

Spider silk-inspired functional materials with tailored surface properties for biomedical applications

**Doctoral thesis
(Dissertation)**

In consideration of the academic grade of

Doctor rerum naturalium (Dr. rer. nat)

by the University of Bayreuth

and The University of Melbourne (Australia)

In fulfilments of the requirements of the degree of

Doctor of Philosophy (PhD)

In agreement with a joint-degree-arrangement

Sarah Lentz

From Steffeln, Germany
ORCID: 0000-0003-0404-1216

Bayreuth 2022

Spider silk-inspired functional materials with tailored surface properties for biomedical applications

**Doctoral thesis
(Dissertation)**

In consideration of the academic grade of

Doctor rerum naturalium (Dr. rer. nat)

by the University of Bayreuth

and The University of Melbourne (Australia)

In fulfilments of the requirements of the degree of

Doctor of Philosophy (PhD)

In agreement with a joint-degree-arrangement

Sarah Lentz

From Steffeln, Germany
ORCID: 0000-0003-0404-1216

Bayreuth 2022

For my family

The work described in this thesis was carried out at the Department of Biomaterials within the Bayreuth School of Mathematical and Natural Sciences (BayNAT) at the University of Bayreuth and the Polymer Science Group, School of Chemical Engineering at the University of Melbourne from July 2017 to January 2022 under the supervision of Prof. Dr. Thomas Scheibel and Prof. Dr. Greg Qiao as a Joint PhD degree within the DAAD Bayreuth-Melbourne Polymer/Colloid Network.

This is a full reprint of the thesis submitted to obtain the academic degree of doctor of natural sciences (Dr. rer. nat.) and approved by the Bayreuth Graduate School of Mathematical and Natural Sciences (BayNAT) of the University of Bayreuth.

Thesis submitted: 28.01.2022

Date of defence: 07.07.2022

Acting director of BayNAT: Prof. Dr. Hans Keppler

Doctoral committee

Prof. Dr. Thomas Scheibel	(reviewer)
Prof. Dr. Greg Qiao	(reviewer)
Prof. Dr. Andreas Walther	(reviewer)
Prof. Dr. Hans-Werner Schmidt	(chairman)
Prof. Dr. Andreas Möglich	

Abstract

Biomaterials science is an increasingly important and constantly evolving field of science. Only intensive cooperation between different disciplines and a deep understanding of the physical and chemical interactions within developed materials and the biological system as a whole lead to the successful development of new biomaterials. Biocompatibility plays a central role here. It must be possible to assess whether the material is compatible with the respective application, e.g., implantation in hard or soft tissue. Here, a further distinction can be made between structural and surface compatibility. Structural compatibility covers the structure, shape, and mechanical property interactions in a biological environment. Surface compatibility summarizes the adaptation of chemical, physical, biological, and morphological surface properties to the biological environment. Consequently, the surface properties of a biomaterial are crucial for its biocompatibility and interactions with the host system.

Materials used as biomaterials must fulfill a wide range of requirements. They should have excellent mechanical stability, be biocompatible and, depending on the requirements, bioinert or bioactive. For example, bioactive biomaterials are used to increase or control interaction with cells. Synthetic polymers usually have excellent mechanical properties but then lack biocompatibility, whereas natural polymers often have excellent biocompatibility but then are mechanically very weak and therefore not suitable for applications with high mechanical stress. A promising material that exhibits the advantages of both classes of polymers is spider silk. Spider silk has been used since ancient times as wound dressings and suture material as it is mechanically resilient and elastic and elicits little to no immune response. Natural spider silk cannot be used as a biomaterial on a large scale due to the cannibalistic behavior of most spider species and changing quality of silk.

Therefore, this work presents two approaches utilizing materials inspired from natural spider silk to create functional, modifiable, mechanically resilient, and biocompatible coatings. The first approach is bioengineered recombinant spider silk proteins. Before biotechnological production, these proteins produced can be genetically modified in *E.Coli* bacteria. In this work, twelve different spider silk protein variants are used and investigated concerning their biocompatibility, biodegradability, and interaction with proteins, cells, and human blood. These spider silk protein variants are non-toxic and can be resorbed by the body as they consist solely of amino acids. The second approach is based on synthetic

polypeptides prepared by the continuous assembly polymerization (CAP) method, published for the first time, using reversible-addition-fragmentation chain-transfer (RAFT) polymerization, or CAP-RAFT. Polypeptides were selected based on amino acids found in natural spider silk (L-lysine and L-glutamic acid). These coatings based on synthetic polypeptides were investigated concerning secondary structure and biodegradability. CAP-RAFT was established as a viable strategy to prepare surface-limited cross-linked polypeptide films with precise film thickness control and novel properties such as specific secondary structure formation and biodegradation. This variability of secondary structure combined with enzymatic degradation shows high potential for numerous biological applications.

In the present work, secondary structure formation and assembly of the spider silk-inspired materials on coatings were investigated in detail. Firstly, the effect of coating thickness on the structural properties (β -sheet fraction) was investigated from the nanoscale to the microscale. A coating thickness-dependent assembly and phase separation model is presented. In addition, the orientation of β -sheets in recombinant spider silk coatings was investigated.

Another important aspect of surface biocompatibility is the structure-property relationship of these spider silk-based materials. Concerning applications in the biomedical field, the interaction between material and biological environment is essential. Several aspects are studied in detail: specifically surface charge, surface chemistry, surface topography, and surface hydrophilicity. These aspects were analyzed to understand the interaction with proteins, cells, and blood as well as their biodegradability. Based on the results of the respective studies, it was possible to categorize the different spider silk variants into bioinert and bioactive variants and assign their subsequent potential biomedical applications. Positively charged spider silk protein variants are bioactive and have the most significant interaction with cells and blood. Modification with the cell-binding peptide improved cell adhesion of all variants used. Amino acid sequences based on the natural *Araneus diadematus* fibroin (ADF) 3 protein showed significantly faster enzymatic degradation than the protein variants based on the amino acid sequence of ADF4. The introduction of three-dimensional patterns on the coating surface can significantly increase the adhesion of cells to material (negatively charged variant), which shows little adhesion of cells as a smooth coating.

In this dissertation, the structure formation, assembly, and structure-property relationships of spider silk-inspired materials were systematically investigated. These spider silk-

inspired materials possessed a high potential for application in various biomedicine fields due to the diverse modification possibilities in terms of morphology, amino acid sequence, and charge.

Zusammenfassung

Die Biomaterialwissenschaft ist ein immer wichtiger werdender Forschungsbereich. Er zeichnet sich durch intensive Kooperation zwischen verschiedenen Fachbereichen und das tiefgehende Verständnis der physikalischen und chemischen Wechselwirkungen von verwendetem Material und biologischen System zur erfolgreichen Entwicklung neuer Biomaterialien aus. Der Aspekt der Biokompatibilität spielt hier eine zentrale Rolle. Es muss eine Einschätzung erfolgen, ob das Material für das jeweilige Anwendungsgebiet, z.B. Implantation in Hart- oder Weichgewebe oder Verbrauchsmaterialien, die in Kontakt mit Körperflüssigkeiten kommen, kompatibel ist. Hier kann nochmals zwischen Struktur- und Oberflächenkompatibilität differenziert werden. Die Strukturkompatibilität umfasst die Aspekte Struktur, Form und mechanische Eigenschaften eines Materials in Wechselwirkung mit einer biologischen Umgebung. Die Oberflächenkompatibilität fasst die Anpassung der chemischen, physikalischen, biologischen und morphologischen Oberflächeneigenschaften an das biologische System zusammen. Dies führt dazu, dass die Oberflächeneigenschaften eines Biomaterials entscheidend für seine Biokompatibilität und Interaktionen mit dem Wirtssystem sind.

Biomaterialien müssen vielfältige Anforderungen erfüllen. Zum einen sollen sie über hervorragende mechanische Stabilität verfügen, zum anderen sollen sie biokompatibel sein. Je nach Anforderung sollten sie beispielsweise bioinert sein, also keine Wechselwirkung mit der biologischen Umgebung eingehen. Bioaktive Biomaterialien hingegen werden zum Beispiel verwendet, um die Interaktion mit Zellen zu erhöhen oder zu steuern. Synthetische Polymere verfügen oft über sehr gute mechanische Eigenschaften, weisen jedoch unzureichende Biokompatibilität auf. Wohingegen natürliche Polymere oft sehr gute Biokompatibilität aufweisen, dann aber mechanisch sehr schwach und deswegen für Anwendungen mit hoher mechanischer Belastung nicht geeignet sind. Ein vielversprechendes Material, das die Vorteile der beiden Polymerklassen verbindet, ist Spinnenseide. Seide wird schon seit der Antike in Wundauflagen und Nahtmaterial verwendet, da das Material mechanisch belastbar und elastisch ist, aber auch wenig bis keine Immunantwort auslöst. Natürliche Spinnenseide kann aufgrund von kannibalistischem Verhalten der meisten Spinnenarten und wechselnder Qualität der Seide nicht als Material im großen Maßstab gewonnen werden. Daher werden in dieser Arbeit zwei Ansätze präsentiert, bei denen von der natürlichen Spinnenseide inspirierte

rekombinante und synthetische Materialien verwendet werden um funktionelle, modifizierbare, mechanisch belastbare und biokompatible Beschichtungen zu schaffen.

Der erste Ansatz sind biotechnologisch hergestellten rekombinanten Spinnenseidenproteine. Die Proteine können bereits vor der Expression in *E.Coli* Bakterien genetisch modifiziert werden. In dieser Arbeit werden zwölf verschiedene Spinnenseidenproteinvarianten verwendet, und hinsichtlich ihrer Biokompatibilität, Bioabbaubarkeit und Interaktion mit Proteinen, Zellen und humanem Blut untersucht. Alle diese Spinnenseidenproteinvarianten sind nicht toxisch und können vom Körper resorbiert werden, da sie ausschließlich aus Aminosäuren bestehen. Der zweite Ansatz basiert auf synthetischen Polypeptiden die durch die erstmals veröffentlichte Methode der kontinuierlichen Assemblierungspolymerisation (CAP, continuous assembly polymerisation) mittels reversibler Additions-Fragmentierungs-Kettenübertragungspolymerisation (RAFT polymerization, reversible-addition-fragmentation chain-transfer polymerization), kurz CAP-RAFT, hergestellt wurden. Es wurden Polypeptide ausgewählt, die auf Aminosäuren basieren, welche auch in der natürlichen Spinnenseide zu finden sind (L-Lysin und L-Glutaminsäure). Diese auf synthetischen Polypeptiden basierenden Beschichtungen wurden hinsichtlich Sekundärstruktur und Bioabbaubarkeit untersucht. CAP-RAFT konnte als eine praktikable Strategie zur Herstellung von oberflächenbegrenzten, vernetzten Polypeptidfilmen mit präziser Schichtdickenkontrolle und neuer Eigenschaften wie spezifische Sekundärstrukturbildung und biologischen Abbau etabliert werden. Diese Variabilität der Sekundärstruktur in Verbindung mit dem enzymatischen Abbau zeigt ein hohes Potenzial für zahlreiche Anwendungen.

In der vorliegenden Arbeit wurde die Sekundärstrukturbildung und die Assemblierung der Spinnenseiden-inspirierten Materialien an Beschichtungen eingehend untersucht. Zum einen wurde der Einfluss der Schichtdicke auf die strukturellen Eigenschaften (β -Faltblatt Anteil) von nanoskaligen bis hin zum mikroskaligen Bereich untersucht. Es wird ein schichtdickenabhängiges Assemblierungs- und Phasenseparationsmodell präsentiert. Außerdem wurde die Orientierung der β -Faltblätter in rekombinanten Spinnenseidenbeschichtungen untersucht.

Ein weiterer wichtiger Aspekt der Oberflächenbiokompatibilität ist die Betrachtung der Struktur-Eigenschaftsbeziehung dieser Spinnenseiden-basierten Materialien. Im Hinblick auf Anwendungen im biomedizinischen Bereich ist die Wechselwirkung zwischen Material

und biologischer Umgebung essentiell. Es werden mehrere Aspekte eingehend untersucht: der Einfluss der Oberflächenladung, der Oberflächenchemie, sprich der Modifikation mit zellbindenden Peptidsequenzen, der Oberflächentopographie und der Hydrophilie der Oberfläche. All diese Aspekte wurden analysiert um den Einfluss dieser auf die Interaktion mit Proteinen, Zellen und Blut und auf die Bioabbaubarkeit zu verstehen. Ausgehend von den Resultaten der jeweiligen Studien war es möglich, die verschiedenen Spinnenseidenvarianten, die sich in ihrer Aminosäuresequenz und Ladung unterschieden, in bioinerte und bioaktive Varianten zu kategorisieren und ihnen mögliche biomedizinische Anwendungen zuzuordnen. Es konnte gezeigt werden, dass positiv geladene Spinnenseidenproteinvarianten bioaktiv sind und die größte Interaktion mit Zellen und Blut aufweisen. Eine Modifikation mit dem zellbindenden Peptid führte zu einer verbesserten Zelladhäsion aller verwendeten Varianten. Aminosäuresequenzen basierend auf dem natürlichen *Araneus diadematus* Fibroin 3 Protein zeigten einen deutlich schnelleren enzymatischen Abbau als die Proteinvarianten, die auf der Aminosäuresequenz des *Araneus diadematus* Fibroin 4 basieren. Die Einführung von dreidimensionalen Mustern auf der Beschichtungsoberfläche kann die Adhäsion von Zellen auf der negativ geladenen Variante eADF4(C16), welche als glatte Beschichtung kaum Adhäsion von Zellen zeigt, signifikant erhöhen.

In dieser Dissertation wurde systematisch die Strukturbildung, Assemblierung und die Struktur-Eigenschaftsbeziehungen Spinnenseiden-inspirierter Materialien untersucht. Durch die vielfältigen Modifikationsmöglichkeiten hinsichtlich Morphologie, Aminosäuresequenz und Ladung besitzen diese Spinnenseiden-inspirierten Materialien ein hohes Potential in verschiedenen Bereichen der Biomedizin Anwendung zu finden.

Eidesstattliche Versicherungen und Erklärungen

(§ 9 Satz 2 Nr. 3 PromO BayNAT)

Hiermit versichere ich eidesstattlich, dass ich die Arbeit selbstständig verfasst und keine anderen als die von mir angegebenen Quellen und Hilfsmittel benutzt habe (vgl. Art. 64 Abs. 1 Satz 6 BayHSchG).

(§ 9 Satz 2 Nr. 3 PromO BayNAT)

Hiermit erkläre ich, dass ich die Dissertation nicht bereits zur Erlangung eines akademischen Grades eingereicht habe und dass ich nicht bereits diese oder eine gleichartige Doktorprüfung endgültig nicht bestanden habe.

(§ 9 Satz 2 Nr. 4 PromO BayNAT)

Hiermit erkläre ich, dass ich Hilfe von gewerblichen Promotionsberatern bzw. -vermittlern oder ähnlichen Dienstleistern weder bisher in Anspruch genommen habe noch künftig in Anspruch nehmen werde.

(§ 9 Satz 2 Nr. 7 PromO BayNAT)

Hiermit erkläre ich mein Einverständnis, dass die elektronische Fassung meiner Dissertation unter Wahrung meiner Urheberrechte und des Datenschutzes einer gesonderten Überprüfung unterzogen werden kann.

(§ 9 Satz 2 Nr. 8 PromO BayNAT)

Hiermit erkläre ich mein Einverständnis, dass bei Verdacht wissenschaftlichen Fehlverhaltens Ermittlungen durch universitätsinterne Organe der wissenschaftlichen Selbstkontrolle stattfinden können.

Bayreuth,

Declaration of Authorship

This declaration is to certify that:

- i. The thesis comprises only my original work towards the degree of Doctor of Philosophy (PhD) except where indicated in the Preface;
- ii. Due acknowledgment has been made in the text to all other material used;
- iii. The thesis is less than 100,000 words in length, exclusive of tables, bibliographies, appendices, and footnotes.

Sarah Lentz
2022

Preface

This thesis is divided into three parts, where each chapter of this thesis is presented as a self-contained manuscript. The following chapters are intended for submission.

- i. The introduction on Part I - Chapter 1 on pages 1 - 22 is written by Sarah Lentz.
- ii. Texts on methods and instrumentation in Part I - Chapter 2 on pages 23 - 43 are written by Sarah Lentz.
- iii. The synopsis in Part I - Chapter 3 on pages 44 - 70 is written by Sarah Lentz.
- iv. The text in Part II - Chapter 1 on pages 71 - 90 is taken from “Ultra-thin spider silk films: insights into silk assembly on surfaces”, ACS Appl. Polym. Mater. 2019, 1, 3366-3374.
 - Sarah Lentz performed the synthesis and purification of the protein processed the spider silk protein into films.
 - Sarah Lentz performed the characterization of the recombinant spider silk films presented in this chapter with GATR-FTIR, AFM, water contact angle measurements.
 - The ATR- and transmission FTIR measurements were performed by Martin Müller.
 - The phase separation model was developed by Christian Borkner and Sarah Lentz.
 - The writing of the original draft and the visualization of the results was done by Sarah Lentz and Christian Borkner.
 - The review and the editing of the manuscript were done by all authors.
 - The conceptualization of this project was done by Christian Borkner, Andreas Fery and Thomas Scheibel.
 - The funding for this project was raised by Andreas Fery and Thomas Scheibel.

- v. The text in Part II - Chapter 2 on pages 91 - 110 is taken from „ Dichroic FTIR-spectroscopy characterization of β -sheet orientation in spider silk films on silicon substrates “, J. Phys. Chem. B, 2021, 125, 1061 - 1071.
- Sarah Lentz performed the synthesis and purification of the protein and processed the recombinant spider silk proteins into films.
 - The experiments were performed by Mirjam Hofmaier, Sarah Lentz and Birgit Urban.
 - The writing of the original draft and the visualization of the results was done by Mirjam Hofmaier, Martin Müller, and Sarah Lentz.
 - The review and the editing of the manuscript were done by all authors.
 - The conceptualization of this project was done by Martin Müller, Andreas Fery, and Thomas Scheibel.
 - Christian Borkner was involved in the discussion of the results.
 - The funding for this project was raised by Andreas Fery and Thomas Scheibel.
- vi. The text in Part III - Chapter 1 on pages 111 - 146 is taken from „ Structure-property relationship based on the amino acid composition of recombinant spider silk proteins for potential biomedical applications “, ACS Applied Materials & Interfaces, 14 (22), 31751 - 31766.
- Sarah Lentz performed the synthesis and purification of the proteins eADF4(C16), eADF4(κ 16), eADF3(AQ)₁₂, and eADF3(AQ)₂₄. Vanessa Trossmann performed the design, synthesis, and purification of the protein eADF4(Ω 16).
 - The design of the experiments was performed by Sarah Lentz, Vanessa Trossmann and Thomas Scheibel.
 - Sarah Lentz produced the films and performed the AFM, KPFM, GATR-FTIR, and water contact angle measurements.
 - Christian Borkner, Vivien Beyersdorfer, Vanessa Trossman and Sarah Lentz performed the enzymatic degradation.
 - Christian Borkner and Sarah Lentz performed the QCM-D measurements.

- Sarah Lentz performed the blood coagulation tests as part of a collaboration with Markus Rottmar (EMPA).
 - Vanessa Trossmann and Sarah Lentz performed the cell culture tests.
 - The writing of the original draft and the visualization of the results was done by Vanessa Trossmann and Sarah Lentz.
 - Sarah Lentz, Vanessa Trossmann and Thomas Scheibel conceptualized the study.
 - Thomas Scheibel supervised the studies and edited the paper.
 - The funding for this project was raised by Thomas Scheibel.
- vi. The text in Part III - Chapter 2 on pages 147 - 157 is taken from “Surface Modification of Spider Silk Particles to Direct Biomolecular Corona Formation”, ACS Applied Materials & Interfaces, 12 (22), 24635-24643.
- The design of the experiments was performed by Alessia Weiss, Heike Herold, Sarah Lentz, Frank Caruso, and Thomas Scheibel.
 - Heike Herold and Sarah Lentz prepared and characterized the spider silk particles.
 - Alessia Weiss performed the characterization using SDS-PAGE and all mass spectrometry studies and the respective data analysis.
 - Sarah Lentz produced the spider silk films and performed the blood coagulation assays.
 - Quinn Besford performed statistical analysis of the blood assay data.
 - Matt Faria assisted with the analysis of the mass spectrometry data.
 - Ching-Seng Ang performed mass spectrometry experiments and protein identification.
 - Thomas Scheibel and Frank Caruso supervised the studies and edited the paper.
 - The preparation of the original draft was performed by Alessia Weiss, Heike Herold and Sarah Lentz.
 - The funding for this project was raised by Frank Caruso and Thomas Scheibel.

- vii. The text in Part III - Chapter 3 on pages 158 - 187 is taken from “Selective Topography Directed Cell Adhesion on Spider Silk Surfaces”, (submitted to Advanced Functional Interfaces).
- Sarah Lentz designed, produced the photolithographic masters and produced the patterned recombinant spider silk films.
 - Sarah Lentz did the physicochemical analysis of the used recombinant spider silk films.
 - Vanessa Trossmann and Sarah Lentz performed the cell culture experiments and analyzed them using different microscopic methods.
 - Vanessa Trossmann performed the CLSM measurements.
 - Sarah Lentz performed the SEM analysis of the patterned films.
 - Sarah Lentz and Vanessa Trossmann wrote the original draft of the manuscript.
 - Sarah Lentz, Vanessa Trossmann and Thomas Scheibel conceptualized the study.
 - All authors revised and approved the final version of the manuscript.
 - The funding for this project was raised by Thomas Scheibel.
- viii. The text in Part III - Chapter 4 on pages 188 - 201 is taken from “Designing of spider silk proteins for human induced pluripotent stem cell-based cardiac tissue engineering”, Materials Today Bio, 2021, 11, 100114.
- Tillmann Esser, Vanessa Trossmann carried out cell-culture-related experimental work and analyzed the data.
 - Sarah Lentz did the physicochemical analysis of the used recombinant spider silk variant films.
 - Tillmann Esser, Vanessa Trossmann, Felix Engel and Thomas Scheibel wrote the original draft of the manuscript.
 - Felix Engel and Thomas Scheibel conceptualized and supervised the study.
 - All authors revised and approved the final version of the manuscript.
 - The funding for this project was raised by Felix Engel and Thomas Scheibel.

- ix. The text in Part IV - Chapter 1 on pages 202 - 306 is taken from “Mimicry of silk utilizing synthetic polypeptides “, (under review Progress in Polymer Science).
- This review was written by Nicholas Chan and Sarah Lentz in equal parts.
- x. The text in Part IV - Chapter 2 on pages 307 - 334 is taken from “Crosslinked polypeptide films via RAFT mediated continuous assembly of polymers”, Angewandte Chemie International Edition, e202112842.
- Nicholas Chan performed the synthesis and NMR analysis of the monomers, the RAFT agents and the crosslinked polypeptide films via RAFT mediated continuous assembly of polymers.
 - The design of the experiments was performed by N.C and S.L.
 - Nicholas Chan performed the AFM measurements of the polypeptide films. Sarah Lentz performed the correlative AFM measurements and the ATR-FTIR and the resulting secondary structure analysis.
 - Sarah Lentz performed the enzymatic degradation.
 - The writing of the original draft and the visualization of the results was done by Nicholas Chan.
 - Thomas Scheibel, Paul Gurr, Shereen Tan and Greg Qiao supervised the studies and edited the paper.
 - All authors revised and approved the final version of the manuscript.
 - The funding for this project was raised by Greg Qiao and Thomas Scheibel.
- xi. The appendix on pages 335 - 346 is written by Sarah Lentz.

Manuscripts

The following manuscripts have been produced during this Joint PhD candidature with the University of Bayreuth as home university and the University of Melbourne as host university:

1. Borkner, C. B.[#], **Lentz, S.[#]**, Müller, M., Fery, A., & Scheibel, T. (2019). Ultrathin Spider Silk Films: Insights into Spider Silk Assembly on Surfaces. *ACS Applied Polymer Materials*, 1(12), 3366-3374.
2. Hofmaier, M., Urban, B., **Lentz, S.**, Borkner, C. B., Scheibel, T., Fery, A., & Müller, M. (2021). Dichroic Fourier Transform Infrared Spectroscopy Characterization of the β -Sheet Orientation in Spider Silk Films on Silicon Substrates. *The Journal of Physical Chemistry B*, 125(4), 1061-1071.
3. Weiss, A. C.[#], Herold, H. M.[#], **Lentz, S.**, Faria, M., Besford, Q. A., Ang, C. S., Caruso, C. & Scheibel, T. (2020). Surface Modification of Spider Silk Particles to Direct Biomolecular Corona Formation. *ACS Applied Materials & Interfaces*, 12 (22), 24635-24643.
4. **Lentz, S.[#]**, Trossmann, V.T.[#], Borkner, C.B., Beyersdorfer, V., Rottmar, M. & Scheibel, T. (2022). Structure-property relationship based on the amino acid composition of recombinant spider silk proteins for potential biomedical applications, *ACS Applied Materials & Interfaces*, 14 (22), 31751 -31766.
5. **Lentz, S.[#]**, Trossmann, V.T.[#] & Scheibel, T. (2022). Selective Topography Directed Cell Adhesion on Spider Silk Surfaces. submitted to *Advanced Functional Interfaces*.
6. Chan, N.[#], **Lentz, S.[#]**, Gurr, P., Scheibel, T. & Qiao, G. (2021). Mimicry of silk utilizing synthetic polypeptides, under review in *Progress in Polymer Science*
7. Esser, T.[#], Trossmann, V.T.[#], **Lentz, S.**, Felix B. Engel, and Thomas Scheibel (2021). Designing of spider silk proteins for human induced pluripotent stem cell-based cardiac tissue engineering, *Materials Today Bio*, 11, 100114.

8. Chan, N., **Lentz, S.**, Gurr, P. A., Tan, S., Scheibel, T., & Qiao, G. G. (2021). Crosslinked Polypeptide Films via RAFT-Mediated Continuous Assembly of Polymers. *Angewandte Chemie International Edition*, e202112842.

Scientific presentations

1. SFB 840 PhD Symposium, 06.08.2016, „Coatings Made of Recombinant Spider Silk Proteins”, TP A8“, oral presentation.
2. SFB 840 PhD Symposium, 12.07.2017, „Coatings Made of Recombinant Spider Silk Proteins, TP A8“, oral presentation.
3. SFB 840 PhD Symposium, 12.04.2018, „Coatings Made of Recombinant Spider Silk Proteins, TP A8“, oral presentation.
4. CSIRO, Melbourne and PSG group at the University of Melbourne, 01/2019, „Spider Silk Proteins & More: From Natural Models to Materials Applications.”, oral presentation.
5. 9th Australian Colloid & Interface Symposium (ACIS), Hobart (TAS), 07.02.2019, „Ultra-Thin Spider Silk Films: Insights into Silk Assembly on Surfaces”, oral presentation.
6. 5th Euro BioMat 2019, Weimar, 08.05.2019, „Negatively Charged Spider Silk Surfaces Prevent Blood Clotting. “short oral presentation and poster.
7. IPF Get Together 2019, 08.05.2019, „Investigation of Phase Separation and Self-Organization Properties of Ultrathin Spider Silk Coatings “, oral presentation.
8. Werkstoffwoche 2019, Dresden, 19.09.2019, „Einfluss der Oberflächenmorphologie und der Nettoladung von spinnenseiden-basierten Materialien auf die Interaktionen mit Blut”, oral presentation.
9. Workshop Series: Building an International Career, 2021, online, 17.11.2021, “Building an International Network”, oral presentation.

Acknowledgments

This thesis would not have been possible without the tremendous support of countless people. The last 4.5 years have been a crazy roller coaster ride with many good but also some sobering moments full of funny moments and events with my lab mates, exciting results, being a lateral entrant in a Joint PhD program, incredible research experiences, including traveling at the other end of the world and a pandemic that thwarts all plans. I would not have pulled this off without your constant support and coaxing.

First, I would like to thank my supervisor Prof. Thomas Scheibel. You agreed to take me as a student coming from physical chemistry and never worked with proteins before. I am really grateful for this chance. I would also like to thank you for giving me the freedom to develop my own ideas and skills while constantly pushing me in the right direction. Above all, I would like to thank you for the trust you placed in me when you gave me the opportunity to do the Joint PhD. I will cherish the great experiences and the network I created for a long time to come. Furthermore, I would also like to thank you for your patience, perseverance, and time you have mentored me.

Secondly, I want to thank my supervisor Prof. Greg Qiao. I am very grateful to you for giving me the opportunity to do a Joint PhD and get closer to polymer chemistry again. Our long discussions and later in my candidature, the Zoom meetings helped me a lot to get a deeper understanding of polymer chemistry. Thank you for always standing behind me when I was again struggling with Australian bureaucracy. In the same line, I would like to thank Dr. Paul Gurr, who helped me a lot during my time in Melbourne. I want to thank my committee chair A/Prof Dr. Kathryn Mumford, for her thoughtfulness and understanding. You have been a very supportive chair. I would also like to thank the whole polymer science group for welcoming me with open arms and being very supportive the whole time in Melbourne. I would like to thank Nick Chan, who had to put up with me the most, as he had to overcome the same hurdles as me as my Australian counterpart as a Joint PhD. It was a happy coincidence that we were chosen as Joint PhDs. Your fun, loud and engaging nature made working with you very enjoyable. We complement each other well in our strengths and have achieved great results in a short time. The time with Ada and you in Germany were also enjoyable, and I love that we managed to be in the right country at each other's wedding.

Additionally, I would like to thank all my cooperation partners for the interesting research that resulted from the lively exchange and great ideas, especially Prof. Dr. Andreas Fery, Dr. Martin Müller and Mirjam Hofmeier from the IPF in Dresden.

I would also like to thank the DAAD and the Bayreuth-Melbourne Polymer/Colloid Network that supported my Joint PhD stays in Melbourne.

Furthermore, I want to thank the past and present members of the Fiberlab who were supportive throughout my PhD. I had so much fun with you at all BBQs, the thanksgiving and Christmas parties, and the two fiber retreats.

I could not have gone through this time without Vanessa, Vanessa, Annika, Anika, and Merisa. Our jungle office has evolved from working colleagues to deep friendships. I am thrilled that we have always supported each other and helped each other beyond our self-imposed limits. I especially appreciate that you are honest and intervene when necessary. The Jungle office has shown how productive different perspectives, life experiences, and academic backgrounds can be, especially Vanessa. I sincerely hope that our group will continue beyond the PhD years.

Finally, I would like to thank my friends and family. My loving husband Michi has put up with me for 14 years now. We have mastered all the ups and downs and I cannot tell you how grateful I am for your everlasting support. Throughout my studies, you had my back and often took a back seat when I was stressed. I look forward to coming home every day and leaving my stress at the door because of your calm, level-headed and empathetic manner. Above all, I would like to thank my parents, Hermann and Heike, for everything. You have gone through so much with me. Who would have thought that I still get grown-up. You have always accepted and supported me as I am. For that, I am very grateful. I want to thank my siblings Christoph and Britta for their support. Especially Britta, for the hours of conversations that gave me an often-needed break. I would also like to thank all my friends (Vali, Tim, Jasmin, Fritzi, Nadine, Julian, Felix, Yannic, and Inga) who accompanied and dragged me through my studies. Last but not least, I would like to thank my long-time friends (Flora, Veronika, Anja, Annice, Benny, Jojo, and Thorsten), who are always there for me, even after several broken promises to return to the Eifel.

Table of contents

Abstract	I
Zusammenfassung	V
Eidesstattliche Versicherungen und Erklärungen	IX
Declaration of Authorship	X
Preface	XI
Manuscripts	XVI
Scientific presentations	XVIII
Acknowledgments	XIX
Table of contents	XXI
Part I – Chapter 1 - Introduction	1
Part I – Chapter 1.1 - Polymers.....	1
<i>Part I – Chapter 1.1.1 - Block copolymers</i>	3
<i>Part I – Chapter 1.1.2 - (Synthetic) Polypeptides and proteins</i>	6
<i>Part I – Chapter 1.1.3 - Definition of Polypeptides, Poly (amino acids) and proteins</i>	6
<i>Part I – Chapter 1.1.4 - Poly(amino acid) synthesis</i>	8
<i>Part I – Chapter 1.1.5 - NCA-ROP of polypeptides</i>	9
<i>Part I – Chapter 1.1.6 - Grafting-from and Grafting-to methods</i>	11
<i>Part I – Chapter 1.1.7 - Natural polypeptides - natural spider silk</i>	12
<i>Part I – Chapter 1.1.8 - Recombinant polypeptides - recombinant spider silk</i>	15
Part I – Chapter 1.2 - Biomaterials.....	20
Part I - Chapter 2 – Methods and Instrumentation	23
Part I – Chapter 2.1 - Methods.....	23
<i>Part I – Chapter 2.1.1 - Purification of recombinant spider silk proteins</i>	23
<i>Part I – Chapter 2.1.2 - Formation of a coating</i>	24
Part I – Chapter 2.2 - Instrumentation.....	26
<i>Part I – Chapter 2.2.1 - Atomic force microscopy</i>	26
<i>Part I – Chapter 2.2.2 - Scanning electron microscopy</i>	27

<i>Part I – Chapter 2.2.3 - Fluorescence microscopy</i>	28
<i>Part I – Chapter 2.2.4 - ζ-Potential</i>	31
<i>Part I – Chapter 2.2.5 - Sodium dodecyl sulfate-polyacrylamide gel electrophoresis</i>	32
<i>Part I – Chapter 2.2.6 - Fourier transform infrared spectroscopy</i>	34
<i>Part I – Chapter 2.2.7 - Circular dichroism</i>	37
<i>Part I – Chapter 2.2.8 - Quartz crystal microbalance with dissipation monitoring</i>	39
<i>Part I – Chapter 2.2.9 - Maskless lithography</i>	41
<i>Part I – Chapter 2.2.10 - Water contact angle measurement</i>	42
Part I - Chapter 3 – Synopsis and Aim of the thesis	44
Part I – Chapter 3.1 - Aim of the thesis	44
Part I – Chapter - 3.2 Synopsis	46
<i>I – Processing and Assembly of Spider Silk Inspired Materials into Films</i>	49
<i>II – Structure-property relationship of spider silk inspired materials</i>	55
Part I - References	61
Part II – Mechanism of structure formation and microphase separation of recombinant spider silk proteins on surfaces	71
Part II - Chapter 1 – Ultra-thin spider silk films: Insights into silk assembly on surfaces	71
Part II - Chapter 2 – Dichroic FTIR spectroscopy characterization of β-sheet orientation in spider silk films on silicon substrates	91
Part III – Bioselectivity of recombinant spider silk surfaces	111
<i>Part III - Chapter 1 – Structure-property relationship based on the amino acid composition of recombinant spider silk proteins for potential biomedical applications</i>	111
<i>Part III - Chapter 2 – Surface Modification of Spider Silk Particles to Direct Biomolecular Corona Formation</i>	134
<i>Part III - Chapter 3 – Selective Topography Directed Cell Adhesion on Spider Silk Surfaces</i>	145
<i>Part III - Chapter 4 – Designing of spider silk proteins for hiPSC-based cardiac tissue engineering</i>	178
Part IV - Spider silk inspired functional materials	192
<i>Part IV - Chapter 1 – Mimicry of silk utilizing synthetic polypeptides</i>	192

<i>Part IV - Chapter 2 - Crosslinked polypeptide films via RAFT mediated continuous assembly of polymers</i>	<i>237</i>
Part V – Appendix	265
<i>Part V – 1 - List of Abbreviations.....</i>	<i>265</i>
<i>Part V – 2 - List of Figures.....</i>	<i>268</i>
<i>Part V – 3 - List of Tables</i>	<i>276</i>

Part I – Chapter 1 - Introduction

Part I – Chapter 1.1 - Polymers

A polymer is a macromolecule built up by covalently bound smaller molecules, called monomers.¹ The chemical reaction of linking these smallest building blocks (monomers) is called polymerization.

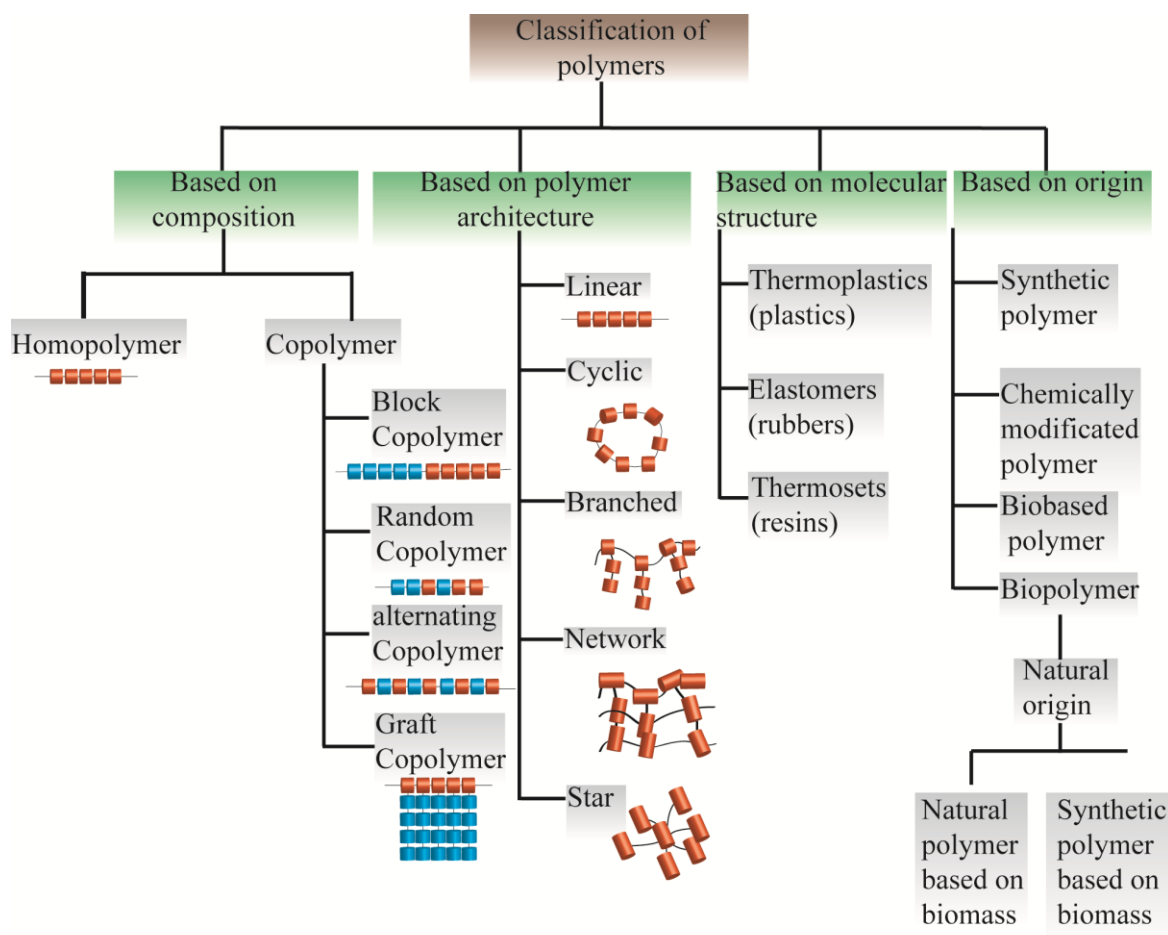


Figure 1: This is a schematic overview of the classification of polymers according to composition, architecture, molecular structure, and origin. Figure created based on ¹⁻³.

Polymers can be classified according to several criteria. Polymers can be divided into homopolymers, and copolymers.^{1,3} Homopolymers are the most used synthetic polymers.^{1,3} They have only one building block (i.e., monomer, orange block **Figure 1**), often an alkene, e.g., ethylene and methylmethacrylate.^{1,3} Copolymers comprise more than one type of monomer, and two or more monomers can be linked differently. There are four major classes of copolymers (**Figure 1**), the grafted polymer, where one type of monomer acts as a backbone, and the other type of monomer is grafted onto it as a side chain. Other classes

are alternating copolymers, where the two monomers are alternating or block copolymers, in which two blocks of monomers are covalently bound linearly.³ The last category is random or statistical copolymers.³ Another classification criterion is polymer architecture. Polymers are distinguished whether they are linear, cyclic, branched, star-shaped, or networked.^{1, 3} The third kind of classification is the molecular structure. Thermoplastic polymers are solid at room temperature (RT) but become soft upon heating, making them suitable for processing. They also have ordered crystalline and non-ordered amorphous regions. Thermoplasts can be amorphous or semi-crystalline.^{1, 3, 4} Single polymer chains are held together by van-der-Waals forces, which entangle them and make them hard at RT.^{1, 3} Elastomers, such as rubber, are polymers, which are moderately and randomly crosslinked. Therefore, they can recover their original dimension after stretching.^{1, 3} Thermoplasts are the hardest polymers. Such resins are highly crosslinked, which means that the single polymer chains are crosslinked with each other. The higher the crosslinking degree, the more rigid and brittle a polymer is. The last kind of classification is based on the origin of the polymers. Organic polymers can be divided into synthetic polymers, chemically modified polymers, and biopolymers.¹ Synthetic polymers are tailor-made polymers derived from petroleum. This class of polymers can be designated as mass polymers because famous representatives like polyethylene (PE), polystyrene (PS), polyvinylchloride (PVC), and polypropylene (PP) are produced in millions of tons per annum.^{1, 3} Naturally occurring polymers can be chemically modified and comprise the second class.⁵ Cellulose ether is produced 100 000 t/a in Germany.⁶ It is a derivative of cellulose, where parts or all hydrogens are substituted with hydroxyl groups.^{6, 7} There is a broad range of applications for these chemically modified polymers, like in cosmetic industry, in pharmaceutical applications as emulgators and detergents.^{6, 8} For this thesis, the most important class of polymers is biopolymers (**Figure 1**, bottom right). They are divided into two subclasses, the biopolymers based on natural resources and synthetic polymers, which mimic biofunctionality.² The polymers based on natural resources can be further divided into natural polymers on a biomass basis and synthetic polymers on a biomass basis.² Polymers like Chitin, cellulose, starch, and proteins are natural polymers produced by living organisms.² Synthetic polymers based on biomass are, for example, polylactic acid, ethylene, and polyamide. The basic building blocks are extracted from natural resources and then chemically modified and polymerized.² Polymers with bifunctionality can be divided into biologically degradable polymers and polymers for biomedical applications.² Biologically degradable polymers are defined as materials whose

origin is not necessarily natural but are able to degrade when exposed to microorganisms, aerobic fully, and anaerobic processes.⁹ Polymers for biomedical applications are defined in terms of their properties like biocompatibility, and non-toxicity.¹⁰ Synthetic poly(lactic-co-glycolic acid) (PLGA) is widely considered as a important example of this group for biomedical applications.¹⁰

Part I – Chapter 1.1.1 - Block copolymers

Block copolymers (BCPs) play an essential role in this thesis. Therefore, this polymeric class is described more in detail. BCPs are macromolecules that consist of at least two different covalently bonded homopolymer segments (**Figure 1**).^{1, 11, 12} Depending on the number and the arrangement of the different blocks, a differentiation is made between diblock copolymers $(A)_n(B)_n$, triblock copolymers $(A)_x(B)_y(A)_z$ or $(A)_x(B)_y(C)_z$ and multiblock copolymers $-(A)_x(B)_y)_z-$.^{1, 11-13} Different geometries are possible like graft copolymers or star copolymers.^{1, 11, 12} In general, BCPs are amphiphilic, comprising a combination of hydrophilic and hydrophobic blocks. Thus, BCPs can act as a stabilizer at interfaces or as an interface builder, for example, at polymer/polymer interfaces or metal/polymer interfaces.¹⁴⁻¹⁶ The block copolymer properties are tunable by changing the proportions of blocks A, B, C, the shape of the polymer, or the length of the polymer.¹⁴⁻¹⁶

When these blocks are connected covalently, there is always a degree of incompatibility caused by the different solubility of the blocks.¹⁷ This incompatibility leads to copolymer self-assembly and ordered structures on the nanometer scale (**Figure 2**).¹⁸ If the blocks have different solubilities, similar blocks tend to increase their interaction, and different blocks try to minimize the interactions. The mixing enthalpy ΔH_m and the mixing entropy ΔS_m competing against each other.

The Gibbs-Helmholtz equation describes the phase separation behavior thermodynamically.^{14, 16} Here ΔG_m is the free mixing enthalpie, ΔH_m is the mixing enthalpie and ΔS_m is the mixing entropy and T is the temperature.^{14, 16}

$$\Delta G_m = \Delta H_m - T\Delta S_m$$

(1)

Block copolymer blocks are only fully miscible when $\Delta G_m < 0$.¹⁴⁻¹⁶ This is not the case in most block copolymers.¹⁴⁻¹⁶ This leads to self-assembly and phase separation of the block copolymer with a minimum interface between the polymer blocks.^{18, 19} This organization in block copolymers is widely known as microphase separation.¹⁴⁻¹⁷ Microphase separation

is an essential equilibrium process to stabilize thermodynamic and entropic forces.¹⁴⁻¹⁷ The self-consistent mean-field theory describes the phase separation behavior of AB block copolymers. In this theory, the enthalpy of mixing/demixing ΔH_m is proportional to the so-called Flory-Huggins segment-segment interaction parameter χ_{AB} , and the temperature T is inversely proportional to this interaction parameter.¹⁴⁻¹⁶

$$\chi_{AB} = \frac{C_A}{T} + C_B \quad (2)$$

C_A and C_B are empirical constants and depend on the block copolymer.¹⁴⁻¹⁶ **Figure 2** shows an exemplary, theoretical phase diagram of a block copolymer with two different blocks. The product of χ -parameter and degree of polymerization N is displayed as the y-axis. The fraction of polymer A is displayed as the x-axis.¹⁸ The disordered phase is formed above a specific temperature. In this phase, the two blocks mix homogeneously.¹⁸ By decreasing the temperature, the χ -parameter increases, and the blocks tend to separate into ordered microstructures with structures around 10-100 nm.^{14, 16, 18}

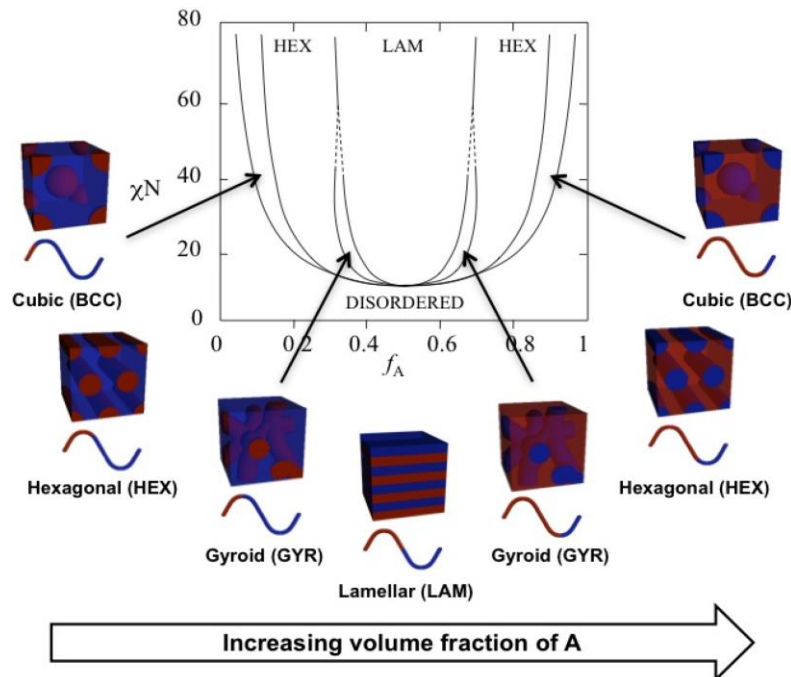


Figure 2: The figure shows an exemplary, theoretical phase diagram of a diblock copolymer. The x-axis displays the fraction of block A. The y-axis shows the Flory-Huggins interaction parameter, the χ -parameter, and N stands for the total degree of polymerization. If the volume fraction of block A is increased, equilibrium morphologies of AB diblock copolymers change from body-centered cubic (BCC) to hexagonal cylinders (HEX) to gyroid (GYR) to lamellar (LAM) phases in bulk.¹⁷

As shown in **Figure 2**, different microphases can occur. On the left, the body-centered cubic (BCC) phase with block A (red) as the minority phase occurs with a low amount of

block A in the BCP. By increasing the proportion of block A the phase change to hexagonal cylinders (HEX) and then to a gyroid (GYR) phase; if both polymers are nearly equally distributed in the BCP, a lamellar microstructure is formed.^{14, 16, 18} If the proportion of block A is above 50 % ($f_a > 0.5$), block A forms the majority phase of the BCP with the same microphases (**Figure 2**).^{14, 16, 18} The following parameters determine the particular microstructure:

1. Flory-Huggins segment-segment interaction parameter χ_{AB}
2. The degree of polymerization N
3. Molecular weight
4. The volume fraction f_a and f_b
5. The overall polymer architecture (di-, tri- BCP, star BCP) (**Figure 3**)

When the number of different blocks is increased, for example, there are three interaction parameters and two composition variables that have to be taken into account for three blocks. This substantially complicates the phase separation behavior, and the number of phases also increases.¹⁸ There are various possibilities to synthesize BCPs. Due to the advanced polymer synthesis strategies, controlled polymerization techniques with precisely controlled molecular weight and defined architectures can be processed (**Figure 3**).¹⁸

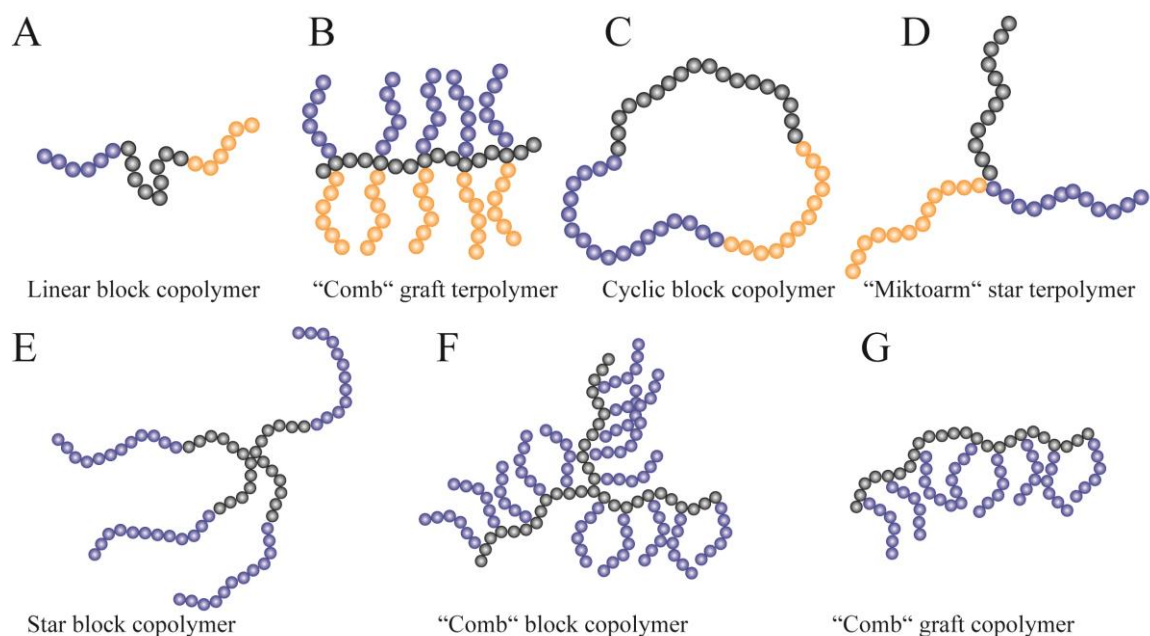


Figure 3: Representative architectures of different kinds of block copolymers. A - D represents the most common terblock copolymers, namely linear BCP (A), "Comb" graft terpolymer (B), Cyclic BCP (C), and miktoarm star terpolymer (D). E - G represents complex polymer structures like star BCP (E), "Comb" star copolymer (F), and "Comb" graft polymer (G). The figure was drawn according to¹⁸

Part I – Chapter 1.1.2 - (Synthetic) Polypeptides and proteins

Polypeptides (PP) and proteins are used for a major class of biocompatible and biodegradable functional materials made of renewable resources.^{20, 21} A distinction must be drawn between polypeptides and proteins. Polypeptides and proteins are composed of up to 20 different aa and are monodisperse or rather consist of polypeptides arranged in a biofunctional manner.^{20, 22-24} Polypeptides comprise less than 100 amino acids, proteins more than 100 amino acids. The research focuses mainly on producing advanced protein materials with tailored functions for applications in the field of drug delivery such as implant technology, artificial organs, tissue regeneration. Further protein-based materials can be used for microelectronic devices, stimuli-responsive materials, for energy capture and storage, and various separation techniques.^{20, 21} The most challenging issue is that the materials have to preserve their function over a long time period.^{20, 21} Within a human body, the body reacts with a rejection reaction in case of failure.^{20, 21} Since biomaterials based on protein they are often biocompatible; they offer a promising alternative to synthetic polymers or materials.^{20, 21}

Part I – Chapter 1.1.3 - Definition of Polypeptides, Poly (amino acids) and proteins

Polypeptides and proteins are defined as biopolymers which are composed of amino acid residues connected by peptide bonds formed by a condensation reaction of the carboxylic group of one amino acid (aa) (**Figure 4**, aa with R₁) with the amino group of the second amino acid (**Figure 4**, aa with R₂) upon the removal of one water molecule.^{20, 22, 23}

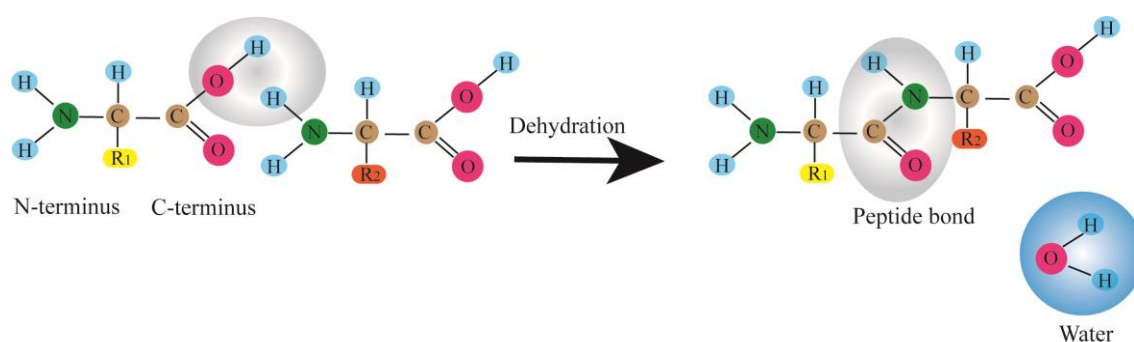


Figure 4: Schematic representation of the formation of a peptide bond by a condensation reaction of the C-terminus of AA1 and the N-terminus of AA2, which results in the removal of one water molecule. Figure adapted from ^{20, 22, 23, 25}.

The formation of polypeptides and proteins can be regarded as a sequential amino acid reaction.^{20, 22, 23} 20 natural amino acids can be used to form these sequences, all comprising different properties, charges and side chains (**Figure 5**).^{20, 22, 23}

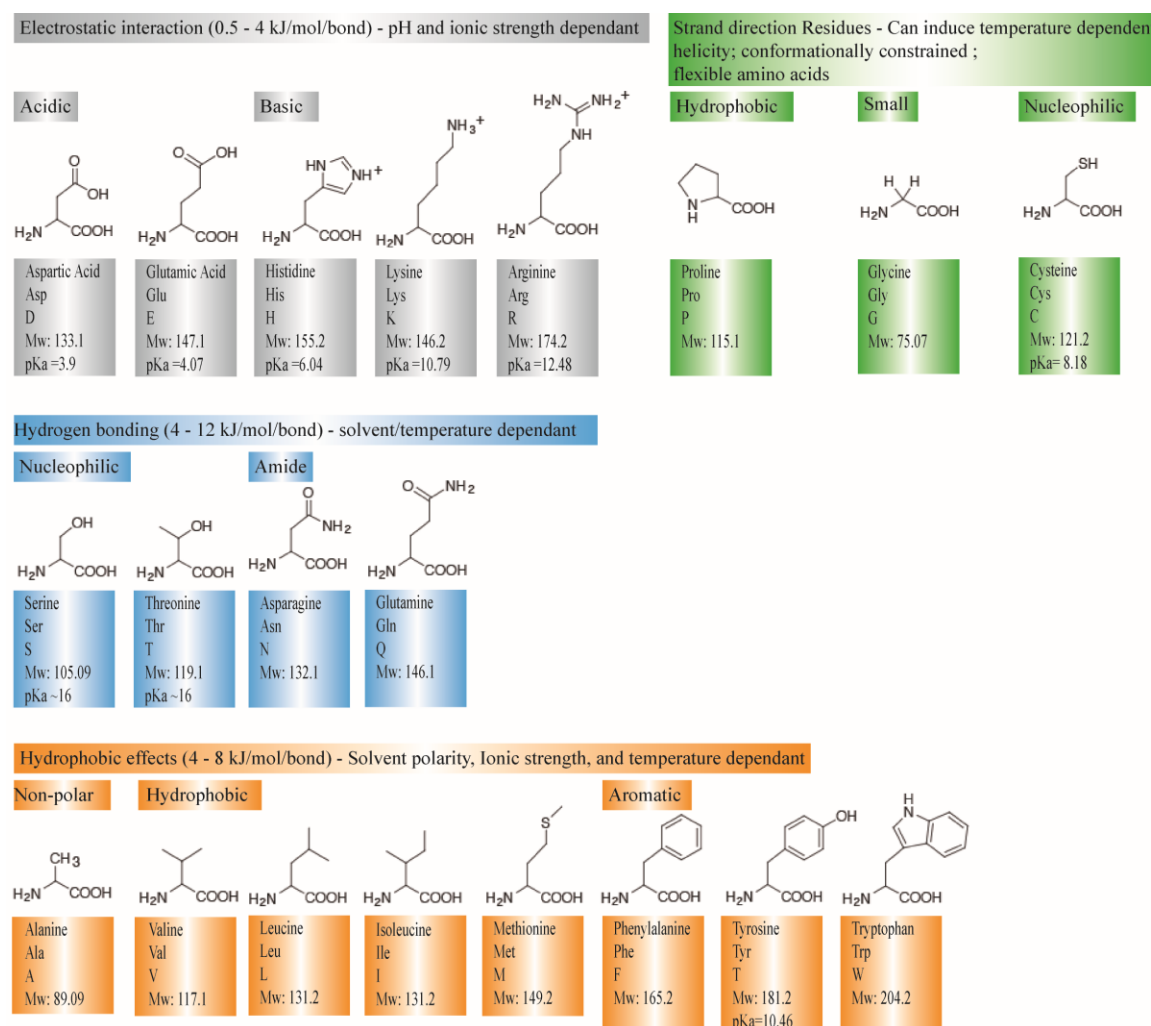


Figure 5: Overview of 20 naturally used amino acids of proteins. The amino acids are divided into different classes. The separation was done according to their effects and properties. Each amino acid is shown with its chemical structure, name, and abbreviations of this and molecular weight. Figure adapted from²⁶.

The amino acid sequence is defined as the first level of a structure called the primary structure (**Figure 6**).²² The primary structure can fold into thermodynamically stable α -helices, β -turns, β -sheets, and random coil, comprising a dynamically stable secondary structure (**Figure 6**).²² The secondary structure defines the local conformation of the protein backbone.²² Furthermore, the secondary structure is stabilized by hydrogen bonding.²⁷

The next level of protein structure is the tertiary structure. This level refers to the 3D structure of a protein. There are several types of long-range interactions involved in this 3D folding process.²² The sectioning of these interactions is shown in **Figure 6**. Electrostatic interactions occur between positively and negatively charged aa. They will form an ionic bonding.²² Hydrogen bondings are formed in the polypeptide chain and will additionally stabilize the shape of the protein.²² Hydrophobic interactions contribute to the folding process of a protein.²⁸ The hydrophilic amino acid will mainly orientate toward the aqueous environment. Hydrophobic amino acids will try to avoid the formation of an interface with the aqueous environment and center to the core of the protein (**Figure 6**).²² The highest level of protein structure is called the quaternary structure and refers to the interactions of multiple polypeptide chains.²²

Primary protein structure

- Amino acid sequence

GSSAAAAAAAAAS

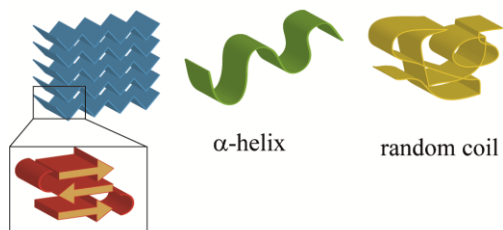
GPGGY GPENQGPS GPGGY GPGGP

Secondary protein structure

- Amino acid sequence linked by hydrogen bonds

- Local folding

- Short distance interactions

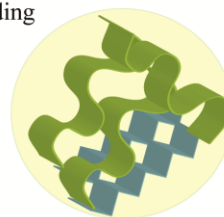


β -sheet crystallite with β -turns

Tertiary protein structure

- Distant interactions between secondary structure elements

- Additional folding



Quaternary protein structure

- multiple amino acid chains interacting

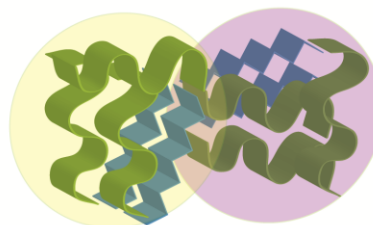


Figure 6: Four levels of a PP and protein structures. Firstly, the amino acid sequence is the lowest hierarchical level, which assembles into secondary structure elements like β -sheets, α -helices, or remains unordered as random coil. The secondary structure elements assemble into the tertiary protein structure. When multiple protein chains interact, the quaternary protein structure is formed.

Part I – Chapter 1.1.4 - Poly(amino acid) synthesis

Polycondensation reactions of amino acids to produce proteins are essential for every kind of life on earth.²⁰ This kind of reaction enables the specific processing of polymers with various amino acids.²⁰ The first human-made polymerization route for poly (amino acids) was the solid-phase peptide synthesis (SPPS) reported by Merrifield in 1963.²⁰ The

principle of this technique relies on a solid polymeric, functional resin, like chloromethylstyrene-divinylbenzene in the Merrifield method, which is used for sequential conjugation of the desired amino acids with the solid interface.²⁰ The isolation of the product is a straightforward route using filtration or centrifugation.²⁰ But there are several drawbacks of this method; the biggest drawback is the limitation of approximately 100 aa repeat units without losing massively yield.²⁰ Another drawback is that this method is very time-consuming and expensive.²⁰ A polymerization technique that overcomes this drawback is N-carboxyanhydride ring-opening polymerization (NCA ROP).^{20, 21} This technique is appealing because of its efficiency, scalability, and simplicity.^{20, 21} NCA ROP exhibits the possibility of producing higher molecular weight polymers cost-effectively.^{20, 21} It is also possible to direct the structure and the stereochemistry of the resulting polymer.^{20, 21} By using NCA ROP a polydispersity less than 1.10 can be achieved.²⁰

Part I – Chapter 1.1.5 - NCA-ROP of polypeptides

First, the precursors have to be synthesized. For this purpose, two different methods are possible, the Leuchs' synthesis, which was discovered accidentally by Leuchs over a century ago by trying to distill N-ethoxycarbonyl amino acid chlorides and N-methoxycarbonyl amino acids chlorides.²⁰ The Fuch-Farthing method is another synthesis strategy.²⁰ Both synthesis strategies are shown in **Figure 7A** and **B**.

The mechanism in **Figure 7A** starts with an α -amino acid, which is N-alkylcarbonyl-protected or N-benzyloxycarbonyl-protected and reacts with an acid halide.²⁰ Commonly used acid halide agents are the agent used by Leuchs: thionyl chloride, phosphorous pentachloride, phosphorous trichloride, and dichloro methy methyl ether. Leuchs' method also has some drawbacks, such as the yield is limited, a high cyclization temperature is necessary, and the purification is complicated.²⁰ One approach to overcome the high cyclization temperatures is to use acid bromides. Using this kind of agent, the cyclization temperature can be lowered below room temperature.²⁰ The rate of cyclization also depends on the substituent group of the α -amino acid, namely in this order: -methyl < -ethyl < -allyl < -benzyloxycarbonyl.²⁰

A more preferred route to obtain NCA monomers in high yields is the Fuchs-Farthing method displayed in **Figure 7B**. There, free, unprotected α -amino acids are directly phosgenated in an anhydrous solvent under reflux.²⁰ Possible solvents are tetrahydrofuran (THF), dioxane, ethyl acetate, toluene, and chlorinated hydrocarbons. Their key feature is

that they do not interact with the phosgenating agent.²⁰ Commonly, triphosgene is used because this agent is solid at room temperature and is easier and safer to handle as phosgene gas.²⁰ As shown in **Figure 7B**, the first step of the reaction is the addition of triphosgene and heat. In this step, the triphosgene breaks down to phosgene molecules under anhydrous conditions. One hydrochloric acid molecule is a side product of the reaction during the phosgenation and formation of the N-chloroformyl amino acid intermediate. In the second reaction step, the cyclization of the intermediate molecule and the loss of a second HCl molecule can be obtained by finishing the reaction to an NCA monomer.²⁰

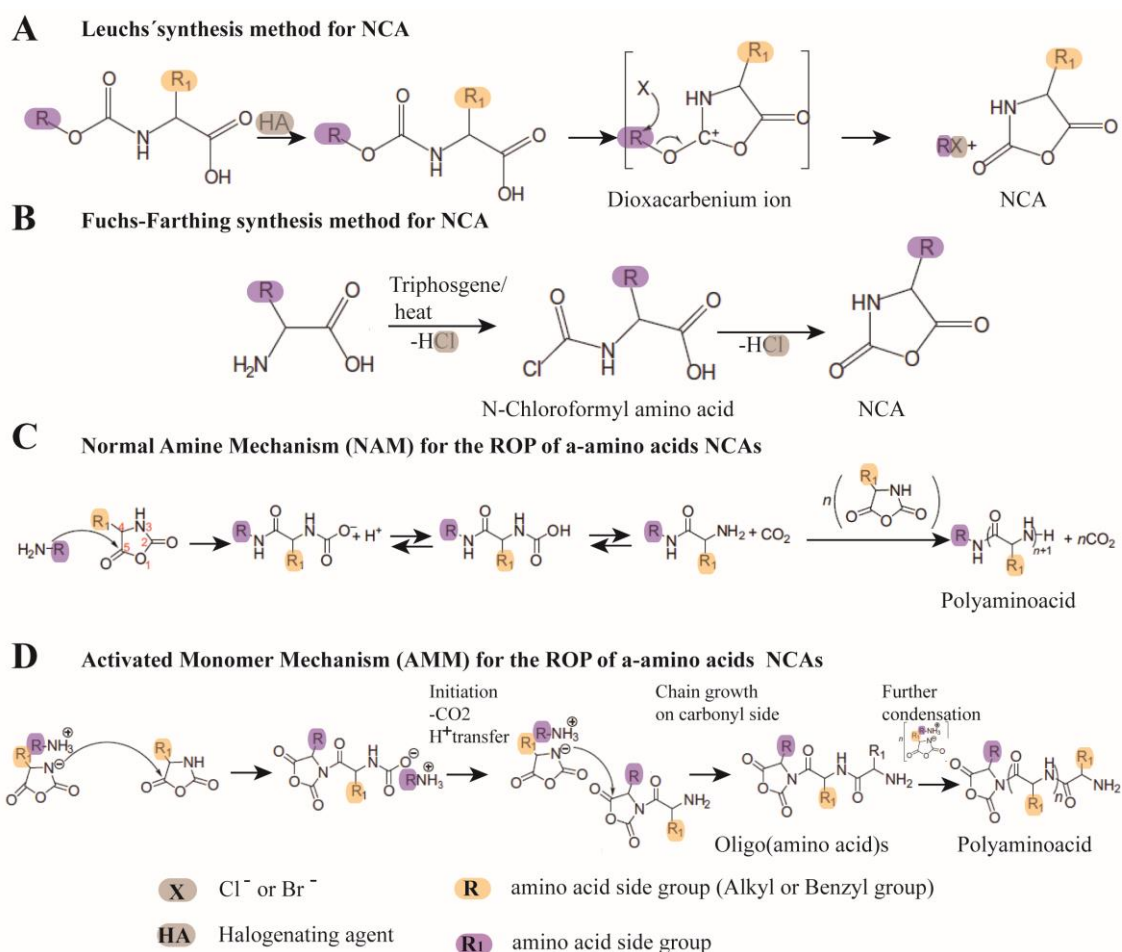


Figure 7: Overview of poly(amino acid) synthesis using the NCA method. (A) displays the Leuchs method of NCA synthesis. (B) shows the Fuchs Farthing method of NCA production. (C) is a schematic presentation of the normal amine mechanism (NAM) for ROP of α -AA NCAs. (D) represents the mechanism of the activated monomer mechanism (AMM). Figure adapted from ^{20, 21}.

The crucial step in NCA monomer synthesis is their purification. Many side reactions happen during the polycondensation reaction.²⁰ These side products, like HCl, N-chloroformyl amino acids, HCl amino salts, have to be removed to yield pure NCA

monomers.²⁰ After establishing a suitable purification strategy, the NCA monomers can be processed into poly (amino acids). Two synthesis routes are common for this ring-opening polymerization (ROP), the normal amine mechanism of poly(amino acid) synthesis (NAM) and the activated monomer mechanism of poly(amino acid) synthesis (AMM) (**Figure 7C and D**).^{20, 21} Both ROP strategies are straightforward because the NCA monomer interacts with a suitable nucleophilic/basic initiator to obtain poly (amino acids).^{20, 21} An advantage of the NCA ROP is the easy processing, the narrow PDI, reactive chain ends, molecular weight dependence on stoichiometric ratios of monomer/initiator, and the low synthesis temperature (RT).^{20, 21} By using the NAM synthesis route, nonionic, nucleophilic (basic) initiators with one accessible hydrogen atom, like primary and secondary amines, alcohols, and water, can be used as the initiator.²⁰ The NCA molecule is attacked by a nucleophilic attack at the 5-CO position. An unstable carbamic acid results in proton transfer.²⁰ A primary amine terminal group is formed upon the loss of CO₂. The active species is then at the N-terminal end of the molecule. Another NCA monomer can be added subsequently. The monomer/initiator ratio determines the resulting molecular weight of the poly(amino acid). In contrast to NAM, AMM is initiated by bases.²⁰ Here, with the help of tertiary amines or metal alkoxides, the 3-N position of the NCA monomer ring is attacked to obtain an NCA anion (**Figure 7D**).²⁰ This NCA anion initiates the chain propagation by attacking another NCA monomer at the 5-CO position to yield another NCA anion.²⁰ CO₂ is formed upon decarboxylation and proton transfer, recovering the amine.²⁰

In summary, AMM is used when high molecular weights are desired, but AMM results in broader PDI's than NAM.²⁹

Part I – Chapter 1.1.6 - Grafting-from and Grafting-to methods

The grafting-from and grafting-to approaches are versatile methods to apply polymer brushes to a solid surface.^{21, 30-34} The principle of both methods is shown in **Figure 8**. The grafting-to process relies on a functional group that is immobilized on a substrate and a preformed end-functionalized polymer (peptide) chain in solution. The end group of the peptide chain can be grafted-to the solid substrate via polycondensation, living anionic, cationic, radical, or ring-opening metathesis polymerization (**Figure 8A**).^{21, 35} The grafting to approach is a two-step polymerization. The first step is the diffusion of the preformed polymer (peptide) chain, which is free in the solution, to the complementary immobilized

group at the substrate.³⁵ The second step is the reaction of these complementary functional groups.³⁵ The drawback of this approach is that it is limited to an unfunctional, simple polymer chain without coexisting other functional groups.³⁵ Another drawback is the low grafting density and, because of that, resulting in a thin-film thickness of a few nanometers.³⁵ The grafting-from approach reaches higher grafting density and film thickness because the polymer (peptide) chains are formed in-situ from the modified surface of the substrate via radical or living polymerizations methods (**Figure 8B**).^{21, 35}

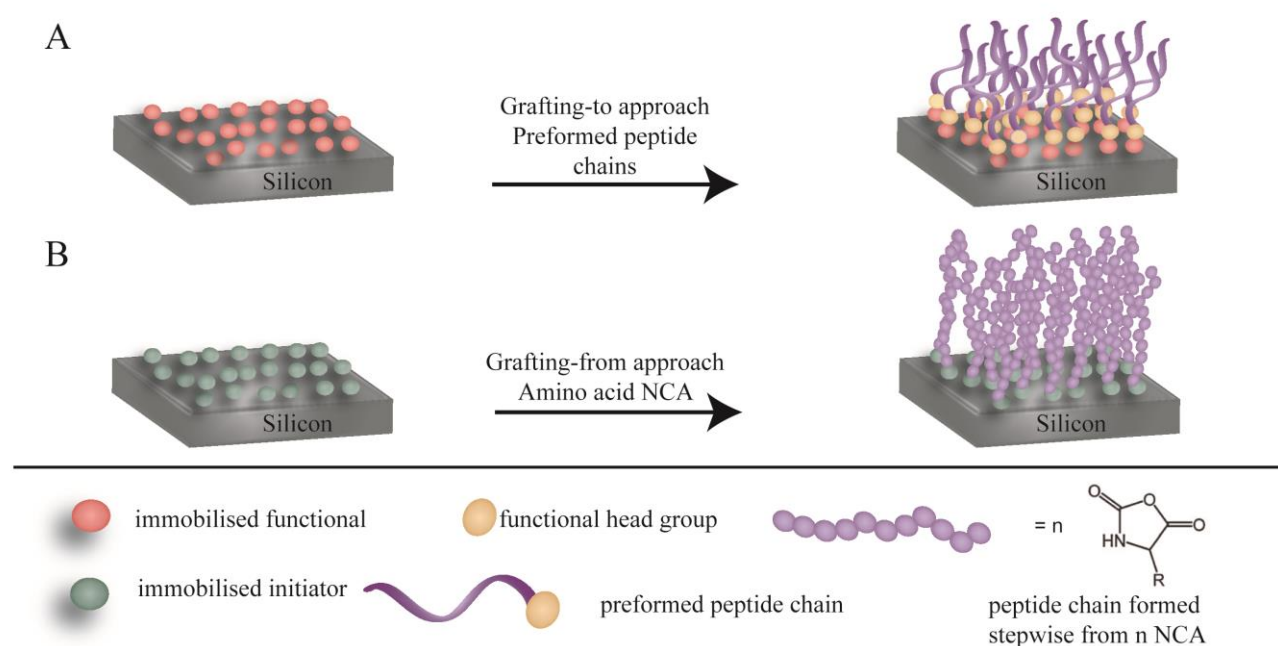


Figure 8: The principle of grafting to (A) and grafting from (B) methods are shown exemplarily for NCA ROP. Figure created based on ²¹.

The grafting-from approach has the initiator of the polymerization immobilized on the surface.²¹ And by adding, for example, the NCA monomers to the substrate, the polymerization proceeds from the surface via polycondensation.²¹ In both methods, a polymer brush is formed, determining the surface properties.³²

Part I – Chapter 1.1.7 - Natural polypeptides - natural spider silk

Spiders have many different families and classes. Orb-weaver spiders are probably the most well-known silk producers.³⁶ These orb-weaving spiders belong to the largest family of *Araneidae* with more than 2600 described species.³⁶

Spider silk fibers are fascinating materials because of their outstanding mechanical properties combining moderate strength and high extensibility, yielding a toughness that is unreached by human-made fibers .^{37 38}

Female orb-weaving spiders can produce up to seven different silk types.^{39, 40} Each of these seven silks has different properties suitable for various purposes.⁴⁰ The name of the silk derives from the spinning gland where the respective silk proteins are produced.⁴¹ **Figure 9** shows the web of *Araneus diadematus*. The web is built of five different silks (1-5). Furthermore, two different silks, namely the *Aciniform silk* (6) and the *Tubuliform silk* (7), are used to protect the offspring or to wrap prey (6).⁴¹

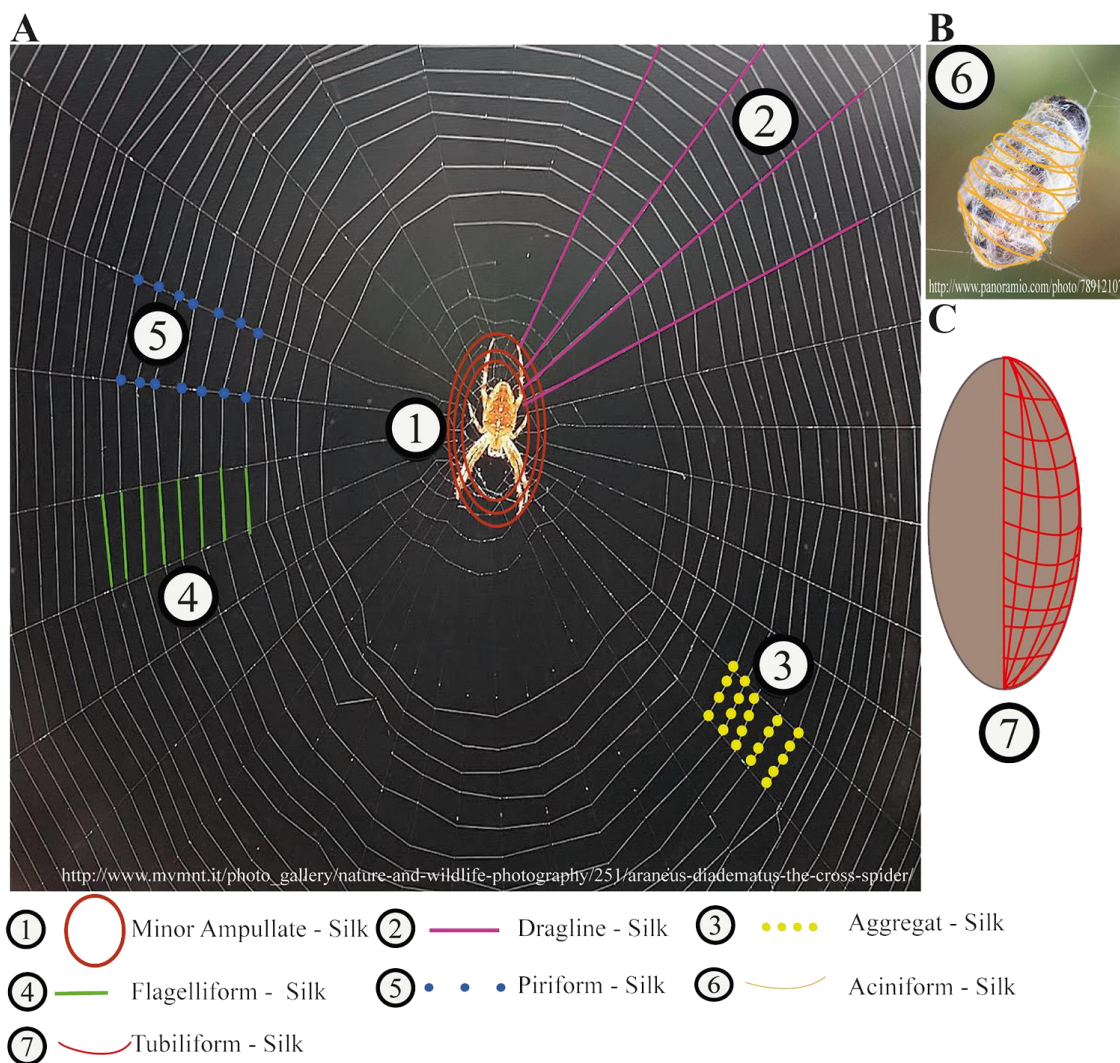


Figure 9: This figure shows the seven different kinds of spider silk produced by *Araneus diadematus*: (1) *Minor Ampullate* silk (2) *Dragline* silk (3) *Aggregate* silk (4) *Flagelliform* silk (5) *Piriform* silk (6) *Aciniform* silk (7) *Tubuliform* silk. Figure created based on ^{40, 42}.

Our research focuses on the *dragline silk* (**Figure 9(2)**) of the spider *Araneus diadematus*. This silk represents the lifeline of the spider.⁴¹ The proteins of this dragline silk are produced in the major ampullate gland.³⁸ Two protein classes, which mainly differ in their proline content, are named MaSp1 and MaSp2 and have mostly a molecular weight of approximately 250-350 kDa.^{37-39, 42} More than 50 % of the amino acid sequence consists of glycine and alanine residues.^{39, 43, 44} The MaSP protein can be divided into a large repetitive core domain flanked by two non-repetitive termini.^{39, 42, 45} The repetitive core domain consists of highly conserved sequence motifs comprising 20-40 amino acids repeated more than a hundred times.⁴⁶ There are three central consensus motifs, the polyalanine motif A_n with $n = 4-12$, GGX with $X = Y, L$ or Q , and GPGXX (mainly in MaSp2) with $X = Q, G$ or Y .^{42, 45}

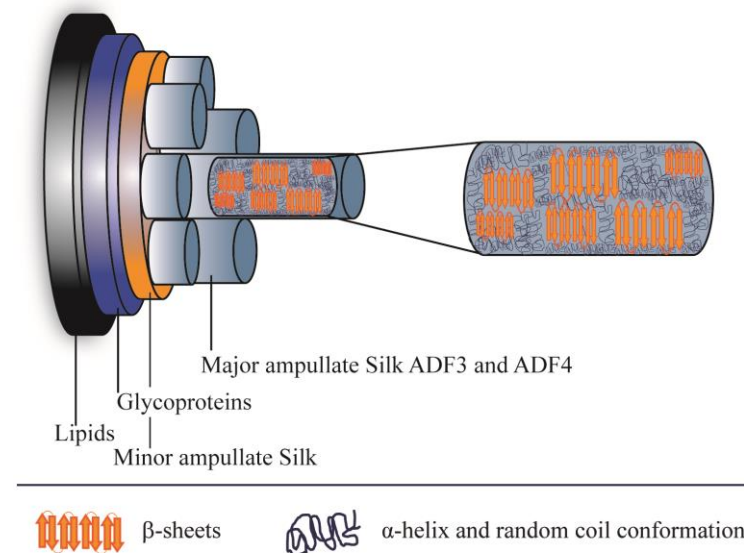


Figure 10: Core-shell model of an *Araneus diadematus* dragline silk fiber. The fiber can be divided into four parts. The outer shell is a lipid layer. The second layer is the glycoprotein layer, which protects the inner layer, the *minor ampullate silk ADF1, and ADF2*. The core is semi-crystalline *major ampullate silk* comprising at least two MaSp named ADF3 and ADF4 and consists of fibrils representing the crystalline part of the silk. Figure created based on ^{42, 43, 45}.

The outstanding mechanical properties of the dragline are based on the hierarchical structure of the silk (**Figure 10**). This hierarchical structure can be divided into four parts.^{42, 43, 45} The core consists of proteins produced in the *major ampullate gland*.^{42, 43, 45} These proteins can form micro- and nanofibrils directed along the fiber axis by inter- and intramolecular assembly of β -sheets embedded in an amorphous glycin-rich matrix.

Combining these amorphous and crystalline regions (11-35%) is responsible for the outstanding mechanical properties. The tensile strength is a result of the nonpolar hydrophobic crystalline regions. The elasticity results from the hydrophilic amorphous matrix comprising random coils, α -helices, and β -turns.⁴⁷⁻⁴⁹ The three shells of the spider silk fiber are built of lipids, glycoproteins, and minor ampullate silk to protect the core against environmental damage or microbes.⁵⁰

Part I – Chapter 1.1.8 - Recombinant polypeptides - recombinant spider silk

Most spiders show aggressive territorial and cannibalistic behavior.⁴² Therefore, it is not feasible to farm them. Another drawback of natural spider silk is the inhomogeneity in silk composition caused by variations of nutrition and habitat.⁴²

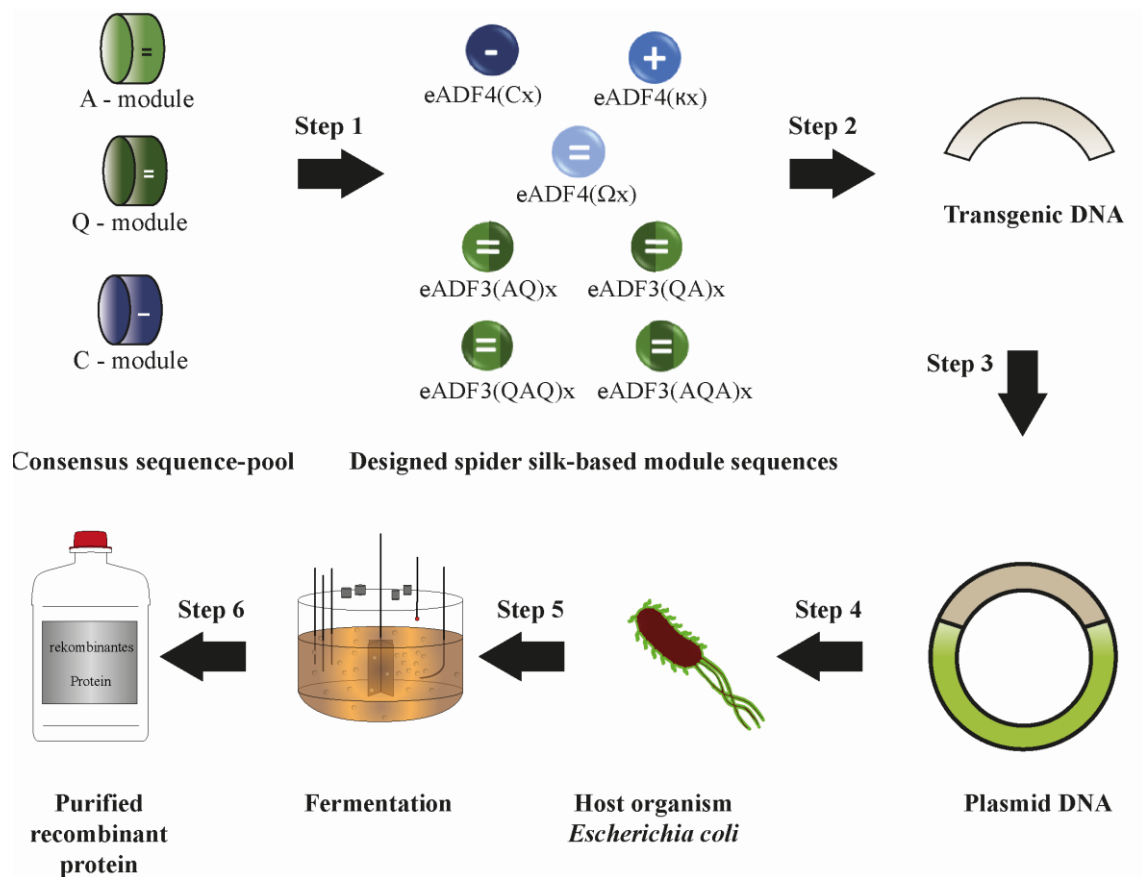


Figure 11: Schematic overview of recombinant spider silk production from the consensus sequence pool (Step 1) to the technical approach. The designed spider silk module sequences are translated in Step 2 to transgenic DNA, which is then transferred to a plasmid (Step 3), which can be introduced in the host organism *E.coli* (Step 4) for recombinant expression (Step 5) in fermenters. After the biotechnological production, the protein is purified using different purification steps (Step 6) and, upon lyophilization, yields a white protein powder. Figure adapted from ⁴¹.

For these reasons, a process of recombinant production of spider silk proteins was developed using *Escherichia coli* (*E.coli*) as the host organism.⁵¹

The production pathway is displayed in **Figure 11**. A sequence pool was designed based on the identified repetitive consensus sequences of the dragline silk from the European garden cross spider *Araneus diadematus*.⁵² Codon optimization was done to ensure that the genetic information is applicable for translation in *E.coli* bacteria.⁴⁰ Furthermore, the amino acid modules were multimerized and transferred into a suitable expression vector.⁴⁰ After the transformation of the expression vector into *E.coli*, the protein is produced, purified, and lyophilized.⁵³ Spider silk proteins can be processed into various morphologies like films, fibers, non-woven meshes, foams, hydrogels, particles, and capsules (**Figure 12D**). Figure 12 schematically shows the used spider silk peptides and proteins in this thesis. Three spider silk peptides and protein variants derive from the so-called C-module. The amino acid sequence of one module is shown in **Figure 13A**. The C-module can be divided into two blocks. One hydrophobic block and one hydrophilic block.⁵¹ Thus, you can say that spider silk can be regarded as an amphiphilic multiblock polymer.^{54, 55}

By substitution of one amino acid (presented in the one-letter code in **Figure 13**), the negatively charged C-module can obtain a neutral charge (E vs. Q)⁵² or positive charge (E vs. L).⁵⁶ **Figure 12B** shows the ADF3-derived spider silk variants eADF3(AQ)_x. The hydrophobic (A-module) and the hydrophilic block (Q-module) are divided into two modules.⁵⁷ Both blocks of these variants have a neutral net charge.⁵⁷ These recombinant spider silk proteins can be genetically fused with biofunctional peptide tags like the synthetic integrin-recognition motif RGD⁵⁸, the polyanionic glutamic acid tag E₈G⁵⁹, or the polycationic arginine tag R₈G⁶⁰ at the C-terminal end of the recombinant protein (**Figure 12C**).

The terminal primary amine (-NH₂) and the carboxyl group flanking the N- and the C termini of the protein as well as the amine and sulfhydryl (-SH) groups of the side chains of lysine and cysteine comprise the options to conjugate targets covalently to the protein.

The protein powder needs to be dissolved in solvents like hexafluoro-2-propanol (HFIP), formic acid (FA), and aqueous buffers to process the spider silk proteins. Organic solvents are suitable for archiving highly concentrated protein solutions with protein concentrations from 20 w/v % up to 60 w/v %.⁵¹ This is not possible with aqueous solutions in a one-step process. First, recombinant spider silk proteins must be dissolved in a chaotropic salt

solution like Guadiniumthiocyanate) and dialyzed against an aqueous buffer like ammonium hydrogen carbonate or Tris/HCl.⁵⁶ The secondary structure changes by using different solvents for film casting.⁵⁶ For example, HFIP induces α -helical structures to the spider silk proteins during solvent evaporation.⁶¹ In contrast, FA induces a higher β -sheet content leading to water-insoluble films.⁶¹ Likewise, it is possible to post-treat the spider silk materials, e.g., films, with cosmotropic salt solutions, monovalent alcohols, heat, post-stretching, and water vapor.^{49, 56, 61}

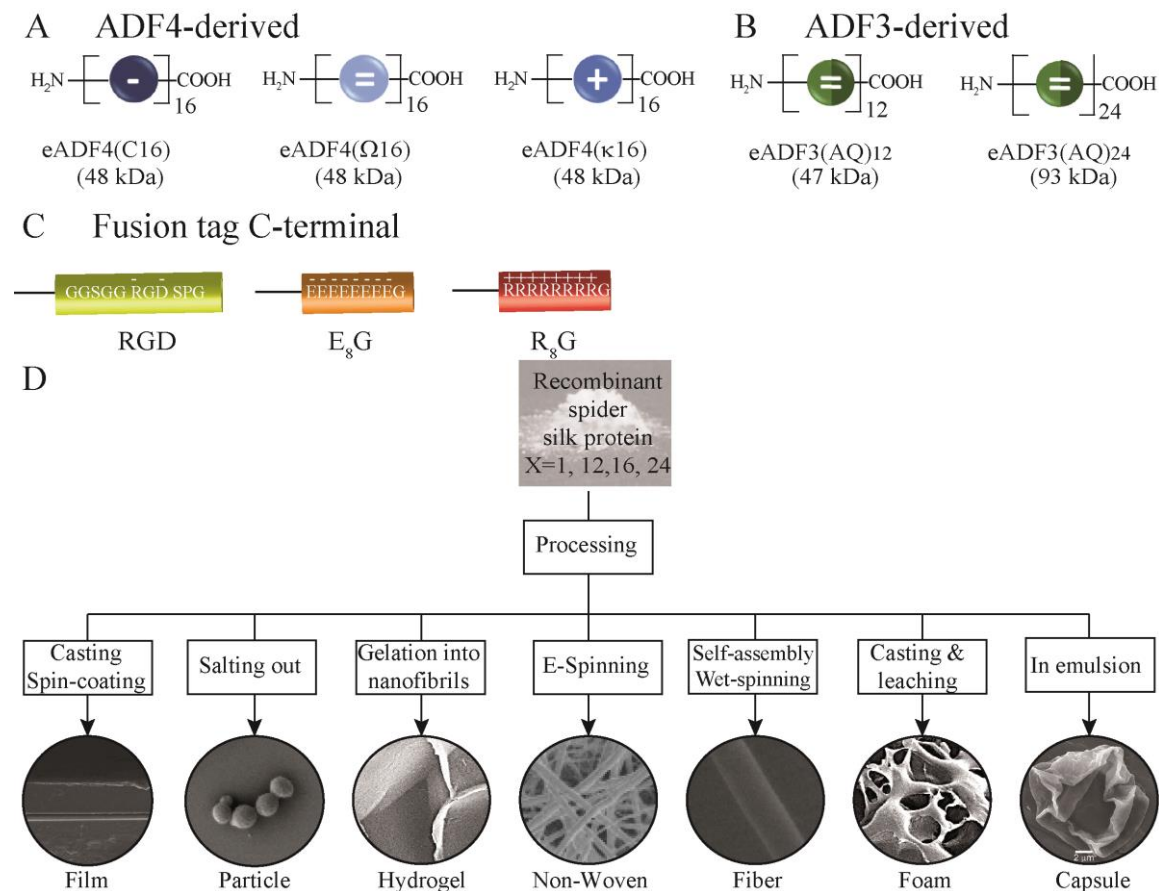


Figure 12: Names, net-charges, and molecular weight of the spider silk proteins and peptides used in this thesis. The ADF4 derived spider silk variants eADF4(C16), eADF4(κ16), and eADF4(Ω16) with corresponding charge and molecular weight are depicted in (A). Furthermore, (B) shows the ADF3-derived spider silk variants, eADF3(AQ)₁₂ and eADF3(AQ)₂₄. All recombinant spider silk variants in (A) and (B) can be genetically engineered and fused with functional tags, in this thesis with C-terminal tags like -RGD, -E₈G, or -R₈G⁶⁰ (C). After protein purification, the recombinant spider silk proteins are a lyophilized white powder that can be processed using various processing methods into different morphologies like films, fibers, non-woven meshes, foams, hydrogels, particles, and capsules (D). Figure was adapted from ⁶².

Part I – Chapter 1.1.1.1 - Phase separation behavior of recombinant spider silk

Some working groups have already observed phase separation behavior in natural and recombinant silk proteins.^{61, 63-65}

Rabotyagova et al. produced recombinant spider silk proteins, which are block copolymer-like and called HBA_x with $x = 1, 2, 6$. This HBA_x consists of a histidine tag (H), a hydrophobic pAla block, and a glycin-rich block.⁴⁸ *Rabotyagova et al.* found correlations between the number and order of repeating units and the secondary structure obtained in aqueous solutions.⁴⁸ By increasing the number of repetitions from H(AB)₂ to H(AB)₁₂, the protein changed from the unstructured phase (compare Phase diagram, phase DIS in **Figure 2**) to a lamellar phase (**Figure 13D**).⁴⁸

The phase separation behavior of recombinant spider silk proteins was already investigated for cast films with a film thickness of 1-2 μm .⁶¹ Dependent on the substrate hydrophilicity, a phase separation model for eADF4(C16) was developed. **Figure 13A** represents the amino acid sequence of one C-module of eADF4(C16).⁶¹ **Figure 13B** represents the possible orientation of the protein chains at the phase interface. **Figure 13C** is the proposed phase separation model of *Wohlrab et al.* upon assembly on surfaces with the dependency on substrate hydrophilicity.⁶¹

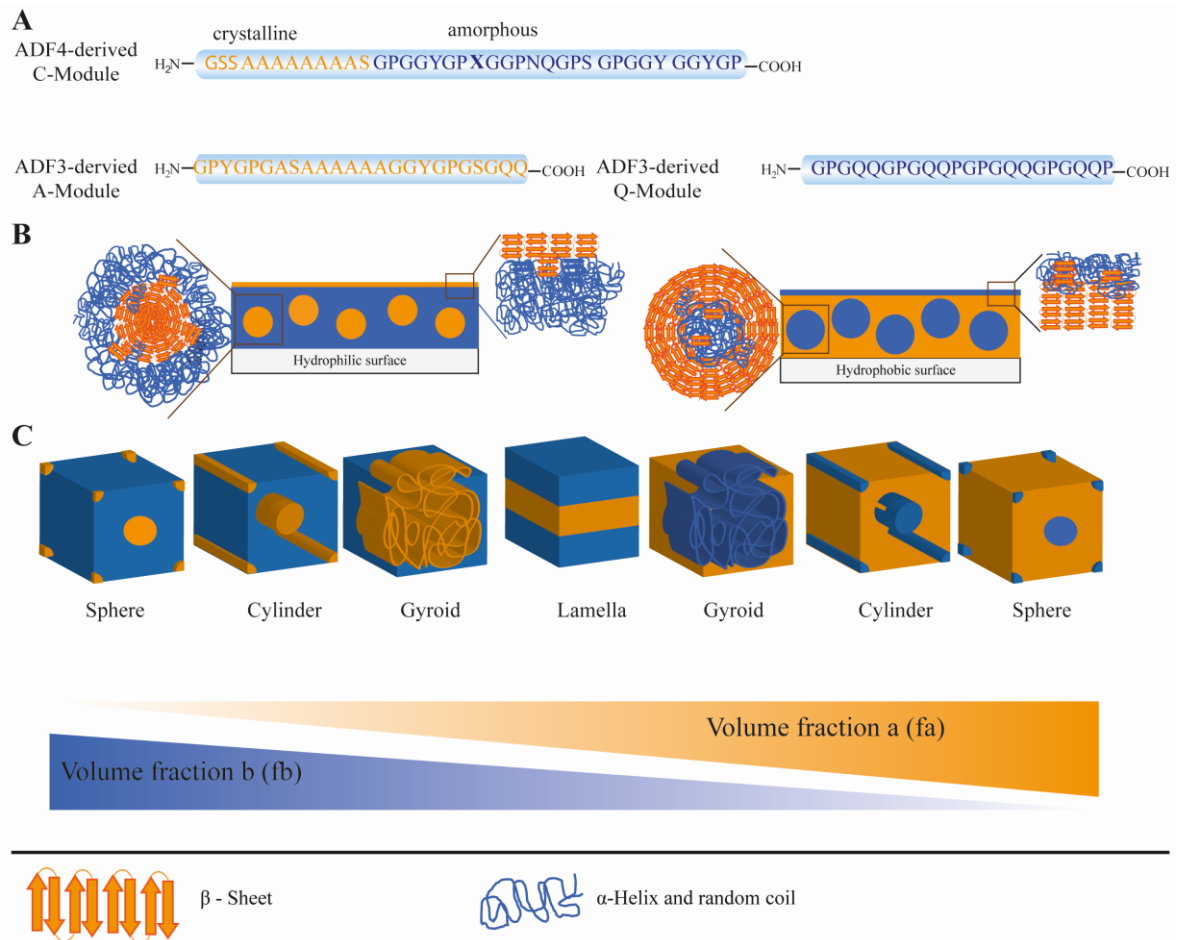


Figure 13: Schematic figure displaying the different blocks of the amino acid sequence of the eADF4-derived C-module and the eADF3-derived A- and Q-module (A). The microphase separation model, according to *Wohlrab et al.*, is shown in (B) for a hydrophilic and a hydrophobic substrate.⁶¹ The microphase separation of polymer chains depending on the fraction of the crystalline block A f_a (orange) and amorphous block B (dark blue) is depicted in (C). Figure B was adapted from ⁶¹.

Upon assembly, the amorphous and the crystalline blocks separate from each other and influence the substrate wettability. Water contact angle measurements of cast eADF4(C16) films show that films that were cast on hydrophobic polytetrafluoroethylene (PTFE) result in more hydrophilic contact angles ($41.7^\circ \pm 6.3^\circ$) than eADF4(C16) films, which were cast on glass ($74.4^\circ \pm 8.5^\circ$).⁶¹ The microphase separation model indicates that the amorphous phase forms the majority phase on hydrophilic surfaces. The β -sheets are separated and embedded in an amorphous matrix and orientated towards the air/film interface.⁶¹ eADF4(C16) on hydrophobic surfaces show a reversed-phase separation behavior.⁶¹ Further experiments were performed to verify this model. Secondary structure analysis using FTIR and enzymatic degradation with α -chymotrypsin confirmed the model.⁶¹

Part I – Chapter 1.2 - Biomaterials

The first biomaterials were used more than 2000 years ago. For example, gold was used in odontology.⁶⁶ But the research field and the term biomaterial are much younger. Williams defined 1987 the term biomaterial as all materials which come into contact with body tissues or fluids, e.g., the implantation of a material within these tissues.⁶⁷ More precisely, a non-viable material with synthetic or natural origin that can be used as a partial or complete biological substitute of the body for a certain time to maintain or amend the quality of life.⁶⁸ The interdisciplinary research field of biomaterials has grown exponentially over the last 50 years.⁶⁹ Nowadays, biomaterials are used in, e.g., hip or knee replacements, dental implants, breast implants, stents, or contact lenses.⁶⁹

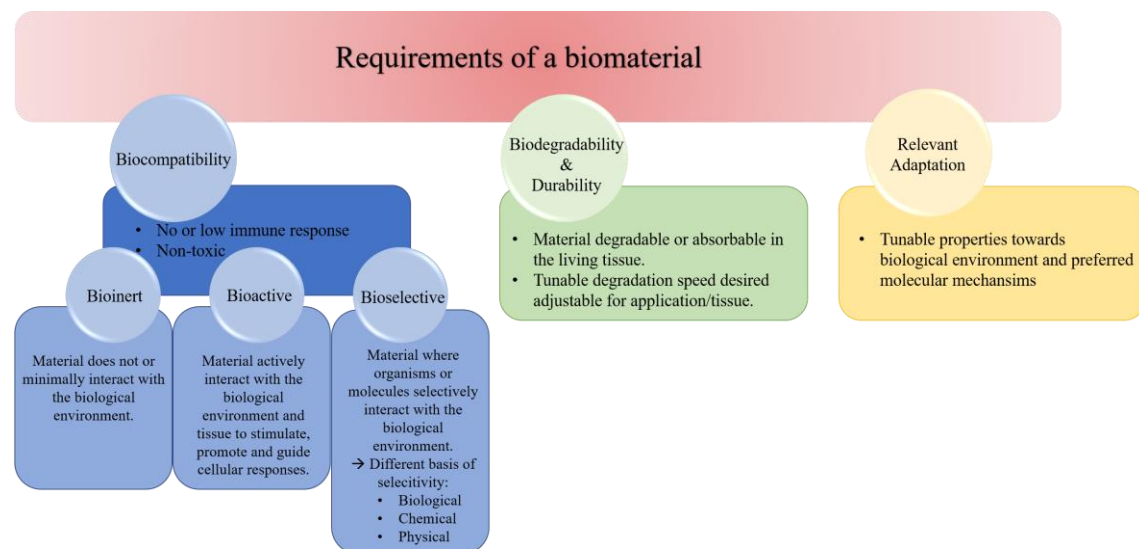


Figure 14: Requirements of a biomaterial and biomaterial surfaces. The three most important points are that the material is biocompatible, biodegradable, and can be adapted towards the biological environment. Sometimes, biodegradability is not desired; instead, durability is more important for the used biomaterial, such as hip implants. A biomaterial surface can be described from two different perspectives, the physicochemical perspective, where the surface morphology, mechanical properties, and hydrophilicity are the most determining factors; the biological perspective, where the biocompatibility and no or low immune response are desired. Surface engineering can be useful to achieve the requirements of a biomaterial. Methods like self-assembly of polymers or proteins or chemical coupling are methods for surface modifications.

There are specific requirements that biomaterials have to fulfill (**Figure 14**). Firstly, the materials need to be biocompatible. By coming into contact with body tissue, the material should not cause an immune response and has to be non-toxic. Biomaterials can be subdivided into three different classes. The first class is bioinert materials. These materials

do not interact with the biological environment, and the interaction is not desired.⁶⁶⁻⁶⁹ In contrast to the bioactive materials, here, the interaction between the material and the tissue is desired and aims to promote or guide the response of cellular growth, e.g., in tissue or bone regeneration.⁷⁰ The third class is bioselective materials. Selectivity can be defined in many ways and is gradable in contrast to specificity.⁷¹ Here, bioselectivity is defined as a term for selective interactions with the biological environment resulting from biological, chemical, and physical aspects. Consequently, bioselective surfaces are surfaces where the affinity for cells or molecules is enhanced or reduced.^{68, 69}

Another important aspect is the biodegradability and the durability of a biomaterial.^{52, 72, 73} The biomaterial should be ideally biodegradable but within a defined time span tailored for the application. Sometimes, no degradation is desired because the implant should replace a joint. For example, a scaffold for bone regeneration should not be degraded within two days because the osteoblasts will need more time to regenerate.⁷⁴ At best, the material can be adapted to the needed properties of the application.^{52, 68, 69, 74} In most cases, the biomaterial surface is the crucial part because it is ubiquitous in the biological environment. Moreover, many materials still lack biocompatibility; hence, the physicochemical properties of the biomaterial surface are of utmost importance to cope with this problem, especially *in vivo*.⁶⁸ Therefore, the biological response to physicochemical properties of biomaterial surfaces is highly relevant for developing new biomaterials. Here, also three different perspectives are highly relevant. Firstly, from the biomaterials engineering perspective, every physicochemical property can highly affect the selectivity of the biomaterial surface (**Figure 15**). The characterization of the physicochemical properties of natural and synthetic surfaces is highly important to understand their basis for bioselectivity. If this knowledge is gained, it is possible to develop biomaterial surfaces with enhanced selectivity with different properties. From the biological perspective, the biocompatibility and the biochemical signals can be tuned. From a surface engineering perspective, the introduction of new functions is possible using various methods like self-assembly, click chemistry or RAFT polymerisation (**Figure 15**).

Nowadays, there are more requirements on a biomaterial than being bioinert.⁷⁵ For some applications, integrating the material in the biological environment is desired.⁷⁵ Synthetic polymers lack monodispersity and sequence control. It is primarily a statistical distribution of composition and sequence, resulting in low reproducibility and material tunability.⁷⁵ One

advantage is often the easy and cheap production of these materials. A class of biomaterials that overcome these drawbacks are recombinant proteins. Recombinantly produced proteins comprise monodispersity, precise amino acid composition, biodegradability, and biocompatibility.⁷⁵ Furthermore, they can be genetically modified with various peptide sequences, introducing additional functionalities.⁷⁵

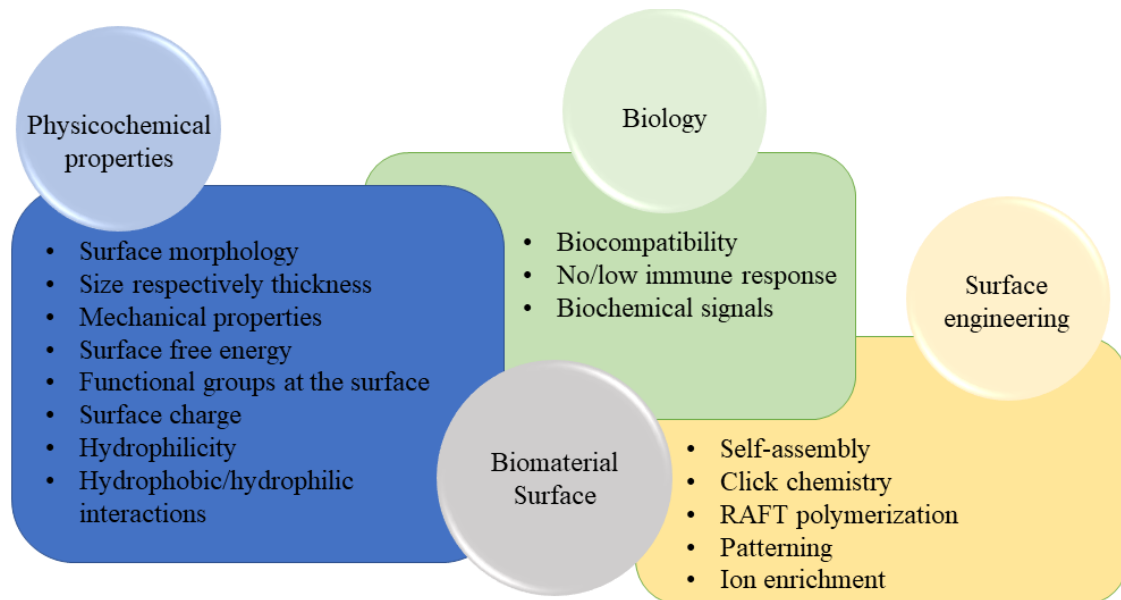


Figure 15: Requirements and properties of a biomaterial surface. The physicochemical properties affect the biocompatibility of a biomaterial. These properties are valuable parameters to tune the biomaterial surface. The biological perspective of the surface is highly important because biocompatibility and the immune response are the most important factors for a good biomaterial surface. Surface engineering is useful to achieve the desired surface properties. Figure created based on findings of ^{52, 68, 69}.

Part I - Chapter 2 – Methods and Instrumentation

In this chapter, the fundamental methods, the theoretical principles, and the setup of the devices used in this thesis are briefly described. Detailed experimental protocols are described in the associated chapters.

Part I – Chapter 2.1 - Methods

Part I – Chapter 2.1.1 - Purification of recombinant spider silk proteins

An appropriate purification strategy of the recombinant spider silk proteins is crucial to obtain reproducible and pure recombinant spider silk proteins. The purification of recombinant spider silk proteins begins with cell lysis and cell disruption since the target protein is otherwise not accessible. (**Figure 16**, green star indicates target protein, brown cylinders depict *E.coli* bacteria). Either ultrasonication or high-pressure homogenization can be used to disrupt the cells. These processes result in the so-called cell lysate. Further, the cell lysate is heated up to around 70°C to remove impurities or *E.Coli*-derived proteins because they are not as heat stable as the recombinant spider silk proteins. In this step, the recombinant spider silk protein is in the supernatant. A centrifugation step is performed to remove the precipitated impurities. Then, the recombinant spider silk protein is precipitated using ammonium sulfate. The protein pellet is washed multiple times until the supernatant is clear, and then the protein pellet is frozen and lyophilized. Afterwards, a white protein powder is obtained.

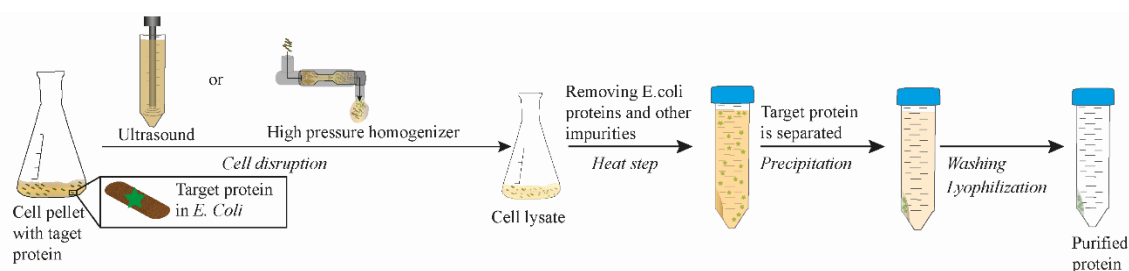


Figure 16: Purification strategy of recombinant spider silk proteins. The obtained cell pellet with the target protein is lysed, and the cells get disrupted using ultrasound or high-pressure homogenization. The cell lysate is heated to around 70 °C to precipitate all *E.coli*-derived proteins and other impurities. The cell debris is removed using centrifugation. The purification continues with a precipitation step with ammonium sulfate and vigorously washing. After multiple washing steps, the pure protein can be lyophilized. The green star indicates the target protein. The brown cylinders depict *E.coli* bacteria.

Part I – Chapter 2.1.2 - Formation of a coating

In this chapter, the principles of the preparation methods of coatings used in this thesis are presented briefly.

Part I – Chapter 2.1.2.1 - Spin-coating

Spin-coating is a technique to apply thin films from solutions on various substrate surfaces.⁷⁶ It is commonly used in many research fields like microelectronic packing⁷⁷, colloidal crystal assembly⁷⁸, or spider silk assembly.⁷⁹ Several parameters influence the film thickness: spinning velocity ν , the concentration of the polymeric solution c_0 , the solvent, molar mass M and molar mass distribution.⁷⁶ Coatings between a few nm to a few μm can be obtained homogeneously with this method.⁸⁰

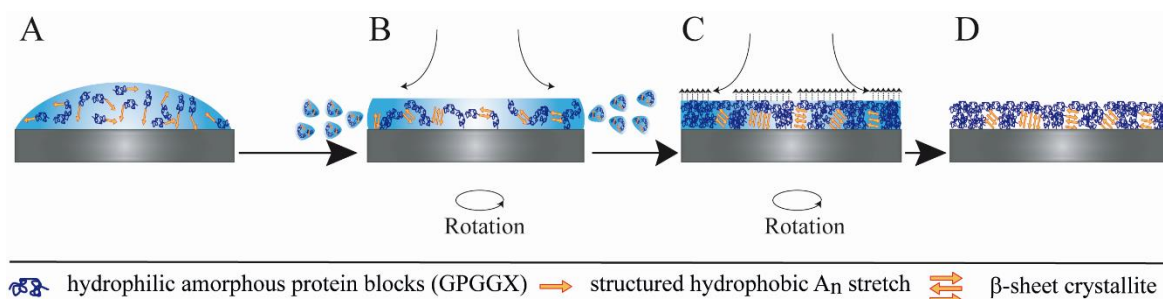


Figure 17: Schematic representation of spider silk film formation upon spin-coating.^{76, 80} The protein solution is applied onto the substrate (A), and then rotational forces are applied to the substrate. The excess protein solution is slung away from the substrate, the protein molecules come close together (B), and the solvent evaporates completely (C→D).

Figure 17 shows the spin-coating procedure schematically.⁸⁰ The spider silk protein solution is applied to the substrate (**Figure 17A**). A rotating plate is accelerated to high revolutions per minute (rpm), and most of the solution is flung off the side because of centripetal forces (**Figure 17B**).^{76, 80, 81} In combination with the surface tension of the solution, the applied drop is pulled into an even and homogeneous coating.^{76, 80, 81} During the whole rotating process, the solvent evaporates because of the airflow and the low vapor pressure of the solvent (**Figure 17C**).^{76, 80, 81} A plasticized film results.^{76, 80, 81} After complete evaporation of the solvent, only the molecules, e.g., the spider silk molecules, remain as a film on the surface.^{76, 80, 81}

Roughly, the thickness t of a spin-coated film is indirectly proportional to the square root of the angular velocity ν (rotating speed) (**Equation 1**).⁸⁰

$$t \propto \frac{1}{\sqrt{v}}$$

(1)

Simply said: If the spin-coating velocity is increased four times, the films will be only half as thick.⁸⁰

However, film thickness depends on more parameters like the protein concentration, solvent, solvent viscosity, vapor pressure, temperature, and local humidity.⁸⁰

Part I – Chapter 2.1.2.2 - Drop-casting

Drop casting is a simple and straightforward method for producing films with thicknesses from nano to micrometer.^{49, 53, 61} The process is shown in **Figure 18**. Upon dropping, the unordered, dissolved protein molecules are randomly distributed (**Figure 18A**). Induced by the evaporation of the solvent, the protein molecules begin to assemble, triggered by desolvation and surface contact (**Figure 18B**).^{49, 53, 61} After solvent evaporation, only the self-assembled protein molecules remain a homogeneous film on the surface. The resulting film thickness and secondary structure of the proteins depend on the protein concentration, the used solvent, and the vapor pressure of the solvent.^{49, 53, 61}

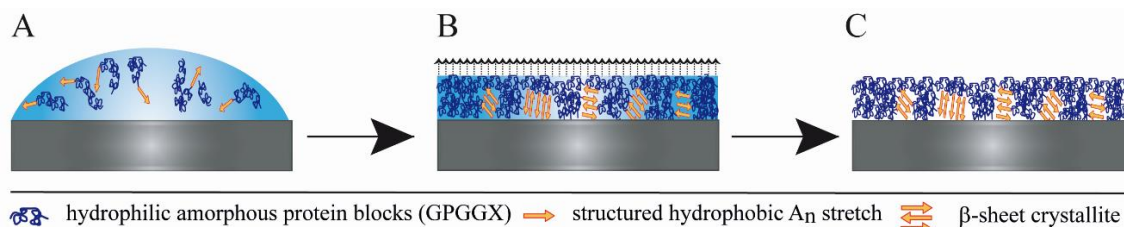


Figure 18. Formation of a coating using drop-casting. The dissolved protein is applied to the surface. The protein molecules, which can be divided into hydrophilic, amorphous blocks, and hydrophobic polyalanine stretches, are randomly distributed in the droplet. (A) The solvent starts to evaporate, the degree of freedom of the proteins decreases due to the declining volume of the solvent. (B) The protein molecules come closer together and start to self-assemble. (B) After the complete evaporation of the solvent, a homogenous, self-assembled film is formed. (C)

Part I – Chapter 2.2 - Instrumentation

Part I – Chapter 2.2.1 - Atomic force microscopy

Atomic force microscopy (AFM) is a powerful, non-destructive, high-resolution, non-optical imaging method to analyze surfaces.⁸²⁻⁸⁵ It is a powerful tool since information about topography, electrical, magnetical, mechanical, and chemical properties can be determined in air, fluids, or vacuum with this technique.⁸²⁻⁸⁶ The most commonly used operation mode of an AFM to detect topographical features from submicron to nanometer length scale is the tapping mode (**Figure 19C**).⁸³ An oscillating cantilever is actuated near it used to scan the surface of the sample regarding topography and roughness. The principle of an AFM measurement is that the cantilever is actuated near the surface and scans line per line.⁸³ The position of the cantilever is changed due to the forces between the tip and the surface. These changes are detected by the changes of deflection of the laser beam using a photodetector (**Figure 19A**). The forces can be repulsive (short-range Coulomb interaction) or attractive (van der Waals force) (**Figure 19B**).

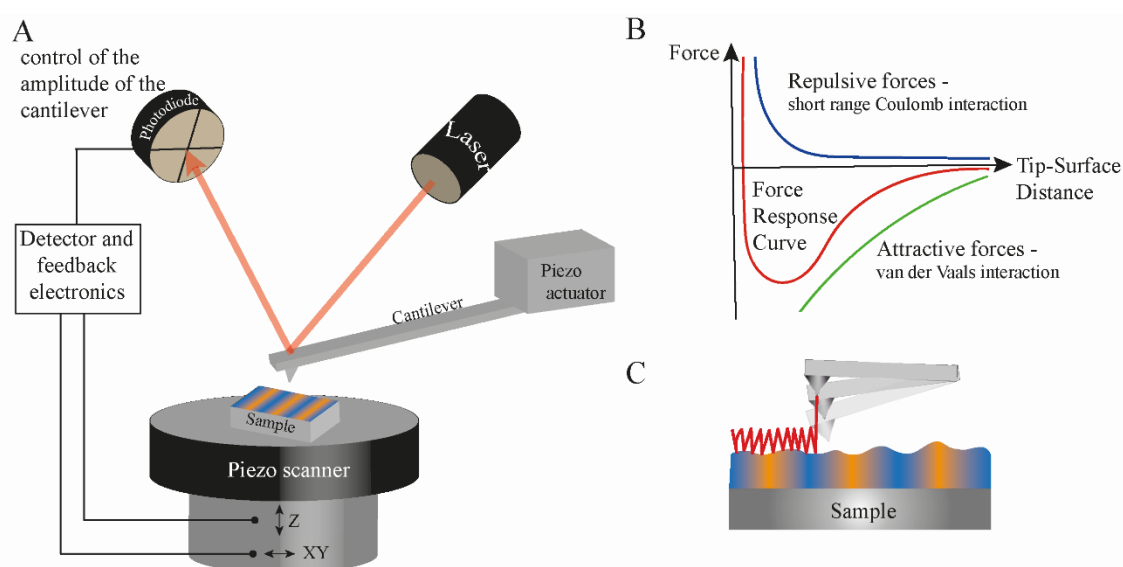


Figure 19: Schematic setup of the fundamental functionality of an Atomic force microscope (AFM): The sample is placed on the sample plate, which is movable in x, y, and z-direction driven by a piezoelectric motor. A laser beam is focused on the backside of a cantilever to record the changes in the cantilever deflections during scanning of the surface. A position-sensitive photodiode is used to detect the reflection of the laser beam. A piezoelectric scanner controls the lateral and vertical position of the AFM cantilever by getting feedback relative to the sample surface (A). Depending on the distance to the surface of the sample, the deflection of the cantilever changes. Different interaction forces apply depending on the distance between the tip and the surface of the sample (B). If the distance of the cantilever is approximate 100 nm from the surface, it gets attracted upon

van der Waals forces. (C) schematically shows the tapping mode. Figure based on descriptions and adapted figures from⁸²⁻⁸⁵.

Part I – Chapter 2.2.2 - Scanning electron microscopy

Scanning electron microscopy (SEM) is a common technique to image and analyze the surface of a specimen with an electron beam on a nanometer to micrometer scale.⁸⁷ An electron beam is generated from a cathode and accelerated by a voltage difference (1 – 300 kV) between cathode and anode, focused by electromagnetic lenses to a beam size between 1 nm - 0.1 μm .^{87, 88} The distance between the sample and the lower polepiece, where the electron beam arises, is called working distance (WD). When the electron beam hits the surface of the sample, a change in atom density occurs due to the solid sample density. Various scattering events occur through interactions of the beam electrons and the sample atoms.⁸⁷⁻⁸⁹ These scattering events aim to transfer the energy from the electron beam to the sample atoms.⁸⁷⁻⁸⁹

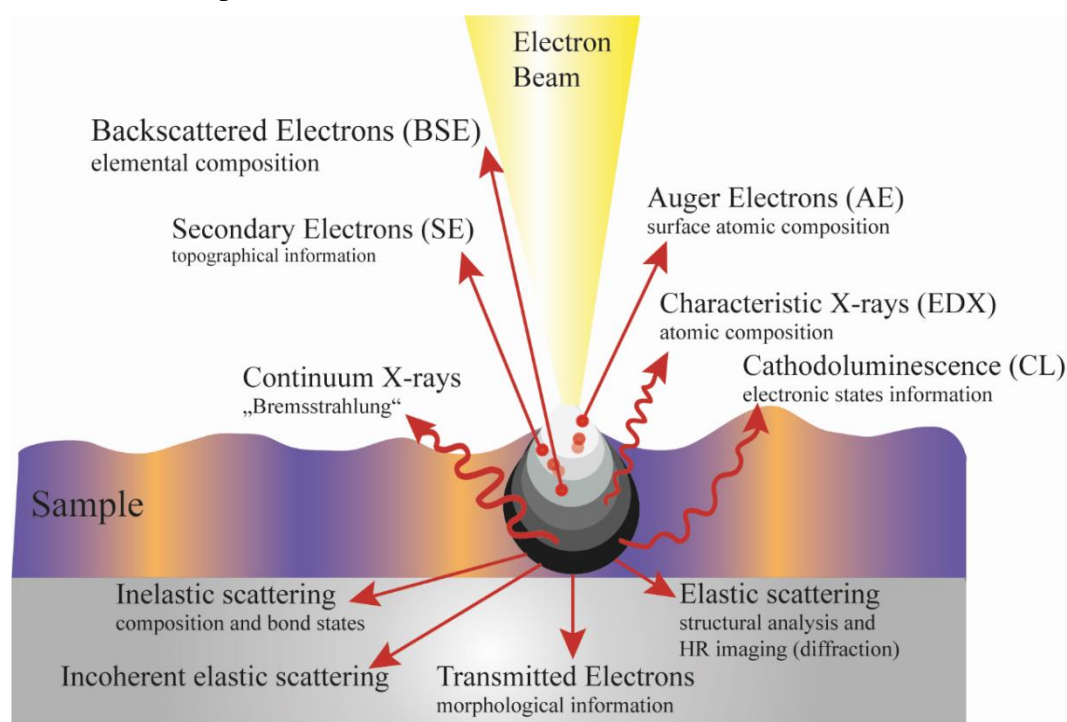


Figure 20: Generation of different electrons in the diffusion cloud by the interaction of an electron beam with a solid sample.^{88, 90} The different emitted and transmitted electrons (backscattered electrons (BSE), secondary electrons (SE), Auger electrons (AE) and transmitted electrons), the characteristic X-rays (EDX), cathodoluminescence (CL), and Bremsstrahlung provide different information concerning the analyzed matter. The corresponding information is shown below the electrons. Figure adapted from⁸⁷⁻⁹⁰.

The primary electron beam / sample interactions generate different emitted and transmitted electrons. Elastic and inelastic scattering are atomic processes that are not caused by single

scattering events but more by electron diffusion and energy loss of the electron energy by lateral spreading.⁸⁷⁻⁸⁹ Depending on the electron energy and the sample density, the volume and the penetration depth of the possible interactions vary from 10 nm - 10 μm .⁸⁷⁻⁸⁹ The entirety of the interaction volume is called diffusion cloud.⁸⁷⁻⁸⁹ There, secondary (SE), backscattered (BSE) and Auger electrons (AE), and characteristic X-rays (EDX) are produced, giving lots of information on the topography, the crystal structure, and the elemental and atomic composition of the sample (**Figure 20**).⁸⁷⁻⁹⁰

Part I – Chapter 2.2.3 - Fluorescence microscopy

Fluorescence is the property of atoms and molecules to absorb light with a distinct wavelength and subsequently emit light at a higher wavelength.⁹¹ Molecules that can fluoresce are called fluorophores.⁹¹ Fluorescence can be described using the Jablonski diagram (Figure 21 A).^{91,92} The absorption of a photon by a molecule causes the excitation of an electron from the ground state S_0 to an excited state (S_1). Subsequently, it emits to the ground state (S_0) with a loss of energy (fluorescence emission) (**Figure 21A**).^{91, 93} The normalized absorption and emission spectral profile for the fluorophore Alexa fluoro 555 is shown (**Figure 21B**).⁹⁴ Both spectra comprise a span of wavelengths even if the light source is monochromatic.^{91, 94} The excitation peak is at 555 nm, and the emission peak is at 565 nm.⁹⁴ The difference between the two peaks is called the Stokes shift.⁹¹ The setup of a widefield-fluorescence microscope comprises different parts such as an eyepiece, and a camera where the resulting images can be observed or recorded, a bright light source, usually a mercury, xenon, or metal halide lamp, emission filter sets containing excitation filter, dichroic mirror, and an excitation filter and an objective (**Figure 21C**).^{91, 93} The dichromatic mirror is positioned between the emission -and the excitation filter. The excitation filter transmits light in the range of the excitation of the fluorophore to the sample. The dichromatic mirror transmits the longer wavelength (emission) light towards the detector (camera), while the shorter wavelength (absorption) light is directed to the objective and the sample.⁹¹ The emission filter blocks any wavelengths other than the desired wavelength range before the fluorescent wavelengths form an image.⁹¹ Epifluorescence microscopy illuminates the entire wide field of view, and the fluorescent light has the same path backward the objective (**Figure 21D**). If a sample is illuminated in the opposite direction to the fluorescence wavelength detection, it is called Epi-fluorescence (**Figure 21D**).⁹³ The advantages of epifluorescence are fast detection, deep

penetration depth, and low signal loss. However, a disadvantage is the background fluorescence from objects outside the focal plane or the surrounding media, yielding low-contrast images.⁹⁵ For samples, where the interface between the substrate and the cells is the focus of interest, another technique called total internal reflection microscopy (TIRF) is the best choice. Here, only a very thin layer of fluorescent molecules close to the substrate interface is excited by an evanescent wave (**Figure 21E**).⁹⁶ This evanescent wave, has the same frequency as the excitation light and occurs if the incident light is totally reflected at an interface of two transparent media with a refractive index mismatch. The evanescent wave travels at an angle that the light is completely reflected from the medium with the higher refractive index (substrate, e.g. glass, n_2) to the medium with the lower refractive index (water, n_1).^{96, 97} The critical angle θ_c can be determined with Snell's law (**Equation 4**).

$$\theta_c = \sin^{-1} \left(\frac{n_1}{n_2} \right) \quad (4)$$

Even if the excited light is completely reflected, the evanescent wave can propagate into the sample and excite only fluorescent molecules in the first hundreds of nanometers of the interface (**Figure 21E**).⁹⁷⁻¹⁰¹

The laser beam (illumination, green, **Figure 21E**) focuses on the objective's rear aperture.⁹⁶ A total internal reflection is obtained if the angle of incidence is above the critical angle θ_c .⁹⁶ The advantages of TIRF microscopy are the rapid detection, the high resolution at the interface, and the low background fluorescence.^{95, 96} The disadvantage of this technique is the small penetration depth of the evanescent wave.^{95, 96} Only the first few 100 nm can be measured at high resolution.^{95, 96}

Another fluorescence microscopy method is needed for thick or three-dimensional samples, confocal laser scanning microscopy (CLSM).⁹⁵ CLSM uses a focused laser beam (point scanning) for optical sectioning.¹⁰² This means that with the CLSM technique, it is possible to extract fluorescent light from a single plane in a thick sample. The fluorescent light passes a pinhole before it is detected. The pinhole allows only light from the focal plane to pass; all other light is excluded. (**Figure 21F**).¹⁰² By stacking single plane CLSM images using different focal planes in the z-direction, obtaining a 3D image of the sample is

possible.¹⁰² The advantages of CLSM are that no out-of-focus background can be detected, and sectioning along the z-axis is possible, however, CLSM is slow in detection.^{95, 102}

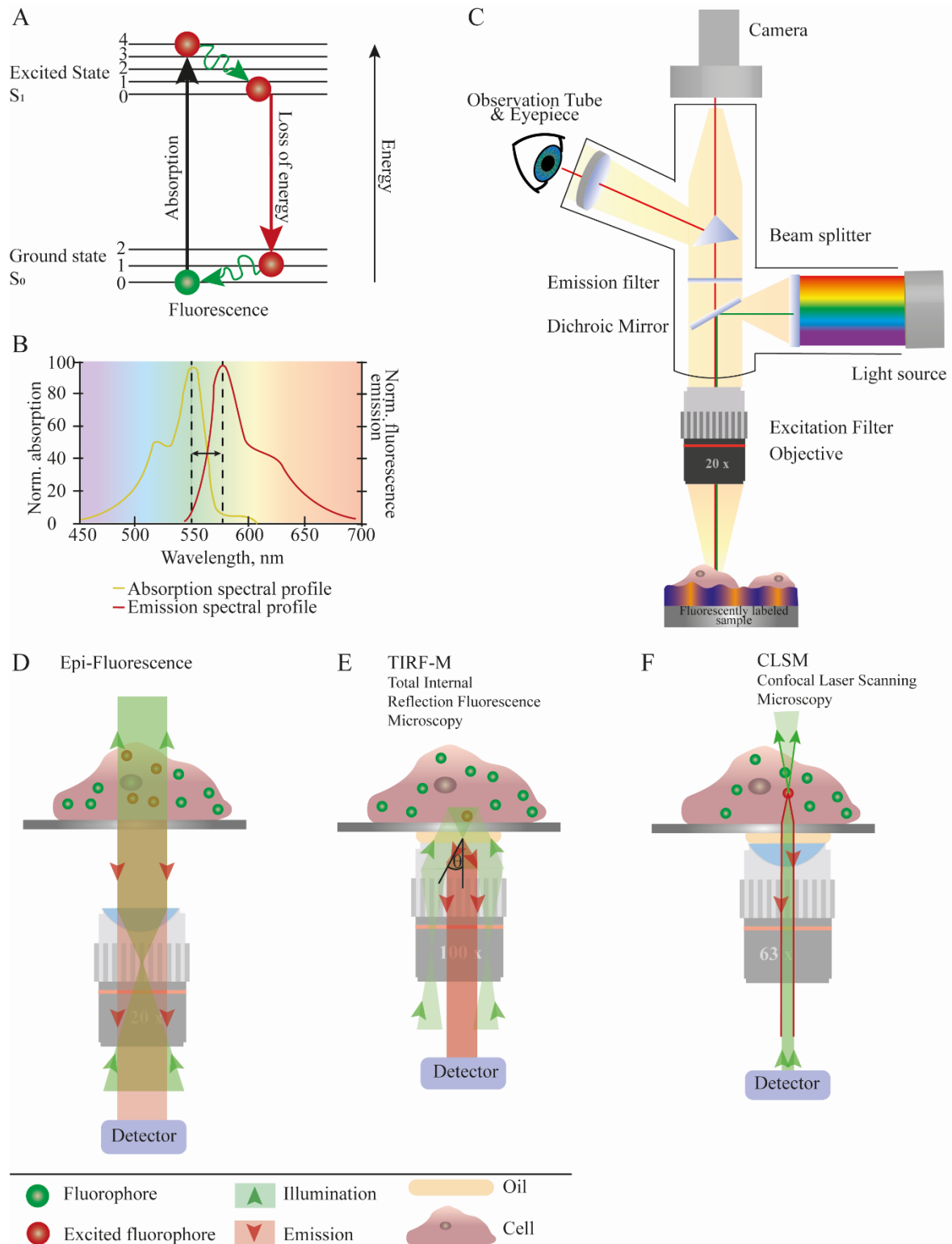


Figure 21: Fluorescence is the property of molecules to absorb light with a distinct wavelength and to emit light at higher wavelengths. In this process, the electron jumps from the ground state S_0 to an excited state (S_1) and then subsequently emits with a loss of energy back to the ground state. (A) The fluorophore absorption profile of Alexa fluoro 555 is

shown as an example. The difference between the absorption spectral profile and the emission spectral profile is called the Stokes shift. (B) The setup of a standard widefield fluorescence microscope (Epi) is shown in (C). The simplified light paths and the penetration of the light for Epi-Fluorescence (D), TIRF-M (E), and CLSM (F) are depicted in (D), (E), and (F). Excited fluorophores are depicted in red, non-excited fluorophores in green. Epi-Fluorescence penetrates the whole cell, and all fluorophores in the light path are excited (D). Using TIRF-M, the incidence angle of the light can be varied to achieve total internal reflection. This leads to the effect that only the fluorophores in the first 200 nm of the cell are excited (E). CLSM comprises the variation of the penetration depth. The laser can scan the cell layer by layer using galvanometer mirrors and excite different fluorophores by varying the scanning depth. Figure adapted from^{91, 92, 94, 98-106}.

Part I – Chapter 2.2.4 - ζ -Potential

Measuring ζ -Potential or the electrokinetic potential (unit, mV) is an important method to characterize the surface functionality and stability of colloidal particles. The primary obtained information is the surface charge depending on the properties of the surrounding medium like pH and ionic strength of the buffer. If a particle comes into contact with the surrounding liquid, the functional groups on the surface will interact with the ubiquitous liquid resulting in a surface charge caused by the attraction of oppositely charged ions. The arrangement of these so-called counter ions around the particle surface is called the electrochemical double layer. The ζ -potential is the sum of the surface potential of the particle surface and the accumulated double layer (**Figure 22**). This electrochemical double layer consists of a stationary and a diffuse layer (**Figure 22**). The stationary layer is formed directly at the particle surface, and the oppositely charged ions are immobilized due to strong interactions with the particle surface, also called Stern layer. Connected to this layer is the diffuse layer, where the ions are less attracted by the particle surface, and the distance to the surface is higher (**Figure 22**). In this layer, the ions can move. The border between these two layers is called the slipping lane. This is the part of the electrochemical double layer that contributes to the net charge of the particle. Therefore, the potential at this plane is defined as ζ -potential.^{22, 107-110}

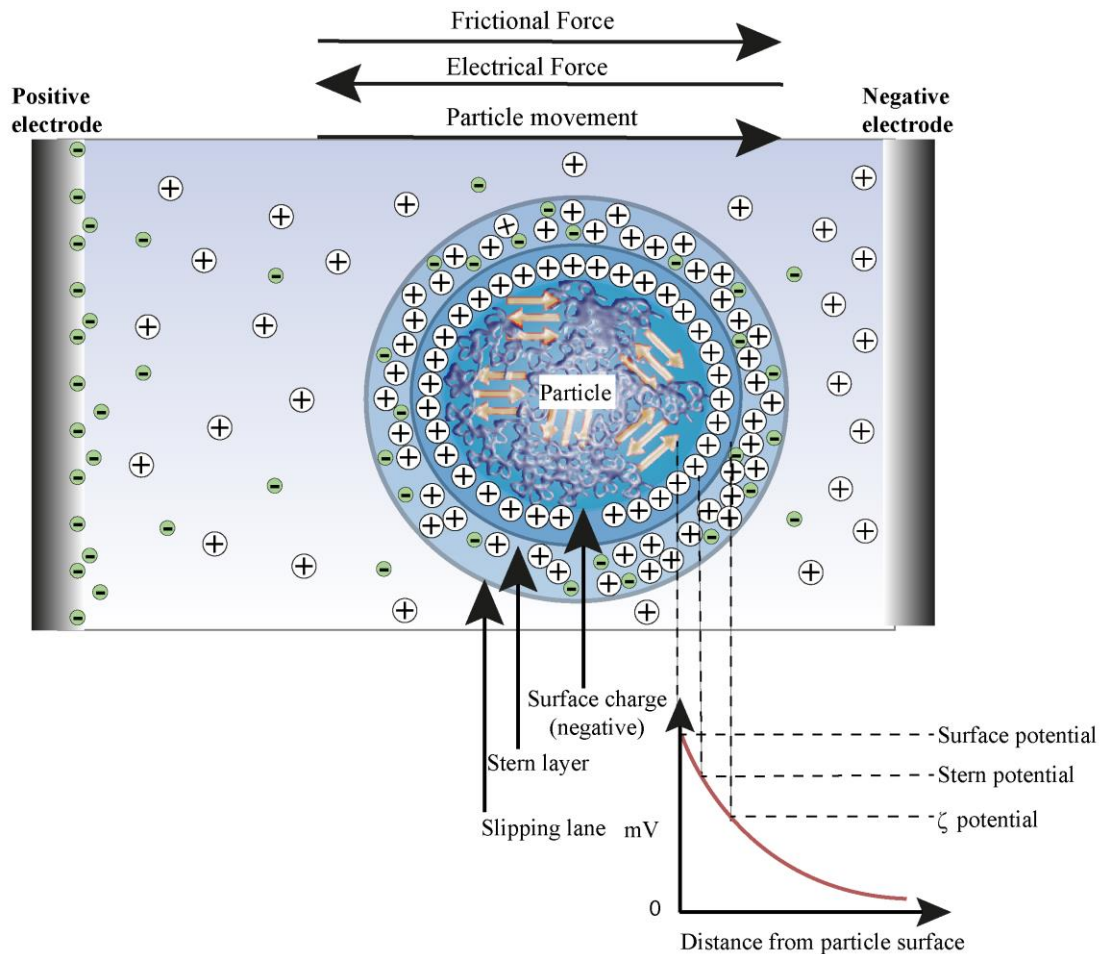


Figure 22: A negatively charged (spider silk) protein particle suspended in an aqueous buffer. The negatively charged particle is migrating towards the positive electrode. Figure adapted from ¹¹¹.

Part I – Chapter 2.2.5 - Sodium dodecyl sulfate-polyacrylamide gel electrophoresis

Sodium dodecyl sulfate-polyacrylamide gel electrophoresis (SDS-PAGE) separates mixtures of proteins by molecular weight.^{112, 113} The negatively charged detergent SDS denatures proteins and binds to them. Therefore, the original charge is overlarge. The proteins are less tangled and comprise a uniform negative net charge (**Figure 23A**).^{112, 113} The now negatively charged proteins migrate towards a positive electrode proportional to their molecular weight with different velocities if an electric field is applied (**Figure 23**).^{112, 113} A copolymerization of acrylamide monomers and a crosslinker results in mechanically and chemically stable polyacrylamide gels in which the pore size can be controlled by the total acrylamide concentration the concentration of the crosslinker.¹¹³ In the stacking gel (4.5 % acrylamide), which comprises larger pores and lower pH, the proteins are applied to the gel before the electric field is turned on (**Figure 23BII**).^{112, 113} After applying the

electric field, the proteins line up in the stacking gel and enter at the same time the resolving gel (10-15 % acrylamide), which comprises smaller pores and higher pH independent of the molecular weight of the protein.^{112, 113} The tighter polyacrylamide mesh slows the proteins down and separates them by molecular weight (**Figure 23BIV**).^{112, 113} Bigger proteins get tangled in the small pores and need more time to travel through the tight mesh.^{112, 113} A molecular weight ruler, also called ladder, is also applied to the gel to analyze the molecular weight of the sample in comparison to itself.^{112, 113} After finishing the separation process, the gel needs to be stained to make the separated band visible.¹¹²⁻¹¹⁵ Commonly used methods are Coomassie brilliant blue and silver staining.¹¹⁴⁻¹¹⁶ The number of bands will give you the number of different proteins in the sample, which is an indicator of the purity of the sample. The height of the bands compared to the ladder indicated the molecular weight of the protein.¹¹²⁻¹¹⁶

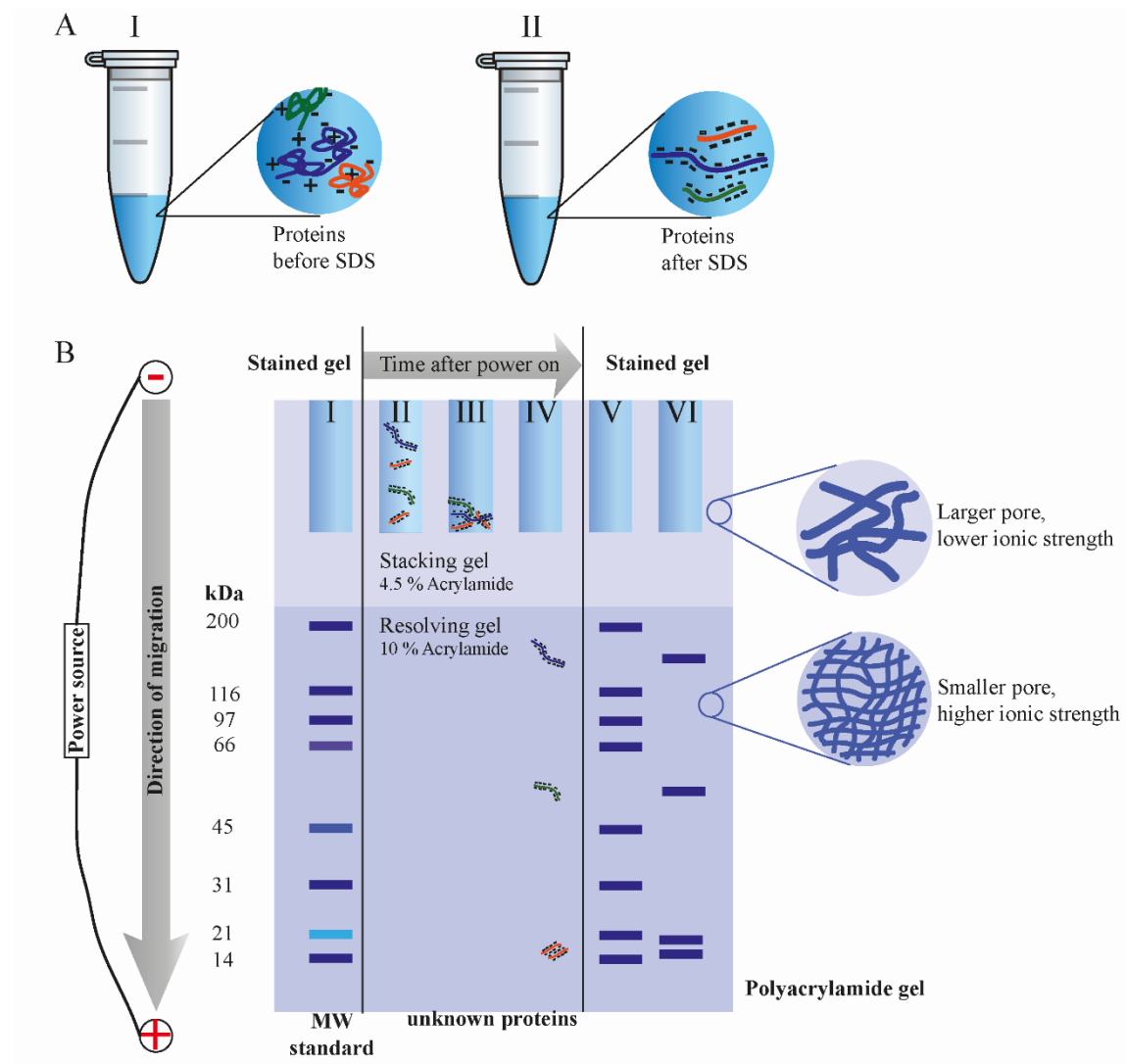


Figure 23: A mixture of proteins are in solution with a different charge without consistency (A-I) is mixed with sodium dodecyl sulfate (SDS). The negatively charged SDS binds

evenly because of its long aliphatic tail to the protein. The SDS has a strong binding affinity; thus, the original charges of the protein are overpowered upon the addition of SDS. A direct charge/length relationship is established for most proteins (A-II). After adding SDS to the protein mixture, the solution can be applied to a polyacrylamide gel. A schematic setup of a polyacrylamide gel is shown (B). The upper part of the gel is the so-called stacking gel. Here, the protein mixture is applied into one pocket of the gel. This polyacrylamide gel has larger pores and a lower ionic strength than the lower part of the gel, the resolving gel. Here, the acrylamide concentration is increased, and thus the pores are smaller and comprise higher pH. In general, all polyacrylamide gels are running with molecular weight (MW) standard sample. It is a molecular ruler for the unknown protein samples (B-I). The negatively charged proteins travel to the cathode if an electric field is applied. In the beginning, the proteins are collected in the stacking gel in the looser polyacrylamide mesh (B-II-III). Then all proteins enter the resolving gel simultaneously and separate, dependent on their molecular weight. Bigger molecules get entangled in the smaller pores of the resolving gel. Smaller molecules can pass the gel faster. After finishing the separation, the separated proteins can be visualized upon staining with Coomassie brilliant blue or silver staining (BI; V-VI). Figure was created based on ¹¹²⁻¹¹⁶.

Part I – Chapter 2.2.6 - Fourier transform infrared spectroscopy

Fourier transform infrared spectroscopy (FTIR) is a non-destructive, vibrational spectroscopy method commonly used to characterize materials concerning structure, orientation, composition, and dynamics.^{110, 117} In IR-spectroscopy, radiation in the mid-infrared range is used (**Figure 24A**). The unit commonly used in FTIR for the wavenumber is the reciprocal of the wavelength (cm^{-1}). Two regions are mainly used in FTIR spectroscopy, the group frequency region ($\sim 4000 \text{ cm}^{-1} - 1400 \text{ cm}^{-1}$) and the fingerprint region ($\sim 1400 \text{ cm}^{-1} - 400 \text{ cm}^{-1}$) (**Figure 24A**).^{110, 117} The principle of FTIR spectroscopy is that a sample is irradiated with polychromatic light. This means all wavenumbers at the same time. This means that the sample absorbs energy.^{110, 118} These energy equivalents in the range of wavelength corresponds to the energy of a vibration mode of a compound.^{110, 118} These modes can be symmetric or asymmetric stretching modes or bending modes (**Figure 24B**).^{110, 118} Four different experimental setups were used: the grazing angle attenuated total reflection (GATR) - FTIR, the single beam single reflectance ATR - FTIR (SBSR ATR - FTIR), transmission (Trans -) FTIR and Dichroic FTIR (**Figure 24B-F**).¹¹⁰ GATR-FTIR is the most sensitive method because the GATR-crystal comprises a bigger area than the usual ATR crystal. In general, a distinction is made between ATR and transmission IR spectroscopy. For the attenuated total reflection IR spectroscopy (ATR), IR light passes through the Ge-crystal, interacts with the crystal/sample interface, and propagates as an evanescent wave along the surface.^{110, 119, 120} However, for the transmission technique, the IR beam directly passes the sample. Some wavelengths will be

absorbed by the sample, and the remaining wavelengths will be transmitted to the detector (**Figure 24E**). The grazing incidence IR concept is based on IR light reflected on the surface of the sample with an angle near the grazing incidence.¹¹⁰ The result is a standing wave formed by the superposition of the incoming and reflected IR light.¹¹⁰ Therefore, the formed electric field is parallel polarized to the surface normal.¹¹⁰ This means that GATR-FTIR works only with the E_z component of the electric field (**Figure 24F**).¹¹⁰

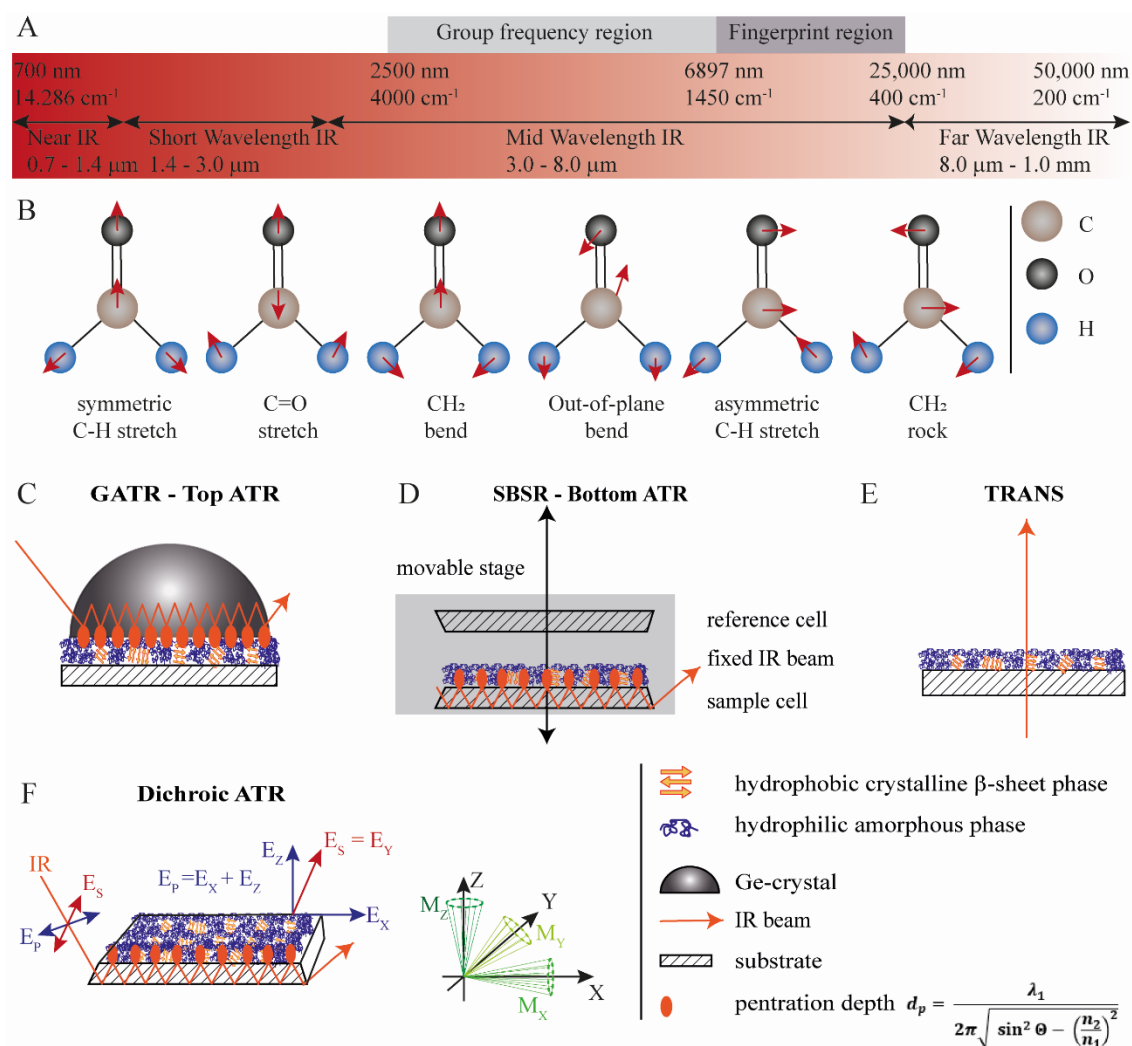


Figure 24: The infrared wavelength region with corresponding wavenumbers is shown (A). The fingerprint region reaches from 400 cm^{-1} to 1450 cm^{-1} , the group frequency region from 1450 cm^{-1} to 4000 cm^{-1} .¹¹⁰ The different vibration modes of molecules are exemplarily shown for formaldehyde (B).¹¹⁰ The grazing incidence angle attenuated total reflection (GATR) IR principle is shown. The surface of a coating is measured at the interface air/coating. The penetration depth of the IR beam is marked (C).¹¹⁰ The single-beam-sample-reference (SBSR) cell is an individual setup from the IPF in Dresden. Here, the sample is directly coated onto the sample cell, and the IR beam can penetrate the sample cell so that the bottom of the film can be measured.¹²¹ The IR beam penetrates the whole sample in the case of transmission measurements (E).¹¹⁰ Dichroic ATR-FTIR is a method where parallel (p) and vertical (s) polarized IR light is measured individually. The parameter which can be determined with this method is the so-called dichroic ratio RT.

This is the ratio of the integrated absorbances of p- and s-polarized light (F). Figure created based on ¹¹⁰.

The single-beam-sample-reference FTIR (SBSR) is a special setup to simultaneously measure ATR-FTIR in-situ for sample and reference measurement (**Figure 24D**).¹²¹ The orientation of polymeric films can be determined with IR dichroism. IR dichroism is defined as different absorption of parallel (p) and vertical (s) polarized IR light. The determined parameter is the so-called order parameter R^T which is the ratio between the integrated absorbances of p- and s-polarized light.¹¹⁰ An order parameter of one reflects perfect parallel axial orientation.¹¹⁰ In contrast to an order parameter of zero, which implies no order. An order parameter of 0.5 reflects a perfectly vertical orientation.¹¹⁰

Part I – Chapter 2.2.7 - Circular dichroism

Circular dichroism (CD) spectroscopy is an analytical absorption spectroscopy technique based on circularly polarized light to investigate molecules with chirality through their optical activity. CD-spectroscopy is a widely used method for structural analysis of secondary structure-forming molecules and protein conformation analysis, based on the absorption difference of right - and left circular polarized (RPL/LPL, **Figure 25A**) light through an asymmetric chromophore. The unequally absorbed left- and right-handed circular polarized light can be measured and quantified. Chiral molecules which are optically active absorb preferentially to one direction of RPL/LPL.¹²²⁻¹²⁴

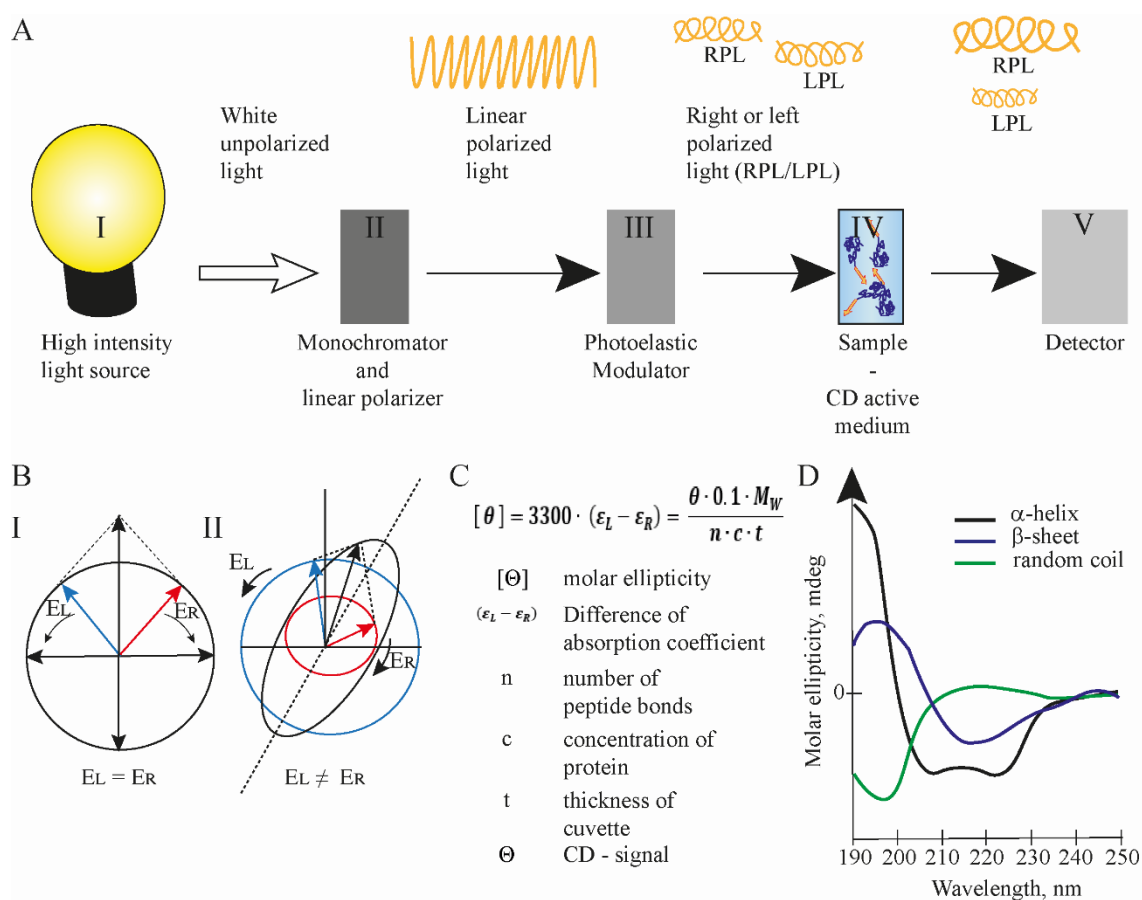


Figure 25: A) Schematic setup of a CD-spectrometer: White unpolarized light is generated from a high-intensity light source (I). The light is transformed into single wavelength, linear polarized light passing a monochromator and a linear polarizer (II). The photoelastic modulator splits the light into right or left polarized light (RPL/LPL) (III). The RPL/LPL passes the CD active medium (IV). Due to the chiral molecules preference, the proportion of RPL or LPL increases, and the photomultiplier (V) transforms the signal into a voltage, from which the ellipticity is calculated. The linearly polarized light can be seen as a superposition of RPL/LPL. If RPL and LPL are absorbed equally by the sample, then no CD signal is detectable (B-i), but if RPL/LPL are absorbed unequally, then ellipticity can be measured as a function of wavelength. But this ellipticity is still dependent on the sample concentration, the thickness of the cuvette, the number of peptide bonds, and the CD signal.

According to the Lambert-Beer-Law, the concentration-independent molar ellipticity $[\theta]$ can be calculated with the equation (C). Also, the relationship between the differential absorption coefficient of RPL/LPL and the molar ellipticity is given. D) Representative CD-spectra of polypeptides and proteins with α -helical (black), β -sheet, and random coil (green) conformation are shown. The curve characteristics for each secondary structure element can be found in table 1. Figure created based on ¹²⁴.

Perpendicular to the propagation direction of a light beam oscillates electromagnetic waves containing electric and magnetic field components. The polarization of the electromagnetic wave is determined by the direction of the components. Electric and magnetic fields oscillate in many different directions if the light is not polarized (white). If the light propagates along a single plane, it is referred to as linear polarized light. A 90° phase difference of two electromagnetic wave planes, rotating as the light beam propagates, is defined as circular polarized light. A symmetrical molecule will adsorb left (E_L) or right-handed (E_R) components of the electromagnetic wave with the same intensity (**Figure 25BI**). Optically, respectively, CD-active molecules can be described by their chirality or molecule structure asymmetry, e.g., each peptide bond provides a chiral C-atom. Depending on the refractive index of the CD-active medium, the velocity of the light passing through will change (Figure 25 A-IV \rightarrow V, RPL/LPL). Therefore, E_L and E_R of circular polarized light will be absorbed unequally, resulting in elliptically polarized light (**Figure 25BII**). The magnitude of CD has measured as an angle parameter called ellipticity (θ , [mdeg]). To obtain a concentration (c) independent specific value for the CD-active medium, the molar ellipticity $[\theta]$ can be calculated using the formula in **Figure 25C**. The differential absorption of left and right circularly polarized light is the ellipticity, which is obtained from a measurement with a CD instrument (**Figure 25A**). ($\epsilon_L - \epsilon_R$) is the difference of the molar extinction coefficients, and due to historical reasons, CD data is presented as molar ellipticity. The formula in **Figure 25C** gives the relationship of $[\theta]$ and ($\epsilon_L - \epsilon_R$).¹²²⁻¹²⁴

CD-spectroscopy is a well-established method in secondary structure analysis of proteins and polypeptides. Using CD spectra can give an estimation in which proportion the structure elements are present in the protein. Representative, ideal CD-spectra for α -helical (black), β -sheet, and random coil (green) conformations are depicted in **Figure 25C**. Key points for the estimation of a specific secondary structure are given in **Table 1**.¹²²⁻¹²⁴

Table 1: Maxima and minima for certain secondary structure elements in CD-spectra.^{122,}

123

Secondary structure element	Maximum/Maxima, nm	Minimum/Minima, nm
α-Helix	192	208 and 222
β - sheet	196	218
<i>random coil</i>	212	195

The schematic setup of such a CD-spectrometer is depicted in Figure 26A. White unpolarized light from a high-intensity light source (A-I) passes a polarizer and a monochromator (A-II) and is then linear polarized. A single wavelength can pass the photoelastic modulator (A-III), converting the linear polarized light into LCP and RCP. As the LCP/RCP passes the CD active medium (A-IV), the circularly polarized light absorbs preferentially in one direction, both components are detected in the photomultiplier (V) and generate a voltage which is then transferred into the ellipticity for each wavelength.¹²²⁻¹²⁴

Part I – Chapter 2.2.8 - Quartz crystal microbalance with dissipation monitoring

The quartz crystal microbalance with dissipation monitoring (QCM-D) is a surface-sensitive, label-free technique based on a quartz sensor that measures mass changes at the surface of a QCM-D sensor with a resolution in the nanoscale (**Figure 26A**).^{125, 126} This sensor is a piezoelectric sensor which can be modified with proteins and polymers to analyze the adsorption behavior onto these materials.^{127, 128} Therefore, the sensor can be oscillated at a specific frequency by applying a voltage. With the assumption that the deposited mass on the quartz behaves like the quartz crystal itself and the total adsorbed mass comprise only 2 % of the QCM-D sensor weight, the resonant frequency changes linearly due to a mass accumulation at the quartz surface (**Figure 26B**, Δh reflects the change in thickness). The relationship was stated first by Sauerbrey in 1959.¹²⁵ With the Sauerbrey equation, the mass of a rigid adhesive layer can be calculated (**Figure 26 G**). Here, C stands as a mass sensitivity constant, which depends on the properties of the used quartz crystal. n reflects the number of the frequency overtone, which is always an odd multiple of the fundamental frequency (1, 3, 5, 7...).¹²⁹ Respectively also the thickness of the adsorbed layer can be determined using the ratio of calculated mass from the Sauerbrey equation with the effective density of the adsorbed layer ρ_{eff} (**Figure 26G**).¹²⁹⁻¹³¹ Therefore, mass adsorption can be monitored *in-situ* (**Figure 26B**).¹²⁷⁻¹²⁹ In combination with the changes in dissipation D or Δd (**Figure 26G**), this method provides information about the

state of molecular layers bound to the sensor surface, the relating mass, thickness, and viscoelastic properties of the adsorbed layer.^{127, 128, 129} Mathematically, the dissipation D can be described by the ratio of the dissipated energy during an oscillation circle E_{lost} and the total energy during an oscillation circle E_{stored} (**Figure 26G**).¹²⁹⁻¹³¹ By turning off the voltage, one oscillation cycle is finished, and the decay curve can be recorded.¹²⁹⁻¹³¹ The adsorption of rigid particles leads to a longer decay curve of the (**Figure 26C, E**) than softer molecules, e.g., proteins (**Figure 26D, F**).¹²⁷ The energy loss respectively the dissipation is smaller for rigid layers than for soft layers (compare green curves, **Figure 26C, D**).^{127, 129}

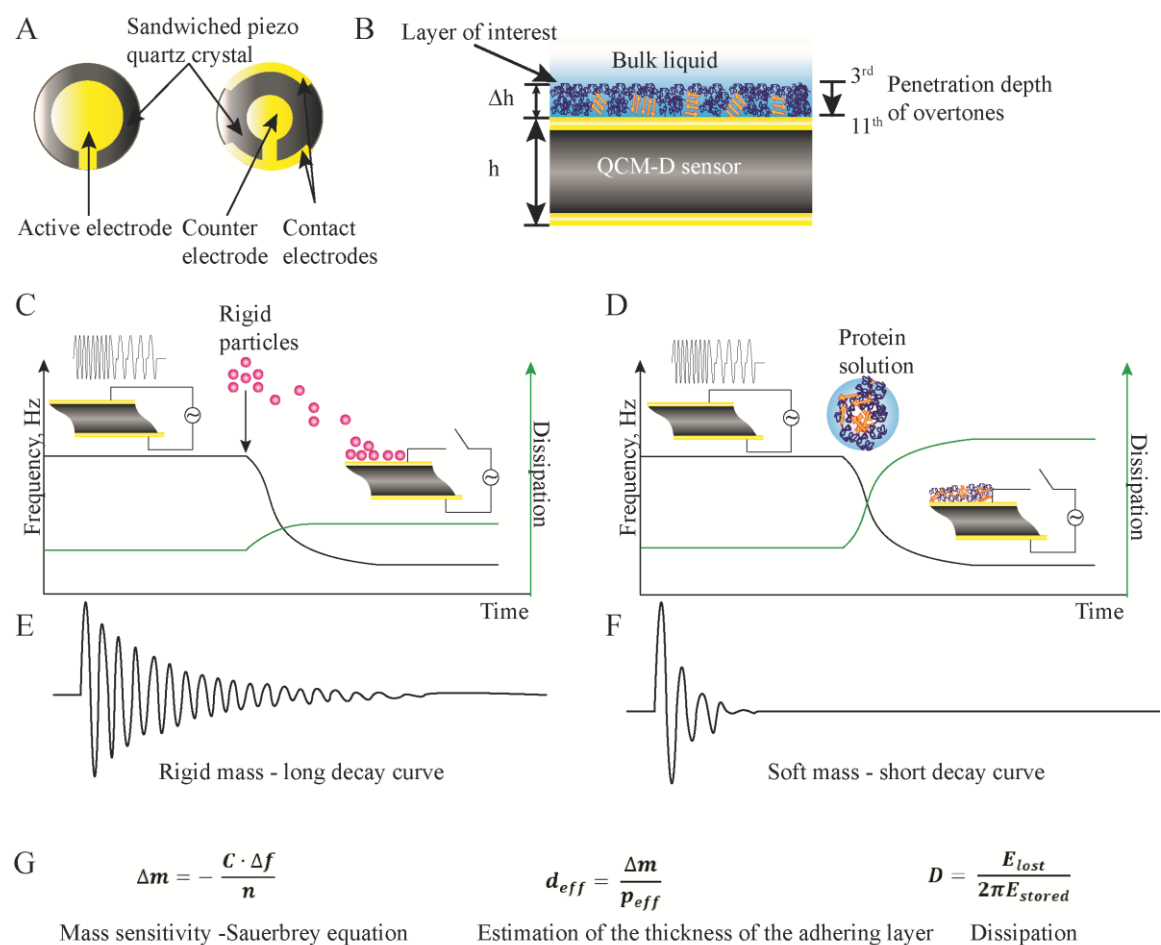


Figure 26: Schematic illustration of a QCM-D sensor chip: The active and counter electrode sandwich a piezo quartz crystal (A). The frequency changes if mass (layer of interest) is absorbed to the sensor surface. The penetration depth of the different overtones of the fundamental frequency increases with increasing odd numbers (B). The course of frequency and dissipation in situ for the adsorption of rigid particles (C) follow the Sauerbrey equation (G). In contrast to the course of frequency and dissipation for rigid particles, the course for Δf and ΔD of soft materials like proteins are displayed in (D). The resulting decay curves are shown below each diagram (E for C) and F for D). The relevant equations for the determination of adsorbed mass (Sauerbrey equation), the estimation of

the thickness of the adsorbed layer, and the dissipation are shown in (G). Figure adapted from ^{125, 126, 129, 132}.

Part I – Chapter 2.2.9 - Maskless lithography

Maskless lithography is short for solid photomask-free photolithography and provides particular advantages compared to other lithography techniques.¹³³⁻¹³⁵ It is a cheap and fast technology because the applied mask is digital and can be transferred to the photoresist using a system including an μ -LCD matrix, a filter, and a focusing lens (**Figure 27A**).¹³³⁻¹³⁵ While ordinary photolithography uses structured masks that are fixed to the photoresist layer to project the desired structure onto the photoresist during exposure, maskless photolithography uses a μ -LCD matrix. This is used to project the desired structure onto the photoresist layer by darkening individual pixels using the digital mask previously designed in a graphics program. **Figure 27A** shows the structure of the so-called SmartPrint® device. The μ -LCD matrix first darkens the light on the areas where black pixels are present in the designed "digital mask" and passes through the other areas. A monochromatic filter then filters out the wavelengths that are not in the blue region of the spectrum since the light in the wavelength range of 430-470 nm is needed to expose the photoresist layer. The generated image is focused onto the photoresist layer in the desired size via the objective lenses (**Figure 27B**).¹³⁶ By using different objective lenses, the size of the produced patterns can be changed.¹³⁶ For the 1x objective, one pixel represents $\sim 7 \mu\text{m}$. Using the 2.5 x objective, one pixel represents $\sim 2 \mu\text{m}$.¹³⁶ The production of patterned photoresist is depicted in **Figure 27C**. First, a homogenous photoresist layer needs to be prepared using spin-coating. Then, the photoresist is exposed to the digital masking using the Smartprint device.¹³⁶ Following exposure, immersing the exposed photoresist to a developer solution removes the exposed portions of the photoresist. After developing the photoresist in the developer solution, the remaining photoresist is the master for preparing PDMS stamps. This technique makes it possible to generate 3D patterned stamps quickly with various geometries and sizes in the micrometer range.¹³⁶

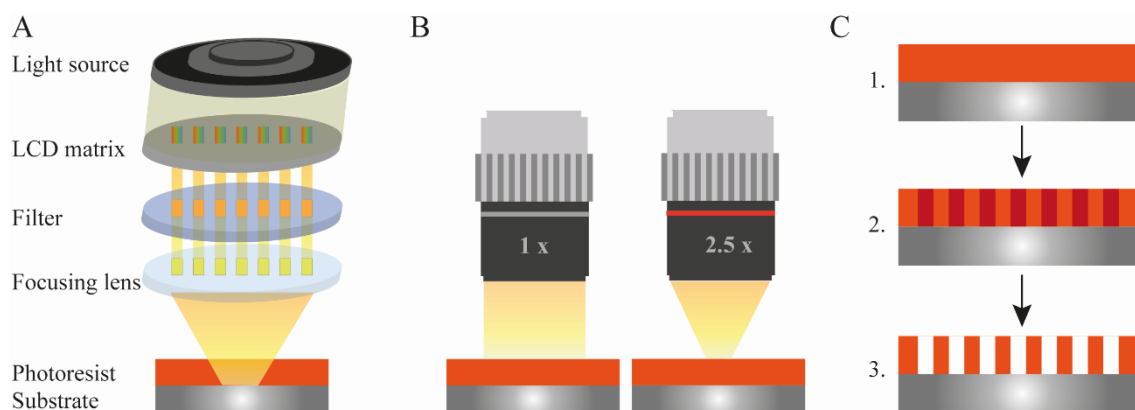


Figure 27: The maskless lithography device (Smartprint®) setup consists of a light source that passes an LCD matrix, a filter, and gets focused by a focusing lens and directly exposed to a photoresist (A). The device comprises two different objectives. The 2.5x objective narrows the light beam compared to the 1x objective. This results in smaller features while using the 2.5x objective (B). The processing of patterning photoresists is schematically depicted in (C). The photoresist should be a homogeneous coating (1), then the photoresist coating is exposed to the light beam, which exposes the areas from the digital mask (2). The exposed photoresist is immersed in the developer solution, and then the exposed parts will be removed, and the remaining photoresists reflects the pattern of the digital mask. Figure adapted from ¹³⁶.

Part I – Chapter 2.2.10 - Water contact angle measurement

The water contact angle is geometrically defined as the angle formed by a water droplet in contact with a flat surface.¹³⁷ Three phases come in contact at the interface of the droplet: the solid phase, which represents the substrate (S); the liquid of the droplet (L), and the surrounding gas at an equilibrium state (G) (**Figure 28A**).^{137, 138} Measuring a sessile drop on a solid surface without changes of the three-phase boundary, the measurement is defined as static.¹³⁷ This is the most commonly used method to determine quick, straightforward, and quantitative the wettability of a substrate. The three phases are assumed as thermodynamically stable, and each interface comprises a free energy (γ_{SG} , γ_{SL} , and γ_{LG}).^{137, 138} With these assumptions, it is possible to use the Young-Laplace equation (**Figure 28A**) to calculate the water contact angle θ .¹³⁷⁻¹³⁹ The resulting angle is a quantitative measure of the wettability of a substrate by a liquid, here a water droplet. A water contact angle of 0° is defined as complete wetting.¹³⁷⁻¹³⁹ Every contact angle above 0° up to 180° comprises partially wetting. However, it is common sense that contact angles above 90° are regarded as bad wetting behavior and specify the underlying material as

hydrophobic. The theoretical limit of the contact angle is 180° , which describes the non-wetting state (**Figure 28A**).¹³⁷⁻¹³⁹

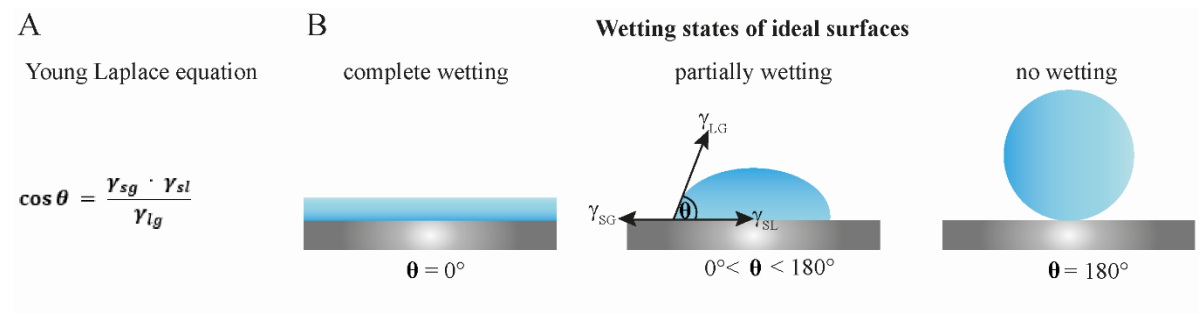


Figure 28: The Young Laplace equation describes the relation between the specific surface energy γ_{SG} of a substrate, a water drop γ_{SL} and the surface tension of the water drop γ_{LG} and the corresponding contact angle θ (A). Three ideal degrees of wetness exist, the partially, the complete and the non-wetting state. A water contact angle of 0° defines the complete wetting. A water contact angle between 0° and 180° comprises partially wetting. No wetting state is defined with a water contact angle above 180° (B). Figure was created based on^{137, 138, 140}.

Part I - Chapter 3 – Synopsis and Aim of the thesis

Part I – Chapter 3.1 - Aim of the thesis

Replacing petroleum-based polymers in medical and technical applications with biocompatible, biodegradable materials from sustainable sources is nowadays a major challenge. Spider silk-inspired materials are promising candidates, as they show good biocompatibility, biodegradability, and excellent mechanical properties. One possibility to obtain such materials is based on the recombinant production of spider silk proteins. This production method offers the advantage that the properties of spider silk can already be adapted at the genetic level. For example, different charges and/or cell-specific binding motifs can be introduced. Furthermore, these recombinant spider silk proteins can be produced on a large scale with consistent quality. Several variants were investigated in this thesis to extend the applicability of recombinant spider silk proteins comprising different amino acid sequences, net charges, and modifications at the C-terminal end of the protein (e.g. cell-binding motifs). The main focus was on coatings made of spider silk-inspired materials and how they can be applied in the biomedical field. A fundamental understanding of how these spider silk-inspired materials assemble is essential to find the most suitable application. Therefore, assembly studies of an already established, negatively charged variant were performed to understand the structure-property relationship of recombinant spider silk proteins. Furthermore, coatings made of methacrylated poly-L-Glutamic acid (PLGMA) and poly-L-Lysine (PLLMA) were produced using a newly developed polymerization method for synthetic polypeptides. Both coatings were extensively tested concerning the resulting coating thickness, secondary structure, and surface properties. Assembly mechanisms for both systems are proposed in this thesis.

One main goal of improving biomaterials is to make them specific and adjustable. However, the most crucial factor is the interaction of the material's surface with the surrounding biological environment. Long-term use of implants, e.g., breast implants, or medical tubings, e.g. catheters, for short usage can lead to complications due to host responses to the biomaterial. Such pathophysiological complications include scar tissue formation and encapsulation of the material in the body, which often occurs in periprosthetic capsular fibrosis with silicone breast implants. This could lead to severe consequences, such as sepsis or death. The crucial step in the body's response to foreign materials is the formation of a protein layer on the surface of the material, the so-called

protein corona, within the first moments after coming into contact with the material. Spider silk-inspired materials could be suitable to trick the host organism's immune response.

Therefore, an in-depth analysis of biocompatibility, bioselectivity, biodegradability, and surface properties of recombinant spider silk morphologies/assemblies (films, particles) was performed. Based on these results, recombinant spider silk proteins with tailored properties were categorized into different groups like bioinert or bioactive, promoting or preventing blood clotting, and fast or slow biodegradation. Specific applications were proposed. Therefore, parts of this work aimed to investigate the blood coagulation behavior or cell adhesion by introducing different peptide motifs like the cell-binding motifs RGD, the biomineralization motif E₈G, or the cell-penetrating motif R₈G or non-specific interactions (topography and wettability). One promising method is introducing specific cell adhesion peptides, such as RGD, to spider silk proteins by molecular cloning. This modification of the proteins is advantageous because the produced variants can be used directly after purification. After film production, possible influences of the functionalization on the assembly behavior, structure, wettability, roughness, and cell adhesion were investigated.

Furthermore, the efficiency of the differently charged recombinant spider silk proteins or the introduced RGD sequences should be analyzed using in vitro cell culture. The cell adhesion behavior on the neutrally charged variants eADF3(AQ)₁₂, eADF3(AQ)₂₄, and eADF4(Ω16), the positively charged eADF4(κ16), and the negatively charged eADF4(C16) were tested using fibroblasts, neuronal cells, and keratinocytes. The eADF4-derived and RGD-modified variants were further tested with human-induced pluripotent stem cell-based cardiomyocytes. Flat and patterned films made of eADF4(C16) were tested with eight different cell lines, namely human skin fibroblasts BJ, mouse Balb 3T3 fibroblasts, human osteoblasts MG63, rat neuronal cells B50, murine neuronal cells NG108, rat Schwann cells RN22, murine myoblasts C2C2 and human keratinocytes HaCaT. The arrangement, shape, and orientation of the cells often determine their function. Therefore, topographical patterns were introduced in silk films. Since surface structures alone can decisively improve the interaction between cells and biomaterials, patterned eADF4(C16) silk films were prepared. In addition to biochemical signals and topography, the hydrophobicity of the surface influences cell adhesion. Thus, coatings of different spider silk variants with different wettabilities were prepared and further characterized. The last part of the thesis deals with materials of a synthetic origin and tries to mimic the

extraordinary properties of silk materials. An overview and assessment of synthetic polymers that aim to mimic spider silk properties are given in this part. Also, a novel method for producing synthetically cross-linked polypeptide films is provided, and they are investigated concerning properties and biodegradability.

Part I – Chapter - 3.2 Synopsis

This thesis contains eight publications presented in **Parts II-IV**. Their common theme is the assembly of spider silk-inspired materials to yield in coatings, to understand their assembly mechanisms, the structure-property relationship, and to adjust cell adhesion by chemical or physical modifications of these materials in a controllable manner.

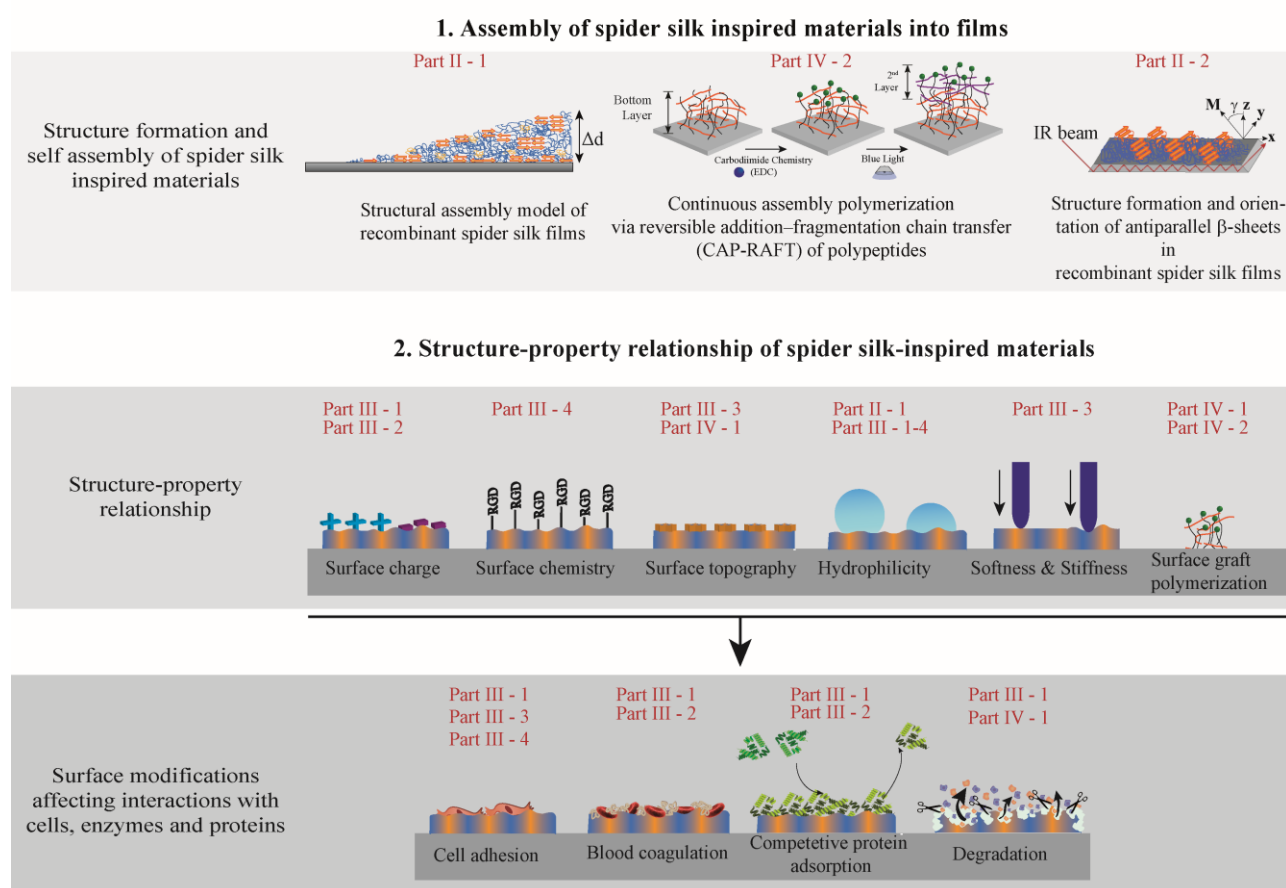


Figure 29: Structure of the thesis. This thesis is divided into two main topics, the assembly of spider silk-inspired materials into films and the structure-property relationship of spider silk-inspired materials. The first part is developing a thickness-dependent structural assembly and phase separation model for recombinant spider silk proteins from the nanoscale up to the microscale (Part II-1) and studying the structure formation of recombinant spider silk proteins and the orientation of β -sheet crystals within these films (Part II-2). A method for continuous assembly polymerization via reversible addition-fragmentation chain transfer (CAP-RAFT) of polypeptides into crosslinked film with

tunable layer thickness is developed (Part IV-2) as well. The second main topic is the structure-property relationship of the spider silk-inspired materials concerning various surface properties and modifications and their effects on degradation biocompatibility, such as blood coagulation behavior, protein adsorption, and cell adhesion behavior.

The first part of the thesis is divided into two chapters (**Part II Chapter 1** Ultra-thin spider silk films: Insights into silk Assembly on surfaces and **Part II Chapter 2** Dichroic FTIR spectroscopy characterization of β -sheet orientation in spider silk films on silicon substrates). The structure formation and the self-assembly of recombinant spider silk films made of the negatively charged recombinant spider silk protein variant eADF4(C16) concerning different film thicknesses from the nanoscale (3-4 nm) to the microscale (1 μ m) are investigated in detail. With this study, the phase separation of the hydrophilic, amorphous parts (GGPXX) and the hydrophobic crystalline parts (polyalanine blocks) of the recombinant spider silk protein are investigated. A thickness-dependent phase separation model is proposed based on the resulting secondary structure proportions, especially the β -sheet proportion and the water contact angles. The conformational changes during post-treatment with methanol are investigated in both studies concerning β -sheet content.

Furthermore, in the second chapter, the orientation of the β -sheet crystals in nano- and microscale eADF4(C16) films is analyzed concerning the order parameter of the β -sheet structures concerning uniaxial orientation. In-depth FTIR analysis, namely dichroic ATR - and TRANS-FTIR spectroscopy, as well as lineshape analysis, the assignment of the secondary structure elements of the amide I band to specific vibrations, and the transition dipole moment directions of the β -sheets were used to calculate the experimental dichroic ratio. Additionally, the second study provides an analytic concept to analyze the out-of-plane orientation of oriented natural and synthetic proteins and polymers.

The third part of this thesis contains two submitted publications and two published articles concerning the bioselectivity of recombinant spider silk proteins. The first chapter (**III-1** Structure-property relationship based on the amino acid composition of recombinant spider silk proteins for biomedical applications) describes a systematic investigation of five different recombinant spider silk proteins with different net charges and amino acid compositions, in the viewpoints of physicochemical properties, biocompatibility, and biodegradability.

The second chapter (**III-2** Surface modification of spider silk particles to direct biomolecular corona formation) investigates the effects of the net charge of recombinant spider silk surfaces on the formation of a biomolecular corona and the resulting macroscopic effects like blood clotting and fibrin formation. Here, different recombinantly engineered spider silk variants are used, all comprising different surface charges or terminal modifications with short peptide tags, to analyze the biocompatibility concerning whole human blood.

The third chapter (**III-3** Selective Topography Directed Cell Adhesion on Spider Silk Surfaces) demonstrates the effect of a patterned surface compared to a flat film concerning cell adhesion behavior. The first chapter of this part shows that mammalian cells do not willingly attach and proliferate on flat films of the negatively charged recombinant spider silk protein variant eADF4(C16). Introducing a gradient with different sized patterns like circles, triangles or squares, changes the behavior of the cells utterly. They like to attach to the patterned surface of eADF4(C16), although the amino acid composition of the protein was not changed.

The fourth chapter (**III-4**) is a systematic study of three differently charged recombinant spider silk protein variants and their RGD modified pendants as promising candidates for materials in cardiac tissue engineering. The recombinant spider silk protein films were tested concerning the suitability for cardiomyocyte attachment, contractions, and response to pharmacological treatment.

The fourth part of the thesis is about spider silk-inspired functional materials and contains two chapters. The first chapter (**IV-1** Mimicry of silk utilizing synthetic polypeptides) is a review article on applying synthetic polymerization techniques molecularly inspired by silk proteins. A closer look is taken at the physicochemical properties of silk, how the β -sheets are formed, and in which regions. Chemical and structural similarities to silk form the basis of the reviewed works. They mainly used polymerization strategies for polypeptides like NCA-ROP or chemoenzymatic degradation are reviewed. Furthermore, these silk mimics are assessed from the synthetic production (molecular), the structure formation (mesoscopic), and the processing into different morphologies with various properties (macroscopic) to possible applications.

As an example of silk mimicry, crosslinked polypeptide films based on Poly-L-glutamic acid and Poly-L-Lysine are produced in the second chapter (**IV-2** Crosslinked polypeptide

films via RAFT mediated continuous assembly of polymers). This publication describes crosslinked polypeptide films formed upon continuous assembly via reversible addition-fragmentation chain transfer (CAP-RAFT). This novel polymerization method produces densely crosslinked polypeptide films with unusual secondary structure composition. Another advantage of this method is the control of the polypeptide film thickness and biodegradability.

The following chapters provide a summary of the central aspects. Detailed correlations, classification, and experimental data can be taken from the corresponding publications.

I – Processing and Assembly of Spider Silk Inspired Materials into Films

Although various processing methods are available for (bio-) polymers, such as film casting, spin-coating, dip-coating, or (soft) lithographic techniques, little was known on the assembly- and phase separation behavior of spider silk-inspired materials into films at the beginning of this thesis. As part of this thesis, two publications on the assembly of the recombinant spider silk protein eADF4(C16), a review article about mimicry of silk using synthetic polymers, and one publication on a novel assembly method of synthetic polypeptides will close this gap to the same respect.

As silks are protein-based materials, research into mimicry and understanding the assembly of these materials often starts at a molecular level. These spider silk-inspired materials can be synthesized using many different techniques. Recombinant methods involve manipulation on a genetic level with the help of bacterial plasmids to force microorganisms to produce proteins with specific sequences.^{141, 142} Here, it is possible to introduce modifications like an integrin-binding tag (e.g. RGD) or a different net charge by exchanging single amino acids before protein production.^{52, 58, 143} The advantage of this production method is that recombinantly produced spider silk proteins comprise a monodisperse molecular weight and a very defined amino acid sequence. Silk-like proteins synthesized in this fashion are amongst the most popular and extensively studied routes for achieving silk mimicry and have already been extensively reviewed.^{45, 144, 145} The other common method for synthesizing specific sequences is using solid-state peptide synthesis, but the size of these peptides is restricted and lacks a high throughput. Therefore, this method was not used in this thesis.^{146, 147} Alternative polymerization methods for synthesizing polypeptides are N-carboxyanhydride ring-opening polymerization (NCA

ROP)^{31, 148-150} and chemoenzymatic polymerization^{151, 152}, which can also lead to spider silk inspired materials. The biggest disadvantage of both polymerization methods is the issue of sequence control of the resulting polypeptide. However, both provide interesting methods for synthesizing polypeptides with amino acids as molecular building blocks. Depending on the polymerization method, they can be arranged in random or alternating blocks.

Natural silks vary in their primary structure, but they share fundamental amino acid motifs. The primary structure of silk comprises different amino acid sequence motifs, such as short alanine-rich hydrophobic blocks (e.g., polyalanine blocks with 5-10 residues) and hydrophilic glycine-rich blocks.¹⁵³⁻¹⁵⁵ The hydrophobic blocks associate with each other to form rigid β -sheet nanocrystals, while the hydrophilic regions gain rather α -helical, β -turn, β -spiral or amorphous structures. Many studies revealed that β -sheet crystals are the determining part by defining the properties of silk by allocating stiff and crosslinked crystalline domains embedded in an amorphous glycine-rich matrix. In this thesis, recombinant spider silks inspired by dragline spider silk were mainly used. Dragline spider silk differs between different species but generally consists primarily of two different major ampullate spidroins (MaSps) (~200-350 kDa), named MaSp1 and MaSp2. However, recent studies have begun to investigate MaSp3 and MaSp4.¹⁵⁶⁻¹⁵⁹ Numerous motifs are common within these proteins, including poly(L-alanine) (PLA_l), GGX, and GPGXX motifs (almost exclusively in MaSp2), where P is proline and X is often tyrosine, glutamine or leucine. The frequency of these motifs primarily affects the overall amino acid composition and helps differentiate the two MaSp proteins. For example, the proline content in MaSp1 is less than 1%, while it is greater than 10% for MaSp2. MaSp proteins consist of highly repetitive units of around 30-60 residues, including these motifs. The β -sheet nanocrystalline regions, which are partially responsible for the superior mechanical properties, are based on PLA_l blocks. These are made up of 5-14 residues depending on their species of origin and MaSp. Subsequently, hydrophobic association stacks these β -sheets to form aligned nanocrystals with dimensions of ~ 2 nm × 5 nm × 6 nm, much smaller than that of silkworm silk. The combination of nanocrystal alignment parallel to the fiber axis and size is responsible for the superior mechanical properties, especially the strength and toughness, which is approximately double that of silkworm silk.¹⁶⁰⁻¹⁶² Apart from these regions are the glycine-rich regions, which include the aforementioned GGX and GPGXX motifs and, subsequently, are less well-defined and consist of a mix of secondary

structures.¹⁶³⁻¹⁶⁷ This more amorphous region then provides the desired matrix for the β -sheet crystals to attain the desired mobility within, thus achieving superior flexibility and elasticity. The repetitive core is flanked by non-repetitive regions existing at the ends of the polypeptide sequence of the primarily helical terminal domains.^{159, 168}

In my studies, I focused on assembling spider silk-inspired materials into films. For this purpose, the purified and dried recombinant spider silk proteins must be solved. Dissolution or denaturation is done in organic and aqueous solvents, ionic liquids, strong acids (formic acid), or solutions of chaotropic salts like guanidine thiocyanate (GuaSCN). In this thesis, the studies of the phase separation behaviour of eADF4(C16) (**Part II-1**) and the systematic investigation of various recombinant spider silk variants (eADF3(AQ)₁₂, eADF3(AQ)₂₄, eADF4(C16), eADF4(C16)-RGD, eADF4(κ 16), eADF4(κ 16)-RGD, eADF4(Ω 16) and eADF4(Ω 16)-RGD), **Part III-1,3,4**) concerning structure-property relationship were performed using formic acid as solvent. Hexafluoroisopropanol (HFIP) was used as a solvent in the study concerning β -sheet orientation (Part II-2). In **Part III-2**, besides films, also particulate systems were investigated. These were precipitated from aqueous solutions. Prior to precipitation, the recombinant spider silk powder was denatured with GuaSCN solution and then dialyzed against an aqueous buffer.¹⁴³ The crosslinked synthetic polypeptide films using CAP-RAFT were performed in organic solvents.

Three different processing methods were performed. Firstly, the nano - to micrometer thick films in **Part II 1-2** were spin-coated. Here, the recombinant spider silk solution is applied to the substrate, and then the substrate is rotated with a defined speed, and excess solution is flung away (see **Part I-2.1.2.1**). Secondly, in **Part III-1-4**, films in the micrometer range were investigated. Here, the films were drop cast onto a substrate and then dried in atmospheric conditions (see **Part I-2.1.2.2**). Thirdly, the crosslinked polypeptide films were assembled via the novel polymerization method: continuous assembly of polymers via reversible addition-fragmentation chain transfer (CAP-RAFT).

For block copolymers, it is known that a layer thickness-dependent assembly and phase separation behavior occurs in (ultra-)thin films. A substrate-dependent phase separation model for films in the micrometer range was established for eADF4(C16) by *Wohlrab et al.* It was shown that eADF4(C16) exhibits block copolymer characteristics and that the primary structure (amino acid sequence) of eADF4(C16) can be described by the presence of hydrophilic and hydrophobic block similar to an AB multiblock copolymer. Another hypothesis to be investigated was whether the phase separation of eADF4(C16) films also

exhibits a film thickness dependence. This hypothesis was investigated by characterizing the secondary structure and surface properties of (ultra-) thin eADF4(C16) films from the protein layer with a thickness of only a few nanometers. A corresponding phase separation model of eADF4(C16) nanofilms up to the bulk films described by *Wohlrab et al.* with a layer thickness in the micrometer range was established, proposed, and discussed. If a coating has a film thickness below 100 nm, they are referred to as nanomaterials, which have different properties compared to bulk materials. The nomenclature we defined here was based on their thickness or the number of protein layers: monolayer, bilayer, multilayer. A monolayer was a coating with a thickness of 3-5 nm. This coating thickness is the size range of a β -sheet nanocrystal (~ 5 nm), the silk nanofibrils ($d \sim 2$ nm), or a molecular monolayer ($d \sim 1.5$ nm). This coating was the thinnest homogeneous coating that could be produced using spin-coating. Therefore, in this thesis, we used the term monolayer, which should not mean molecular monolayer. For layers with a coating thickness of approximately 8 nm (bilayer), the water contact angle was $\theta_{\text{Bilayer}} = 63^\circ \pm 2^\circ$, but increased with increasing coating thickness to $\theta_{\text{Multilayer, 33 nm}} = 71^\circ \pm 4^\circ$ to $\theta_{\text{Multilayer, 625 nm}} = 91^\circ \pm 6^\circ$. This $\theta_{\text{Multilayer, 625 nm}}$ shows similar water contact angles as *Wohlrab et al.* observed with eADF4(C16) films cast on glass substrates.⁶¹ The contact angles show a clear dependence on the film thickness. However, the comparison of these data does not take the influence of the substrates, the net charge of the protein, genetic modifications with peptide tags, and differences in surface roughness on the water contact angle of the coatings into account.

Therefore, in **Chapter III-1**, the investigation of the surface properties of recombinant spider silk on substrates was systematically extended to different substrates, namely mica, polystyrene, silica, and glass. All these studies in **Part III-1** are performed with microfilms with the same coating thickness, and the structure-property relationship is discussed in detail (**I-3.2.2**).

In addition to the thickness-dependent surface properties (contact angle), the structural properties were investigated as a function of layer thickness. For this purpose, the relative-folded β -sheet fraction (B) of eADF4(C16) films in the thickness range from 3-5 nm (monolayer) up to the micrometer range before (bpt) and after post-treatment (apt) with methanol (**Part II 1-2**) are investigated (**Part I-1**).

Films with a thickness of up to 600 nm were spin-coated, and microfilms were drop cast. β -sheet proportion (B) is determined using the deconvolution and curve fitting of the amide

I band of an FTIR spectrum of the eADF4(C16) film. The amide I band is mainly a superposition of C=O stretching vibrations of the protein backbone of different vibrational energies.^{64, 169} It is determined in its vibrational energy by the chemical and structural environment of the respective carbonyl group of the peptide bond, i.e., it depends directly on the secondary structure of the protein backbone and can therefore be used for the quantitative analysis of the different secondary structures. The relative secondary structure fractions can be determined by Fourier self-deconvolution and subsequent peak fitting to the unfolded amide-I band.^{53, 64, 169} eADF4(C16) monolayers ($d = 3-5$ nm) have a B_{bpt} of $14.2\% \pm 2.7\%$. When the layer thickness increases (bilayer), B_{bpt} decreases slightly to $12.7\% \pm 1.8\%$ and subsequently increases again with further increasing film thickness until a saturation value of $B_{\text{bpt}} = 18\%$ to 21% is reached in the range $d > 65$ nm. Although the significance of this difference between monolayer and bilayer is small, attention should still be paid to this slight decrease in B_{bpt} from the monolayer and bilayer, which indicates a minimum in B_{bpt} , which can be explained by the intra- and intermolecular interactions of the protein with other protein molecules or the surface. During spin-coating, a thin film of the spider silk solution is formed on the substrate. The formic acid evaporates, and a solid but mainly unstructured spider silk film is formed due to the fast evaporation of the solvent. A possible explanation for a higher B_{bpt} of the monolayer than the bilayer is that the first adsorbed predominantly unstructured layer forms hydrophobic interactions with the surface of the substrate. Such an interaction is based on the displacement of water from the protein and substrate surface. As a result, carbonyl groups of the protein backbone can interact with the silicon oxide layer of the surface of the silicon substrate, which can lead to a possible change in the vibrational energy of the C=O bond. In the bilayer film, a predominantly amorphous second layer is added to this higher-ordered first protein layer, which leads to a decrease in B_{bpt} . In turn, increasing the layer thickness increases the likelihood of inter- and intramolecular interaction of the molecules since the recombinant spider silk molecules (except for those at the interfaces) can now interact in all three spatial directions, and B_{bpt} increases.

Furthermore, the orientation of the β -sheets in micro- and nanometer-thick films cast out of HFIP is investigated in detail. In-depth structural analyses of the β -sheets in eADF4(C16) coatings are performed using dichroic transmission - and attenuated total reflection FTIR (**Part II-2**). The experimental dichroic ratio is used to determine the order parameter of the β -sheets, which indicates the orientation of the β -sheet in the amorphous matrix to the

surface. Nanofilms resulted in an order parameter of $S \sim 0.40$, which correlates to the tilt angle of the β -sheets. This means that nanofilms made of eADF4(C16) contain β -sheets tilted with an angle of 39° to the surface normal. In contrast, micrometer thick films out of eADF4(C16) showed an order parameter of ~ 0 , which means that the β -sheets showed no apparent order in these films.

Additionally, it was found that the structure formation of eADF4(C16) coatings during post-treatment with methanol follows a pseudo-first-order kinetic with an increasing β -sheet proportion and a decreasing unordered proportion. The increase of β -sheets upon post-treatment with MeOH was also already observed in the study in **Part II - 1**. Both studies showed that, regardless of the solvent, the post-treatment with MeOH led to the nearly complete conversion of β -sheets. We calculated the proportion of hydrophobic blocks in eADF4(C16) with 34 %, which correlates tightly with the β -sheet proportion. Consequently, the water contact angle measurements showed that these post-treated films are water-insoluble. In **Part III - 4**, recombinant spider silk films made of six different variants (eADF4(C16), eADF4(C16)-RGD, eADF4(κ 16), eADF4(κ 16)-RGD, eADF4(Ω 16) and eADF4(Ω 16)-RGD) were cast on APTES-functionalized glass slides out of formic acid/water (5:1). Here, no post-treatment was necessary as the β -sheet content was already nearly at the maximal theoretically possible β -sheet proportion. Also, the patterned films in **Part III - 3** do not need additional post-treatment to be water-insoluble. The FTIR spectra of the patterned films already showed a β -sheet dominated amide I band around 1630 cm^{-1} .

Another approach of yield nanofilms made of silk-inspired materials is the assembly of crosslinked polypeptide films. In this thesis, a novel polymerization method is presented, a continuous assembly of polymers via reversible addition-fragmentation chain transfer (CAP-RAFT). The film properties are dictated by their structural features, and subsequent control thereof using unique fabrication strategies is essential. Herein, **Part IV - II** reports a facile method of creating densely crosslinked polypeptide films with unusually high random coil conformations through continuous assembly polymerization *via* reversible addition-fragmentation chain transfer (CAP-RAFT). CAP-RAFT was fundamentally investigated using methacrylated poly-L-lysine (PLLMA) and methacrylated poly-L-glutamic acid (PLGMA). Careful technique refinement resulted in up to $36.1 \pm 1.1 \text{ nm}$ thick films, which could be increased to $94.9 \pm 8.2 \text{ nm}$ after using this strategy multiple times. PLLMA and PLGMA films were found to have 30-50% random coil conformations.

II – Structure-property relationship of spider silk inspired materials

The interest in spider silk-inspired materials as new high-performance materials has grown because of their extraordinary mechanical properties. However, there is still a significant knowledge gap regarding the relationship between amino acid sequence, secondary structure, and resulting properties.^{170, 171} To predict the resulting properties, various recombinant spider silk variants with different amino acid sequences, charges, or genetic modifications were extensively studied to understand the relationships between sequence chemistry, processing, and structure. Furthermore, the in **Part I-3-I** stated assembly model of recombinant spider silk proteins would help understand the results. Firstly, the sequence design, namely the proportions and length of the hydrophobic polyalanine stretches compared to the amorphous, hydrophilic parts of the amino acid sequences, the introduction of charged amino acids, or the addition of the integrin-binding tag RGD are parameters that influence the resulting material properties.

The interactions between and within the protein molecules are of utmost importance because the macroscopic characteristics are caused by the nanoscale assembly of the protein molecules, which are highly influenced by the (genetically) engineered design.^{170, 171} **Table 2** summarizes all the used spider silk-inspired materials used in this thesis, mainly flat films were investigated, but also two other morphologies (particles and patterned films).

This part of the synopsis is divided into two different sections. Firstly, the structure-property relationship of spider silk inspired-materials, which means how the structure affects, for example, the response of the material towards degradation with enzymes and incubation with human blood or proteins; secondly, the investigation of which properties or modifications of the surface affect the response of mammalian cells. The main focus of these studies was the influence of the charge of the protein, the surface chemistry, the surface topography, and the wettability of the surfaces on the interaction with cells, proteins, and human blood. All of the eight publications in this thesis illuminate these aspects from different perspectives. The two publications in **Part II** focus on the negatively charged recombinant spider silk variant eADF4(C16) and investigate the assembly mechanism thickness-dependently. The main focus lies on the secondary structure of the protein, mainly the β -sheet proportion and how the β -sheets are arranged in the film. These studies lack application-related studies like biocompatibility studies with mammalian cells, adsorption of important proteins, or compatibility with human blood.

Table 2: Overview of proteins and synthetic polypeptides used in this study.

Recombinant spider silk protein/ Polypeptide	Flat films	Other Morphologies
ADF4-derived		
eADF4(C16)	Part II-1, II-2, III-1, III-2, III-3, III-4	Particles: Part III-2 Patterned films: III-3
eADF4(κ16)	Part III-1, III-2	Particles: Part III-2
eADF4(Ω16)	Part III-1	n/a
ADF3-derived		
eADF3(AQ)₁₂	Part III-1	n/a
eADF3(AQ)₂₄	Part III-1	n/a
ADF4-derived and terminal peptide tag		
eADF4(C16)-RGD	Part III-1, III-2, III-4	Particles: Part III-2
eADF4(κ16)-RGD	Part III-4	n/a
eADF4(Ω16)-RGD	Part III-4	n/a
eADF4(C16)-E₈G	n/a	Particles: Part III-2
eADF4(C16)-E_sG	n/a	Particles: Part III-2
Synthetic polypeptide		
Poly-L-Lysine	n/a	Crosslinked films: Part IV-2
Poly-L-Glutamic acid	n/a	Crosslinked films: Part IV-2

Therefore, **Part III** aims to be more application related. The first study, **Part III-1**, investigates five recombinant spider silk variants in detail and classifies them based on their results of various tests for biomedical applications (**Figure 30**).

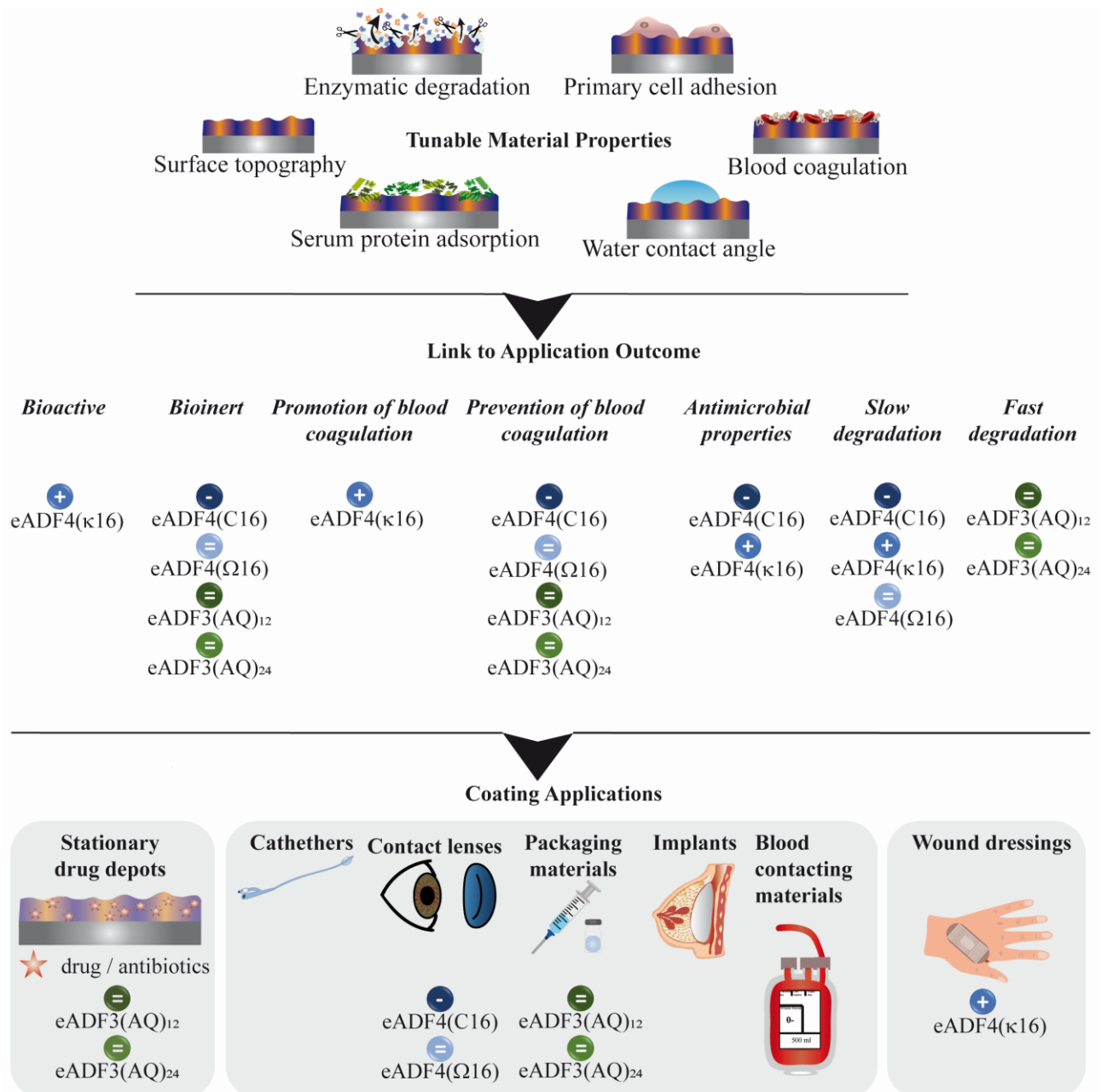


Figure 30: Classification of five different recombinant spider silk variants for coating applications based on their properties. Figure adapted from ¹⁷³.

The morphological investigation with AFM showed relatively smooth films with roughness values below 10 nm for all variants. The water contact angles (WCA) on four different substrates (Mica, polystyrene, glass, and silicon) results in the finding that for eADF3-derived uncharged variants, the WCA is always around the same level (69°-81°) regardless of the underlying substrate. The higher molecular weight of eADF3(AQ)₂₄ (96 kDa) did not affect the WCA. The eADF4-derived variants also show a trend independently from the substrate. The negatively charged variant always show the highest WCA, followed by the positively charged variant, and the uncharged variant eADF4(Ω 16) consistently showed

the most hydrophilic wettability. The degradation with two enzymes, a protease mix type XIV (PXIV), which mimics the cocktail of metalloproteases present in the gut, and a collagenase mix representing a model for wound environment, is used as model enzymes to study the degradability of recombinant spider silk coatings. The degradability is also amino acid specific. All ADF3-derived variants are nearly completely degraded within the first day, while all ADF4-derived variants show better resistance to the enzymes and degrade slower, with around 40-50 % after 15 days.

Furthermore, the biocompatibility of these recombinant spider silk proteins was tested using QCM-D protein adsorptions studies and using incubation in whole human blood. The finding here is that the positively charged recombinant spider silk protein eADF4(κ 16) promotes blood clotting, which is also strengthened by the highest adsorption (QCM-D) of three essential serum proteins, namely fibrinogen, HSA, and IgG. Additionally, the cell adhesion of fibroblasts, keratinocytes, and neuronal cells is tested on materials made of the five recombinant spider silk protein variants. Likewise, here, materials of the positively charged recombinant spider silk protein eADF4(κ 16) show more adhered cells than the other recombinant spider silk coatings. The cells do not like to attach to the negatively and uncharged variants. This behavior makes them suitable for applications where no cell attachment is desired, like coatings for catheters or stents. The positively charged variant could be used, where blood clotting is desired, such as wound dressing. Fast-degrading biocompatible materials like the uncharged ADF3-derived variants eADF3(AQ)₁₂ and eADF3(AQ)₂₄ are possible candidates for stationary drug depots.

The publication (**Part III-2**) studies the formation of a biomolecular corona around a recombinant spider silk protein particle. Here, we assess the influence of the rss protein net charge on the biomolecular corona composition with in-depth proteomics after incubation with whole human blood. For the positively charged variant eADF4(κ 16), an enrichment of fibrinogen is found in the biomolecular corona related to blood clotting. This finding confirms the findings of the study in **Part III-1**. The genetic modification with a peptide tag like -RGD, -E₈G, and R₈G show no significant change in the biomolecular corona formation.

The publication **Part III-4** shows a significant improvement of the growth of human-induced pluripotent stem cell (hiPSC)-derived cardiomyocytes on all RDG modified variants regardless of the charge (eADF4(C16)-RGD, eADF4(κ 16)-RGD and eADF4(Ω 16)-RGD). The positively charged recombinant spider silk protein variant

eADF4(κ 16) also exhibits good cellular growth of these hiPSC-derived cardiomyocytes but with a different morphology. Here the cardiomyocytes show less spreading and smaller appearance than the RGD-modified variants. All six investigated variants showed a patchy morphology using AFM phase imaging, which could support cell attachment. The WCA decrease with all six variants ($\sim 50^\circ$) compared to the silanized glass ($\sim 80^\circ$) without a recombinant spider silk protein coating. These results follow the phase separation model of *Wohlrab et al.* that the hydrophobicity is inverted by coating a substrate with recombinant spider silk protein. The β -sheet proportion for all six variants is in the range of 26-31%, which indicates stable coatings. Various cell culture studies, including contraction of the hiSPC-derived cardiomyocytes, show that recombinant spider silk protein coatings could be suitable materials for cardiac tissue engineering, as they grow selectively on RGD-modified and/or positively charged variants.

Another possibility of modifying recombinant spider silk protein coating surfaces is changing their morphology from flat to patterned. It is shown that the wettability of a surface is closely related to its roughness respectively, topography. The fabrication of these patterned films is done using maskless lithography. A photoresist is exposed with a pattern, then developed, and a PDMS replica is cast. This PDMS replica is used to produce the patterned recombinant spider silk protein films. The recombinant spider silk protein solution is cast into a well-plate, and the PDMS was put on top, acting as a stamp. After evaporation of the solvent, the PDMS stamp is removed, resulting in a patterned recombinant spider silk protein film (**Figure 31**).

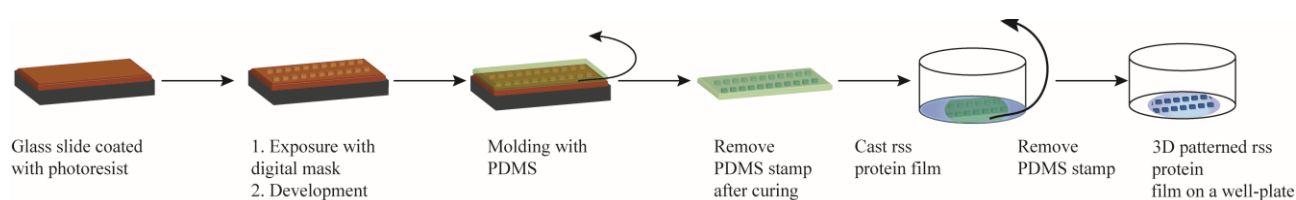


Figure 31: Schematic illustration of the fabrication of patterned recombinant spider silk protein films.

This publication focuses on improving cell adhesion using a patterned surface as a tool to make the negatively charged eADF4(C16) more attractive for cells to attach. This is the first time that patterned films other than lines made of recombinant spider silk protein are presented. Patterns with different numbers of edges and a size gradient are used since different cell types comprise different sizes too. Eight different cell lines are used: a human fibroblast cell line named BJ and a murine cell line Balb3T3; human osteoblasts MG63;

three neuronal cell lines, hybrid cells NG108, rat B50 and RN22 Schwann cells, mouse C2C12 myoblasts and human keratinocytes HaCaT. All cell lines show an improved cell attachment. The bigger the size of the cells, the likelier they go-to patterns in size range of themselves. All cell lines prefer intruding patterns compared to protruding patterns. Correlative measurements are performed to combine SEM and CLSM measurements into one image. The patterns are better visible with the SEM, and the cytoskeleton and the cell nucleus are better visible with CLSM (**Figure 32**).

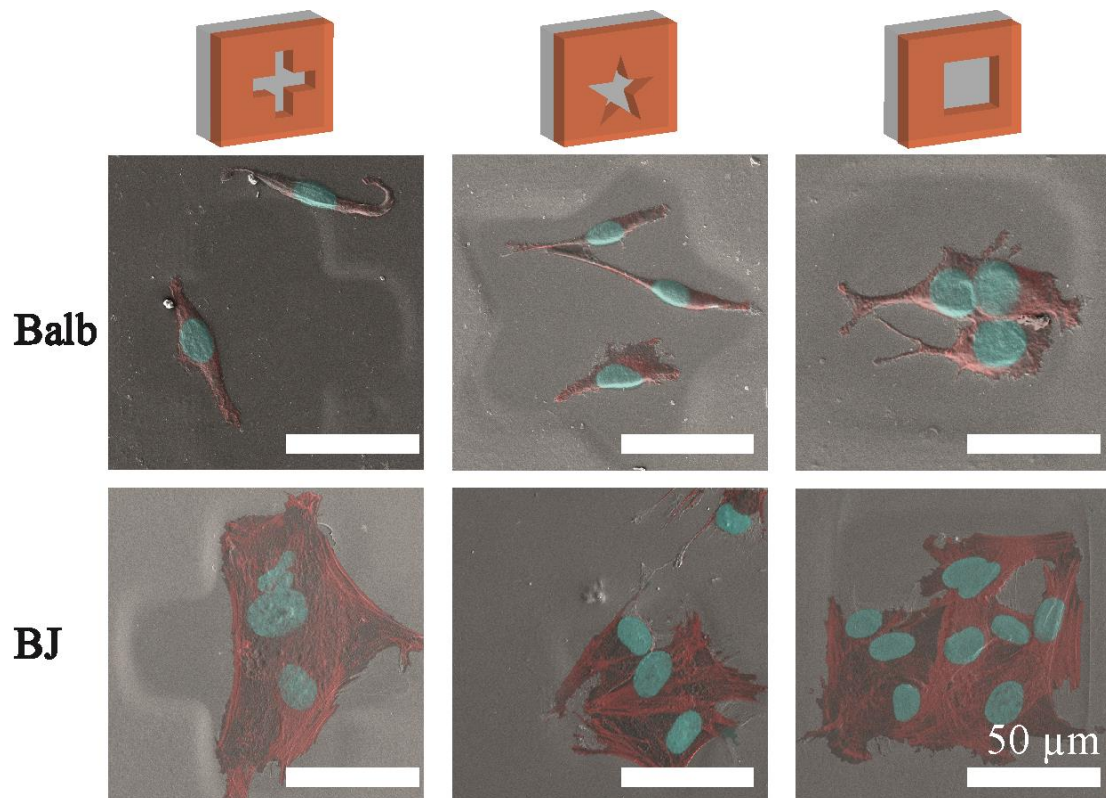


Figure 32: Correlative measurements of murine (Balb) and human (BJ) fibroblasts adhered to three different intruding patterns in a recombinant spider silk protein film.

Part I - References

1. Lechner, M.; Gehrke, K.; Nordmeier, E. H., *Makromolekulare Chemie: Ein Lehrbuch für Chemiker, Physiker, Materialwissenschaftler und Verfahrenstechniker*. Springer-Verlag: **2013**.
2. Lang, G. Herstellung und Charakterisierung von Fasern aus rekombinanten Spinnenseidenproteinen und deren potentielle Applikationen. Universität Bayreuth, 2015.
3. Tieke, B., *Makromolekulare Chemie: Eine Einführung*. John Wiley & Sons: 2014.
4. Davies, J. T., On the shapes of molecules of poly-amino acids and proteins at interfaces. *Biochimica et Biophysica Acta* **1953**, *11*, 165-177.
5. Jonas, U.; van den Brom, C. R.; Brunsen, A.; Roskamp, R., Surface attached polymeric hydrogel films. *Handbook of Biofunctional Surfaces*. Pan Stanford Publishing **2013**, 277.
6. Wüstenberg, T., *Cellulose und Cellulosederivate: Grundlagen, Wirkungen und Applikationen*. Behr's Verlag DE: **2013**.
7. Chang, C.; Zhang, L., Cellulose-based hydrogels: Present status and application prospects. *Carbohydrate Polymers* **2011**, *84* (1), 40-53.
8. Application of Cellulose Ether. <http://celluloseether.com/cm-cellulose/> (accessed **05.03.2020**).
9. Abhilash, M.; Thomas, D., 15 - Biopolymers for Biocomposites and Chemical Sensor Applications. In *Biopolymer Composites in Electronics*, Sadasivuni, K. K.; Ponnamma, D.; Kim, J.; Cabibihan, J. J.; AlMaadeed, M. A., Eds. Elsevier: **2017**; pp 405-435.
10. Wei, Q.; Deng, N.-N.; Guo, J.; Deng, J., Synthetic Polymers for Biomedical Applications %J International Journal of Biomaterials. **2018**, *2*.
11. Cowie, J. M., *Chemie und Physik der synthetischen Polymeren: ein Lehrbuch*. Vieweg: **1997**.
12. Tieke, B., *Makromolekulare Chemie: Eine Einführung*. John Wiley & Sons: 2012.
13. Guldin, S., *Inorganic nanoarchitectures by organic self-assembly*. Springer Science & Business Media: **2013**.
14. Rubinstein, M.; Colby, R., *Polymers physics*. Oxford Oxford, UK: 2003; Vol. 767.
15. Sperling, L. H., *Introduction to physical polymer science*. John Wiley & Sons: **2005**.
16. Hans-Jürgen Butt, K. G., Michael Kappl, *Physics and Chemistry of Interfaces*. **2003**.
17. Swann, J. M. G.; Topham, P. D., Design and Application of Nanoscale Actuators Using Block-Copolymers. *Polymers* **2010**, *2* (4), 454-469.
18. Feng, H.; Lu, X.; Wang, W.; Kang, N.-G.; Mays, J. W., Block Copolymers: Synthesis, Self-Assembly, and Applications. *Polymers* **2017**, *9* (10), 494.
19. Popescu, M.-T.; Lontos, G.; Avgeropoulos, A.; Voulgari, E.; Avgoustakis, K.; Tsitsilianis, C., Injectable Hydrogel: Amplifying the pH Sensitivity of a Triblock Copolypeptide by Conjugating the N-Termini via Dynamic Covalent Bonding. *ACS Applied Materials & Interfaces* **2016**, *8* (27), 17539-17548.
20. Khuphe, M.; Thornton, P. D., 7 - Poly(amino acids). In *Engineering of Biomaterials for Drug Delivery Systems*, Parambath, A., Ed. Woodhead Publishing: **2018**; pp 199-228.
21. Wibowo, S. H.; Sulistio, A.; Wong, E. H. H.; Blencowe, A.; Qiao, G. G., Polypeptide films via N-carboxyanhydride ring-opening polymerization (NCA-ROP): past, present and future. *Chemical Communications* **2014**, *50* (39), 4971.

22. Berg, J. M.; Stryer, L.; Tymoczko, J. L., *Stryer Biochemie*. Springer-Verlag: 2015.
23. Ivanova, E. P.; Bazaka, K.; Crawford, R. J., 3 - Advanced synthetic polymer biomaterials derived from organic sources. In *New Functional Biomaterials for Medicine and Healthcare*, Ivanova, E. P.; Bazaka, K.; Crawford, R. J., Eds. Woodhead Publishing: 2014; pp 71-99.
24. Hadjichristidis, N.; Iatrou, H.; Pitsikalis, M.; Sakellariou, G., Synthesis of Well-Defined Polypeptide-Based Materials via the Ring-Opening Polymerization of α -Amino Acid N-Carboxyanhydrides. *Chemical Reviews* **2009**, *109* (11), 5528-5578.
25. Gutiérrez, T. J., *Reactive and Functional Polymers Volume Four: Surface, Interface, Biodegradability, Compostability and Recycling*. Springer Nature: 2020.
26. Mart, R. J.; Osborne, R. D.; Stevens, M. M.; Ulijn, R. V., Peptide-based stimuli-responsive biomaterials. *Soft Matter* **2006**, *2* (10), 822-835.
27. Parry, D. A.; Squire, J. M., *Fibrous Proteins: Structures and Mechanisms*. Springer: **2017**.
28. Kadakeri, S.; Arul, M. R.; Bordett, R.; Duraisamy, N.; Naik, H.; Rudraiah, S., 6 - Protein synthesis and characterization. In *Artificial Protein and Peptide Nanofibers*, Wei, G.; Kumbar, S. G., Eds. Woodhead Publishing: 2020; pp 121-161.
29. Alexander, H., *Physikalische Grundlagen der Elektronenmikroskopie*. Teubner: **1997**.
30. Deming, T. J., Methodologies for preparation of synthetic block copolypeptides: materials with future promise in drug delivery. *Advanced Drug Delivery Reviews* **2002**, *54* (8), 1145-1155.
31. Deming, T. J., Synthetic polypeptides for biomedical applications. *Progress in Polymer Science* **2007**, *32* (8), 858-875.
32. Minko, S., Grafting on Solid Surfaces: "Grafting to" and "Grafting from" Methods. In *Polymer Surfaces and Interfaces: Characterization, Modification and Applications*, Stamm, M., Ed. Springer Berlin Heidelberg: Berlin, Heidelberg, 2008; pp 215-234.
33. Shirbin, S. J.; Lam, S. J.; Chan, N. J.-A.; Ozmen, M. M.; Fu, Q.; O'Brien-Simpson, N.; Reynolds, E. C.; Qiao, G. G., Polypeptide-Based Macroporous Cryogels with Inherent Antimicrobial Properties: The Importance of a Macroporous Structure. *ACS Macro Letters* **2016**, *5* (5), 552-557.
34. Lu, H.; Wang, J.; Song, Z.; Yin, L.; Zhang, Y.; Tang, H.; Tu, C.; Lin, Y.; Cheng, J., Recent advances in amino acid N-carboxyanhydrides and synthetic polypeptides: chemistry, self-assembly and biological applications. *Chemical Communications* **2014**, *50* (2), 139-155.
35. Hansson, S.; Trouillet, V.; Tischer, T.; Goldmann, A. S.; Carlmark, A.; Barner-Kowollik, C.; Malmström, E., Grafting Efficiency of Synthetic Polymers onto Biomaterials: A Comparative Study of Grafting-from versus Grafting-to. *Biomacromolecules* **2013**, *14* (1), 64-74.
36. SCHARFF, N.; CODDINGTON, J. A., A phylogenetic analysis of the orb-weaving spider family Araneidae (Arachnida, Araneae). *Zoological Journal of the Linnean Society* **2008**, *120* (4), 355-434.
37. Exler, J. H.; Hümmerich, D.; Scheibel, T., The Amphiphilic Properties of Spider Silks Are Important for Spinning. *Angewandte Chemie International Edition* **2007**, *46* (19), 3559-3562.
38. Heidebrecht, A.; Eisoldt, L.; Diehl, J.; Schmidt, A.; Geffers, M.; Lang, G.; Scheibel, T., Biomimetic Fibers Made of Recombinant Spidroins with the Same Toughness as Natural Spider Silk. **2015**, *27* (13), 2189-2194.
39. Asakura, T.; Tasei, Y.; Matsuda, H.; Naito, A., Dynamics of Alanine Methyl Groups in Alanine Oligopeptides and Spider Dragline Silks with Different Packing

- Structures As Studied by ^{13}C Solid-State NMR Relaxation. *Macromolecules* **2018**, *51* (17), 6746-6756.
40. Vendrely, C.; Scheibel, T., Biotechnological Production of Spider-Silk Proteins Enables New Applications. *Macromolecular bioscience* **2007**, *7* (4), 401-409.
 41. Borkner, C. B.; Elsner, M. B.; Scheibel, T., Coatings and Films Made of Silk Proteins. *ACS Applied Materials & Interfaces* **2014**, *6* (18), 15611-15625.
 42. Eisoldt, L.; Smith, A.; Scheibel, T., Decoding the secrets of spider silk. *Materials Today* **2011**, *14* (3), 80-86.
 43. Huemmerich, D.; Scheibel, T.; Vollrath, F.; Cohen, S.; Gat, U.; Ittah, S., Novel Assembly Properties of Recombinant Spider Dragline Silk Proteins. *Current Biology* **2004**, *14* (22), 2070-2074.
 44. Huemmerich, D.; Helsen, C. W.; Quedzuweit, S.; Oschmann, J.; Rudolph, R.; Scheibel, T., Primary structure elements of spider dragline silks and their contribution to protein solubility. *Biochemistry* **2004**, *43* (42), 13604-13612.
 45. Humenik, M.; Smith, A. M.; Scheibel, T., Recombinant Spider Silks—Biopolymers with Potential for Future Applications. *Polymers* **2011**, *3* (1), 640.
 46. Humenik, M.; Smith, A. M.; Arndt, S.; Scheibel, T., Ion and seed dependent fibril assembly of a spidroin core domain. *Journal of Structural Biology* **2015**, *191* (2), 130-138.
 47. Ketten, S.; Buehler, M. J., Nanostructure and molecular mechanics of spider dragline silk protein assemblies. *Journal of The Royal Society Interface* **2010**, *7* (53), 1709-1721.
 48. Rabotyagova, O. S.; Cebe, P.; Kaplan, D. L., Self-assembly of genetically engineered spider silk block copolymers. *Biomacromolecules* **2009**, *10* (2), 229-236.
 49. Slotta, U.; Tammer, M.; Kremer, F.; Koelsch, P.; Scheibel, T., Structural analysis of spider silk films. *Supramolecular Chemistry* **2006**, *18* (5), 465-471.
 50. Augsten, K.; Mühlig, P.; Herrmann, C., Glycoproteins and skin-core structure in *Nephila clavipes* spider silk observed by light and electron microscopy. *Scanning* **2000**, *22* (1), 12-15.
 51. Slotta, U.; Mougin, N.; Römer, L.; Leimer, A. H., Synthetic spider silk proteins and threads. *Chemical Engineering Progress* **2012**, *108* (5), 43-49.
 52. Kumari, S.; Lang, G.; DeSimone, E.; Spengler, C.; Trossmann, V. T.; Lücker, S.; Hudel, M.; Jacobs, K.; Krämer, N.; Scheibel, T., Engineered spider silk-based 2D and 3D materials prevent microbial infestation. *Materials Today* **2020**, *41*, 21-33.
 53. Spieß, K.; Wohlrab, S.; Scheibel, T., Structural characterization and functionalization of engineered spider silk films. *Soft Matter* **2010**, *6* (17), 4168-4174.
 54. Chen, J.; Hu, J.; Zuo, P.; Shi, J.; Yang, M., Facile preparation of recombinant spider eggcase silk spheres via an HFIP-on-Oil approach. *International Journal of Biological Macromolecules* **2018**, *116*, 1146-1152.
 55. Borkner, C. B.; Lentz, S.; Müller, M.; Fery, A.; Scheibel, T., Ultrathin Spider Silk Films: Insights into Spider Silk Assembly on Surfaces. *ACS Applied Polymer Materials* **2019**, *1* (12), 3366-3374.
 56. Doblhofer, E.; Heidebrecht, A.; Scheibel, T., To spin or not to spin: spider silk fibers and more. *Applied Microbiology and Biotechnology* **2015**, *99* (22), 9361-9380.
 57. Heidebrecht, A.; Eisoldt, L.; Diehl, J.; Schmidt, A.; Geffers, M.; Lang, G.; Scheibel, T., Biomimetic fibers made of recombinant spidroins with the same toughness as natural spider silk. *Advanced Materials* **2015**, *27* (13), 2189-2194.
 58. Wohlrab, S.; Müller, S.; Schmidt, A.; Neubauer, S.; Kessler, H.; Leal-Egaña, A.; Scheibel, T., Cell adhesion and proliferation on RGD-modified recombinant spider silk proteins. *Biomaterials* **2012**, *33* (28), 6650-6659.
 59. Weiss, A. C. G.; Herold, H. M.; Lentz, S.; Faria, M.; Besford, Q. A.; Ang, C.-S.; Caruso, F.; Scheibel, T., Surface Modification of Spider Silk Particles to Direct

- Biomolecular Corona Formation. *ACS Applied Materials & Interfaces* **2020**, *12* (22), 24635-24643.
60. Schierling, M. B.; Doblhofer, E.; Scheibel, T., Cellular uptake of drug loaded spider silk particles. *Biomaterials Science* **2016**, *4* (10), 1515-1523.
61. Wohlrab, S.; Spieß, K.; Scheibel, T., Varying surface hydrophobicities of coatings made of recombinant spider silk proteins. *Journal of Materials Chemistry* **2012**, *22* (41), 22050-22054.
62. Aigner, T. B.; DeSimone, E. K.; Scheibel, T., Biofabrication using recombinant spider silk proteins as a biomaterial. **2017**.
63. Rammensee, S.; Slotta, U.; Scheibel, T.; Bausch, A. R., Assembly mechanism of recombinant spider silk proteins. *Proceedings of the National Academy of Sciences* **2008**, *105* (18), 6590-6595.
64. Hu, X.; Kaplan, D.; Cebe, P., Determining Beta-Sheet Crystallinity in Fibrous Proteins by Thermal Analysis and Infrared Spectroscopy. *Macromolecules* **2006**, *39* (18), 6161-6170.
65. Gebhardt, R.; Vendrely, C.; Burghammer, M.; Riek, C., Characterization of the boundary zone of a cast protein drop: fibroin β -sheet and nanofibril formation. *Langmuir* **2009**, *25* (11), 6307-6311.
66. Ratner, B. D., Biomaterials Science: An Interdisciplinary Endeavor. In *Biomaterials Science*, Ratner, B. D.; Hoffman, A. S.; Schoen, F. J.; Lemons, J. E., Eds. Academic Press: San Diego, 1996; pp 1-8.
67. Williams, D. F., Tissue-biomaterial interactions. *Journal of Materials Science* **1987**, *22* (10), 3421-3445.
68. Rahmati, M.; Silva, E. A.; Reseland, J. E.; Heyward, C.; Haugen, H. J., Biological responses to physicochemical properties of biomaterial surface. *Chemical Society Reviews* **2020**, *49* (15), 5178-5224.
69. Kapusetti, G.; More, N.; Choppadandi, M., Introduction to Ideal Characteristics and Advanced Biomedical Applications of Biomaterials. In *Biomedical Engineering and its Applications in Healthcare*, Paul, S., Ed. Springer Singapore: Singapore, **2019**; pp 171-204.
70. Turksen, K., *Cell Biology and Translational Medicine, Volume 1: Stem Cells in Regenerative Medicine: Advances and Challenges*. Springer: **2018**; Vol. 1079.
71. J. Vessman, R. I. S., J.F. van Staden, K. Danzer, W. Lindner, D.T. Burns, A. Fajgelj, and H. Müller, Selectivity in Analytical Chemistry (IUPAC Recommendations 2001). *Chemistry International -- Newsmagazine for IUPAC* **2002**, *24* (1), 21-22.
72. Müller-Herrmann, S.; Scheibel, T., Enzymatic Degradation of Films, Particles, and Nonwoven Meshes Made of a Recombinant Spider Silk Protein. *ACS Biomaterials Science & Engineering* **2015**, *1* (4), 247-259.
73. Zeplin, P. H.; Maksimovikj, N. C.; Jordan, M. C.; Nickel, J.; Lang, G.; Leimer, A. H.; Römer, L.; Scheibel, T., Spider Silk Coatings as a Bioshield to Reduce Periprosthetic Fibrous Capsule Formation. *Advanced Functional Materials* **2014**, *24* (18), 2658-2666.
74. Sanz-Herrera, J. A.; García-Aznar, J. M.; Doblaré, M., On scaffold designing for bone regeneration: A computational multiscale approach. *Acta Biomaterialia* **2009**, *5* (1), 219-229.
75. Mulyasmita, W.; Madl, C. M.; Heilshorn, S. C., 2.2 Protein-Engineered Biomaterials: Synthesis and Characterization. In *Comprehensive Biomaterials II*, Ducheyne, P., Ed. Elsevier: Oxford **2017**; pp 18-40.

76. Schubert, D.; Dunkel, T., Spin coating from a molecular point of view: its concentration regimes, influence of molar mass and distribution. *Mat Res Innovat* **2003**, *7* (5), 314-321.
77. Rymaszewski, E. J.; Klopfenstein, A. G., *Microelectronics Packaging Handbook: Semiconductor Packaging*. Springer: **1997**.
78. Jiang, P.; McFarland, M. J., Large-Scale Fabrication of Wafer-Size Colloidal Crystals, Macroporous Polymers and Nanocomposites by Spin-Coating. *Journal of the American Chemical Society* **2004**, *126* (42), 13778-13786.
79. Junghans, F.; Morawietz, M.; Conrad, U.; Scheibel, T.; Heilmann, A.; Spohn, U., Preparation and mechanical properties of layers made of recombinant spider silk proteins and silk from silk worm. *Applied Physics A* **2006**, *82* (2), 253-260.
80. Ltd, O. Spin Coating: A Guide to Theory and Techniques. <https://www.ossila.com/pages/spin-coating#spin-coating-general-theory> (accessed **26.04.2019**).
81. Ikeno, M., Spin coating method. Google Patents: **1993**.
82. Binnig, G.; Quate, C. F.; Gerber, C., Atomic Force Microscope. *Physical Review Letters* **1986**, *56* (9), 930-933.
83. Khan, M. K.; Wang, Q. Y.; Fitzpatrick, M. E., 1 - Atomic force microscopy (AFM) for materials characterization. In *Materials Characterization Using Nondestructive Evaluation (NDE) Methods*, Hübschen, G.; Altpeter, I.; Tschuncky, R.; Herrmann, H.-G., Eds. Woodhead Publishing: **2016**; pp 1-16.
84. Pang, G. K. H.; Baba-Kishi, K. Z.; Patel, A., Topographic and phase-contrast imaging in atomic force microscopy. *Ultramicroscopy* **2000**, *81* (2), 35-40.
85. Stark, M.; Möller, C.; Müller, D. J.; Guckenberger, R., From Images to Interactions: High-Resolution Phase Imaging in Tapping-Mode Atomic Force Microscopy. *Biophysical Journal* **2001**, *80* (6), 3009-3018.
86. Shinato, K. W.; Huang, F.; Jin, Y., Principle and application of atomic force microscopy (AFM) for nanoscale investigation of metal corrosion. *Corrosion Reviews* **2020**, *38* (5), 423-432.
87. Goldstein, J. I.; Newbury, D. E.; Michael, J. R.; Ritchie, N. W.; Scott, J. H. J.; Joy, D. C., *Scanning electron microscopy and X-ray microanalysis*. Springer: **2018**.
88. Inkson, B. J., 2 - Scanning electron microscopy (SEM) and transmission electron microscopy (TEM) for materials characterization. In *Materials Characterization Using Nondestructive Evaluation (NDE) Methods*, Hübschen, G.; Altpeter, I.; Tschuncky, R.; Herrmann, H.-G., Eds. Woodhead Publishing: **2016**; pp 17-43.
89. Flegler, S. L.; Heckman, J. W.; Klomparens, K. L., *Elektronenmikroskopie: Grundlagen, Methoden, Anwendungen*. Spektrum-Akademischer Vlg: **1995**.
90. Keevend, K.; Coenen, T.; Herrmann, I. K., Correlative cathodoluminescence electron microscopy bioimaging: towards single protein labelling with ultrastructural context. *Nanoscale* **2020**, *12* (29), 15588-15603.
91. Murphy, D. B.; Davidson, M. W., Fluorescence Microscopy. In *Fundamentals of Light Microscopy and Electronic Imaging* **2012**; pp 199-231.
92. Jablonski, A., Efficiency of Anti-Stokes Fluorescence in Dyes. *Nature* **1933**, *131* (3319), 839-840.
93. Lichtman, J. W.; Conchello, J.-A., Fluorescence microscopy. *Nature Methods* **2005**, *2* (12), 910-919.
94. Berlier, J. E.; Rothe, A.; Buller, G.; Bradford, J.; Gray, D. R.; Filanoski, B. J.; Telford, W. G.; Yue, S.; Liu, J.; Cheung, C.-Y.; Chang, W.; Hirsch, J. D.; Beechem Rosaria P. Haugland, J. M.; Haugland, R. P., Quantitative Comparison of Long-wavelength

- Alexa Fluor Dyes to Cy Dyes: Fluorescence of the Dyes and Their Bioconjugates. *Journal of Histochemistry & Cytochemistry* **2003**, *51* (12), 1699-1712.
95. Shin, K.; Song, Y. H.; Goh, Y.; Lee, K. T., Two-Dimensional and Three-Dimensional Single Particle Tracking of Upconverting Nanoparticles in Living Cells. *International Journal of Molecular Sciences* **2019**, *20* (6), 1424.
96. Murphy, D. B.; Davidson, M. W., Fluorescence Imaging of Dynamic Molecular Processes. In *Fundamentals of Light Microscopy and Electronic Imaging*, **2012**; pp 233-263.
97. Sparkes, I.; Graumann, K.; Martinière, A.; Schoberer, J.; Wang, P.; Osterrieder, A., Bleach it, switch it, bounce it, pull it: Using lasers to reveal plant cell dynamics. *Journal of experimental botany* **2010**, *62*, 1-7.
98. Johnson, A.; Gnyliukh, N.; Kaufmann, W. A.; Narasimhan, M.; Vert, G.; Bednarek, S. Y.; Friml, J., Experimental toolbox for quantitative evaluation of clathrin-mediated endocytosis in the plant model. *Journal of Cell Science* **2020**, *133* (15), jcs248062.
99. Krieger, J. W.; Singh, A. P.; Bag, N.; Garbe, C. S.; Saunders, T. E.; Langowski, J.; Wohland, T., Imaging fluorescence (cross-) correlation spectroscopy in live cells and organisms. *Nature Protocols* **2015**, *10* (12), 1948-1974.
100. Liu, S.; Wang, Z.-g.; Zhang, Z.-L.; Pang, D.-W., Tracking single viruses infecting their host cells using quantum dots. *Chemical Society reviews* **2015**, *45*.
101. Schermelleh, L.; Ferrand, A.; Huser, T.; Eggeling, C.; Sauer, M.; Biehlmaier, O.; Drummen, G. P. C., Super-resolution microscopy demystified. *Nature Cell Biology* **2019**, *21* (1), 72-84.
102. Murphy, D. B.; Davidson, M. W., Confocal Laser Scanning Microscopy. In *Fundamentals of Light Microscopy and Electronic Imaging* **2012**; pp 265-305.
103. Chudakov, D. M.; Matz, M. V.; Lukyanov, S.; Lukyanov, K. A., Fluorescent Proteins and Their Applications in Imaging Living Cells and Tissues. *Physiological Reviews* **2010**, *90* (3), 1103-1163.
104. Elliott, A. D., Confocal Microscopy: Principles and Modern Practices. *Current Protocols in Cytometry* **2020**, *92* (1), e68.
105. Wu, H.; Qiao, Y., Microscopy techniques for protocell characterization. *Polymer Testing* **2021**, *93*, 106935.
106. Murphy, D. B.; Davidson, M. W., Fundamentals of Light Microscopy. In *Fundamentals of Light Microscopy and Electronic Imaging* **2012**; pp 1-19.
107. Bhattacharjee, S., DLS and zeta potential – What they are and what they are not? *Journal of Controlled Release* **2016**, *235*, 337-351.
108. Clogston, J. D.; Patri, A. K., Zeta Potential Measurement. In *Characterization of Nanoparticles Intended for Drug Delivery*, McNeil, S. E., Ed. Humana Press: Totowa, NJ **2011**; pp 63-70.
109. Salopek, B.; Krasic, D.; Filipovic, S., Measurement and application of zeta-potential. *Rudarsko-geolosko-naftni zbornik* **1992**, *4* (1), 147.
110. Stamm, M., Polymer surfaces and interfaces. *Characterization, Modification and Applications*; Springer: Berlin, Germany, **2008**.
111. Zasoski, R. J., Zeta potential. In *Encyclopedia of Soil Science*, Chesworth, W., Ed. Springer Netherlands: Dordrecht **2008**; pp 841-845.
112. Clark, D.; Held, A.; Pazdernik, N., *Molekulare Biotechnologie: Grundlagen und Anwendungen*. Spektrum Akademischer Verlag: **2009**.
113. Janson, J.-C., *Protein purification: principles, high resolution methods, and applications*. John Wiley & Sons: **2012**; Vol. 151.

114. Chevallet, M.; Luche, S.; Rabilloud, T., Silver staining of proteins in polyacrylamide gels. *Nature Protocols* **2006**, *1* (4), 1852-1858.
115. Wray, W.; Boulikas, T.; Wray, V. P.; Hancock, R., Silver staining of proteins in polyacrylamide gels. *Analytical Biochemistry* **1981**, *118* (1), 197-203.
116. Brunelle, J. L.; Green, R., Chapter Thirteen - Coomassie Blue Staining. In *Methods in Enzymology*, Lorsch, J., Ed. Academic Press: **2014**; Vol. 541, pp 161-167.
117. Ling, S.; Dinjaski, N.; Ebrahimi, D.; Wong, J. Y.; Kaplan, D. L.; Buehler, M. J., Conformation Transitions of Recombinant Spidroins via Integration of Time-Resolved FTIR Spectroscopy and Molecular Dynamic Simulation. *ACS Biomaterials Science & Engineering* **2016**.
118. Koenig, J. L., Spectroscopy of polymers. *Elsevier*: **1999**.
119. Behlke, J.; Kleinpeter, E.; Kraft, R.; Laßmann, G.; Pfeil, W.; Rohde, K.; Welfle, H., Methoden in der Proteinanalytik. *Springer-Verlag*: **2013**.
120. Güldenhaupt, J., ATR-FTIR-spektroskopische Untersuchungen von membrangebundenem Ras **2010**.
121. Müller, M.; Torger, B.; Bittrich, E.; Kaul, E.; Ionov, L.; Uhlmann, P.; Stamm, M., In-situ ATR-FTIR for characterization of thin biorelated polymer films. *Thin Solid Films* **2014**, *556*, 1-8.
122. Greenfield, N. J., Using circular dichroism spectra to estimate protein secondary structure. *Nature protocols* **2006**, *1* (6), 2876-2890.
123. Lottspeich, F.; Zorbas, H., Bioanalytik, *Spektrum Akademischer Verlag* **1998**.
124. Raja, P. M. V.; Barron, A. R., Circular Dichroism Spectroscopy and its Application for Determination of Secondary Structure of Optically Active Species **2021**.
125. Sauerbrey, G., Verwendung von Schwingquarzen zur Wägung dünner Schichten und zur Mikrowägung. *Zeitschrift für Physik A Hadrons and Nuclei*, **1959**, *155* (2), 206-222.
126. Geddes, N. J.; Paschinger, E. M.; Furlong, D. N.; Caruso, F.; Hoffmann, C. L.; Rabolt, J. F., Surface chemical activation of quartz crystal microbalance gold electrodes — analysis by frequency changes, contact angle measurements and grazing angle FTIR. *Thin Solid Films* **1995**, *260* (2), 192-199.
127. Fang, J.; Ren, C.; Zhu, T.; Wang, K.; Jiang, Z.; Ma, Y., Comparison of the different responses of surface plasmon resonance and quartz crystal microbalance techniques at solid–liquid interfaces under various experimental conditions. *Analyst* **2015**, *140* (4), 1323-1336.
128. Liu, G.; Zhang, G., QCM-D Studies on Polymer Behavior at Interfaces, *Springer*, **2013**.
129. Tonda-Turo, C.; Carmagnola, I.; Ciardelli, G., Quartz Crystal Microbalance With Dissipation Monitoring: A Powerful Method to Predict the in vivo Behavior of Bioengineered Surfaces. *Frontiers in Bioengineering and Biotechnology* **2018**, *6*.
130. Alexander, T. E.; Lozeau, L. D.; Camesano, T. A., QCM-D characterization of time-dependence of bacterial adhesion. *Cell Surf* **2019**, *5*, 100024.
131. Vörös, J., The Density and Refractive Index of Adsorbing Protein Layers. *Biophysical Journal* **2004**, *87* (1), 553-561.
132. Höök, F.; Kasemo, B.; Nylander, T.; Fant, C.; Sott, K.; Elwing, H., Variations in Coupled Water, Viscoelastic Properties, and Film Thickness of a Mefp-1 Protein Film during Adsorption and Cross-Linking: A Quartz Crystal Microbalance with Dissipation Monitoring, Ellipsometry, and Surface Plasmon Resonance Study. *Analytical Chemistry* **2001**, *73* (24), 5796-5804.
133. Bueno-Blanco, C.; Svatek, S. A.; Lin, D. Y.; Martínez, M.; Watanabe, K.; Taniguchi, T.; Antolín, E. In Enabling high efficiencies in MoS homojunction solar cells,

- 2021 *IEEE 48th Photovoltaic Specialists Conference (PVSC)*, 20-25 June 2021; **2021**; pp 0165-0170.
134. Ryu, Y. K.; Carrascoso, F.; López-Nebreda, R.; Agraït, N.; Frisenda, R.; Castellanos-Gomez, A., Microheater Actuators as a Versatile Platform for Strain Engineering in 2D Materials. *Nano Letters* **2020**, *20* (7), 5339-5345.
135. Shulga, A. G.; Yamamura, A.; Tsuzuku, K.; Dragoman, R. M.; Dirin, D. N.; Watanabe, S.; Kovalenko, M. V.; Takeya, J.; Loi, M. A., Patterned Quantum Dot Photosensitive FETs for Medium Frequency Optoelectronics. *Advanced Materials Technologies* **2019**, *4* (9), 1900054.
136. <http://www.smartforcetechnologies.com/products/smartprint>, zuletzt aufgerufen: **20.11.2019**.
137. Findenegg, G. H.; Herminghaus, S., Wetting: Statics and dynamics. *Current Opinion in Colloid & Interface Science* **1997**, *2* (3), 301-307.
138. Israelachvili, J. N., Intermolecular and surface forces, *Academic Press*, **2011**.
139. Quéré, D., Wetting and Roughness. *Annual Review of Materials Research* **2008**, *38* (1), 71-99.
140. Dörfler, H.-D., Grenzflächen und kolloid-disperse Systeme Physik und Chemie ; mit 88 Tabellen, *Springer*, **2002**.
141. Saric, M.; Scheibel, T., Engineering of silk proteins for materials applications. *Current Opinions in Biotechnology* **2019**, *60*, 213-220.
142. Wang, J.; Scheibel, T., Recombinant Production of Mussel Byssus Inspired Proteins. *Biotechnology Journal* **2018**, *13* (12), 1800146.
143. Doblhofer, E.; Scheibel, T., Engineering of recombinant spider silk proteins allows defined uptake and release of substances. *Journal of pharmaceutical sciences* **2015**, *104* (3), 988-994.
144. Tokareva, O.; Michalczechen-Lacerda, V. A.; Rech, E. L.; Kaplan, D. L., Recombinant DNA production of spider silk proteins. *Microbial Biotechnology* **2013**, *6* (6), 651-663.
145. Spiess, K.; Lammel, A.; Scheibel, T., Recombinant Spider Silk Proteins for Applications in Biomaterials. *Macromolecular Bioscience* **2010**, *10* (9), 998-1007.
146. Varnava, K. G.; Sarojini, V., Making Solid-Phase Peptide Synthesis Greener: A Review of the Literature. *Chemistry – An Asian Journal* **2019**, *14* (8), 1088-1097.
147. Amblard, M.; Fehrentz, J.-A.; Martinez, J.; Subra, G., Methods and protocols of modern solid phase peptide synthesis. *Molecular Biotechnology* **2006**, *33* (3), 239-254.
148. He, X.; Fan, J.; Wooley, K. L., Stimuli-Triggered Sol–Gel Transitions of Polypeptides Derived from α -Amino Acid N-Carboxyanhydride (NCA) Polymerizations. *Chemistry – An Asian Journal* **2016**, *11* (4), 437-447.
149. Rasines Mazo, A.; Allison-Logan, S.; Karimi, F.; Chan, N. J.-A.; Qiu, W.; Duan, W.; O'Brien-Simpson, N. M.; Qiao, G. G., Ring opening polymerization of α -amino acids: advances in synthesis, architecture and applications of polypeptides and their hybrids. *Chemical Society Reviews* **2020**.
150. Huang, J.; Heise, A., Stimuli responsive synthetic polypeptides derived from N-carboxyanhydride (NCA) polymerisation. *Chemical Society Reviews* **2013**, *42* (17), 7373-7390.
151. Tsuchiya, K.; Numata, K., Chemoenzymatic Synthesis of Polypeptides for Use as Functional and Structural Materials. *Macromolecular Bioscience* **2017**, *17* (11), 1700177.
152. Numata, K., Poly(amino acid)s/polypeptides as potential functional and structural materials. *Polymer Journal* **2015**, *47* (8), 537-545.
153. Hardy, J. G.; Römer, L. M.; Scheibel, T. R., Polymeric materials based on silk proteins. *Polymer* **2008**, *49* (20), 4309-4327.

154. Hardy, J. G.; Scheibel, T. R., Composite materials based on silk proteins. *Progress in Polymer Science* **2010**, *35* (9), 1093-1115.
155. Huang, W.; Ling, S.; Li, C.; Omenetto, F. G.; Kaplan, D. L., Silkworm silk-based materials and devices generated using bio-nanotechnology. *Chemical Society Reviews* **2018**, *47* (17), 6486-6504.
156. Brooks, A. E.; Steinkraus, H. B.; Nelson, S. R.; Lewis, R. V., An Investigation of the Divergence of Major Ampullate Silk Fibers from *Nephila clavipes* and *Argiope aurantia*. *Biomacromolecules* **2005**, *6* (6), 3095-3099.
157. Saric, M.; Eisoldt, L.; Döring, V.; Scheibel, T., Interplay of Different Major Ampullate Spidroins during Assembly and Implications for Fiber Mechanics. **2021**, *33* (9), 2006499.
158. Correa-Garhwal, S. M.; Clarke, T. H.; Janssen, M.; Crevecoeur, L.; McQuillan, B. N.; Simpson, A. H.; Vink, C. J.; Hayashi, C. Y., Spidroins and Silk Fibers of Aquatic Spiders. *Sci Rep* **2019**, *9* (1), 13656.
159. Xu, M.; Lewis, R. V. J. P. o. t. N. A. o. S., Structure of a protein superfiber: spider dragline silk. **1990**, *87* (18), 7120-7124.
160. Plaza, G. R.; Pérez-Rigueiro, J.; Riekkel, C.; Perea, G. B.; Agulló-Rueda, F.; Burghammer, M.; Guinea, G. V.; Elices, M., Relationship between microstructure and mechanical properties in spider silk fibers: identification of two regimes in the microstructural changes. *Soft Matter* **2012**, *8* (22), 6015-6026.
161. Grubb, D. T.; Jelinski, L. W., Fiber Morphology of Spider Silk: The Effects of Tensile Deformation. *Macromolecules* **1997**, *30* (10), 2860-2867.
162. Riekkel, C.; Bränden, C.; Craig, C.; Ferrero, C.; Heidelbach, F.; Müller, M., Aspects of X-ray diffraction on single spider fibers. *International Journal of Biological Macromolecules* **1999**, *24* (2), 179-186.
163. Winkler, S.; Kaplan, D. L., Molecular biology of spider silk. *Reviews in Molecular Biotechnology* **2000**, *74* (2), 85-93.
164. Kümmerlen, J.; Van Beek, J.; Vollrath, F.; Meier, B., Local structure in spider dragline silk investigated by two-dimensional spin-diffusion nuclear magnetic resonance. *Macromolecules* **1996**, *29* (8), 2920-2928.
165. Hijirida, D. H.; Do, K. G.; Michal, C.; Wong, S.; Zax, D.; Jelinski, L. W., ¹³C NMR of *Nephila clavipes* major ampullate silk gland. *Biophysical Journal* **1996**, *71* (6), 3442-3447.
166. Liu, Y.; Spenner, A.; Porter, D.; Vollrath, F., Proline and processing of spider silks. *Biomacromolecules* **2008**, *9* (1), 116-121.
167. Holland, G. P.; Jenkins, J. E.; Creager, M. S.; Lewis, R. V.; Yarger, J. L., Quantifying the fraction of glycine and alanine in β -sheet and helical conformations in spider dragline silk using solid-state NMR. *Chemical communications* **2008**, (43), 5568-5570.
168. Bauer, J.; Scheibel, T. J. B., Conformational stability and interplay of helical N- and C-terminal domains with implications on major ampullate spidroin assembly. **2017**, *18* (3), 835-845.
169. Hu, X.; Kaplan, D.; Cebe, P., Dynamic Protein–Water Relationships during β -Sheet Formation. *Macromolecules* **2008**, *41* (11), 3939-3948.
170. Krishnaji, S. T.; Bratzel, G.; Kinahan, M. E.; Kluge, J. A.; Staii, C.; Wong, J. Y.; Buehler, M. J.; Kaplan, D. L., Sequence–Structure–Property Relationships of Recombinant Spider Silk Proteins: Integration of Biopolymer Design, Processing, and Modeling. *Advanced Functional Materials* **2013**, *23* (2), 241-253.
171. Yarger, J. L.; Cherry, B. R.; van der Vaart, A., Uncovering the structure–function relationship in spider silk. *Nature Reviews Materials* **2018**, *3* (3), 18008.

172. Esser, T. U.; Trossmann, V. T.; Lentz, S.; Engel, F. B.; Scheibel, T., Designing of spider silk proteins for human induced pluripotent stem cell-based cardiac tissue engineering. *Materials Today Bio* **2021**, *11*, 100114.
173. Lentz, S; Trossmann, V. T.; Borkner, C. B.; Beyersdorfer, V., Rottmar, M.; Scheibel, T., Structure-Property Relationship Based on the Amino Acid Composition of Recombinant Spider Silk Proteins for Potential Biomedical Applications. *Advanced Functional Materials* **2022**, *14* (28), 31751-31766.

Part II – Mechanism of structure formation and microphase separation of recombinant spider silk proteins on surfaces

Part II - Chapter 1 – Ultra-thin spider silk films: Insights into silk assembly on surfaces

Part II – Chapter 1.1 - Chapter perspective and contribution

This work investigates the self-assembly and folding of negatively charged recombinant spider silk (rss) protein films (eADF4(C16)) on silicon substrates in dependency on the film thickness and the number of silk protein layers. A model for recombinant spider silk protein folding is proposed based on microphase separation theories, which are already well-known for block copolymers combined with the folding properties of the rss protein eADF4(C16).

This chapter is one of my first author papers. Here, I performed the synthesis, purification, and processing of the recombinant spider silk proteins into films. The characterization of the recombinant spider silk films using GATR-FTIR, AFM, and water contact angle measurements was performed by myself. The ATR- and transmission FTIR measurements were performed by Martin Müller. The phase separation model was developed by Christian Borkner and myself. The writing of the original draft and the visualization of the results was done by Christian Borkner and me. The review and the editing of the manuscript were done by all authors. The conceptualization of this project was done by Christian Borkner, Andreas Fery and Thomas Scheibel. The funding for this project was provided by Andreas Fery and Thomas Scheibel. This study was done in cooperation with the Leibniz Institute in Dresden with Prof. Andreas Fery and Dr. Martin Müller. This paper is published in ACS Applied Polymer Science: “Ultra-thin spider silk films: insights into silk assembly on surfaces”, ACS Appl. Polym. Mater. 2019, 1, 3366-3374.

The permission of reprint was granted by ACS Applied Polymer Science: Reprinted (adapted) with permission from Ultra-thin spider silk films: insights into silk assembly on surfaces”, ACS Appl. Polym. Mater. 2019, 1, 3366-3374. Copyright 2021 American Chemical Society.

Ultrathin Spider Silk Films: Insights into Spider Silk Assembly on Surfaces

Christian B. Borkner,^{†,¶} Sarah Lentz,^{†,¶} Martin Müller,^{‡,○} Andreas Fery,^{‡,◆} and Thomas Scheibel^{*,†,§,||,⊥}

[†]Lehrstuhl Biomaterialien, Fakultät für Ingenieurwissenschaften, Universität Bayreuth, Prof.-Rüdiger-Bormann-Strasse 1, 95447 Bayreuth, Germany

[‡]Leibniz-Institut für Polymerforschung Dresden (e.V.), Institute of Physical Chemistry and Polymer Physics, Hohe Strasse 6, D-01069 Dresden, Germany

[○]Technische Universität Dresden, Chair for Physical Chemistry of Polymeric Materials, 01069 Dresden, Germany

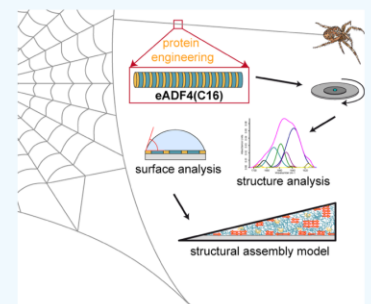
[◆]Technische Universität Dresden, Chair for Macromolecular Chemistry, 01062 Dresden, Germany

[§]Bayerisches Polymerinstitut (BPI), Bayreuther Zentrum für Kolloide und Grenzflächen (BZKG), ^{||}Bayreuther Zentrum für Molekulare Biowissenschaften (BZMB), [⊥]Bayreuther Materialzentrum (BayMAT), Universität Bayreuth, Universitätsstrasse 30, 95440 Bayreuth, Germany

Supporting Information

ABSTRACT: β -Sheets in natural spider dragline silk proteins are typically formed by polyalanine (A_n) as well as alanine-glycine (AG) and GGA sequences flanking these A_n regions. The hydrophobic β -sheet-rich regions are embedded in a hydrophilic amorphous matrix, and this phenomenon can be reflected as microphase separation, similar to that of block copolymers. Microphase separation occurs not only in fibers but also in cast spider silk films. Micellar-like structures form within the bulk of the film, while substrate surface as well as the film/air interface trigger explicit secondary structure formation in these layers. So far, only limited information is available concerning the mechanism of film assembly and microphase separation of spider silk proteins on surfaces. In this work, self-assembly and folding of eADF4(C16) was analyzed on steady silicon surfaces, dependent on the spider silk layer number and thickness. Based on the results, a model for structural features of spider silk films is proposed, combining block copolymer microphase separation theory with folding properties of recombinant eADF4(C16).

KEYWORDS: spider silk, protein structure, self-assembly, spin-coating, microphase separation



1. INTRODUCTION

Silks, like keratin and collagen,^{1–3} are protein fibers, and the underlying proteins have highly repetitive amino acid sequences. Among silk producers, web-spinning spiders (*Araneae*) have probably the highest variety of specialized silk materials. Female orb-weaving spiders such as the European garden spider *Araneus diadematus* can produce up to seven different types of silk with task-dependent properties, up to five of which are utilized in their webs.⁴

The engineered spider silk protein eADF4(C16) is based on the consensus sequence of the core domain of *A. diadematus* fibroin 4 (ADF4), which belongs to the class of major ampullate spidroin 2 (MaSp2), characterized by proline-rich sequences. Figure 1 illustrates the key elements of the primary structure of amphiphilic eADF4(C16) and the related secondary structure elements upon processing.⁵ The amino acid consensus motif of the core domain of ADF4 is called C-module (sequence: GSSAAAAAAS GPGGY GPENQGPS GPGGY GPGGP) and is repeated 16 times in the recombinant protein.⁶ eADF4(C16) is an amphiphilic protein with

polyalanine stretches reflecting hydrophobic and glycine-rich regions reflecting hydrophilic blocks. These polyalanine stretches (pAla; A_n) fold into β -sheets upon fiber assembly.^{7,8} Therein, antiparallel β -sheets are formed by assembly of several individual pAla β -strands. The surrounding elastin-like sequences (GPGGX, X = Y, P) and glutamic acid containing motifs (GPENQGPS) form an amorphous phase.^{8–14} From a polymer perspective, recombinant spider silk can be regarded as a semicrystalline material where β -sheets from several protein chains form β -sheet crystallites, which are embedded in an amorphous matrix.^{15,16} Micrometer-thick films cast of eADF4(C16) show a secondary structure similar to that of natural spider silk fibers and have a β -sheet content (B) between 34 and 52% depending on parameters like solvent, post-treatment, and substrate material on which the films are cast.^{17–20}

Received: August 24, 2019

Accepted: October 30, 2019

Published: October 30, 2019

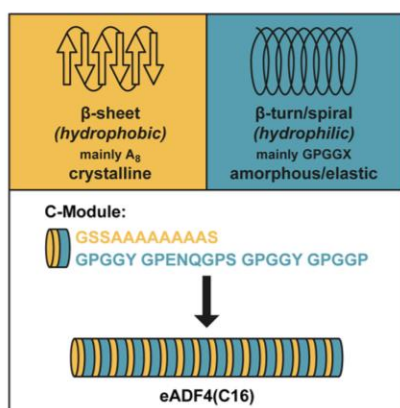


Figure 1. Primary structure (amino acid sequence) of the amphiphilic C-module and corresponding secondary structure elements in recombinant spider silk protein eADF4(C16). The two-color code indicates the block-copolymer-like structure where the hydrophobic part of the amino acid sequence is shown in yellow and the hydrophilic part is shown in blue.

Unlike synthetic polymers, recombinant proteins have a polydispersity index of 1.0. eADF4(C16) can be considered as a block copolymer with the motif (AB)₁₆, where block A is hydrophobic and block B is hydrophilic (illustrated in Figure 1 by a two-color code of sequence stretches, A: yellow, B: blue).¹⁶ Block copolymers can in principle undergo microphase separation. Therein, similar blocks try to maximize and dissimilar blocks try to minimize their interaction, yielding separation into microdomains.^{21–24} Such microphase separation behavior has indeed been previously reported for silk proteins, including eADF4(C16),^{18,25,26} *Bombyx mori* silkworm silk fibroin,^{27,28} multiblock copolymers based on *B. mori* and other spider silk proteins,^{29,30} as well as other protein-based block copolymers.³¹ Microphase separation occurs in diluted solutions, lyotropic liquid crystalline phases, and in the solid phase.^{22,23} Phase separation and the structure of silk proteins were first described in the 1990s for the silk of the domestic silkworm *B. mori* at the water/air interface.^{32–34}

Recently, recombinant spider silk proteins based on primary structure elements of spider silk proteins of the MaSp1 class (having a low proline content) were analyzed concerning their behavior when processed into films. The used proteins, named HBA_x ($x = 1, 2, 6$), comprised a histidine-tag (H) for purification, a pAla/glycine-rich block (A) forming hydrophobic β -sheets, and a noncrystalline glycine-rich block (B).³⁵ The proteins were processed into Langmuir Blodgett films showing microphase separation of the hydrophilic and hydrophobic blocks at the air/silk and silk/substrate interfaces depending on the surface pressure³⁶ and a sequence-dependent secondary structure formation (β -sheets) in cast films of HBA₃ and HAB₃ due to the varying number of blocks.^{30,37,38}

When eADF4(C16) was cast into microfilms with a thickness of 1–2 μm , microphase separation occurred depending on the hydrophobicity of the substrate and the film thickness. On hydrophilic substrates, the hydrophilic blocks were oriented toward the substrate and hydrophobic pAla patches were oriented toward the film/air interface. Within the bulk of the film, pAla β -sheets formed β -sheet crystallites embedded in a hydrophilic Gly-rich matrix.¹⁸

Here, spider silk films of eADF4(C16) were produced by spin-coating, yielding homogeneous thin silk films with low surface roughness.^{39–41} The aim of this study was to identify the influence of the increasing number of silk layers (starting with a monolayer) on protein structure and surface properties of respective spider silk films. The term monolayer refers to the thinnest possible homogeneous layer of spider silk protein (3–4 nm). This film thickness matches with the previously reported monolayer thickness of *B. mori* silk fibroin films.⁴² Lee et al. investigated the colorimetric fingerprints of aperiodic nanopatterned silk fibroin monolayers with the dimensions for β -sheets of 5 nm and corresponding β -strands of 2 nm.⁴² Zha et al. assembled eADF4(C16) into nanofibers using simultaneous supramolecular assembly and adsorption in a one-pot approach.^{43,44} The thinnest possible coating with nanofibrils was observed with dimensions of 2–3 nm thickness and 10 nm width.^{43,44}

The present study enabled a deeper insight into structure formation and microphase separation properties of spider silk layers starting at the nanoscale, passing the mesoscale, and reaching the bulk (i.e., the microscale).

2. RESULTS

2.1. Processing of Ultrathin Spider Silk Films.

Homogenous thin eADF4(C16) films were prepared using spin-coating.^{45,46} Figure 2A shows exemplary atomic force microscopy (AFM) images (topography) of eADF4(C16) films made of 1, 2, 10, and 50 mg/mL eADF4(C16) solutions.

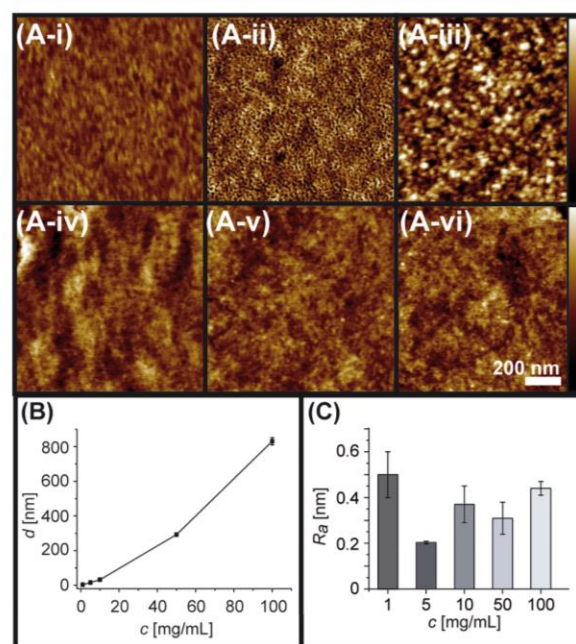


Figure 2. (A) AFM height images of thin eADF4(C16) films made using spin-coating exemplarily shown for solutions containing (i) 1, (ii) 2, (iii) 5, (iv) 10, (v) 50, and (vi) 100 mg/mL eADF4(C16) (height bar: 2 nm) on a silicon wafer. (B) Protein concentration dependency (1, 5, 10, 50, and 100 mg/mL) of the film thickness using constant spin-coating parameters. (C) Average roughness (R_a) of films prepared at protein concentrations of 1, 5, 10, 50, and 100 mg/mL (3–800 nm, respectively) on silicon measured in an area of 25 μm^2 .

Additional AFM images are shown in the Supporting Information (Figure S1). Figure 2B illustrates the concentration dependence of the coating thickness in a range of 1–100 mg/mL, leading to film thicknesses from 3 to 800 nm with an average surface roughness (R_a) of <1.0 nm for all prepared films (Figure 2C). Thus, spin-coating allowed controlled processing of ultrathin silk films by simply varying the silk concentration in solution. Observation of microphase separation in thin silk films by AFM was limited by the small size of hydrophilic (23 amino acids) and hydrophobic (12 amino acids) blocks combined with the similar physical properties (stiffness/softness; adhesion between tip and surface) of the two different blocks in the C-module. The spider silk film processed from 1 mg/mL protein solution showed vertically aligned segments (Figure 2A-i), whereas the 2 mg/mL film showed mesophasic features and a smooth surface (Figure 2A-ii). Through further increase of the protein concentration to 10 and 50 mg/mL eADF4(C16), the structural features of the films became more blurred and cloudier (Figure 2A-iii and A-iv).

2.2. Secondary Structure and Contact Angle Analysis.

In the following, nanofilms are depicted as films with a thickness of 1 to ~100 nm; films in the range of 100 nm to ~999 nm are called submicrofilms, and films thicker than 1 μm are called microfilms. The relative β -sheet content (B) of spin-coated nano- and (sub)microfilms ($d = 3\text{--}800\text{ nm}$) after spin-coating and before (bpt) or after (apt) post-treatment with methanol vapor was determined using grazing angle attenuated total reflectance (GATR)-Fourier transform infrared (FTIR) spectroscopy measurements and data treatment using Fourier self-deconvolution (FSD) and curve fitting of the amide I band, yielding the β -sheet content shown in Figure 3A (see Supporting Information, Figure S3 and S4). The amide I band is mainly a superposition of C=O stretching vibrations from the amide groups of the protein backbone, and they are influenced considering their vibration energy by intra- and intermolecular coupling due to their specific/defined secondary structural surroundings.^{47,48} In eADF4(C16) nanofilms ($d = 3\text{--}4\text{ nm}$), a relative β -sheet content of $B_{\text{bpt}} = 14.2 \pm 2.7\%$ was obtained before post-treatment. The thickness of the thinnest prepared eADF4(C16) nanofilm was similar to the thickness of β -sheet platelets and nanofilaments reported for silkworm silk fibroin and eADF4 nanofibrils ($d = 2\text{--}5\text{ nm}$).^{41,43,49} When the film thickness was increased, B_{bpt} also increased. A steady increase in B_{bpt} could be observed with an increasing film thickness of nano- and (sub)microfilms until a saturation was reached with a relative β -sheet content of $B_{\text{bpt}} = 18\text{--}21\%$ at $d > 65\text{ nm}$.

The steady increase of B_{bpt} from mono- to bilayered nanofilms to (sub)microfilms can be explained by the intra- and intermolecular interactions of the protein and the interaction of eADF4(C16) molecules with the silicon wafer surface. Due to the fast evaporation of formic acid, which was used as solvent for eADF4(C16), the silk molecules were frozen in a metastable partially unstructured state and did not have time for folding into secondary structures like β -sheets. In the thinnest produced nanofilm, the silk molecules had no protein neighbor in the z -direction, and interactions with other molecules were only possible in the xy -plane. The B_{bpt} determined in the films when $d < 10\text{ nm}$ can be explained by interactions of the protein backbone with the surface of the substrate. If the molecules were forced to the surface in a monolayer, the carbonyl group (C=O) could only interact

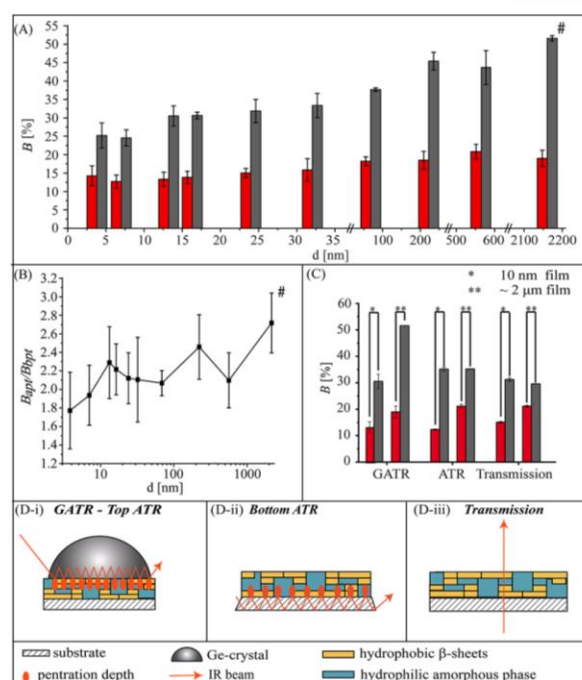


Figure 3. (A) β -sheet content B of spin-coated eADF4(C16) films before (bpt) and after post-treatment (apt, gray) in methanol atmosphere dependent on film thickness d (red). (B) Ratio of the relative average β -sheet content after (B_{apt}) and before post-treatment (B_{bpt}) reflects the increase in B due to post-treatment in a methanol atmosphere. Connecting lines are auxiliary lines to guide the eye. Microfilms with a thickness of $\sim 2\ \mu\text{m}$ were prepared by drop-casting. (C) β -sheet content B before (bpt, red) and after post-treatment (apt, gray) in a methanol atmosphere measured using three different FTIR techniques, namely GATR, ATR, and transmission. (D) Schematic representation of different FTIR techniques: (i) shows the GATR setup, where the film is measured on the surface facing the air. (ii) The complementary measurement setup. There, the substrate/film interface is measured using attenuated total reflection with the ATR mode. (iii) Representation of a transmission measurement, where parts of the IR beam penetrate the entire sample. Signals derived from the spin-coated eADF4(C16) films depended on the used FTIR technique.

with the silicon oxide (SiO_2) layer, which covered the silicon wafer surface. However, the probability to form pAla–pAla interactions increased in a multilayer. The increase in layer thickness raised the probability (gain in the degree of freedom of translation) to form inter- and intramolecular interactions (pAla–pAla; β -sheets), leading to a rise of B_{bpt} . The volume phase also increased with the layer thickness. An increasing volume phase caused a higher degree of the amorphous silk phase, in which β -crystallites could more readily grow with less confinement from the silicon/silk and the silk/air interface.

Post-treatment of spider silk films in methanol atmosphere led to an increasing β -sheet content (rearrangement of pAla stretches into β -sheets) due to dehydration (Figure 3A and Supporting Information, Figures S3 and S4).^{39,50–52} The post-treatment in methanol vapor led to temporary swelling of the spider silk films.⁵³ Here, we assume that the differences in B_{apt} in nano and (sub-)microfilms occur from the limited diffusion of methanol vapor to the bulk of the microfilm because the conversion of pAla-patches to β -sheet starts at the

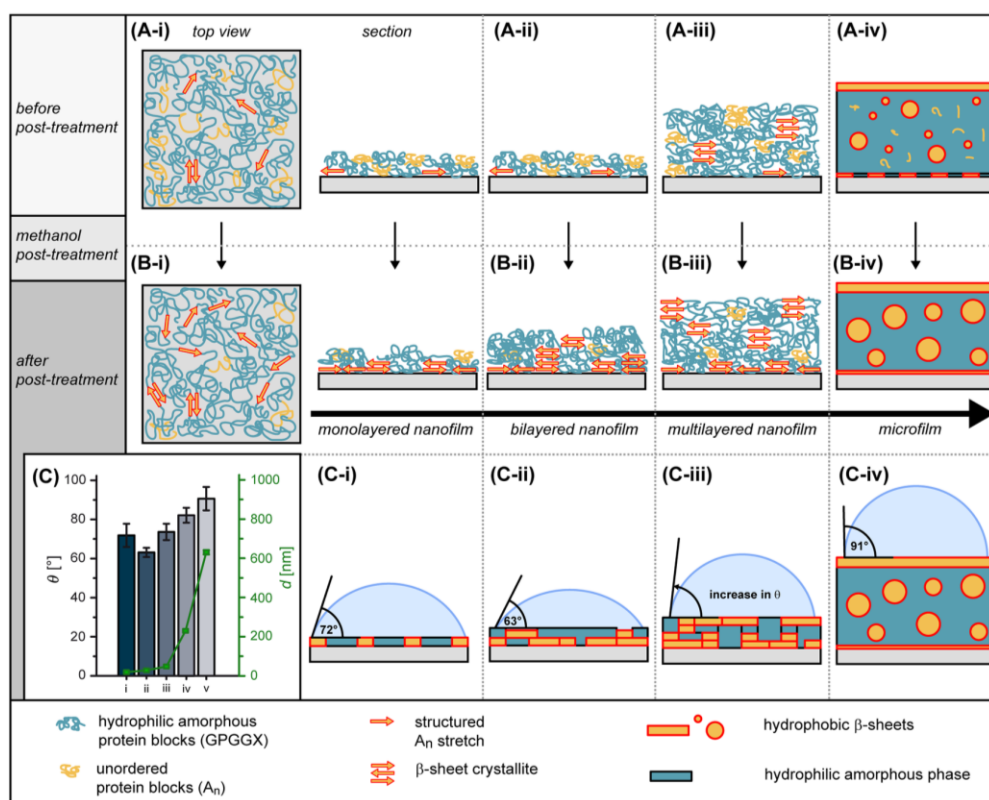


Figure 4. Structural assembly model for eADF4(C16) films dependent on the film thickness from the nano- to microscale. A detailed structural model for films (A) directly after spin-coating and drying and (B) after post-treatment with methanol. (C) Static water contact angle on post-treated spider silk films with simplified separation scheme and illustrated wetting behavior. In all panels (A–C): (i) monolayered nanofilms showed 2D separation of the hydrophilic and hydrophobic phases, (ii) bilayered nanofilms showed a pAla-enriched phase at the silicon/air interface leading to exposition of the hydrophilic phase at the protein/air interface, (iii) multilayered nanofilms yielded pAla-rich surface/protein interfaces and β -sheet-rich protein/air interfaces, which are hydrophobic,¹⁸ and (iv) microfilms showed microphase separation in the bulk film as previously reported by Wohlrab et al., in which β -sheet crystallites are separated at the protein/air interface as well as embedded as micelle-like inclusions in the amorphous matrix.¹⁸

interface and therefore limits the diffusion of the methanol vapor to the deeper layers of the film. After the post-treatment in methanol, the films were stored in air to allow the methanol to evaporate completely. B_{apt} was always measured with dry films. The film thickness was only temporarily influenced by the post-treatment.⁵³ At the beginning, Hu et al. stated that structural water can act as a “mobility enhancer” and increases the flexibility and the extensibility, but exposure to nonaqueous solvents yields in β -sheet formation. In all cases, post-treatment led to an increase in B . Figure 3B shows the ratio ($B_{\text{apt}}/B_{\text{bpt}}$) of the β -sheet content after (B_{apt}) and before post-treatment (B_{bpt}). The lowest rise in B upon post-treatment was observed for spider silk monolayers ($d \approx 4$ nm) ($B_{\text{apt}}/B_{\text{bpt}} = 1.8 \pm 0.4$). The error of $B_{\text{apt}}/B_{\text{bpt}}$ was calculated using Gauß law of propagation. If the layer thickness was doubled ($d \approx 8$ nm), $B_{\text{apt}}/B_{\text{bpt}}$ increased to 1.9 ± 0.3 and reached 2.3 ± 0.4 at $d \approx 13$ nm. In the case of the monolayer ($d < 5$ nm), the β -sheet content increased from 14.2 ± 2.7 to $25.2 \pm 3.4\%$ upon post-treatment, which was only half of the B_{apt} for eADF4(C16) microfilms because the number of pAla/pAla interactions was limited in the monolayer. Intra- and intermolecular pAla interactions could be formed only in the xy -direction, which significantly decreased the probability for these interactions. In

comparison, B_{bpt} and B_{apt} of drop-cast eADF4(C16) films with a thickness of ~ 2 μm on silicon were also investigated (Figure S2), where B increased from $B_{\text{bpt}} = 19.0 \pm 2.2\%$ to $B_{\text{apt}} = 51.6 \pm 0.7\%$ with $B_{\text{apt}}/B_{\text{bpt}} = 2.7 \pm 0.3$. This reflects the maximum relative β -sheet content $B_{\text{max,apt}}$ of post-treated eADF4(C16) films reported in literature (on glass: $35.7 \pm 1.7\%$;¹⁸ on polystyrene: $41.0 \pm 0.3\%$;¹⁸ 45.2% ¹⁹ by post-treatment with methanol, and 52.1% ²⁰ by post-treatment with $\text{K}_x\text{H}_{3-x}\text{PO}_4$). As stated above, in the case of films before post-treatment, the carbonyl group ($\text{C}=\text{O}$) could interact only with the silicon oxide layer. When the film thickness was increased, the conformational freedom, increasing volume phase, and the probability for each molecule/pAla stretch to form β -sheets increased due to the increasing number of interaction partners in each layer (z -direction). This led to an increase in B with increasing film thickness until the maximum in B_{bpt} and B_{apt} was reached at a film thickness of about 90–220 nm.

The high B_{apt} of microfilms on silicon indicates the separation of the hydrophobic β -sheet structures at the protein/air interface, considering the theoretical penetration depth d_p of the IR-irradiation during GATR-ATR measurements of 313 nm at 1590 cm^{-1} and 292 nm at 1705 cm^{-1} (see

Supporting Information, Table S1 and FTIR spectra Figures S3 and S4)).

Due to the limited penetration depth of the IR beam, two additional FTIR methods were used besides GATR-FTIR to gain a deeper insight into the distribution of β -sheet structures in eADF4(C16) nano- ($d = 10$ nm) and microfilms ($d = 1$ μ m). Schematic setups of the three different measuring modes are shown in Figure 3C. With the GATR-FTIR setup, the air/silk interface was measured (Figure 3D-i). With the ATR-FTIR setup, it was possible to measure the spider silk film structure at the silicon/silk interface (Figure 3D-ii). The third setup measured the transmission of the FTIR beam through the whole silk film (Figure 3D-iii, Supporting Information Table S2). The results from these three setups showed that, depending on which interface (silicon/silk or silk/air) was investigated, different β -sheet contents were observed. B_{bpt} showed in all three setups similar values for nano- and (sub-)microfilms as shown in detail for the GATR setup (Figure 3A, see FTIR spectra Supporting Information, GATR Figures S3 and S4, ATR Figure S5, and transmission Figure S6). In contrast to B_{bpt} the proportions of signals at the silicon/silk interface (ATR-FTIR) resulted in different values for B_{apt} . Nano- and microfilms contained the same amount of β -sheets ($B_{10\text{nm}} = 35.2 \pm 0.7\%$; $B_{1\mu\text{m}} = 35.2 \pm 0.5\%$). This could be explained by limited diffusion of methanol during the post-treatment process for the (sub-) microfilms because the β -sheets on the interface air/film formed a more compact layer through which the methanol vapor could no longer diffuse freely. Therefore, the bulk (middle) and lower part of the film showed less β -sheet content (see Supporting Information, Figure S7).

Transmission FTIR provided the overall β -sheet content of the films. Interestingly, B of the nanofilms doubled ($B_{\text{bpt}} = 15.1 \pm 0.3\%$ to $B_{\text{apt}} = 31.2 \pm 0.6\%$) upon methanol post-treatment, whereas B_{bpt} in microfilms was already $21.1 \pm 0.4\%$ and only slightly increased to $B_{\text{apt}} = 29.6 \pm 0.2\%$ after methanol post-treatment.

3. DISCUSSION

Structural Assembly of Spider Silk Proteins on Surfaces Depends on the Number of Layers/Film Thickness. An interesting observation was the increase in B until saturation by increasing the spider silk film thickness. Analysis of B combined with the surface wetting properties of the spin-coated thin spider silk films led to a structural assembly model for eADF4(C16) films depending on the number of protein layers (Figure 4).

Blocks in polymers (here: hydrophobic and hydrophilic sequence motifs of the C-module) are only miscible if they interact through specific interactions such as hydrogen bonds, charge-charge, and hydrophobic interactions, which yields structuring/folding of the protein. In eADF4(C16), the hydrophilic Gly-rich blocks do not significantly interact with the more hydrophobic pAla blocks, and therefore, interactions between identical blocks are preferred. Due to the covalent connection (i.e., the polypeptide backbone) of the hydrophilic and the hydrophobic block, the molecules could not undergo macroscopic phase separation in the solid-state, i.e., in contact with a substrate's surface. If one considers eADF4(C16) an amphiphilic block copolymer with the architecture $(AB)_{16}$, it is possible to calculate the volume fraction ϕ_A for the hydrophobic block and ϕ_B for the hydrophilic block. The amino acid sequence of the C-module (Figure 1) is divided

into 12 amino acids which correspond to the hydrophobic block A and 23 amino acids which correspond to the amorphous, hydrophilic block B. For $(AB)_{16}$ polymers, the ratio of block A to the total number of aa in the sequence is a value for the expected type of microphase formation. It results in $\phi_A = 0.34$ for the hydrophobic block, which is also the theoretical β -sheet content of eADF4(C16). At $\phi_A = 0.35$ – 0.65 , alternating lamellar structures for A and B would be observed.⁵⁴ In contrast, at $0.2 < \phi_A < 0.35$, cylindrical structures would be observed for the hydrophobic block.⁵⁴ These theoretical volume fractions fit very well with the observed B as obtained from the transmission FTIR measurements (Figure 3D). There, the overall B was $31.2 \pm 0.6\%$ for the 8 nm nanofilm and $29.6 \pm 0.2\%$ for the 2 μ m microfilm. Interestingly, B_{apt} of the 2 μ m eADF4(C16) film was significantly higher when measuring in the GATR mode. These led to the assumption that microphase separation is the driving force for the increase of β -sheet content after post-treatment. The methanol cannot diffuse deeply into the film, and therefore, the bulk phase of the (sub-)microfilm has less β -sheet content than the surface where the methanol can convert the pAla patches into β -sheets.

In contrast to cast films, where the silk molecules formed bigger β -sheet crystallites during the drying process, spin-coating of eADF4(C16) out of formic acid led to metastable and mainly unstructured silk films due to the fast evaporation of the solvent during the spin-coating process. In thin films, the microstructure was also influenced by the protein/substrate (surface field) and protein/air interface as well as the thickness (i.e., the number of layers) of the protein film.^{55–57}

Surface wetting properties of post-treated eADF4(C16) films were analyzed as an indicator of the structural properties of the protein/air interphase. Due to the low crystallinity (low β -sheet content) of the metastable silk films, it was not possible to determine the water contact angle before post-treatment. The eADF4(C16) monolayer was composed of statistically distributed and mainly unfolded hydrophilic and hydrophobic blocks (Figure 4A-i). Upon post-treatment, the β -sheet content was increased, and the films turned water-stable because methanol induced refolding and restructuring at the surface. The hydrophobic pAla stretches further interacted with the substrate and were surrounded by the hydrophilic phase, but microphase separation could only occur in the xy -direction (Figure 4B-i). Figure 4C shows the static water contact angle θ of post-treated eADF4(C16) films, dependent on the film thickness. Water contact angle measurements of as-cast films (bpt) are not possible due to their water solubility.³⁹ The statistical distribution of hydrophobic and hydrophilic blocks at the protein/air interface in monolayers yielded an “intermediate” contact angle of $72 \pm 6^\circ$, and Figure 4C-i illustrates the contact angle dependence on the statistical distribution of hydrophilic and hydrophobic blocks in the monolayer. At $5 < d < 10$ nm, the protein layer at the substrate/protein interface could interact with the substrate in a monolayer-like manner, and the protein layer at the protein/air interface was mainly unstructured (Figure 4A-ii). Upon post-treatment, β -sheets also formed in the z -direction between the layers. The morphology of thin block copolymer films, in general, depends on the influence of the surface field on the biopolymer/protein and the film thickness. The morphology and the microstructure in thin films can significantly differ from the structure in the bulk, which explains the observed results.⁵⁸ The silk system changed its properties upon

increasing the film thickness due to the interplay of folding and microphase separation. At $5 < d < 10$ nm, microphase separation was mainly influenced by the surface field, while in thicker films, additional protein folding processes took place independent of the surface. For as-spin-coated films, the probability of forming β -sheets further increased with thickness/number of layers (Figure 4A-iii). Accordingly, the β -sheet content increased with increasing film thickness before as well as after post-treatment. In post-treated multilayered films, the hydrophilic and hydrophobic blocks could also form bigger volumes of individual blocks during microphase separation (Figure 4B-iii). The hydrophobic β -sheets oriented toward the protein/air interface with increasing film thickness (Figure 4C-iii). On top of the initial pAla-rich layer at the substrate/protein interface, a hydrophilic phase was formed in which hydrophobic patches were embedded if a critical film thickness between 90 and 250 nm was reached. In the latter, the β -sheet amount before (B_{ppt}) and after (B_{apt}) post-treatment reached its maximum. In this film thickness range, the β -sheet content was more or less constant, but the surface water contact angle at the protein/air interface still increased until a film thickness of 600 nm was reached. This can be explained by the formation of hydrophobic β -sheet-rich patches (increasing micellar character¹⁸) with increasing film thickness. Before post-treatment, only smaller hydrophobic patches were formed (Figure 4A-iii), and post-treatment led to the formation of bigger β -sheet crystallites as well as to increased separation of hydrophobic blocks at the protein/air interface (Figure 4B-iii). A more distinct separation of hydrophilic and hydrophobic blocks occurred in thick films ($\sim 2 \mu\text{m}$ produced by drop casting) as previously reported by Wohlrab et al.¹⁸ Exposition of hydrophobic β -crystallites at the protein/air interface led to a hydrophobic surface (Figure 4A-iv, B-iv, C-iv). The GATR measurements (Figure 3D-i) as well as the ATR-FTIR measurements indicated that the $2 \mu\text{m}$ film showed a very high β -sheet content at the protein/air interface ($B_{\text{apt}} = 51.6 \pm 0.7\%$, $d_p \sim 300$ nm), which confirmed the proposed microphase separation model (Figure 4A-iv, B-iv, C-iv). More than 85% of the overall β -sheet content ($29.6 \pm 0.2\%$) was oriented toward both surfaces (silicon/protein and protein/air). Hence, in the center of the films, only approximately 15% of the formed β -sheets were located and generated a micellar-like phase, as detected previously. For the 8 nm film, where all three FTIR setups can detect the entire signal of the film, B_{apt} was nearly identical for all setups ($B_{\text{apt}} \sim 32\%$), which fits very well to the theoretically calculated maximum β -sheet content ($\phi_A = 0.35$, $B_{\text{apt,max}} = 35\%$).

4. CONCLUSION

Spin-coating of eADF4(C16) allowed controlling film thickness by simply varying the concentration of the protein in solution while keeping all other spin-coating parameters constant. The resulting films showed low average surface roughness ($R_a < 1$ nm). Secondary structure and surface properties (surface hydrophilicity) of eADF4(C16) films changed upon varying the number of silk layers/film thickness and post-treatment. In eADF4(C16) films, different physical properties of the hydrophilic and hydrophobic amino acid sequence blocks led to microphase separation. β -Sheet structures mainly occurred at the substrate/protein interface, especially in very thin films. When the film thickness was increased (and more protein layers were added), the proteins could interact in all three directions. The β -sheet content (B_{ppt}

B_{apt}) reached its maximum for spin-coated eADF4(C16) films at a film thickness of ~ 100 nm, but the surface properties (protein/air interface) of silk films changed until a film thickness of $d > 600$ nm, where the water contact angle was identical to that of cast bulk silk films.

5. EXPERIMENTAL SECTION

Materials. If not stated otherwise, all chemicals were purchased from Roth (Karlsruhe, Germany) in analytical grade. eADF4(C16) (salt-free) was purchased from AMSilk GmbH (Planegg/München, Germany). The used water was ultrapure and obtained by using a Merck Millipore system (Billerica, MA, United States).

Processing of eADF4(C16) into Nano- and (Sub)microfilms. Polished (111) silicon wafers (CrysTec GmbH, Berlin, Germany) were cut into 1×1 cm pieces and cleaned by rinsing with acetone and heating using snow-jetting prior to coating. eADF4(C16) was dissolved in formic acid at desired concentrations. Silk solutions ($V = 20 \mu\text{L}$) were placed in the center of the substrate and spin-coated ($f_{\text{rot}} = 4000$ rpm, $a_{\text{rot}} = 1800$ rpm/s, $t = 30$ s) using a I-EC 101 DT-19456 Spin-Coater (Headway Research Inc., Garland, United States). Silk microfilms with a thickness of $d \sim 2 \mu\text{m}$ were prepared by casting. The silk solution was cast on silicon wafers at 1 mg/cm^2 and dried overnight at ambient conditions. For post-treatment, samples were placed in a desiccator with 20 mL methanol at the bottom. The desiccator was evacuated ($p = 10\text{--}1$ mbar) to generate a saturated methanol atmosphere, and samples were incubated overnight.

Atomic Force Microscopy. For surface morphology characterization film, surfaces were analyzed in tapping mode using a Dimension 3100 Nanoscope V (Bruker, Karlsruhe, Germany) with a resolution of 512 by 512 data points at 0.5 to 1 Hz. Silicon cantilevers (OTESPA-R3, Bruker, Karlsruhe, Germany) were used with a force constant of 26 N m^{-1} . The average roughness R_a was calculated in an area of $25 \mu\text{m}^2$.

Film Thickness Measurements. For thickness measurements of spin-coated films, samples were scratched using a sharp tweezer, and the scratched area was measured perpendicular to the direction of the scratch. For analysis of the film thickness, STEP and DEPTH routine of Nanoscope Analysis 1.5 Software (Bruker, Karlsruhe, Germany) was used. Silk microfilms were cast on the polished side (top) of silicon wafers. To generate a sharp breaking edge, the silicon wafer substrate was scratched underneath and broken afterward. The defined breaking edge was analyzed by scanning electron microscopy (SEM) using a Leo 1530 Gemini (Zeiss, Oberkochen, Germany) at an accelerating voltage of 3 kV. Samples were sputtered with 1.3 nm platinum.

GATR-FTIR. Fourier transform infrared spectroscopy was performed using the VariGATR grazing angle attenuated total reflection accessory (Harrick Scientific Products Inc., Pleasantville, United States) using a Bruker Tensor 27 FTIR-spectrometer with an MCT detector (Bruker, Rheinstetten, Germany). For absorbance measurements, a grazing angle of 62° was used. One-hundred and forty scans from 4000 cm^{-1} to 800 cm^{-1} were averaged at a resolution of 2 cm^{-1} . The penetration depth d_p of the evanescent wave depends on the refractive indices of the germanium crystal (n_1) and of the sample (n_2 , silk film at the silicon wafer), angle of incidence (α), and the wavelength of the incident light (λ), as shown in eq 1.⁵⁹

$$d_p = \frac{\lambda}{2\pi n_1 \left(\sin^2(\alpha) - \left(\frac{n_2}{n_1} \right)^2 \right)^{1/2}} \quad (1)$$

For $\alpha = 62^\circ$ (1.0821 rad), $n_1 = 4$ of germanium crystal ($T = 20^\circ \text{C}$, $\lambda_{\text{IR}} = 6 \mu\text{m}$),⁶⁰ and $n_2 = 1.5$ of silk proteins,⁴⁰ the penetration depth d_p was calculated in the amide I region ($\nu = 1705$ to 1590 cm^{-1}) to be $d_p = 293\text{--}313$ nm (Supporting Information Table S1).

The relative error $\sigma_{B_d}^{\text{rel}}/B_d^{\text{rel}}$ (with $B_d^{\text{rel}} = B_{\text{apt}}/B_{\text{ppt}}$, $\sigma_{B_d}^{\text{rel}}$: absolute error of B_d^{rel}) for specific film thicknesses d was calculated using the Gauß law of

error propagation using eq 2. $\sigma_{B_{x,d}}$ ($x = \text{apt, bpt}$) is the standard deviation of $B_{x,d}$ ($x = \text{apt, bpt}$) for a specific film thicknesses d .

$$\left(\frac{\sigma_{B_d^{\text{total}}}}{B_d^{\text{total}}}\right)^2 = \left(\frac{\sigma_{B_{\text{apt},d}}}{B_{\text{apt},d}}\right)^2 + \left(\frac{\sigma_{B_{\text{bpt},d}}}{B_{\text{bpt},d}}\right)^2 \quad (2)$$

Preparation of Films for ATR and Transmission FTIR Measurements. eADF4(C16) was dissolved in formic acid at desired concentrations. Thin spider silk films ($\ll 1 \mu\text{m}$) were prepared by spin coating. Therefore, diluted silk solutions ($V = 200 \mu\text{L}$, $c \geq 1 \text{ mg/mL}$) were placed in the center of trapezoidal silicon (Si) internal reflection elements (IRE, $50 \times 20 \times 2 \text{ mm}^3$, see below) and spin-coated ($f_{\text{rot}} = 4500 \text{ rpm}$, $t = 30 \text{ s}$) using a commercial Spin-Coater (SCT-10, LOT ORIEL, Darmstadt, Germany). The Spin-coater was equipped with a home-built rotating plate (Al), in which a mount (deepening) for fixation of the IRE was milled. After spin-coating, the total area of Si IRE and the lower half area of the silicon crystal ($50 \times 10 \text{ mm}^2$) was cleaned with water using a tissue. Thick silk films ($\sim 2 \mu\text{m}$) were prepared by casting, i.e., placing a concentrated silk solution ($V \geq 10 \mu\text{L}$, $c \geq 50 \text{ mg/mL}$) as spot in the middle of the upper half area ($50 \times 10 \text{ mm}^2$) of Si IRE followed by drying under gentle N_2 gas stream optionally using a heatable metal support at $T = 50 \text{ }^\circ\text{C}$. For post-treatment (vapor phase), samples (silk coated IREs) were placed on a base in a closed crystallizing dish filled with $250 \mu\text{L}$ of methanol not directly contacting the sample. Samples were incubated overnight.

ATR and Transmission FTIR Spectroscopy. An FTIR spectrometer (Tensor II, BRUKER-Optics GmbH, Ettlingen, Germany) equipped with global source and either deuterated triglycine sulfate (DTGS) or a mercurium–cadmium–telluride (MCT) detector was used in the mid-IR range. FTIR spectra were recorded in the wavenumber range between $4000\text{--}400 \text{ cm}^{-1}$ at 2 cm^{-1} spectral resolution, and 50 scans were done. Both modes, transmission (TRANS) FTIR and attenuated total reflection (ATR) FTIR, were used.

TRANS-FTIR was applied at silicon (Si) internal reflection elements (IRE), which were fixed in constructed sample holders (M. Ulrich, M.M., IPF Dresden). The IR beam transmitted the Si IRE at minimum focal area ($< 5 \text{ mm}$) in the FTIR sample chamber. TRANS FTIR absorbance spectra $A(\nu)$ were recorded from spider silk coated (spin coated or cast) Si IREs as the sample intensity $I_S(\nu)$ and clean (plasma cleaner, Harrick, Ossining, NY, United States) uncoated Si IREs as the reference intensity $I_R(\nu)$ and processed according to $A(\nu) = -\log [I_S(\nu)/I_R(\nu)]$.

ATR-FTIR was applied at trapezoidal Si IREs ($50 \times 20 \times 2 \text{ mm}^3$, see above) allowing an incident and leaving angle of 45° . Si IREs were fixed in sample holders (M. Ulrich, M.M., IPF Dresden) located in a commercial pseudodouble-beam-ATR device (OPTISPEC, Neerach, Switzerland) operated according to the single-beam-sample-reference (SBSR) concept of Fringeli.⁶¹ In principle, the (spin-coated or cast) silk film was located at the upper half area ($50 \times 10 \text{ mm}^2$) of the front side of Si IRE, which was achieved by cleaning the lower half area ($50 \times 10 \text{ mm}^2$) from silk material. Sample $I_S(\nu)$ and reference $I_R(\nu)$ intensities were measured by alternately shuttling the upper and lower half of the Si IRE into the IR beam using a lift, and absorbance spectra were computed similar to that of TRANS-FTIR according to $A(\nu) = -\log [I_S(\nu)/I_R(\nu)]$.

Fourier Self-Deconvolution and Curve Fitting. To determine the fractions of individual secondary structures, the amide I region (1595 cm^{-1} to 1705 cm^{-1}) was analyzed by Fourier self-deconvolution (FSD) with subsequent curve fitting according to Hu et al. using the Software Opus 6.5 (Bruker Optics Corp., Billerica, MA, United States).⁴⁷

Water Contact Angle. To analyze surface wettability, static water contact angles on surfaces were analyzed using the OCA contact angle system (DataPhysics Instruments GmbH, Filderstadt, Germany). A water droplet of $2 \mu\text{L}$ was placed on the surface, and the contact angles were determined using the SCA 20 software (DataPhysics Instruments GmbH, Filderstadt, Germany) and a Laplace–Young fit.

■ ASSOCIATED CONTENT

Supporting Information

The Supporting Information is available free of charge on the ACS Publications website at DOI: 10.1021/acsapm.9b00792.

AFM topography pictures of films at all concentrations showing 3 different pictures sizes ($1, 9, \text{ and } 625 \mu\text{m}^2$) (Figure S1); representative SEM image of the thickness of a microfilm (Figure S2); normalized spectra of all three used FTIR methods with a magnification of the amide I band region (Figures S3–S7); values of the penetration depth of the IR beam (Table S1); summary of the values for the β -sheet content of the three FTIR methods with standard derivation (Table S2) (PDF)

■ AUTHOR INFORMATION

Corresponding Author

*E-mail: thomas.scheibel@bm.uni-bayreuth.de

ORCID

Martin Müller: 0000-0001-8961-4604

Andreas Fery: 0000-0001-6692-3762

Thomas Scheibel: 0000-0002-0457-2423

Author Contributions

[†]C.B.B. and S.L. contributed equally. Conceptualization: C.B.B., A.F., and T.S.; methodology: C.B.B., S.L., M.M., A.F., and T.S.; investigation: C.B.B., S.L., and M.M.; writing of original draft: C.B.B. and S.L.; review and editing: S.L., M.M., A.F., and T.S.; visualization: C.B.B. and S.L.; supervision: A.F. and T.S.; funding: A.F. and T.S.

Funding

This work is supported by Grants DFG SCHE603/23-1 and DFG FE600/29-1.

Notes

The authors declare no competing financial interest.

■ ACKNOWLEDGMENTS

We thank Martin Humenik for helpful discussion regarding the manuscript and Markus Hund for support during AFM measurements. We thank Birgit Urban for the ATR and the transmission FTIR measurements. We thank Prof. Laforsch for access to the Harrick VariGATR.

■ REFERENCES

- (1) Craig, C. L. Evolution of arthropod silks. *Annu. Rev. Entomol.* **1997**, *42*, 231–267.
- (2) Sutherland, T. D.; Young, J. H.; Weisman, S.; Hayashi, C. Y.; Merritt, D. J. Insect silk: One name, many materials. *Annu. Rev. Entomol.* **2010**, *55*, 171–188.
- (3) Vollrath, F.; Porter, D. Spider silk as archetypal protein elastomer. *Soft Matter* **2006**, *2* (5), 377–385.
- (4) Lintz, E. S.; Scheibel, T. R. Dragline, Egg Stalk and Byssus: A Comparison of Outstanding Protein Fibers and Their Potential for Developing New Materials. *Adv. Funct. Mater.* **2013**, *23* (36), 4467–4482.
- (5) Exler, J. H.; Hummerich, D.; Scheibel, T. The amphiphilic properties of spider silks are important for spinning. *Angew. Chem., Int. Ed.* **2007**, *46* (19), 3559–3562.
- (6) Huemmerich, D.; Helsen, C. W.; Quedzuweit, S.; Oschmann, J.; Rudolph, R.; Scheibel, T. Primary structure elements of spider dragline silks and their contribution to protein solubility. *Biochemistry* **2004**, *43* (42), 13604–13612.

- (7) Boyle, A. L. Applications of de novo designed peptides. *Peptide Applications in Biomedicine, Biotechnology and Bioengineering* 2018, 51–86.
- (8) Boyle, A. L. 3: Applications of de novo designed peptides. In *Peptide Applications in Biomedicine, Biotechnology and Bioengineering*; Koutsopoulos, S., Ed.; Woodhead Publishing: 2018; pp 51–86.
- (9) Eisoldt, L.; Smith, A.; Scheibel, T. Decoding the Secrets of Spider Silk. *Mater. Today* 2011, 14 (3), 80–86.
- (10) Brooks, A. E.; Nelson, S. R.; Jones, J. A.; Koenig, C.; Hinman, M.; Stricker, S.; Lewis, R. V. Distinct contributions of model MaSp1 and MaSp2 like peptides to the mechanical properties of synthetic major ampullate silk fibers as revealed in silico. *Nanotechnol., Sci. Appl.* 2008, 1, 9–16.
- (11) Keten, S.; Buehler, M. J. Nanostructure and molecular mechanics of spider dragline silk protein assemblies. *J. R. Soc., Interface* 2010, 7 (53), 1709–21.
- (12) Rabotyagova, O. S.; Cebe, P.; Kaplan, D. L. Role of Polyalanine Domains in β -Sheet Formation in Spider Silk Block Copolymers. *Macromol. Biosci.* 2010, 10 (1), 49–59.
- (13) Tokareva, O.; Jacobsen, M.; Buehler, M.; Wong, J.; Kaplan, D. L. Structure-function-property-design interplay in biopolymers: Spider silk. *Acta Biomater.* 2014, 10 (4), 1612–1626.
- (14) Boyle, A. L.; Woolfson, D. N. De novo designed peptides for biological applications. *Chem. Soc. Rev.* 2011, 40 (8), 4295–4306.
- (15) Lefèvre, T.; Rousseau, M.-E.; Pézolet, M. Protein Secondary Structure and Orientation in Silk as Revealed by Raman Spectromicroscopy. *Biophys. J.* 2007, 92 (8), 2885–2895.
- (16) Pappu, R. V.; Wang, X.; Vitalis, A.; Crick, S. L. A polymer physics perspective on driving forces and mechanisms for protein aggregation. *Arch. Biochem. Biophys.* 2008, 469 (1), 132–141.
- (17) Keerl, D.; Scheibel, T. Characterization of natural and biomimetic spider silk fibers. *Bioinspired, Biomimetic Nanobiomater.* 2012, 1 (BBN2), 83–94.
- (18) Wohlrab, S.; Spieß, K.; Scheibel, T. Varying surface hydrophobicities of coatings made of recombinant spider silk proteins. *J. Mater. Chem.* 2012, 22 (41), 22050–22054.
- (19) Slotta, U.; Tammer, M.; Kremer, F.; Koelsch, P.; Scheibel, T. Structural analysis of spider silk films. *Supramol. Chem.* 2006, 18 (5), 465–471.
- (20) Spiess, K.; Lammel, A.; Scheibel, T. Recombinant Spider Silk Proteins for Applications in Biomaterials. *Macromol. Biosci.* 2010, 10 (9), 998–1007.
- (21) Darling, S. B. Directing the self-assembly of block copolymers. *Prog. Polym. Sci.* 2007, 32 (10), 1152–1204.
- (22) Förster, S.; Plantenberg, T. From self-organizing polymers to nanohybrid and biomaterials. *Angew. Chem., Int. Ed.* 2002, 41 (5), 688–714.
- (23) Mai, Y.; Eisenberg, A. Self-assembly of block copolymers. *Chem. Soc. Rev.* 2012, 41 (18), 5969–5985.
- (24) Hu, H.; Gopinadhan, M.; Osuji, C. O. Directed self-assembly of block copolymers: a tutorial review of strategies for enabling nanotechnology with soft matter. *Soft Matter* 2014, 10 (22), 3867–89.
- (25) Rammensee, S.; Slotta, U.; Scheibel, T.; Bausch, A. R. Assembly mechanism of recombinant spider silk proteins. *Proc. Natl. Acad. Sci. U. S. A.* 2008, 105 (18), 6590–6595.
- (26) Hermanson, K. D.; Huemmerich, D.; Scheibel, T.; Bausch, A. R. Engineered microcapsules fabricated from reconstituted spider silk. *Adv. Mater.* 2007, 19 (14), 1810–1815.
- (27) Hu, X.; Lu, Q.; Kaplan, D. L.; Cebe, P. Microphase Separation Controlled β -Sheet Crystallization Kinetics in Fibrous Proteins. *Macromolecules* 2009, 42 (6), 2079–2087.
- (28) Gebhardt, R.; Vendrely, C.; Burghammer, M.; Riek, C. Characterization of the Boundary Zone of a Cast Protein Drop: Fibroin β -Sheet and Nanofibril Formation. *Langmuir* 2009, 25 (11), 6307–6311.
- (29) Rathore, O.; Sogah, D. Y. Nanostructure formation through β -sheet self-assembly in silk-based materials. *Macromolecules* 2001, 34 (5), 1477–1486.
- (30) Krishnaji, S. K.; Huang, W.; Cebe, P.; Kaplan, D. L. Influence of Solution Parameters on Phase Diagram of Recombinant Spider Silk-Like Block Copolymers. *Macromol. Chem. Phys.* 2014, 215, 1230–1238.
- (31) Rabotyagova, O. S.; Cebe, P.; Kaplan, D. L. Protein-Based Block Copolymers. *Biomacromolecules* 2011, 12 (2), 269–289.
- (32) Müller, W. S.; Samuelson, L. A.; Fossey, S. A.; Kaplan, D. L. Formation and Characterization of Langmuir Silk Films. *Langmuir* 1993, 9 (7), 1857–1861.
- (33) Valluzzi, R.; Gido, S. P.; Müller, W.; Kaplan, D. L. Orientation of silk III at the air-water interface. *Int. J. Biol. Macromol.* 1999, 24, 237–242.
- (34) Valluzzi, R.; Gido, S. P.; Zhang, W.; Müller, W. S.; Kaplan, D. L. Trigonal Crystal Structure of *Bombyx mori* Silk Incorporating a Threefold Helical Chain Conformation Found at the Air-Water Interface. *Macromolecules* 1996, 29, 8606–8614.
- (35) Rabotyagova, O. S.; Cebe, P.; Kaplan, D. L. Self-Assembly of Genetically Engineered Spider Silk Block Copolymers. *Biomacromolecules* 2009, 10 (2), 229–236.
- (36) Krishnaji, S. T.; Huang, W.; Rabotyagova, O.; Kharlampieva, E.; Choi, I.; Tsukruk, V. V.; Naik, R.; Cebe, P.; Kaplan, D. L. Thin Film Assembly of Spider-like Block Copolymers. *Langmuir* 2011, 27 (3), 1000–1008.
- (37) Krishnaji, S. T.; Bratzel, G.; Kinahan, M. E.; Kluge, J. A.; Staii, C.; Wong, J. Y.; Buehler, M. J.; Kaplan, D. L. Sequence-Structure-Property Relationships of Recombinant Spider Silk Proteins: Integration of Biopolymer Design, Processing and Modeling. *Adv. Funct. Mater.* 2013, 23 (23), 241–253.
- (38) Tokareva, O. S.; Lin, S.; Jacobsen, M. M.; Huang, W.; Rizzo, D.; Li, D.; Simon, M.; Staii, C.; Cebe, P.; Wong, J. Y.; Buehler, M. J.; Kaplan, D. L. Effect of sequence features on assembly of spider silk block copolymers. *J. Struct. Biol.* 2014, 186 (3), 412–9.
- (39) Borkner, C. B.; Elsner, M. B.; Scheibel, T. Coatings and Films Made of Silk Proteins. *ACS Appl. Mater. Interfaces* 2014, 6 (18), 15611–15625.
- (40) Jiang, C. Y.; Wang, X. Y.; Gunawidjaja, R.; Lin, Y. H.; Gupta, M. K.; Kaplan, D. L.; Naik, R. R.; Tsukruk, V. V. Mechanical properties of robust ultrathin silk fibroin films. *Adv. Funct. Mater.* 2007, 17 (13), 2229–2237.
- (41) Tao, H.; Kaplan, D. L.; Omenetto, F. G. Silk Materials - A Road to Sustainable High Technology. *Adv. Mater.* 2012, 24 (21), 2824–2837.
- (42) Lee, S. Y.; Amsden, J. J.; Boriskina, S. V.; Gopinath, A.; Mitropoulos, A.; Kaplan, D. L.; Omenetto, F. G.; Dal Negro, L. Spatial and spectral detection of protein monolayers with deterministic aperiodic arrays of metal nanoparticles. *Proc. Natl. Acad. Sci. U. S. A.* 2010, 107 (27), 12086–12090.
- (43) Huemmerich, D.; Scheibel, T.; Vollrath, F.; Cohen, S.; Gat, U.; Ittah, S. Novel Assembly Properties of Recombinant Spider Dragline Silk Proteins. *Curr. Biol.* 2004, 14 (22), 2070–2074.
- (44) Zha, R. H.; Delparastan, P.; Fink, T. D.; Bauer, J.; Scheibel, T.; Messersmith, P. B. Universal nanothin silk coatings via controlled spinrod self-assembly. *Biomater. Sci.* 2019, 7 (2), 683–695.
- (45) Metwalli, E.; Slotta, U.; Darko, C.; Roth, S. V.; Scheibel, T.; Papadakis, C. M. Structural changes of thin films from recombinant spider silk proteins upon post-treatment. *Appl. Phys. A: Mater. Sci. Process.* 2007, 89 (3), 655–661.
- (46) Junghans, F.; Morawietz, M.; Conrad, U.; Scheibel, T.; Heilmann, A.; Spohn, U. Preparation and mechanical properties of layers made of recombinant spider silk proteins and silk from silk worm. *Appl. Phys. A: Mater. Sci. Process.* 2006, 82 (2), 253–260.
- (47) Hu, X.; Kaplan, D.; Cebe, P. Determining β -sheet crystallinity in fibrous proteins by thermal analysis and infrared spectroscopy. *Macromolecules* 2006, 39 (18), 6161–6170.
- (48) Hu, X.; Kaplan, D.; Cebe, P. Dynamic protein-water relationships during β -sheet formation. *Macromolecules* 2008, 41 (11), 3939–3948.
- (49) Bates, F. S. Polymer-Polymer Phase-Behavior. *Science* 1991, 251 (4996), 898–905.

- (50) Cheng, Y.; Koh, L.-D.; Li, D.; Ji, B.; Han, M.-Y.; Zhang, Y.-W. On the strength of β -sheet crystallites of Bombyx mori silk fibroin. *J. R. Soc., Interface* **2014**, *11* (96), 20140305–20140305.
- (51) Hu, X.; Kaplan, D.; Cebe, P. Dynamic Protein–Water Relationships during β -Sheet Formation. *Macromolecules* **2008**, *41* (11), 3939–3948.
- (52) Rathore, O.; Sogah, D. Y. Self-Assembly of β -Sheets into Nanostructures by Poly(alanine) Segments Incorporated in Multi-block Copolymers Inspired by Spider Silk. *J. Am. Chem. Soc.* **2001**, *123* (22), 5231–5239.
- (53) Aigner, T.; Scheibel, T. Self-Rolling Refillable Tubular Enzyme Containers Made of Recombinant Spider Silk and Chitosan. *ACS Appl. Mater. Interfaces* **2019**, *11* (17), 15290–15297.
- (54) Mai, Y.; Zhang, F.; Feng, X. Polymer-directed synthesis of metal oxide-containing nanomaterials for electrochemical energy storage. *Nanoscale* **2014**, *6* (1), 106–121.
- (55) Knoll, A.; Horvat, A.; Lyakhova, K. S.; Krausch, G.; Sevink, G. J. A.; Zvelindovsky, A. V.; Magerle, R. Phase behavior in thin films of cylinder-forming block copolymers. *Phys. Rev. Lett.* **2002**, *89* (3) DOI: 10.1103/PhysRevLett.89.035501.
- (56) Knoll, A.; Magerle, R.; Krausch, G. Phase behavior in thin films of cylinder-forming ABA block copolymers: Experiments. *J. Chem. Phys.* **2004**, *120* (2), 1105–1116.
- (57) Krausch, G.; Magerle, R. Nanostructured thin films via self-assembly of block copolymers. *Adv. Mater.* **2002**, *14* (21), 1579–1583.
- (58) Karim, A.; Singh, N.; Sikka, M.; Bates, F. S.; Dozier, W. D.; Felcher, G. P. Ordering in Asymmetric Poly (Ethylene-Propylene)-Poly (Ethylethylene) Diblock Copolymer Thin-Films. *J. Chem. Phys.* **1994**, *100* (2), 1620–1629.
- (59) Mirabella, F. M. *Internal Reflection Spectroscopy: Theory and Application*; Marcel Dekker, Inc.: New York, United States, 1993.
- (60) Li, H. H. Refractive-Index of Silicon and Germanium and Its Wavelength and Temperature Derivatives. *J. Phys. Chem. Ref. Data* **1980**, *9* (3), 561–658.
- (61) Lindon, J. C.; Tranter, G. E.; Koppenaal, D. *Encyclopedia of Spectroscopy and Spectrometry*; Academic Press: 2016.

Supporting Information

Ultra-Thin Spider Silk Films: Insights into Spider Silk Assembly on Surfaces

*Christian B. Borkner^a ‡, Sarah Lentz^a ‡, Martin Müller^b, Andreas Fery^b and Thomas Scheibel^{a, c, d, e} **

^a Lehrstuhl Biomaterialien, Fakultät für Ingenieurwissenschaften, Universität Bayreuth, Prof.-Rüdiger-Bormann-Str. 1, 95447 Bayreuth, Germany

* Corresponding author, E-Mail: thomas.scheibel@bm.uni-bayreuth.de

^b Leibniz Institute of Polymer Research Dresden, Institute of Physical Chemistry and Polymer Physics, Hohe Str. 6, 01069 Dresden, Germany

^c Bayerisches Polymerinstitut (BPI), Bayreuther Zentrum für Kolloide und Grenzflächen (BZKG)

^d Bayreuther Zentrum für Molekulare Biowissenschaften (BZMB)

^e Bayreuther Materialzentrum (BayMAT)

^{c-e} Universität Bayreuth, Universitätsstr. 30, 95440 Bayreuth, Germany

‡ contributed equally

The supporting information includes seven figures and two tables.

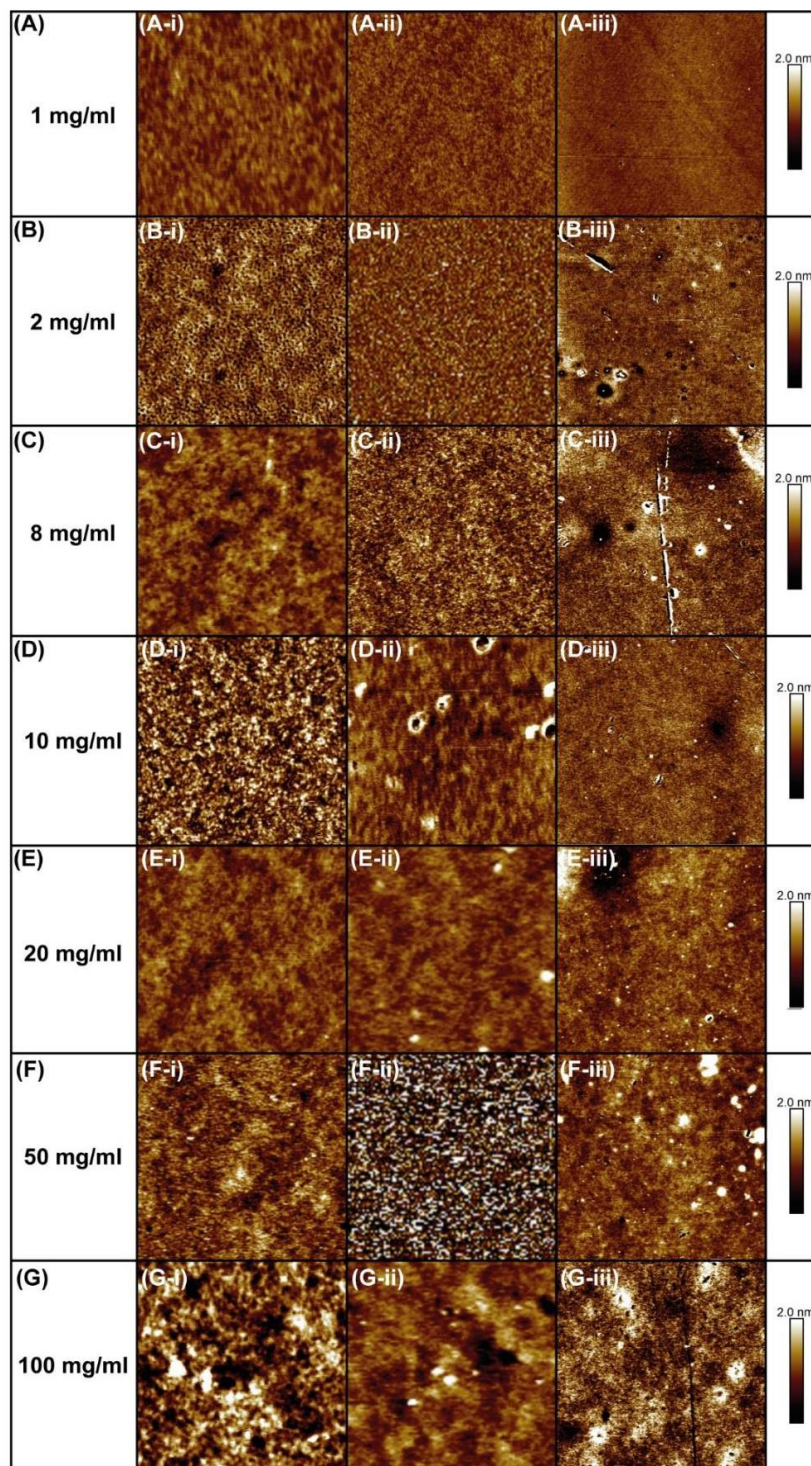


Figure S1. AFM topography images of eADF4(C16) films spin-coated with (A) 1 mg/ml, (B) 2 mg/ml, (C) 8 mg/ml, (D) 10 mg/ml, (E) 20 mg/ml, (F) 50 mg/ml and (G) 100 mg/ml eADF4(C16). Image size of (i) 1 μm x 1 μm , (ii) 3 μm x 3 μm and (iii) 15 μm x 15 μm .

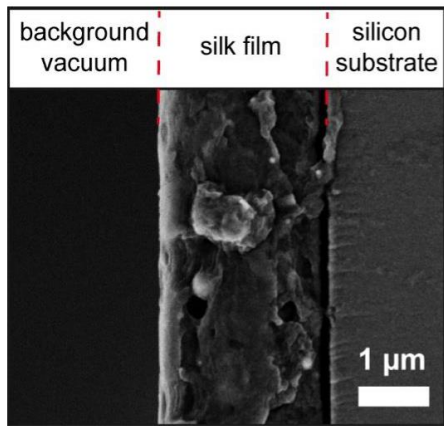


Figure S2. Exemplary SEM picture of a breaking edge of a cast eADF4(C16)-microfilm on a silicon wafer surface used for film thickness measurement.

Table S1. Calculated values of penetration depth d_p of the germanium ATR-crystal for the wave numbers ν of the amide I band.

ν , cm^{-1}	d_p , nm	ν , cm^{-1}	d_p , nm	ν , cm^{-1}	d_p , nm	ν , cm^{-1}	d_p , nm
1590	313	1619	307	1648	302	1677	296
1591	312	1620	307	1649	301	1678	296
1592	312	1621	307	1650	301	1679	296
1593	312	1622	306	1651	301	1680	296
1594	312	1623	306	1652	301	1681	296
1595	312	1624	306	1653	301	1682	295
1596	311	1625	306	1654	300	1683	295
1597	311	1626	306	1655	300	1684	295
1598	311	1627	305	1656	300	1685	295
1599	311	1628	305	1657	300	1686	295
1600	311	1629	305	1658	300	1687	295
1601	310	1630	305	1659	300	1688	294
1602	310	1631	305	1660	299	1689	294
1603	310	1632	305	1661	299	1690	294
1604	310	1633	304	1662	299	1691	294
1605	310	1634	304	1663	299	1692	294
1606	309	1635	304	1664	299	1693	294
1607	309	1636	304	1665	299	1694	293
1608	309	1637	304	1666	298	1695	293
1609	309	1638	303	1667	298	1696	293
1610	309	1639	303	1668	298	1697	293
1611	309	1640	303	1669	298	1698	293
1612	308	1641	303	1670	298	1699	293
1613	308	1642	303	1671	297	1700	292
1614	308	1643	303	1672	297	1701	292
1615	308	1644	302	1673	297	1702	292
1616	308	1645	302	1674	297	1703	292
1617	307	1646	302	1675	297	1704	292
1618	307	1647	302	1676	297	1705	291

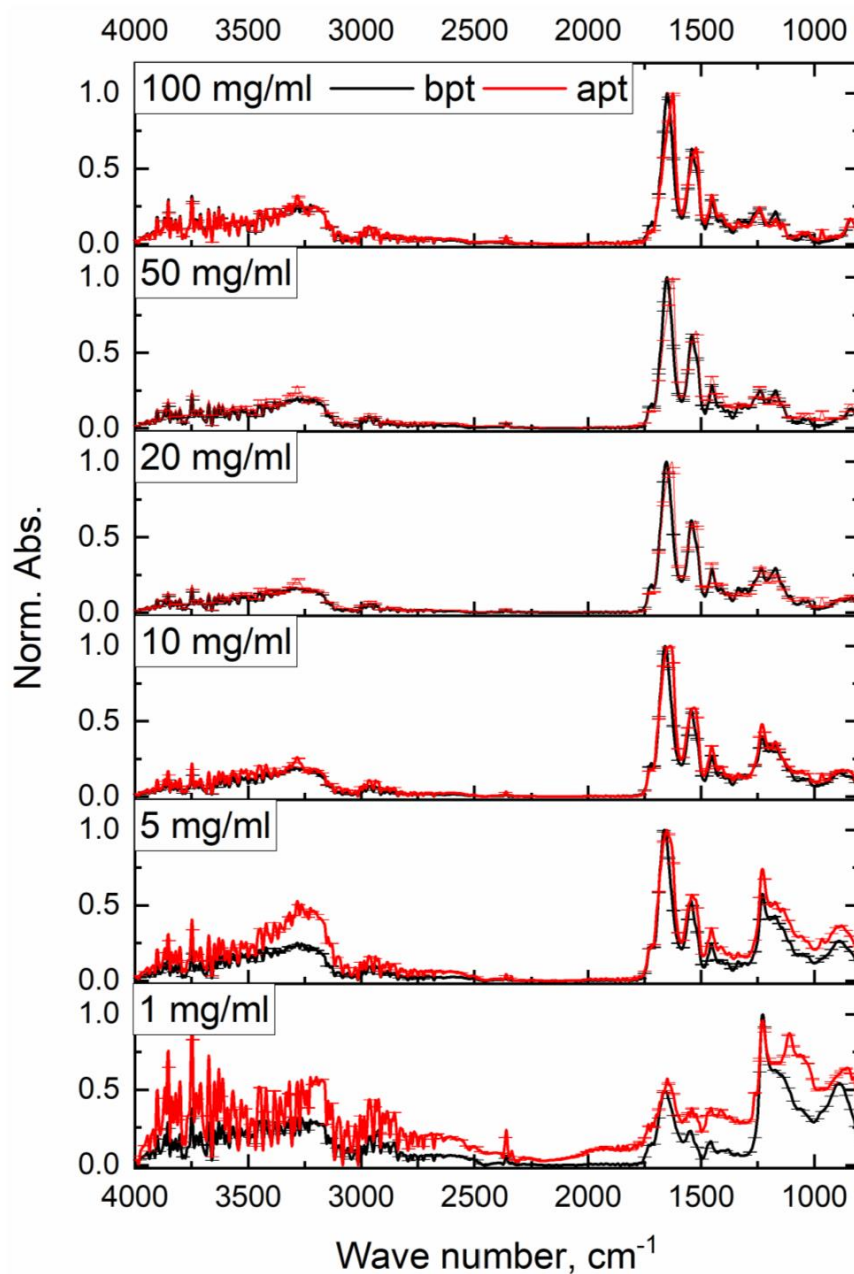


Figure S3: Averaged ($n = 3$) and normalized (to maximum) full spectra of GATR measurements of recombinant spider silk protein films with concentrations of (1, 5, 10, 20, 50, 100) mg/ml. The black lines are the GATR-FTIR spectra before post-treatment (bpt) and the red lines represent the spectra of recombinant spider silk films after post-treatment (apt). In the interest of clarity only 150 error bars per curve are shown.

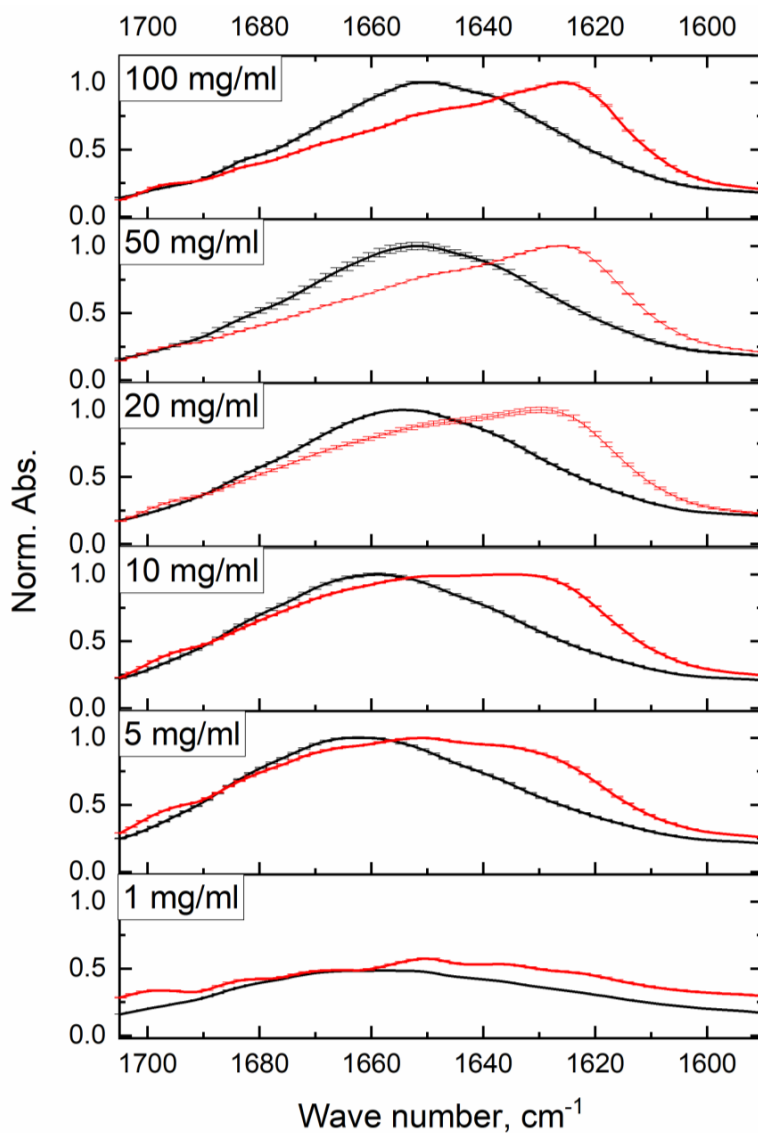


Figure S4: Averaged ($n = 3$) and normalized (to maximum) spectra of GATR measurements of the amide I band of recombinant spider silk protein films with concentrations of (1, 5, 10, 20, 50, 100) mg/ml. The black lines are the GATR-FTIR spectra before post-treatment (bpt) and the red lines represent the spectra of recombinant spider silk films after post-treatment (apt). In the interest of clarity, only 150 error bars per curve are shown.

Table S2. B_{bpt} and B_{apt} with corresponding standard derivations (SD) of nano- and microfilms of eADF4(C16) measured using three different FTIR-setups (GATR, SBSR, and Transmission-FTIR)

FTIR	10 nm film				1 μ m film			
	B_{bpt} , %	SD, %	B_{apt} , %	SD, %	B_{bpt} , %	SD, %	B_{apt} , %	SD, %
GATR	13.3	1.9	30.5	2.7	19.0	2.2	51.6	0.7
SBSR	12.3	0.2	35.2	0.7	21.1	0.7	35.2	0.5
Transmission	15.1	0.3	31.2	0.6	21.1	0.4	29.6	0.2

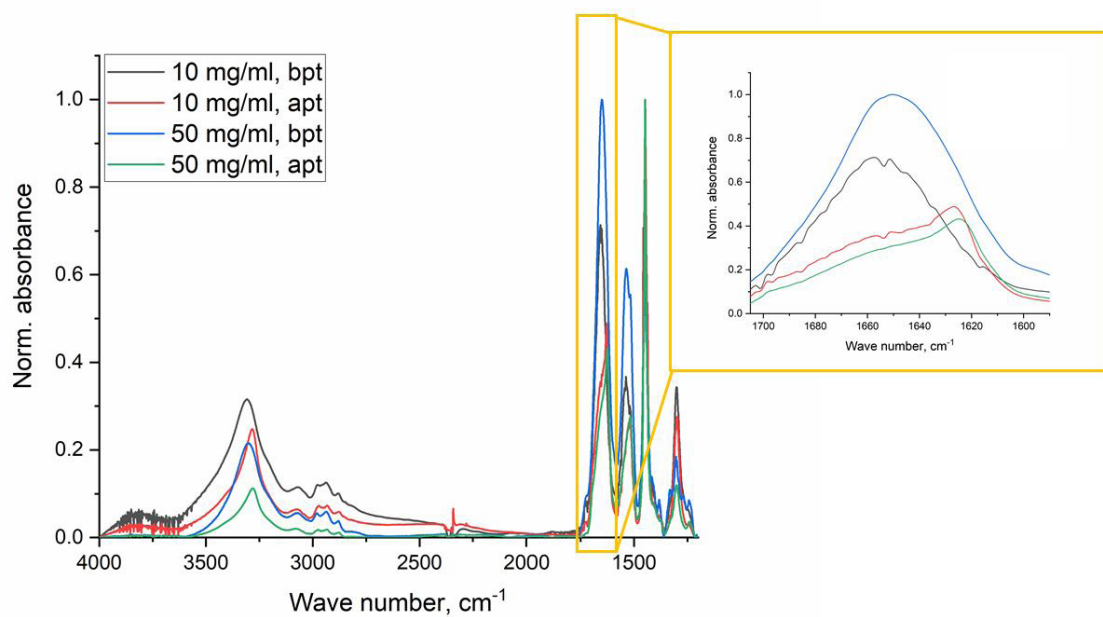


Figure S5: Normalized SBSR FTIR spectra of recombinant spider silk films with concentrations of 10 mg/ml and 50 mg/ml before (bpt) and after (apt) post-treatment with methanol.

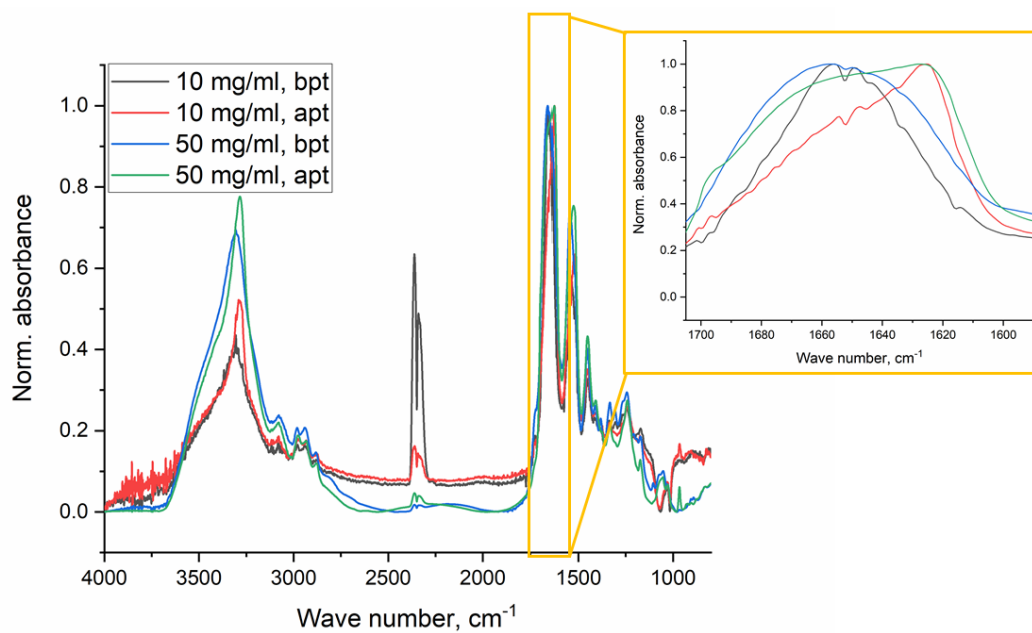


Figure S6: Normalized Transmission FTIR spectra of recombinant spider silk films with concentrations of 10 mg/ml and 50 mg/ml before (bpt) and after (apt) post-treatment with methanol.

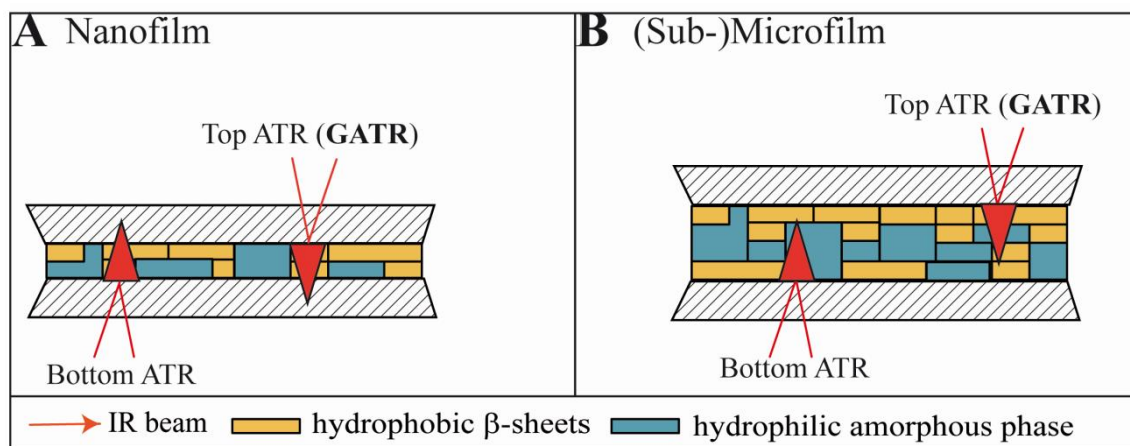


Figure S7: GATR FTIR in comparison to SBSR FTIR yields different B for nano- (A) and (sub) microfilms (B).

Part II - Chapter 2 – Dichroic FTIR spectroscopy characterization of β -sheet orientation in spider silk films on silicon substrates

Part II – Chapter 2.1 - Chapter perspective and contribution

This study focuses on the structure formation of thin, intermediate, and thick confined recombinant spider silk (rss) films. Therefore, the rss protein eADF4(C16) was deposited onto planar and nanoscratched silicon substrates. The kinetic of the post-treatment with MeOH and the orientation of the β -sheets in the films were investigated. This was realized using measuring the dichroic ATR-FTIR. The dichroic ratios of the amide I band assigned to the mode of antiparallel β -sheets were used to calculate the molecular order parameter S and the tilt angle of the β to the surface normal. For thin and intermediate films, it was found that they reveal a high order parameter of 0.40, which indicates that the β -sheets stacks are vertically oriented with tilt angles of $\gamma \sim 39^\circ$. Thick films showed a lower order parameter $S \sim 0$. A pseudo-first kinetics order was found for the folding kinetics upon post-treatment with methanol. This suggested a transition from an unfolded to a folded state.

I performed the synthesis and the purification of the protein and processed the recombinant spider silk protein into films. The methodology was performed by Mirjam Hofmaier, Sarah Lentz and Birgit Urban. The writing of the original draft and the visualization of the results was done by Mirjam Hofmaier, Martin Müller and Sarah Lentz. The review and the editing of the manuscript were done by all authors. The conceptualization of this project was done by Martin Müller, Andreas Fery and Thomas Scheibel. Christian Borkner was involved in the discussion of the results. The funding for this project was provided by Andreas Fery and Thomas Scheibel.

This study was done in cooperation with the Leibniz Institute in Dresden with Prof. Andreas Fery, Dr. Martin Müller, and Mirjam Hofmeier. This study is published in the Journal of Physical Chemistry (<https://doi.org/10.1021/acs.jpcc.0c09395>). Since the authors signed the co-authorization form, this publication is also part of the thesis at the University of Melbourne.

The permission of reprint was granted by The Journal of Physical Chemistry B: Reprinted (adapted) with permission from: “Dichroic Fourier Transform Infrared Spectroscopy Characterization of the β -Sheet Orientation in Spider Silk Films on Silicon Substrates”, Mirjam Hofmaier, Birgit Urban, Sarah Lentz, Christian B. Borkner, Thomas Scheibel,

Andreas Fery, and Martin Müller, *The Journal of Physical Chemistry B* 2021 125 (4), 1061-1071, DOI: 10.1021/acs.jpcc.0c09395. Copyright 2021 American Chemical Society.

Part II – Chapter 2.2 - Full Paper

Dichroic Fourier Transform Infrared Spectroscopy Characterization of the β -Sheet Orientation in Spider Silk Films on Silicon Substrates

Mirjam Hofmaier, Birgit Urban, Sarah Lentz, Christian B. Borkner, Thomas Scheibel, Andreas Fery, and Martin Müller*



Cite This: *J. Phys. Chem. B* 2021, 125, 1061–1071



Read Online

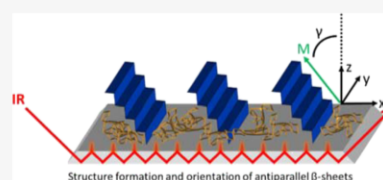
ACCESS |

Metrics & More

Article Recommendations

Supporting Information

ABSTRACT: Orientation analysis of the β -sheet structure within films of the established recombinant spider silk protein eADF4(C16) was performed using a concept based on dichroic transmission- and attenuated total reflection-Fourier transform infrared spectroscopy, lineshape analysis, assignment of amide I components to specific vibration modes, and transition dipole moment directions of β -sheet structures. Based on the experimental dichroic ratio R , the order parameter S of β -sheet structures was calculated with respect to uniaxial orientation. Films of eADF4(C16) were deposited on untexturized (Si) and unidirectionally scratched silicon substrates (Si-sc) and post-treated with MeOH vapor. Freshly cast thin and thick eADF4(C16) films out of hexafluoroisopropanol featured β -sheet contents of $\approx 6\%$, which increased to $>30\%$ after MeOH post-treatment in dependence of time. Pseudo-first order folding kinetics were obtained, suggesting a transition from an unfolded to a folded state. In MeOH post-treated thin films with diameters in the nanometer range, a significant orientation of β -sheets was obtained regardless of the texturization of the silicon substrate (Si, Si-sc). This was rationalized by dichroic ratios of the amide I component at 1696 cm^{-1} assigned to the $(0, \pi)$ mode of antiparallel β -sheet structures, whose transition dipole moment M is located in parallel to both β -sheet plane and chain direction. The calculated high molecular order parameter $S \approx 0.40$ suggested vertically (out-of-plane) oriented antiparallel β -sheet stacks with tilt angles of $\gamma \approx 39^\circ$ to the surface normal. Microscale (thick) films, in contrast, revealed low order parameters $S \approx 0$. Scanning force microscopy on thin eADF4 films at silicon substrates showed dewetted polymer film structures rather at the micro-scale. These findings give new insights in the role of the β -sheet crystallite orientation for the mechanical properties of spider silk materials.



INTRODUCTION

Silks are protein-based fibers with unique properties, which are used for various purposes in nature such as cocoons by silkworms (*Bombyx mori*) or as webs by spiders.^{1,2} The combination of outstanding mechanical properties (tensile strength and elasticity) and the high biocompatibility, biodegradability, as well as low immunoreactivity and lack of allergenicity makes silks very appealing for applications in the textile industry or biomedicine.³ Because of these applications and industrial interests, fundamental research work on silk structures and properties has been increasingly performed in the past decades.

However, while silkworms are cultured since millennia to produce silk fibers in sufficient amounts for industrial and research purposes, spiders cannot be cultured at a large scale because of their cannibalistic behavior. To get access to spider silk proteins and materials made thereof, they have to be recombinantly produced.⁴ Recombinant spider silk proteins can be designed, which are based on the primary structure of the fibroin 4 of the dragline of the European garden spider *Araneus diadematus* (ADF4).^{5,6} The engineered spider silk protein eADF4(C16), which is used in this work, consists of 16 repetitive modules (C-modules) each comprising 35 amino

acids. This C-module contains a hydrophobic crystalline block (GSSAAAAAAS) and a hydrophilic amorphous block (GPGGYGPENQGPSGGYGPGGP) forming an amphiphilic diblock copolymer in an AB type manner.⁷ eADF4(C16) features are comparable to those of block copolymers comprising acrylates or olefins, which self-assemble into phase-separated nanostructures driven by, for example, block length ratio and Flory Huggins interaction parameters.⁸

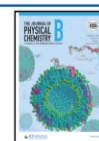
Especially, the molecular structure of processable silk materials like fibers and films with respect to conformation and orientation is of key interest, since a broad range of modern surface and interface analytical techniques is available for these systems giving new physical chemistry insights.

So far, fundamental research has been concentrated on structure formation and phase separation processes of silk materials in fibrils, fibers,⁹ and thick (micron-sized) and thin

Received: October 16, 2020

Revised: December 7, 2020

Published: January 12, 2021



coatings.¹⁰ The separation of β -sheet crystals in 2D films was found at the protein/air interface and also their embedding in a Gly-rich matrix.³ “Two-dimensional (2D)”-separation of the crystalline and the amorphous phases was observed for monolayered nanofilms. In bilayered nanofilms the β -sheets enriched at the protein/substrate interface, and in multilayered nanofilms the crystalline phases were mainly localized at the protein/air- and the protein/substrate-interfaces.¹¹ Although quite some knowledge exists on the orientation of β -sheet crystals in fibers,^{12,13} so far, no detailed information about the orientation of β -sheet nanocrystals within spider silk films was achieved.

The present study aims at closing this gap by applying an analytical concept based on dichroic transmission (TRANS) and attenuated total reflection (ATR) Fourier transform infrared (FTIR) spectroscopy using parallel (P) and vertical (S) polarized IR. This analytical concept includes the identification of amide I components by lineshape analysis (LSA), their assignment to the vibration modes and transition dipole moment (TDM) directions of typical ordered secondary structures like parallel and antiparallel β -sheets and the calculation of the order parameter S based on experimental dichroic ratio R and TDM. While this concept has been formerly applied to characterize the in-plane orientation in thin films of multilayered charged α -helical polypeptides,¹⁴ herein, it is applied to thin eADF4(C16) films containing significant β -sheet content after post-treatment in MeOH vapor.^{3,11,16} Complementarily, circular dichroism (CD) and scanning force microscopy (SFM) were used for analysis.

MATERIALS AND METHODS

Reagents and Materials. eADF4(C16) was obtained from AMSilk GmbH (Planegg/Munich, Germany). eADF4(C16) solutions were prepared in hexafluoroisopropanol (HFIP) at two concentrations, namely, $c = 1$ and 50 mg/mL.

Silicon substrates for TRANS- and ATR-FTIR measurements (2 mm thick trapezoidal internal reflection elements, IRE, with areas of 48×20 mm² and 52×20 mm² on front and backside, Komlas GmbH, Berlin) were cleaned and texturized on the front side using mechanical treatment with a nanoparticulate diamond grinding material (Wagner CoAG, Lotzwil, Switzerland), which resulted in parallel nanogrooves with widths of 50–70 nm and depths of 5–8 nm, as reported previously.¹⁵ These scratched silicon substrates are further denoted Si-sc. Untreated silicon substrates were used as a reference and are further denoted Si.

Deposition of eADF4(C16) Films. eADF4(C16) solution (50 μ L) was spread on Si and Si-sc substrates forming a spot size with rectangular dimensions of 40×6 mm². HFIP was completely evaporated using a nitrogen flow. Post-treatment in MeOH vapor was performed in closed glass vessels.¹⁶

Scanning Force Microscopy. SFM measurements were carried out using Nanostation II (ultramicroscope, Bruker Nano GmbH, Berlin, Germany), enabling optical (Carl Zeiss, Jena) and force microscopy. The noncontact mode was applied using tips from Nanosensors (Darmstadt, Germany). Analyzed Si and Si-sc samples were identical to those used for FTIR spectroscopic measurements. Film thickness was measured based on topography images of zones carefully cut using a scalpel, considering the height difference between the undamaged film and bare silicon. SFM images and roughness analysis were performed using the respective Software tool of Nanostation II (Bruker Nano GmbH, Berlin, Germany).

Spectroscopic Reflectometry. The film thickness of eADF4(C16) films was determined using the thin-film measurement system (MProbeVis-MSP) of Semiconsoft Inc. (Southborough, MA, USA.), which includes a tungsten-halogen (5 W) light source, a fiber optics probe, and a F4 vis spectrometer with a Si detector in the wavelength range of 400–1100 nm.

Universal Surface Tester. The thickness of eADF4(C16) films was analyzed using a universal surface tester (UST, Innowep GmbH) with a steel ball tip (0.8 mm). Five measurements were carried out and the average was calculated.

Confocal Laser Scanning Microscopy. Thickness measurements of eADF4(C16) films were carried out using a confocal laser scanning microscope (μ Surf Expert Revolver) with a 10X objective revolver and a resolution of 200 nm. The average of three different measurements was calculated.

Circular Dichroism. CD spectroscopy was used to characterize eADF4(C16) solutions and films. Far-UV CD spectra were measured using a J810 spectral polarimeter (Jasco GmbH, Groß-Umstadt, Germany). CD spectra of eADF4(C16) solutions (1 mg/mL in HFIP) were measured using quartz cuvettes with 1 mm path length. CD spectra of eADF4(C16) films were measured after casting and drying 100 μ L of 1 mg/mL of eADF4(C16) solutions in HFIP at a surface of 1 mm quartz cuvettes (area of around 1 cm²). The quantitative secondary structure evaluation of eADF4(C16) was done using the “CD-PRO-Analysis” tool applying the “CONTIN” option of Jasco Software Spectra Manager Version 2 (Version 2.06.00, Build 6 from JASCO GmbH, Groß-Umstadt, Germany), which is based on least square fitting of CD data by polypeptide- or protein-based reference data sets introduced by Provencher¹⁷ and Sreerama.¹⁸ Errors of secondary structure fractions were based on standard deviations between three independent samples.

FTIR Spectroscopy. The characterization of the eADF4(C16) films was performed by either TRANS-FTIR or ATR-FTIR spectroscopy using polarized IR light. A TENSOR II spectrometer (BRUKER Optics GmbH, Ettlingen Germany), continuously purged with nitrogen and equipped with a global source and MCT detector, was used with TRANS- and ATR-FTIR attachments. For TRANS-FTIR measurements, Si and Si-sc substrates were placed in constructed sample holders, allowing the IR light to penetrate the sample at the focal plane. For ATR-FTIR measurements, Si and Si-sc substrates were placed in constructed sample holders located in a single-beam-sample-reference (SBSR) device (Optispec Neerach, Switzerland).¹⁹ Briefly, the trapezoidal IRE was divided into an upper sample and lower reference half with respective 48×10 mm² front areas. Single-channel intensity spectra were recorded from the upper sample (I) and lower reference half (I_0) by alternate shuttling into a fixed IR beam by a vertical lift. Computing $A(\nu) = -\log(I(\nu)/I_0(\nu))$ revealed absorbance spectra $A(\nu)$ with proper baselines and low contributions of atmospheric water vapor. Generally, FTIR spectra were recorded at a resolution of 2 cm⁻¹ with a zero filling factor of 2. IR light was achieved with parallel (P) polarization and with vertical (S) polarization concerning the laboratory (i.e., spectrometer) plane using a wire grid polarizer (SPECAC, UK). The polarizer was located after passing the sample before the detector for both techniques (ATR-, TRANS-FTIR). P- and S-polarized absorbance FTIR spectra (A_p , A_s) were recorded by co-adding 50 scans of the respective reference

Table 1. Thickness and Number of Measurements (#) of eADF4(C16) Coatings Cast out of HFIP Solutions (1 and 50 mg/mL) on Si Substrates

conc. eADF4(C16)	method				
	thickness/[nm]				
	SR/[nm]	SFM/[nm]	UST/[nm]	CLSM/[nm]	average/[nm]
50 mg/mL (thick)	2795 ± 950 (#20)	^b	2060 ± 410 (#5)	1780 ± 190 (#3)	1920 ± 140
1 mg/mL (thin)	34 ± 11 (#13)	21 ± 6 (#3)	^a	^a	28 ± 6

^aFilm thickness is below the detection limit. ^bTechnically not measurable.

($I_{P,S}^0$) and sample intensity spectra ($I_{P,S}$), respectively, and calculating A_P and A_S according to eq 1.

$$A_{P,S} = -\log(I_{P,S}/I_{0,P,S}) \quad (1)$$

To check for undesired time-dependent variations, the polarized spectra (P, S) were measured with the sequence “P–S–P”. The first P-polarized spectrum was then compared to the second one. Integrated band areas B_P and B_S were used for the dichroic ratio R determination of the amide bands, according to $R = B_P/B_S$.

Dichroic TRANS–FTIR Spectroscopy. Dichroic TRANS–FTIR spectroscopy (see Figure S1A) was applied at Si and Si-sc IRE. A polarizer with P- and S-setting generated polarized IR light with an electrical field vector (E) oscillating either in parallel (E_P) or vertically (E_S), concerning the incident plane along the x -axis of the used Si IRE.

TRANS–FTIR Spectra Measured in P- and S-Polarization. TRANS dichroic ratios R^T were calculated for selected IR bands based on their integrated areas B_P^T and B_S^T according to eq 2.

$$R^T = B_P^T/B_S^T \quad (2)$$

For the quantitative analysis of dichroic TRANS–FTIR data, previously published concepts were applied by Zbinden for polymer systems²⁰ and by Fringeli for low molecular liquid crystalline²¹ and lipid systems.²² The general experimental setup is shown in Figure S1A. The basic equation of dichroism^{20,23} includes the square of the scalar product of electric field vector E and TDM vector M , resulting in the measurable absorbance A given in eq 3.

$$A = (E \cdot M)^2 = |E|^2 \cdot |M|^2 \cdot \cos^2(E \cdot M) \\ = (E_x M_x + E_y M_y + E_z M_z)^2 = A_x + A_y + A_z \quad (3)$$

Maximum absorbance A is obtained, if the angle between E vector and M vector is 0° , and minimum A is obtained, if the angle between those is 90° . For TRANS–FTIR mode only, the two electrical field components E_x and E_y are valid leading to eq 4.

$$R^T = (E_x M_x)^2 / (E_y M_y)^2 = A_x / A_y \quad (4)$$

Based on a model of the partial axial orientation,²⁰ the following relation (eq 5) is valid between the dichroic ratio R^T , the angle between the TDM M and the molecular main axis θ , and the orientation parameter S' when the main molecular chain axis is distributed within a cone envelope, and calculating A_x and A_y according to eq 3.

$$R^T = (\sin^2 \theta + S') / (2 \sin^2 \theta + S') \quad (5)$$

θ values can be either found in the literature or rationalized by molecular modeling. The more common molecular order

parameter S can be received from the orientation parameter S'^{22} using the following eq 6.

$$S' = 2 / (3S) - 2/3 \quad (6)$$

Finally, inserting eq 6 in eq 5 leads to eq 7, which has been further used herein.

$$S = \frac{(1 - R^T)}{(2R^T + 1)} \cdot \frac{2}{(3 \cos^2 \theta - 1)} \quad (7)$$

Assuming $\theta = 0^\circ$, an experimental value $R^T = 0$ results in $S = 1$, meaning that the molecular chain axis are perfectly aligned in parallel with respect to the texturization direction. Whereas $R^T = \infty$ (for $\theta = 0^\circ$) results in $S = -1/2$, indicating that the molecular chain axes are perfectly aligned vertically with respect to the texturization direction. S is directly related to the opening angle γ of the model cone (see Figure S1C) using eq 8. Values of γ close to 54.7° (“magic angle”) correspond to low S values, indicating a low degree of the unidirectional alignment of stiff molecular chains.

$$\gamma = \arccos(2/3S + 1/3)^{1/2} \quad (8)$$

Dichroic ATR–FTIR Spectroscopy. Dichroic ATR–FTIR spectroscopy (Figure S1B) was performed on texturized (Si-sc) and untexturized (Si) planar silicon IRE applying the SBSR concept¹⁹ to obtain well-compensated ATR–FTIR spectra. The quantitative analysis of dichroic ATR–FTIR data^{21,22} is directly related to that of dichroic TRANS–FTIR data²⁰ described above, which was applied to α -helical polypeptides therein.¹² In eq 9, the experimental dichroic ratio R^{ATR} in the ATR mode is given by dividing B_P^{ATR} and B_S^{ATR} , which are the integrated absorbances of a given band measured with either P- and S-polarized light, respectively.

$$R^{ATR} = B_P^{ATR} / B_S^{ATR} \quad (9)$$

Unlike TRANS–FTIR for ATR–FTIR mode, the E vectors oscillating either in parallel (E_P , eq 10a) or vertically (E_S , eq 10b) with respect to the normal plane of the substrate (E_x/E_z plane, see Figure S1B) are composed of the three relative electrical field components E_x , E_y , and E_z .

$$E_P = (E_x^2 + E_z^2)^{1/2} \quad (10a)$$

$$E_S = E_y \quad (10b)$$

Applying the basic dichroism eq 3, all three electrical field components E_x , E_y , and E_z are considered and the dichroic ratio R^{ATR} as denoted in eq 11.

$$R^{ATR} = (A_x + A_z) / A_y = (E_x M_x + E_z M_z)^2 / (E_y M_y)^2 \quad (11)$$

Based on the partial axial orientation model of Zbinden²⁰ and calculating A_x , A_y , and A_z according to eq 3 ATR–FTIR

analysis can be performed optionally in x -, y -, or z -directions based on the directional dichroic ratios R_x^{ATR} , R_y^{ATR} and R_z^{ATR} as defined in eqs 12a - c.

$$R_x^{\text{ATR}} = \frac{(E_x^2 + E_z^2)}{E_y^2} \cdot \frac{2 \cos^2 \theta + S'}{\sin^2 \theta + S'} \quad (x\text{-axis}) \quad (12a)$$

$$R_y^{\text{ATR}} = \frac{(E_x^2 + E_z^2)}{E_y^2} \cdot \frac{\sin^2 \theta + S'}{2 \cos^2 \theta + S'} \quad (y\text{-axis}) \quad (12b)$$

$$R_z^{\text{ATR}} = \frac{E_x^2}{E_y^2} + \frac{E_z^2}{E_y^2} \cdot \frac{2 \cos^2 \theta + S'}{\sin^2 \theta + S'} \quad (z\text{-axis}) \quad (12c)$$

The relative electric field components E_x , E_y , and E_z of the evanescent wave (Figure S1B) are composed of constants (e.g., refractive indices), which are listed for the case of thin films ($d = 28$ nm) and thick films ($d = 1920$ nm) in Table S1 (thickness values see Table 1), and can be calculated according to Harrick.²⁴ The E_x , E_y , and E_z values for these two film thicknesses were calculated by interpolating between the respective values of infinitely thin and thick films (see Supporting Information).

The directional dichroic ratios R_x^{ATR} , R_y^{ATR} and R_z^{ATR} can be converted into their respective directional dichroic ratios R_x^{T} , R_y^{T} and R_z^{T} (eqs 13a - c) for TRANS mode by substituting $(\sin^2 \theta + S')/(2 \cos^2 \theta + S')$ with R^{T} according to eq 5.

$$R_x^{\text{T}} = 1/R_x^{\text{ATR}} \cdot \frac{(E_x^2 + E_z^2)}{E_y^2} \quad (x\text{-axis}) \quad (13a)$$

$$R_y^{\text{T}} = R_y^{\text{ATR}} \cdot \frac{E_y^2}{(E_x^2 + E_z^2)} \quad (y\text{-axis}) \quad (13b)$$

$$R_z^{\text{T}} = \frac{E_z^2}{(R_z^{\text{ATR}} \cdot E_y^2 - E_x^2)} \quad (z\text{-axis}) \quad (13c)$$

These three directional dichroic ratios R_x^{T} , R_y^{T} and R_z^{T} can be inserted in eq 7, respectively, and the corresponding three directional order parameters S_x , S_y , and S_z are calculated. S_x , S_y , and S_z denote optional order parameters, which are based on the assumption of the orientation with respect to either x -, y -, or z -directions. The one correct directional order parameter (e.g., S_z) can be obtained by excluding the two others (e.g., S_x and S_y), if, for example, the values of S_x and S_y are negative and significantly low and if the value of S_z is positive and significantly high (e.g., $S_z > 0.2$).

LSA for the Quantification of Secondary Structure Elements and Their Orientation. Quantitative access to secondary structure elements and their orientation within thin eADF4(C16) films was obtained using LSA. LSA is based on the representation of the measured absorbance $A(\nu)$ by the sum of absorbances of multiple (i) components, $A_i(\nu)$, according to eq 14.

$$A(\nu) = \sum A_i(\nu) \quad (14)$$

Every component i is determined by the parameters' wavenumber position of component maximum (ν_i^{max}), half-width at half-height (w_i), and component area (B_i). A mixture of 50% Lorentzian and 50% Gaussian lineshape was used, which is an arbitrary setting as it was discussed by Chirgadze²⁵ for IR analysis of polypeptides, according to eq 15.

$$A_i(\nu) = 0.5(B_i w_i) / \pi [(\nu - \nu_i^{\text{max}})^2 + w_i^2] + 0.5 B_i / w_i (\ln 2 / \pi)^{0.5} \exp(-\ln 2 (\nu - \nu_i^{\text{max}})^2 / w_i^2) \quad (15)$$

The parameters ν_i^{max} , w_i , and B_i for each component A_i were optimized iteratively with the conditions of minimizing the residual difference $D = A(\nu) - \sum A_i(\nu)$ (least-squares condition) using the algorithm of Levenberg–Marquardt. The curve fitting tool of OPUS software (Bruker Optics GmbH, Ettlingen) was applied. FTIR spectra were cut to a wavenumber range of 1715–1585 cm^{-1} and baseline corrected by setting the absorbance at 1715 and 1585 cm^{-1} to zero. The number i and positions ν_i^{max} of band components A_i were identified by calculating the second derivative of all spectra to be analyzed using the respective tool of OPUS software (25 smoothing points), where negative peaks in the second derivative spectra indicated relevant components. Additionally, difference spectra between differently hydrated states were calculated and ν_i^{max} was rationalized to get a minimum number of components for the amide I band, which are all confirmed by the second derivative spectra, knowledge on the secondary structure composition of eADF4(C16), and theoretically calculated wavenumber positions for these secondary structures. Final ν_i^{max} values were determined for each component i by averaging the ν_i^{max} values of the respective i th component. Conclusively, five components at $\nu^{\text{max}} = 1696$, 1675, 1658, 1650, 1625 cm^{-1} were considered, all five of which were assigned to secondary structures according to the literature,^{28–30} as summarized in Table S2.

Values for half-widths for each i th component were arbitrarily set to $w_i = 20$ cm^{-1} because the LSA runs (see above) resulted in w_i values close to this value, with one exception. A half-width of $w = 50$ cm^{-1} was chosen for the unordered component at 1658 cm^{-1} , which is in agreement with half-widths for synthetic polypeptides and silk fibroin in the unordered coil state reported by Chirgadze.²⁵ Finally, in the quantitative LSA run, all spectra were fitted using the values of ν_i^{max} and w_i of Table S2, and only component areas B_i were allowed to relax freely. Finally, secondary structure portions Q were calculated by rationing the respective amide I component integrals assigned to typical secondary structures, as shown in Table S2, and the sum of all amide I component band areas followed by multiplication with 100% under the assumption that all used amide I components have comparable absorption coefficients as critically addressed by Barth.²⁶ For the amide I band, the unordered coil content was calculated according to eq 16a considering only the B_{1658} component in the numerator, while the β -sheet content was calculated considering the B_{1625} component in the numerator according to eq 16b.

$$Q_{\text{unordered}} = B_{1658} / (B_{1696} + B_{1675} + B_{1658} + B_{1650} + B_{1625}) \quad (16a)$$

$$Q_{\beta\text{-sheet}} = B_{1625} / (B_{1696} + B_{1675} + B_{1658} + B_{1650} + B_{1625}) \quad (16b)$$

RESULTS AND DISCUSSION

Films of eADF4(C16) were cast out of HFIP solutions onto silicon substrates and further treated in MeOH vapor (MeOH post-treatment) for 24 h. To examine the influence of the substrate morphology on the secondary structure formation and orientation after MeOH post-treatment, both, nano-

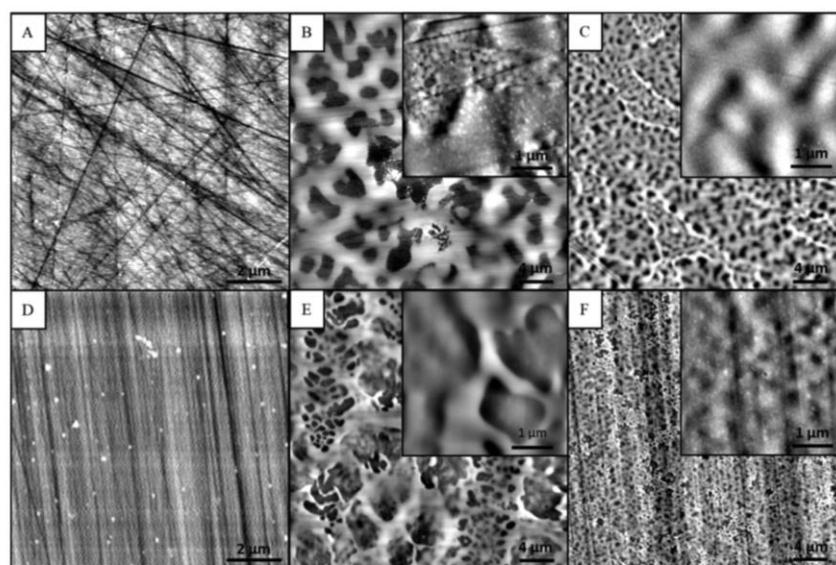


Figure 1. SFM topographic images of untexturized Si substrates (A) and unidirectionally texturized Si-sc substrates (D), SFM images of thin eADF4(C16) films before post-treatment on Si (B) and Si-sc (E) and after subsequent post-treatment in MeOH vapor (1 h) on Si (C) and Si-sc (F).

scratched silicon substrates (Si-sc) as well as untreated ones (Si) were used. Additionally, two different film thicknesses were used to investigate the effect of this parameter on the secondary structure formation and orientation. eADF4(C16) films were analyzed directly after casting in the initial state and after MeOH post-treatment, respectively.

Microscopic Structure of Spider Silk Coatings. *Thickness.* The average thicknesses of eADF4(C16) coatings were determined using spectroscopic reflectometry (SR), SFM, UST, and confocal laser scanning microscopy (CLSM). The results are summarized in Table 1.

eADF4(C16) films cast from 1 mg/mL and 50 mg/mL of solutions in HFIP showed different thickness values within various samples and various sample positions, and thus have rather large standard deviations. Thickness ranges were found with average values from 1780 (CLSM) to 2750 nm (SR) for 50 mg/mL and 21 (SFM) to 34 nm (SR) for 1 mg/mL of spider silk solutions. Based thereon, mean averaged thickness values of $d = 28$ nm (1 mg/mL) denoted as thin and $d = 1920$ nm (50 mg/mL) denoted as thick were calculated (Table 1, last column). These averaged thickness values were used to calculate the electric field components E_x , E_y , and E_z (see Materials and Methods section), whose values critically depend on thickness d via the depth of penetration d_p (eq S5) and via the chosen optical media model including the respective refractive indices n_1 , n_2 , and n_3 (eq S4a–c).

Microstructure. In Figure 1, SFM images of untexturized (Si) (A), bare scratched silicon (Si-sc) (D) and thin eADF4(C16) films deposited from the HFIP solution before (B,E), and after MeOH post-treatment (C,F) are shown. Nanogrooves are visible with no distinct (Figure 1A) or with unidirectional alignment (Figure 1D) featuring widths of around 50–100 nm and depths up to 5 nm for the applied uncoated Si and Si-sc substrates, respectively. For both polymer deposited substrates, the nanogrooves appeared to be overcoated with eADF4(C16) but still visible (Figure 1B,E). Before MeOH post-treatment, a dewetted polymer film

structure at the silicon/polymer/air interface could be obtained with a coarse porous appearance, and the roughness analysis provided a value of RMS = 19.7 nm for Si and RMS = 15.79 nm for Si-sc. After MeOH post-treatment, the dewetted structure changed significantly from rather coarse to rather grain (fine) (Figure 1C,F), and the RMS value changed to 14.9 and 4.21 nm, respectively. This morphology change might be rationalized by both the different surface energies of the solvent HFIP used for deposition and of MeOH used for post-treatment and their different selectivities for amorphous and crystalline domains within eADF4(C16) films. However, for both substrates, these dewetted structures cannot be correlated with, for example, crystalline domain sizes, which for block copolymers typically have few nanometers, because the applied SFM resolution is too low. For thick eADF4(C16) films on Si (Figure S3A) or Si-sc (Figure S3B), the grooves were no longer visible and neither the dewetted surface structure before nor a change after MeOH post-treatment (Figure S3C,D) as found for thin films, could be observed, because the eADF4(C16) film was too thick and completely masked dewetting at the silicon/polymer interface. This observation is in line with the obtained lower RMS values before MeOH post-treatment (Si: 4.15 nm; Si-sc: 9.64 nm) compared to the thin eADF4(C16) film, which also changed to their respective lower values (Si: 1.31 nm; Si-sc: 1.11 nm). Conclusively, the SFM analysis data on thin eADF4(C16) films evidenced dewetted polymer film structures and gave qualitative hints for changes in size of these dewetted structures after MeOH post-treatment, while for thick films neither such dewetting nor such changes could be observed.

Secondary Structure in Spider Silk Coatings. Secondary structure analysis was performed using FTIR spectroscopy and CD. FTIR spectroscopic analysis of protein conformation is based on the position and lineshape of the amide I band, which has been provided earlier in the pioneering work of Miyazawa, Blout, and Krimm.^{27–30} Therein, correlations between wavenumber positions of amide I and amide II

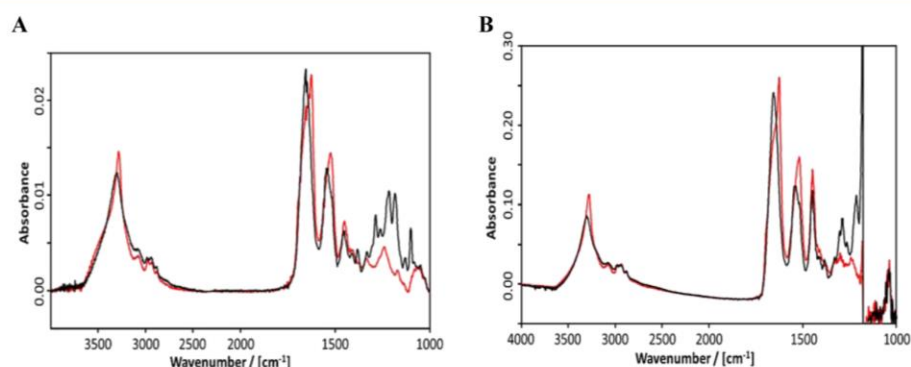


Figure 2. TRANS-FITIR (A) and ATR-FITIR (B) spectra (unpolarized) of thin (cast from 1 mg/mL HFIP solutions) eADF4(C16) films on Si-sc before (black) and after MeOH post-treatment (red).

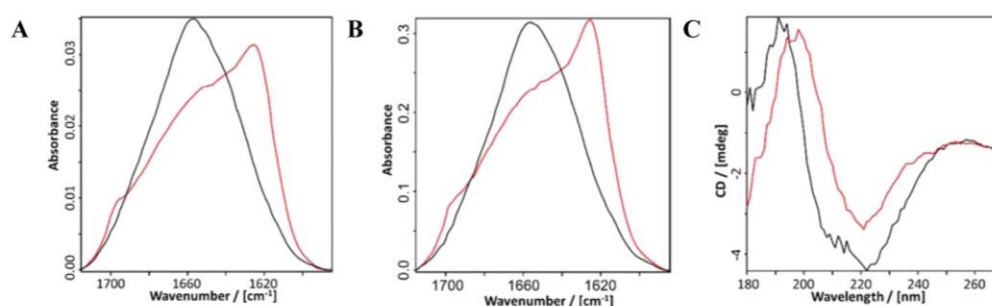


Figure 3. TRANS-FITIR (A) and ATR-FITIR (B) spectra of thin eADF4(C16) films on texturized Si-sc IRE as-cast (black) and after MeOH post-treatment (red). Representative CD spectra (C) of eADF4(C16) films as-cast (black) and after MeOH post-treatment (red).

band components and typical protein secondary structures were provided based on normal coordinate analysis at model amide compounds and perturbation theory at infinitely long polypeptides with intra- and intermolecularly coupled (H-bonded) amide group units.

In Figure 2, TRANS-FITIR (A) and ATR-FITIR spectra (B) of thin eADF4(C16) films before and after MeOH post-treatment are given in an extended wavenumber range. The former showed IR bands with around 10 times lower intensities compared to the latter. For the TRANS- and ATR-FITIR spectra, position and lineshape changes were observed in the spectral ranges between 3500 and 3000, 1700–1600, and 1600–1500 cm⁻¹, in which the respective diagnostic amide A ($\nu(\text{NH})$), amide I (80% $\nu(\text{C}=\text{O})$), and amide II (60% $\delta(\text{NH})$) bands appeared.^{28–30} Below 1400 cm⁻¹, incompensation features appeared because of the intense Si–O stretching band of the Si/SiO_xH_y substrate.

In Figure 3, more detailed baseline corrected (see Materials and Methods) TRANS-FITIR (A) and ATR-FITIR spectra (B) of thin eADF4(C16) films on texturized Si-sc substrates (IRE) are shown in the amide I band range before (black) and after MeOH post-treatment (red, Figure 3).

For both, ATR-FITIR and TRANS-FITIR, the as-cast state showed an amide I band position at 1658 cm⁻¹, while after MeOH post-treatment, a shifted amide I position at 1625 cm⁻¹ could be seen with a broad shoulder at around 1658 cm⁻¹ and a small narrow peak at 1696 cm⁻¹. These findings were found for both Si-sc as well as Si substrates (Figure S4). The wavenumber position at 1658 cm⁻¹ could be assigned to the unperturbed amide I vibration (i.e., vibration lacking specific

interactions with neighboring peptide groups), which is typical for unordered structures. Wavenumber positions at 1625 and 1696 cm⁻¹ could be assigned to β -sheet structures.^{28–30} To quantify the β -sheet content, LSA was performed as described in the Materials and Methods section. The results are summarized in Table 2 for Si and Si-sc substrates.

As-cast films showed a β -sheet content of around 6%, which increased to 33% after MeOH post-treatment. An increasing β -

Table 2. β -Sheet Content of eADF4(C16) Solutions, eADF4(C16) Coatings on Substrates as Indicated and eADF4(C16) Fibers³¹ before and after Post-Treatment in MeOH Vapor Determined Using FTIR and CD Spectroscopy^a

eADF4(C16)	<i>c</i> [mg/mL]	CD (%)	TRANS-FITIR (%)	ATR-FITIR (%)
solution, HFIP	10	<i>b</i>	<i>b</i>	8.8
film, Si-sc	1	<i>b</i>	6.7	6.5
	50	<i>b</i>	<i>c</i>	11.0
film, quartz		6.4	<i>b</i>	<i>b</i>
	1	<i>b</i>	29.6	31.1
film, MeOH-vapor, Si-sc				
	50	<i>b</i>	<i>c</i>	35.4
film, MeOH-vapor, Si	1	<i>b</i>	31.8	32.8
film, MeOH-vapor, quartz	1	38.0	<i>b</i>	<i>b</i>

^aNo standard deviation was obtained higher than $\pm 3.7\%$. ^bNot determined because of low CD transparency or low IR intensity. ^cNot determined because of too high IR intensity.

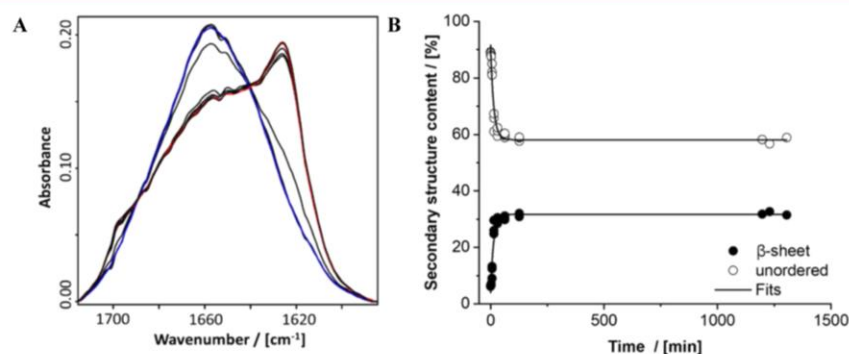


Figure 4. (A) ATR-FTIR spectra of thin eADF4(C16) films on Si-sc during post-treatment in MeOH vapor at $t = 0$ min (blue), time points between $t = 1$ min, $t = 120$ min (black), and $t = 24$ h (red). (B) Plot of the β -sheet content and content of unordered structures vs time at 1625 and 1658 cm^{-1} . Kinetic curves showed good reproducibility.

sheet content was obtained with increasing film thickness in as-cast films. After MeOH post-treatment, similar β -sheet contents were reached for thin (31%) and thick films (35%). HFIP is well known to promote either unordered or helical secondary structures in proteins. An earlier work of Ikeda reported random coil structures for poly(cysteine) dissolved in HFIP,³² whereas Kishore³³ detected 3_{10} helices for *B. mori* silk fibroin and peptides derived therefrom in HFIP using NMR and CD. Recombinant spider silk proteins dissolved in HFIP showed a higher α -helical content as those dissolved in formic acid.^{10,34,35} For eADF4(C16), the β -sheet content increased upon film formation.^{35,36} The MeOH post-treatment of recombinant spider silk films led to a further increase of the β -sheet content. During MeOH post-treatment, the film swelled and the polyaniline stretches had the possibility to undergo a rearrangement into β -sheets.³ The values of eADF4(C16) films after MeOH post-treatment (Si and Si-sc) in Table 2 confirmed nearly complete conversion of the polyaniline stretches to β -sheets reaching the maximal theoretical β -sheet content for eADF4(C16) of 35%.³

Additionally, CD was applied in the far UV range to confirm the structural changes observed using FTIR measurements. Quartz substrates were used instead of silicon ones because of limited UV/vis TRANS and wavelength range. While FTIR spectroscopy is highly sensitive for the β -sheet structure, CD spectroscopy is known to be more sensitive for α -helical and less sensitive for β -sheet structures.^{37,38} Qualitatively, in the spectrum before post-treatment, which is shown in Figure 3C (black), the typical negative doublet was observed for α -helical structures at around 208 nm (split π - π^* transition of amide chromophore) and 222 nm (n - π^* transition) and a positive signal at around 190 nm (split π - π^* transition).³⁷ The ratio of the positive signal (190 nm) and negative doublet signal (208, 222 nm) was around 1:2. Knowing that for pure α -helical polypeptides this ratio is around 2:1 and that random coil polypeptides feature a negative signal at 195 nm (π - π^* transition) beside α -helical structures, an additional portion of unordered structures could be concluded. After MeOH post-treatment, the band at 208 nm was absent in the respective CD spectrum (Figure 3C, red), the intensity of the whole spectrum was decreased and the intensity ratio of the signal at 190 nm compared to that at 220 nm was still around 1:2. Knowing that CD spectra of antiparallel β -sheet polypeptides have a positive signal at 195 nm (split π - π^* transition) and a negative one at 218 nm (split π - π^* transition), the formation of antiparallel β -

sheet structures could be concluded after MeOH post-treatment within residual unordered secondary structures (amorphous matrix).

Additionally, also the quantitative evaluation of the secondary structure was performed based on least square fitting of CD data by reference data sets.^{22,23} eADF4(C16) films on quartz substrates revealed β -sheet contents of around 6% before and of around 38% after MeOH post-treatment (Table 2, Figure 3), which is in accordance with the FTIR results.³

Folding Kinetics. Furthermore, ATR-FTIR spectra of as-cast eADF4(C16) films were recorded during post-treatment in MeOH vapor between 0 and 24 h, which are given in Figure 4.

Qualitatively, significant time-dependent changes of the amide I lineshape were observed, whereby the initial maximum at 1658 cm^{-1} evolved indicative for the unordered structure shifted to one at 1625 cm^{-1} and a shoulder at 1696 cm^{-1} indicative for the β -sheet structure. Moreover, an isosbestic point was found at around 1640 cm^{-1} between the two maxima at 1658 and 1625 cm^{-1} , which suggested a direct transition from unordered to β -sheet state within the eADF4(C16) film. Quantitative kinetic information was obtained using LSA (see Materials and Methods section). Plotting the relative area with respect to the total area of the amide I components at 1625 and 1658 cm^{-1} versus time suggested an exponentially damped β -sheet increase and exponentially decreasing function concerning unordered structures. Hence, the data points were fitted using the following empirical equations (eqs 17a, 17b), taking an exponential and constant contribution into account. The constants $B_{1658,0}$ and $B_{1625,0}$ correspond to either the final residual amount of the unordered structure, and the already converted initial amount of the β -sheet structure, respectively

$$B_{1658}(t) = B_{1658,0} \exp(-k_1 t) + b_1 \quad (17a)$$

$$B_{1625}(t) = B_{1625,0}(1 - \exp(-k_2 t)) + b_2 \quad (17b)$$

Interestingly, identical empirical (apparent) kinetic constants $k_1 = 0.073 \pm 0.009 \text{ min}^{-1}$ and $k_2 = 0.075 \pm 0.010 \text{ min}^{-1}$ were obtained, supporting a two-state model of the secondary structure conversion following pseudo-first order kinetics claimed as a simple analytical concept for protein folding.³⁹

These found kinetic constants k_1 and k_2 might be compared to those obtained from folding data for more or less related silk

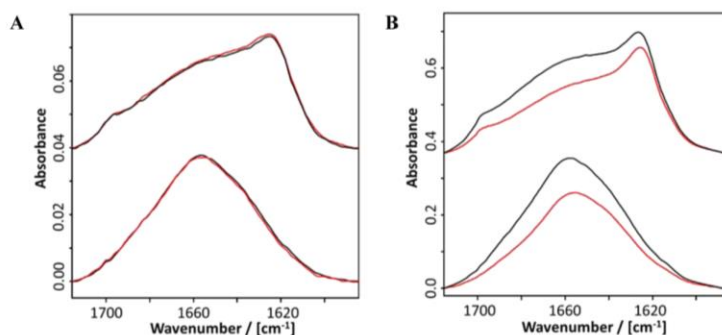


Figure 5. Typical dichroic TRANS-FTIR (A) and ATR-FTIR (B) spectra of thin eADF4(C16) films before (bottom) and after MeOH post-treatment (top) in P-polarization (black) and S-polarization (red) on Si-sc substrates.

material systems. While folding kinetics within films of eADF4(C16) have so far not been obtained, recently kinetic data on post-treatment have been reported of eADF4(C16) fiber mats using a series of alcohol vapors.³¹ For the therein presented respective MeOH post-treatment data, an empirical kinetic constant of $k = 0.366 \pm 0.045 \text{ min}^{-1}$ could be determined for the β -sheet formation by fitting according to eq 17b. The higher k value (factor of around five) compared to the k_1 and k_2 values reported herein might be explained by the larger surface area of fibers (all sides accessible) for the MeOH vapor, compared to that of films (only top side accessible).

Molecular Orientation in Spider Silk Coatings. The orientation of the structural elements of eADF4(C16) films was analyzed using dichroic TRANS-FTIR and dichroic ATR-FTIR spectroscopy with parallelly and vertically polarized IR light. The analysis of the respective dichroic ratios $R = B_p/B_s$ was performed in accordance to Zbinden²⁰ and Fringeli,^{21,22} as summarized in the Materials and Methods section.

TRANS-FTIR Dichroism. In Figure 5A, typical dichroic TRANS-FTIR spectra of thin eADF4(C16) as-cast films on Si-sc substrates are given before (bottom) and after MeOH post-treatment (top). Qualitatively, no significant differences were obtained of the TRANS-FTIR spectra in P- and S-polarization. Quantitatively, before MeOH post-treatment (bottom) a dichroic ratio of $R^T = B_p/B_s \approx 1$ was obtained for the main amide I band component at 1658 cm^{-1} , which is the value for an isotropic sample ($R_{\text{ISO}}^T = 1$).¹⁹ Inserting this R^T value into eq 7, consequently, as-cast films revealed low values of $S \approx 0$ for the 1658 cm^{-1} component, and thus the unordered secondary structure regardless of the choice of θ . This was not surprising, because no directional orientation was expected in unordered structures.

After MeOH post-treatment, the lineshape of the amide I band, in the dichroic TRANS-FTIR spectra (see above) changed, but all the amide I components revealed $R^T \approx 1$, and thus low values of $S \approx 0$ resulted for the corresponding secondary structures regardless of the choice of θ . Especially, the component at 1696 cm^{-1} assigned to the $(0, \pi)$ mode of the antiparallel β -sheet, whose angle between TDM M and molecular axis was known to be $\theta = 0^{28-30}$ (see above), revealed such a low value of $S \approx 0$. Additionally, thick eADF4(C16) films showed similar behavior on the Si-sc substrate.

Because dichroic TRANS-FTIR analysis exclusively probes 2D in-plane molecular orientations within eADF4(C16) coatings using the two electrical field vectors E_x and E_y

oscillating within the x/y -plane, no in-plane orientation was concluded at Si-sc. The same result was found for thin and thick films on untexturized Si substrates (Table S6, Supporting Information). Conclusively, TRANS-FTIR analysis indicated that the antiparallel β -sheet structure of eADF4(C16) films had no distinct orientation in the substrate plane, neither for Si nor for Si-sc substrates.

ATR-FTIR Dichroism. ATR-FTIR analysis allows to probe molecular orientations based on three electrical field components E_x , E_y , and E_z and, therefore, is sensitive to both 2D in-plane orientations in the x/y -plane via E_x and E_y as well as a one-dimensional out-of-plane orientation with respect to the z -axis via E_z . In Figure 5B, typical dichroic ATR-FTIR spectra are given of thin eADF4(C16) as-cast films on Si-sc substrates before (bottom) and after MeOH post-treatment (top). Qualitatively, significant differences were obtained for P- and S-polarization with respect to the lineshape and intensity of the amide I band, which already suggested considerable orientation features. Quantitative evaluation was based on the amide I component at 1696 cm^{-1} . The intensity of the 1696 cm^{-1} component was determined with respect to ATR-FTIR spectra recorded in the P- and S-polarization using LSA. This weak component could be exclusively assigned to the pure $(0, \pi)$ mode^{10,35,36} of the antiparallel β -sheet structure, while the more intense component at 1625 cm^{-1} originated from the overlap of the $(\pi, 0)$ modes of both antiparallel and parallel β -sheet structures²⁸⁻³⁰ and could, therefore, not be used for further analysis. Importantly, the angle θ between M of the $(0, \pi)$ mode at 1696 cm^{-1} and both the plane and polypeptide chain direction in the antiparallel β -sheet elementary unit is known to be approximately 0° ("parallel" or "in-plane" mode). Hence, this θ value can be directly inserted in eq 7, from which the order parameter S could be calculated based on the experimental R^{ATR} value. The relevant dichroic ATR-FTIR orientation data are summarized in Figure 6.

For thin eADF4(C16) films, an experimental value of $R^{\text{ATR}} = 1.67$ was obtained after MeOH post-treatment, which is significantly higher than the dichroic ratio of an isotropic thin film $R_{\text{ISO}}^{\text{ATR}} = 1.16$ (Figure 6, grey-green bar pair). For respective thick films, $R^{\text{ATR}} = 1.94$ was determined, which is close to the value $R_{\text{ISO}}^{\text{ATR}} = 2.00$ for an isotropic thick film (Figure 6, grey-orange bar pair). In the following three bar pairs (Figure 6, green-orange), the optional directional order parameters S_x , S_y , and S_z are given for thin (green) and thick films (orange) based on the experimental R^{ATR} values of 1.67 (thin) and 1.94 (thick). S_x , S_y , and S_z were calculated, as it is described in the

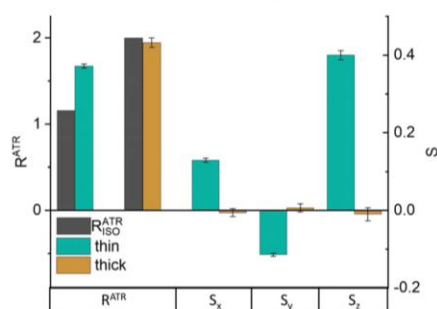


Figure 6. Dichroic ratios R_x^{ATR} , R_y^{ATR} , and R_z^{ATR} with respect to the β -sheet component at 1696 cm^{-1} and order parameter S_x , S_y , and S_z of eADF4(C16) films on Si-sc after MeOH post-treatment. Calculation of S_x , S_y , and S_z is based on the assumption that β -sheet planes are located either in-plane (S_x , S_y) or out-of-plane (S_z) to a planar substrate and that M is located in parallel ($\theta = 0^\circ$) to the β -sheet plane and chain direction.

Materials and Methods section (eqs 13a, 13b, and 13c), and are related to three assumed orientations of antiparallel β -sheets relative to the three space fixed orientation axes x , y , and z of Si-sc.

Thereby, the assumption of antiparallel β -sheets oriented in-plane along the x axis revealed a positive low value of $S_x = 0.13$, from which no significant orientation could be concluded along the x -axis. The assumption of antiparallel β -sheets oriented in-plane along the y axis revealed an unreasonable negative low value of $S_y = -0.11$, which in turn excluded this assumption. Hence, both assumptions did not suggest the in-plane orientation of antiparallel β -sheets, which was also supported by the TRANS-FTIR orientation data ($S = 0$). However, the assumption of antiparallel β -sheets oriented out-of-plane along the z -axis resulted in a high order parameter of $S = 0.40$. Hence, together with the information of the TRANS-FTIR data, the conclusion was drawn that the out-of-plane arrangement of antiparallel β -sheets is favored in thin eADF4(C16) films. Therefore, β -sheets are not lying in parallel but standing vertically to the substrate plane with an approximate tilt angle of $\gamma = 39^\circ$, which was calculated using eq 8. Finally, for thick eADF4(C16) films, low positive or negative values of S_x , S_y , and S_z were the result of the respective assumptions, so that neither in-plane nor out-of-plane orientations of β -sheets were concluded. Presumably, for thick eADF4(C16) films, confinement effects prevail neither from the planar substrate nor from the unidirectionally scratched grooves. Conclusively, a detailed structural model could be established of thin eADF4(C16) coatings on Si-sc substrates (Figure 7).

Dominant hydrophobic antiparallel β -sheet crystallites are embedded in an amorphous hydrophilic polypeptide matrix of the less ordered secondary structure³⁹ and are located rather vertically (out-of-plane) and not in parallel (in-plane) to the substrate plane. The polypeptide chain direction within antiparallel β -sheet crystallites runs vertically with respect to the β -sheet pleats, that is, in the z -direction in relation to the substrate plane.

Originally it was expected that in-plane texturization of silicon substrates (Si-sc) should cause the in-plane orientation of β -sheet crystallites. However, no significant deviation was observed of the order parameters between eADF4(C16) films cast on untexturized Si (Table S6) and those on Si-sc

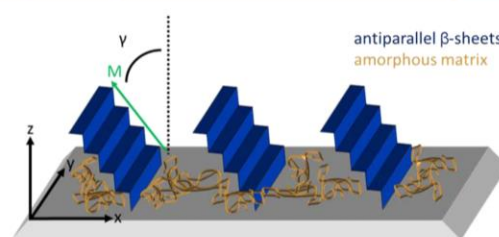


Figure 7. Out-of-plane arrangement of antiparallel β -sheets within MeOH post-treated thin eADF4(C16) films in relation to the Si or Si-sc substrate plane. Antiparallel β -sheet crystallites are embedded in an amorphous polypeptide matrix of the less ordered secondary structure.⁴⁰ The green arrow indicates the direction of TDM (M) of the $(0, \pi)$ amide I mode at 1696 cm^{-1} assigned to antiparallel β -sheets.

substrates (Figure 6) based on both dichroic TRANS-FTIR and ATR-FTIR analysis. If the β -sheet crystallites were oriented in-plane, a more significant effect would have been observed of the in-plane texturization on such an orientation should. Thus, the absence of in-plane texturization effects confirmed the out-of-plane orientation of β -crystallites on silicon substrates.

CONCLUSIONS

An analytical concept based on dichroic ATR- and TRANS-FTIR spectroscopy, including LSA, assignment of amide I band components to protein secondary structures, and calculation of order parameters based on their TDM was used to characterize model spider silk films of eADF4(C16) at silicon substrates with respect to conformation and uniaxial orientation of ordered structural motifs.

Both nanoscale and microscale films of eADF4(C16) were deposited out of 1 and 50 mg/mL of HFIP solutions at untreated (Si) and unidirectionally scratched (Si-sc) silicon substrates and post-treated in MeOH vapor.

First, as-cast eADF4(C16) films revealed low- β -sheet (<6%) and high content of unordered structures (>71%) before MeOH post-treatment, while increased β -sheet contents (>30%) and decreased contents of unordered structures (<63%) were detected by TRANS- and ATR-FTIR after MeOH post-treatment on both substrate types in accordance with previous studies.

Second, the folding kinetics of eADF4(C16) films upon MeOH post-treatment showed pseudo-first order kinetics with β -sheets increasing at the expense of the unfolded unordered structures, suggesting a two-state kinetic model.

Third, after MeOH post-treatment, an out-of-plane orientation of antiparallel β -sheets was detected using dichroic ATR-FTIR because of its sensitivity for the z -axis via the electrical field component E_z , which is normal to Si substrates. IR dichroism was based on the amide I component at 1696 cm^{-1} assigned to the parallel vibration mode $(0, \pi)$ of the antiparallel β -sheet structure within thin eADF4(C16) films. From the dichroic ratio $R^{\text{ATR}} = 1.67$, an order parameter of $S \approx 0.40$ was calculated (thin film) on Si and Si-sc (molecular tilt angle $\gamma = 39^\circ$), suggesting that antiparallel β -sheet structures rather stand vertically than lay parallelly to the substrate. No significant effects were found for substrate in-plane texturization (Si-sc) on these orientation features confirming the out-of-plane arrangement of β -sheet crystallites.

In summary, we discovered that thin films of the MeOH post-treated eADF4(C16) feature antiparallel β -sheet crystallites embedded in an amorphous polypeptide matrix with a significant out-of-plane orientation independently of the texturization of the silicon substrates. Obviously, dichroic ATR–FTIR spectroscopy enabled novel insights into the molecular orientation in thin spider silk films putatively having an impact on the mechanical properties of spider silk fibers. Future work will address the influence of other substrate parameters like substrate chemistry as well as the primary structure of spider silk proteins on orientation. Moreover, the introduced analytical concept will be applied on further oriented natural and synthetic protein systems, with respect to out-of-plane orientation.

■ ASSOCIATED CONTENT

Supporting Information

The Supporting Information is available free of charge at <https://pubs.acs.org/doi/10.1021/acs.jpcb.0c09395>.

Calculation and values of electrical field components, data treatments, additional atomic force microscopy data for thin and thick films at Si and Si-sc, additional dichroic ratio-based data of amide I components measured by TRANS– and ATR–FTIR at Si and Si-sc, and additional FTIR spectra at Si and Si-sc (PDF)

■ AUTHOR INFORMATION

Corresponding Author

Martin Müller – Institute of Physical Chemistry and Polymer Physics, Leibniz Institute of Polymer Research Dresden (IPF), D-01069 Dresden, Germany; Chair of Macromolecular Chemistry, Technical University of Dresden (TUD), D-01062 Dresden, Germany; orcid.org/0000-0001-8961-4604; Email: mamuller@ipfdd.de

Authors

Mirjam Hofmaier – Institute of Physical Chemistry and Polymer Physics, Leibniz Institute of Polymer Research Dresden (IPF), D-01069 Dresden, Germany; Chair of Macromolecular Chemistry, Technical University of Dresden (TUD), D-01062 Dresden, Germany

Birgit Urban – Institute of Physical Chemistry and Polymer Physics, Leibniz Institute of Polymer Research Dresden (IPF), D-01069 Dresden, Germany

Sarah Lentz – Chair of Biomaterials, University of Bayreuth, D-95447 Bayreuth, Germany

Christian B. Borkner – Chair of Biomaterials, University of Bayreuth, D-95447 Bayreuth, Germany

Thomas Scheibel – Chair of Biomaterials, University of Bayreuth, D-95447 Bayreuth, Germany

Andreas Fery – Institute of Physical Chemistry and Polymer Physics, Leibniz Institute of Polymer Research Dresden (IPF), D-01069 Dresden, Germany; Chair of Physical Chemistry of Polymeric Materials, Technical University Dresden (TUD), D-01069 Dresden, Germany

Complete contact information is available at: <https://pubs.acs.org/doi/10.1021/acs.jpcb.0c09395>

Notes

The authors declare no competing financial interest.

■ ACKNOWLEDGMENTS

This work was funded by the Deutsche Forschungsgemeinschaft (DFG, German Research Foundation) – Projektnummer 410 872 515. Astrid Drechsler is acknowledged for CLSM and Andre Knapp for UST measurements.

■ REFERENCES

- (1) Vollrath, F.; Porter, D. Spider silk as archetypal protein elastomer. *Soft Matter* **2006**, *2*, 377–385.
- (2) Lin, L. H.; Edmonds, D. T.; Vollrath, F. Structural engineering of an orb-spider's web. *Nature* **1995**, *373*, 146–148.
- (3) Borkner, C. B.; Elsner, M. B.; Scheibel, T. Coatings and films made of silk proteins. *ACS Appl. Mater. Interfaces* **2014**, *6*, 15611–15625.
- (4) Elgar, M. A.; Nash, D. R. Sexual cannibalism in the garden spider *Araneus Diadematus*. *Anim. Behav.* **1988**, *36*, 1511–1517.
- (5) Huemmerich, D.; Helsen, C. W.; Quedzuweit, S.; Oschmann, J.; Rudolph, R.; Scheibel, T. Primary structure elements of spider dragline silks and their contribution to protein solubility. *Biochemistry* **2004**, *43*, 13604–13612.
- (6) Wohlrab, S.; Müller, S.; Schmidt, A.; Neubauer, S.; Kessler, H.; Leal-Egaña, A.; Scheibel, T. Cell adhesion and proliferation on RGD-modified recombinant spider silk proteins. *Biomaterials* **2012**, *33*, 6650–6659.
- (7) Humenik, M.; Magdeburg, M.; Scheibel, T. Influence of repeat numbers on self-assembly rates of repetitive recombinant spider silk proteins. *J. Struct. Biol.* **2014**, *186*, 431–437.
- (8) Bates, F. S.; Fredrickson, G. H. Block Copolymers-Designer Soft Materials. *Phys. Today* **1999**, *52*, 32–38.
- (9) Heidebrecht, A.; Eisoldt, L.; Diehl, J.; Schmidt, A.; Geffers, M.; Lang, G.; Scheibel, T. Biomimetic fibers made of recombinant spider silks with the same toughness as natural spider silk. *Adv. Mater.* **2015**, *27*, 2189–2194.
- (10) Wohlrab, S.; Spieß, K.; Scheibel, T. Varying surface hydrophobicities of coatings made of recombinant spider silk proteins. *J. Mater. Chem.* **2012**, *22*, 22050–22054.
- (11) Borkner, C. B.; Lentz, S.; Müller, M.; Fery, A.; Scheibel, T. Ultrathin Spider Silk Films: Insights into Spider Silk Assembly on Surfaces. *ACS Appl. Polym. Mater.* **2019**, *1*, 3366–3374.
- (12) Anton, A. M.; Heidebrecht, A.; Mahmood, N.; Beiner, M.; Scheibel, T.; Kremer, F. Foundation of the Outstanding Toughness in Biomimetic and Natural Spider Silk. *Biomacromolecules* **2017**, *18*, 3954–3962.
- (13) Lefèvre, T.; Rousseau, M. E.; Pérolet, M. Determination of Molecular Orientation in Protein Films and Fibres by Raman Microspectroscopy. *Can. J. Anal. Sci. Spectrosc.* **2004**, *50*, 41–48.
- (14) Müller, M.; Ouyang, W.; Kessler, B. Dichroic ATR-FTIR spectroscopy on oriented α -helical poly(L-lysine) multilayered with polyanions. *Spectrochim. Acta, Part A* **2010**, *77*, 709–716.
- (15) Müller, M. Orientation of α -Helical Poly(L-lysine) in Consecutively Adsorbed Polyelectrolyte Multilayers on Texturized Silicon Substrates. *Biomacromolecules* **2001**, *2*, 262–269.
- (16) Spiess, K.; Ene, R.; Keenan, C. D.; Senker, J.; Kremer, F.; Scheibel, T. Impact of initial solvent on thermal stability and mechanical properties of recombinant spider silk films. *J. Mater. Chem.* **2011**, *21*, 13594–13604.
- (17) Provencher, S. W.; Gloeckner, J. Estimation of globular protein secondary structure from circular dichroism. *Biochemistry* **1981**, *20*, 33–37.
- (18) Sreerama, N.; Woody, R. W. Estimation of protein secondary structure from circular dichroism spectra: comparison of CONTIN, SELCON, and CDSSTR methods with an expanded reference set. *Anal. Biochem.* **2000**, *287*, 252–260.
- (19) Fringeli, U. P. ATR and Reflectance IR spectroscopy, Applications. *Encyclopedia of Spectroscopy and Spectrometry*; Lindon, J. C., Tranter, G. E., Holmes, J. L., Eds.; Academic Press, 2000.
- (20) Zbinden, R. *IR-Spectroscopy of High Polymers*; Academic Press: NY, 1964.

- (21) Fringeli, U. P.; Schadt, M.; Rihak, P.; Günthard, H. H. Z. *Naturforsch., A: Phys., Phys. Chem., Kosmophys.* **1976**, *31*, 1098.
- (22) Fringeli, U. P. The structure of lipids and proteins studied by attenuated total reflection (ATR) infrared spectroscopy. *Z. Naturforsch., C: J. Biosci.* **1977**, *32*, 20–45.
- (23) Michl, J.; Thulstrup, E. W. *Spectroscopy with Polarized Light*; VCH Publishers: New York, 1986.
- (24) Harrick, N. J. *Internal Reflection Spectroscopy*; Harrick Sci. Corp.: Ossining, New York, 1979.
- (25) Chirgadze, Y. N.; Shestopalov, B. V.; Venyaminov, S. Y. Intensities and other spectral parameters of infrared amide bands of polypeptides in the β - and random forms. *Biopolymers* **1973**, *12*, 1337–1351.
- (26) Barth, A. Infrared spectroscopy of proteins. *Biochim. Biophys. Acta* **2007**, *1767*, 1073–1101.
- (27) Miyazawa, T.; Shimanouchi, T.; Mizushima, S. I. Normal vibrations of N-methylacetamide. *J. Chem. Phys.* **1958**, *29*, 611–616.
- (28) Miyazawa, T. Perturbation treatment of the characteristic vibrations of polypeptide chains in various configurations. *J. Chem. Phys.* **1960**, *32*, 1647–1652.
- (29) Miyazawa, T.; Blout, E. R. The infrared spectra of polypeptides in various conformations: Amide I and II bands. *J. Am. Chem. Soc.* **1961**, *83*, 712–719.
- (30) Krimm, S. Infrared spectra and chain conformation of proteins. *J. Mol. Biol.* **1962**, *4*, 528–540.
- (31) Lang, G.; Neugirg, B. R.; Kluge, D.; Fery, A.; Scheibel, T. Mechanical testing of engineered spider silk filaments provides insights into molecular features on a mesoscale. *ACS Appl. Mater. Interfaces* **2017**, *9*, 892–900.
- (32) Tomiyama, T.; Ikeda, S. A Double Solvent-Induced β -Coil Transition of Poly-(S-[(3-hydroxypropyl)carbamoylmethyl]-L-cysteine) in Aqueous Hexafluoro-2-propanol Mixtures. *Polym. J.* **1981**, *13*, 1111–1117.
- (33) Ha, S.-W.; Asakura, T.; Kishore, R. Distinctive influence of two hexafluoro solvents on the structural stabilization of Bombyx mori silk fibroin protein and its derived peptides: ^{13}C NMR and CD studies. *Biomacromolecules* **2006**, *7*, 18–23.
- (34) Stephens, J. S.; Fahnestock, S. R.; Farmer, R. S.; Küick, K. L.; Chase, D. B.; Rabolt, J. F. Effects of Electrospinning and Solution Casting Protocols on the Secondary Structure of a Genetically Engineered Dragline Spider Silk Analogue Investigated via Fourier Transform Raman Spectroscopy. *Biomacromolecules* **2005**, *6*, 1405–1413.
- (35) Huemmerich, D.; Slotta, U.; Scheibel, T. Processing and modification of films made from recombinant spider silk proteins. *Appl. Phys. A* **2006**, *82*, 219–222.
- (36) Spieß, K.; Wohlrab, S.; Scheibel, T. Structural characterization and functionalization of engineered spider silk films. *Soft Matter* **2010**, *6*, 4168–4174.
- (37) Rodger, A.; Norden, B. *Circular Dichroism & Linear Dichroism*; Oxford University Press Inc.: New York, 1997.
- (38) Berova, N.; Nakanishi, K.; Woody, R. W. *Circular Dichroism*, 2nd ed.; Wiley-VCH, 2000.
- (39) Anfinsen, C. B.; Scheraga, H. A. Experimental and theoretical aspects of protein folding. *Adv. Protein Chem.* **1975**, *29*, 205–300.
- (40) Heim, M.; Römer, L.; Scheibel, T. Hierarchical structures made of proteins. The complex architecture of spider webs and their constituent silk proteins. *Chem. Soc. Rev.* **2010**, *39*, 156–164.

Supporting Information

Dichroic FTIR Spectroscopy Characterization of β -sheet Orientation in Spider Silk Films on Silicon Substrates

Mirjam Hofmaier^{1,2}, Birgit Urban¹, Sarah Lentz⁴, Christian B. Borkner⁴, Thomas Scheibel⁴, Andreas Fery^{1,3}, Martin Müller^{1,2,*}

1. Leibniz Institute of Polymer Research Dresden (IPF), Institute of Physical Chemistry and Polymer Physics, Hohe Strasse 6, D-01069 Dresden

2. Technical University of Dresden (TUD), Chair of Macromolecular Chemistry, Mommsenstraße 4, D-01062 Dresden

3. Technical University Dresden (TUD), Chair of Physical Chemistry of Polymeric Materials, D-01069 Dresden

4. University of Bayreuth, Chair of Biomaterials, Prof.-Rüdiger-Bormann-Str. 1, D-95447 Bayreuth

*To whom correspondence should be addressed

Email: mamuller@ipfdd.de

Principles of dichroic FTIR-spectroscopy

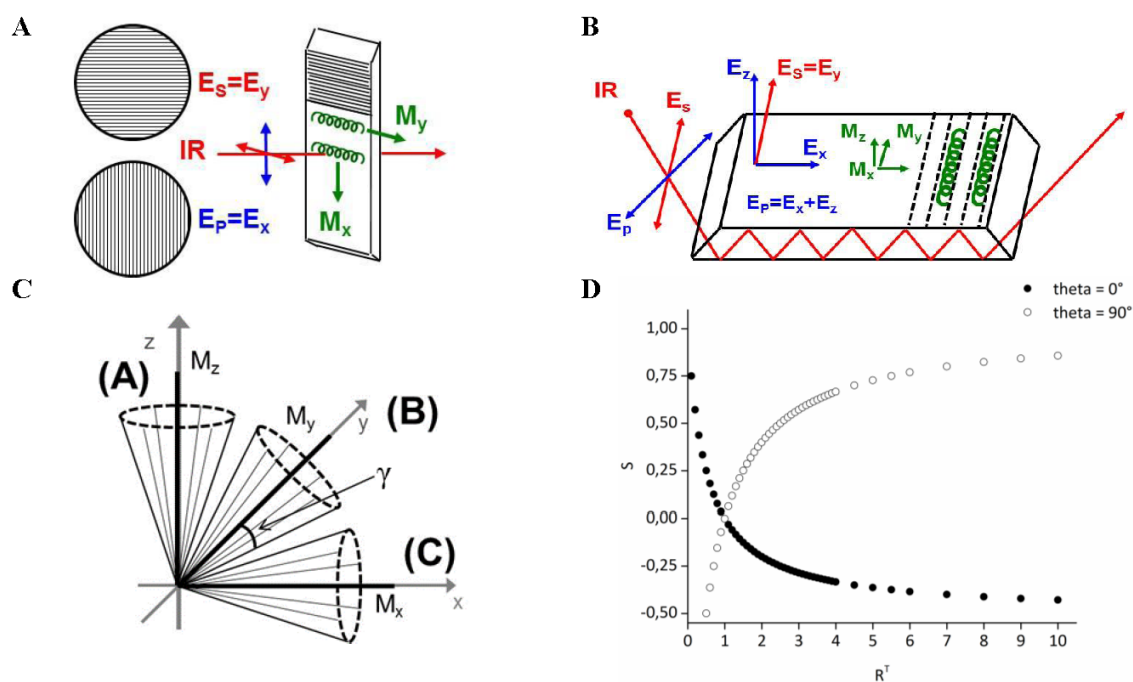


Fig. S1 Principles of dichroic TRANS-FTIR (A) and dichroic ATR-FTIR spectroscopy (B) of oriented polymer films on texturized substrates; grooves are located between the drawn dotted lines. (C) Cone based orientation models describe distributions of oriented molecular chains along either x-, y- or z-axis. The respective angles θ are zero between the transition dipole moments M_x , M_y , and M_z and the respective molecular axis. The angle γ is the opening angle of the cone model. (D) Plot of the order parameter S versus the dichroic ratio R^T for the two extreme cases with angles of $\theta = 0^\circ$ and $\theta = 90^\circ$ according to eq. (8).

S1

Electrical field components

Tab. S1 Values of relative electrical field components E_x , E_y , E_z used herein according to [1] for thin films ($d = 28$ nm) and thick films ($d = 1920$ nm) (see Tab. 2).

Layer system	E_x	E_y	E_z
Si / eADF4(C16) film, $d = 28$ nm / air $n_1 = 3.5 / n_2 = 1.5 / n_3 = 1.0$	1.407	1.481	0.751
Si / eADF4(C16) film, $d = 1920$ nm / air $n_1 = 3.5 / n_2 = 1.5 / n_3 = 1.0$	1.378	1.565	1.732

The following equations (S1)-(S3) were used ¹ for calculation of the relative electrical field components E_x , E_y and E_z :

$$E_x = \frac{2 \cos a_{TOT} \sqrt{\sin^2 a_{TOT} - n_{31}^2}}{\sqrt{1 - n_{31}^2} \sqrt{(1 - n_{31}^2) \sin^2 a_{TOT} - n_{31}^2}} \quad (S 1)$$

$$E_y = \frac{2 \cos a_{TOT}}{\sqrt{1 - n_{31}^2}} \quad (S 2)$$

$$E_z = \frac{2 \cos a_{TOT} \sin a_{TOT} - n_{32}^2}{\sqrt{1 - n_{31}^2} \sqrt{1 + n_{31}^2 \sin^2 a_{TOT} - n_{31}^2}} \quad (S 3)$$

with $n_{31} = n_3/n_1$ and $n_{32} = n_3/n_2$. α is the critical angle of incidence. Denoting films with thicknesses of $d \rightarrow 0$ nm, with $n_1 = 3.5$ for silicon, $n_2 = 1.5$ for protein and $n_3 = 1$ for air and thick films with $d \rightarrow \infty$ nm n_3 (air) must be replaced by n_2 (polymer), while the other refractive index settings are kept. Besides, E_x and E_y , especially E_z is sensitive to film thickness d . Therefore, to get more precise values of E_x , E_y and E_z , an empirical interpolation formula was applied from Fringeli ², which scales the respective differences $E^{THIN} - E^{THICK}$ using an exponentially damped function as follows (S 4a – S 4c):

$$E_x^{INTER} = E_x^{THIN} + (E_x^{THICK} - E_x^{THIN}) * \exp(-d/d_p) \quad (S 4a)$$

$$E_y^{INTER} = E_y^{THIN} + (E_y^{THICK} - E_y^{THIN}) * \exp(-d/d_p) \quad (S 4b)$$

$$E_z^{INTER} = E_z^{THIN} + (E_z^{THICK} - E_z^{THIN}) * \exp(-d/d_p) \quad (S 4c)$$

d_p is the penetration depth, which is defined as the distance d from the substrate surface, where the electrical field is decayed to $1/e$ with respect to the surface according to Harrick ¹:

$$d_p = \frac{\lambda}{2\pi \sqrt{\sin^2 \alpha - \left(\frac{n_1}{n_2}\right)^2}} \quad (S 5)$$

λ is the wavelength, α the angle of incidence, and n_1 and n_2 the refractive indexes of the film (n_1) and the substrate (n_2).

Lineshape analysis

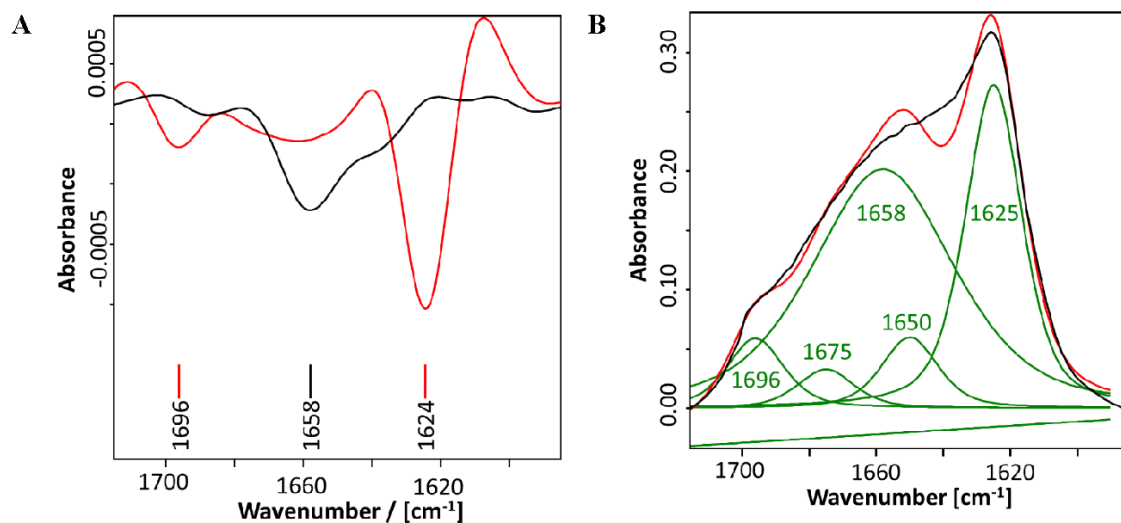


Fig. S2 (A) Second derivative FTIR spectra of eADF4(C16) films cast from HFIP ($c_{\text{solution}} = 1 \text{ mg/ml}$) before (black) and after post-treatment using MeOH vapour (red). Respective secondary structure diagnostic minima are indicated. (B) Exemplary curve fitting (LSA) of ATR-FTIR spectra of eADF4(C16) films ($c_{\text{solution}} = 1 \text{ mg/ml}$) after MeOH vapour post-treatment. Measured ATR-FTIR spectrum (black), fitted spectrum (red) and underlying five components (green, Table S2) and baseline (green) are shown.

Tab. S2 Wavenumber positions ν^{max}_i of Amide I bands in FTIR spectra of eADF4(C16) and assignment to secondary structures according to the literature.^{3,4,5} Selected half-widths w_i in cm^{-1} are given in brackets.

Amide I / [cm^{-1}]	1696 (20)	1675 (20)	1658 (50)	1650 (20)	1625 (20)
Secondary structure	β -sheet	β -turn	unordered	α -helix	β -sheet

Additional SFM data

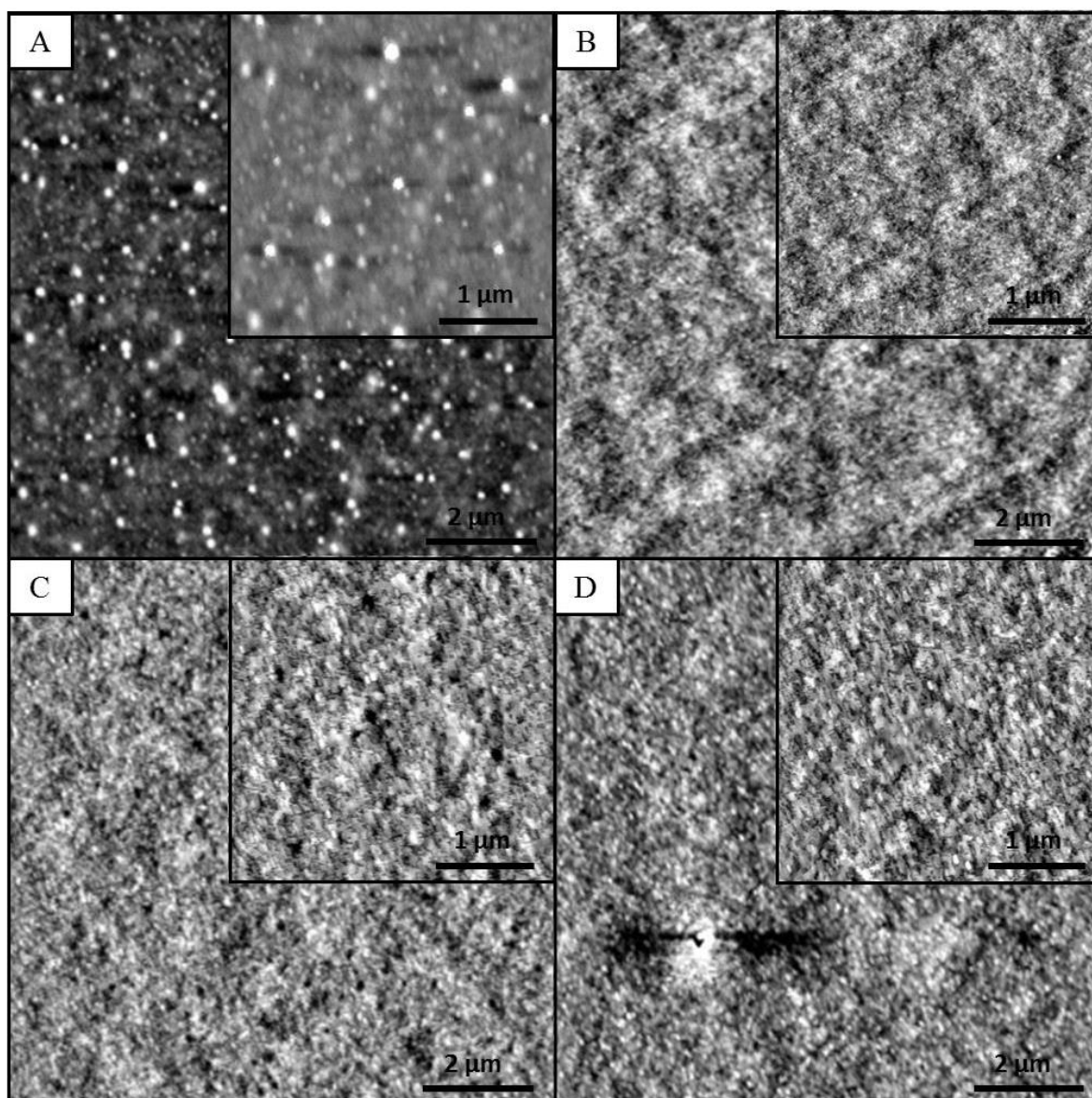


Fig. S3 SFM images (10 x 10 μm) of thick as-cast eADF4(C16) films before post-treatment on Si (A) and Si-sc (B) and after subsequent post-treatment using MeOH vapor (1 h) on Si (C) and Si-sc (D).

Additional dichroic ratio-based data**Dichroic ratios of Amide I components measured using TRANS-FTIR on Si-Sc**

Tab. S3 Main wavenumber position, the angle between TDM and molecular plane/axis θ and measured dichroic ratio R^T of post-treated thin eADF4(C16) films on Si-sc. Measurements were repeated three times.

	TRANS-FTIR Si-sc	TRANS- FTIR Si-sc	TRANS-FTIR Si-sc	TRANS-FTIR Si-sc
Position / [cm^{-1}]	1675	1658	1650	1625
θ / [$^\circ$]	(not known)	(not known)	(not known)	(not known)
R^T (exp)	0.97 ± 0.12	1.01 ± 0.04	0.93 ± 0.18	0.98 ± 0.04

Dichroic ratios of Amide I components measured using ATR-FTIR at Si-sc

Tab. S4 Main wavenumber position, angle between TDM and molecular plane/axis θ , measured dichroic ratio R^{ATR} and calculated dichroic ratio R_x^T , R_y^T , R_z^T (assuming x-, y- or z-axis orientation), respectively, using eqs. 14a, 14b, 14c of post-treated thin eADF4(C16) films on Si-sc. ($n = 3$).

	ATR-FTIR Si-sc	ATR- FTIR Si-sc	ATR-FTIR Si-sc	ATR-FTIR Si-sc
Position / [cm^{-1}]	1675	1658	1650	1625
θ / [$^\circ$]	(not known)	(not known)	(not known)	(not known)
R^{ATR} (exp)	2.05 ± 0.04	1.44 ± 0.02	1.16 ± 0.02	1.09 ± 0.00
R_x^T	0.56 ± 0.01	0.80 ± 0.01	1.00 ± 0.01	1.06 ± 0.00
R_y^T	1.77 ± 0.03	1.24 ± 0.02	1.00 ± 0.01	0.94 ± 0.00
R_z^T	0.22 ± 0.01	0.48 ± 0.02	1.01 ± 0.06	1.35 ± 0.03

Dichroic ratios measured using ATR-FTIR on Si-sc

Tab. S5 Dichroic ratios R_x^{ATR} , R_y^{ATR} , R_z^{ATR} , R_x^T , R_y^T , R_z^T with respect to β -sheet content at 1696 cm^{-1} , and order parameter S_x , S_y , S_z of post-treated eADF4(C16) films on Si-sc substrates. Calculation of S_x , S_y and S_z is based on the assumptions that β -sheet planes are located either *in-plane* (S_x , S_y) or *out-of-plane* (S_z) to the planar substrate and that M is located in parallel ($\theta = 0^\circ$) to the β -sheet plane and chain direction. The number of measurements is given in brackets (#).

Sample	TRANS-FTIR (#3) 1 mg/ml	ATR-FTIR (#3) 1 mg/ml	ATR-FTIR (#2) 50 mg/ml
$R^{T, ATR}_{ISO}$ (theo.)	1.00	1.16	2.00
R^{ATR} (exp.)	---	1.67 ± 0.03	1.94 ± 0.06
R_x^T	1.02 ± 0.01	0.69 ± 0.01	1.03 ± 0.03
R_y^T	---	1.44 ± 0.02	0.97 ± 0.03
R_z^T	---	0.31 ± 0.01	1.05 ± 0.05
S_x	0.00 ± 0.01	0.13 ± 0.01	-0.01 ± 0.01
S_y	---	-0.11 ± 0.00	0.01 ± 0.01
S_z	---	0.40 ± 0.01	-0.02 ± 0.02

Dichroic ratios measured using ATR-FTIR on Si

Tab. S6 Main wavenumber positions, angle between TDM and molecular plane/axis, experimental dichroic ratio R^{ATR} , calculated dichroic ratio R_x^T , R_y^T , R_z^T (β -sheet component at 1696 cm^{-1}) and order parameter S_x , S_y , S_z are shown for eADF4(C16) post-treated films on untexturized Si substrates. Calculations of S_x , S_y , S_z are based on the assumption that β -sheet planes are located either *in-plane* (S_x , S_y) or *out-of-plane* (S_z) to the planar substrate and that TDM is located in parallel ($\theta = 0^\circ$) to the β -sheet plane and to chain direction. The number of measurements is given in brackets (#).

	TRANS-FTIR (#3) 50 mg/ml	ATR-FTIR (#2) 1 mg/ml	ATR-FTIR (#3) 50 mg/ml
Position / [cm^{-1}]	1696	1696	1696
θ / [$^\circ$]	0	0	0
R^{ATR} (exp)	---	1.67 ± 0.04	1.86 ± 0.02
R_x^T	1.07 ± 0.01	0.69 ± 0.02	1.07 ± 0.01
R_y^T	---	1.44 ± 0.04	0.93 ± 0.01
R_z^T	---	0.34 ± 0.02	1.13 ± 0.02
S_x	-0.02 ± 0.00	0.13 ± 0.01	-0.02 ± 0.00
S_y	---	-0.11 ± 0.01	0.02 ± 0.00
S_z	---	0.40 ± 0.02	-0.04 ± 0.01

Additional FTIR spectra on Si and Si-sc

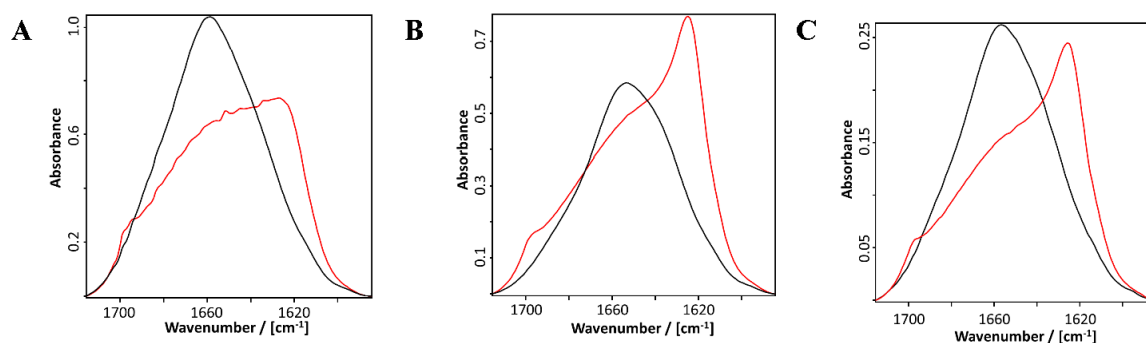


Fig. S4 Typical TRANS-FTIR (A) and ATR-FTIR spectra (unpolarised) of eADF4(C16) thick (B) and thin (C) films before (black) and after MeOH post-treatment (red) on Si substrates.

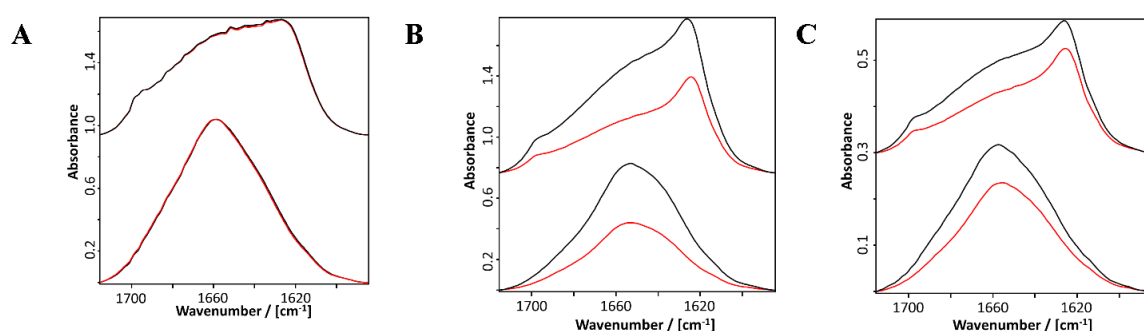


Fig. S5 Typical dichroic TRANS-FTIR (A) and ATR-FTIR-spectra of eADF4(C16) thick films (B) thin films (C) as-cast (bottom) and after MeOH post-treatment (top) in P-polarisation (black) and S-polarisation (red) on Si substrates.

References

1. Harrick, N. J. *Internal reflection Spectroscopy*; Harrick Sci. Corp.: Ossining: New York, **1979**.
2. Fringeli, U. P. *ATR and Reflectance IR spectroscopy. Applications*; In *Encyclopedia of Spectroscopy and Spectrometry*. Lindon, J. C., Tranter, G. E., Holmes, J. L. Eds. Academic Press, **2000**.
3. Miyazawa, T.; Shimanouchi, T.; Mizushima, S, I. Normal vibrations of N-methylacetamide. *J. Chem. Phys.* **1958**, *29* (3), 611-616.
4. Miyazawa, T. Perturbation treatment of the characteristic vibrations of polypeptide chains in various configurations. *J. Chem. Phys.* **1960**, *32*, 1647-1652.
5. Miyazawa, T.; Blout, E. R. The infrared spectra of polypeptides in various conformations: Amide I and II bands. *J. Amer. Chem. Soc.* **1961**, *83*, 712-719.

Part III – Bioselectivity of recombinant spider silk surfaces

Part III - Chapter 1 – Structure-property relationship based on the amino acid composition of recombinant spider silk proteins for potential biomedical applications

Part III – Chapter 1.1 - Chapter perspective and contribution

This publication is one of my first author papers. This publication is focused on the surface properties of recombinant spider silk proteins depending on their amino acid composition and net charge. This study systematically investigates the wettability, the biocompatibility with three kinds of mammalian cells and whole human blood, the biodegradability towards protease and collagenase and the topography of five different recombinant spider silk protein films.

I performed the synthesis and purification of the proteins eADF4(C16), eADF4(κ 16), eADF3(AQ)₁₂, and eADF3(AQ)₂₄. Vanessa Trossmann performed the design, synthesis, and purification of the protein eADF4(Ω 16). The design of the experiments was performed by Vanessa Trossmann and myself. I produced the films and performed the AFM, KPFM, GATR-FTIR, and water contact angle measurements. Christian Borkner, Vivien Beyersdorfer, Vanessa Trossman and myself performed the enzymatic degradation. Christian Borkner and Sarah Lentz performed the QCM-D measurements. I performed the blood coagulation tests as part of a collaboration with Markus Rottmar (EMPA). Vanessa Trossmann and I performed the cell culture tests. The writing of the original draft and the visualization of the results was done by Vanessa Trossmann and myself. Thomas Scheibel supervised the studies and edited the paper.

The permission of reprint was granted by ACS Applied Materials & Interfaces: Reprinted (adapted) with permission from „, Structure–Property Relationship Based on the Amino Acid Composition of Recombinant Spider Silk Proteins for Potential Biomedical Applications, “Sarah Lentz, Vanessa T. Trossmann, Christian B. Borkner, Vivien Beyersdorfer, Markus Rottmar, and Thomas Scheibel, ACS Applied Materials & Interfaces **2022** 14 (28), 31751-31766, DOI: 10.1021/acsami.2c09590. Copyright 2022 American Chemical Society.

Part III – Chapter 1.2 - Full Paper

ACS APPLIED MATERIALS
& INTERFACES

www.acsami.org

Research Article

Structure–Property Relationship Based on the Amino Acid Composition of Recombinant Spider Silk Proteins for Potential Biomedical Applications

Sarah Lentz, Vanessa T. Trossmann, Christian B. Borkner, Vivien Beyersdorfer, Markus Rottmar, and Thomas Scheibel*

Cite This: *ACS Appl. Mater. Interfaces* 2022, 14, 31751–31766

Read Online

ACCESS |

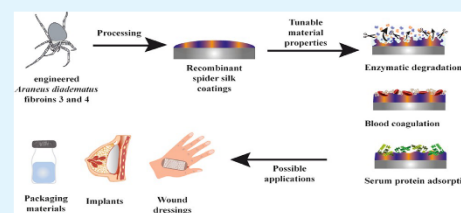
Metrics & More

Article Recommendations

Supporting Information

ABSTRACT: Improving biomaterials by engineering application-specific and adjustable properties is of increasing interest. Most of the commonly available materials fulfill the mechanical and physical requirements of relevant biomedical applications, but they lack biological functionality, including biocompatibility and prevention of microbial infestation. Thus, research has focused on customizable, application-specific, and modifiable surface coatings to cope with the limitations of existing biomaterials. In the case of adjustable degradation and configurable interaction with body fluids and cells, these coatings enlarge the applicability of the underlying biomaterials. Silks are interesting coating materials, e.g., for implants, since they exhibit excellent biocompatibility and mechanical properties. Herein, we present putative implant coatings made of five engineered recombinant spider silk proteins derived from the European garden spider *Araneus diadematus* fibroins (ADF), differing in amino acid sequence and charge. We analyzed the influence of the underlying amino acid composition on wetting behavior, blood compatibility, biodegradability, serum protein adsorption, and cell adhesion. The outcome of the comparison indicates that spider silk coatings can be engineered for explicit biomedical applications.

KEYWORDS: recombinant spider silk proteins, blood coagulation, enzymatic degradation, cell adhesion, protein adsorption, surface properties



1. INTRODUCTION

One main goal of biomaterials' development is the improvement of their application specificity.¹ However, the performance of a biomaterial strongly depends on its interaction with the surrounding biological environment, which is mainly driven by interactions on the material's surface.^{2,3} The crucial step in this process is the formation of a protein layer on the surface of the material within a short time after contact.^{2–6} Protein–material interactions are influenced and directed by the properties of the material as well as the body fluid, such as general composition, size, charge, stability, folding, and structure of included proteins. In the case of the biomaterial, its chemical composition, charge, hydrophobicity, wettability, topography, and structure are highly important.^{7,8} A protein layer formed on the material surface, also named a biocorona, affects subsequent cellular mechanisms, such as cell adhesion, since protein segments accessible for cell surface receptors might influence their adhesion and further cell fate.^{2,8,9} However, the foreign body response, inflammation, fibrous capsule formation, and thus a potential rejection reaction of the body are also determined by the adsorbed protein

layer.^{2,10,11} Since several material surface properties, including roughness, wettability, and charge, trigger responses upon contact with body fluids, such as protein adsorption and cell-related behavior,^{2,4,7–9,12} the control of surface properties of biomaterials is one key factor for their successful application in biomedical applications, tissue engineering, and regenerative medicine.^{3,7,13} However, depending on the desired field of application, the demands on biomaterials' surface properties are quite different. The class of bioinert materials should interact minimally with the host environment, while bioactive and biospecific materials should actively interact with the biological surrounding and adjacent tissue to stimulate, promote, and guide cellular responses.^{1,3,13–16}

Received: May 29, 2022

Accepted: June 20, 2022

Published: July 5, 2022



ACS Publications

© 2022 American Chemical Society

31751

<https://doi.org/10.1021/acsami.2c09590>
ACS Appl. Mater. Interfaces 2022, 14, 31751–31766

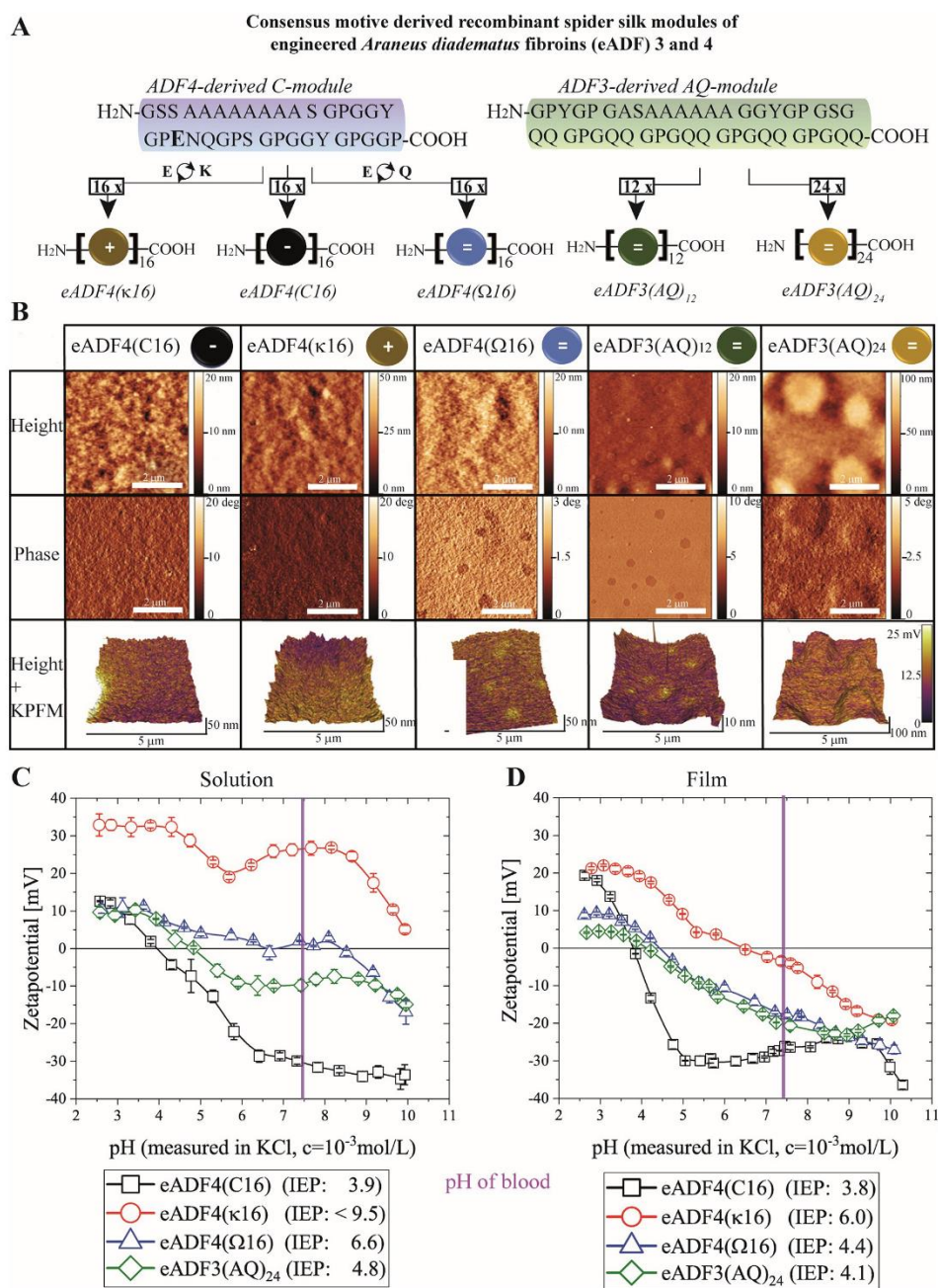


Figure 1. (A) Schematic representation of the amino acid consensus sequences of ADF3 and ADF4 named AQ- and C-modules and the resulting engineered *A. diadematus* fibroins *eADF3(AQ)₁₂* (48 kDa), *eADF3(AQ)₂₄* (96 kDa), *eADF4(C16)* (48 kDa), *eADF4(κ16)* (48 kDa), and *eADF4(Ω16)* (48 kDa). ⊕ depicts the positive net charge, ⊖ depicts the negative net charge, and ⊙ depicts the zero net charge. (B) Atomic force microscopy (AFM) images of dry protein films. The last lane depicts Kelvin probe force microscopy (KPFM) images, showing the surface potential (mV) of the spider silk films related to the cantilever overlaid by topography images of these films. (C) Representative ζ potential curves of recombinant spider silk proteins in solution versus pH. (D) Representative streaming potential curves of recombinant spider silk films versus pH. The films made of the recombinant spider silk proteins are the negatively charged variant *eADF4(C16)* (black curves), the positively charged variant *eADF4(κ16)* (red curves), and the uncharged variants *eADF4(Ω16)* (blue curve) and *eADF3(AQ)₂₄* (green curves). ($n = 3$ at each pH value.) The purple line indicates the pH of human blood of ~ 7.4 .³⁷

31752

<https://doi.org/10.1021/acsami.2c09590>
 ACS Appl. Mater. Interfaces 2022, 14, 31751–31766

On the one hand, bioinert surfaces are used for many different biomedical contact materials interacting with blood, tear fluid, urine, or saliva.^{12,17} Thereby, it must be distinguished between *in vivo* applications, including cardiovascular stents, urine or intravascular catheters, guidewires and ocular devices, or medical devices, which come in direct contact with the patient, and *ex vivo* applications related to diagnostics and analytical methods of body fluids or biopsies.^{12,17} In this context, it is important to mention that blood-contacting devices, such as catheters, artificial heart bladders, or stents, should not only prevent adhesion with the surrounding tissues but also inhibit thrombosis and immunological responses.^{3,17–19} Today, the most commonly used materials for such applications are polymeric materials, such as polyurethanes (PUs), poly(tetrafluoroethylene) (PTFE), latex, and silicone-based materials, due to their easy processing and suitable physical properties. However, several of these materials comprise low biocompatibility, increased susceptibility to infection, risk of incrustation, or trigger inflammatory responses as serious disadvantages.^{18,20,21} On the other hand, bioactive surfaces are specifically designed, modified, and functionalized to actively engage with the surrounding tissue for their application in drug delivery as a local depot of bioactive substances as well as in tissue engineering and regeneration to support cellular responses, including adhesion, proliferation, or differentiation.^{13–16,22}

From the problems associated with bone tissues, including implant loosening, poor healing, and permanent defect or infections, it is clear that such bioactive implants should support tissue integration, prevent microbial infections, and stimulate cells.²³ As mentioned before, many implants are made of polymeric materials but also metals, ceramics, and composites are used, and in addition to difficulties in processing, they also have serious disadvantages in terms of biocompatibility, degradability, and foreign body reaction.²⁴ In recent years, customizable, application-specific, and modifiable surface coatings have become more and more important to overcome the known limitations and drawbacks of different biomaterials.^{13,15,17,23,25} These coatings could be generated using materials like phosphorylcholine or polymers, such as poly(ethylene glycol) (PEG), and naturally occurring biopolymers and proteins, such as extracellular matrix components (e.g., hyaluronic acid and collagen I) or chitosan, as well as hydroxyapatite or silver.^{15,17,23,25}

In this context, coatings made of recombinant silk proteins are promising candidates for modifying a wide range of biomaterials, because they are biocompatible, do not trigger an inflammatory response, and can be adapted to a specific application. Since recombinant spider silk-based materials consist of amino acids, they are nontoxic and biodegradable and, therefore, well suited for various biomedical applications.^{18,26–30} The dragline spider silk of the European garden spider *Araneus diadematus* comprises at least two major ampullate spidroins (MaSp), the so-called *A. diadematus* fibroins (ADF) 3 and 4.^{31–33} A sequence alignment of ADF3 and ADF4 revealed a pairwise identity of 58.1%, mainly deriving from polyalanine and amorphous sequence motifs containing glycine and proline residues (Figure S11). Although showing similar amounts of proline, alanine, and glycine residues, they differ significantly in the content of glutamine and serine residues, with ADF4 containing more serine and fewer glutamine residues than ADF3.³¹ ADF3 represents a more hydrophilic spider silk protein based on the amino acid

composition, while ADF4 has a more hydrophobic character.³³ In an established recombinant approach, consensus sequences of the core domains of both proteins, namely, eADF4(C), eADF3(Q), and eADF3(A), have been multimerized, resulting in eADF4(C16) and eADF3(AQ)₁₂ or eADF3(AQ)₂₄ (Figure 1A).^{32,34} To investigate the impact of protein net charge more closely, the uncharged eADF4(Ω16) variant and the positively charged eADF4(κ16) variant were developed.^{29,35,36}

Here, recombinant spider silk film surfaces were analyzed concerning their suitability for biomedical applications based on their amino acid composition. We gained insights into the surface properties of spider silk coatings concerning the impact of the underlying amino acid composition including the charge. With these findings, we identified possible biomedical application fields of coatings made of each variant.

2. RESULTS AND DISCUSSION

2.1. Surface Topography and Surface Potential.

Atomic force microscopy (AFM) was used to image the surface topography of spider silk films made of five different spider silk variants, as depicted in Figure 1. Both the eADF3- and the eADF4-derived variants showed smooth and relatively featureless surfaces (Figure 1B). The root-mean-square (rms) roughness of all spider silk films was below 5 nm (Figure S12).

Films made of eADF3(AQ)₁₂ and eADF3(AQ)₂₄ showed large patches on the surface, with eADF3(AQ)₂₄ being bigger than that of eADF3(AQ)₁₂, likely due to the larger molecular weight of this protein. Interestingly, the phase image of the uncharged eADF4(Ω16) showed similar patches as observed for eADF3(AQ)₁₂, while the charged variants eADF4(C16) and eADF4(κ16) showed no patchy areas. The surface potential of the detected nanostructures and phase-separated domains were visualized using Kelvin probe force microscopy (KPFM). KPFM measurements qualitatively showed that the patchy character of the phase images of eADF4(Ω16), eADF3(AQ)₁₂, and eADF3(AQ)₂₄ arose from phase separation of the hydrophilic and hydrophobic motifs of the proteins, indicative of phase-separated (slightly more hydrophobic) β -sheets, which increase the surface potential compared to non- β -sheet areas of the surface.^{38–40} Coatings made of recombinant spider silk protein films will mostly be in contact with body fluids. The most important body fluid is human blood with a pH of 7.4.³⁷ Therefore, electrokinetic measurements, namely, streaming potential measurements of recombinant spider silk coatings and ζ -potential measurements of recombinant spider silk proteins in solution versus pH, were performed to show the surface charge behavior over the pH range from 2.5 to 10 (Figure 1C,D). Furthermore, an isoelectric focusing (IEF) gel electrophoresis of soluble, dialyzed proteins (Figure S13) was conducted to determine the isoelectric point (IEP) of the spider silk variants. Since a homogeneous gel staining was not possible for the used spider silk proteins, a subsequent western blot analysis was conducted detecting the N-terminally fused T7-tag with a horseradish peroxidase (HRP)-conjugated T7-antibody. The theoretical expected and the experimentally determined IEPs are shown in Table 1. Recombinant spider silk films on silicon were used for streaming potential measurements, and, therefore, the water contact angles on silicon were important for discussing the streaming potential results. Recombinant spider silk protein films showed water contact angles (WCAs) from 50° (eADF4(Ω16)) to 55° (eADF4(κ16)) to more hydrophobic

Table 1. Comparison of Isoelectric Points (IEPs) of Recombinant Spider Silk Proteins^a

protein	calculated IEP (mV)	IEP estimated from IEF gel	ζ -potential (solution) (mV)	streaming potential (film) (mV)
eADF4(C16)	3.5	4.5	3.9	3.8
eADF4(κ 16)	9.7	>8.3	>9.5	6.0
eADF4(Ω 16)	7.7	7.8–8.3	6.6	4.4
eADF3(AQ) ₂₄	7.8	8.3	4.8	4.1

^aCalculated theoretical IEPs, IEPs estimated from an IEF gel electrophoresis (pH gradient gel), and IEPs of ζ -potential measurements of recombinant spider silk proteins in solution versus IEPs of streaming potential measurements ($n = 3$ at each pH).

WCA of 70° (eADF4(C16)) up to ~80° (eADF3(AQ)₂₄) (see Figure 2).

For the negatively charged variant eADF4(C16), the theoretical IEP of 3.5 was close to the measured IEP in solution (IEP_{C16,solution} = 3.9) and on films (IEP_{C16,film} = 3.8). With a large band at around 4.5, the IEP derived from the IEF gel analysis was also in a similar range (Figure S13). eADF4(C16) is the most acidic recombinant spider silk protein investigated in this study because of its amino acid sequence, which comprises 16 additional COOH-groups from glutamic acid residues in the repetitive units. The eADF4(κ 16) variant is positively charged because the glutamic acid in its consensus motif is substituted by 16 basic lysines. In solution, eADF4(κ 16) showed a positive ζ -potential over the entire pH range, which is a typical curve course for protonated samples. The theoretical IEP is at 9.7. The IEP was not observable in the electrokinetic measurements in solution, probably because of too much dissolved CO₂. Additionally, with the IEF gel analysis, it was also not possible to make a precise statement

for soluble eADF4(κ 16) because the used IEF setup was only designed for the separation of proteins with an IEP range between 3.0 and 8.5 according to the manufacturer. Due to the fact that eADF4(κ 16) stays inside the gel pocket and only a very light band was visible, we assume an IEP of above 8.5 (Figure S13). The streaming potential of eADF4(κ 16) films showed a different course of the curve (Figure 1). This is due to the more hydrophobic surface of the film (WCA ~ 55°) compared to that of eADF4(κ 16) in solution. In the eADF4(Ω 16) variant, the 16 glutamic acid in the repetitive unit are substituted with 16 glutamine residues. Consequently, the eADF4(Ω 16) protein comprises more amide functional groups than eADF4(C16). The IEP in solution is a bit lower than the theoretical IEP (7.7), but the curve between pH 6 and 8.5 is always close to zero (Table 1 and Figure 2C). In the IEF gel analysis, three bands were detected for eADF4(Ω 16) in an IEP range between 7.8 and 8.3 (Figure S13), which are close to the theoretical IEP. It is a known mechanism that *Escherichia coli* bacteria start protein degradation N-terminally,^{41,42} and, for instance, the missing of methionine as the first amino acid is already known for recombinant spider silk proteins.³⁰ As a consequence, the free N-terminal amino group is located at different amino acid residues, which could influence the IEP of uncharged proteins more than the IEP of highly charged proteins explaining the three bands for eADF4(Ω 16). Furthermore, the IEF gel also showed three bands in the same IEP range between 7.8 and 8.3 for the uncharged eADF3(AQ)₁₂ (Figure S13). For eADF3(AQ)₂₄ only one band was detectable at an IEP of around 8.3, which corresponded with the theoretical IEP. Streaming potentials of only one of the eADF3-derived variants were measured, because eADF4-(AQ)₁₂ and eADF3(AQ)₂₄ just differ in molecular weight. The ζ -potential in solution is more acidic (IEP: 4.8) than the

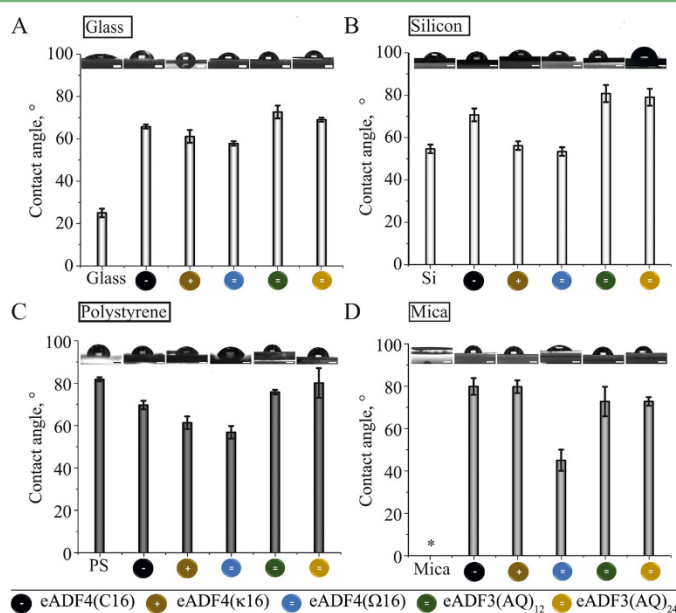


Figure 2. Water contact angles (static drop) of spider silk films in comparison to blank substrates; (A) glass, (B) silicon, (C) polystyrene (PS), and (D) mica. The recombinant spider silk films were post-treated with methanol overnight prior to water contact angle measurements. *Contact angle measurements were not possible due to the complete spreading of the water droplet. Scale bars are 1 mm ($n = 9$).

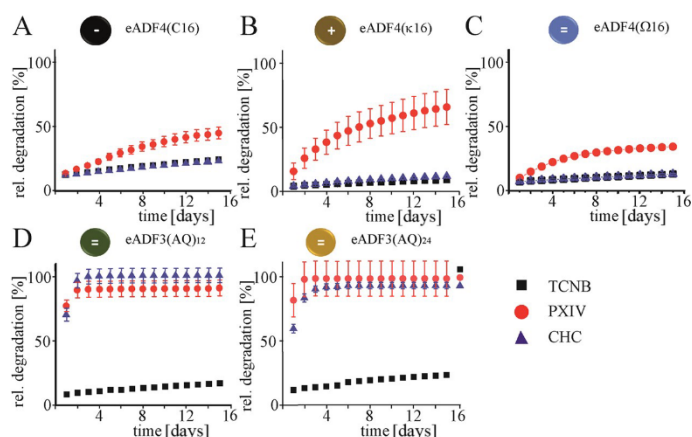


Figure 3. Enzymatic degradation of eADF4(C16) (A), eADF4(κ 16) (B), eADF4(Ω 16) (C), eADF3(AQ)₁₂ (D) eADF3(AQ)₂₄ (E) films in the presence of protease mixture PXIV of *S. griseus* and collagenase CHC from *C. histolyticum* (type IA), as indicated over 15 days at room temperature (RT). The TCNB samples contained no enzyme and served as controls. The enzyme and buffer solutions were exchanged every 24 h ($n = 2$).

theoretical IEP (IEP: 7.8) as well as the streaming potential (IEP: 4.1).

2.2. Wetting Behavior and Secondary Structure of Recombinant Spider Silk Protein Films. The substrate on which spider silk films are cast on has an impact on spider silk phase separation and on the spider silk film surface properties.^{18,38,39} Therefore, in addition to silicium, as stated above, additional surfaces with different hydrophobicities, such as mica, glass, and polystyrene (PS), were used as substrates to analyze the water contact angle (WCA). The structural differences (secondary structure) of the silk films were analyzed using grazing angle attenuated total reflection Fourier transform infrared spectroscopy (GATR-FTIR) before and after post-treatment with MeOH. As cast, the normalized GATR-FTIR spectra of all recombinant spider silk films showed a unimodal peak around 1658–1661 cm^{-1} , assigned to random coil structures (Figure S14). After post-treatment with MeOH vapor, the GATR-FTIR spectra showed a bimodal curve shape. The β -sheet content increased for all variants, as seen by a shift of the maximum of the GATR-FTIR spectra to the β -sheet-assigned area (1628–1630 cm^{-1}) (Figure S14).⁴³ For eADF4(C16) and eADF4(Ω 16) films, there was no apparent difference in the secondary structure content on the different substrates. eADF4(κ 16) films cast on mica showed a higher random coil content than on the other substrates (higher peak at 1658 cm^{-1}) (Figure S14). For eADF3-derived proteins, a bimodal curve shape could be observed, and for all four substrates, the random coil content was higher than for the eADF4-derived variants (Figure S14). In principle, the increase in the β -sheet content turned the recombinant spider silk films water-insoluble.³⁹ Therefore, all WCA measurements were performed after post-treatment. The WCA of uncoated mica was close to zero, and the drop spread entirely over the surface immediately after its contact with the surface.⁴⁴

The contact angle increased with increasing surface hydrophobicity from mica to glass to silicon to polystyrene (Figure 2). eADF3-derived variants showed WCAs between 69° and 81° regardless of the underlying substrate on all four different substrates. Furthermore, there was no significant difference between the WCA of eADF3(AQ)₁₂ and eADF3(AQ)₂₄ on the same substrate, indicating that the molecular

weight in this case did not affect WCA. eADF4-derived variants showed different behavior (Figure 2), and the WCA decreased in the order of eADF4(C16) > eADF4(κ 16) > eADF4(Ω 16) independent of the underlying substrate.

In general, as reported previously,³⁹ upon coating with recombinant spider silk proteins, all surfaces showed an inverted WCA compared to the uncoated substrates. Here, inverted WCA means that surfaces that were hydrophobic before coating turned more hydrophilic upon coating with spider silk proteins. Vice versa, uncoated, hydrophilic substrates turned more hydrophobic upon spider silk coating. Strikingly, the underlying substrate had less influence on the film formation of the uncharged recombinant spider silk variants, and the uncharged eADF4(Ω 16) surfaces always showed the lowest WCAs. These results led to the assumption that the charge of the protein plays an important role in the resulting water contact angles and, thus, surface hydrophilicity and wetting behavior. The ratios between the WCA of the uncoated and the coated substrates showed a clear trend regardless of the absolute values. This led to the assumption that the increase/decrease of WCA is independent of the protein but specific to the substrates; e.g., coating glass with recombinant spider silk proteins led to a 40% increase of WCA compared to that of the uncoated substrate (see Table S11).

2.3. Biodegradation of Spider Silk Films. To analyze the biodegradability of spider silk films, they were incubated in the presence of protease mixture PXIV from *Streptomyces griseus* (type XIV) and a collagenase (CHC) from *Clostridium histolyticum* (type IA), which reflects model enzymes for digestive and wound proteases, respectively, and represents prominent candidates for evaluating the proteolytic stability of silk proteins.^{45–49} As expected, enzymatic degradation was highly dependent on the underlying amino acid sequence (Figure 3). Films of both recombinant eADF3 spider silk variants were almost completely degraded within the first 48 h in the presence of both enzymatic mixtures, because the ADF3-derived variants are more hydrophilic than ADF4-derived variants. It is known that a hydrophilic network allows a fast inflow of the enzymes in the bulk material, leading to increased cleavage of the peptide bonds.⁵⁰ In contrast, eADF4-based films could not be digested by collagenase CHC. The

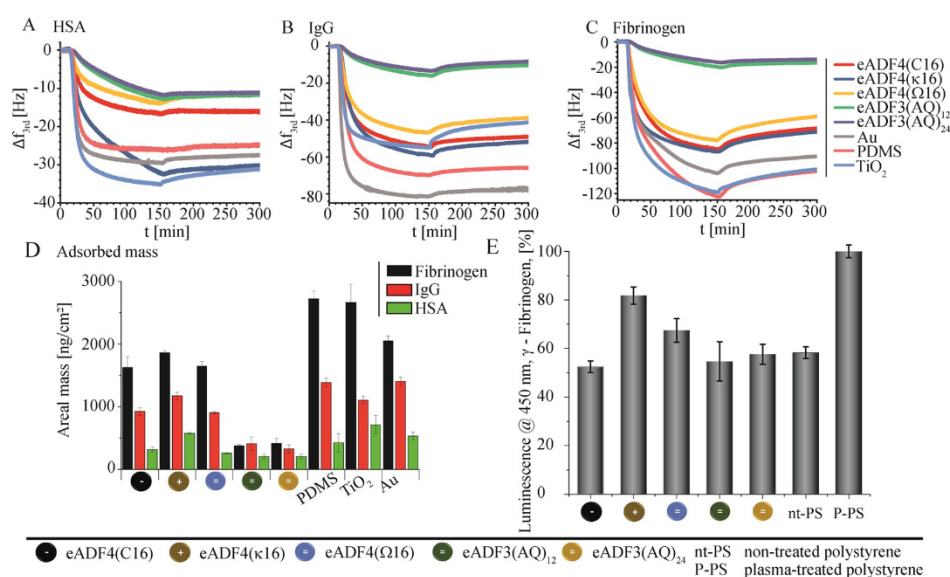


Figure 4. Third overtone (Δf_{3rd}) of quartz crystal frequency of protein adsorption is shown for the spider silk films. (A) HSA, (B) IgG, and (C) fibrinogen were added to various surfaces, as depicted in the legend. All samples were washed with PBS buffer for 150 min until 300 min to remove the loosely adsorbed protein. The adsorbed areal mass of serum proteins was calculated using the Sauerbrey equation or the viscoelastic Kelvin–Voigt model, depending on the protein behavior. The blank Au–QCM-D surface, TiO₂, and PDMS were used as reference substrates. (D) The adsorbed areal mass is shown at maximum during serum protein adsorption before the PBS buffer flow and desorption started. The amount of the adsorbed mass to spider silk films is in the order of eADF4(κ 16) > eADF4(C16) \approx eADF4(Ω 16) > eADF3(AQ)₁₂ \approx eADF3(AQ)₂₄ ($n = 3$). (E) Indirect enzyme-linked immunosorbent assay (ELISA) determining the restructuring of human fibrinogen by detecting the usually hidden carboxyl-terminal peptide of the γ -chain using a monoclonal mouse anti- γ -chain antibody (2 $\mu\text{g mL}^{-1}$) and a secondary antibody with a HRP function (1:10 000). Luminescence was measured at 450 nm. Nontreated and oxygen plasma polystyrene served as control.

measured signal was as low as for the buffer control and, thus, a result of washing. Protease XIV digested eADF4-based films but to a much lower extent than ADF3-based ones. Among the eADF4 variants, films of the positively charged eADF4(κ 16) showed the fastest proteolytic degradation (Figure 3A–C). After 15 days, approximately 45% of the eADF4(C16) films, 35% of the eADF4(Ω 16) films, and 70% of the eADF4(κ 16) spider silk films were degraded by protease XIV. Proteases of the mix PXIV exhibit an unspecific cleavage pattern, while the collagenases of mix CHC cleave at $-P/X\downarrow G/P/-$ (with X representing a neutral amino acid).⁴⁵ In eADF4-based proteins, only one such pattern, namely, $-P/S/G/P/-$ could be found. In contrast, eADF3(AQ)-based proteins showed the $-P/Y/G/P/-$ and three further $-P/G/Q/Q/G/P/-$ amino acid motifs. We assume that all motifs in eADF3(AQ)-based proteins could be cleaved by the CHC collagenase mix and that the serine in eADF4-based variants reduced the enzyme interaction.

The previously published results showed that soluble, unstructured eADF4(C16) proteins are degraded orders of magnitude faster than β -sheet-rich spider silk films.⁴⁵ In a soluble state, the intrinsically unstructured spider silk proteins are freely accessible to enzymes leading to enhanced enzymatic interaction and degradation rate.⁴⁵ In contrast, in the bulk state in the films, the protein sequence is densely packed,³⁸ leading to a decelerated enzymatic degradation rate.⁴⁵

2.4. Formation of a Protein Layer on Spider Silk Film Surfaces. **2.4.1. Adsorption of Essential Blood Serum Proteins.** The first response to the implantation of biomaterials is the formation of a protein layer on its surface. Therefore,

controlling protein adsorption is crucial for enhancing the biocompatibility of a material.^{2–6} Protein adsorption on biomaterial surfaces is influenced by a multitude of parameters, including chemical composition, charge, wettability, and topography.^{2–5} Thus, protein adsorption on spider silk films was determined using three essential blood proteins, human serum albumin (HSA), immunoglobulin G (IgG), and fibrinogen (Fib).⁶ Quartz crystal microbalance (QCM) measurements allowed calculating the adsorbed mass of the respective proteins on the spider silk films in situ based on the third overtone of the frequency of the respective protein (Figure 4A–C). Therefore, the three essential blood proteins were floated 150 min over coatings of recombinant spider silk proteins and three reference materials poly(dimethylsiloxane) (PDMS), TiO₂, and gold (Au), which are often used in biomedical applications. After 150 min, the coatings were flushed for another 150 min with phosphate-buffered saline (PBS) buffer to remove the loosely bound protein from the surface. The adsorbed mass (Figure 4D) represents the adsorbed mass after washing with 1 \times PBS. A slight change in frequency was observed for all three blood proteins by washing the films with 1 \times PBS. As a consequence, just small amounts of proteins were loosely bound to the surface. Strikingly, fibrinogen was less prone to adsorb on silk surfaces than on the control materials (Figure 4C,D). Comparing films made of the spider silk variants, the adsorption of fibrinogen and IgG was higher on films made of eADF4 variants than on that of eADF3 variants (Figure 4), indicating a clear sequence but not really charge-dependent protein adsorption, as eADF4(Ω 16) is also uncharged. The direct comparison of

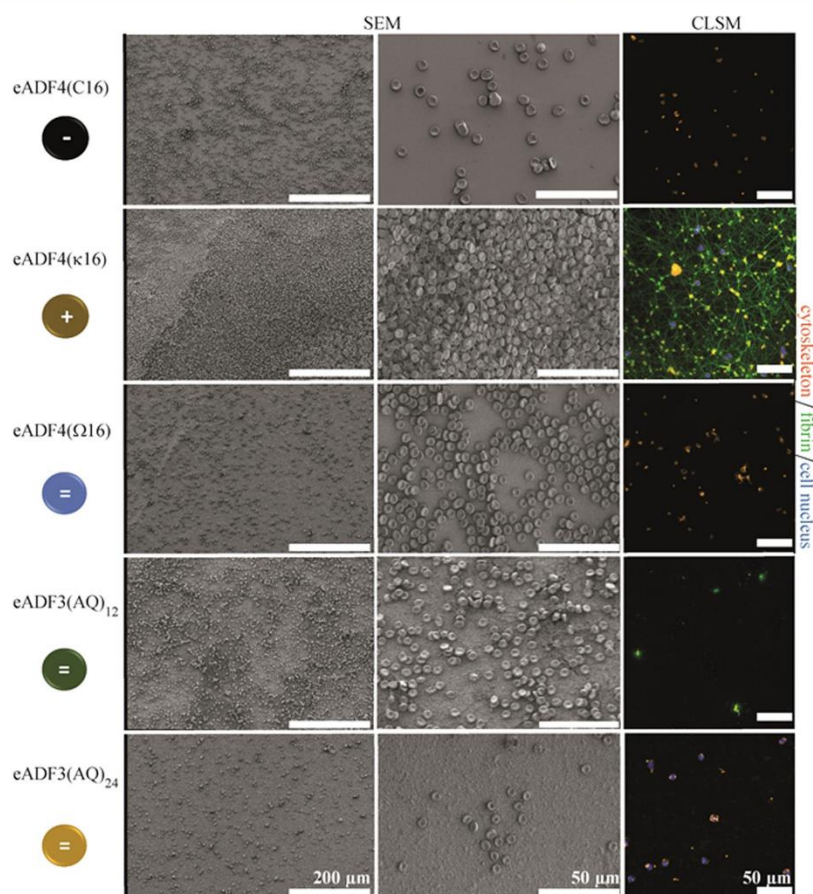


Figure 5. SEM and CLSM images of spider silk films incubated in whole human blood at dynamic conditions (10 rpm) for 35 min. The blood incubated samples were immuno-stained to visualize the cytoskeleton, fibrin (green), and the cell nuclei (blue) (CLSM) or they were dehydrated and sputter-coated with 10 nm gold (SEM). Scale bars are as indicated for the first row of 200 μm and for the last two rows of 50 μm ($n = 3$).

uncharged spider silk variants showed that the protein adsorption on eADF3(AQ)₁₂ and eADF4(AQ)₂₄ was significantly decreased compared to that on eADF4(Ω16). This finding is likely based on a higher hydrophobicity of ADF4-based materials. Several studies support this finding, as fibrinogen adsorption is enhanced on hydrophobic surfaces.^{6,51,52} However, in addition to the sequence-dependent differences of protein adsorption between eADF3 and eADF4 variants, a clear surface charge effect could be observed when only considering differently charged eADF4 spider silk proteins. While the negatively charged eADF4(C16) and uncharged eADF4(Ω16) surfaces adsorbed nearly the same amount of proteins, the positively charged eADF4(κ16) variant exhibited higher protein adsorption for all investigated serum proteins (Figure 4D). Thus, the combination of a positively charged and hydrophobic surface led to higher protein adsorption, as all other spider silk variant films showed lower protein adsorption. This supports the assumption that a combination of amino acid composition and charge of a coating is the reason for specific protein adsorption. Generally, the spider silk film surfaces showed a protein adsorption behavior for the model proteins in the order of eADF4(κ16) >

eADF4(C16) \approx eADF4(Ω16) > eADF3(AQ)₁₂ \approx eADF3(AQ)₂₄. A study by Kidoaki and Matsuda analyzing the same serum proteins showed that surfaces with carboxyl functional groups generally showed the lowest protein adsorption. In that case, fibrinogen adsorption was stronger compared to that of albumin and IgG adsorption.⁵³ Our results indicated that the adsorption of the selected model proteins is dependent on the amino acid sequence as well as the surface charge of spider silk films or a combination of both. Since albumin and fibrinogen are negatively charged at physiological pH,⁵⁴ a mostly electrostatically driven interaction of negatively charged proteins and positively charged spider silk films could be an explanation for the results of eADF4 variants, with almost identical primary structures differing only in individual residues.^{55,56} Since hydrophilic material surfaces with a neutral charge seemed to be more resistant to protein adsorption,⁵⁷ and eADF3 variants are more hydrophilic than eADF4 variants, the reduced protein adsorption noted there is more likely dependent on the underlying (hydrophilic) primary structure.

2.4.2. Conformational Changes of Fibrinogen during Adsorption on Spider Silk Surfaces. Serum proteins adsorbed

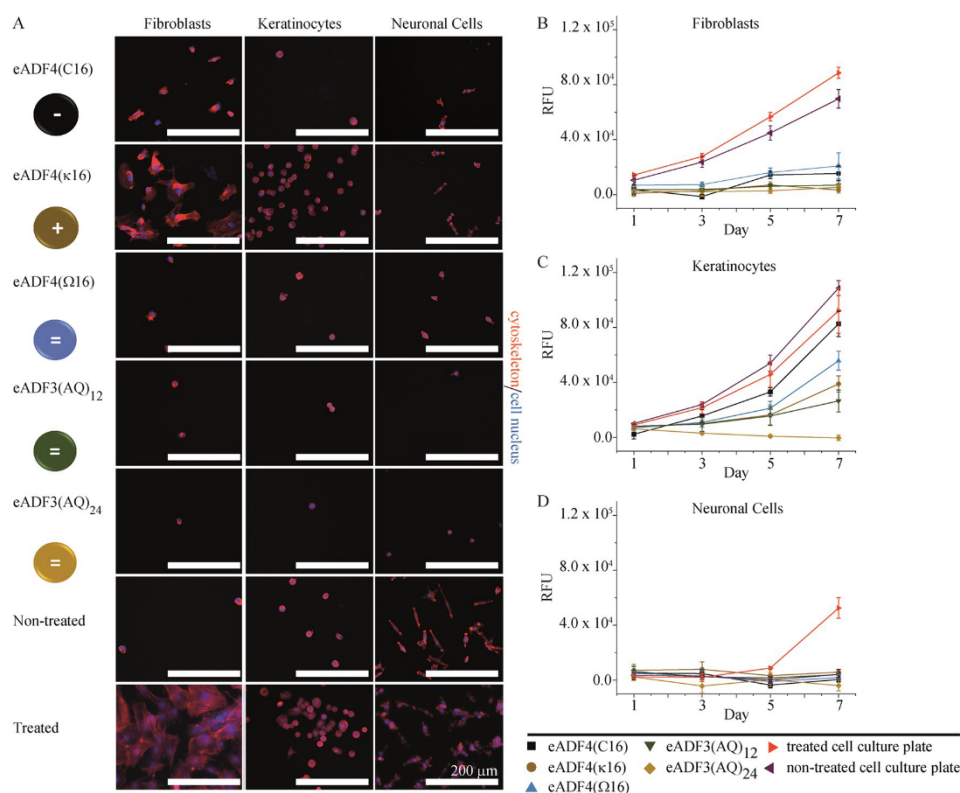


Figure 6. Adhesion and proliferation of human BJ fibroblasts, human HaCaT keratinocytes, and rat B50 neuronal cells on spider silk films made of eADF4(C16), eADF4(κ16), eADF4(Ω16), eADF3(AQ)₁₂, and eADF4(AQ)₂₄ and polystyrene surfaces as controls. (A) Primary cell adhesion in the presence of PCS was analyzed using fluorescence microscopy after 4 h of cultivation. Cell nuclei and F-actin cytoskeleton were stained using DAPI (blue) and phalloidin–rhodamine (red), respectively. (B–D) Proliferation of mammalian cells over 7 days was investigated by measuring the resorufin fluorescence of metabolized resazurin of the cell titer blue assay on days 1, 3, 5, and 7 ($n = 3$).

on biomaterial surfaces can influence a biomaterial's behavior; for instance, fibrinogen can trigger platelet adhesion and blood coagulation on such a surface.⁶ Interestingly, it is not the total amount of surface-bound fibrinogen but its conformation and the accessibility of cryptic binding sites, exposed by the restructuring of fibrinogen during adsorption, that are decisive for subsequent platelet interaction and blood coagulation, enhancing the risk of cardiovascular diseases.^{6,58,59} Thus, in addition to the quantification of total fibrinogen mass using QCM-D, the conformational changes of fibrinogen due to adsorption on spider silk surfaces were analyzed. Therefore, an indirect enzyme-linked immunosorbent assay (ELISA) with the mouse monoclonal antibody 2.G2.H9 explicitly binding to the carboxyl-terminal peptide of the human fibrinogen γ -chain was conducted to detect conformation-specific accessibility (Figure 4E).^{59,59} For eADF4-based films, the highest amount of restructured fibrinogen was obtained in the case of the positively charged eADF4(κ16) variant, followed by the uncharged eADF4(Ω16) and the negatively charged eADF4(C16) variant (Figure 4E). Interestingly, the conformational change of fibrinogen on uncharged eADF3(AQ)₁₂ and eADF3(AQ)₂₄ films was at a similar level as for the negatively charged eADF4(C16) variant.

Comparing adsorption (QCM-D) and conformational changes (ELISA) of fibrinogen on spider silk film surfaces

showed that generally less fibrinogen is adsorbed on hydrophilic eADF3 variants, but restructuring takes place in all cases. Although eADF4(C16) films showed a higher total adsorption, the conformational changes of fibrinogen were at similar levels compared to that of eADF3 variants. Furthermore, the level of fibrinogen restructuring was only slightly enhanced on uncharged eADF4(Ω16) films compared to those of eADF4(C16) and eADF3(AQ)-based ones. These results rebut a fibrinogen restructuring based on the spider silk sequences. Since the highest fibrinogen restructuring takes place on the positively charged eADF4(κ16) variant, which at the same time also adsorbs the highest fibrinogen amount, the combination of a hydrophobic amino acid sequence with a positive charge seems to trigger the unfavorable conformational change of fibrinogen. As mentioned before, hydrophilic material surfaces with a neutral charge are more resistant to protein adsorption,⁵⁷ which could explain the better performance of eADF3-based variants. Furthermore, the negative charge of fibrinogen at physiological pH⁵² could explain its enhanced interaction with aminated and, thus, positively charged surfaces compared to negatively charged, carboxylated surfaces.^{55,56}

2.5. Interaction of Human Blood with Spider Silk Film Surfaces. In addition to the protein adsorption and fibrinogen conformation analysis, spider silk films were also analyzed for

inducing blood coagulation to complete the blood compatibility analysis of spider silk surfaces. As mentioned before, the control of blood coagulation, to either prevent or promote it, is of utmost importance for biomedical applications. Blood coagulation is a complex cascade influenced by different factors, including protein adsorption and restructuring, platelet adhesion and their activation, coagulation, and thrombosis.^{6,11} Here, the spider silk films were analyzed regarding blood clotting and fibrin formation, which were mainly enhanced on the positively charged, hydrophobic eADF4(κ 16) films (Figure 5). Scanning electron microscopy (SEM) and confocal laser scanning microscopy (CLSM) of stained fibrin networks revealed that surfaces made of uncharged eADF3(AQ)₁₂, eADF3(AQ)₂₄, eADF4(Ω 16), or the negatively charged eADF4(C16) did not induce blood clotting or fibrin formation since only erythrocytes were detectable. However, the positively charged eADF4(κ 16) induced severe blood clotting and fibrin formation, as depicted previously,⁶⁰ with erythrocytes being entrapped in a fibrillar fibrin network (Figure 5). The results of the blood coagulation assay are in line with the serum protein adsorption and the fibrinogen restructuring (Figure 4). Especially the adsorption and restructuring of fibrinogen are central processes triggering subsequent platelet activation and the blood coagulation cascade.^{6,58,59} Furthermore, fibrinogen represents the precursor molecule of fibrin, which is the predominant structural component in blood coagulation/clotting and thrombus formation.⁶ Since positively charged eADF4(κ 16) surfaces exhibited the highest amount and restructuring of adsorbed fibrinogen, enhanced blood coagulation and fibrin expression have been expectable. These results are in accordance with a previous study on the formation of a biomolecular corona on spider silk films and particles made of eADF4(C16) and eADF4(κ 16), showing enhanced protein adsorption, fibrin network formation, and blood clotting on the positively charged silk, independent of the morphology.⁶⁰

In this study, erythrocytes were also visible on all investigated samples, but the whole human blood was in a coagulated state after contact with eADF4(κ 16) materials, while it was still liquid in the case of eADF4(C16) ones.⁶⁰ This finding confirmed that the adsorption of erythrocytes on surfaces has a negligible effect on subsequent blood coagulation and thrombus formation.

Sperling et al. have already shown that the coagulation and the fibrin network formation are enhanced on positively charged surfaces but not on negatively or uncharged surfaces, supporting our findings.⁵² The blood coagulation response on the positively charged eADF4(κ 16) could be based on negatively charged proteins or molecules, e.g., heparin interacting via ionic interactions or activating further blood coagulation cascades.⁵²

2.6. Mammalian Cell Interaction with Spider Silk Films. For biomedical applications, tissue encapsulation is another important issue and should either be prevented, e.g., for catheters¹⁸ or implants,²⁷ or specific cell adhesion should be supported, e.g., in tissue regeneration.³⁰ Surface charge, in accordance with surface roughness or wettability, can regulate cell adhesion on a material.^{8,18,22} It is relevant to determine the relationship between the underlying spider silk protein sequence and cellular adhesion and growth. Therefore, primary cell adhesion after 4 h and cell growth over 7 days on spider silk films were investigated using three mammalian cell lines (human dermal fibroblasts (BJ), rat neuronal cells (B50),

human keratinocytes (HaCaT); Figure 6). The primary cell adhesion after 4 h was analyzed using fluorescence microscopy of stained cell nuclei (4',6'-diamidino-2-phenylindole (DAPI)) and the F-actin cytoskeleton (phalloidin) (Figure 6A). Fluorescence microscopy revealed indeed that the positively charged spider silk film surface supported early cell attachment and expression of F-actin stress fibers; however, cells also attached to eADF4(C16) and eADF4(Ω 16) surfaces. In contrast, only a few cells adhered to uncharged eADF(AQ)₁₂ and eADF3(AQ)₂₄ spider silk films, showing a round morphology without spreading or enhanced F-actin production. These results showed a sequence-dependent cell adhesion, indicating that the more hydrophobic eADF4 spider silk variants promote primary cell adhesion. The cell proliferation assay of these mammalian cell lines showed that none of the investigated spider silk surfaces promoted cell growth as strong as polystyrene surfaces (Figure 6B–D). Since eADF4 and eADF3 amino acid sequences do not contain any specific cell interaction motifs,⁶¹ mainly the structural arrangement of hydrophobic and hydrophilic parts and to a lower extent the different charges are responsible for the primary cell interaction. Usually, cells prefer positively charged surfaces for cell adhesion due to their negatively charged cell surface.^{38–40} One previously published study analyzed cardiomyocyte attachment on non-post-treated eADF4(C16), eADF4(κ 16), and eADF4(Ω 16) films cast from formic acid on glass substrates and showed that only the positively charged variant promoted cardiomyocyte attachment.⁴⁰ Another study showed that mammalian cells could grow on post-treated eADF4(κ 16) but not on eADF4(C16) coatings cast from aqueous solutions on catheter surfaces.¹⁸ However, in comparison to our results, these studies used different substrates, pretreatments, solvents, and post-treatment methods, making a direct correlation difficult. Thus, we conclude that cell adhesion could be influenced by these parameters to be cytophilic or cytophobic. We assume that the pretreatment with ozone used here to enable a homogeneous film formation led to a different structural assembly of the amino acid sequence of eADF4-based variants compared to the other studies using the same spider silk variants. Thus, the surface properties could be changed leading to a reduced mammalian cell interaction. However, if an application requires cell adhesion and growth, spider silk proteins have to be further modified and functionalized (e.g., with an RGD-motif) to enable cell attachment and growth on silk scaffolds, as shown previously.^{30,40} Thus, in correlation with protein adsorption (Figure 4) and blood coagulation (Figure 5), the negatively charged eADF4(C16) and the uncharged eADF4(Ω 16), eADF3(AQ)₁₂, and eADF3(AQ)₂₄ variants reflect promising coating materials for, e.g., catheters (as shown previously)¹⁸ or stents, where interactions with cells should be decreased.

3. CONCLUSIONS

The interaction of a biomaterial with the surrounding biological environment is crucial for its performance, and it is eligible if this is controllable depending on the application.^{2,3} Since the implant surfaces come in direct contact with different physiological body fluids, the surfaces of medical devices that should not interact with these fluids, like catheters, implants, or contact lenses,^{12,17} as well as packaging materials, have to be modified, e.g., with coatings, to protect or stabilize such implants.^{62,63} Further, surfaces could enhance wound healing by activating blood coagulation^{64,65} or act as a stationary drug

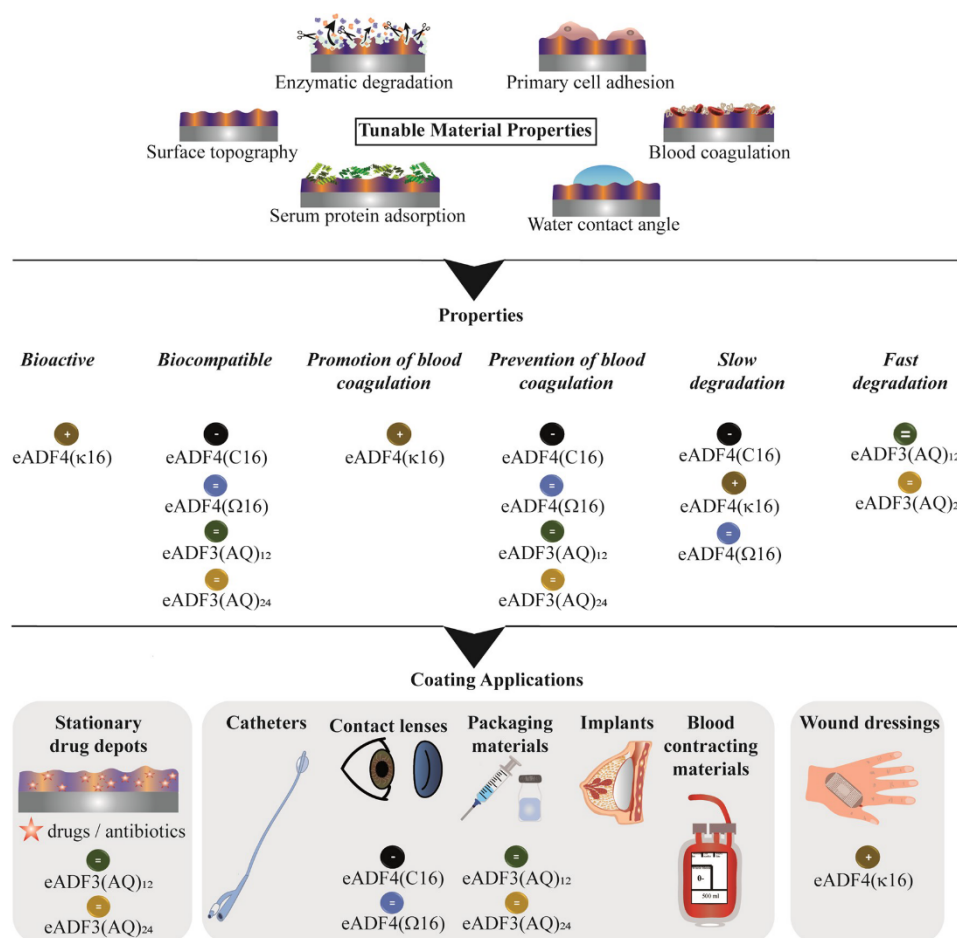


Figure 7. Summary of properties and tentative biomedical applications for films made of five different spider silk variants.

depot releasing bioactive molecules.⁶³ Particularly, with regard to the mentioned applications, recombinant spider silk materials interact differently with serum proteins, whole human blood, and mammalian cells depending on the underlying protein sequence (Figure 7).

Among the tested spider silk derivatives, eADF4(C16) and eADF4(Ω 16) are promising candidates for applications as a coating material for implants or medical devices coming in direct contact with different physiological body fluids, as well as storage materials for, e.g., drugs or growth factors with long lifetime. Films made of both proteins are biocompatible and combine necessary requirements, including a smooth surface, slow biodegradation and resistance against proteolytic enzymes, low adsorption and conformational change of blood serum proteins, (partial) microbial repellence, no blood coagulation, and cell repellence of different mammalian cell lines.

Since films made of eADF3(AQ)₁₂ and eADF3(AQ)₂₄ also combine these important features except long-time stability, they are promising candidates for similar applications but where fast biodegradation is desired. Furthermore, due to their fast biodegradation, coatings made thereof are appropriate

candidates for stationary depots releasing bioactive substances, such as drugs or antibiotics.

In contrast, coatings made of the positively charged eADF4(κ 16) seem to be biologically active, as they promote the adsorption of blood serum proteins, blood coagulation, and cell adhesion of selected mammalian cell lines. Nevertheless, coatings made thereof are also degradable by digestive proteases. Due to the enhanced stimulation of blood coagulation, eADF4(κ 16) films are promising candidates for, e.g., wound dressings.

4. EXPERIMENTAL SECTION

4.1. Materials. All chemicals were purchased from Roth (Karlsruhe, Germany) with analytical grade if not stated otherwise. eADF4(C16) was purchased from AMSilk GmbH (Planegg/München, Germany). The IEF SERVAGel IEF 3–10 Starter kit was purchased from Serva. Protease mixture (PXIV) from *S. griseus* (type XIV), collagenase (CHC) from *C. histolyticum* (type IA), formic acid, human fibrinogen, recombinant human albumin (HSA), and immunoglobulin (IgG) from rabbit serum were purchased from Sigma-Aldrich (Munich, Germany). Bovine fibrinogen was purchased from TCI (TCI Europe N.V., Zwijndrecht, Belgium). 5/6-Carboxyfluorescein succinimidyl ester (NHIS-fluorescein) was pur-

chased from Thermo Fisher Scientific (Darmstadt, Germany). Dimethylformamide (DMF) and ethanol were purchased from VWR (Darmstadt, Germany). Poly(dimethylsiloxane) (PDMS) (Sylgard 184 Silicone Elastomer) was purchased from Dow Corning (Wiesbaden, Germany). Q-Sense Ti sensor chips (QSX 310 Ti) were purchased from LOT-QuantumDesign GmbH (Darmstadt, Germany). The used water was ultrapure (Milli-Q) and obtained using a Merck Millipore system (Billerica, MA). Antibodies for fibrinogen ELISA were purchased from Santa Cruz Animal Health. ECL Western Plus and LimuLight detection solutions were purchased from Merck. The cell titer blue assay was purchased from Promega.

4.2. Production of eADF4(Ω 16), eADF4(κ 16), eADF3(AQ)₁₂, and eADF3(AQ)₂₄. Silk proteins were recombinantly produced using *E. coli* (BL21 gold (DE3)) in a fermenter using the fed-batch technique.³² The recombinant spider silk proteins eADF3(AQ)₁₂ and eADF3(AQ)₂₄ were purified using a heating step and ammonium sulfate precipitation, as described previously.³² eADF4(κ 16) was produced as reported earlier.²⁹ eADF4(Ω 16) was also purified, as described previously.³⁶

4.3. Processing of eADF3 and eADF4 Spider Silk Proteins into Films. For film casting, all eADF3- and eADF4-based recombinant spider silk proteins were dissolved in formic acid at a concentration of 5 mg mL⁻¹ for 1–2 h at room temperature. Since different substrates and sample sizes were necessary for the performed characterization methods, the appropriate film casting procedures are explained at the beginning of each respective analysis paragraph.

4.4. Characterization of Surface Topography and Surface Potential of Spider Silk Films. **4.4.1. Preparation of Protein Films.**

The recombinant spider silk films were cast ($c = 5$ mg mL⁻¹) onto freshly RCA-cleaned, ozone-treated Si-wafers. The post-treatment was performed in MeOH_{abs} vapor overnight.

4.4.2. Atomic Force Microscopy (AFM). For surface morphology characterization, film surfaces were analyzed in tapping mode using a Dimension 3100 Nanoscope V (Bruker, Karlsruhe, Germany) with a resolution of 512 to 512 data points at 0.12 to 1 Hz. Silicon cantilevers (OTESPA-R3, Bruker, Karlsruhe, Germany) were used with a force constant of 26 N m⁻¹. The average roughness R_a was calculated in an area of 25 μm^2 . Silicon cantilevers (OTESPA-R3, Bruker, Karlsruhe, Germany) were used with a force constant of 26 N m⁻¹. The average arithmetic roughness R_a was calculated in an area of 25 μm^2 .

4.4.3. Kelvin Probe Force Microscopy (KPFM). For analyzing the surface potential of spider silk films, KPFM measurements were performed on a Cypher ES (Oxford Instruments, Asylum Research, Santa Barbara) in air at an ambient temperature and pressure. The instrument was operated in a dual-frequency mode (DFM). Topographic images were recorded simultaneously with KPFM images (512 \times 512 lines, 1 Hz, 5 $\mu\text{m} \times 5 \mu\text{m}$). An asylum electrolever tip with a conductive coating (Ti/Ir) (Asylec.01-R2, $f = 75$ kHz, $k = 2.8$ N m⁻¹) was used for KPFM measurements.

4.5. Electrokinetic Measurements of Spider Silk Proteins.

4.5.1. Streaming Potential Measurements of Recombinant Spider Silk Films. Si-wafers (2 cm \times 1 cm) were cleaned with alkaline RCA cleaning. Therefore, the Si-wafers were placed into a Teflon sample holder and a mixture consisting of ammonia hydroxide, hydrogen peroxide, and Milli-Q-water (1:1:5). The Si-wafers were stirred for 1 h, at 70 °C, and afterward thoroughly rinsed with MQ-water and dried with a N₂ flow. The recombinant spider silk films were cast by drop-casting. Therefore, all recombinant spider silk proteins were dissolved in formic acid ($c = 5$ mg mL⁻¹). The Si-wafer surfaces were activated using O₂-plasma (Plasma Technology, Mini-Flecto, 1 min, 100% power, 0.1 mbar, 100% O₂). Afterward, 200 μL of the recombinant spider silk solution was cast onto the Si-wafer and the formic acid was evaporated overnight. Then, the dried films were placed in a methanol atmosphere for 24 h post-treat the films. Finally, the films were dried at room temperature. The ζ -potential was determined with streaming potential measurements using a SurPASS 3 (Anton Paar, Austria). The post-treated recombinant spider silk films were inserted into the cylindrical cell equipped with Ag/AgCl electrodes. As electrolyte solution, KCl ($c = 0.001$ M) was used. The

pressure changed during the measurement in the range of 600–200 mbar. The acidic or alkaline pH region measurements were started at neutral pH. 0.1 M HCl or 0.1 M KOH solutions were used for pH adjustment. The measurement was repeated at least twice for each recombinant spider silk protein with three measurements at each pH. The ζ -potential was calculated according to Smoluchowski.

4.5.2. Electrokinetic Measurements of Soluble Spider Silk Proteins. For characterizing the isoelectric point of proteins in solution, the hydrophilic eADF3(AQ)₂₄ was directly dissolved in 1 mM potassium chloride (KCl) at a concentration of 1 mg mL⁻¹. The hydrophobic eADF4-based proteins were dissolved in 6 M guanidinium thiocyanate (GuaSCN) at a concentration of 1–2 mg mL⁻¹ for 30 min at room temperature and dialyzed against 0.001 M KCl overnight. The dialysis was conducted using membranes with a molecular weight cutoff of 6–8 kDa at room temperature (eADF4(C16), eADF4(κ 16)) and at 4 °C for eADF4(Ω 16). The pH-dependent electrokinetic measurements in solution were performed via electrophoresis with a Zetasizer Ultra Red from Malvern Instruments Ltd. and an MPT-3 autotitrator. For the pH-dependent ζ -potential measurements, the recombinant spider silk proteins, dissolved in 0.001 M KCl, were titrated by adding either 0.1 M KOH or HCl aqueous solutions until pH 10 or 2.5. Three measurements were recorded for each sample at each pH value.

4.5.3. Isoelectric Focusing by Gel Electrophoresis. For isoelectric focusing (IEF) of the recombinant spider silk proteins, the IEF gel electrophoresis starter kit (pH 3–10, SERVA) was conducted according to the manufacturer's protocol. Therefore, all proteins were dissolved in 6 M GuaSCN and dialyzed against 10 mM Tris/HCl (pH 7.5) overnight using again membranes with a molecular weight cutoff of 6–8 kDa at room temperature (eADF4(C16), eADF4(κ 16), eADF3(AQ)₁₂, and eADF3(AQ)₂₄) and at 4 °C for eADF4(Ω 16). Protein samples were mixed with an IEF sample loading buffer. Five micrograms of the appropriate protein was loaded on IEF gels (pH 3–10). For IEF gel electrophoresis, the related anode and cathode buffers were used. Gel electrophoresis was conducted for 60 min at 100 V, 60 min at 200 V, and 30 min at 500 V. After gel electrophoresis, one IEF standard marker band was separated and silver-stained. A western blot was conducted with the remaining gel to transfer the proteins to a PVDF membrane and to allow detection of the fused T7-tag by interaction with an HRP-conjugated T7-antibody. After blocking the membrane with 5% w/v milk powder in 1 \times PBS and incubation with a conjugated T7-antibody (1:5000 dilution in 1 \times PBS), protein bands were visualized by incubating the membrane with the LumiLight detection solution for 15 min in the dark at room temperature. Chemiluminescence was detected on a Hoefer device (Hoefer, Germany).

4.6. Wetting Behavior of Recombinant Spider Silk Films on Different Substrates. **4.6.1. Preparation of Protein Films.**

For analyzing the influence of different substrates on the wetting behavior of spider silk films, polished (111) silicon wafers (CrysTec GmbH, Berlin, Germany), RCA-cleaned glass slides, and mica sheets were cut into pieces of 1 cm² and cleaned by rinsing with toluene, acetone, water, and acetone before coating. Polystyrene (PS) surfaces were rinsed with ethanol. Silk solutions ($V = 200 \mu\text{L}$) were placed in the substrate center and dried overnight at ambient conditions to obtain films with 0.5 mg protein per 1 cm². For post-treatment, samples were placed in a desiccator with 20 mL methanol at the bottom. The desiccator was evacuated ($p = 10^{-1}$ mbar) to generate a saturated methanol atmosphere, and samples were incubated overnight.

4.6.2. Fourier Transform Infrared (FTIR) Spectroscopy. For determining the secondary structure of spider silk films, grazing angle attenuated total reflection (GATR) FTIR spectroscopy was performed using the VariGATR accessory (Harrick Scientific Products Inc., Pleasantville) on a Bruker Tensor 27 FTIR-spectrometer with an MCT detector (Bruker, Rheinstetten, Germany). For absorbance measurements, a grazing angle of 62° was used. One hundred and forty scans from 4000 to 800 nm⁻¹ were averaged at a resolution of 2 cm⁻¹.

4.6.3. Water Contact Angle Measurements. To analyze wettability, static contact angles of water were determined on

different spider silk films on various substrates using the OEG contact angle system (Surftens Universal, OEG, Frankfurt(Oder), Germany). Contact angles were analyzed using the SURFTENS software (OEG, Frankfurt(Oder), Germany) and a Laplace Young fit.

4.7. Biodegradation of Recombinant Spider Silk Films.

4.7.1. Protein Labeling. Recombinant spider silk proteins were dissolved in 6 M GuaSCN and dialyzed against 20 mM *N*-(2-hydroxyethyl)piperazine-*N'*-ethanesulfonic acid (HEPES) (pH 7.1) using membranes with a molecular weight cutoff of 6–8 kDa at room temperature (eADF4(C16), eADF4(κ 16), eADF3(AQ)₁₂, and eADF3(AQ)₂₄) and at 4 °C for eADF4(Ω 16). A 10-fold molar excess of the NHS-fluorescein was dissolved in dimethylformamide (DMF) and added to the protein solution (1 h, RT), with the exception of eADF4(Ω 16) (1 h, 4 °C). The labeled proteins were precipitated using 1 M potassium phosphate (K-Pi, pH 7.0) overnight (4 °C). The resulting particles were thoroughly washed three times using a water–DMF mixture (1:1, v/v), followed by pure water to remove salt and a nonspecifically bound fluorescence dye. Afterward, the labeled protein particles were dissolved in 6 M GdmSCN and dialyzed against ammonium bicarbonate buffer (20 mM, pH 9.0) to remove the remaining free fluorescein. Ammonium bicarbonate was chosen, as it decomposes into the volatile components NH₃, CO₂, and H₂O during the lyophilization process without any remaining salts. The success of labeling was confirmed by UV/vis analysis (Nanodrop ND 1000, Thermo Scientific), and the determined degree of labeling (η (fluorescein)/ η (protein)) was 0.90 for eADF4(C16), 1.93 for eADF4(κ 16), 1.33 for eADF4(Ω 16), 0.86 for eADF3(AQ)₁₂, and 1.26 for eADF3(AQ)₂₄. Afterward, the proteins were freeze-dried (Alpha 1-2 LD plus freeze dryer, Martin Christ Gefriertrocknungsanlagen GmbH, Germany).

4.7.2. Preparation of Protein Films. For degradation experiments, fluorescein-labeled protein solutions were cast in nontreated 48-well plates (Nunc, Thermo Scientific, Germany) and dried at ambient conditions overnight to obtain films with 0.5 mg protein per 1 cm². For post-treatment, 250 μ L of 75% ethanol was added onto the films and air-dried overnight at ambient conditions.

4.7.3. Enzymatic Degradation Assay. Degradation experiments were performed according to Müller-Herrmann and Scheibel.⁵³ Experiments were performed in the TCNB buffer (50 mM Tris/HCl, 10 mM CaCl₂, 150 mM NaCl, 0.05% Brij 35, pH 7.5) at room temperature. The fluorescein-labeled eADF3 and eADF4 spider silk films were incubated with 250 μ L of PKIV or CHC solution (175 μ g mL⁻¹ in TCNB buffer) for 15 days. Control experiments without enzymes were conducted in 250 μ L of TCNB buffer. Buffers and enzyme solutions were changed every 24 h. The experiments were performed in sextuplicates, and the fluorescence intensity of the supernatant was measured every day using a Mithras LB940 plate reader system (Berthold Technologies, Germany) (λ_{exc} = 485 nm, λ_{em} = 535 nm) in a black plate (Nunc, Thermo Scientific, Germany). To calculate the protein concentration in the supernatant and determine the relative degradation ($m_{degraded}/m_{initial}$) of the protein, a calibration curve was made for the labeled proteins.

4.8. Protein Adsorption on Recombinant Spider Silk Films.

4.8.1. Sensor Chip Coatings. For quantifying protein adsorption on spider silk films, QCM-D resonators (5 MHz, AT-cut, Cr/Au; Quartz Pro Sweden AB, Järfälla, Sweden) were cleaned using a 10 min UV/ozone treatment (PSD-Pro Series, Novascan, Ames). For spider silk coating, chips were spin-coated (67 rps, 3 s acceleration ramp, 30 s; K.L.M. SCE-150 jr, Schaefer Technologie GmbH, Germany) with a 30 μ L protein solution (4 mg mL⁻¹) in formic acid, yielding spider silk films with a thickness of 15–20 nm.⁵² The coated sensor chips were post-treated in a methanol atmosphere overnight and mounted in the standard Q-Sense flow module (QFM 401, Biolin Scientific, Västra Frölunda, Sweden). For PDMS coating of QCM-D resonators, thin PDMS films were applied to resonators, as reported by Bračić et al.⁶⁵ A stock solution of 10% (w/w) PDMS with a base-to-curing agent ratio of 10:1 (w/w) was prepared by dissolving the reaction mixture in toluene and shaking overnight. For resonator coatings, the PDMS solution was diluted with toluene to 0.5% (w/w) followed by shaking overnight. Sensor chips were spin-coated (83 rps, 3 s

acceleration ramp, 60 s) with 40 μ L of PDMS solution (0.5% (w/w)). The PDMS-coated sensor chips were cured overnight at 80 °C in a drying cabinet. Such a spin-coating process leads to films with a thickness of 23.1 \pm 1.1 nm if applied on silicon wafers. Film thickness was determined by scratching the film with a scalpel, measuring the scratched area using AFM, and applying step analysis using NanoScope Analysis 1.5 (Bruker, Karlsruhe, Germany).

4.8.2. Blood Serum Protein Solutions. Fibrinogen was layered on top of 1 \times PBS and gently agitated in an Eppendorf thermomixer (300 rpm, 37 °C; Eppendorf AG, Hamburg, Germany) overnight. IgG and HAS were reconstituted in 1 \times PBS overnight at 4 °C. Protein concentrations were determined in the UV/vis region using a Nanodrop ND 1000 ($E_{280\text{ nm}}^{1\%}$ (Fibrinogen) = 15.1, $E_{279\text{ nm}}^{1\%}$ (HSA) = 5.3, $E_{280\text{ nm}}^{1\%}$ (IgG) = 14.0) and set to 1 mg mL⁻¹. Working aliquots of HSA and IgG were stored at -20 °C. Fibrinogen solutions were freshly prepared before usage.

4.8.3. QCM-D Measurements. All equilibration and adsorption steps were performed in a 1 \times PBS buffer at a volume flow of 10 mL min⁻¹ at 21 °C with a Q-Sense E4 (Biolin Scientific, Västra Frölunda, Sweden). The coated sensor chips were equilibrated in PBS buffer and then flushed with 1 mg mL⁻¹ of the particular blood serum proteins for 135 min, followed by a 210 min buffer flow. Frequency and dissipation data were monitored for the 3rd, 5th, 9th, and 11th overtones. The change in the areal mass density $\Delta\rho_A$ for a specific overtone *n* is proportional to the change in frequency Δf and is described by the Sauerbrey equation (eq 1)⁵⁷

$$\Delta\rho_A = -\frac{\rho_q h_q \Delta f}{f_0 n} = -C \frac{\Delta f}{n} \quad (1)$$

The mass sensitivity constant *C* depends on the density (ρ_q), the thickness (h_q), and the fundamental frequency (f_0) of the quartz crystal.⁶⁸ The Sauerbrey equation can be used to estimate the mass change of a rigidly adsorbed layer on the chip surface in air or vacuum and also in the liquid medium, as long as the damping of oscillation is not sufficiently large.⁶⁹ If the damping is too large, a viscoelastic model has to be applied, which will consider the change in the dissipation factor *D* by measuring the oscillation decay.⁶⁸ The hydrodynamic thickness can be calculated by fitting Δf and ΔD at different overtones using the Voigt model with Q-tools software (Biolin Scientific, Västra Frölunda, Sweden). Areal mass was estimated by the conversion of thickness into mass using the bulk density (1370 kg m⁻³) of the protein–material. The areal mass of HSA on all surfaces, as well as fibrinogen and IgG adsorption on eADF3(AQ)₁₂ and eADF3(AQ)₂₄, was determined using the Sauerbrey equation due to the more rigid character of these thin adsorbed serum protein layers. The Voigt model was used for the areal mass calculation of all other samples due to their more viscoelastic character.

4.9. Quantification of Conformational Changes during Fibrinogen Adsorption on Recombinant Spider Silk Films.

4.9.1. Preparation of Films. For investigating conformational changes of human fibrinogen during protein adsorption on spider silk surfaces, nontreated 96-well polystyrene tissue culture plates (Nunc, Thermo Scientific, Germany) were pretreated using UV/ozone (PSD-Pro Series, Novascan, Ames) for 10 min to enable a homogeneous film formation after solvent evaporation. 42 μ L of the respective spider silk solution was drop-cast in each well and dried overnight at ambient conditions to obtain films containing 0.5 mg protein per 1 cm². For post-treatment, 100 μ L of ethanol (75% v/v) was added to each film, removed after 1 h incubation, and evaporated overnight to induce β -sheets to make the films water-insoluble.

4.9.2. Indirect Enzyme-Linked Immunosorbent Assay (ELISA). Human plasma fibrinogen (Sigma-Aldrich, Germany) was resolubilized in a 0.9% (w/v) saline solution at a concentration of 1 mg mL⁻¹ at RT. 50 μ L of fibrinogen solution was pipetted on films and control wells to obtain a protein amount of 50 μ g per well (five wells per condition). Uncoated wells on the spider silk film-containing plate, as well as an oxygen plasma pretreated (60 s, 100% O₂) 96-well polystyrene plate, served as controls (five wells per condition). The

samples were incubated overnight at 4 °C to allow fibrinogen adsorption and restructuring on the different surfaces. After removal of the fibrinogen solution, the samples were washed twice using 150 μL 1 \times PBS. The samples were incubated with 150 μL blocking solution (1% w/v bovine serum albumin in 1 \times PBS) for 5 h to block nonspecific protein interactions. Afterward, the samples were again washed twice using 1 \times PBS and incubated with 100 μL monoclonal mouse antifibrinogen γ primary antibody (IgG1, sc-81620, clone 2.G2.H9, 2 $\mu\text{g mL}^{-1}$ in blocking solution, Santa Cruz Biotechnology, Germany) for 90 min at RT. After another round of washing with 1 \times PBS, 100 μL of the secondary antibody carrying a horseradish peroxidase (HRP) function (m-IgG1 BP-HRP, sc-525415, 1:10 000 v/v in 1 \times PBS, Santa Cruz Biotechnology, Germany) was added to the samples and incubated for 90 min. The samples were washed again with 1 \times PBS and developed with 50 μL of ECL Plus substrate solution (1:50 v/v solution A and solution B) for 15 min. Several controls (three wells per condition) were added to the assay, namely, 100 μL of pure fibrinogen, substrate, primary, and secondary antibody solutions, as well as adsorbed fibrinogen incubated with either one or both antibodies with or without substrate solution to detect nonspecific protein binding or substrate degradation. The luminescence of the resulting product correlating with fibrinogen adsorption was quantified at a wavelength of 450 nm using an endpoint measurement on a SpectraMax iD5 plate reader system (Molecular Devices, Germany).

4.10. Interaction of Human Blood with Recombinant Spider Silk Films. **4.10.1. Preparation of Films.** After solving in formic acid, recombinant spider silk proteins ($c = 10 \text{ mg mL}^{-1}$) were cast onto piranha cleaned (3:1 ratio H_2SO_4 and H_2O_2 (30%), 15 min, RT) cover borosilicate glass and dried overnight. For post-treatment, the samples were placed in a methanol-saturated atmosphere overnight. Afterward, the recombinant spider silk proteins were dried at room temperature.

4.10.2. Blood Coagulation Assays. According to the described procedure, the blood coagulation assays were performed with whole human blood.^{69,70} Human blood was collected from healthy human volunteers by standard venipuncture into S-Monovette tubes (Sarstedt), partially heparinized to a final concentration of 0.43 IU mL^{-1} , and used within 1 h upon withdrawal. Informed consent was obtained in compliance with the ethics approval BASEC No. PB_2016-00816 from the local ethics committee, St. Gallen, Switzerland. Spider silk films were placed in custom Teflon molds, incubated with whole human blood on an orbital shaker (Polymax, Heidolph) for 35 and 40 min, washed with PBS, and then prepared for SEM or CLSM imaging, as described previously.⁷⁰ Two independent experiments were performed with duplicate samples each and analyzed by CLSM ($n = 2$) and SEM ($n = 2$). Representative images are depicted.

4.11. Mammalian Cell Culture on Recombinant Spider Silk Films. **4.11.1. Preparation of Films.** Nontreated 48-well and 96-well polystyrene tissue culture plates (Nunc, Thermo Scientific, Germany) were pretreated using UV/ozone (PSD-Pro Series, Novascan, Ames) for 10 min to ensure a homogeneous film formation after solvent evaporation.

One hundred microliters (48-well plates) and 32 μL (96-well plates) of silk solutions were drop-cast in appropriate wells and dried overnight at ambient conditions to obtain films showing 0.5 mg protein per 1 cm^2 after solvent evaporation. For post-treatment, 250 μL (48-well plate) or 100 μL (96-well plate) of 75% (v/v) ethanol were added to each film and evaporated overnight to induce β -sheets and make the films water-insoluble. Before cell culture analysis, spider silk films were sterilized using UV treatment for 30 min and washed once with 1 \times PBS.

4.11.2. Mammalian Cell Cultivation. Human BJ fibroblasts (ATCC, CRL-2522) were cultivated in Eagle's minimum essential medium (EMEM) (LGC Standards GmbH, Germany), and human HaCaT keratinocytes (CLS, cell lines service, Germany) and rat B50 neuronal cells (ECACC, Public Health, England) were cultivated in Dulbecco's modified Eagle's medium (DMEM) (Biosell GmbH, Germany) supplemented with 10% (v/v) fetal calf serum (FCS)

(Biosell GmbH, Germany) 1% (v/v) GlutaMAX (Gibco, Thermo Scientific) and 0.1% (v/v) gentamycin sulfate (Sigma-Aldrich, Germany) in a cell culture incubator (HERAcell 150i, Thermo Scientific, Germany) in a controlled atmosphere (5% CO_2 , 95% relative humidity) at 37 °C. BJ fibroblasts, HaCaT keratinocytes, and B50 neuronal cells were subcultured using trypsinization. Cell viability and cell number were determined using trypan blue (Sigma-Aldrich, U.K.) and an automated cell counter (TC20, BioRad Laboratories Ltd, U.K.). All cell culture experiments were conducted with media containing 10% (v/v) FCS, 1% (v/v) GlutaMAX, and 0.1% (v/v) gentamycin sulfate.

4.11.3. Initial Cell Adhesion on Silk Films. To evaluate early cell attachment, all three cell lines were seeded at a density of 10 000 cells per cm^2 on spider silk films and control plates (treated (Nunclon, Thermo Scientific, Germany) and nontreated (Nunc, Thermo Scientific, Germany) 48-well polystyrene tissue culture plates) ($n = 3$). After 4 h of incubation in a cell culture incubator (HERAcell 150i, Thermo Scientific, Germany) in a humidified atmosphere (5% CO_2) at 37 °C, the cells were washed with 1 \times PBS and fixed using 3.7% (v/v) paraformaldehyde (Carl Roth, Germany) in 1 \times PBS at ambient conditions. Cell samples were incubated in 0.1% (v/v) Triton X-100 (Carl Roth, Germany) in 1 \times PBS to permeabilize the cell membrane prior to fluorescence staining. The cell nuclei were stained using 300 nM 4',6-diamidino-2-phenylindole and dihydrochloride (DAPI, Thermo Scientific), while F-actin cytoskeleton was visualized using 200 nM phalloidin-rhodamine (Sigma-Aldrich, Germany). Primary cell adhesion was analyzed using a fluorescence microscope (DMI3000B, Leica, Germany) and the associated LAS X software (Leica, Germany).

4.11.4. Cell Proliferation on Silk Films. To evaluate cell growth on spider silk films, all three cell lines were seeded at a density of 5000 cells per cm^2 on spider silk films and control plates (treated (Nunclon, Thermo Scientific, Germany) and nontreated (Nunc, Thermo Scientific, Germany) 48-well polystyrene tissue culture plates) ($n = 4$) and incubated at 37 °C in a humidified atmosphere (5% CO_2) in a cell culture incubator (HERAcell 150i, Thermo Scientific, Germany). After 1, 3, 5, and 7 days of incubation, cell viability and growth were analyzed using the cell titer blue assay (AlamarBlue, Promega, Germany). Therefore, cell samples were washed with 1 \times PBS and incubated with 150 μL of 10% (v/v) cell titer blue reagent in appropriate cell culture media in a humidified atmosphere (5% CO_2) in a cell culture incubator (HERAcell 150i, Thermo Scientific, Germany) at 37 °C. As mammalian cells can metabolize resazurin (blue) to resofurin (pink), cell viability and thus cell growth could be determined by measuring the resofurin fluorescence at 590 nm. A sample without cells was used as a blank control to determine the self-degradation of resazurin during the incubation time. After incubation, 100 μL of the supernatant was pipetted to a black 96-well plate (Nunc, Thermo Scientific, Germany) and measured at 590 nm using a Mithras LB940 plate reader system (Berthold Technologies, Germany).

■ ASSOCIATED CONTENT

Supporting Information

The Supporting Information is available free of charge at <https://pubs.acs.org/doi/10.1021/acsami.2c09590>.

Sequence comparison, amino acid sequence blast, root-mean-square roughness of spider silk films, IEF gel and western blot of soluble spider silk proteins, normalized FTIR spectra on different substrates in the amide I region, and the ratio of water contact angles (PDF)

■ AUTHOR INFORMATION

Corresponding Author

Thomas Scheibel – Lehrstuhl Biomaterialien, Fakultät für Ingenieurwissenschaften, Universität Bayreuth, 95447 Bayreuth, Germany; Bayerisches Polymerinstitut (BPI),

Bayreuther Zentrum für Kolloide und Grenzflächen (BZKG),
Bayreuther Zentrum für Molekulare Biowissenschaften
(BZMB), Bayreuther Materialzentrum (BayMAT),
Universität Bayreuth, 95440 Bayreuth, Germany;
orcid.org/0000-0002-0457-2423;
Email: thomas.scheibel@bm.uni-bayreuth.de

Authors

Sarah Lentz – Lehrstuhl Biomaterialien, Fakultät für
Ingenieurwissenschaften, Universität Bayreuth, 95447
Bayreuth, Germany

Vanessa T. Trossmann – Lehrstuhl Biomaterialien, Fakultät
für Ingenieurwissenschaften, Universität Bayreuth, 95447
Bayreuth, Germany

Christian B. Borkner – Lehrstuhl Biomaterialien, Fakultät für
Ingenieurwissenschaften, Universität Bayreuth, 95447
Bayreuth, Germany

Vivien Beyersdorfer – Lehrstuhl Biomaterialien, Fakultät für
Ingenieurwissenschaften, Universität Bayreuth, 95447
Bayreuth, Germany

Markus Rottmar – Laboratory for Materials-Biology
Interactions, Empa Swiss Federal Laboratories for Materials
Science and Technology, CH-9014 St. Gallen, Switzerland;
orcid.org/0000-0001-7636-428X

Complete contact information is available at:
<https://pubs.acs.org/10.1021/acsami.2c09590>

Author Contributions

S.L. and V.T.T. contributed equally to this work. The design of the experiments was performed by S.L., V.T.T., and T.S. S.L. produced the films and performed the AFM, KPFM, GATR-FTIR, and the water contact angle measurements. V.T.T. designed and produced the eADF4(Q16) variant. C.B.B., V.B., S.L., and V.T.T. performed the enzymatic degradation. C.B.B. and S.L. performed the QCM-D measurements. S.L. and M.R. performed the blood coagulation tests. V.T.T. and S.L. performed the cell culture tests. S.L. performed the electrokinetic measurements. V.T.T. performed the IEF gel electrophoresis, western blot, and the ELISA test. Preparation of the paper was performed by V.T.T. and S.L. T.S. supervised the studies and edited the paper.

Funding

This project has been funded by the Deutsche Forschungsgemeinschaft (DFG, German Research Foundation) project numbers 326998133–TRR225 subproject C01 (T.S.) and DFG SCHE603/23-1 (T.S.).

Notes

The authors declare the following competing financial interest(s): T.S. is a cofounder and shareholder of AmSilk GmbH.

ACKNOWLEDGMENTS

The authors thank Prof. Laforsch for access to the HARRICK VariGATR, Anja Caspari for the streaming potential measurements, and PD Dr. Alla Synytska for the possibility to measure the electrokinetic measurements.

REFERENCES

(1) Bhat, S.; Kumar, A. Biomaterials and bioengineering tomorrow's healthcare. *Biomatter* **2013**, *3*, No. e24717.
(2) Kyriakides, T. R. Molecular Events at Tissue–Biomaterial Interface. In *Host Response to Biomaterials* Badyal, S. F., Ed.; Academic Press: Oxford, 2015; Chapter 5, pp 81–116.

(3) Wei, Q.; Becherer, T.; Angioletti-Uberti, S.; Dzubiella, J.; Wischke, C.; Neffe, A. T.; Lendlein, A.; Ballauff, M.; Haag, R. Protein Interactions with Polymer Coatings and Biomaterials. *Angew. Chem., Int. Ed.* **2014**, *53*, 8004–8031.

(4) Wilson, C. J.; Clegg, R. E.; Leavesley, D. L.; Pearcy, M. J. Mediation of biomaterial–cell interactions by adsorbed proteins: a review. *Tissue Eng.* **2005**, *11*, 1–18.

(5) Horbett, T. A.; Latour, R. A. Adsorbed Proteins on Biomaterials. In *Biomaterials Science*, 4th ed.; Wagner, W. R.; Sakiyama-Elbert, S. E.; Zhang, G.; Yaszemski, M. J., Eds.; Academic Press, 2020; Chapter 2.1.2, pp 645–660.

(6) Xu, L.-C.; Bauer, J. W.; Siedlecki, C. A. Proteins, platelets, and blood coagulation at biomaterial interfaces. *Colloids Surf., B* **2014**, *124*, 49–68.

(7) Visalakshan, R. M.; MacGregor, M. N.; Sasidharan, S.; Ghazaryan, A.; Mierczynska-Vasilev, A. M.; Morsbach, S.; Mailänder, V.; Landfester, K.; Hayball, J. D.; Vasilev, K. Biomaterial Surface Hydrophobicity-Mediated Serum Protein Adsorption and Immune Responses. *ACS Appl. Mater. Interfaces* **2019**, *11*, 27615–27623.

(8) Hoshiba, T.; Yoshikawa, C.; Sakakibara, K. Characterization of Initial Cell Adhesion on Charged Polymer Substrates in Serum-Containing and Serum-Free Media. *Langmuir* **2018**, *34*, 4043–4051.

(9) Keselowsky, B. G.; Collard, D. M.; García, A. J. Surface chemistry modulates fibronectin conformation and directs integrin binding and specificity to control cell adhesion. *J. Biomed. Mater. Res., Part A* **2003**, *66A*, 247–259.

(10) Anderson, J. M.; Rodriguez, A.; Chang, D. T. Foreign body reaction to biomaterials. *Semin. Immunol.* **2008**, *20*, 86–100.

(11) Anderson, J. M. Biological Responses to Materials. *Annu. Rev. Mater. Res.* **2001**, *31*, 81–110.

(12) Luensmann, D.; Jones, L. Protein deposition on contact lenses: The past, the present, and the future. *Contact Lens Anterior Eye* **2012**, *35*, 53–64.

(13) Pagel, M.; Beck-Sickingler, A. G. Multifunctional biomaterial coatings: synthetic challenges and biological activity. *Biol. Chem.* **2017**, *398*, 3–22.

(14) Mertgen, A.-S.; Trossmann, V. T.; Guex, A. G.; Maniura-Weber, K.; Scheibel, T.; Rottmar, M. Multifunctional Biomaterials: Combining Material Modification Strategies for Engineering of Cell-Contacting Surfaces. *ACS Appl. Mater. Interfaces* **2020**, *12*, 21342–21367.

(15) Pacelli, S.; Manoharan, V.; Desalvo, A.; Lomis, N.; Jodha, K. S.; Prakash, S.; Paul, A. Tailoring biomaterial surface properties to modulate host-implant interactions: implication in cardiovascular and bone therapy. *J. Mater. Chem. B* **2016**, *4*, 1586–1599.

(16) Kyzioł, K.; Kaczmarek, L.; Kyzioł, A. Surface Functionalization of Biomaterials. *Handbook of Composites from Renewable Materials*; John Wiley & Sons, Inc., 2017; Vol. 4, pp 457–490.

(17) Wyman, P. Hydrophilic Coatings for Biomedical Applications in and Ex Vivo. *Coatings for Biomedical Applications*; Elsevier, 2012; pp 3–42.

(18) Borkner, C. B.; Wohlrab, S.; Möller, E.; Lang, G.; Scheibel, T. Surface Modification of Polymeric Biomaterials Using Recombinant Spider Silk Proteins. *ACS Biomater. Sci. Eng.* **2017**, *3*, 767–775.

(19) Qi, P.; Maitz, M. F.; Huang, N. Surface modification of cardiovascular materials and implants. *Surf. Coat. Technol.* **2013**, *233*, 80–90.

(20) Lawrence, E. L.; Turner, I. G. Materials for urinary catheters: a review of their history and development in the UK. *Med. Eng. Phys.* **2005**, *27*, 443–453.

(21) Braun, U.; Lorenz, E.; Weimann, C.; Sturm, H.; Karimov, I.; Ettl, J.; Meier, R.; Wohlgemuth, W. A.; Berger, H.; Wildgruber, M. Mechanic and surface properties of central-venous port catheters after removal: A comparison of polyurethane and silicon rubber materials. *J. Mech. Behav. Biomed. Mater.* **2016**, *64*, 281–291.

(22) Zhang, H.; Zheng, X.; Ahmed, W.; Yao, Y.; Bai, J.; Chen, Y.; Gao, C. Design and Applications of Cell-Selective Surfaces and Interfaces. *Biomacromolecules* **2018**, *19*, 1746–1763.

- (23) Borchering, K.; Schmidmaier, G.; Hofmann, G. O.; Wildemann, B. The rationale behind implant coatings to promote osteointegration, bone healing or regeneration. *Injury* 2021, 52, S106–S111.
- (24) Kiradzhyska, D. D.; Mantcheva, R. Overview of Biocompatible Materials and Their Use in Medicine. *Folia Med.* 2019, 61, 34–40.
- (25) Zhang, B. G. X.; Myers, D. E.; Wallace, G. G.; Brandt, M.; Choong, P. F. M. Bioactive coatings for orthopaedic implants—recent trends in development of implant coatings. *Int. J. Mol. Sci.* 2014, 15, 11878–11921.
- (26) Borkner, C. B.; Elsner, M. B.; Scheibel, T. Coatings and films made of silk proteins. *ACS Appl. Mater. Interfaces* 2014, 6, 15611–15625.
- (27) Zepflin, P. H.; Maksimovikj, N. C.; Jordan, M. C.; Nickel, J.; Lang, G.; Leimer, A. H.; Römer, L.; Scheibel, T. Spider silk coatings as a bioshield to reduce periprosthetic fibrous capsule formation. *Adv. Funct. Mater.* 2014, 24, 2658–2666.
- (28) Aigner, T. B.; DeSimone, E.; Scheibel, T. Biomedical Applications of Recombinant Silk-Based Materials. *Adv. Mater.* 2018, 30, No. 1704636.
- (29) Doblhofer, E.; Schmid, J.; Rieß, M.; Daab, M.; Suntinger, M.; Habel, C.; Bargel, H.; Hugenschmidt, C.; Rosenfeldt, S.; Brey, J.; Scheibel, T. Structural Insights into Water-Based Spider Silk Protein–Nanoclay Composites with Excellent Gas and Water Vapor Barrier Properties. *ACS Appl. Mater. Interfaces* 2016, 8, 25535–25543.
- (30) Wohrlab, S.; Müller, S.; Schmidt, A.; Neubauer, S.; Kessler, H.; Leal-Egana, A.; Scheibel, T. Cell adhesion and proliferation on RGD-modified recombinant spider silk proteins. *Biomaterials* 2012, 33, 6650–6659.
- (31) Guerette, P. A.; Ginzinger, D. G.; Weber, B. H. F.; Gosline, J. M. Silk Properties Determined by Gland-Specific Expression of a Spider Fibroin Gene Family. *Science* 1996, 272, 112–115.
- (32) Huemmerich, D.; Helsen, C. W.; Quedzuweit, S.; Oschmann, J.; Rudolph, R.; Scheibel, T. Primary Structure Elements of Spider Dragline Silks and Their Contribution to Protein Solubility. *Biochemistry* 2004, 43, 13604–13612.
- (33) Eissoldt, L.; Smith, A.; Scheibel, T. Decoding the secrets of spider silk. *Mater. Today* 2011, 14, 80–86.
- (34) Heidebrecht, A.; Eissoldt, L.; Diehl, J.; Schmidt, A.; Geffers, M.; Lang, G.; Scheibel, T. Biomimetic Fibers Made of Recombinant Spidroins with the Same Toughness as Natural Spider Silk. *Adv. Mater.* 2015, 27, 2189–2194.
- (35) Kumari, S.; Lang, G.; DeSimone, E.; Spengler, C.; Trossmann, V. T.; Lückner, S.; Hudel, M.; Jacobs, K.; Krämer, N.; Scheibel, T. Data for microbe resistant engineered recombinant spider silk protein based 2D and 3D materials. *Data Brief* 2020, 32, No. 106305.
- (36) Kumari, S.; Lang, G.; DeSimone, E.; Spengler, C.; Trossmann, V. T.; Lückner, S.; Hudel, M.; Jacobs, K.; Krämer, N.; Scheibel, T. Engineered spider silk-based 2D and 3D materials prevent microbial infestation. *Mater. Today* 2020, 41, 21.
- (37) Kellum, J. A. Determinants of blood pH in health and disease. *Crit. Care* 2000, 4, No. 6.
- (38) Borkner, C. B.; Lentz, S.; Müller, M.; Fery, A.; Scheibel, T. Ultrathin Spider Silk Films: Insights into Spider Silk Assembly on Surfaces. *ACS Appl. Polym. Mater.* 2019, 1, 3366–3374.
- (39) Wohrlab, S.; Spieß, K.; Scheibel, T. Varying surface hydrophobicities of coatings made of recombinant spider silk proteins. *J. Mater. Chem.* 2012, 22, 22050–22054.
- (40) Esser, T. U.; Trossmann, V. T.; Lentz, S.; Engel, F. B.; Scheibel, T. Designing of spider silk proteins for human induced pluripotent stem cell-based cardiac tissue engineering. *Mater. Today Bio* 2021, 11, No. 100114.
- (41) Varshavsky, A. The N-end rule pathway and regulation by proteolysis. *Protein Sci.* 2011, 20, 1298–1345.
- (42) Humbard, M. A.; Surkov, S.; De Donatis, G. M.; Jenkins, L. M.; Maurizi, M. R. The N-degradome of *Escherichia coli*: limited proteolysis in vivo generates a large pool of proteins bearing N-degrons. *J. Biol. Chem.* 2013, 288, 28913–28924.
- (43) Hu, X.; Kaplan, D.; Cebe, P. Determining beta-sheet crystallinity in fibrous proteins by thermal analysis and infrared spectroscopy. *Macromolecules* 2006, 39, 6161–6170.
- (44) Metya, A.; Ghose, D.; Ray, N. R. Development of hydrophobicity of mica surfaces by ion beam sputtering. *Appl. Surf. Sci.* 2014, 293, 18–23.
- (45) Müller-Herrmann, S.; Scheibel, T. Enzymatic Degradation of Films, Particles, and Nonwoven Meshes Made of a Recombinant Spider Silk Protein. *ACS Biomater. Sci. Eng.* 2015, 1, 247–259.
- (46) Li, M.; Ogiso, M.; Minoura, N. Enzymatic degradation behavior of porous silk fibroin sheets. *Biomaterials* 2003, 24, 357–365.
- (47) Zhao, C.; Wu, X.; Zhang, Q.; Yan, S.; Li, M. Enzymatic degradation of *Antheraea pernyi* silk fibroin 3D scaffolds and fibers. *Int. J. Biol. Macromol.* 2011, 48, 249–255.
- (48) Bauer, C. A.; Löfqvist, B.; Pettersson, G. Studies on the catalytic mechanism of a serine protease from *Streptomyces griseus*. *Eur. J. Biochem.* 1974, 41, 45–49.
- (49) Wolters, G. H. J.; Vos-Scheperkeuter, G. H.; Lin, H.-C.; van Schilfhaarde, R. Different roles of class I and class II *Clostridium histolyticum* collagenase in rat pancreatic islet isolation. *Diabetes* 1995, 44, 227–233.
- (50) Maziz, A.; Leprette, O.; Boyer, L.; Blaché, C.; Bergaud, C. Tuning the properties of silk fibroin biomaterial via chemical cross-linking. *Biomed. Phys. Eng. Express* 2018, 4, No. 065012.
- (51) Rodrigues, S. N.; Gonçalves, I. C.; Martins, M. C. L.; Barbosa, M. A.; Ratner, B. D. Fibrinogen adsorption, platelet adhesion and activation on mixed hydroxyl-/methyl-terminated self-assembled monolayers. *Biomaterials* 2006, 27, 5357–5367.
- (52) Sperling, C.; Maitz, M. F.; Grasso, S.; Werner, C.; Kanse, S. M.; Positivity, A. Charged Surface Triggers Coagulation Activation Through Factor VII Activating Protease (FSAP). *ACS Appl. Mater. Interfaces* 2017, 9, 40107–40116.
- (53) Kidoaki, S.; Matsuda, T. Adhesion Forces of the Blood Plasma Proteins on Self-Assembled Monolayer Surfaces of Alkanethiolates with Different Functional Groups Measured by an Atomic Force Microscope. *Langmuir* 1999, 15, 7639–7646.
- (54) Bernabeu, P.; Caprani, A. Influence of surface charge on adsorption of fibrinogen and/or albumin on a rotating disc electrode of platinum and carbon. *Biomaterials* 1990, 11, 258–264.
- (55) Agashe, M.; Raut, V.; Stuart, S. J.; Latour, R. A. Molecular Simulation To Characterize the Adsorption Behavior of a Fibrinogen γ -Chain Fragment. *Langmuir* 2005, 21, 1103–1117.
- (56) Evans-Nguyen, K. M.; Tolles, L. R.; Gorkun, O. V.; Lord, S. T.; Schoenfisch, M. H. Interactions of Thrombin with Fibrinogen Adsorbed on Methyl-, Hydroxyl-, Amine-, and Carboxyl-Terminated Self-Assembled Monolayers. *Biochemistry* 2005, 44, 15561–15568.
- (57) Ostuni, E.; Chapman, R. G.; Holmlin, R. E.; Takayama, S.; Whitesides, G. M. A Survey of Structure–Property Relationships of Surfaces that Resist the Adsorption of Protein. *Langmuir* 2001, 17, 5605–5620.
- (58) Sivaraman, B.; Latour, R. A. The relationship between platelet adhesion on surfaces and the structure versus the amount of adsorbed fibrinogen. *Biomaterials* 2010, 31, 832–839.
- (59) Lovely, R. S.; Kazmierczak, S. C.; Massaro, J. M.; D’Agostino, R. B., Sr.; O’Donnell, C. J.; Farrell, D. H. Gamma’ fibrinogen: evaluation of a new assay for study of associations with cardiovascular disease. *Clin. Chem.* 2010, 56, 781–788.
- (60) Weiss, A. C. G.; Herold, H. M.; Lentz, S.; Faria, M.; Besford, Q. A.; Ang, C.-S.; Caruso, F.; Scheibel, T. Surface Modification of Spider Silk Particles to Direct Biomolecular Corona Formation. *ACS Appl. Mater. Interfaces* 2020, 12, 24635–24643.
- (61) Leal-Egana, A.; Lang, G.; Mauerer, C.; Wickinghoff, J.; Weber, M.; Geimer, S.; Scheibel, T. Interactions of Fibroblasts with Different Morphologies Made of an Engineered Spider Silk Protein. *Adv. Mater.* 2012, 14, B67–B75.
- (62) Kazmierska, K.; Ciach, T. Bioactive Coatings for Minimally Invasive Medical Devices: Surface Modification in the Service of Medicine. *Recent Pat. Biomed. Eng.* 2010, 2, 1–14.

(63) Böttcher, H. Bioactive Sol-Gel Coatings. *J. Prakt. Chem.* **2000**, *342*, 427–436.

(64) Li, Z.; Milionis, A.; Zheng, Y.; Yee, M.; Codispoti, L.; Tan, F.; Poulidakos, D.; Yap, C. H. Superhydrophobic hemostatic nanofiber composites for fast clotting and minimal adhesion. *Nat. Commun.* **2019**, *10*, No. 5562.

(65) Shiu, H. T.; Goss, B.; Lutton, C.; Crawford, R.; Xiao, Y. Controlling whole blood activation and resultant clot properties by carboxyl and alkyl functional groups on material surfaces: a possible therapeutic approach for enhancing bone healing. *J. Mater. Chem. B* **2014**, *2*, 3009–3021.

(66) Bračić, M.; Mohan, T.; Kargl, R.; Griesser, T.; Hribernik, S.; Köstler, S.; Stana-Kleinschek, K.; Fras-Zemljič, L. Preparation of PDMS ultrathin films and patterned surface modification with cellulose. *RSC Adv.* **2014**, *4* (23), 11955–11961.

(67) Sauerbrey, G. Verwendung von Schwingquarzen zur Wägung dünner Schichten und zur Mikrowägung. *Z. Physik* **1959**, *155* (2), 206–222.

(68) Liu, G.; Zhang, G. Basic principles of QCM-D. In *QCM-D Studies on Polymer Behavior at Interfaces*; Springer, 2013; pp 1–8.

(69) Liu, G.; Zhang, G. *QCM-D Studies on Polymer Behavior at Interfaces*; Springer, 2013.

(70) Weidenbacher, L.; Müller, E.; Guex, A. G.; Zündel, M.; Schweizer, P.; Marina, V.; Adlhart, C.; Vejsadová, L.; Pauer, R.; Spiecker, E.; Maniura-Weber, K.; Ferguson, S. J.; Rossi, R. M.; Rottmar, M.; Fortunato, G. In Vitro Endothelialization of Surface-Integrated Nanofiber Networks for Stretchable Blood Interfaces. *ACS Appl. Mater. Interfaces* **2019**, *11* (6), 5740–5751.

Supporting Information

Structure-property relationship based on the amino acid composition of recombinant spider silk proteins for potential biomedical applications

Sarah Lentz^{‡,†}, Vanessa T. Trossmann^{‡,†}, Christian B. Borkner[‡], Vivien Beyersdorfer[‡],

Markus Rottmar[§] and Thomas Scheibel^{,‡,x}*

[‡] Lehrstuhl Biomaterialien, Fakultät für Ingenieurwissenschaften, Universität Bayreuth,

Rüdiger-Bormann-Str. 1, 95447 Bayreuth, Germany

[§] Laboratory for Materials-Biology Interactions, Empa Swiss Federal Laboratories for

Materials Science and Technology, CH-9014 St. Gallen, Switzerland

** Bayerisches Polymerinstitut (BPI), Bayreuther Zentrum für Kolloide und Grenzflächen*

(BZKG), Bayreuther Zentrum für Molekulare Biowissenschaften (BZMB), Bayreuther

Materialzentrum (BayMAT), Universität Bayreuth, Universitätsstr. 30, 95440 Bayreuth,

Germany

E-Mail: thomas.scheibel@bm.uni-bayreuth.de

[†] contributed equally

^x corresponding author

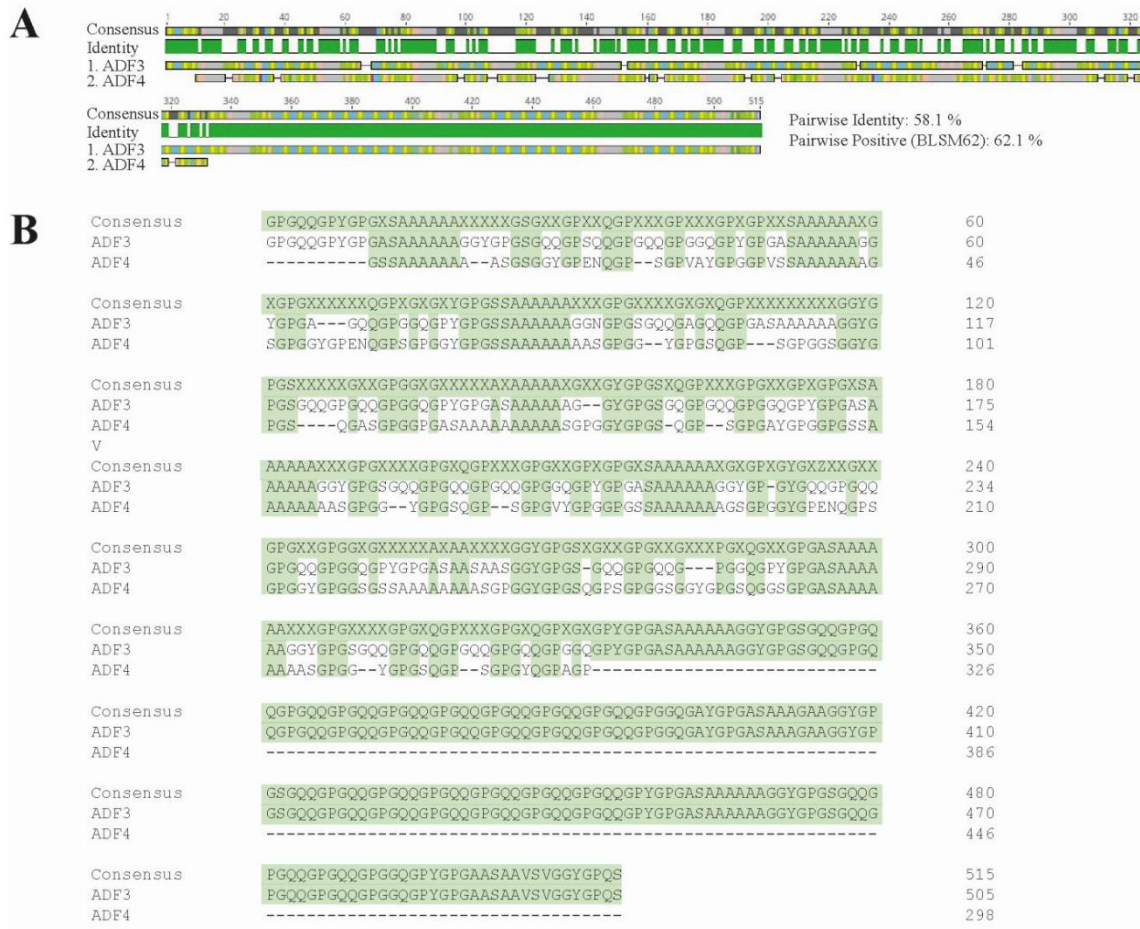


Figure SI 1: A) Sequence comparison of natural amino acid sequences of *Araneus diadematus* fibroin 3 and 4. Homology and identity of both amino acid sequences are shown. B) Amino acid sequence blast of the so far identified parts of the natural amino acid sequences ADF3 and ADF4. The algorithm BLSM62 was used for the comparison. The known sequence of ADF3 comprises 505 aa and that of ADF4 298aa.

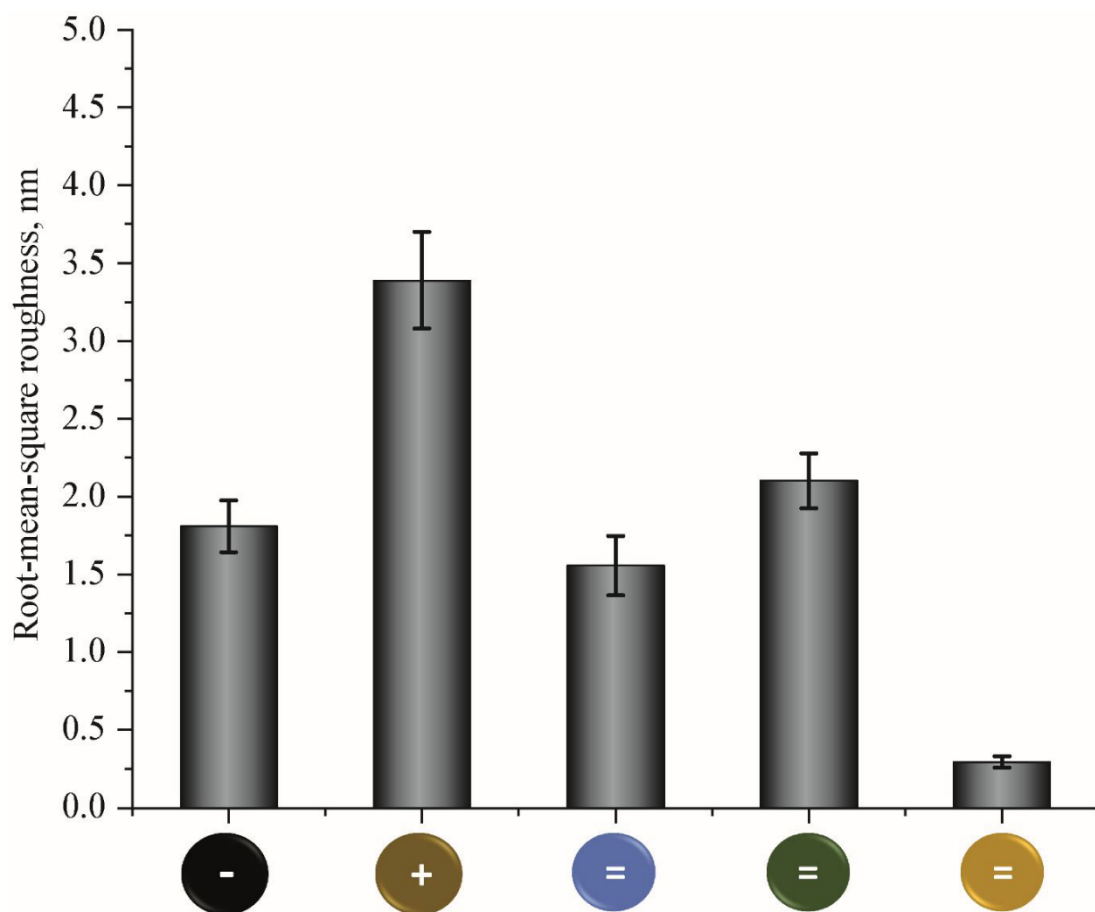


Figure SI 2: Root-mean-square roughness (nm) of recombinant spider silk films as shown in figure 1. The black button reflects the negatively charged eADF4(C16), the brown one the positively charged eADF4(κ 16), the blue one the uncharged variant eADF4(Ω 16), and the green one depicts for eADF3(AQ)₁₂ and the yellow one for eADF3(AQ)₂₄.

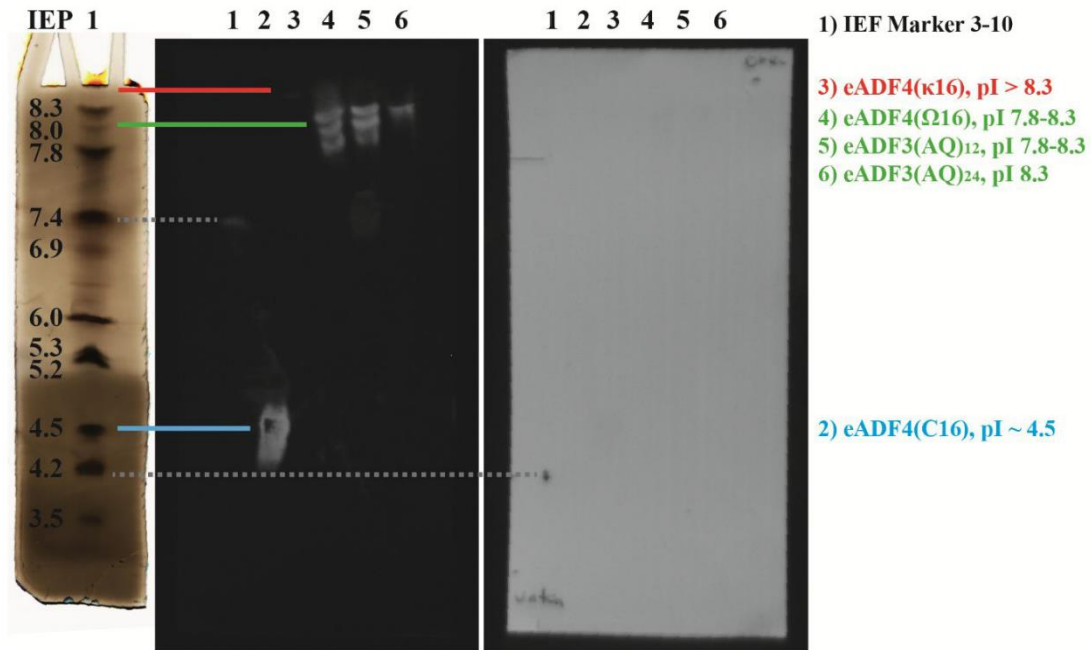


Figure SI 3: Isoelectric focussing (IEF) of soluble recombinant spider silk proteins eADF4(C16), eADF4(κ 16), eADF4(Ω 16), eADF3(AQ)₁₂ and eADF3(AQ)₂₄ for determination of the isoelectric point (IEP). An IEF gel electrophoresis using the SERVA *GeI*TM IEF 3-10 Starter Kit was performed with dialyzed, soluble spider silk proteins in native state according to manufacturers protocol. The subsequent western blot enabled protein visualization by detecting the N-terminally fused T7-tag using an HRP-conjugated T7 antibody (1:5000), since a homogeneous protein staining, e.g. silver staining, was not possible due to individual protein characteristics. However, the IEF marker was additionally silver stained for a better allocation of the individual IEP-indicating bands. The grey dashed lines show the bands visible on the blot that were used for classification.

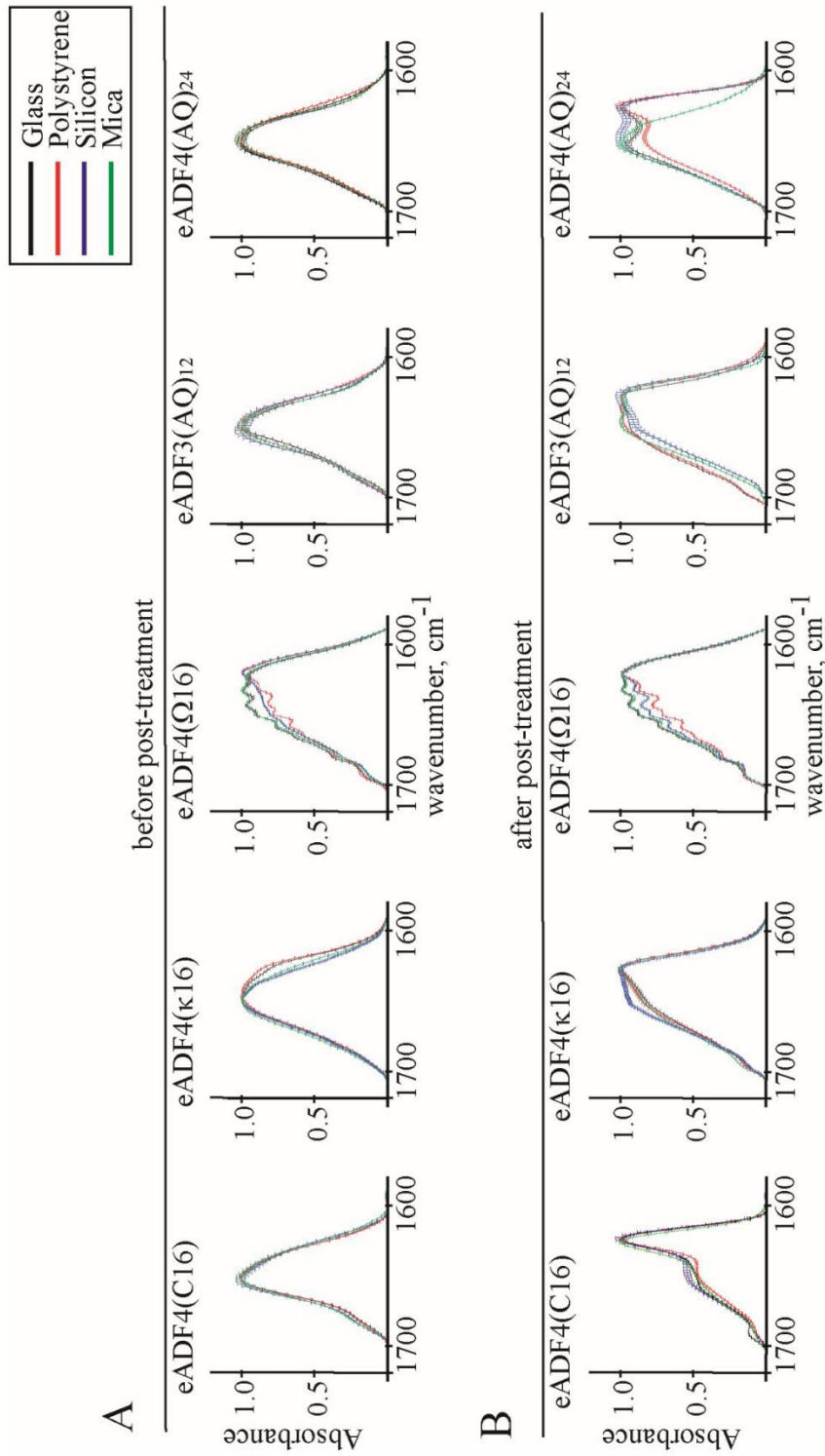


Figure SI 4: Normalized FTIR-spectra (amide I band) of (A) recombinant spider silk films as-cast and (B) after post-treatment with methanol. Films were cast on glass (black), polystyrene (red), silicon (blue) and mica (green). Samples were analyzed in quintuplets. Post-treatment leads to a peak shift from ~ 1660 cm^{-1} (mainly random coil) to ~ 1626 cm^{-1} (mainly β -sheet).

Table SI 1: Ratio of water contact angles of uncoated substrates to recombinant spider silk coated substrates.

Protein	Glass/Protein	PS/Protein	Si/Protein	Mica/Protein
eADF4(C16)	0.4	1.2	0.8	0.01
eADF4(κ 16)	0.4	1.3	1.0	0.01
eADF4(Ω 16)	0.4	1.4	1.0	0.02
eADF3(AQ) ₁₂	0.4	1.1	0.7	0.01
eADF3(AQ) ₂₄	0.4	1.0	0.7	0.01
Average \pm SD	0.4 \pm 0.0	1.2 \pm 0.2	0.8 \pm 0.2	0.01 \pm 0.0

Part III - Chapter 2 – Surface Modification of Spider Silk Particles to Direct Biomolecular Corona Formation

Part III – Chapter 2.1 - Chapter perspective and contribution

In this chapter, recombinant spider silk (rss) coatings and spherical rss protein particles were investigated concerning key physicochemical properties that direct the biological response to biomaterials. The used rss variants comprised different charges and genetic modifications with C-terminal tags like RGD, E₈G, and R₈G. The focus of this chapter lies in the interaction of the rss proteins with whole human blood. The formation of a biomolecular corona was investigated concerning the biomolecular corona composition, which also affects macroscopic effects such as fibrin formation and blood clotting. The outcome of this study was that fibrinogen-based proteins are the dominant species in the biomolecular corona for the positively charged eADF4(κ 16) particles. Negatively charged spider silk particles consisting of either eADF4(C16), eADF4(C16)-E₈G, eADF4(C16)-RGD, or eADF4(C16)-R₈G, and the close-to-neutral charged (eADF4(C16)/ κ 16) blend particles adsorbed predominantly lactotransferrin and complement C3. This outcome assumes that positively charged rss protein eADF4(κ 16) promotes blood clotting and the negatively charged variants prevent blood clotting.

The design of the experiments was performed by Alessia Weiss, Heike Herold, Sarah Lentz, Frank Caruso, and Thomas Scheibel. Heike Herold and Sarah Lentz prepared and characterized the spider silk particles. Alessia Weiss performed the characterization using SDS-PAGE and all mass spectrometry studies and the respective data analysis. Sarah Lentz produced the spider silk films and performed the blood coagulation assays. Quinn Besford performed statistical analysis of the blood assay data. Matt Faria assisted with the analysis of the mass spectrometry data. Ching-Seng Ang performed mass spectrometry experiments and protein identification. Thomas Scheibel and Frank Caruso supervised the studies and edited the paper. The preparation of the original draft was performed by Alessia Weiss, Heike Herold and Sarah Lentz.

This paper is published in ACS Applied Materials and Interfaces: Surface Modification of Spider Silk Particles to Direct Biomolecular Corona Formation, ACS Applied Materials & Interfaces 2020 12 (22), 24635-24643, DOI: 10.1021/acsami.0c06344.

The permission of reprint was granted by ACS Applied Materials & Interfaces: Reprinted (adapted) with permission from „Surface Modification of Spider Silk Particles to Direct

Biomolecular Corona Formation, “Alessia C. G. Weiss, Heike M. Herold, Sarah Lentz, Matthew Faria, Quinn A. Besford, Ching-Seng Ang, Frank Caruso, and Thomas Scheibel, *ACS Applied Materials & Interfaces* **2020** 12 (22), 24635-24643, DOI: 10.1021/acsami.0c06344. Copyright 2021 American Chemical Society.

Part III – Chapter 2.2 - Full Paper

Surface Modification of Spider Silk Particles to Direct Biomolecular Corona Formation

Alessia C. G. Weiss,[†] Heike M. Herold,[†] Sarah Lentz, Matthew Faria, Quinn A. Besford, Ching-Seng Ang, Frank Caruso,* and Thomas Scheibel*Cite This: *ACS Appl. Mater. Interfaces* 2020, 12, 24635–24643

Read Online

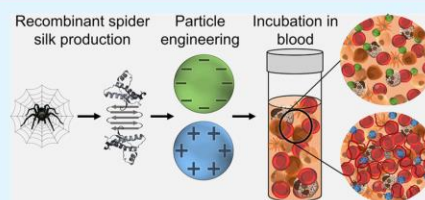
ACCESS |

Metrics & More

Article Recommendations

ABSTRACT: In recent years, spider silk-based materials have attracted attention because of their biocompatibility, processability, and biodegradability. For their potential use in biomaterial applications, i.e., as drug delivery systems and implant coatings for tissue regeneration, it is vital to understand the interactions between the silk biomaterial surface and the biological environment. Like most polymeric carrier systems, spider silk material surfaces can adsorb proteins when in contact with blood, resulting in the formation of a biomolecular corona. Here, we assessed the effect of surface net charge of materials made of recombinant spider silk on the biomolecular corona composition. In-depth proteomic analysis of the biomolecular corona revealed that positively charged spider silk materials interacted predominantly with fibrinogen-based proteins. This fibrinogen enrichment correlated with blood clotting observed for both positively charged spider silk films and particles. In contrast, negative surface charges prevented blood clotting. Genetic engineering allows the fine-tuning of surface properties of the spider silk particles providing a whole set of recombinant spider silk proteins with different charges or peptide tags to be used for, for example, drug delivery or cell docking, and several of these were analyzed concerning the composition of their biomolecular corona. Taken together this study demonstrates how the surface net charge of recombinant spider silk surfaces affects the composition of the biomolecular corona, which in turn affects macroscopic effects such as fibrin formation and blood clotting.

KEYWORDS: recombinant spider silk, spider silk hybrid proteins, proteomics analysis, fibrinogen, drug delivery



INTRODUCTION

Biomaterials exposed to complex biological fluids, such as blood, interact with a variety of different proteins, sugars, and lipids, and thus a layer forms on their surfaces, known as the biomolecular corona.^{1–6} The biomolecular corona is a two-component system consisting of an inner layer, often referred to as the “hard” biomolecular corona, and an outer layer of associated proteins, the so-called “soft” biomolecular corona.^{7–11} The presence of the biomolecular corona changes the synthetic identity of biomaterials, including their surface chemistry and topography, to a biological identity.^{12,13} Biological identity means the composition, i.e., the type and amount of adsorbed proteins.¹³ This biological identity, in turn, influences the physiological response in vivo, such as cytotoxicity and cellular association.^{1,9–11,13–16} Extensive efforts have been made to understand the correlation between the material design, and the biomolecular corona composition, however, there is still limited knowledge about how the presence of adsorbed proteins affects interactions between biomaterials and their environment.

The surface net charge of a material has a profound impact on the composition of the biomolecular corona. It is well-known that the abundance of proteins is higher on charged

surfaces compared to charge-neutral materials.^{12–14} Furthermore, proteins with a pI > 5.5 preferably adsorb on negatively charged surfaces, whereas proteins with a pI < 5.5 favor positively charged surfaces.¹⁵ Extensive efforts have been directed toward evaluating the impact of such material design parameters on the protein fingerprint.^{16–20} Identifying proteins that are significant in mediating physiological responses may assist in understanding the correlation between material design and its physiological performance.

Biopolymers play an increasingly important role as biomaterials for medical applications, e.g., in tissue engineering and drug delivery. Materials made from spider silk proteins are promising candidates for a variety of biomedical applications, as they are largely biocompatible and nontoxic and show reduced/no immunoreactivity.²¹ Importantly, there is no need for removal of spider silk-based biomaterials after implantation,

Received: April 6, 2020

Accepted: May 5, 2020

Published: May 5, 2020



as once the biomaterial is in contact with the body, the spider silk material decomposes over time (from weeks to months) in vivo into nontoxic degradation products (i.e., amino acids).^{22–24}

The recombinant production of spider silk proteins allows precise genetic engineering. Depending on the area of application, diverse morphologies, such as fibers,²⁵ nonwoven meshes,²⁶ hydrogels,²⁷ films,²⁸ and particles²⁹ can be produced. Particles produced from recombinant spider silk are especially interesting for use in therapeutic and diagnostic applications. They have been previously shown to be suitable drug delivery vehicles for low-molecular-weight model drug substances³⁰ as well as protein delivery,³¹ for coating of magnetic particles intended for use in diagnostic imaging,³² or as a carrier system for a new vaccination strategy if antigenic peptides are incorporated by genetic engineering.³³ Silk films can be used in tissue engineering, wound healing applications, or as coatings of implants. Although cell attachment on eADF4-(C16) spider silk films is weak, it can be significantly enhanced by implementation of, for example, an integrin-recognition RGD sequence as a tag onto the eADF4(C16) protein.³⁴ Films prepared from polycationic spider silk eADF4(κ 16) have successfully been employed for specific interaction with cardiomyocytes.³⁵ Moreover, spider silk coatings of catheters revealed their potential as biomedical coatings to shield unfavorable attachment of cells, and strikingly, spider silk coatings of silicone implants have been shown to improve their biocompatibility in vivo by reducing the risk of unwanted side effects such as fibrosis.³⁶

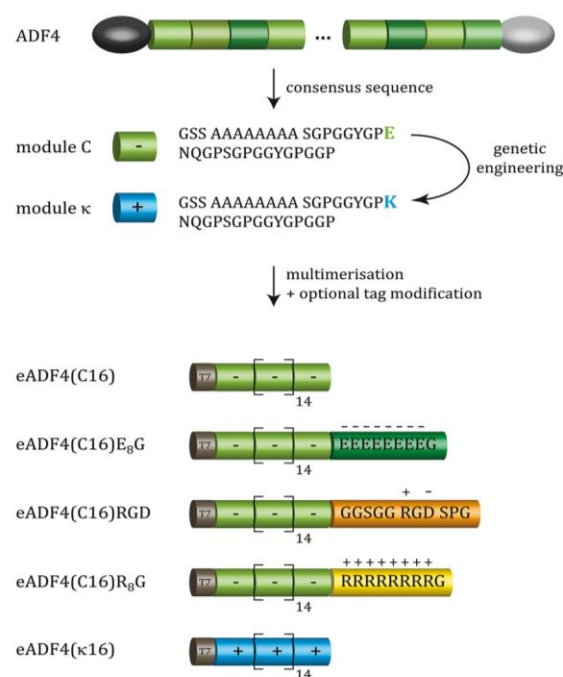
In spite of the broad field of applications of spider silk-derived materials and their successful evaluation for in vivo applications, little is known about interactions of spider silk materials with plasma proteins. In this work, we investigated the impact of spider silk material surface charges on the biomolecular corona formed upon exposure to human whole blood using a genetically engineered spider silk platform. Combining in-depth proteomics analyses with imaging microscopy, we demonstrated that positively charged particles and surfaces attracted a broad variety of fibrinogen-based proteins. Understanding the consequences of material properties, such as surface charge on the composition of the biomolecular corona and hence the physiological responses is crucial for improvement of the biocompatibility of biomaterials.

RESULTS AND DISCUSSION

Spider Silk Variants with Different Net Charges.

Materials made of different eADF4 variants were used (Scheme 1) to examine the influence of a materials' surface net charge and the contribution of (functional) peptide tags on the interaction with blood proteins. eADF4(C16) is derived from the highly repetitive *Araneus diadematus* fibroin 4 core sequence and contains one negatively charged amino acid (glutamic acid) per amino acid sequence block, the so-called C-module. The 16 repeat units of module C in eADF4(C16) result in a negatively charged polyanionic protein, hence C16-based materials exhibit a negative surface net charge.³⁷ Besides unmodified eADF4(C16), four variants thereof were produced to investigate the effect of different tags and charge distributions (Scheme 1). eADF4(C16) was carboxyl-terminally modified eADF4(C16) fused with a polyanionic octaglutamic-acid tag E₈G (eADF4(C16)E₈G). Furthermore, the RGD motif (eADF4(C16)RGD)³⁴ or a polycationic octa-

Scheme 1. Schematic Illustration of the Different Spider Silk Variants Used in This Study^a



^aPolyanionic eADF4(C16)³⁷ consists of 16 repeats of a repetitive amino acid motif (module C) derived from the repetitive core domain of the natural silk protein ADF4. Genetic engineering, i.e., exchanging the glutamic acid (E) in module C to lysine (K) gives rise to the cationic κ module and multimerization yields the polycationic eADF4(κ 16).³⁹ Optionally, further tags have been added to eADF4(C16) by means of genetic engineering to generate eADF4(C16)RGD,³⁴ eADF4(C16)R₈G,³⁸ or eADF4(C16)E₈G (this work).

arginine tag R₈G (eADF4(C16)R₈G,³⁸ and the polycationic variant eADF4(κ 16)³⁹ comprising the positively charged amino acid residue lysine instead of glutamic acid in each of the 16 κ modules were studied (Scheme 1), as well as a blend of negatively charged eADF4(C16) and positively charged eADF4(κ 16). The major focus of this study was on the influence of spider silk particle surface charge or surface-presented peptide tags on binding of proteins from human blood. An overview of selected properties of particles from the assessed spider silk variants is given in Table 1.

Zeta-potential data of the spider silk particles confirmed the charges of particles made of the individual spider silk variants (Table 1). The surface net charge of eADF4(C16) particles yielded a zeta potential of -27 ± 1 mV. The negatively charged E₈G-tag further decreased the zeta potential to -32 ± 2 mV. Fusion of a positively charged octa-arginine resulted in a zeta potential of -21 ± 1 mV. The RGD tag contributed one negatively as well as one positively charged amino acid residue, resulting in a similar surface charge as the unmodified eADF4(C16). In contrast, the positive charges arising from the 16 κ modules resulted in a zeta potential of $+15 \pm 1$ mV. The blend of eADF4(C16) and eADF4(κ 16) in particles revealed a near-to-neutral surface charge. The heterogeneity of the examined silk types with various surface charges and differing surface-exposed peptide sequences allowed a detailed

Table 1. Charge Distributions, Molecular Weight (MW), and Zeta Potential (ζ) Data of the Individual Spider Silk Variants^a

	no. of positively and negatively charged amino acid residues		resulting net charge	theoretical pI	ζ (mV)	MW (Da)
eADF4(C16)	+2	-17	-15	3.48	-27 ± 1	47 698
eADF4(C16)E ₈ G	+2	-25	-23	3.31	-32 ± 2	48 788
eADF4(C16)R ₈ G	+10	-17	-7	4.57	-21 ± 1	49 005
eADF4(C16)RGD	+3	-18	-15	3.64	-24 ± 3	48 583
eADF4(κ 16)	+18	-1	+17	9.70	+15 ± 1	47 683
eADF4(C16/ κ 16) blend	+20	-18	+2	n/a	-6 ± 8	n/a

^aCharges include those originating from N- and C- termini and those originating from amino acid residues being charged at physiological conditions (pH 7.4). Note that all spider silk proteins comprise an amino-terminal T7 tag, which contributes one positive charge. Theoretical pI and MW of the individual spider silk proteins were calculated using ProtParam. Zeta potential data of silk particles were taken from Schierling et al.³⁸ measured in 1/11 PBS except for variant eADF4(C16)E₈G. Data for eADF4(C16/ κ 16) blend particles are taken from Elsner et al.⁴⁰ in 10 mM KCl, pH 5.5. n/a, not applicable.

study on how spider silk particle surface characteristics relate to the formation and composition of a biomolecular corona.

The silk materials were used to analyze how different surface net charges affect the physiological response of the spider silk materials upon contact with human whole blood (Figure 1). SEM imaging and proteomic analyses were performed allowing correlation of the composition of the biomolecular coronae to blood clotting effects.

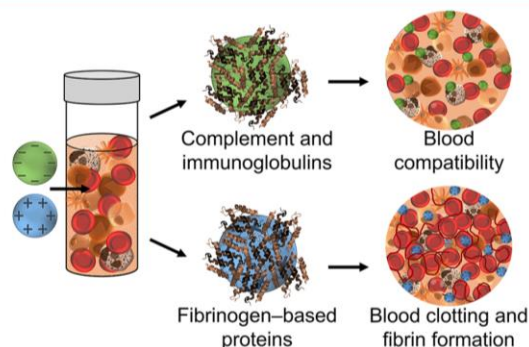


Figure 1. Proteomic analyses revealed that different proteins were attracted upon incubation in human whole blood based on spider silk particles of different surface charge. Negatively charged particles predominantly attracted complement and immunoglobulins, whereby positively charged particles adsorbed mainly fibrinogen-based proteins.

Surface Charge Correlated with Blood Clotting. To begin with, interactions of negatively (eADF4(C16)) and positively (eADF4(κ 16)) charged spider silk materials were investigated upon contact with freshly drawn human blood (Figure 2). Therefore, 2D spider silk films and microparticles were prepared and exposed to human blood. Scanning electron microscopy (SEM) and digital images of both planar films and particles manufactured from the negatively charged eADF4(C16) showed macroscopic blood compatibility, i.e., no signs of blood clotting or fibrin formation (Figure 2a–c). Some erythrocytes, however, changed their shape from completely round to cells with a frayed outline that occurred as a result of sample preparation.⁴¹ In contrast, the presence of the positively charged eADF4(κ 16) films and particles in blood resulted in fibrin formation and blood clotting (Figure 2d–f). One basis for blood-clotting is thrombin-based fibrinogen

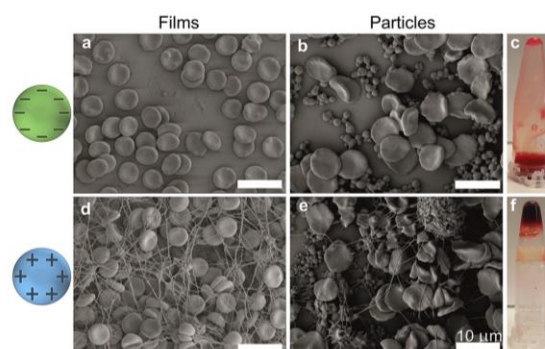


Figure 2. (a, b, d, e) Scanning electron microscopy (SEM) and (c, f) digital images of (a, d) spider silk films and (b, e) particles prepared from (a–c) negatively (eADF4(C16)) and (d–f) positively (eADF4(κ 16)) charged spider silk materials following incubation in whole human blood. The scale bars are 10 μ m.

cleavage yielding insoluble fibrin fibers, forming a network leading to blood coagulation.^{42–44}

Fibrinogen-Based Proteins Predominantly Adsorb on Positively Charged Spider Silk Particles. For in-depth proteomic and sodium dodecyl sulfate-polyacrylamide gel electrophoresis (SDS-PAGE) analyses of the biomolecular coronae formed on the surface of spider silk particles, the study was extended to further spider silk variants with modified surface net charge or with functional peptide tags (e.g., RGD-tag) (Table 1). SDS-PAGE of proteins eluted off the spider silk particles showed slight differences concerning the identified proteins in the coronae among negatively (eADF4(C16), eADF4(C16)E₈G, eADF4(C16)RGD, eADF4(C16)R₈G), and close-to-neutral charged (eADF4(C16/ κ 16) blend) particles, but more severe differences in comparison to positively charged (eADF4(κ 16)) particles (Figure 3a). Low-molecular-weight proteins adsorbed as predominant species on negatively and close-to-neutral charged spider silk particles, whereas the positively charged particles additionally adsorbed high- and medium-molecular-weight proteins. Mass spectrometry was performed on the basis of a recently published method to identify these proteins.¹⁰ Three replicates of each spider silk particle type were examined following incubation in human whole blood. The protein composition of whole human blood alone was determined as well, to analyze enrichment of specific proteins in the respective biomolecular corona in comparison to the incubation media. A normalized spectral abundance

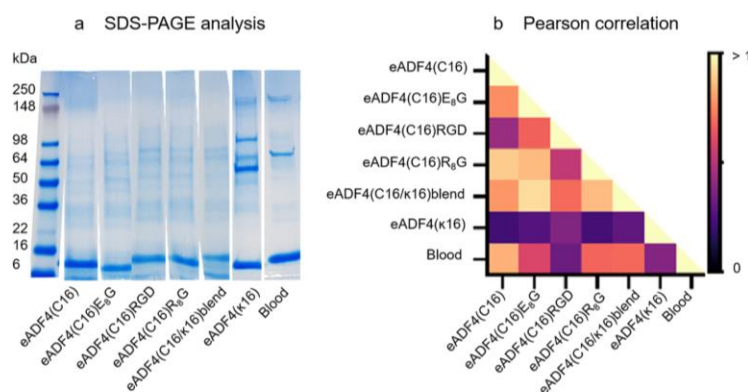


Figure 3. (a) Cropped Coomassie blue-stained SDS-PAGE of proteins identified in the biomolecular coronae of spider silk particles eADF4(C16), eADF4(C16)E₈G, eADF4(C16)RGD, eADF4(C16)R₈G, eADF4(C16/κ16) blend, and eADF4(κ16) following incubation in human whole blood. A reference band associated with particular molecular weights (left) and a sample of the incubation media alone is shown for comparison. (b) Pearson correlation analysis of the relative abundance (NSAF) of identified secreted proteins in the biomolecular coronae of spider silk particles. Data are presented as averages across all replicates. Lighter colors correlate with more similar biomolecular coronae.

factor (NSAF), describing the relative abundance of each protein in a complex protein solution, was next determined.⁴⁵ For mass spectrometry sample preparation, red blood cell (RBC) lysis was performed following incubation in whole blood, leading to the detection of additional intracellular proteins. As intracellular proteins are not present in the plasma and therefore can cause wrong interpretations of the proteomics data, all intracellular proteins were not used within the “raw data” for further analyses. This data set is referred to as the “processed protein abundance” data set. The relative abundance of proteins detected within the biomolecular corona of the different spider silk particles after incubation in human whole blood was compared using Pearson correlation (Figure 3b). Pearson correlation revealed that the biomolecular coronae of the negatively and close-to-neutral charged particles differed from those of the positively surface charged particles. Furthermore, the negatively and neutrally charged particles both exhibited coronae that were similar to the composition of human whole blood, whereas the composition of that of eADF4(κ16) was significantly different.

The abundance of individual corona proteins was investigated. Therefore, a raw expression analysis (Figure 4a) and an enrichment analysis (Figure 4b) were performed. The raw expression analysis lists proteins based on the relative abundance identified in each biomolecular corona, whereby the enrichment analysis identified proteins that were over-represented in a particular coronae in comparison to the incubation media.

Serum albumin was identified as the main species in the raw expression analysis for all spider silk particles because of its high abundance in human plasma. For the negatively surface charged spider silk particles, as well as for the close-to-neutral charged particles, lactotransferrin, protein S100-A8, protein S100-A9, Ig kappa chain C region, complement C1q, and complement C3 were adsorbed with a high preference. Similar adsorption trends were obtained from the enrichment analysis: Lactotransferrin and complement C3 were identified as main proteins in the coronae of negatively and close-to-neutral charged particles. Transferrins, complement, and immunoglobulins are generally implicated in complement and inflammation responses.^{46–51} Their adsorption to particles has been

shown to promote phagocytic uptake.^{51–58} In contrast, both analyses identified fibrinogen-based proteins (fibrinogen beta chain, fibrinogen gamma chain, and fibrinogen alpha chain) as the most abundant proteins in the coronae of the positively charged eADF4(κ16) particles. The average molecular weight of human fibrinogen is ~340 kDa.⁵⁹ The observed bands in the SDS-PAGE gel (Figure 3) may be indicative of the high abundance of the different fibrinogen chains (α , β , and γ), which were subsequently confirmed using quantitative proteomics analysis. Fibrin promotes blood clotting by forming bridges between blood platelets through binding to surface membrane fibrinogen receptors. Furthermore, in the presence of thrombin and blood clotting factors, fibrinogen forms fibrin strands, which develop into an extensive interconnected fibrin network. These networks are the basis for the formation of mature fibrin clots as seen in Figure 2.⁶⁰ Similar adsorption trends were found by Sakulku et al. investigating the *in vivo* biomolecular corona of differently charged superparamagnetic nanoparticles.⁶¹

CONCLUSION

We have presented an investigation on how the surface net charge of spider silk materials affect the composition of the biomolecular corona upon contact with human whole blood. Our data allowed the direct correlation of proteomics data to clotting. Fibrinogen-based proteins were detected to be the dominant species of adsorbed proteins on positively charged eADF4(κ16) spider silk particles. In contrast, negatively charged spider silk particles consisting of either eADF4(C16), eADF4(C16)E₈G, eADF4(C16)RGD, or eADF4(C16)R₈G, and the close-to-neutral charged (eADF4(C16/κ16) blend) particles adsorbed predominantly lactotransferrin and complement C3. Surface charge plays the most prominent role in biomolecular corona formation, whereas peptide tags exposed on a particle's surface had only a minor influence on corona formation. We hypothesize that the high abundance of fibrinogen-based proteins in the biomolecular coronae of eADF4(κ16) particles triggered blood clotting and fibrin formation on particles as well as on planar silk-coated surfaces. Our work assists in understanding influencing variables of

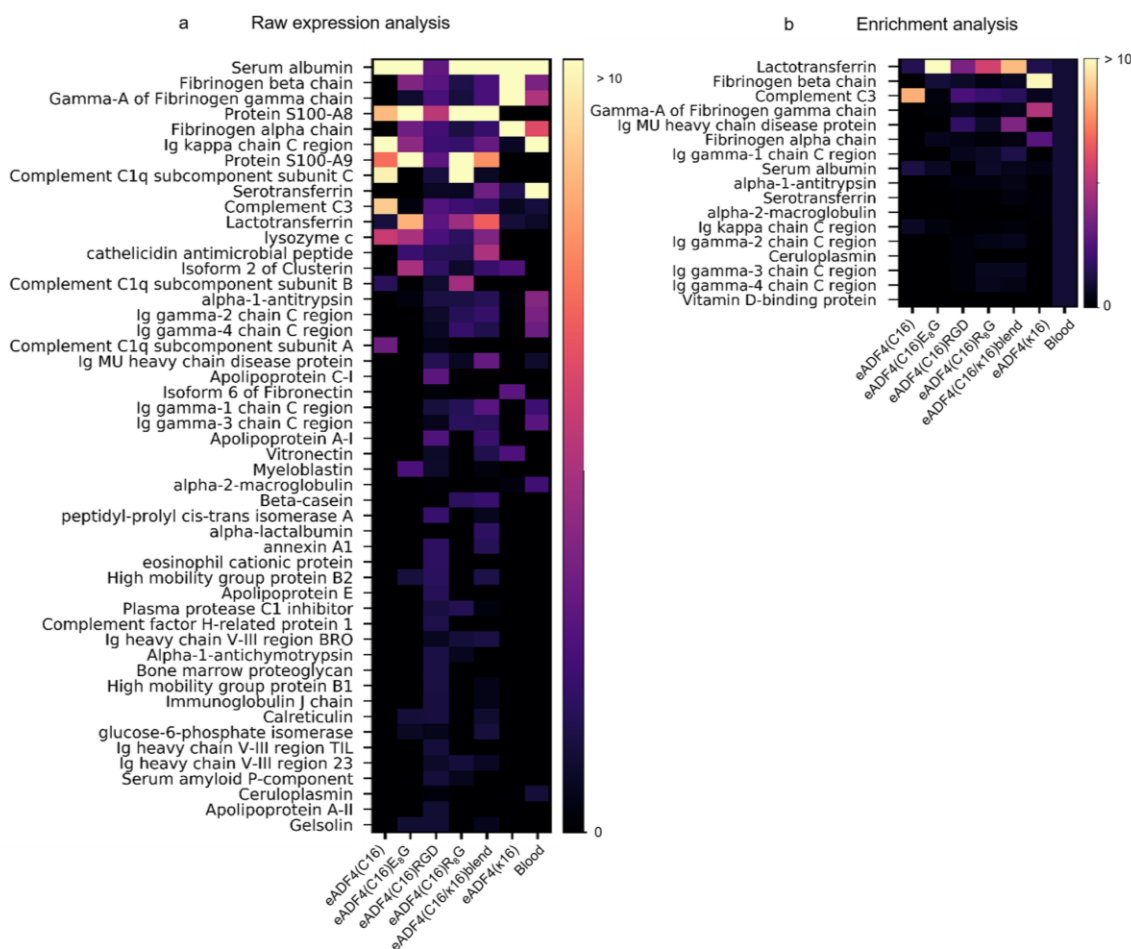


Figure 4. (a) Raw expression analysis of proteins identified in the coronae of negatively (eADF4(C16), eADF4(C16)E₈G, eADF4(C16)RGD, eADF4(C16)R₈G), close-to-neutral (eADF4(C16/κ16) blend), and positively (eADF4(κ16)) charged spider silk particles after incubation in human blood. The top 50 proteins are displayed in accordance with their maximum enrichment across all examined samples. The order is from top to bottom. (b) Enrichment analysis of proteins identified in the coronae of the analyzed spider silk particles following incubation in human blood. Proteins not found in blood were excluded. Lighter colors indicate a high abundance on a particle surface when compared to the incubation media.

polymeric particles such as surface charge and peptide tags on the composition of the biomolecular corona upon contact with blood. It may allow us to specifically tailor polymer- and especially spider silk-based materials to individual biomedical applications using genetic engineering.

EXPERIMENTAL SECTION

Materials. All chemicals were of analytic grade. They were used without further purification. High-purity water (Milli-Q water) was obtained from an inline Millipore RiOs/Origin water purification system (Millipore Corporation, Massachusetts, USA) or Milli-Q system (Billerica, MA, USA) with a resistivity of >18.2 MΩ cm. Biomolecular corona characterization was done using Dulbecco's phosphate-buffered saline (DPBS), ammonium bicarbonate (NH₄HCO₃, 99.0%), acetonitrile (ACN) (99.5%), DL-dithiothreitol (DTT, 99.0%), iodoacetamide (IAA), trypsin from porcine pancreas (proteomics grade), trifluoroacetic acid (TFA, 99.0%), and formic acid (FA, 95.0%) all purchased from Aldrich (Missouri, USA). BioRad 4–20% Mini-PROTEAN TGX stain-free protein bis-tris gels and 10X tris/glycine/sodium dodecyl sulfate running buffer were purchased

from BioRad (California, USA). LDS sample buffer (4X), NuPAGE sample reducing agent (10X), SeeBlue prestained protein standard, and SimplyBlue safe stain were purchased from Thermo Fisher (Scoresby VIC 3179, Australia). Lysis of red blood cells (RBCs) was carried out using Pharm Lyse buffer from BD Bioscience (Victoria, Australia). eADF4(C16) was purchased from AMSilk GmbH (Planegg/München, Germany). Formic acid (99.0%), methanol (p.a.), ethanol (p.a.), formaldehyde, and glutaraldehyde were purchased from Sigma-Aldrich (Sigma-Aldrich, München, Germany). All other chemicals and solvents were purchased from Roth (Karlsruhe, Germany) in analytical grade. They were used without further purification. Cover borosilicate glass were purchased from VWR (Ø = 19 mm, Karlsruhe, Germany). Polished (111) silicon wafers were purchased from CrysTec GmbH (Berlin, Germany).

Genetic Design of eADF4(C16)E₈G. The genetically engineered spider silk proteins used in this study are all variants of eADF4(C16), the genetic design of which has been described by Huemmerich et al.³⁷ Shortly, a consensus sequence of the repetitive core domain of the spiderin ADF4 of the European garden spider *Araneus diadematus* has been derived (protein sequence of module C: GSS AAAAAAAAA

SGPGGY GPENQ GPSGPGGYGPGGP), back-translated into a nucleotide sequence and repeated 16 times. Additionally, a nucleotide sequence encoding a T7 tag (peptide sequence: MASMTGGQMQMGR, spacer: GS) has been fused to the 5' end for detection purposes.³⁷ The cloning cassette developed by the authors allows the addition of tags to the recombinant proteins using a seamless cloning strategy. Here, a new silk variant, eADF4(C16)E₈G, has been created. In analogy to the tag fusion strategy presented for the recombinant silk protein eADF4(C16)RGD by Wohlrab et al.,³⁴ two synthetic oligonucleotides were annealed (E₈ tag fwd GATCCATGGGCGAAGAAGAGGAA GAGGAAGAAGAGGGCT AATGAA and E₈ tag rev AGCTTTCATTAGCCCTCTCTTTCCTTCTCTTCTTTCGCCCCA TG), encoding the E₈G peptide with the oligonucleotide design generating sticky ends mimicking a *Bam*HI and *Hind*III restriction site, suitable for integration into a pCS cloning vector, allowing fusion with the eADF4(C16) gene and further subcloning into the pET expression vector. Successful cloning was verified by sequencing.

Recombinant Spider Silk Protein Production. Spider silk proteins were produced recombinantly in *E. coli* and purified as described previously.³⁷ Shortly, bacterial cells were transformed with a pET vector containing the respective gene constructs. Gene expression was induced by addition of Isopropyl β -D-1-thiogalactopyranoside (IPTG) to the fermentation broth; cells were lysed by ultrasonication, cell debris removed by centrifugation, and the heat-stable silk proteins separated by heat denaturation of bacterial proteins. Proteins were precipitated using ammonium sulfate and lyophilized for storage.

Particle Production and Characterization. Particles were produced according to a previously described method.⁵² Spider silk proteins were dissolved in guanidinium thiocyanate and dialyzed against Tris buffer (pH 7.5), and spider silk protein concentrations were adjusted to 0.5 mg mL⁻¹ prior to particle formation, which was induced by the addition of potassium phosphate at a final concentration of 1 M (pH 7.5). eADF4(C16/ κ 16) blends were obtained by mixing eADF4(C16) and eADF4(κ 16) protein solutions in a one-to-one ratio before particle production. The particles were washed thoroughly and redispersed in water until further use. Size and zeta-potential measurements of the particles were undertaken using a Zetasizer Nano-ZS (Malvern Instruments, Malvern, UK) equipped with a He-Ne ion laser (λ = 633 nm). Particle size and size distribution were measured using dynamic light scattering. The particles' electrophoretic mobility was measured in 1/11 PBS and their zeta potential calculated from the electrophoretic mobility according to the theory of Smoluchowsky.⁶³

Spider Silk Film Formation. Cover borosilicate glass was cleaned using piranha cleaning (the glass covers were immersed in a 3:1 ratio of sulfuric acid (H₂SO₄) and 30% hydrogen peroxide for 15 min at RT). After piranha cleaning, the cover glass was rinsed with Milli-Q water and 100% ethanol (EtOH) and air-dried. eADF4(C16) and eADF4(κ 16) were dissolved in formic acid at desired concentrations (1 mg cm⁻²) and were overhead shaken for 30 min. Afterward, the silk solutions were centrifuged to remove aggregates (14 437 g, RT, 15 min). The silk solutions were cast on cover borosilicate glass at 1 mg cm⁻² on a balanced plate and dried overnight at ambient conditions. For post-treatment, the samples were placed in a methanol-saturated atmosphere in a desiccator overnight.

Incubation of Spider Silk Materials in Human Whole Blood. Blood was collected from a healthy human volunteer and stored in sodium heparin vacuettes (Greiner Bio-One). Informed consent was obtained in compliance with the University of Melbourne human ethics approval 1443420 and the Australian National Health and Medical Research Council Statement on Ethical Conduct in Human Research or ethics approval BASEC No. PB 2016-00816 from the local ethics committee, St. Gallen, Switzerland.

Spider silk particles (10 μ L of 1 mg mL⁻¹ spider silk particles dispersed in DPBS) were immersed in human whole blood (500 μ L) for 1 h at 37 °C (Eppendorf Thermomixer Comfort, Germany). RBC lysis was performed using Pharm Lyse buffer at 20 \times blood volume and topped up to 4 mL using 1 \times PBS before pelleting the white blood

cells (WBC) and particles (500 g, 40 min). Unbound and loosely bound proteins were removed by washing the particles and WBCs followed by multiple centrifugation (300 g, 3 min) and resuspension steps (DPBS, 3 \times), followed by washing steps without redispersion (in DPBS (3 \times)) to remove the WBCs.

For SEM analysis, recombinant spider silk particles were resuspended in water at a concentration of 1 mg mL⁻¹, and 100 μ L of this suspension was cast on a 0.5 cm² silica wafer surface and air-dried. After immobilization of the particles to the silica wafer surface, the samples were sterilized with 70% EtOH for 2 min in sterile 12-well plates and air-dried. Spider silk films were prepared as depicted above and then placed in well plates. Blood was collected into S-monovettes with a heparin concentration of 0.43 IU/mL and used within 1 h after withdrawal. Five hundred microliters per sample of the blood was transferred into well plates on top of the substrate and incubated with the immobilized spider silk particles or films (10 rpm, RT, 35 min.). After incubation, the blood was removed from the samples, and the samples were fixed with Karnovsky fixing solution and dehydrated with EtOH (50, 70, 80, 90, and 100%), dried overnight, and sputtered with 10 nm gold prior to SEM analysis.

SDS-PAGE and sample preparation was done as published previously.¹⁰

Mass Spectrometry, Protein Identification, and Proteomics Data Processing. Sample preparation, protein identification via liquid chromatography coupled with tandem mass spectrometry (LC-MS/MS), protein identification, and data processing were carried out as described recently.^{10,64} Briefly, in-gel digested samples were analyzed by LC-MS/MS using Q-Exactive plus mass spectrometer (Thermo Scientific). The spectrometer was equipped with a nanoflow reversed-phase-HPLC (Ultimate 3000 RSLC, Dionex). The nano-LC system had an Acclaim Pepmap nanotrap column (Dionex C18, 100 \AA , 75 μ m \times 2 cm) and an Acclaim Pepmap RSLC analytical column (Dionex C18, 100 \AA , 75 μ m \times 50 cm). All spectra were measured in positive mode using full scan MS spectra scanning from m/z 375–1400 at 70 000 resolution with AGC target of 3e⁶ with maximum accumulation time of 50 ms. Lockmass of 445.120024 was used. The 15 most intense peptide ions with charge states $\geq 2-5$ were isolated with an isolation window of 1.2 m/z and fragmented with normalized collision energy of 30 at 17500 resolution. Data were analyzed using the PatternLab for Proteomics 4.0 suite including the Comet search engine.⁶⁵ Searches and filtering of peptide spectrum matches and protein quantification were performed as published previously.¹⁰

AUTHOR INFORMATION

Corresponding Authors

Frank Caruso – ARC Centre of Excellence in Convergent Bio-Nano Science and Technology and the Department of Chemical Engineering, The University of Melbourne, Victoria 3010, Australia; orcid.org/0000-0002-0197-497X; Email: fcarus@unimelb.edu.au

Thomas Scheibel – Lehrstuhl für Biomaterialien, Bayreuther Zentrum für Kolloide und Grenzflächen (BZKG), Bayreuther Zentrum für Molekulare Biowissenschaften (BZMB), Bayreuther Materialzentrum (BayMAT), and Bayerisches Polymerinstitut (BPI), Universität Bayreuth, Bayreuth 95447, Germany; orcid.org/0000-0002-0457-2423; Email: thomas.scheibel@bm.uni-bayreuth.de

Authors

Alessia C. G. Weiss – ARC Centre of Excellence in Convergent Bio-Nano Science and Technology and the Department of Chemical Engineering, The University of Melbourne, Victoria 3010, Australia

Heike M. Herold – Lehrstuhl für Biomaterialien, Universität Bayreuth, Bayreuth 95447, Germany

Sarah Lentz – Lehrstuhl für Biomaterialien, Universität Bayreuth, Bayreuth 95447, Germany

Matthew Faria – ARC Centre of Excellence in Convergent Bio-Nano Science and Technology and Systems Biology Laboratory, School of Mathematics and Statistics, and the Department of Biomedical Engineering, The University of Melbourne, Parkville, Victoria 3052, Australia

Quinn A. Besford – Leibniz-Institute für Polymerforschung, Dresden 01069, Germany; orcid.org/0000-0002-1779-9176

Ching-Seng Ang – Bio21 Molecular Science and Biotechnology Institute, The University of Melbourne, Parkville, Victoria 3010, Australia

Complete contact information is available at:
<https://pubs.acs.org/10.1021/acsami.0c06344>

Author Contributions

†A.C.G.W. and H.M.H. contributed equally to this work. The design of the experiments was performed by A.C.G.W., H.M.H., S.L., F.C., and T.S.. Preparation of the paper was performed by A.C.G.W., H.M.H., and S.L. H.M.H. and S.L. prepared and characterized the spider silk particles. A.C.G.W. performed characterization via SDS-PAGE and all mass spectrometry studies and the respective data analysis. S.L. produced the spider silk films and performed the blood coagulation assays. Q.A.B. performed statistical analysis of the blood assay data. M.F. assisted with analysis of the mass spectrometry data. C.-S.A. performed mass spectrometry experiments and protein identification. T.S. and F.C. supervised the studies and edited the paper.

Notes

The authors declare the following competing financial interest(s): T.S. is co-founder and share-holder of AMSilk GmbH, Germany.

ACKNOWLEDGMENTS

This research was conducted and funded by the Australian Research Council (ARC) Centre of Excellence in Convergent Bio-Nano Science and Technology (project CE140100036) (F.C.) and the Deutsche Forschungsgemeinschaft (DFG, German Research Foundation) through SFB 840 subproject A8 (T.S.). F.C. acknowledges the award of an NHMRC Senior Principal Research Fellowship (GNT1135806). A.C.G.W. acknowledges funding from The University of Melbourne through Melbourne International Research Scholarships. A.C.G.W., H.M.H., S.L., F.C. and T.S. acknowledge funding from the German Academic Exchange Service (DAAD) through its thematic network Bayreuth-Melbourne Colloid/Polymer Network sponsored from funds of the Federal Ministry of Education and Research (BMBF). We thank Markus Rottmar and Eike Müller for help with collecting blood samples and further thank Vanessa Neubauer for fermentation and purification of the protein eADF4(C16)_{E₃}G.

REFERENCES

- (1) Giulimondi, F.; Digiacomo, L.; Pozzi, D.; Palchetti, S.; Vulpis, E.; Capriotti, A. L.; Chiozzi, R. Z.; Lagana, A.; Amenitsch, H.; Masuelli, L.; Peruzzi, G.; Mahmoudi, M.; Screpanti, I.; Zingoni, A.; Caracciolo, G. Interplay of Protein Corona and Immune Cells Controls Blood Residency of Liposomes. *Nat. Commun.* **2019**, *10*, 3686.
- (2) Hadjideometriou, M.; Kostarelos, K. Evolution of the Nanoparticle Corona. *Nat. Nanotechnol.* **2017**, *12*, 288–290.
- (3) Weiss, A. C. G.; Kempe, K.; Förster, S.; Caruso, F. Microfluidic Examination of the “Hard” Biomolecular Corona Formed on

Engineered Particles in Different Biological Milieu. *Biomacromolecules* **2018**, *19*, 2580–2594.

- (4) Fadeel, B. Hide and Seek: Nanomaterial Interactions with the Immune System. *Front. Immunol.* **2019**, *10*, 133.
- (5) Moghimi, S. M.; Hunter, A. C.; Murray, J. C. Long-Circulating and Target-Specific Nanoparticles: Theory to Practice. *Pharmacol. Rev.* **2001**, *53*, 283–318.
- (6) Milani, S.; Baldelli Bombelli, F.; Pitek, A. S.; Dawson, K. A.; Rädler, J. Reversible Versus Irreversible Binding of Transferrin to Polystyrene Nanoparticles: Soft and Hard Corona. *ACS Nano* **2012**, *6*, 2532–2541.
- (7) Docter, D.; Westmeier, D.; Markiewicz, M.; Stolte, S.; Knauer, S. K.; Stauber, R. H. The Nanoparticle Biomolecule Corona: Lessons Learned – Challenge Accepted? *Chem. Soc. Rev.* **2015**, *44*, 6094–6121.
- (8) García-Álvarez, R.; Hadjideometriou, M.; Sánchez-Iglesias, A.; Liz-Marzán, L. M.; Kostarelos, K. In Vivo Formation of Protein Corona on Gold Nanoparticles. The Effect of Their Size and Shape. *Nanoscale* **2018**, *10*, 1256–1264.
- (9) Walkey, C. D.; Olsen, J. B.; Guo, H.; Emili, A.; Chan, W. C. W. Nanoparticle Size and Surface Chemistry Determine Serum Protein Adsorption and Macrophage Uptake. *J. Am. Chem. Soc.* **2012**, *134*, 2139–2147.
- (10) Weiss, A. C. G.; Kelly, H. G.; Faria, M.; Besford, Q. A.; Wheatley, A. K.; Ang, C.-S.; Crampin, E. J.; Caruso, F.; Kent, S. J. Link between Low-Fouling and Stealth: A Whole Blood Biomolecular Corona and Cellular Association Analysis on Nanoengineered Particles. *ACS Nano* **2019**, *13*, 4980–4991.
- (11) Tenzer, S.; Docter, D.; Rosfa, S.; Wlodarski, A.; Kuharev, J.; Rekić, A.; Knauer, S. K.; Bantz, C.; Nawroth, T.; Bier, C.; Sirirattanapan, J.; Mann, W.; Treuel, L.; Zellner, R.; Maskos, M.; Schild, H.; Stauber, R. H. Nanoparticle Size Is a Critical Physicochemical Determinant of the Human Blood Plasma Corona: A Comprehensive Quantitative Proteomic Analysis. *ACS Nano* **2011**, *5*, 7155–7167.
- (12) Wang, B.; Blin, T.; Kaminen, A.; Ge, X.; Pilkington, E. H.; Quinn, J. F.; Whittaker, M. R.; Davis, T. P.; Ke, P. C.; Ding, F. Brushed Polyethylene Glycol and Phosphorylcholine for Grafting Nanoparticles against Protein Binding. *Polym. Chem.* **2016**, *7*, 6875–6879.
- (13) García, K. P.; Zarschler, K.; Barbaro, L.; Barreto, J. A.; O'Malley, W.; Spiccia, L.; Stephan, H.; Graham, B. Zwitterionic-Coated “Stealth” Nanoparticles for Biomedical Applications: Recent Advances in Countering Biomolecular Corona Formation and Uptake by the Mononuclear Phagocyte System. *Small* **2014**, *10*, 2516–2529.
- (14) Riley, K. R.; Sims, C. M.; Wood, I. T.; Vanderah, D. J.; Walker, M. L. Short-Chained Oligo(Ethylene Oxide)-Functionalized Gold Nanoparticles: Realization of Significant Protein Resistance. *Anal. Bioanal. Chem.* **2018**, *410*, 145–154.
- (15) Gossmann, R.; Fahrlander, E.; Hummel, M.; Mulac, D.; Brockmeyer, J.; Langer, K. Comparative Examination of Adsorption of Serum Proteins on Hsa- and Plga-Based Nanoparticles Using Sds-Page and Lc-MS. *Eur. J. Pharm. Biopharm.* **2015**, *93*, 80–87.
- (16) Shreffler, J. W.; Pullan, J. E.; Dailey, K. M.; Mallik, S.; Brooks, A. E. Overcoming Hurdles in Nanoparticle Clinical Translation: The Influence of Experimental Design and Surface Modification. *Int. J. Mol. Sci.* **2019**, *20*, 6056.
- (17) Nienhaus, K.; Nienhaus, G. U. Towards a Molecular-Level Understanding of the Protein Corona around Nanoparticles – Recent Advances and Persisting Challenges. *Curr. Opin. Biomed. Eng.* **2019**, *10*, 11–22.
- (18) Mahmoudi, M.; Bertrand, N.; Zope, H.; Farokhzad, O. C. Emerging Understanding of the Protein Corona at the Nano-Bio Interfaces. *Nano Today* **2016**, *11*, 817–832.
- (19) Foroozandeh, P.; Aziz, A. A. Merging Worlds of Nanomaterials and Biological Environment: Factors Governing Protein Corona Formation on Nanoparticles and Its Biological Consequences. *Nanoscale Res. Lett.* **2015**, *10*, 221.

24641

<https://dx.doi.org/10.1021/acsami.0c06344>
ACS Appl. Mater. Interfaces **2020**, *12*, 24635–24643

- (20) Sakulkhu, U.; Mahmoudi, M.; Maurizi, L.; Salaklang, J.; Hofmann, H. Protein Corona Composition of Superparamagnetic Iron Oxide Nanoparticles with Various Physico-Chemical Properties and Coatings. *Sci. Rep.* **2015**, *4*, 5020.
- (21) Leal-Egana, A.; Scheibel, T. Silk-Based Materials for Biomedical Applications. *Biotechnol. Appl. Biochem.* **2010**, *55*, 155–167.
- (22) Müller-Herrmann, S.; Scheibel, T. Enzymatic Degradation of Films, Particles, and Nonwoven Meshes Made of a Recombinant Spider Silk Protein. *ACS Biomater. Sci. Eng.* **2015**, *1*, 247–259.
- (23) Kumari, S.; Bargel, H.; Anby, M. U.; Lafargue, D.; Scheibel, T. Recombinant Spider Silk Hydrogels for Sustained Release of Biologicals. *ACS Biomater. Sci. Eng.* **2018**, *4*, 1750–1759.
- (24) Spiess, K.; Lammel, A.; Scheibel, T. Recombinant Spider Silk Proteins for Applications in Biomaterials. *Macromol. Biosci.* **2010**, *10*, 998–1007.
- (25) Heidebrecht, A.; Eisoldt, L.; Diehl, J.; Schmidt, A.; Geffers, M.; Lang, G.; Scheibel, T. Biomimetic Fibers Made of Recombinant Spidroins with the Same Toughness as Natural Spider Silk. *Adv. Mater.* **2015**, *27*, 2189–2194.
- (26) Lang, G.; Jokisch, S.; Scheibel, T. Air Filter Devices Including Nonwoven Meshes of Electrospun Recombinant Spider Silk Proteins. *J. Visualized Exp.* **2013**, No. e50492.
- (27) Schacht, K.; Scheibel, T. Controlled Hydrogel Formation of a Recombinant Spider Silk Protein. *Biomacromolecules* **2011**, *12*, 2488–2495.
- (28) Spieß, K.; Wohlrab, S.; Scheibel, T. Structural Characterization and Functionalization of Engineered Spider Silk Films. *Soft Matter* **2010**, *6*, 4168–4174.
- (29) Slotta, U. K.; Rammensee, S.; Gorb, S.; Scheibel, T. An Engineered Spider Silk Protein Forms Microspheres. *Angew. Chem., Int. Ed.* **2008**, *47*, 4592–4594.
- (30) Lammel, A.; Schwab, M.; Hofer, M.; Winter, G.; Scheibel, T. Recombinant Spider Silk Particles as Drug Delivery Vehicles. *Biomaterials* **2011**, *32*, 2233–2240.
- (31) Hofer, M.; Winter, G.; Myschik, J. Recombinant Spider Silk Particles for Controlled Delivery of Protein Drugs. *Biomaterials* **2012**, *33*, 1554–1562.
- (32) Mickoleit, F.; Borkner, C. B.; Toro-Nahuelpan, M.; Herold, H. M.; Maier, D. S.; Plitzko, J. M.; Scheibel, T.; Schüler, D. In Vivo Coating of Bacterial Magnetic Nanoparticles by Magnetosome Expression of Spider Silk-Inspired Peptides. *Biomacromolecules* **2018**, *19*, 962–972.
- (33) Lucke, M.; Mottas, L.; Herbst, T.; Hotz, C.; Römer, L.; Schierling, M.; Herold, H. M.; Slotta, U.; Spinetti, T.; Scheibel, T.; Winter, G.; Bourquin, C.; Engert, J. Engineered Hybrid Spider Silk Particles as Delivery System for Peptide Vaccines. *Biomaterials* **2018**, *172*, 105–115.
- (34) Wohlrab, S.; Müller, S.; Schmidt, A.; Neubauer, S.; Kessler, H.; Leal-Egana, A.; Scheibel, T. Cell Adhesion and Proliferation on Rgd-Modified Recombinant Spider Silk Proteins. *Biomaterials* **2012**, *33*, 6650–6659.
- (35) Petzold, J.; Aigner, T. B.; Touska, F.; Zimmermann, K.; Scheibel, T.; Engel, F. B. Surface Features of Recombinant Spider Silk Protein eADF4(K16)-Made Materials Are Well-Suited for Cardiac Tissue Engineering. *Adv. Funct. Mater.* **2017**, *27*, 1701427.
- (36) Zeplin, P. H.; Maksimovikj, N. C.; Jordan, M. C.; Nickel, J.; Lang, G.; Leimer, A. H.; Roemer, L.; Scheibel, T. Spider Silk Coatings as a Bioshield to Reduce Periprosthetic Fibrous Capsule Formation. *Adv. Funct. Mater.* **2014**, *24*, 2658–2666.
- (37) Hümmerich, D.; Helsen, C. W.; Quedzuweit, S.; Oschmann, J.; Rudolph, R.; Scheibel, T. Primary Structure Elements of Spider Dragline Silks and Their Contribution to Protein Solubility. *Biochemistry* **2004**, *43*, 13604–13612.
- (38) Schierling, M. B.; Doblhofer, E.; Scheibel, T. Cellular Uptake of Drug Loaded Spider Silk Particles. *Biomater. Sci.* **2016**, *4*, 1515–1523.
- (39) Doblhofer, E.; Scheibel, T. Engineering of Recombinant Spider Silk Proteins Allows Defined Uptake and Release of Substances. *J. Pharm. Sci.* **2015**, *104*, 988–994.
- (40) Elsner, M. B.; Herold, H. M.; Müller-Herrmann, S.; Bargel, H.; Scheibel, T. Enhanced Cellular Uptake of Engineered Spider Silk Particles. *Biomater. Sci.* **2015**, *3*, 543–551.
- (41) Blasi, B.; D'alessandro, A.; Ramundo, N.; Zolla, L. Red Blood Cell Storage and Cell Morphology. *Transfusion medicine* **2012**, *22*, 90–96.
- (42) Markl, J.; Sadava, D.; Hillis, D. M.; Heller, H. C.; Hacker, S. D. Kreislaufsysteme. In *Purves Biologie*; Markl, J., Ed. Springer: Berlin, 2019; pp 1497–1529.
- (43) Smith, G. F. Fibrinogen-Fibrin Conversion. The Mechanism of Fibrin-Polymer Formation in Solution. *Biochem. J.* **1980**, *185*, 1–11.
- (44) Blombäck, B.; Hessel, B.; Hogg, D.; Therkildsen, L. A Two-Step Fibrinogen–Fibrin Transition in Blood Coagulation. *Nature* **1978**, *275*, 501–505.
- (45) Paoletti, A. C.; Parmely, T. J.; Tomomori-Sato, C.; Sato, S.; Zhu, D.; Conaway, R. C.; Conaway, J. W.; Florens, L.; Washburn, M. P. Quantitative Proteomic Analysis of Distinct Mammalian Mediator Complexes Using Normalized Spectral Abundance Factors. *Proc. Natl. Acad. Sci. U. S. A.* **2006**, *103*, 18928–18933.
- (46) Merle, N. S.; Noe, R.; Halbwachs-Mecarelli, L.; Fremeaux-Bacchi, V.; Roumenina, L. T. Complement System Part II: Role in Immunity. *Front. Immunol.* **2015**, *6*, 257.
- (47) Frank, M. M.; Fries, L. F. The Role of Complement in Inflammation and Phagocytosis. *Immunol. Today* **1991**, *12*, 322–326.
- (48) Xu, X.; Ho, W.; Zhang, X.; Bertrand, N.; Farokhzad, O. Cancer Nanomedicine: From Targeted Delivery to Combination Therapy. *Trends Mol. Med.* **2015**, *21*, 223–232.
- (49) Mornet, S.; Vasseur, S.; Grasset, F.; Duguet, E. Magnetic Nanoparticle Design for Medical Diagnosis and Therapy. *J. Mater. Chem.* **2004**, *14*, 2161–2175.
- (50) Frank, M. M.; Fries, L. F. The Role of Complement in Inflammation and Phagocytosis. *Immunol. Today* **1991**, *12*, 322–326.
- (51) Simon, J.; Müller, L. K.; Kokkinopoulou, M.; Lieberwirth, I.; Morsbach, S.; Landfester, K.; Mailänder, V. Exploiting the Biomolecular Corona: Pre-Coating of Nanoparticles Enables Controlled Cellular Interactions. *Nanoscale* **2018**, *10*, 10731–10739.
- (52) Mahmoudi, M.; Lynch, I.; Ejtehadi, M. R.; Monopoli, M. P.; Bombelli, F. B.; Laurent, S. Protein-Nanoparticle Interactions: Opportunities and Challenges. *Chem. Rev.* **2011**, *111*, 5610–5637.
- (53) Quach, Q. H.; Kah, J. C. Y. Non-Specific Adsorption of Complement Proteins Affects Complement Activation Pathways of Gold Nanomaterials. *Nanotoxicology* **2017**, *11*, 382.
- (54) Tonigold, M.; Simon, J.; Estupiñán, D.; Kokkinopoulou, M.; Reinholz, J.; Kintzel, U.; Kaltbeitzel, A.; Renz, P.; Domogalla, M. P.; Steinbrink, K.; Lieberwirth, I.; Crespy, D.; Landfester, K.; Mailänder, V. Pre-Adsorption of Antibodies Enables Targeting of Nanocarriers Despite a Biomolecular Corona. *Nat. Nanotechnol.* **2018**, *13*, 862–875.
- (55) Quach, Q. H.; Kah, J. C. Y. Non-Specific Adsorption of Complement Proteins Affects Complement Activation Pathways of Gold Nanomaterials. *Nanotoxicology* **2017**, *11*, 1–39.
- (56) Cai, R.; Chen, C. Protein Corona in Vivo: Dynamic Complement Proteins-Mediated Opsonization and Immune Modulation. *Sci. Bull.* **2017**, *62*, 976–977.
- (57) Guan, J.; Shen, Q.; Zhang, Z.; Jiang, Z.; Yang, Y.; Lou, M.; Qian, J.; Lu, W.; Zhan, C. Enhanced Immunocompatibility of Ligand-Targeted Liposomes by Attenuating Natural Igm Absorption. *Nat. Commun.* **2018**, *9*, 2982.
- (58) Schlothauer, T.; Herter, S.; Koller, C. F.; Grau-Richards, S.; Steinhart, V.; Spick, C.; Kubbies, M.; Klein, C.; Umaña, P.; Mössner, E. Novel Human Igg1 and Igg4 Fc-Engineered Antibodies with Completely Abolished Immune Effector Functions. *Protein Eng., Des. Sel.* **2016**, *29*, 457–466.
- (59) Fantl, P.; Ward, H. A. Molecular Weight of Human Fibrinogen Derived from Phosphorus Determinations. *Biochem. J.* **1965**, *96*, 886–889.
- (60) Besser, M. W.; MacDonald, S. G. Acquired Hypofibrinogenemia: Current Perspectives. *J. Blood Med.* **2016**, *7*, 217–225.

(61) Sakulkhu, U.; Maurizi, L.; Mahmoudi, M.; Motazacker, M.; Vries, M.; Gramoun, A.; Ollivier Beuzelin, M. G.; Vallée, J. P.; Rezaee, F.; Hofmann, H. Ex Situ Evaluation of the Composition of Protein Corona of Intravenously Injected Superparamagnetic Nanoparticles in Rats. *Nanoscale* **2014**, *6*, 11439–11450.

(62) Lammel, A.; Schwab, M.; Slotta, U.; Winter, G.; Scheibel, T. Processing Conditions for the Formation of Spider Silk Microspheres. *ChemSusChem* **2008**, *1*, 413–416.

(63) Hunter, R. J. *Zeta Potential in Colloid Science: Principles and Applications*; Academic Press: London, 1981.

(64) Weiss, A. C. G.; Kempe, K.; Förster, S.; Caruso, F. Microfluidic Examination of the "Hard" Biomolecular Corona Formed on Engineered Particles in Different Biological Milieu. *Biomacromolecules* **2018**, *19*, 2580–2594.

(65) Carvalho, P. C.; Lima, D. B.; Leprevost, F. V.; Santos, M. D. M.; Fischer, J. S. G.; Aquino, P. F.; Moresco, J. J.; Yates, J. R.; Barbosa, V. C. PatternLab for Proteomics 4.0: A One-stop Shop for Analyzing Shotgun Proteomic Data. *Nat. Protoc.* **2016**, *11*, 102–117.

Part III - Chapter 3 – Selective Topography Directed Cell Adhesion on Spider Silk Surfaces

Part III – Chapter 3.1 - Chapter perspective and contribution

This chapter is one of my first author papers.

Here I designed and manufactured the photolithographic masters and produced the patterned recombinant spider silk films I performed the physicochemical analysis of the used recombinant spider silk films. The cell culture experiments and the microscopical analysis were performed by Vanessa Trossmann and myself. I performed the SEM analysis of the patterned films with and without cells. The manuscript and the visualization were done by Vanessa Trossmann and myself. Together with Vanessa Trossmann and Thomas Scheibel, we conceptualized the study. All authors revised and approved the final version of the manuscript.

This manuscript is submitted to *Advanced Functional Interfaces* and currently under review.

Part III – Chapter 3.2 Full paper

WILEY-VCH

Selective Topography Directed Cell

Adhesion on Spider Silk Surfaces

*Sarah Lentz[‡], Vanessa Tanja Trossmann[‡] and Thomas Scheibel**

Sarah Lentz[‡], Vanessa T. Trossmann[‡]

Lehrstuhl Biomaterialien, Fakultät für Ingenieurwissenschaften, Universität Bayreuth, Prof-
Rüdiger-Bormann-Str. 1, 95447 Bayreuth, Germany

Thomas Scheibel*

Bayerisches Polymerinstitut (BPI), Bayreuther Zentrum für Kolloide und Grenzflächen
(BZKG), Bayreuther Zentrum für Molekulare Biowissenschaften (BZMB), Bayreuther
Materialzentrum (BayMAT), Universität Bayreuth, Universitätsstr. 30, 95447 Bayreuth,
Germany

Lehrstuhl Biomaterialien, Fakultät für Ingenieurwissenschaften, Universität Bayreuth, Prof-
Rüdiger-Bormann-Str. 1, 95447 Bayreuth, Germany

E-Mail: thomas.scheibel@bm.uni-bayreuth.de

Keywords: bioselectivity; contact guidance; correlative microscopy; gradient materials;
geometric confinement

Abstract

For tissue engineering applications, guided cell interaction with a biomaterial surface is one essential feature, since in natural tissue cells constantly interact with their extracellular matrix, which provides different topographical, mechanical and biochemical stimuli. Therefore, the introduction of topographical surface features is one promising approach to direct material-cell interactions. In this study, maskless lithography and soft lithographic methods were used to produce recombinant spider silk films with size gradient patterns, including grooves, circles, squares, triangles and stars, to enhance specific cell attachment. The influence of surface features on cell behavior was analyzed using eight different cell lines. It could be shown that surface indentations provide cellular attachment sites and guiding structures for restructuring, aligning, and adopting cell morphology, with a relation of cell to feature size for some of the cell lines investigated. Therefore, specific topographical surface modifications could be used to guide selective cell adhesion, allowing the generation of tissue-specifically modified implant surfaces in the future.

1. Introduction

The interactions of a biomaterial surface with the surrounding biological environment are decisive for the successful performance of a biomaterial.^[1] The natural surrounding of cells exposes various external stimuli, including topographical surface features, mechanical properties, or biochemical factors that depend on the composition of the extracellular matrix (ECM).^[2] Thus, surface modifications have been investigated to trigger cellular responses, including attachment and alignment of cells for advanced tissue integration.^[3] One focus has been on engineering the biomaterial implant surface with topographical features to influence

WILEY-VCH

biological responses after cell-material contact.^[1c, 4] It is well known that substrate topography triggers several important cellular responses after the first cell-surface interaction, such as adhesion, migration, differentiation, morphological changes, and intracellular signalling of cells.^[1c, 3a, 4d-f, 5] It must be emphasized that anisotropic topographical surface structures in the nanometer as well as in the low micrometer range are perceived by the cells and can cause diverse cellular responses.^[4d, 5b, 5c, 6] Although surface topography can influence cell adhesion on material surfaces, the appropriate cell response is highly dependent on the respective cell type, and the dimensions and nature of the topographical surface features also play a decisive role.^[4e] Thus, for developing biomaterials and implants for tissue engineering applications, it is crucial to know the requirements of tissue-specific cells of the target tissue to adapt the surface topography.^[4d-f]

Several studies could show that cells can recognize and sense different surface patterns in various dimensions, sizes, and shapes and could bridge smaller patterns. Interestingly, F-actin assembly correlated with the respective surface pattern, e.g., aligned with grooves or on pillar structures.^[3a, 4d, 6b, 7] One systematic study analyzed the organization of the cytoskeleton as well as the connection of adhesion forces and surface topography using AFM-based single-cell force spectroscopy. It was concluded that micro-structured surfaces decreased early and enhanced long-term cell adhesion, as adhesion forces increased continuously over time, while nanotopographical surfaces only supported initial cell attachment (< 1h), connected to a different organization of intracellular components and spreading behavior of the cells.^[6b] A surface-modified chip (TopoChip) was developed and contained over 2000 different microtopographies on its surface based on circles, triangles, and rectangles to identify specific topographies influencing differentiation of tonsil-derived stromal cells^[8], tenocytes^[9], or primary human keratinocytes.^[10] Structural features and guiding topographies on a biomaterial surface, such as grooves or pores, could mimic the structural, fibrillar composition and

WILEY-VCH

landscape of the natural extracellular environment leading to a controlled cellular interaction and guidance.^[11] In this context, the term contact guidance was used for the first time by P. Weiss, which means the orientation and direction of cell continuation and migration in response to the shape and topography of the substrate's surface.^[12]

On nanopatterned substrates, fibroblasts can respond to the curvature of the underlying substrate and increase their spreading area while reducing their polarization (aspect ratio). However, internal components of the cytoskeleton, such as stress fibers, strongly align along with the underlying topographical pattern.^[13] Microtubules have been shown to be the first cellular component involved in cellular orientation along a grooved surface structure located at the bottom of grooves (first 20 min), while aligned actin microfilament bundles were observed afterwards (40-60 min) at the wall-ridge edges leading to aligned focal contacts after around 3h.^[14] Thus, a biomaterial surface could be modified to become cell-attractive, also known as cytophilic, or cell-repellent, also denoted as cytophobic, by adopting the respective surface topography to trigger the biological response of cells.^[15]

In the present study, flat recombinant spider silk films, which did per se not support cell adhesion^[16], were modified by applying and introducing different shaped and sized surface features using a maskless lithographically produced template to enhance cell interaction. Implant materials based on spider silk are highly biocompatible and do not cause any inflammatory response or foreign body reaction.^[16b, 17] One example are materials made of the recombinant spider silk protein eADF4(C16), which was engineered on the consensus sequence of the *Araneus diadematus* fibroin 4, a spidroin of the European garden spider's dragline silk.^[18] Since eADF4(C16) lacks any cell-binding motifs, cell interaction with flat eADF4(C16) films or coatings is very low.^[16] Furthermore, catheters coated with an eADF4(C16) spider silk protein layer displayed minimal cell interaction.^[16d]

WILEY-VCH

The here introduced features showed an area in the micrometer range, while the height was in the nanometer range. The modification with introduced differently shaped and sized surface patterns supported attachment, morphological restructuring, and alignment of various cell lines on spider silk surfaces.

2. Results and discussion

2.1 Topography modification of recombinant spider silk films

Recombinant eADF4(C16) spider silk scaffolds exhibit promising properties for usage in regenerative and biomedical applications, including high biocompatibility^[17b], slow biodegradation^[19], and repellence against microbes^[20]. However, cell adhesion on unmodified eADF4(C16)-based scaffolds is low since eADF4(C16) lacks any cell interaction sites^[16]. Here, spider silk films were modified by applying topographical surface features, namely indentations or protrusions, to enhance cellular interactions because several cellular responses, including adhesion, spreading, morphological restructuring, migration, and intracellular signaling, are influenced and guided by topographical surface patterns after the first contact of a cell with a material surface.^[1c, 3a, 4d-f, 5] Maskless photolithography was used to fabricate a template (**Figure S1**), for which a glass slide was covered with a photoresist and a digital mask showing the patterns of interest was designed. One digital mask showing size gradients of different structures (circles, hearts, triangles, squares, hexagons, stars, crosses, and grooves) is exemplary shown in **Figure S2**. Such a digital mask can be used for the generation of indentations as well as protrusions on the film surface. The patterns exhibited sizes between around 40 μm and 100 μm and grooves comprised widths from 6 μm to 57 μm . After successful template generation, they were covered with polydimethylsiloxane (PDMS) and cured to generate patterned stamps to be used for subsequent film casting. Since PDMS exhibits

WILEY-VCH

high wear resistance and shows minimal surface interactions due to its chemical inertness, it was ideally suited as a stamp material.^[21] After examining existing literature, it could be concluded that lithography approaches and PDMS molding represent standard, versatile, adjustable, cheap, and high throughput fabrication techniques to generate topographically modified substrate surfaces for cell-contacting surfaces.^[3b, 3c, 4f, 5b, 22]

For patterned film generation, spider silk solutions were cast on ozone pre-treated polystyrene surfaces, and the appropriate stamps were put on top. After solvent evaporation, the stamps could be removed easily due to the minimized interaction of PDMS with the spider silk surface. The PDMS stamps, the maskless photolithographically produced templates, as well as the received patterned spider silk films were analyzed using light microscopy. The generated structures showed good and uniform shape fidelity for all three surfaces with sharp corners and pronounced edges, which were homogeneously distributed over the whole surface. **Figure 1A** displays light microscopy images of eADF4(C16) spider silk films containing gradients of surface indentations. It is visible that the groove gradient on the film surfaces exhibited different widths for ridges and grooves. For the differently shaped topographies, the size gradient of the different patterns was independent of their geometry. The resulting surface features exhibited dimensions in the predicted range of the digital mask. However, the resolution maximum of the lithography approach was reached because the smaller the individual structures became, the less precisely the edges and corners were pronounced, and the shape increasingly approached a circle. Nevertheless, the resolution of the obtained surface patterns on the films did not deteriorate even after repeated usage of the same PDMS stamp or after producing new PDMS stamps from the lithographically produced template. Thus, it is worth mentioning that both, the coated glass slides and the PDMS stamp, can be reused several times (at least up to ten times). Furthermore, this method allows the design and production of very diverse surface structures exhibiting different pattern sizes, heights, and shapes.

WILEY-VCH

Atomic force microscopy (AFM) using tapping mode verified that the patterns had an area size in the micrometer range while the height was in the nanometer range (**Figure 1B**). The average height of each indentation was determined by analyzing several areas of different patterns, revealing that all indentations exhibited similar heights between 100 nm and 125 nm (**Figure SI 3**). Since cells are able to perceive nanometer- and micrometer-scaled topographical surface features, these topographical surface features should stimulate diverse cellular reactions.^[4d, 5b, 5c, 6]

To investigate the influence of the different spider silk film surface topographies on surface hydrophobicity, water contact angles (WCA) were determined using the sessile drop method, and polystyrene (PS) was used as a control (**Figure 1C**). In general, films cast with a PDMS stamp on top showed a higher WCA (above 80°) than films produced upon evaporation of the solvent without a PDMS stamp (50-60°). The high hydrophobicity of PDMS stamps^[23] led to an increase in surface hydrophobicity of spider silk films due to the surface exposure of hydrophobic residues of the silk protein. Interestingly, for PDMS cast films, flat surfaces and surfaces exhibiting indentations or protrusions showed similar WCA. In contrast, air-dried films on PS surfaces without pre-treatment showed the lowest WCA, while a plasma treatment before film casting already led to increased film hydrophobicity. Therefore, also plasma treatment-initiated differences in the spider silk surface.

WILEY-VCH

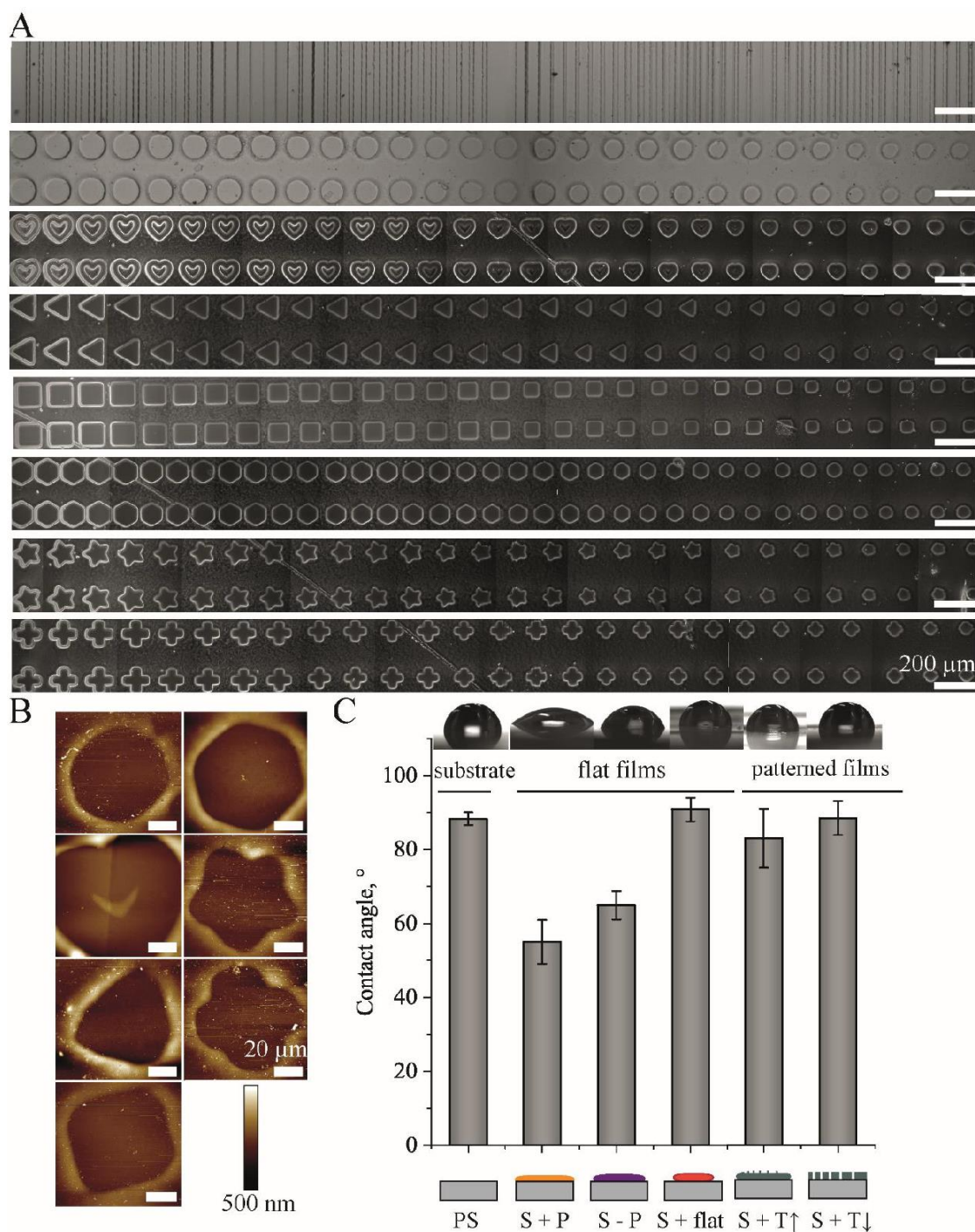


Figure 1: Physicochemical analysis of films with gradient-sized patterns. (A) displays representative light microscope images of the line and pattern gradients. Scale bars: 200 μm . (B) AFM images for height determination. Scale bars: 20 μm . (C) shows water

WILEY-VCH

contact angle measurements on a blank PS substrate (PS), on flat air-dried eADF4(C16) films with (S + P) and without (S – P) plasma treatment, and on silk films cast with flat (S + flat) and patterned (protrusions (S + T↑), indentations (S + T↓)) PDMS stamps on top.

2.2. Influence of indentations and protrusions on cell adhesion

Cell adhesion on flat, unmodified eADF4(C16) films has been shown to be low^[16], and, therefore, the effect of surface topographies (indentations, protrusions) was analyzed in cell culture using human BJ skin fibroblasts (**Figure S4**). Cell binding to spider silk films with grooved, circular, square, and triangular indentations and protrusions was investigated in comparison to that to flat eADF4(C16) films in the presence and absence (w/o) of fetal calf serum (FCS). It is a known effect that upon contact with body fluids, a protein layer immediately adsorbs on the surface of biomaterials, which influences cell adhesion.^[1a, 1c, 24] Shape fidelity and homogenous pattern distribution on topographically modified eADF4(C16) surfaces were verified using light microscopy before cell culture (**Figure S4**). After 4 h adhesion time, unattached BJ fibroblasts were washed off, and adhered cells were fixed and fluorescently stained to visualize cell nuclei (blue) and the F-actin cytoskeleton (red). The fact that 4',6-diamidino-2-phenylindole (DAPI, blue) also interacts with the silk protein to a certain degree was used to stain the film surface and visualize the topographical patterns (**Figure S4**). Comparing similar-sized indentations and protrusions revealed that cells favored the bottom of each topography for primary cell attachment. Thus, in case of indentations, most cells were found inside the patterns (**Figure S4A**). In the case of protrusions, fibroblasts were mainly located around the patterns on the flat spider silk films showing slight morphological adaption (**Figure S4B**). On top of these protrusions, cells could be detected only scarcely. One assumption could be the large interspace and distance between the protrusions leading to

WILEY-VCH

adhesion and spreading around and not on top of the protrusions. Therefore, subsequent cell culture experiments were carried out only on eADF4(C16) films containing indentations.

In general, it could be seen that the stimulation of cells was clearly enhanced if the indentations were in the size range of cells. Nevertheless, too large patterns (compared to the cell size) were not identified as topographical stimuli, while patterns smaller than cells could still be recognized. Due to a local spatial three-dimensional structure, topographical surface features reflected attachment points for cells. Their shape influenced cell morphology by guiding the alignment and orientation of the cells (contact guidance). For instance, F-actin staining visualized that cells aligned along present grooves and edges indicated by an elongated cell morphology regardless of having indentations or protrusions. Additionally, as cell attachment behavior was similar on both surfaces in the presence and absence of FCS, it was concluded that primary cell adhesion ($t < 4$ h) on topographically modified eADF4(C16) films was independent of present serum proteins. Thus, the adsorbed proteins of FCS were not responsible for an unspecific cellular attachment on the biomaterial surface, and the primary cell attachment was mainly driven by surface topography. However, incubating epithelial cells for 12 h on nano- to micrometer scaled grooved silicon oxide coated substrates revealed in a previous study that more cells aligned along the grooves showing media-dependent alignment behavior if FCS was present.^[7d] In our study, the cell attachment of BJ fibroblasts was similar in the absence and presence of FCS, leading to the conclusion that unspecific cell interaction with the spider silk surface was not influenced by other proteins present in the media. Previous studies confirmed this finding on foreign protein independence, as eADF4(C16) coated silicone implants showed a reduced fibrous capsule formation in rats^[16b], and the formed protein corona around particles and films made of eADF4(C16) did not induce blood coagulation.^[25] Based on these results, it was concluded that both the original substrate composition and the incubation time play decisive roles in influencing the cell-material interaction behavior.

2.3 Influence of size and shape of indentations on cell adhesion

Since patterned films made of eADF4(C16) promoted cell adhesion, the effect of pattern size and shape on cell behavior was further analyzed. Eight different cell types from different tissues (BJ skin fibroblasts, Balb 3T3 embryonal fibroblasts, MG63 bone fibroblasts, B50 neuronal cells, NG108 neuronal hybrid cells, RN22 Schwann cells, C2C12 muscle myoblasts, HaCaT skin keratinocytes) were seeded on eADF4(C16) films with size gradients and diverse geometries (between 40 μm and 100 μm) and groove widths (6 μm to 58 μm). Combining different geometries with a size gradient in one stamp enables the evaluation of various parameters. The approach allows a systematic characterization of how the number of edges and corners, the curvature of pattern edges, the total area of the resulting indentation, and the angles of the individual structures influence the adhesion and spreading of several cell types. A three-dimensional overview of the cell structure and morphology was obtained upon staining fluorescently cell nuclei (blue, DAPI) and the F-actin cytoskeleton (red, phalloidin-red) (CLSM, **Figure 2A**). The DAPI background staining of spider silk films was used to visualize the topographical surface indentations. The interaction of DNA intercalating dyes with recombinant spider silk has already been demonstrated with ethidium homodimer, as eADF4(C16)-based hydrogels showed a strong background signal after staining with this dye.^[26]

Human BJ skin fibroblasts strongly responded to surface indentations and preferentially attached inside these surface features with high contact guidance. Outside the indentations, only sporadically cells could be detected. A preferred surface pattern could not be identified, as the BJ cells attached to all structures indistinguishably. However, a correlation between cell size and pattern size was visible. Since BJ fibroblasts displayed a larger cell size than most other investigated cell types, they also showed spreading and alignment in larger structures.

WILEY-VCH

With smaller patterns, one single cell could fill the entire structure. The cells adapted their morphology to the prescribed structure and showed geometric confinement. Moreover, a strong alignment, orientation, and contact guidance of cells along grooved surfaces were visible. Compared to flat spider silk films, spreading and alignment were enhanced on all structured surfaces.

In contrast, the impact of varying surface topographies on the smaller mouse Balb 3T3 fibroblasts seemed to be neglectable. These fibroblasts attached in an aligned morphology even on flat substrates. Looking at larger patterns, the cells adhered inside the indentations but did not align along with the pattern. Nevertheless, if patterns got smaller, a cell-to-pattern size effect could be identified for this cell line. Smaller patterns, which were in the Balb 3T3 fibroblasts size range, showed an effect on cell alignment and orientation of the F-Actin cytoskeleton (especially triangles, circles, squares, hexagons, and crosses).

Since correlative microscopy combines the benefits of different imaging methods, here, SEM and CLSM were used to image and characterize precisely the same area of a sample, i.e., the identical cell. ^[27] SEM imaging elaborated surface topographical features of the spherical indentations and the attached cells, while CLSM enabled the detection of fluorescently stained cellular components, including cell nuclei or the F-actin cytoskeleton. Selected correlative overlays of SEM and CLSM images showing BJ and Balb 3T3 fibroblasts inside the square, star- or cross-shaped indentations were generated (**Figure 2B**). The correlative overlays clearly display focal adhesion and cell anchor sites of attached cells at the edges of the topographical surface patterns.

WILEY-VCH

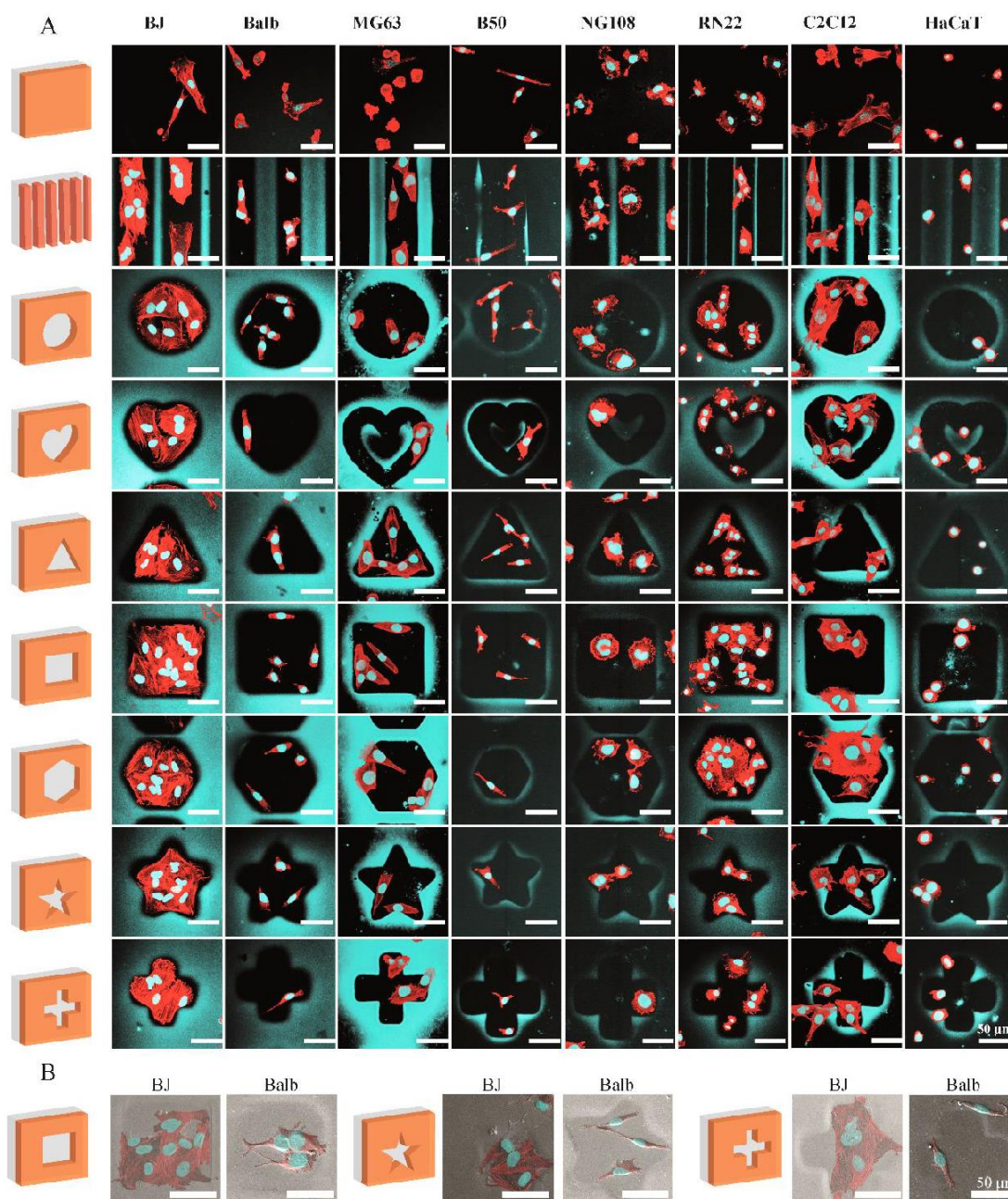


Figure 2: Microscopical analysis of cells within different topographies (indentations). (A) Representative confocal laser scanning microscope (CLSM) images of eight different cell types (BJ skin fibroblasts, Balb 3T3 embryonal fibroblasts, MG63 bone fibroblasts, B50 neuronal cells, NG108 neuronal hybrid cells, RN22 Schwann cells, C2C12 myoblasts, and HaCaT skin keratinocytes) attached on films made of eADF4(C16) showing grooves or topographies (circles, hearts, triangles, squares, hexagons, stars and crosses as indicated).

WILEY-VCH

Flat eADF4(C16) films served as controls. Cell nuclei (blue) and F-actin cytoskeleton (red) were visualized using DAPI and phalloidin-red. DAPI background staining of the spider silk films was used to show the different topographies. Scale bars: 50 μm (B) Correlative microscopy images of attached BJ and Balb 3T3 fibroblasts inside selected topographies. Correlative images display an overlay of SEM (surface topography) and CLSM (fluorescent cell compartment staining) images to create a structural image. For SEM imaging, CLSM samples were dehydrated and platinum sputter-coated. Scale bars: 50 μm .

Interestingly, human MG63 bone fibroblasts strongly reacted to surface patterns. Compared to flat control surfaces (round-shaped cells), MG63 cells displayed cell spreading with focal adhesion formation and adopted their morphology regarding the underlying surface structure on patterned eADF4(C16) films. It seemed that the edges led to contact guidance and cell alignment along with the prescribed surface structure. An adhesion preference of MG63 cells could not be seen, as the cells attached to corners in the cross-shaped as well as along the curved edge in the heart-shaped features. A connection between cell size and pattern size was also visible here. Several cells often interacted with one large surface pattern and aligned therein. If the size of the surface indentation was in the range of the cell size, few cells were able to fill the surface pattern and could adopt their cell morphology to the prescribed structure. Thus, smaller surface patterns showed higher effects.

Rat B50 neuronal cells attached inside the patterns of spider silk films but were not strongly influenced by them. The cells showed a high F-Actin expression and focal adhesion formation and spread inside the different surface patterns. Due to their relatively small cell size, more cells could adhere in one large pattern. Nevertheless, for larger structures, alignment and orientation of the cells along the topographical surface pattern were low compared to that of

WILEY-VCH

other cell lines, such as BJ fibroblasts. Interestingly, this cell line used the feature corners as attachment or anchor points.

Mouse-rat NG108 neuronal cells adhered to all introduced patterns. Cells responded little to the topological guidance of the surface patterns. The cells showed similar cell body size on flat and patterned surfaces and adhered independent of the underlying indentation in a round morphology. Their F-Actin cytoskeleton was clearly pronounced around the cell nuclei, and many stress fibers could be identified, indicating a not favorable surface. The formation of neurons could not be detected. Nevertheless, edges and corners seemed to function as anchor points and induced a slight orientation of NG108 cells.

Rat RN22 Schwann cells were preferentially attached to the deepest part of the structured surface inside the pattern. RN22 adopted their cell shape according to the underlying pattern topography (contact guidance). If there was an edge or a corner present, the cells also aligned in the prescribed shape. Interestingly, too many corners as present in cross- or star-shaped patterns, or patterns including the circle or heart with a round shape seemed to inhibit RN22 alignment. They instead favored hexagons, squares and triangles and adopted their cell orientation towards these topographical structures. Furthermore, a relation between cell and pattern size was identified due to a higher number of cells attached to larger topographical structures, while fewer cells had space in smaller patterns.

Mouse C2C12 myoblasts attached and aligned their cell morphology regarding the underlying surface pattern. Especially, grooves led to enhanced C2C12 cell alignment and contact guidance. The corners and edges seemed to be an attachment or settle point for C2C12 myoblasts. Nevertheless, C2C12 myoblasts were also attached outside the indentation but mainly at the border of a pattern, indicating that they need an anchor point for attachment. C2C12 myoblasts showed a spread morphology on flat surfaces with focal adhesions in

WILEY-VCH

different directions. The orientation of these focal adhesions seemed to be influenced by the topographical structure on patterned surfaces.

In contrast to other investigated cell lines, human HaCaT keratinocytes adhered similarly on all investigated surfaces inside and outside the indentations. HaCaT keratinocytes remained a round morphology independent of the underlying substrate, which was not influenced by corners, edges, or grooves.

Interestingly, while cell adhesion to flat eADF4(C16) spider silk films is low^[16], usage of PDMS stamps led to an increase in surface hydrophobicity followed by more cells attaching to the silk surface than in previous studies (**Figure S3**, **Figure 2**, **Figure 3**). Our analysis further revealed that linear grooves represent the pattern with the highest influence for contact guidance of BJ fibroblasts, Balb 3T3 fibroblasts, MG63 bone fibroblasts, RN22 Schwann cells, and C2C12 myoblasts, which displayed enhanced spreading and strong alignment and orientation of their cell bodies along the straight grooves. In contrast, such modifications did not influence NG108 neuronal cells, B50 cells, and HaCaT keratinocytes. The comparison with existing literature indicated that different types of grooves are the most common topographical surface modifications for guiding cell behavior.^[5b, 7a, 7d, 11, 13, 28] However, some studies investigated also other topographies, for instance, circular pits^[28d, 29] or triangular, circular, rectangular or star-shaped indentations^[30].

Since our system using size gradients of different surface patterns allows the correlation of biomaterial surface modification and cell-type specific effects, overview images of cell-seeded feature gradients were taken using CLSM to identify future tissue- and cell-specific modification strategies for bioselective adhesion. **Figure 3** displays selected representative indentation gradients (squares, hexagons, stars and grooves) for Balb 3T3 and BJ fibroblasts for directly comparing different fibroblast cell lines with each other.

WILEY-VCH

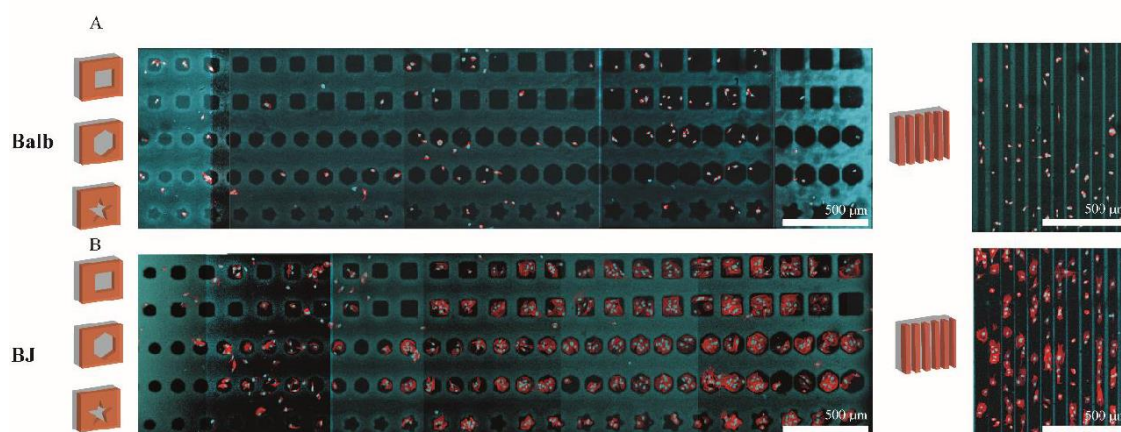


Figure 3: Selected, representative CLSM images of surface topography gradients (squares, hexagons, stars, and grooves) on eADF4(C16) films after seeding of Balb 3T3 (A) and BJ fibroblasts (B). Cell nuclei (blue) and F-actin cytoskeleton (red) were visualized using DAPI and phalloidin-red. DAPI background staining of spider silk films was used to visualize the topographies and size gradients. Scale bars: 500 μm .

The relatively small Balb 3T3 fibroblasts mainly attached inside the generated indentations but showed less orientation or alignment. Nevertheless, it was concluded that surface indentations supported Balb 3T3 cell attachment to eADF4(C16) films, even if contact guidance and morphological cell adaption were not detectable. In contrast, human BJ fibroblasts exhibit larger cell sizes and were strongly influenced by surface indentations. Several fibroblasts were attached inside bigger surface patterns and adapted their cell morphology and body regarding the underlying shape of the pattern (geometric confinement). Our results are in line with another study using BJ fibroblasts and circular indentations (7 μm , 15 μm or 25 μm diameters). BJ fibroblasts adhered inside the large indentations (25 μm) and adopted their morphology by enhancing their cytoskeleton expression (F-actin and tubulin), while most of the smaller ones (7 μm) were covered by the cells. A size-related cell behaviour was described, as fibroblasts entered all indentations, but only cell parts were found inside the structures for smaller ones.^[29b]

WILEY-VCH

Thus, contact guidance was evident, independent of topographical surface features. Interestingly, outside the indentations, only sparse cells have been found. The results clearly showed that the surface modification with topographical features represents a versatile tool to trigger bioselective cell attachment even of cells with similar features, but different origin, e.g. fibroblasts from human and mouse.

3. Conclusion and Outlook

Bioselective biomaterial surfaces for various tissue-specific cell types could be generated using topographical surface features. The here shown maskless lithographical modification process for introducing topographical surface features is straightforward, easy, and versatile. The usage of a size and structure gradient of various surface topographies in combination with eight cell lines differing in cell size and tissue origin set our approach apart from previous ones. The usual cell non-adhesive (cytophobic) spider silk films could be modified using topographical surface patterns to selectively enable cell-type dependent attachment (cytophilic), adopted spreading behavior, contact guidance, and aligned cell morphology. Cellular responses to topography were strongly cell-type specific and dependent on the shape, size, and structure of the applied topographical feature and the interspace between the surface patterns (**Table 1**).

Table 1: Geometry preference of eight selected cell lines.

Cells	Response	Geometry Preference	Cell-Pattern-Size-Effect	Effect
BJ	Very strong	No	Yes	Adhesion to all surface topographies, contact guidance, orientation and alignment regarding prescribed structure, enhanced spreading, in smaller patterns fewer cells, in larger patterns more cells attached, geometric confinement

WILEY-VCH

Balb 3T3	Little	No	No	Adhesion is not affected by surface topographies, most cells adhered inside indentations, only smaller patterns affect cell morphology
MG63	Strong	No	Yes	Adhesion to all surface topographies, contact guidance, edges beneficial for orientation, corners served as anchorage points, in smaller patterns fewer cells, in larger patterns more cells attached
B50	Moderate	No	Yes	Adhesion to all surface topographies, alignment regarding present structures, smaller geometries show stronger effects.
NG108	Little	No	No	Adhesion to all surface topographies, alignment or orientation along with corners and edges visible
RN22	Strong	Yes	Yes	Adhesion to all surface topographies, contact guidance, cell morphology depends on topography, too many corners or circular structures hindered RN22 cell spreading, grooves, triangles, squares, and hexagons were preferred, in smaller patterns fewer cells, in larger patterns more cells attached
C2C12	Moderate	Yes	No	Adhesion to all surface topographies, alignment along edges, grooves preferred, cells need anchorage points, morphology adaption if attachment inside the indentation
HaCaT	No	No	No	Adhesion is not affected by surface topographies, no divergent spreading behavior

However, the correlation between cell and pattern size is significant since cells often reacted on geometrical surface features showing dimensions in their cell size range or slightly above. The here identified cell-specific responses towards geometries allow the generation of tissue-

specifically modified biomaterial implants to enable new routes towards enhanced tissue regeneration by triggering cellular responses (**Figure 4**).

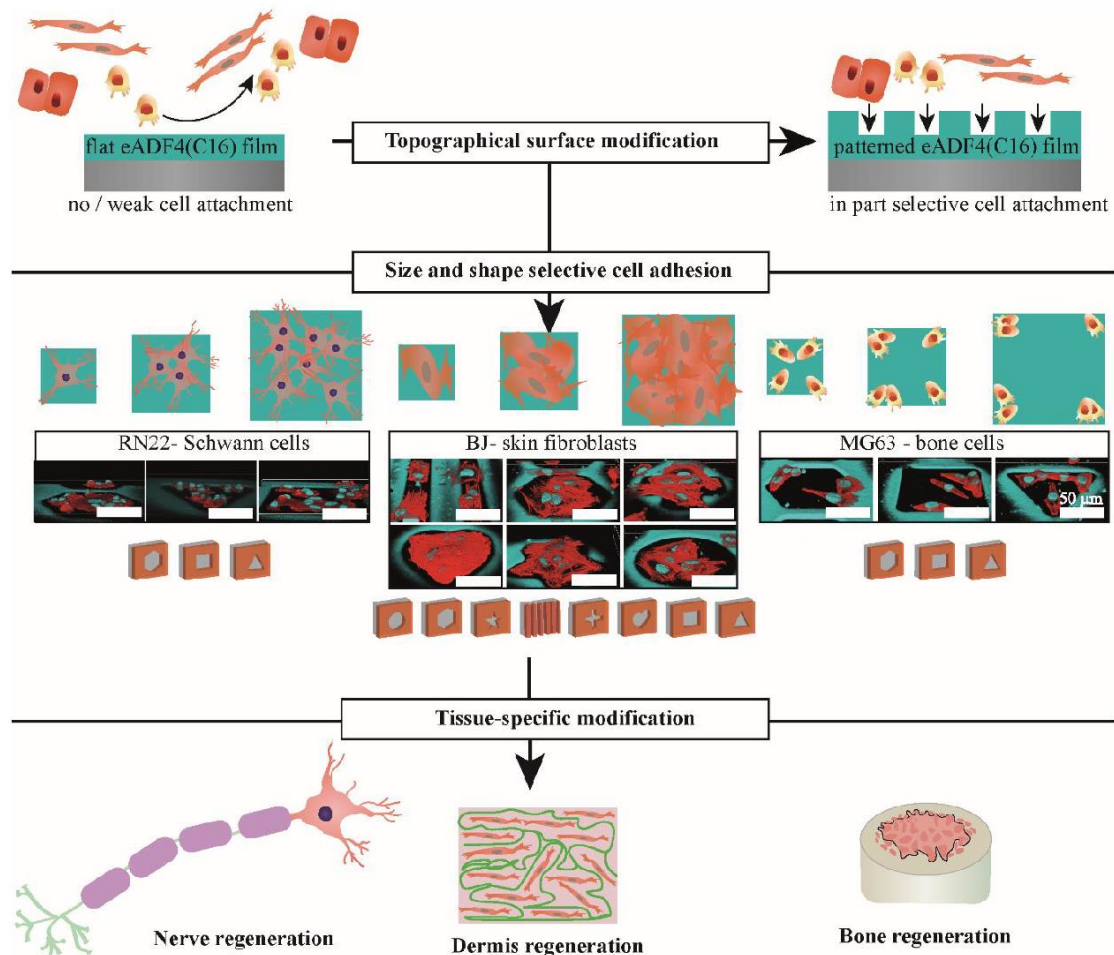


Figure 4: Summary of selected, identified cell-specific responses towards differently shaped and sized topographical surface modifications enabling tissue-specific engineering of biomaterial implant surfaces by stimulating cellular responses.

4. Experimental Section/Methods

Preparation of the photoresist templates. Glass slides (Thermo Fisher Scientific, Germany) with 2.5 cm x 2.5 cm were used as substrates for preparing the photoresist templates after

WILEY-VCH

cleaning with Piranha solution (3:1 H₂SO₄ : H₂O₂, 10 min, RT). The cleaned glass slides were spin-coated with an adhesion promoter (200 μL/ 6.25 cm², 3000 rpm, 20 s, RT, TI prime, Microchemicals GmbH, Ulm Germany). The adhesion promoter was cured 2 min at 120°C to remove any remaining solvent. The photoresist (500 μL/ 6.25 cm², AZ® 4562, Microchemicals GmbH, Ulm, Germany) was spin-coated (4000 rpm, 60s, RT) onto the adhesion promoter layer and then afterwards cured for 8 min at 120 °C.

Photoresist patterning. The patterns (similar sized features, structure gradients) were designed in Adobe Illustrator CC 2021 with 1920 x 1080 pixels dimensions due to the format of the SmartPrint® device (MICROLIGHT3D, La Tronche, France). Using the shape tool, the desired structure was created. The desired dimensions of the pattern were calculated given by the used objective lens (2.5x) of the SmartPrint®. Here one pixel corresponds to 2.84 μm. The digital mask was transferred to the software and was exposed to the photoresist for 90 s. Then the exposed photoresist was developed in developer solution (AZ 400 K, Microchemicals GmbH, Ulm, Germany) for 2 min. Afterwards, the photoresist was washed with MQ water.

PDMS stamp preparation. The PDMS stamp was prepared using Sylgard 184 Silicone Elastomer (1:10 crosslinker : prepolymer, Dow Corning, Wiesbaden, Germany). The PDMS was mixed, and air was removed upon evacuating the PDMS for 10 min. Afterwards, liquid PDMS was poured over the patterned photoresist glass slides. The PDMS was cured for 24 hours at room temperature. Then, the PDMS was baked for 2 h at 70°C, and the stamps were cut out.

Processing of patterned eADF4(C16) spider silk films. Recombinant eADF4(C16) spider silk protein powder (AmSilk GmbH, Germany) was solved in formic acid (VWR, Germany) at a

WILEY-VCH

concentration of 5 mg ml⁻¹ for 1-2 h. Before film casting, the surface of 4-well and 8-well μ -slides (ibiTreat, ibidi GmbH, Germany), polystyrene plates (Thermo Fisher Scientific, Germany), or petridishes (Sarstaedt, Germany) were treated with oxygen plasma (5 min, 100 W, 0.2 mbar, MiniFlecto, plasma technology, Herrenberg-Gültstein, Germany). 100 μ l spider silk solution was pipetted in each well of the 4-well μ -slide, and an appropriate patterned PDMS stamp containing the negative imprints of the respective patterns was placed on the spider silk solution. For flat surfaces, 50 μ l spider silk solution was drop cast in 8-well μ -slides either without PDMS or with an unpatterned PDMS stamp on top. After evaporation of the solvent (at least overnight) at ambient conditions, the PDMS stamps were removed, and the resulting patterned spider silk films were imaged using a Leica DM IL LED microscope with the associated LAS 4.8 software (both Leica, Germany).

Atomic force microscopy. To determine the surface morphology, the patterned eADF4(C16) films were analyzed in tapping mode using a Dimension Icon (Bruker Karlsruhe, Germany) with a resolution of 512 by 512 data points at 0.5 Hz. OTESPA-R3 silicon cantilevers (Bruker, Karlsruhe, Germany) were used with a force constant of 26 N m⁻¹.

Water contact angle measurements. The wettability of the patterned films was analyzed with the sessile drop method using the OEG contact angle system (Surftens Universal, OEG, Frankfurt (Oder), Germany). The shape of the water droplets was analyzed using the SURFTENS software (OEG, Frankfurt (Oder), Germany) and a Laplace Young fit.

Cell culture. Human skin BJ fibroblasts (CRL-2522, ATCC, USA) were cultured in Eagle's Minimum Essential Medium (EMEM, Sigma-Aldrich, Germany) supplemented with 10 % v/v fetal calf serum (FCS, BioSell, Germany), 1 % v/v GlutaMax (Gibco, Thermo Fisher Scientific,

WILEY-VCH

Germany) and 0.1 % v/v gentamycin sulphate (Sigma-Aldrich, Germany). Mouse M-MSV Balb/3T3 fibroblasts (ECACC, Sigma-Aldrich, Germany) were cultured in Dulbecco's modified Eagle's medium (DMEM, BioSell, Germany) supplemented with 10 % v/v fetal calf serum, 1 % v/v GlutaMax and 0.1 % v/v gentamycin sulphate. Human bone MG-63 osteosarcoma fibroblasts (CRL-1427, ATCC, USA) were cultured in EMEM supplemented with 10 % v/v FCS, 1 % v/v GlutaMax, 1 % v/v non-essential amino acids (NEAA, Sigma-Aldrich, Germany) and 0.1 % v/v gentamycin sulphate. Rat nerve B50 neuronal cells (ECACC, Sigma-Aldrich, Germany) were cultured in DMEM supplemented with 10 % v/v fetal calf serum, 1 % v/v GlutaMax and 0.1 % v/v gentamycin sulphate. Mouse C2C12 myoblasts (CLR-1772, ATCC, USA) were cultured in DMEM supplemented with 10 % v/v FCS, 1 % v/v GlutaMax and 0.1 % v/v gentamycin sulphate. Mouse-rat NG108-15 somatic cell hybrids from glio- and neuroblastoma (HB-12317, ATCC, USA) were cultured in DMEM supplemented with 10 % v/v fetal calf serum, 1 % v/v GlutaMax and 0.1 % v/v gentamycin sulphate. Human skin HaCaT keratinocytes (DKFZ, CLS, Germany) were cultured in DMEM supplemented with 10 % v/v fetal calf serum, 1 % v/v GlutaMax and 0.1 % v/v gentamycin sulphate. Immature, bipolar rat RN 22 Schwann cells (ECACC, Sigma-Aldrich, Germany) were cultured in DMEM supplemented with 10 % v/v fetal calf serum, 1 % v/v GlutaMax and 0.1 % v/v gentamycin sulphate.

All cell lines were cultivated under humidified conditions and 5 % CO₂ in a cell culture incubator (Heracell, Thermo Fisher Scientific, Germany) at 37 °C. Sub-culturing of all cell lines was conducted using trypsin/EDTA (BioSell, Germany) at a low concentration of 0.05 % for BJ fibroblasts, Balb/3T3 fibroblasts, C2C12 myoblasts and NG108 hybrids or a higher concentration of 0.25 % for HaCaT keratinocytes, MG-63 osteosarcoma fibroblasts, B50 neuronal cells and RN 22 Schwann cells. Cells were centrifuged (1200 rpm, 5 min, RT) and resuspended in an appropriate fresh medium. Respective cell numbers were determined using

WILEY-VCH

trypan blue (Sigma-Aldrich, Germany) and an automated cell counter (TC20, BioRAD Laboratories, Germany)

Cell adhesion assay and fluorescence staining.

Human BJ fibroblasts were resuspended in EMEM supplemented with 1 % v/v GlutaMax and 0.1 % v/v gentamycin sulphate either without FCS (w/o FCS) or with additionally added 10 % v/v FCS (w FCS) to analyse the impact of present serum proteins in the cell culture media. For all other 4 h cell adhesion assays, cells were resuspended in the appropriate complete cell culture media with added 10 % v/v FCS. The different patterned films made of eADF4(C16) were sterilized for 20-30 min using UV-light of the cell culture hood (Herasafe, Thermo Fisher Scientific, Germany). Prior to use, the surfaces were washed using 1 x phosphate-buffered saline (1xPBS, Sigma-Aldrich, Germany).

On each patterned surface, 10 000 cells per cm² were seeded and incubated for 4 h in a cell culture incubator at 37 °C. Afterwards, cell culture media was soaked off and cells were fixed using 3.7 % v/v para-formaldehyde (Roth, Germany) in 1xPBS for 20-30 min at ambient conditions. Thereafter, the cells were permeabilized using 0.1 % v/v Triton X-100 (Roth, Germany) for 20 min at ambient conditions. Subsequent fluorescence staining of the cell nuclei and the F-Actin cytoskeleton was conducted for 60 min in the dark at RT using 300 nM 4',6-Diamidino-2-phenylindole dihydrochloride (DAPI, Sigma-Aldrich, Germany) and 200 nM Phalloidin tetramethyl rhodamine B isothiocyanate (Phalloidin-red, Sigma-Aldrich, Germany) in 1xPBS, respectively.

Fluorescence and confocal laser scanning microscopy

Fluorescence microscopy of stained cells on patterned spider silk films was conducted using a DMi8 fluorescence microscope and the associated LAS X software (both Leica, Germany).

WILEY-VCH

Overview images of eADF4(C16) films with indentations were taken using a DMI 8 confocal microscope with the associated LAS X software (both Leica, Germany) equipped with a 10x objective and lasers using excitation wavelengths of 405 nm (DAPI) and 552 nm (Phalloidin-Red). Z-stacks were recorded using the 63x objective of the DMI 8 confocal microscope and the same lasers to acquire focused images of cells inside indentations.

Scanning electron microscopy.

The samples were dehydrated using an ethanol dehydration set up for subsequent imaging using scanning electron microscopy. Therefore, 1× PBS was exchanged with 50 % (v/v) ethanol and incubated for 30 min. This step was repeated with 60 %, 70 %, 80 %, 90 % and 100 % (v/v). After the last incubation step, the residual solvent evaporated at ambient conditions. The patterned cell containing spider silk films were fixed on SEM stubs (Plano GmbH, Germany) surrounded by aluminum tape. Afterwards, these samples were sputter-coated with a 2 nm platinum layer using a Leica EM ACE 600 sputter coater (Leica, Germany). SEM was performed on a Thermo Scientific (FEI) Apreo VS device equipped with a Field Emission Gun and an SE2-detector operating at 2 kV (Thermo Fisher Scientific, Germany).

Supporting Information

Supporting information is available from the Wiley Online Library or from the author.

Declaration of competing interest

TS is co-founder and shareholder of the company AMSilk GmbH. All other authors declare that they have no competing financial interests or personal relationships that could have appeared to influence the work reported in the present paper.

Acknowledgements

WILEY-VCH

The authors thank Marcel Höferth for experimental assistance and Hendrik Bargel for help performing the SEM measurements. This work is supported by grant DFG SCHE603/ 23-1. SL and TS acknowledge funding from the German Academic Exchange Service (DAAD) through its thematic network Bayreuth-Melbourne Colloid/Polymer Network sponsored from the Federal Ministry of Education and Research (BMBF) funds. The authors also acknowledge the funding from the Deutsche Forschungsgemeinschaft (DFG, German Research Foundation)-project number 326998133-TRR225 (funded subproject: C01 TS). Support from the Elite Network of Bavaria is also acknowledged (VTT). Sarah Lentz and Vanessa T. Trossmann contributed equally to this work.

Data availability statement

The data that support the findings of this study are available upon reasonable request from the authors.

Credit author statement

SL, VTT and TS designed the study; SL and VTT carried out the experimental work and analyzed the data; TS supervised the study; VTT and SL wrote the original draft; TS edited the paper; SL performed PDMS stamp generation using photolithography, spider silk film processing, AFM, FTIR and WCA measurements, cell culture, light and fluorescence microscopy and SEM, VTT performed spider silk film processing, cell culture, light and fluorescence microscopy and CLSM.

Received: ((will be filled in by the editorial staff))

Revised: ((will be filled in by the editorial staff))

Published online: ((will be filled in by the editorial staff))

References

- [1] a) T. R. Kyriakides, in *Host Response to Biomaterials*, (Ed: S. F. Badylak), Academic Press, Oxford **2015**, p. 81; b) Q. Wei, T. Becherer, S. Angioletti-Uberti, J. Dzubiella, C. Wischke, A. T. Neffe, A. Lendlein, M. Ballauff, R. Haag, *Angew. Chem. Int. Ed. Engl.* **2014**, *53*, 8004; c) D. M. Kalaskar, F. Alshomer, in *In Situ Tissue Regeneration*, (Eds: S. J. Lee, J. J. Yoo, A. Atala), Academic Press, Boston **2016**, p. 137.
- [2] a) T. J. McKee, G. Perlman, M. Morris, S. V. Komarova, *Sci. Rep.* **2019**, *9*, 10542; b) J. K. Kular, S. Basu, R. I. Sharma, *J. Tissue Eng.* **2014**, *5*, 2041731414557112; c) D. Kusindarta, H. Wihadmadyatami, in *Tissue Regeneration*, (Ed: H. A. E. Kaoud) **2018**, p. 65; d) C. Frantz, K. M. Stewart, V. M. Weaver, *J. Cell Sci.* **2010**, *123*, 4195.
- [3] a) J. Rychly, B. J. Nebe, *BioNanoMaterials* **2013**, *14*, 153; b) A.-S. Mertgen, V. T. Trossmann, A. G. Guex, K. Maniura-Weber, T. Scheibel, M. Rottmar, *ACS Appl. Mater. Interfaces* **2020**, *12*, 21342; c) S. Cai, C. Wu, W. Yang, W. Liang, H. Yu, L. Liu, *Nanotechnol. Rev.* **2020**, *9*, 971; d) H. Zhang, X. Zheng, W. Ahmed, Y. Yao, J. Bai, Y. Chen, C. Gao, *Biomacromolecules* **2018**, *19*, 1746; e) E. S. Place, N. D. Evans, M. M. Stevens, *Nat. Mater.* **2009**, *8*, 457; f) K. Kyzioł, L. Kaczmarek, A. Kyzioł, in *Handbook of Composites from Renewable Materials*, **2017**, p. 457; g) R. J. Wade, J. A. Burdick, *Mater. Today* **2012**, *15*, 454; h) H. Amani, H. Arzaghi, M. Bayandori, A. S. Dezfuli, H. Pazoki-Toroudi, A. Shafiee, L. Moradi, *Adv. Mater. Interfaces* **2019**, *6*, 1900572; i) N. R. Richbourg, N. A. Peppas, V. I. Sikavitsas, *J. Tissue Eng. Regen. Med.* **2019**, *13*, 1275.
- [4] a) A. G. Harvey, E. W. Hill, A. Bayat, *Expert Rev. Med. Devices* **2013**, *10*, 257; b) M. Ermis, E. Antmen, V. Hasirci, *Bioact. Mater.* **2018**, *3*, 355; c) E. Luong-Van, I. Rodriguez, H. Y. Low, N. Elmouelhi, B. Lowenhaupt, S. Natarajan, C. T. Lim, R. Prajapati, M. Vyakarnam, K. Cooper, *J. Mater. Res.* **2013**, *28*, 165; d) A. T. Nguyen, S. R. Sathe, E. K. F. Yim, *J. Phys. Condens. Matter* **2016**, *28*, 183001; e) D. W. Hamilton, S. Ghrebi, H. Kim, B. Chehroudi, D. M. Brunette, in *Encyclopedia of biomaterials and biomedical engineering*. New York: Taylor and Francis **2006**, p. 1; f) M. Nikkhah, F. Edalat, S. Manoucheri, A. Khademhosseini, *Biomaterials* **2012**, *33*, 5230.
- [5] a) C.-Y. Yang, W.-Y. Huang, L.-H. Chen, N.-W. Liang, H.-C. Wang, J. Lu, X. Wang, T.-W. Wang, *J. Mater. Chem. B* **2021**, *9*, 567; b) R. G. Flemming, C. J. Murphy, G. A. Abrams, S. L. Goodman, P. F. Nealey, *Biomaterials* **1999**, *20*, 573; c) X. Le, G. E. J. Poinern, N. Ali, C. M. Berry, D. Fawcett, *Int. J. Biomater.* **2013**, *2013*, 782549.
- [6] a) J. Ballester-Beltran, M. Biggs, M. Dalby, M. Salmerón-Sánchez, A. Leal-Egana, *Front. Mater.* **2015**, *2*; b) T. Naganuma, *Nanoscale* **2017**, *9*, 13171.
- [7] a) X. F. Walboomers, W. Monaghan, A. S. G. Curtis, J. A. Jansen, *J. Biomed. Mater. Res.* **1999**, *46*, 212; b) C. Matschegewski, S. Staehlke, R. Loeffler, R. Lange, F. Chai, D. P. Kern, U. Beck, B. J. Nebe, *Biomaterials* **2010**, *31*, 5729; c) C. Mörke, H. Rebl, B. Finke, M. Dubs, P. Nestler, A. Airoudj, V. Roucoules, M. Schnabelrauch, A. Körtge, K. Anselme, C. A. Helm, J. B. Nebe, *ACS Appl. Mater. Interfaces* **2017**, *9*, 10461; d) A. I. Teixeira, G. A. Abrams, P. J. Bertics, C. J. Murphy, P. F. Nealey, *J. Cell Sci.* **2003**, *116*, 1881; e) C. Matschegewski, S. Staehlke, H. Birkholz, R. Lange, U. Beck, K. Engel, J. B. Nebe, *Materials* **2012**, *5*, 1176; f) X. Liu, R. Liu, B. Cao, K. Ye, S. Li, Y. Gu, Z. Pan, J. Ding, *Biomaterials* **2016**, *111*, 27.

- [8] A. S. Vasilevich, F. Mourcin, A. Mentink, F. Hulshof, N. Beijer, Y. Zhao, M. Levers, B. Papenburg, S. Singh, A. E. Carpenter, D. Stamatialis, C. v. Blitterswijk, K. Tarte, J. d. Boer, *Front. Bioeng. Biotechnol.* **2018**, 6.
- [9] S. Vermeulen, A. Vasilevich, D. Tsiapalis, N. Roumans, P. Vroemen, N. R. M. Beijer, A. Dede Eren, D. Zeugolis, J. de Boer, *Acta Biomater.* **2019**, 83, 277.
- [10] S. Zijl, A. S. Vasilevich, P. Viswanathan, A. L. Helling, N. R. M. Beijer, G. Walko, C. Chiappini, J. de Boer, F. M. Watt, *Acta Biomater.* **2019**, 84, 133.
- [11] a) G. Abagnale, A. Sechi, M. Steger, Q. Zhou, C.-C. Kuo, G. Aydin, C. Schalla, G. Müller-Newen, M. Zenke, I. G. Costa, P. van Rijn, A. Gillner, W. Wagner, *Stem Cell Reports* **2017**, 9, 654; b) P. Clark, P. Connolly, A. S. Curtis, J. A. Dow, C. D. Wilkinson, *J. Cell Sci.* **1991**, 99 (Pt 1), 73.
- [12] a) G. A. Dunn, J. P. Heath, *Exp. Cell Res.* **1976**, 101, 1; b) P. Weiss, *J. Exp. Zool.* **1945**, 100, 353.
- [13] A. Mathur, S. W. Moore, M. P. Sheetz, J. Hone, *Acta Biomater.* **2012**, 8, 2595.
- [14] C. Oakley, D. M. Brunette, *J. Cell Sci.* **1993**, 106, 343.
- [15] V. Brunetti, G. Maiorano, L. Rizzello, B. Sorce, S. Sabella, R. Cingolani, P. P. Pompa, *Proc. Natl. Acad. Sci. U S A* **2010**, 107, 6264.
- [16] a) S. Wohlrab, S. Müller, A. Schmidt, S. Neubauer, H. Kessler, A. Leal-Egaña, T. Scheibel, *Biomaterials* **2012**, 33, 6650; b) P. Zeplin, N. Maksimovikj, M. Jordan, J. Nickel, G. Lang, A. Leimer, L. Römer, T. Scheibel, *Adv. Funct. Mater.* **2014**, 24; c) A. Leal-Egaña, G. Lang, C. Mauerer, J. Wickinghoff, M. Weber, S. Geimer, T. Scheibel, *Adv. Engin. Mater.* **2012**, 14, B67; d) C. B. Borkner, S. Wohlrab, E. Möller, G. Lang, T. Scheibel, *ACS Biomater. Sci. Eng.* **2017**, 3, 767.
- [17] a) C. Fredriksson, M. Hedhammar, R. Feinstein, K. Nordling, G. Kratz, J. Johansson, F. Huss, A. Rising, *Materials* **2009**, 2, 1908; b) M. Lucke, I. Mottas, T. Herbst, C. Hotz, L. Römer, M. Schierling, H. M. Herold, U. Slotta, T. Spinetti, T. Scheibel, G. Winter, C. Bourquin, J. Engert, *Biomaterials* **2018**, 172, 105; c) S. Salehi, K. Koeck, T. Scheibel, *Molecules* **2020**, 25, 737; d) T. B. Aigner, E. DeSimone, T. Scheibel, *Adv. Mater.* **2018**, 30, 1704636.
- [18] D. Huemmerich, C. W. Helsen, S. Quedzuweit, J. Oschmann, R. Rudolph, T. Scheibel, *Biochemistry* **2004**, 43, 13604.
- [19] S. Müller-Herrmann, T. Scheibel, *ACS Biomater. Sci. Eng.* **2015**, 1, 247.
- [20] a) S. Kumari, G. Lang, E. DeSimone, C. Spengler, V. T. Trossmann, S. Lücker, M. Hudel, K. Jacobs, N. Krämer, T. Scheibel, *Data Brief* **2020**, 32, 106305; b) S. Kumari, G. Lang, E. DeSimone, C. Spengler, V. T. Trossmann, S. Lücker, M. Hudel, K. Jacobs, N. Krämer, T. Scheibel, *Mater. Today* **2020**, 41, 21.
- [21] a) X. Wei, J. Shen, Z. Gu, Y. Zhu, F. Chen, M. Zhong, L. Yin, Y. Xie, Z. Liu, W. Jin, M. Nouri, L. Chang, *ACS Applied Bio Materials* **2018**, 1, 2167; b) G. Bartalena, Y. Loosli, T. Zambelli, J. G. Snedeker, *Soft Matter* **2012**, 8, 673.
- [22] H. Kavand, H. van Lintel, S. Bakhshi Sichani, S. Bonakdar, H. Kavand, J. Koohsorkhi, P. Renaud, *ACS Appl. Mater. Interfaces* **2019**, 11, 10559.
- [23] A. Mata, A. J. Fleischman, S. Roy, *Biomed. Microdevices* **2005**, 7, 281.
- [24] a) C. J. Wilson, R. E. Clegg, D. I. Leavesley, M. J. Percy, *Tissue Eng.* **2005**, 11, 1; b) J. M. Anderson, A. Rodriguez, D. T. Chang, *Semin. Immunol.* **2008**, 20, 86.
- [25] A. C. G. Weiss, H. M. Herold, S. Lentz, M. Faria, Q. A. Besford, C.-S. Ang, F. Caruso, T. Scheibel, *ACS Appl. Mater. Interfaces* **2020**, 12, 24635.
- [26] a) K. Schacht, T. Jüngst, M. Schweinlin, A. Ewald, J. Groll, T. Scheibel, *Angew. Chem. Int. Ed. Engl.* **2015**, 54, 2816; b) E. DeSimone, K. Schacht, A. Pellert, T. Scheibel, *Biofabrication* **2017**, 9, 044104.

WILEY-VCH

- [27] a) C. Loussert Fonta, B. M. Humbel, *Arch. Biochem. Biophys* **2015**, 581, 98; b) T. Takizawa, J. M. Robinson, *Placenta* **2003**, 24, 557.
- [28] a) A. Leclerc, D. Tremblay, S. Hadjiantoniou, N. V. Bukoreshliev, J. L. Rogowski, M. Godin, A. E. Pelling, *Biomaterials* **2013**, 34, 8097; b) W.-T. Su, Y.-F. Liao, I. M. Chu, *Micron* **2007**, 38, 278; c) A. I. Teixeira, G. A. McKie, J. D. Foley, P. J. Bertics, P. F. Nealey, C. J. Murphy, *Biomaterials* **2006**, 27, 3945; d) M. J. Dalby, D. McCloy, M. Robertson, C. D. W. Wilkinson, R. O. C. Oreffo, *Biomaterials* **2006**, 27, 1306.
- [29] a) A. Mata, L. Hsu, R. Capito, C. Aparicio, K. Henrikson, S. I. Stupp, *Soft Matter* **2009**, 5, 1228; b) C. C. Berry, G. Campbell, A. Spadiccino, M. Robertson, A. S. G. Curtis, *Biomaterials* **2004**, 25, 5781.
- [30] J. Sun, N. Jamilpour, F.-Y. Wang, P. K. Wong, *Biomaterials* **2014**, 35, 3273.

Supplementary Information

Topography directed cell adhesion on spider silk surfaces

Sarah Lentz[‡], Vanessa Trossmann[‡] and Thomas Scheibel

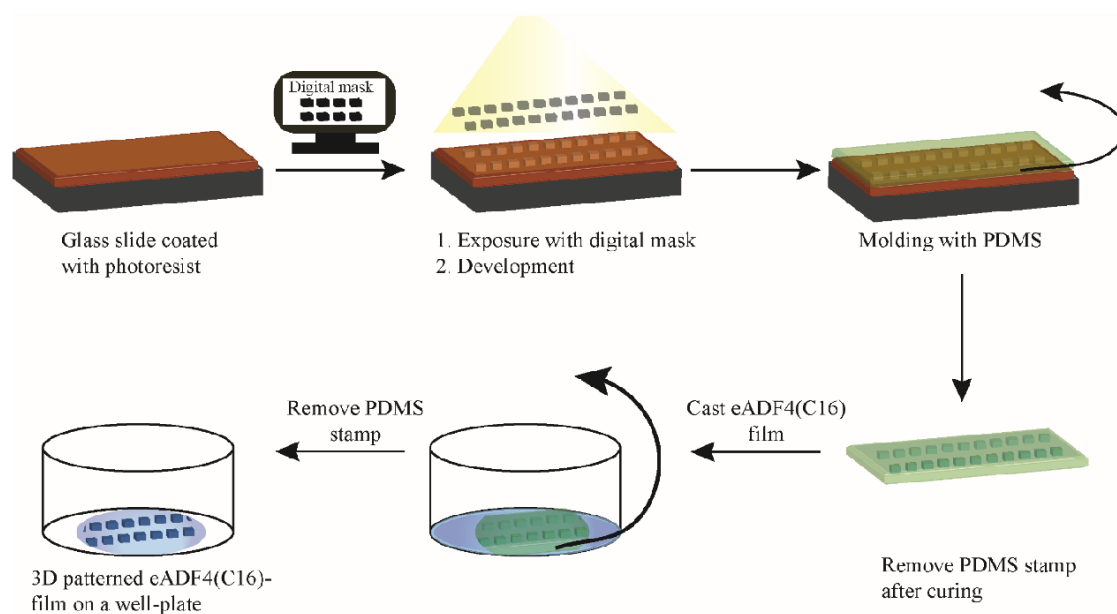


Figure S1: Schematic illustration of the preparation of patterned recombinant spider silk films. The first step is the coating of RCA cleaned glass slides with a photoresist. Then the digital mask is exposed (UV light) to the glass slide. Afterwards, the exposed photoresist is developed in the developer solution. The exposed parts of the photoresist get removed to obtain a template. This template is covered with PDMS and cured to receive an imprint (stamp). The PDMS stamp gets removed. The recombinant spider silk solution is cast into a well-plate. Then, the PDMS stamp is placed in the solution. After the solvent is completely evaporated, the PDMS stamp is removed, and a 3D patterned recombinant spider silk film is the result.

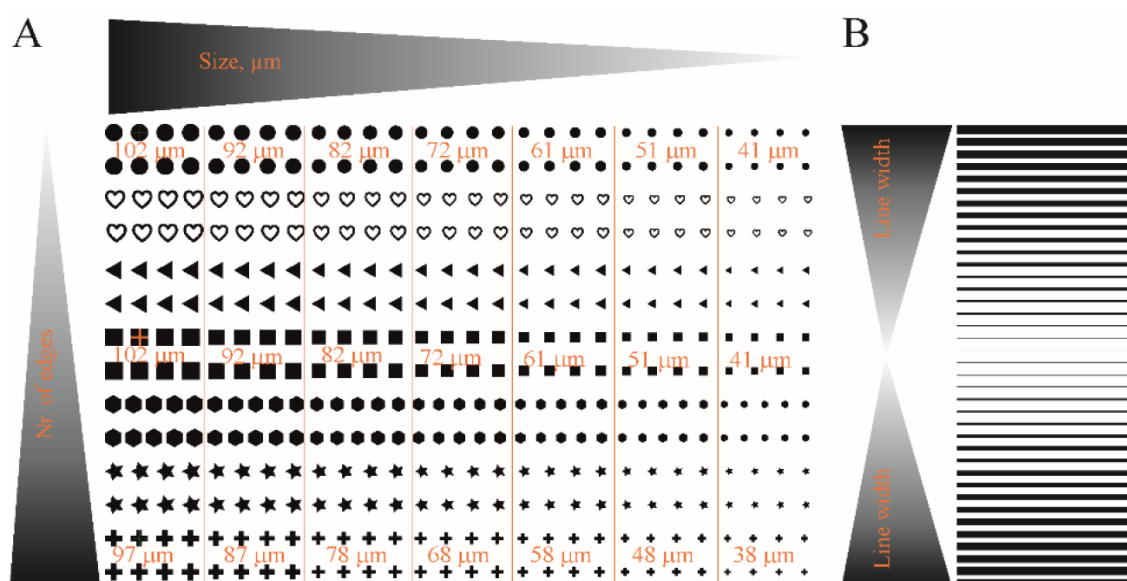


Figure S2: Digital masks showing size gradients of different structures (circles, hearts, triangles, squares, hexagons, stars, and crosses) (A) and grooves exhibiting different groove widths (B). (A) The patterns were arranged regarding their number of corners and their size. The resulting features should show sizes between around 40 μm and 100 μm . (B) the groove gradient is characterized by increasing widths for grooves and ridges.

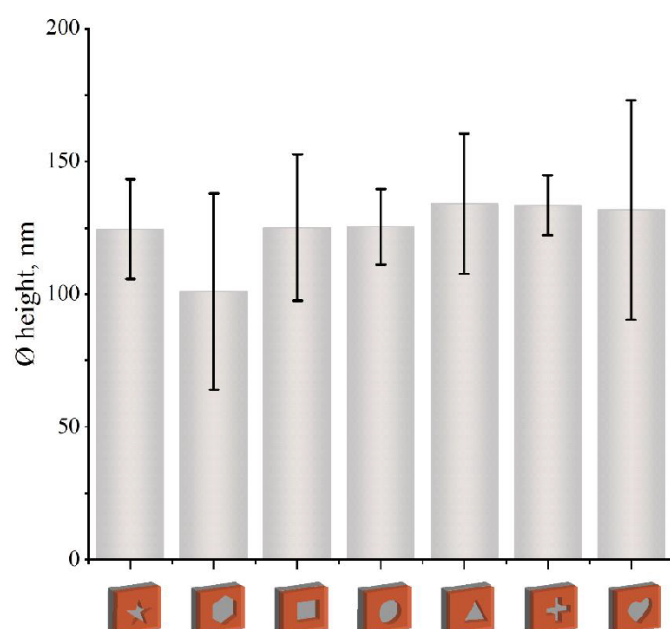


Figure S3: Individual indentation heights of patterns determined using AFM.

WILEY-VCH

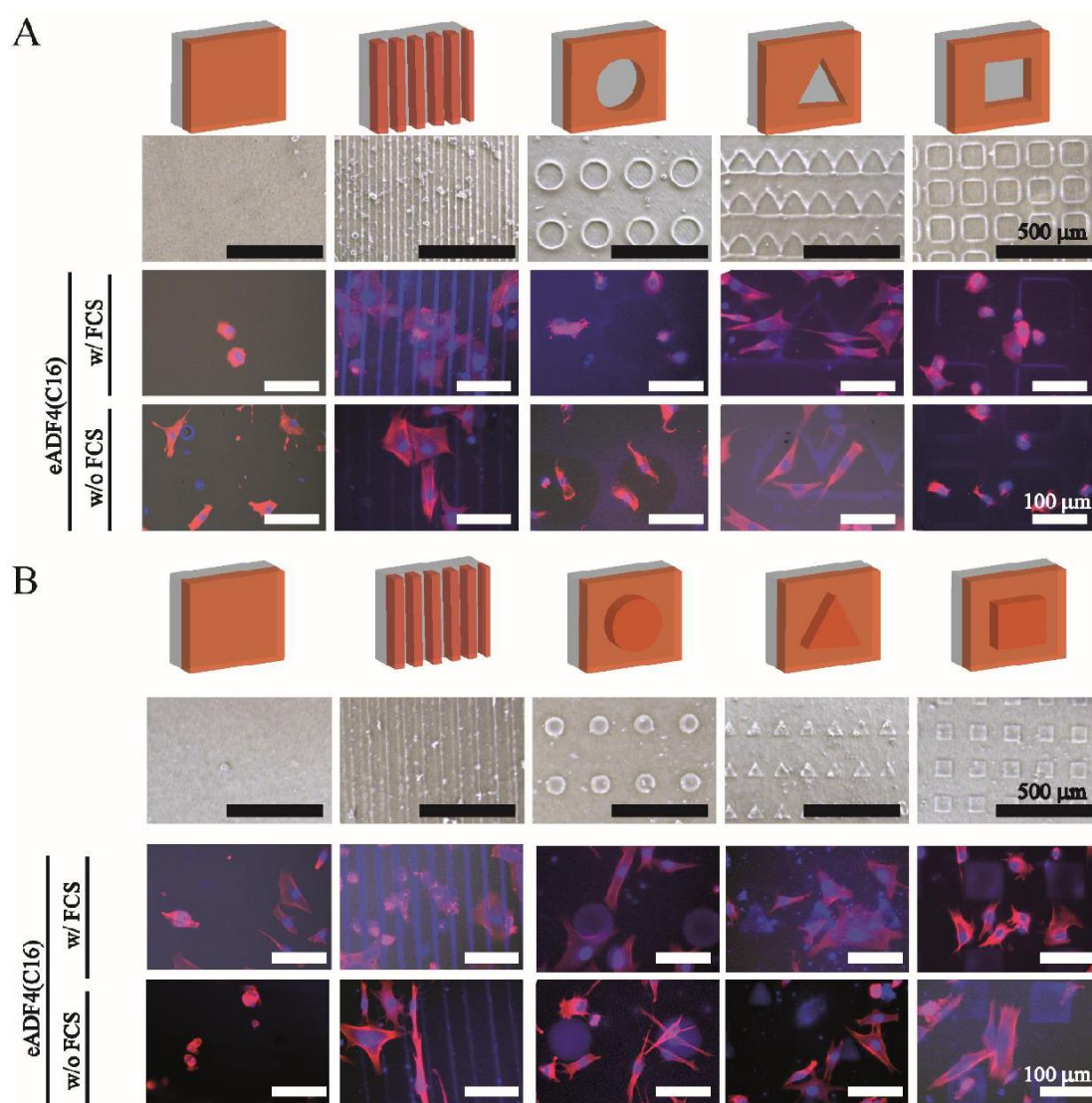


Figure S4: Cell binding to eADF4(C16) films containing indentations (A) or protrusions (B) in the absence and presence of added FCS. Before cell culture experiments, the shape-fidelity of surface topographical patterns was confirmed using light microscopy. Human BJ fibroblasts were seeded for 4 h on flat, grooved and patterned surfaces (circle, triangle and square) made of eADF4(C16) in absence and presence of FCS and subsequently stained with DAPI (blue, cell nuclei) and phalloidin-red (red, F-actin cytoskeleton). Scale bars as indicated.

Part III - Chapter 4 – Designing of spider silk proteins for hiPSC-based cardiac tissue engineering

Part III – Chapter 4.1 - Chapter perspective and contribution

Nowadays, myocardial infarction is one of the most common causes of death because the heart tissue cannot be regenerated. So far, only limited methods for replacing the resulting scar tissue are available.⁷⁰ A new approach could be tissue regeneration using the cell replacement using human induced pluripotent stem cells (hiPSC)-derived cardiomyocytes.⁷⁰ These hiPSC-derived cardiomyocytes could be seeded and cultured to create artificial cardiac tissue. In this chapter, six different recombinantly produced spider silk protein coatings were used as substrates for culturing human-induced pluripotent stem cells (hiPSC)-derived cardiomyocytes for the first time.¹⁷² They attached depending on the used spider silk variant, with different morphologies to the recombinant spider silk coatings. However, they attached contracted and responded to pharmacological treatment onto all RGD-modified variants and the positively charged variant eADF4(κ 16).¹⁷² This evidenced that recombinant spider silk proteins are suitable for hiPSC-based cardiac tissue engineering.

This study was done in cooperation with the university hospital in Erlangen. This chapter is a research article published in *Materials Today Bio*, available online since 15.05.2021. In this paper, I did the physicochemical analysis of the coatings of the used recombinant spider silk variants. I revised the manuscript together with the other authors.

As the author of this Elsevier article, you retain the right to include it in a thesis or dissertation, provided it is not published commercially. Permission is not required, but please ensure that you reference the journal as the original source.

Part III – Chapter 4.2 - Full paper

Materials Today Bio 11 (2021) 100114



Contents lists available at ScienceDirect

Materials Today Bio

journal homepage: www.journals.elsevier.com/materials-today-bio

Designing of spider silk proteins for human induced pluripotent stem cell-based cardiac tissue engineering

T.U. Esser^{a,1}, V.T. Trossmann^{b,1}, S. Lentz^b, F.B. Engel^{a,c,**}, T. Scheibel^{b,d,*}^a Experimental Renal and Cardiovascular Research, Department of Nephropathology, Institute of Pathology, Friedrich-Alexander-Universität Erlangen-Nürnberg (FAU), Erlangen, 91054, Germany^b Lehrstuhl Biomaterialien, Prof.-Rüdiger-Bormann Straße 1, Bayreuth, 95447, Germany^c MURCE, Muscle Research Center Erlangen, Erlangen, Germany^d Bayreuther Zentrum für Kolloide und Grenzflächen (BZKG), Bayerisches Polymerinstitut (BPI), Bayreuther Zentrum für Molekulare Biowissenschaften (BZMB), Bayreuther Materialzentrum (BayMAT), Universitätsstraße 30, Universität Bayreuth, Bayreuth, D-95447, Germany

ABSTRACT

Materials made of recombinant spider silk proteins are promising candidates for cardiac tissue engineering, and their suitability has so far been investigated utilizing primary rat cardiomyocytes. Herein, we expanded the tool box of available spider silk variants and demonstrated for the first time that human induced pluripotent stem cell (hiPSC)-derived cardiomyocytes attach, contract, and respond to pharmacological treatment using phenylephrine and verapamil on explicit spider silk films. The hiPSC-cardiomyocytes contracted for at least 14 days on films made of positively charged engineered *Araneus diadematus* fibroin 4 (eADF4(κ16)) and three different arginyl-glycyl-aspartic acid (RGD)-tagged spider silk variants (positively or negatively charged and uncharged). Notably, hiPSC-cardiomyocytes exhibited different morphologies depending on the spider silk variant used, with less spreading and being smaller on films made of eADF4(κ16) than on RGD-tagged spider silk films. These results indicate that spider silk engineering is a powerful tool to provide new materials suitable for hiPSC-based cardiac tissue engineering.

1. Introduction

Cardiovascular disease is one of the most common causes of death worldwide [1]. Despite great advances in reducing the acute mortality of cardiovascular disease through identification of risk factors (e.g. physical inactivity, high fat diet, high blood pressure, and smoking), education and diagnosis, as well as minimizing cardiomyocyte loss (e.g. antiplatelet therapy, optimized hospitalization, acute percutaneous coronary intervention), the prevalence of heart failure is rising [1]. Thus, there is a great need for novel therapies to improve heart function. Moreover, it is becoming more apparent that data derived from animal models are often not translatable into clinical practice [2–4]. Therefore, researchers in the field are working toward developing predictive human engineered cardiac tissues to model cardiac diseases [5–7], screen for therapeutic drugs [7,8], as well as repair modalities for the injured heart [9–11]. A cornerstone of

this development is the advent of human induced pluripotent stem cells (hiPSCs) and protocols for their efficient differentiation into cardiac lineages [12–15]. The hiPSCs can be derived from patients' own cells and easily modified by the genome editing technology. Clustered Regularly Interspaced Short Palindromic Repeats (CRISPR)/ CRISPR-associated protein 9 (Cas9) to introduce or correct specific mutations or to introduce reporters for monitoring specific processes [16,17].

The most advanced engineered cardiac tissues are based on cast collagen matrices [5,7], in which tissue organization can be enhanced by electrical and mechanical stimulation [18]. However, contractile forces generated by engineered heart tissues (0.05–2 mN/mm² [19]) are still significantly smaller than forces generated by native tissue (approx. 50 mN/mm² [20]). This might, for example, be due to suboptimal mechanical properties of the utilized matrix and the fabrication approach (casting). Only few other materials have been utilized for cardiac tissue

Abbreviations: AFM, atomic force microscopy; APTES, (3-aminopropyl) triethoxysilane; ATR, attenuated total reflection; DPBS, Dulbecco's phosphate-buffered saline; eADF4, Engineered *Araneus diadematus* fibroin 4; EthHD1, ethidium homodimer 1; FT-IR, Fourier-transform infrared (spectroscopy); hiPSC, human-induced pluripotent stem cell; IPTG, isopropyl-β-D-thiogalactoside; SDS-PAGE, sodium dodecyl sulfate-polyacrylamide gel electrophoresis; MALDI-TOF, matrix-assisted laser desorption/ionization time-of-flight.

* Corresponding author. Lehrstuhl Biomaterialien, Prof.-Rüdiger-Bormann Straße 1, Bayreuth, 95447, Germany.

** Corresponding author. Experimental Renal and Cardiovascular Research, Department of Nephropathology, Institute of Pathology, Friedrich-Alexander-Universität Erlangen-Nürnberg (FAU), Erlangen, 91054, Germany.

E-mail addresses: felix.engel@uk-erlangen.de (F.B. Engel), thomas.scheibel@bm.uni-bayreuth.de (T. Scheibel).

¹ Authors contributed equally to the work.

<https://doi.org/10.1016/j.mtbio.2021.100114>

Received 15 March 2021; Received in revised form 1 May 2021; Accepted 8 May 2021

Available online 15 May 2021

2590-0064/© 2021 The Author(s). Published by Elsevier Ltd. This is an open access article under the CC BY-NC-ND license (<http://creativecommons.org/licenses/by-nc-nd/4.0/>).

engineering, such as fibrin [9,18,21] and gelatin methacrylate [22,23]. Expansion of the number of materials suitable for cardiac tissue engineering will be necessary to identify one with optimized mechanical properties and to enable fabrication approaches beyond casting to generate hierarchically structured tissues including, for example, a vasculature, which is required for the creation of thick heart tissues. Limited by the rate of diffusion, the maximum thickness of non-vascularized myocardial tissue *in vitro* generally ranges from 50 to 100 μm , but this can be increased to around 200 μm through perfusion and high oxygen content and even to 0.5 mm when using an advanced perfusion bioreactor [24,25].

In order to identify 3D printable new materials, suitable for tissue engineering, the ones made of silk proteins are promising candidates [26–29]. We have previously demonstrated that materials made of natural silkworm silk and recombinant silk proteins are suitable for cardiac tissue engineering [30–32]. Recombinant spider silk proteins are non-cytotoxic, show no immunogenicity [27,33,34] and can be produced at a large scale with high purity and consistent quality [35–37]. Furthermore, their biological and mechanical properties can be engineered by genetic modifications, and they can be functionalized with growth factors or peptides specific for cardiomyocyte or cardiovascular needs [38–42], which confers a definite advantage over naturally derived (silk) proteins. A further advantage is the processability of recombinant spider silk proteins into 3D scaffolds without the need of additives or crosslinkers, such as hydrogels or foams, which can mimic the environment of natural tissue [43,44]. Our spider silk hydrogels show viscoelastic and shear-thinning behavior and could be 3D bioprinted in the presence or absence of encapsulated cells [38,45].

Our studies are based on the recombinant spider silk protein eADF4(C16), which is composed of 16 repeats of the C-module (Sequence: GSSAAAAAAAASGPGGYGPENQGPSGPGGYGPGGP) based on the *Araneus diadematus* fibroin (ADF4) of the European garden spider [37]. One glutamic acid residue (E) in each C-module yields a negative net charge in eADF4(C16) at neutral pH [37]. Although the material is highly biocompatible, previous studies showed that several cell types could not adhere to films made thereof [39,46], as most cells also have a negatively charged surface and prefer positively charged surfaces for attachment [47,48]. Further, the protein amino acid sequence of

eADF4(C16) lacks any cell-binding motifs [39,46]. When eADF4(C16) is modified with the tripeptide arginyl-glycyl-aspartic acid (RGD) cell adhesion motif or the glutamic acid residues are replaced by lysine ones, yielding the positively charged variant eADF4(κ 16), rat neonatal cardiomyocytes can attach to films made of both proteins [31,32]. These results suggested that materials made of specifically engineered spider silk proteins can be used for cardiac tissue engineering.

In this work, we expanded the number of spider silk variants tested. Further, we showed for the first time that hiPSC-cardiomyocytes can efficiently attach, spread, contract, and respond to pharmacological treatment on films made of explicit eADF4 variants.

2. Materials and methods

If not stated otherwise, all chemicals were purchased from Carl Roth, Germany.

2.1. Production of recombinant spider silk variants

The cell-binding RGD-peptide was genetically fused to the C-terminus of eADF4(κ 16) and the eADF4(Ω 16) variant (Fig. 1A) using our established cloning strategy [37,39]. Therein, all recombinant eADF4-based spider silk variants contain an N-terminally fused T7 tag enabling detection by western blot analysis. While eADF4(C16) was purchased from AMSilk GmbH in a high quality, all other recombinant eADF4-based spider silk proteins were produced via time-dependent fed-batch fermentation in *Escherichia coli* BL21 gold (DE3) as described previously [37]. In brief, the protein synthesis was initialized by adding 0.5 mM isopropyl- β -D-thiogalactoside at 30 °C. While eADF4(C16)-RGD [39] was produced for 4 h, eADF4(κ 16) [41] and eADF4(Ω 16) [40] variants were expressed for 2 h at 37 °C due to faster protein degradation and inclusion body formation. After production, all recombinant spider silk proteins were purified as described previously [37,39–41]. After cell disruption, a heat step was used to denature residual *E. coli* proteins and an ammonium sulfate precipitation to yield spider silk particles. After several washing steps to remove residual *E. coli* DNA or salt, the spider silk particles were lyophilized and stored at –20 °C. The purity of the recombinant spider silk proteins was confirmed by ultraviolet visual (UV–Vis) spectroscopy,

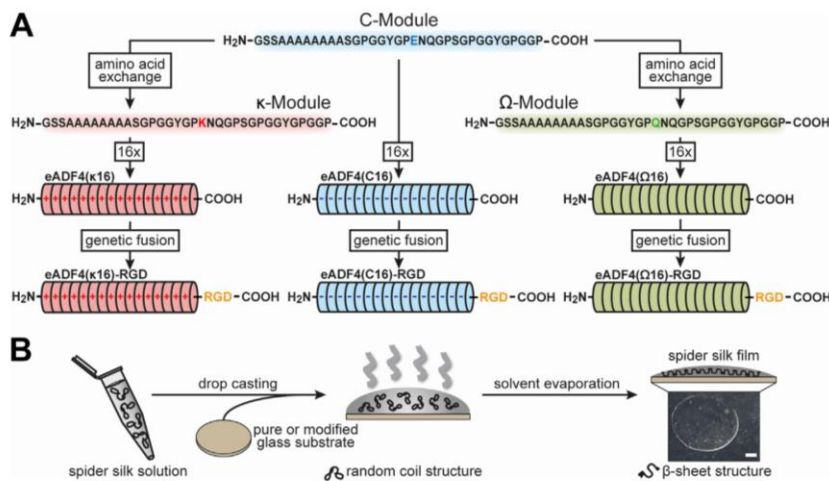


Fig. 1. Design and processing of recombinant spider silk proteins based on ADF4. **A** The negatively charged glutamic acid (E) residue of the C-module, reflecting the consensus sequence of the core domain of the natural *Araneus diadematus* fibroin 4, was replaced by a positively charged lysine (K) or an uncharged glutamine (Q) residue to generate the κ - or the Ω -module, respectively. These modules were repeated 16 times to obtain the charged recombinant spider silk variants eADF4(C16), eADF4(κ 16), or the uncharged eADF4(Ω 16). Additionally, by genetically fusing an integrin-binding sequence RGD at the C-terminus, eADF4(C16)-RGD, eADF4(κ 16)-RGD and eADF4(Ω 16)-RGD were generated. **B** For film casting, the recombinant spider silk proteins were dissolved in a formic acid-water mixture (5:1 v/v). The spider silk solutions were drop-cast on glass substrates to obtain films with 0.5 mg protein per cm^2 . For negatively charged eADF4(C16) variants, the glass substrates were modified using (3-aminopropyl) triethoxysilane (APTES) before film casting to generate a positive surface. During solvent evaporation, β -sheets formed making the spider silk films water-insoluble. Scale bar: 2 mm.

sodium dodecyl sulfate-polyacrylamide gel electrophoresis (SDS-PAGE), Western Blot, fluorescence spectroscopy, and matrix-assisted laser desorption/ionization time-of-flight (MALDI-TOF) mass spectrometry to be >98% as described previously [37,39].

2.2. Spider silk film casting

Recombinant spider silk protein films were cast on glass slides (Thermo Fisher Scientific, Germany) with an area of 1 cm² by a drop-casting process (Fig. 1B). For negatively charged eADF4(C16) variants, glass slides were functionalized using (3-aminopropyl) triethoxysilane (APTES) (Sigma-Aldrich, Germany) before film casting to prevent film detachment due to electrostatic repulsion as described previously [31,32]. In brief, after washing using acetone (VWR, Germany) and water, the glass slides were incubated in ethanol (VWR, Germany)/APTES mixture (250:1 (v/v)) for 5 h at room temperature. Afterwards, the glass slides were incubated for 1 h at 70 °C to stabilize the APTES functionalization. Before film casting, the APTES-functionalized and the pure glass slides were washed using water and ethanol. All eADF4 variants were solved at a concentration of 5 mg/ml in a formic acid/water mixture (5:1 (v/v)) in a step-wise manner in which the protein powder was first solved in formic acid (VWR, Germany) for 30 min before water was added. 100 µL spider silk solution was dropped on glass slides. After evaporation of the solvent, spider silk films containing 0.5 mg spider silk protein per cm² were obtained and stored at dry and dark conditions until further use. Formic acid was used for film casting, as the obtained films were already water-insoluble making a subsequent treatment afterwards unnecessary [49–51]. The resulting films were used as-cast for subsequent experiments without any further washing steps or treatment afterwards.

2.3. Fourier transform infrared spectroscopy

Fourier transform infrared (FT-IR) spectroscopy was performed using a Bruker Tensor 27 FT-IR-spectrometer with Mercury Cadmium Telluride (MCT)-detector (Bruker, Rheinstetten, Germany) coupled with a Hyperion 1000 FT-IR microscope (Bruker Rheinstetten, Germany) with an attenuated total reflection (ATR) lens (20x). The germanium crystal was brought into contact with the sample. The FT-IR spectra were recorded in reflectance mode in a wavenumber range of 4000 cm⁻¹–800 cm⁻¹ with a spectral resolution of 4 cm⁻¹. One hundred scans were recorded for each spectrum. Atmospheric compensation and background spectra in air were applied to each spectrum. The spectra were smoothed with five points, and the baseline was corrected using the rubber band method with 64 baseline points and one iteration. Fourier self-deconvolution (FSD) and curve fitting were performed as described previously [52,53].

2.4. Atomic force microscopy

For surface topography characterization, the recombinant spider silk films on glass were analyzed in tapping mode using a Dimension Icon atomic force microscope (Bruker, Karlsruhe, Germany) with a resolution of 512 to 512 data points at 1 Hz. OTESPA-R3 silicon cantilevers with a spring constant of 26 Nm⁻¹ were used. The scan size was 50 µm–50 µm. Images were processed with Nanoscope analysis 1.5 afterwards, plane fitted and flattened with first-order fits.

2.5. Water contact angle measurements

Water contact angle measurements were conducted on spider silk coatings as well as untreated and silanized glass slides at a SurfTens-universal tensiometer (OEG GmbH, Germany) using the SCA-20 software and the sessile drop method. Therefore, water droplets were applied on the surface of recombinant spider silk films or appropriate glass substrates. After 10 s equilibration time at room temperature an image was taken, and the contact angle was analyzed. (Nine measurements per condition n = 9).

2.6. Human induced pluripotent stem cells culture and cardiac differentiation

Human induced pluripotent stem cells (hiPSCs) were cultured in StemMACS iPS-Brew XF (Miltenyi Biotec, Germany) on Matrigel™-coated multiwell culture plates. Medium change was performed daily. For maintenance culture, hiPSCs were passaged at 75%–80% confluency using ethylene diamine tetra acetic acid (EDTA, 0.5 mM, Thermo Fisher Scientific) and re-plated in StemMACS iPS-Brew XF supplemented with 10 µM rho-associated protein kinase (ROCK)-inhibitor (Y-27632, Selleck Chemicals). For subsequent differentiation, hiPSCs were dissociated into single cells using Accutase (Sigma-Aldrich) and re-plated in StemMACS iPS-Brew XF supplemented with ROCK-inhibitor at a density of ~21,000 cells/cm². A cardiac differentiation protocol based on that described by Lian and coworkers was used [15]. At 80%–90% confluency, cardiac differentiation was initiated by exchanging the culture medium to differentiation medium (M_{Diff}) comprising Roswell Park Memorial Institute (RPMI) 1640 medium (Thermo Fisher Scientific) supplemented with 2% B-27 Minus Insulin (Thermo Fisher Scientific) and 100 µM L-ascorbic acid (Sigma-Aldrich). For the first 24 h (day 0–1), culture medium was further supplemented with 8–10 µM CHIR-99021 (Sigma Aldrich). Subsequently, medium was exchanged to M_{Diff} without additional supplementation. On day 3 of differentiation, medium was exchanged to conditioned M_{Diff} comprising equal parts of fresh M_{Diff} and M_{Diff} from days 1–3 of differentiation, and supplemented with 5 µM IWR-1 (Selleck Chemicals). Fresh M_{Diff} without additional supplementation was added on day 5 of differentiation. Subsequently, on day 7 of differentiation culture medium was exchanged to maintenance medium (M_{Main}) comprising RPMI 1640 supplemented with 2% B-27 Supplement (Thermo Fisher Scientific). Cardiomyocytes were purified by switching to lactate selection medium comprising Glucose-free RPMI 1640 (Thermo Fisher Scientific) supplemented with 5 mM sodium-lactate (Sigma-Aldrich) and 100 mM L-ascorbic acid. Metabolic selection was performed for 4–5 days starting on day 9–11 of differentiation, after which culture medium was changed back to M_{Main} for continued maintenance.

2.7. Cardiomyocyte culture on recombinant spider silk films

Cardiomyocytes were dissociated on day 15–22 of differentiation by incubation with Accutase for 30 min at 37 °C. 200,000 cells in M_{Main} supplemented with 1% RevitaCell (Thermo Fisher Scientific) were seeded per coverslip and left to attach for 24 h. Coverslips were then washed with Dulbecco's phosphate-buffered saline (DPBS, Thermo Fisher Scientific) and subsequently cultured in M_{Main}, with medium changes every 2 days.

2.8. Live-dead-staining

Cardiomyocytes cultured on spider silk films for 72 h were incubated with 1 mM Calcein, 2 mM Ethidium Homodimer-1 (EthHD1) and 5 µg/mL Hoechst 33421 (all Thermo Fisher Scientific) in DPBS for 30 min at 37 °C. Cells were subsequently washed with fresh DPBS and directly mounted onto glass slides using Fluoromount-G (Thermo Fisher Scientific). Samples were imaged immediately on a Keyence BZ-9000 epifluorescence microscope equipped with a 20x Plan Apo objective (Nikon). Calcein⁺ and Ethidium Homodimer-1⁺ cells were counted manually using Hoechst to distinguish autofluorescent debris.

2.9. Immunofluorescence staining

Cardiomyocytes were washed with DPBS and fixed with 4% paraformaldehyde for 15 min at room temperature. Samples were washed

and permeabilized (0.5% Triton X-100 in phosphate buffered saline [PBS]), followed by incubation with blocking buffer (5% bovine serum albumin [BSA], 0.2% Tween-20 in PBS). Samples were incubated with primary antibody overnight at 4 °C. The following antibodies were used at the indicated dilution: anti-sarcomeric α -actinin (abcam, ab9465, 1:500); anti-cardiac troponin-I (abcam, ab56357, 1:500); anti-connexin 43 (abcam, ab11370, 1:250). Secondary antibody incubation was performed for 1 h at room temperature: donkey anti-mouse Alexa Fluor 647 (1:500); donkey anti-rabbit Alexa Fluor 488 (1:500); donkey anti-goat Alexa Fluor 594 (1:500). All antibodies were diluted in blocking buffer. Samples were counterstained with 4',6-diamidino-2-phenylindole (DAPI) and mounted onto glass slides using Fluoromount G. Images were acquired using a laser scanning confocal microscope (LSM 800, Zeiss) equipped with a 20x Plan-APOCHROMAT and a 63x Plan-APOCHROMAT oil immersion objective (both Zeiss).

2.10. Quantification of immunofluorescence staining

For quantification of cardiomyocyte size, images ($\sim 320 \times 320 \mu\text{m}$) of hiPSC-cardiomyocytes, immunofluorescently stained for sarcomeric α -actinin and counterstained with DAPI, were used. Intensity thresholds were set for each image individually, and the area of α -actinin signal was measured. Nuclei were counted and outlined manually, and their size was recorded. All analyses were performed using the Fiji image processing package of ImageJ [54].

2.11. Contraction analysis

Videos of beating cardiomyocytes were recorded at 15 frames per second using a Keyence BZ-9000 microscope equipped with a 20x Plan Fluor objective (Nikon). The number of contractions in each video (10 s) was extrapolated to obtain beats per minute (bpm). The beating frequency calculated from three to four videos were averaged for each sample. Contraction profiles were generated using the MUSCLEMOTION plugin [55] for the image processing software ImageJ/FIJI [54]. For analysis of drug response, baseline contraction behavior was recorded first. Then, 50 μM phenylephrine was added to the culture medium. Videos were recorded after incubating the samples for 10 min at 37 °C. Subsequently, 1 μM verapamil was added, followed by an additional incubation for 10 min at 37 °C and a final recording.

2.12. Statistics

Statistical analyses were conducted in PRISM 5 (GraphPad). Statistical significance was determined by one-way analysis of variance (ANOVA), followed by a *post hoc* test according to Tukey, assuming normal distribution, or two-way ANOVA when indicated. P-values of <0.05 were considered to indicate significant differences between the groups tested.

3. Results and discussion

3.1. Analysis of spider silk variant films as scaffolds for hiPSC cardiomyocytes

Negatively charged eADF4(C16) is based on 16 repeats of the consensus sequence of ADF4 and has been established almost two decades ago [37]. In recent years, modifications of this recombinant protein

comprised the introduction of an RGD-tag in eADF4(C16)-RGD [39]. Furthermore, the exchange of all glutamic acid residues with lysine or glutamine ones, yielded positively charged eADF4(κ 16) [41], and uncharged eADF4(Ω 16) [40], respectively. Herein, to further extend the range of modified spider silk proteins, RGD-fusions with eADF4(κ 16) and eADF4(Ω 16) were generated (Fig. 1A).

Spider silk films were processed on untreated and 3-aminopropyltriethoxysilane (APTES)-functionalized (i.e. silanized) glass substrates at a density of 0.5 mg protein per cm^2 . The differently charged and RGD-modified spider silk proteins were successfully processed into flat films. The positively charged eADF4(κ 16) and uncharged eADF4(Ω 16) variants were stably fixed on the negatively charged glass substrates without treatment beforehand. In contrast, silanization was used to immobilize films made of the negatively charged eADF4(C16) and eADF4(C16)-RGD variants. All films were stable during all experiments, including long-term cell cultivation. No apparent degradation or detachment was detected, confirming results from previous experiments using spider silk films [31,32,34,56].

The secondary structure of recombinant spider silk films was analyzed using FT-IR spectroscopy. In the herein used approach, a subsequent treatment of the spider silk proteins afterwards was not necessary [49–51], since the initial β -sheet content was sufficiently high, after processing from the very beginning, turning the recombinant spider silk films water-insoluble [51,52]. All recombinant spider silk variants showed nearly the same broad curve shape of amide I ($1,600 \text{ cm}^{-1} - 1,700 \text{ cm}^{-1}$) and amide II ($1,570 \text{ cm}^{-1} - 1,540 \text{ cm}^{-1}$) bands (Supplementary Fig. 1A).

Fourier self-deconvolution (FSD) and curve fitting were used to evaluate the secondary structure content of the amide I region (Supplementary Fig. 1B, Table 1) [53].

Primary cell attachment to biomaterial surfaces is influenced by surface topography and, in most cases, by the surface roughness of a material. The surface topography of flat 2D spider silk films was determined without further washing using AFM (Fig. 2A). The height images (Fig. 2A, AFM pictures, upper row) showed a smooth surface topography for eADF4(C16) and eADF4(Ω 16) variants. However, the height AFM pictures indicated circular patches in the cases of eADF4(C16)-RGD, eADF4(Ω 16) and eADF4(Ω 16)-RGD films, which were also visible in the related phase images (Fig. 2A, lower row). These phase images represent the delay of the oscillation of the cantilever in tapping mode. The phase signal is sensitive to different material-related properties like composition, stiffness/softness and viscoelastic properties [57]. These patches on eADF4(C16)-RGD, eADF4(Ω 16) and eADF4(Ω 16)-RGD films (Fig. 2A, lower row) indicated different viscoelastic properties of the patches in comparison to the rest of the film. The patches could result from microphase separation of hydrophobic and hydrophilic parts of the protein as published previously [51,52]. Thereby, during film assembly the hydrophilic parts (GGX and GPGX motifs) of the eADF4-variants separate from the hydrophobic parts (polyalanine stretches), leading to structural patches with crystalline areas embedded in an amorphous matrix. The coupled RGD sequence affected the size of these patches in case of the negatively and uncharged variants, as they were smaller for eADF4(C16)-RGD and eADF4(Ω 16)-RGD compared to eADF4(Ω 16). In contrast, both positively charged films, eADF4(κ 16) and eADF4(κ 16)-RGD, showed a smooth film surface without any patches despite salt crystals distributed over the entire surface. These salt crystals were increasing the apparent total surface roughness.

Table 1

Secondary structure content [%] of recombinant spider silk films determined using FSD analysis according to Hu et al. [53].

Secondary structure	eADF4(C16)	eADF4(C16)-RGD	eADF4(κ 16)	eADF4(κ 16)-RGD	eADF4(Ω 16)	eADF4(Ω 16)-RGD
β -sheets	31.0 \pm 0.4	34.4 \pm 0.9	24.7 \pm 7.9	28.1 \pm 1.0	27.4 \pm 2.0	26.9 \pm 1.4
random coils	35.4 \pm 0.5	34.4 \pm 0.3	36.9 \pm 3.7	34.1 \pm 0.7	34.5 \pm 0.3	34.9 \pm 1.3
α -helices	11.5 \pm 0.3	10.9 \pm 0.1	12.2 \pm 0.7	11.1 \pm 0.4	11.2 \pm 0.3	11.5 \pm 0.5
β -turns	19.7 \pm 0.3	18.8 \pm 0.3	23.4 \pm 1.5	20.1 \pm 0.9	20.1 \pm 1.5	20.4 \pm 0.5
others	2.5 \pm 1.5	1.5 \pm 0.8	2.7 \pm 2.2	6.6 \pm 0.6	6.7 \pm 0.4	6.4 \pm 0.8

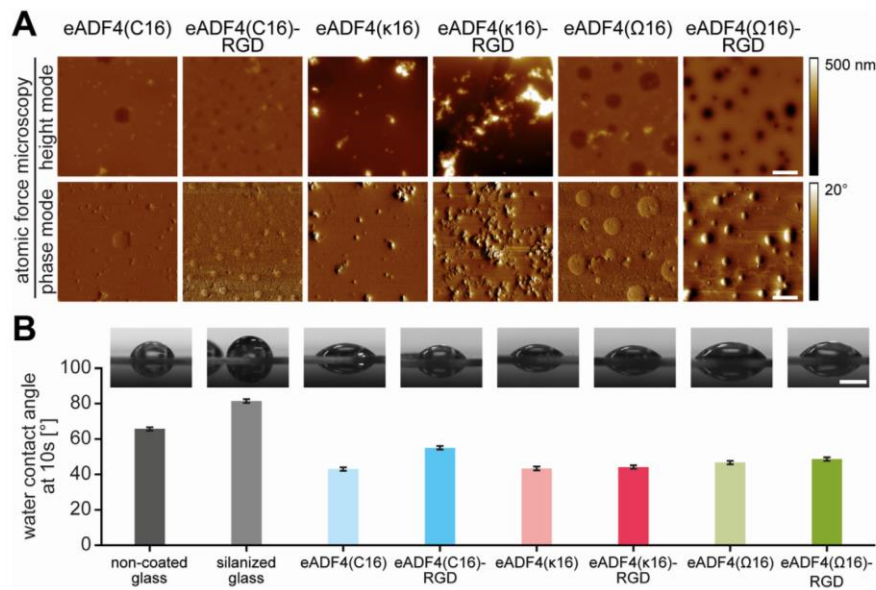


Fig. 2. Spider silk film surface characterization. **A** Film surface topography was determined using atomic force microscopy (AFM) in tapping mode in air. Scale bar: 10 μ m **B** Water contact angles on spider silk films and non-coated and silanized glass materials were determined after 10 s using the sessile drop method. Scale bar: 1 mm.

Finally, water contact angle measurements were performed to evaluate the surface hydrophobicity of the films (Fig. 2B). Surfaces with a water contact angle below 90° are characterized as hydrophilic, while water contact angles above this threshold are indicative of hydrophobic surfaces. Untreated and APTES-functionalized (silanized) glass slides showed contact angles around 66° and 81°, respectively, and are *per se* defined as hydrophilic surfaces. Nevertheless, spider silk surfaces were more hydrophilic, indicated by a better spread water droplet (Fig. 2B). All spider silk variants, except eADF4(C16)-RGD, showed contact angles between 43° and 49°. The slightly higher contact angle of 55° for eADF4(C16)-RGD in comparison to eADF4(C16) confirmed results of a former study [31]. The presence of salt crystals on eADF4(κ 16)-based spider silk films showed no influence on the water contact angle and surface hydrophobicity [32].

3.2. Human induced pluripotent stem cell-cardiomyocytes attach to films of distinct spider silk variants

In order to evaluate the spider silk variants' suitability for human cardiac tissue engineering applications, human induced pluripotent stem cell (hiPSC)-cardiomyocytes were seeded on silk films, and the viability

of attached cells was determined after 3 days using Calcein and Ethidium Homodimer-1 (EthHD1) staining. As a control adhesion matrix, Matrigel™ was used, representing a laminin-rich mixture of extracellular matrix (ECM) proteins. While Matrigel™ is typically used to culture hiPSC-cardiomyocytes *in vitro*, it is not suitable for clinical translation, due to its tumor-related origin and associated safety concerns. In addition, the composition of Matrigel™ is not fully defined and is also subject to lot-to-lot variability [58].

High viability was found on films made of RGD-modified spider silk variants, irrespective of their charge, comparable to the viability of hiPSC-cardiomyocytes on Matrigel™ (Fig. 3A). Similarly, cells on eADF4(κ 16) films exhibited high viability. In contrast, the degree of viability was significantly reduced on eADF4(C16) and eADF4(Ω 16) films (similar to glass controls). Considering the non-cytotoxic nature of spider silk proteins [27,33,34], the reduced viability is probably due to a lack of proper cell attachment. Note, our experience shows also that non-proliferative cardiomyocytes undergo cell death when seeded at very low densities. Importantly, part of the seeded cells is dead as a result of metabolic selection during differentiation and cell dissociation. These dead cells stick to surfaces (in our case also

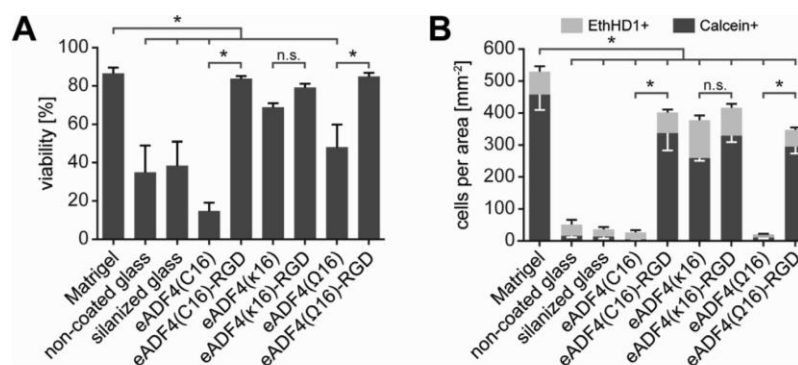


Fig. 3. hiPSC-cardiomyocytes adhere to films made of several spider silk variants. **A** Percentage of viable cells on spider silk films made of different variants 3 days after seeding as determined by Calcein and Ethidium Homodimer-1 (EthHD1) staining. Data are mean \pm standard error (SE) of the mean. *: $p < 0.05$, one-way ANOVA followed by a *post hoc* test according to Tukey. **B** Count of viable (Calcein+) and dead (EthHD1+) cells per area on spider silk films 3 days after seeding. $N = 4$ independent experiments. Data are mean \pm standard error of the mean. *: $p < 0.05$, one-way ANOVA followed by a *post hoc* test according to Tukey.

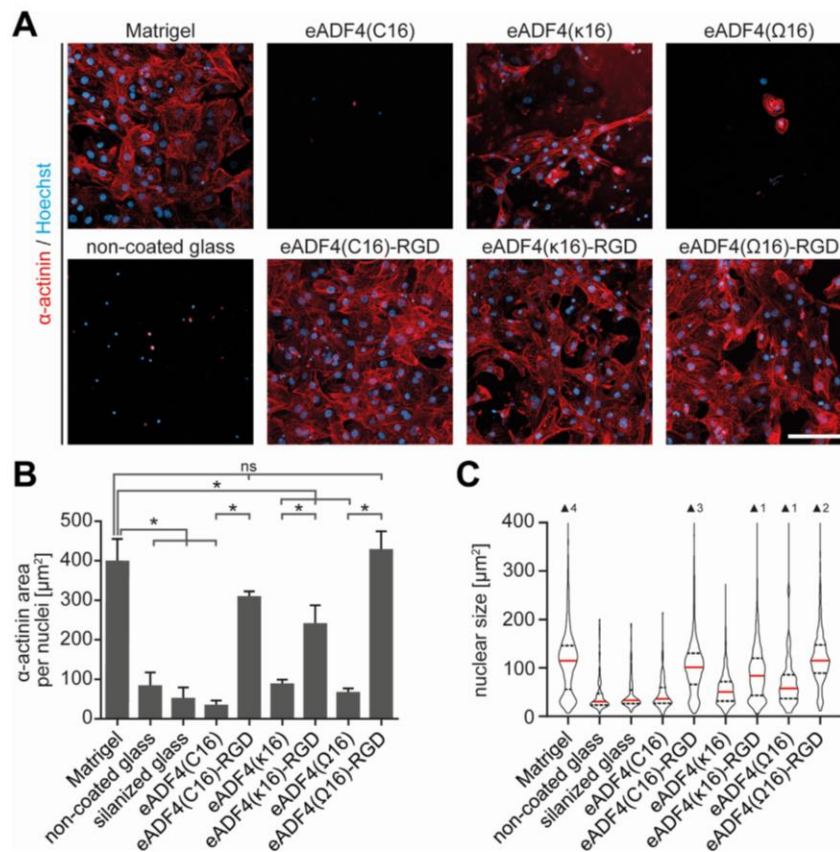


Fig. 4. hiPSC-cardiomyocytes display different morphologies depending on the spider silk variant used as scaffold. **A** Immunofluorescence staining for hiPSC-cardiomyocyte marker protein sarcomeric α -actinin (red) 3 days after seeding. Scale bar: 100 μm . **B** Quantification of sarcomeric α -actinin immunofluorescence signal area, normalized to nuclei count 3 days after seeding. Data from four independent experiments are presented as mean \pm standard error of the mean. *: $p < 0.05$, one-way ANOVA followed by a *post hoc* test according to Tukey. **C** Violin plots of nuclear size 3 days after seeding. Data from four independent experiments are presented ($n = 101$ to 1944). Red lines: median; dashed lines: 1st and 3rd quartile. \blacktriangle : number of data points outside of the depicted range.

non-coated glass) independently of adhesion motifs and thus are overrepresented on films to which hiPSC-derived cardiomyocytes adhere only inefficiently.

To further examine the interaction of hiPSC-cardiomyocytes with the different surfaces, the absolute numbers of live (Calcein⁺) and dead (EthidiumHD1⁺) cells were assessed (Fig. 3B). The number of cells on unmodified eADF4(C16) and eADF4(Q16) films were very low and comparable to glass controls, where only a few viable cells were found. In contrast, the amounts were markedly higher on RGD-modified spider silk variants, as well as eADF4(κ 16). Importantly, the number of viable cells on eADF4(κ 16) films was comparable to that observed for eADF4(κ 16)-RGD ones. No significant differences were observed between the different RGD-modified variants. The observed higher number of attached cells on MatrigelTM, compared to RGD-variant and eADF4(κ 16) films, might be explained by the greater variety of cell adhesion motifs and integrin recognition sites, as MatrigelTM comprises a multitude of extracellular matrix (ECM) proteins [59]. In addition, growth factors present in MatrigelTM might promote attachment.

Attachment on eADF4(κ 16) films appeared to be mediated by its charge, since the primary amino acid sequence of this spider silk sequence contains no cell-binding motif [46], and the cell membrane of mammalian cells is mainly negatively charged and interacts preferentially with polycationic surfaces [32,47,48]. The attachment efficiency to eADF4(κ 16) films was comparable with the efficiencies of eADF4(C16)-RGD or eADF4(Q16)-RGD ones. Interestingly, the RGD-modification of eADF4(κ 16) did not further improve cell attachment. This suggested that the peptide motif of eADF4(κ 16)-RGD has no additional, synergistic effect on initial adhesion to the positively charged surface.

3.3. hiPSC-cardiomyocytes exhibit different morphologies depending on the spider silk variant

Immunofluorescent staining of sarcomeric α -actinin revealed hiPSC-cardiomyocyte spreading on RGD-modified variants, similar to MatrigelTM-controls, 3 days after seeding (Fig. 4A). In contrast, on eADF4(C16) and eADF4(Q16) films, hiPSC-cardiomyocytes remained rounded and did not spread. Notably, while being comparable in number (Fig. 3B), the hiPSC-cardiomyocytes on eADF4(κ 16) films appeared less spread and smaller than those on eADF4(κ 16)-RGD films (Fig. 4A). To obtain an estimation of cardiomyocyte size, the area of α -actinin staining was determined as well as the number of nuclei of a given field of view (Fig. 4B). Our analyses showed that the few cardiomyocytes attached to unmodified variants, irrespective of charge, exhibited the smallest α -actinin areas/nuclei with values comparable to those of cells on glass controls. The analyses further revealed that cardiomyocytes spread most on films made of RGD-variants, with α -actinin/nuclei levels highest for cells grown on MatrigelTM, eADF4(Q16)-RGD and eADF4(C16)-RGD and slightly smaller for cells on eADF4(κ 16)-RGD. Notably, the analyses confirmed that cells on eADF4(κ 16) films exhibited a significantly lower α -actinin area per nuclei compared with cells on eADF4(κ 16)-RGD.

To validate these results, nuclear size was quantified as an indirect indicator of cardiomyocyte cell size. Notably, cells usually maintain a roughly constant nuclear-to-cytoplasmic volume ratio [60]. It has been previously shown that during maturation, the increase in cardiomyocyte size is accompanied by an increase in size of the nuclei [61].

As shown in Fig. 4C, nuclear size data were in agreement with α -actinin area/nuclei data, whereby the average nuclear size was largest

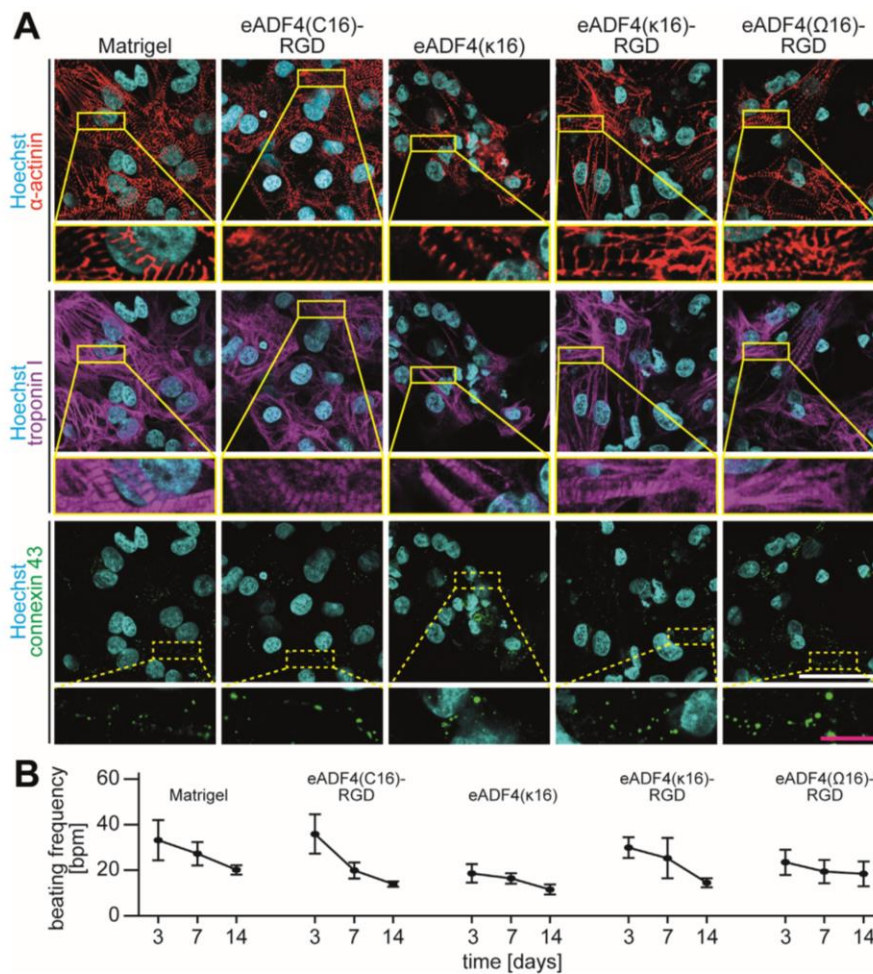


Fig. 5. Long-term cultivation of hiPSC-cardiomyocytes on spider silk films. A Immunofluorescence staining of the hiPSC-cardiomyocyte marker proteins sarcomeric α -actinin (red), cardiac troponin I (magenta) and connexin 43 (green) 14 days after seeding. White scale bar: 50 μ m; magenta scale bar: 10 μ m. B Beating frequency of hiPSC-cardiomyocytes at 3, 7 and 14 days after seeding. Data from 3 independent experiments are presented as mean \pm standard error of the mean.

on eADF4(Ω16)-RGD, surpassing sizes on both eADF4(C16)-RGD and eADF4(κ16)-RGD as well as Matrigel™.

In summary, hiPSC-cardiomyocytes attachment did not correlate with cell size, as hiPSC-cardiomyocytes attached on eADF4(κ16) films were markedly smaller than those attached on films made of RGD-modified variants. These findings are in agreement with reports that RGD-mediated integrin signaling is required for hypertrophic responses in cardiomyocytes [62,63].

3.4. Long-term cultivation of hiPSC-cardiomyocytes on spider silk films

To evaluate the possibility of long-term cultivation of hiPSC-cardiomyocytes on spider silk films, cultures were analyzed for up to 14 days. Immunofluorescent staining for α -actinin revealed a striated pattern, typical for hiPSC-cardiomyocytes, on all RGD-modified spider silk variants, similar to that on Matrigel™ (Fig. 5A). hiPSC-cardiomyocytes cultured on eADF4(κ16) remained smaller, even after this prolonged culture period. Additionally, cardiac troponin I (cTnI), an isoform of troponin I associated with hiPSC-cardiomyocytes maturation, was found in a striated pattern on RGD-modified variants, whereas it appeared more disorganized on eADF4(κ16) (Fig. 5A). Further, the gap junction protein connexin 43 could be identified at cell-to-cell contacts, suggesting electrical

coupling (Fig. 5A). In accordance, spontaneous contractions of hiPSC-cardiomyocytes were observed on films made of RGD-modified variants and eADF4(κ16) as early as 24 h after seeding, and consistently by day 3 of culture. Connexin 43 was not specifically localized to longitudinal termini of cardiomyocytes (i.e. intercalated discs) on either of the matrices investigated, but distributed around the entire cells, suggesting that hiPSC-derived cardiomyocytes did not undergo advanced maturation on spider silk films compared to Matrigel™.

Of note, hiPSC-cardiomyocytes on RGD-modified variants and Matrigel™ contracted synchronously across each field of view, while contractions on eADF4(κ16) were asynchronous (Supplementary Fig. 2), which appears to result from the smaller cell size and, therefore, lower coverage and cell-to-cell contact impairing electrical coupling.

To investigate hiPSC-cardiomyocyte contractility on spider silk variant films over time, cultures were analyzed for up to 14 days, and the beating behavior was recorded (Fig. 5B). An overall reduction in beating frequency was observed with increasing culture time (influence of culture time: $p < 0.05$ determined by two-way ANOVA). However, no significant differences between RGD-modified variants, eADF4(κ16) or Matrigel™ were observed at either time point (day 3, 7 or 14). These findings indicated that films made of these spider silk variants supported long-term culture and did not impair hiPSC-cardiomyocyte contractility.

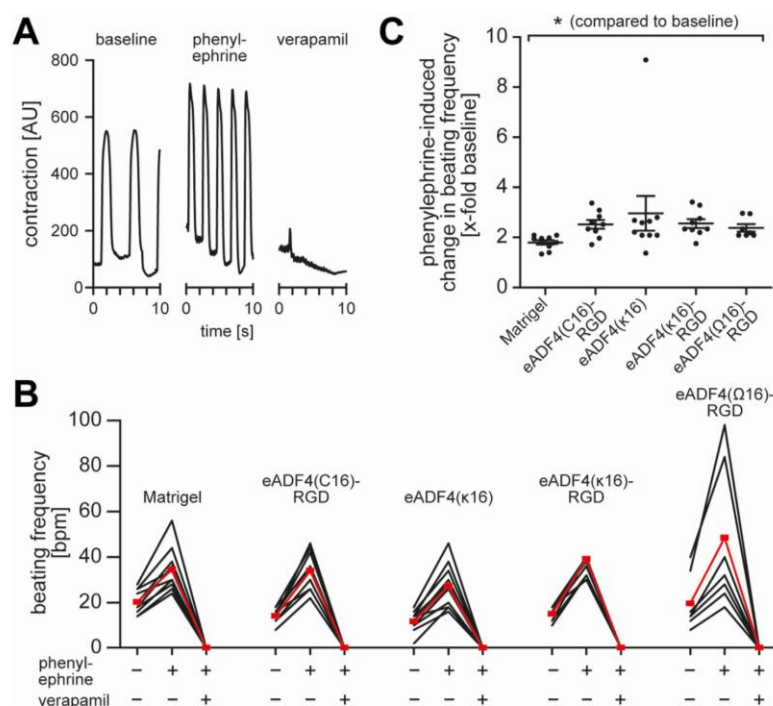


Fig. 6. hiPSC-cardiomyocytes on selected spider silk films are responsive to drug treatment. **A** Scheme of workflow and exemplary contraction profiles of hiPSC-cardiomyocytes at baseline and in response to adrenergic stimulation (50 μ M phenylephrine) and calcium channel blockade (1 μ M verapamil). **B** Beating frequencies of hiPSC-cardiomyocytes upon treatment with phenylephrine and verapamil on spider silk films. Individual samples (n = 7 to 10) are shown in black; means are shown in red. **C** Quantification of the increase in beating frequencies upon phenylephrine treatment. Data from 4 (3 for eADF4(Q16)-RGD) independent experiments are presented as individual data points (black dots) and mean \pm standard error of the mean (gray bars). *: p < 0.05, one-way ANOVA followed by a post hoc test according to Tukey.

3.5. hiPSC-cardiomyocytes on spider silk films respond to pharmacological stimulation

Next, cells were treated with phenylephrine, an adrenergic agonist, and subsequently verapamil, an inhibitor of L-type calcium channels, and the contractions were recorded (Fig. 6A). Phenylephrine induced a significant increase in beating frequency of hiPSC-cardiomyocytes on all spider silk variants tested, while verapamil abolished beating (Fig. 6B and C). A 1.7–2.9-fold increase in beating frequency was detected upon phenylephrine treatment.

4. Conclusion

Two Previous studies have established that spider silk materials made of eADF4 variants are very suitable and promising materials for tissue engineering and biomedical applications, as spider silk materials are highly biocompatible and cause no unspecific immune response [27,33,34]. From the findings presented here, we deduce that these materials are also promising scaffolds for cardiac tissue engineering. Interestingly, while hiPSC-cardiomyocytes could not adhere to eADF4(C16) without additional modification, they could be cultivated on specifically engineered spider silk variants. We conclude that specific modified spider silk variants, tailored to tissue-specific requirements, can be utilized to engineer human cardiac tissues aiming at modeling human diseases, screening for therapeutic drugs, and improving heart function in patients. This is an important observation, as it might allow to design strategies for selective growth of cardiomyocytes in the future, and thus might help in designing hierarchically structured cardiac tissues. Further, hiPSC-cardiomyocytes exhibited selective cell behavior on films made of the different spider silk variants, which might be of advantage for certain applications. The smaller cell size in contact with eADF4(k16) surfaces might allow the generation of cardiac tissues with a higher cardiomyocyte density, which might, therefore, exhibit a higher contractile force. Such a construct could then also be

enlarged by subsequent stimulation with pro-hypertrophic agents. In the context of 3D printing, a smaller cell size might also be of advantage, for example, regarding shear stress.

Credit author statement

TUE, VTT, and SL carried out experimental work and analyzed data; TUE, VTT, FBE, and TS wrote the original draft of the manuscript; FBE and TS conceptualized and supervised the study; all authors revised and approved the final version of the manuscript.

Declaration of competing interest

The authors declare the following financial interests/personal relationships which may be considered as potential competing interests: Prof. Scheibel is co-founder and shareholder of AMSilk GmbH.

Acknowledgments

The authors would like to thank Isabel Schoenauer for assistance in confirming stem cell pluripotency, Jana Petzold for technical advice, as well as Annika Döbl, Kaveh Roshanbinfar and Ingo Thievensen for critical discussions. Support from the Elite Network of Bavaria is also acknowledged. This work was supported by the Deutsche Forschungsgemeinschaft [DFG, German Research Foundation, grant numbers: Projektnummer 326998133 – TRR 225 (subproject C01 to F.B.E. and T.S.) and INST 410/91-1 FUGG (to F.B.E.)].

Appendix A. Supplementary data

Supplementary data to this article can be found online at <https://doi.org/10.1016/j.mtbio.2021.100114>.

References

- [1] S.S. Virani, A. Alonso, E.J. Benjamin, M.S. Bittencourt, C.W. Callaway, A.P. Carson, A.M. Chamberlain, A.R. Chang, S. Cheng, F.N. Delling, L. Djousse, M.S.V. Elkind, J.F. Ferguson, M. Fornage, S.S. Khan, B.M. Kissela, K.L. Knutson, T.W. Kwan, D.T. Lackland, T.T. Lewis, J.H. Lichtman, C.T. Longenecker, M.S. Loop, P.L. Lutsey, S.S. Martin, K. Matsushita, A.E. Moran, M.E. Mussolino, A.M. Perak, W.D. Rosamond, G.A. Roth, U.K.A. Sampson, G.M. Satou, E.B. Schroeder, S.H. Shah, C.M. Shay, N.L. Spartano, A. Stokes, D.L. Tirschwell, L.B. VanWagner, C.W. Tsao, E. American Heart Association Council on, C. Prevention Statistics, S. Stroke Statistics, Heart disease and stroke statistics-2020 update: a report from the American heart association, *Circulation* 141 (2020) e139 e596, <https://doi.org/10.1161/CIR.0000000000000757>.
- [2] S. Lecour, H.E. Botker, G. Condorelli, S.M. Davidson, D. Garcia-Dorado, F.B. Engel, P. Ferdinandy, G. Heusch, R. Madonna, M. Ovize, M. Ruiz-Meana, R. Schulz, J.P. Sluiter, L.W. Van Laake, D.M. Yellon, D.J. Hausenloy, ESC working group cellular biology of the heart: position paper: improving the preclinical assessment of novel cardioprotective therapies, *Cardiovasc. Res.* 104 (2014) 399–411, <https://doi.org/10.1093/cvr/cvt225>.
- [3] S. Clauss, C. Bleyer, D. Schuttler, P. Tomsits, S. Renner, N. Klymiuk, R. Winkl, S. Massberg, E. Wolf, S. Kaab, Animal models of arrhythmia: classic electrophysiology to genetically modified large animals, *Nat. Rev. Cardiol.* 16 (2019) 457–475, <https://doi.org/10.1038/s41569-019-0179-0>.
- [4] C.J. Perry, A.J. Lawrence, Hurdles in basic science translation, *Front. Pharmacol.* 8 (2017) 478, <https://doi.org/10.3389/fphar.2017.00478>.
- [5] M. Tiburcy, J.E. Hudson, P. Balfanz, S. Schlick, T. Meyer, M.L. Chang Liao, E. Levent, F. Raad, S. Zeldner, E. Wingender, J. Riegler, M. Wang, J.D. Gold, I. Kehat, E. Wettwer, U. Ravens, P. Dierckx, L.W. van Laake, M.J. Goumans, S. Khadjeh, K. Toischer, G. Hasenfuss, L.A. Couture, A. Unger, W.A. Linke, T. Araki, B. Neel, G. Keller, L. Gepstein, J.C. Wu, W.H. Zimmermann, Defined engineered human myocardium with advanced maturation for applications in heart failure modeling and repair, *Circulation* 135 (2017) 1832–1847, <https://doi.org/10.1161/CIRCULATIONAHA.116.024145>.
- [6] J.T. Hinson, A. Chopra, N. Nafisi, W.J. Polacheck, C.C. Benson, S. Swist, J. Gorham, L. Yang, S. Schafer, C.C. Sheng, A. Haghghi, J. Homsy, N. Hubner, G. Church, S.A. Cook, W.A. Linke, C.S. Chen, J.G. Seidman, C.E. Seidman, Titin mutations in IPS cells define sarcomere insufficiency as a cause of dilated cardiomyopathy, *Science* 349 (2015) 982–986, <https://doi.org/10.1126/science.1254548>.
- [7] Y. Zhao, N. Rafatian, N.T. Feric, B.J. Cox, R. Aschar-Sobbi, E.Y. Wang, P. Aggarwal, B. Zhang, G. Conant, K. Ronaldson-Bouchard, A. Pahnke, S. Protze, J.H. Lee, L. Davenport Huyer, D. Jekic, A. Wickeler, H.E. Naguib, G.M. Keller, G. Vunjak-Novakovic, U. Brockel, P.H. Backx, M. Radisic, A platform for generation of chamber-specific cardiac tissues and disease modeling, *Cell* 176 (2019) 913–927, <https://doi.org/10.1016/j.cell.2018.11.042>, e18.
- [8] M. Lemme, B.M. Ulmer, M.D. Lemoine, A.T.L. Zech, F. Flenner, U. Ravens, H. Reichenspurner, M. Rol-Garcia, G. Smith, A. Hansen, T. Christ, T. Eschenhagen, Atrial-like engineered heart tissue: an in vitro model of the human atrium, *Stem Cell Rep.* 11 (2018) 1378–1390, <https://doi.org/10.1016/j.stemcr.2018.10.008>.
- [9] P. Menasché, V. Vannieu, A. Hagege, A. Bel, B. Cholley, A. Parouchev, I. Cacciapuoti, R. Al-Daccak, N. Benhamouda, H. Blons, O. Agbulut, L. Tosca, J.H. Troun, J.R. Fabreguettes, V. Bellamy, D. Charron, E. Tartour, G. Tachdjian, M. Desnos, J. Larghero, Transplantation of human embryonic stem cell-derived cardiovascular progenitors for severe ischemic left ventricular dysfunction, *J. Am. Coll. Cardiol.* 71 (2018) 429–438, <https://doi.org/10.1016/j.jacc.2017.11.047>.
- [10] R. Madonna, L.W. Van Laake, H.E. Botker, S.M. Davidson, R. De Caterina, F.B. Engel, T. Eschenhagen, F. Fernandez-Aviles, D.J. Hausenloy, J.S. Hulot, S. Lecour, J. Leor, P. Menasché, M. Pesce, C. Perrino, F. Premier, S. Van Linthout, K. Ytrehus, W.H. Zimmermann, P. Ferdinandy, J.P.G. Sluiter, ESC Working Group on Cellular Biology of the Heart: position paper for Cardiovascular Research: tissue engineering strategies combined with cell therapies for cardiac repair in ischaemic heart disease and heart failure, *Cardiovasc. Res.* 115 (2019) 488–500, <https://doi.org/10.1093/cvr/cvz010>.
- [11] L. Gao, Z.R. Gregorich, W. Zhu, S. Mattapally, Y. Oduk, X. Lou, R. Kannappan, A.V. Borovjagin, G.P. Walcott, A.E. Pollard, V.G. Fast, X. Hu, S.G. Lloyd, Y. Ge, J. Zhang, Large cardiac muscle patches engineered from human induced-pluripotent stem cell derived cardiac cells improve recovery from myocardial infarction in swine, *Circulation* 137 (2018) 1712–1730, <https://doi.org/10.1161/circulationaha.117.030785>.
- [12] L. Cyganek, M. Tiburcy, K. Sekeres, K. Gerstenberg, H. Bohnenberger, C. Lenz, S. Henze, M. Stauske, G. Salinas, W.-H. Zimmermann, G. Hasenfuss, K. Guan, Deep phenotyping of human induced pluripotent stem cell derived atrial and ventricular cardiomyocytes, *JCI Insight* 3 (2018), <https://doi.org/10.1172/jci.insight.99941>.
- [13] J.H. Lee, S.I. Protze, Z. Laksman, P.H. Backx, G.M. Keller, Human pluripotent stem cell-derived atrial and ventricular cardiomyocytes develop from distinct mesoderm populations, *Cell Stem Cell* 21 (2017) 179–194, <https://doi.org/10.1016/j.stem.2017.07.003>, e4.
- [14] S.I. Protze, J. Liu, U. Nussinovitch, L. Ohana, P.H. Backx, L. Gepstein, G.M. Keller, Sinus node cardiomyocytes derived from human pluripotent cells function as a biological pacemaker, *Nat. Biotechnol.* 35 (2016) 56–68, <https://doi.org/10.1038/nbt.3745>.
- [15] X. Lian, J. Zhang, S.M. Azarin, K. Zhu, L.B. Hazellett, X. Bao, C. Hsiao, T.J. Kamp, S.P. Palecek, Directed cardiomyocyte differentiation from human pluripotent stem cells by modulating Wnt/β-catenin signaling under fully defined conditions, *Nat. Protoc.* 8 (2013) 162–175, <https://doi.org/10.1038/nprot.2012.150>.
- [16] C. Long, H. Li, M. Tiburcy, C. Rodriguez-Caycedo, V. Kyrchenko, H. Zhou, Y. Zhang, Y.L. Min, J.M. Shelton, P.P.A. Mammen, N.Y. Liaw, W.H. Zimmermann, R. Bassel-Duby, J.W. Schneider, E.N. Olson, Correction of diverse muscular dystrophy mutations in human engineered heart muscle by single-site genome editing, *Sci. Adv.* 4 (2018), eaap9004, <https://doi.org/10.1126/sciadv.aap9004>.
- [17] Y.H. Sun, H.K.J. Kao, C.W. Chang, A. Merleev, J.L. Overton, D. Pretto, S. Yechikov, E. Mavarakis, N. Chiamvimonvat, J.W. Chan, D.K. Lieu, Human induced pluripotent stem cell line with genetically encoded fluorescent voltage indicator generated via CRISPR for action potential assessment post-cardiogenesis, *Stem Cells* 38 (2020) 90–101, <https://doi.org/10.1002/stem.3085>.
- [18] K. Ronaldson-Bouchard, S.P. Ma, K. Yeager, T. Chen, L. Song, D. Sirabella, K. Morikawa, D. Teles, M. Yazawa, G. Vunjak-Novakovic, Advanced maturation of human cardiac tissue grown from pluripotent stem cells, *Nature* 556 (2018) 239–243, <https://doi.org/10.1038/s41586-018-0016-3>.
- [19] M.N. Hirt, A. Hansen, T. Eschenhagen, Cardiac tissue engineering: state of the art, *Circ. Res.* 114 (2014) 354–367, <https://doi.org/10.1161/CIRCRESAHA.114.300522>.
- [20] G. Hasenfuss, L.A. Mulieri, E.M. Blanchard, C. Holubarsch, B.J. Leavitt, F. Irtelman, N.R. Alpert, Energetics of isometric force development in control and volume-overloaded human myocardium. Comparison with animal species, *Circ. Res.* 68 (1991) 836–846, <https://doi.org/10.1161/01.res.68.3.836>.
- [21] K. Breckwoldt, D. Letuffe-Breniere, I. Mannhardt, T. Schulze, B. Ulmer, T. Werner, A. Benzin, B. Klampe, M.C. Reinsch, S. Laufer, A. Shibamliya, M. Prondzynski, G. Mearini, D. Schade, S. Fuchs, C. Neuber, E. Kramer, U. Saleem, M.L. Schulze, M.L. Rodriguez, T. Eschenhagen, A. Hansen, Differentiation of cardiomyocytes and generation of human engineered heart tissue, *Nat. Protoc.* 12 (2017) 1177–1197, <https://doi.org/10.1038/nprot.2017.033>.
- [22] J. Lee, V. Manoharan, L. Cheung, S. Lee, B.H. Cha, P. Newman, R. Farzad, S. Mehrotra, K. Zhang, F. Khan, M. Ghaderi, Y.D. Lin, S. Afab, P. Mostafalu, M. Miscuglio, J. Li, B.B. Mandal, M.A. Hussain, K.T. Wan, X.S. Tang, A. Khademhosseini, S.R. Shin, Nanoparticle-based hybrid scaffolds for deciphering the role of multimodal cues in cardiac tissue engineering, *ACS Nano* 13 (2019) 12525–12539, <https://doi.org/10.1021/acsnano.9b03050>.
- [23] S.R. Shin, C. Zihlmann, M. Akbari, P. Assawes, L. Cheung, K. Zhang, V. Manoharan, Y.S. Zhang, M. Yuksekkaya, K.T. Wan, M. Nikkiah, M.R. Dokmeci, X.S. Tang, A. Khademhosseini, Reduced graphene oxide-GelMA hybrid hydrogels as scaffolds for cardiac tissue engineering, *Small* 12 (2016) 3677–3689, <https://doi.org/10.1002/smll.201600178>.
- [24] C. Patra, A.R. Bocaccini, F.B. Engel, Vascularisation for cardiac tissue engineering: the extracellular matrix, *Thromb. Haemost.* 113 (2015) 532–547, <https://doi.org/10.1160/TH14-05-0480>.
- [25] T.U. Esser, K. Roshanbinfar, F.B. Engel, Promoting vascularization for tissue engineering constructs: current strategies focusing on HIF-regulating scaffolds, *Expert Opin. Biol. Ther.* 19 (2019) 105–118, <https://doi.org/10.1080/14712598.2019.1561855>.
- [26] Y. Song, H. Wang, F. Yue, Q. Lv, B. Cai, N. Dong, Z. Wang, L. Wang, Silk-based biomaterials for cardiac tissue engineering, *Adv. Healthc. Mater.* (2020), e2000735, <https://doi.org/10.1002/adhm.202000735>.
- [27] S. Salehi, K. Koeck, T. Scheibel, Spider silk for tissue engineering applications, *Molecules* 25 (2020), <https://doi.org/10.3390/molecules25030737>.
- [28] C. Holland, K. Numata, J. Rnjak-Kovacic, F.P. Seib, The biomedical use of silk: past, present, future, *Adv. Healthc. Mater.* 8 (2019), e1800465, <https://doi.org/10.1002/adhm.201800465>.
- [29] B. Kundu, N.E. Kuriand, S. Bano, C. Patra, F.B. Engel, V.K. Yadavalli, S.C. Kundu, Silk proteins for biomedical applications: bioengineering perspectives, *Prog. Polym. Sci.* 39 (2014) 251–267, <https://doi.org/10.1016/j.progpolymsci.2013.09.002>.
- [30] C. Patra, S. Talukdar, T. Novoyatleva, S.R. Velagala, C. Muhlfeld, B. Kundu, S.C. Kundu, F.B. Engel, Silk protein fibroin from *Antheraea mylitta* for cardiac tissue engineering, *Biomaterials* 33 (2012) 2673–2680, <https://doi.org/10.1016/j.biomaterials.2011.12.036>.
- [31] J.P.M. Kramer, T.B. Aigner, J. Petzold, K. Roshanbinfar, T. Scheibel, F.B. Engel, Recombinant spider silk protein eADF4(C16)-RGD coatings are suitable for cardiac tissue engineering, *Sci. Rep.* 10 (2020) 8789, <https://doi.org/10.1038/s41598-020-65786-4>.
- [32] J. Petzold, T.B. Aigner, F. Tanska, K. Zimmermann, T. Scheibel, F.B. Engel, Surface features of recombinant spider silk protein eADF4(kappa 16)-made materials are well-suited for cardiac tissue engineering, *Adv. Funct. Mater.* 27 (2017), <https://doi.org/10.1002/adfm.201701427>.
- [33] D. Steiner, G. Lang, L. Fischer, S. Winkler, T. Fey, P. Grell, T. Scheibel, R.E. Horch, A. Arkudas, Intrinsic vascularization of recombinant eADF4(C16) spider silk matrices in the arteriovenous loop model, *Tissue Eng.* 25 (2019) 1504–1513, <https://doi.org/10.1089/ten.tea.2018.0360>.
- [34] P.H. Zepelin, N.C. Maksimovikj, M.C. Jordan, J. Nickel, G. Lang, A.H. Leimer, L. Römer, T. Scheibel, Spider silk coatings as a bioshield to reduce periprosthetic fibrous capsule formation, *Adv. Funct. Mater.* 24 (2014) 2658–2666, <https://doi.org/10.1002/adfm.201302813>.
- [35] L. DeFrancesco, Hanging on a thread, *Nat. Biotechnol.* 35 (2017) 496–499, <https://doi.org/10.1038/nbt.3894>.
- [36] A. Heidebrecht, T. Scheibel, Recombinant production of spider silk proteins, *Adv. Appl. Microbiol.* 82 (2013) 115–153, <https://doi.org/10.1016/b978-0-12-407679-2.00004-1>.
- [37] D. Huemmerich, C.W. Helsen, S. Quedzuweit, J. Oschmann, R. Rudolph, T. Scheibel, Primary structure elements of spider dragline silks and their contribution to protein solubility, *Biochemistry* 43 (2004) 13604–13612, <https://doi.org/10.1021/bi048983q>.
- [38] K. Schacht, T. Jungst, M. Schweinlin, A. Ewald, J. Groll, T. Scheibel, Biofabrication of cell-loaded 3D spider silk constructs, *Angew. Chem. Int. Ed. Engl.* 54 (2015) 2816–2820, <https://doi.org/10.1002/anie.201409846>.

- [39] S. Wohlrab, S. Müller, A. Schmidt, S. Neubauer, H. Kessler, A. Leal-Egana, T. Scheibel, Cell adhesion and proliferation on RGD-modified recombinant spider silk proteins, *Biomaterials* 33 (2012) 6650–6659, <https://doi.org/10.1016/j.biomaterials.2012.05.069>.
- [40] S. Kumari, G. Lang, E. DeSimone, C. Spengler, V.T. Trossmann, S. Lückner, M. Hudel, K. Jacobs, N. Krämer, T. Scheibel, Engineered spider silk-based 2D and 3D materials prevent microbial infestation, *Mater. Today* (2020), <https://doi.org/10.1016/j.mattod.2020.06.009>.
- [41] E. Doblhofer, T. Scheibel, Engineering of recombinant spider silk proteins allows defined uptake and release of substances, *J. Pharm. Sci.* 104 (2015) 988–994, <https://doi.org/10.1002/jps.24300>.
- [42] M. Saric, T. Scheibel, Engineering of silk proteins for materials applications, *Curr. Opin. Biotechnol.* 60 (2019) 213–220, <https://doi.org/10.1016/j.copbio.2019.05.005>.
- [43] K. Schacht, T. Scheibel, Controlled hydrogel formation of a recombinant spider silk protein, *Biomacromolecules* 12 (2011) 2488–2495, <https://doi.org/10.1021/bm200154k>.
- [44] K. Schacht, J. Vogt, T. Scheibel, Foams made of engineered recombinant spider silk proteins as 3D Scaffolds for cell growth, *ACS Biomater. Sci. Eng.* 2 (2016) 517–525, <https://doi.org/10.1021/acsbomaterials.5b00483>.
- [45] E. DeSimone, K. Schacht, A. Pellert, T. Scheibel, Recombinant spider silk-based bioinks, *Biofabrication* 9 (2017), 044104, <https://doi.org/10.1088/1758-5090/aa90db>.
- [46] A. Leal-Egana, G. Lang, C. Mauerer, J. Wickinghoff, M. Weber, S. Geimer, T. Scheibel, Interactions of fibroblasts with different morphologies made of an engineered spider silk protein, *Adv. Eng. Mater.* 14 (2012) B67–B75, <https://doi.org/10.1002/adem.201180072>.
- [47] A. Blau, Cell adhesion promotion strategies for signal transduction enhancement in microelectrode array in vitro electrophysiology: an introductory overview and critical discussion, *Curr. Opin. Colloid Interface Sci.* 18 (2013) 481–492, <https://doi.org/10.1016/j.cocis.2013.07.005>.
- [48] M. De Rosa, M. Carteni, O. Petillo, A. Calarco, S. Margarucci, F. Rosso, A. De Rosa, E. Farina, P. Grippo, G. Peluso, Cationic polyelectrolyte hydrogel fosters fibroblast spreading, proliferation, and extracellular matrix production: implications for tissue engineering, *J. Cell. Physiol.* 198 (2004) 133–143, <https://doi.org/10.1002/jcp.10397>.
- [49] K. Spiess, R. Ene, C.D. Keenan, J. Senker, F. Kremer, T. Scheibel, Impact of initial solvent on thermal stability and mechanical properties of recombinant spider silk films, *J. Mater. Chem.* 21 (2011) 13594–13604, <https://doi.org/10.1039/c1jm11700a>.
- [50] I.C. Um, H.Y. Kweon, K.G. Lee, Y.H. Park, The role of formic acid in solution stability and crystallization of silk protein polymer, *Int. J. Biol. Macromol.* 33 (2003) 203–213, <https://doi.org/10.1016/j.ijbiomac.2003.08.004>.
- [51] S. Wohlrab, K. Spiess, T. Scheibel, Varying surface hydrophobicities of coatings made of recombinant spider silk proteins, *J. Mater. Chem.* 22 (2012) 22050–22054, <https://doi.org/10.1039/c2jm35075k>.
- [52] C.B. Borkner, S. Lentz, M. Müller, A. Fery, T. Scheibel, Ultrathin spider silk films: insights into spider silk assembly on surfaces, *ACS Appl. Polym. Mater.* 1 (2019) 3366–3374, <https://doi.org/10.1021/acscapm.9b00792>.
- [53] X. Hu, D. Kaplan, P. Cebe, Determining beta-sheet crystallinity in fibrous proteins by thermal analysis and infrared spectroscopy, *Macromolecules* 39 (2006) 6161–6170, <https://doi.org/10.1021/ma0610109>.
- [54] J. Schindelin, I. Arganda-Carreras, E. Frise, V. Kaynig, M. Longair, T. Pietzsch, S. Preibisch, C. Rueden, S. Saalfeld, B. Schmid, J.Y. Tinevez, D.J. White, V. Hartenstein, K. Eliceiri, P. Tomancak, A. Cardona, Fiji: an open-source platform for biological-image analysis, *Nat. Methods* 9 (2012) 676–682, <https://doi.org/10.1038/nmeth.2019>.
- [55] I. Sala, B.J. van Meer, L.G.J. Tertoolen, J. Baekkers, M. Bellin, R.P. Davis, C. Denning, M.A.E. Dieben, T. Eschenhagen, E. Giacomelli, C. Grandela, A. Hansen, E.R. Holman, M.R.M. Jongbloed, S.M. Kamel, C.D. Koopman, Q. Lachaud, I. Mannhardt, M.P.H. Mol, D. Mosqueira, V.V. Orlova, R. Passier, M.C. Ribeiro, U. Saleem, G.L. Smith, F.L. Burton, C.L. Mummery, MUSCLEMOTION: a versatile open software tool to quantify cardiomyocyte and cardiac muscle contraction in vitro and in vivo, *Circ. Res.* 122 (2018) e5–e16, <https://doi.org/10.1161/CIRCRESAHA.117.312067>.
- [56] C.B. Borkner, S. Wohlrab, E. Möller, G. Lang, T. Scheibel, Surface modification of polymeric biomaterials using recombinant spider silk proteins, *ACS Biomater. Sci. Eng.* 3 (2016) 767–775, <https://doi.org/10.1021/acsbomaterials.6b00306>.
- [57] W. Giurlani, E. Berretti, M. Innocenti, A. Lavacchi, Measuring the thickness of metal coatings: a review of the methods, *Coatings* 10 (2020), <https://doi.org/10.3390/coatings10121211>.
- [58] C.S. Hughes, L.M. Postovit, G.A. Lajoie, Matrigel: a complex protein mixture required for optimal growth of cell culture, *Proteomics* 10 (2010) 1886–1890, <https://doi.org/10.1002/pmic.200900758>.
- [59] G. Benton, I. Arnaoutova, J. George, H.K. Kleinman, J. Koblinski, Matrigel: from discovery and ECM mimicry to assays and models for cancer research, *Adv. Drug Deliv. Rev.* 79–80 (2014) 3–18, <https://doi.org/10.1016/j.addr.2014.06.005>.
- [60] L.D. Vukovic, P. Jevtic, L.J. Edens, D.L. Levy, New insights into mechanisms and functions of nuclear size regulation, *Int Rev Cell Mol Biol* 322 (2016) 1–59, <https://doi.org/10.1016/bs.ircmb.2015.11.001>.
- [61] A.M. Gerdes, M.C. Morales, V. Handa, J.A. Moore, M.R. Alvarez, Nuclear size and DNA content in rat cardiac myocytes during growth, maturation and aging, *J. Mol. Cell. Cardiol.* 23 (1991) 833–839, [https://doi.org/10.1016/0022-2828\(91\)90216-9](https://doi.org/10.1016/0022-2828(91)90216-9).
- [62] R.S. Ross, C. Pham, S.Y. Shai, J.I. Goldhaber, C. Fenczik, C.C. Glembotski, M.H. Ginsberg, J.C. Loftus, Beta1 integrins participate in the hypertrophic response of rat ventricular myocytes, *Circ. Res.* 82 (1998) 1160–1172, <https://doi.org/10.1161/01.res.82.11.1160>.
- [63] M. Brancaccio, E. Hirsch, A. Notte, G. Selvetella, G. Lembo, G. Tarone, Integrin signalling: the tug-of-war in heart hypertrophy, *Cardiovasc. Res.* 70 (2006) 422–433, <https://doi.org/10.1016/j.cardiores.2005.12.015>.

1
2
3
4
5
6
7
8
9
10
11
12
13
14
15
16
17
18
19
20
21
22
23
24
25

SUPPLEMENTAL MATERIAL

Designing of spider silk proteins for hiPSC-based cardiac tissue engineering

Tilman U. Esser^{a,e}, Vanessa T. Trossmann^{b,e}, Sarah Lentz^b, Felix B. Engel^{a,c,*},
Thomas Scheibel^{b,d,*}

^aExperimental Renal and Cardiovascular Research, Department of Nephropathology,
Institute of Pathology, Friedrich-Alexander-Universität Erlangen-Nürnberg (FAU),
91054 Erlangen, Germany;

^bLehrstuhl Biomaterialien, Prof.-Rüdiger-Bormann Straße 1, 95447 Bayreuth,
Germany;

^cMURCE, Muscle Research Center Erlangen, Erlangen, Germany.

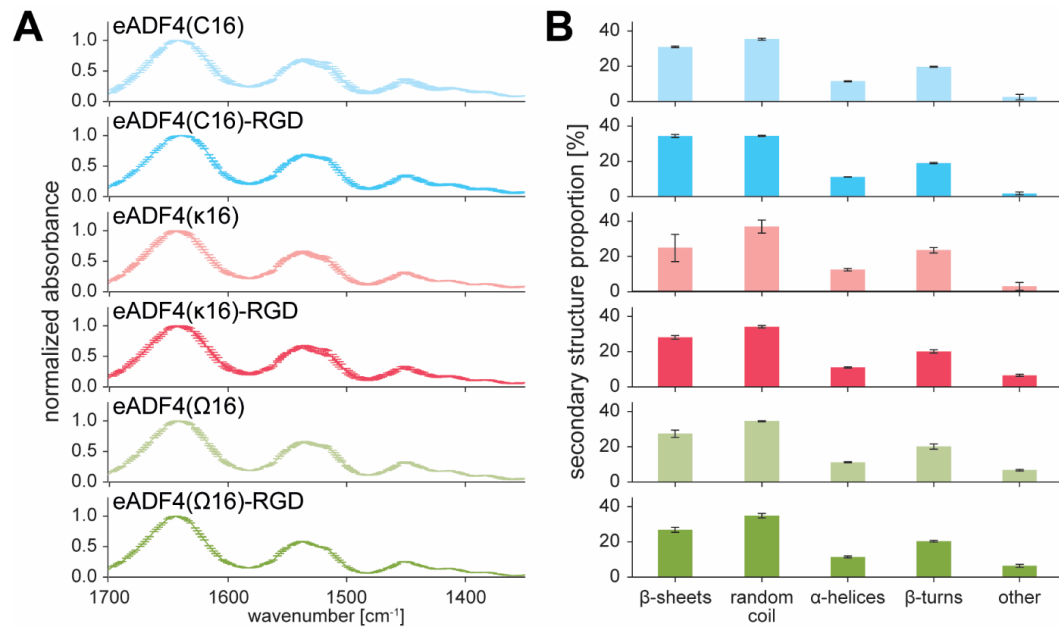
^dBayreuther Zentrum für Kolloide und Grenzflächen (BZKG), Bayerisches
Polymerinstitut (BPI), Bayreuther Zentrum für Molekulare Biowissenschaften (BZMB),
Bayreuther Materialzentrum (BayMAT), Universitätsstraße 30, Universität Bayreuth,
Bayreuth D-95447, Germany,

***Corresponding authors:**

felix.engel@uk-erlangen.de

thomas.scheibel@bm.uni-bayreuth.de

^eauthors contributed equally to the work



26

27

28 **Supplementary Figure 1: Absorbance spectra and Fourier self-deconvoluted**
 29 **secondary structure components of spider silk films**

30 **A** Absorbance spectra of spider silk films showing amide I, II and III bands

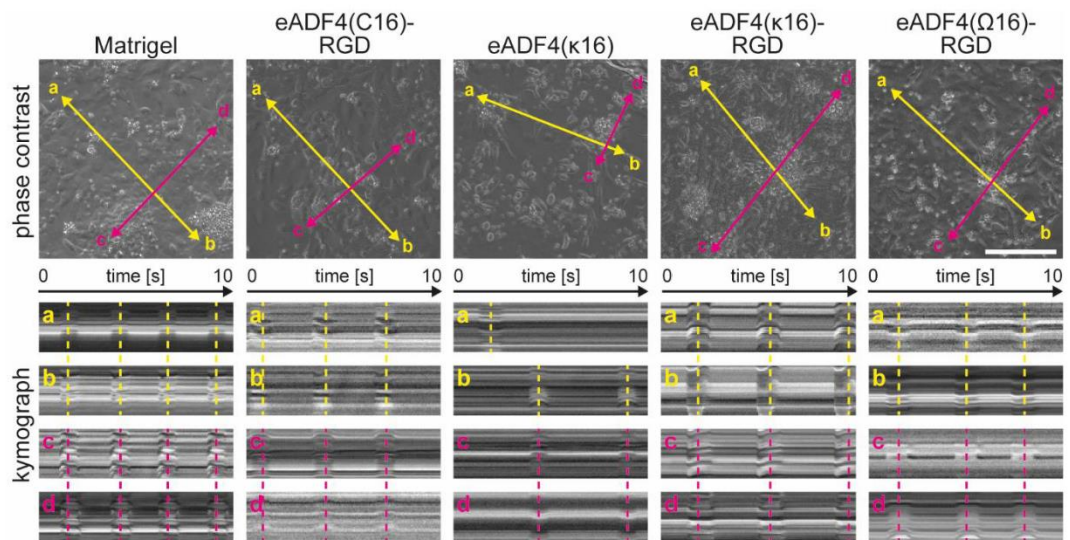
31 determined using attenuated total reflection-Fourier transform infrared (ATR-FTIR)

32 spectroscopy. **B** Secondary structure components were calculated using Fourier self-

33 deconvolution of the amide I band.

34

35



36

37 **Supplementary Figure 2: Synchronous and asynchronous contractions of**
 38 **hiPSC cardiomyocytes on spider silk films**

39 Kymograph analyses of representative videos of hiPSC-cardiomyocytes 3 days after
 40 seeding. *Top row*: still images of videos with arrows indicating kymograph axes.

41 Scale bar: 200 μm . *Bottom rows*: Kymograph plots at positions indicated above (a, b,
 42 c, d). Dashed lines indicate contractions.

Part IV - Spider silk inspired functional materials

In this part, materials with synthetic origin inspired by spider silk are the focus.

Part IV - Chapter 1 – Mimicry of silk utilizing synthetic polypeptides

Part IV – Chapter 1.1 - Chapter perspective and contribution

This chapter reviews synthetic polymerization techniques for new functional materials molecularly inspired by silk proteins. We critically summarized and highlighted the chemical and structural similarities of these synthetic polymers with silk proteins. Furthermore, we went a step further and reviewed the resulting material properties. As such, we explained from a molecular level (synthesis) to a mesoscopic level (structure formation) to a macroscopic level (various morphologies with associated properties) and applications of silk-inspired materials.

This review was written in equal parts with Nicholas Chan. We share the first authorship. This chapter is a research article published in Progress in Polymer Science, Volume 130, July 2022, 101557 with DOI: <https://doi.org/10.1016/j.progpolymsci.2022.101557>.

Permission for reprinting is not required.

Part IV – Chapter 1.2 Full Paper

Progress in Polymer Science 130 (2022) 101557



Contents lists available at ScienceDirect

Progress in Polymer Science

journal homepage: www.elsevier.com/locate/progpolymsci

Mimicry of silk utilizing synthetic polypeptides

Nicholas J. Chan^{a,b,1}, Sarah Lentz^{a,b,1}, Paul A. Gurr^a, Thomas Scheibel^{b,*}, Greg G. Qiao^{a,*}^a Polymer Science Group, Department of Chemical Engineering, University of Melbourne, Parkville, Melbourne, Victoria 3010, Australia^b Chair of Biomaterials, University of Bayreuth, Prof.-Rüdiger-Bormann-Str. 1, Bayreuth D-95447, Germany

ARTICLE INFO

Article history:

Received 25 November 2021

Revised 25 April 2022

Accepted 9 May 2022

Available online 12 May 2022

Keywords:

Silk inspired materials

Biomimicry

 β -sheet

Synthetic polymerization

NCA ROP

Chemoenzymatic

ABSTRACT

For thousands of years, 'silk' and silk-based materials have played an important role for mankind. Today, silk-based materials increasingly find use in novel application areas such as biomedical and advanced technologies. However, natural silks show limitations. To overcome these limitations, chemical polymerization methods have been developed that provide potential avenues to synthetic materials with silk-like features. This article summarizes the physicochemical properties of silks and reviews how the structure-property relationships of silks have inspired material design, for example, by integration of β -sheet forming polypeptide regions. Strategies that utilize N-carboxyanhydride ring-opening polymerization (NCA ROP) for polypeptide synthesis are the primary focus of this review as they provide a versatile platform for polypeptide engineering. Finally, the prospects of silk-inspired material design, such as amorphous polymers featuring β -sheet structures, for the design of high performance polymers are discussed.

© 2022 Published by Elsevier B.V.

1. Introduction

Through evolution, nature often constructs materials with outstanding properties, providing inspiration for material scientists, and forming the basis of biomimicry. The range of properties is diverse – mussel feet show strong adhesion to wet surfaces [1,2], *Morpho* butterfly wings have stunning structural color [3,4], and shark skin-inspired surfaces achieve minimal drag and subsequently increased aerodynamic efficiency [5,6]. One of the most

highly investigated natural materials with excellent mechanical properties is animal silks [7–11].

The superior strength of spider silk is a well-reported example with the dragline silk of the European garden spider possessing a tensile strength, extension at break, and toughness around 1.1 GPa, 30 % and 160 MJ/m³, respectively, (other species have even shown to produce silk with up to 500 MJ/m³ fracture toughness) [12–15]. For comparison, high tensile steel has a similar strength of 1.5 GPa, but a far inferior extension at break of 0.8%, resulting in a much lower toughness (6 MJ/m³). *Bombyx mori* (*B. mori*, i.e., silkworm) silk has a lower tensile strength, extension at break, and toughness than its spider silk counterpart (0.6 GPa, 18%, and 70 MJ/m³, respectively). However, its overall toughness is still far superior to tensile steel [10]. In addition to their remarkable mechanical properties, certain silks have been found to be biocompatible with human cells and provide sufficient support for cellular adhesion [16–18]. Furthermore, as with other proteins, silks are susceptible to enzymatic degradation, making them a strong candidate for utilization in bioapplications [17,19,20]. Although *B. mori* silkworm silk and the regeneration of silk fibers can overcome the issue of scale-up [9], it lacks the mechanical properties of spider silk which may be desired for specific technical applications. In contrast, spider silk is naturally available only at an incredibly low quantity, due to the cannibalistic behavior of spiders making it impractical for large-scale use [9].

As silks are protein-based, research into mimicry often starts at a molecular level. The synthesis of polypeptides can be performed using many different techniques. Recombinant methods involve the manipulation of plasmids transferred into microorganisms to pro-

Abbreviations: ¹³C-NMR, Carbon-13 nuclear magnetic resonance; Abz, Aminobenzoic; ACN, Acetonitrile; ADSCs, Adipose-derived stem cells; AFM, Atomic force microscopy; ATR-FTIR, Attenuated total reflection Fourier transform infrared spectroscopy; ATRP, Atom transfer radical polymerization; b, Block; BzI, Benzyl; CD, Circular dichroism; CGC, Critical gelation concentration; DCM, Dichloromethane; DLS, Dynamic light scattering; DMF, Dimethylformamide; DMSO, Dimethyl sulfoxide; DOX, Doxorubicin; DP, Degree of polymerization; E.Coli, Escherichia Coli; ECM, Extracellular matrix; EDTA, Ethylenediamine tetraacetic acid; FTIR, Fourier transform infrared spectroscopy; g, Grafted; GPa, Gigapascal; HDI, Hexamethylene diisocyanate; HEMA, 2-Hydroxyethylmethacrylate; HFIP, Hexafluoroisopropanol; M θ , Matrigel TM; MALDI-TOF, Matrix-assisted Laser Desorption Ionisation Time of Flight; MeOH, Methanol; MJ, Megajoule; MMA, Methyl methacrylate; NCA ROP, N-carboxyanhydride ring-opening polymerization; PDI, Polydispersity index; pH, Potential of hydrogen; τ , Random; SAXS, Small-angle X-ray scattering; SEM, Scanning electron microscope; sGAG, Sulfonated glycosaminoglycan; SWCNT, Single-wall carbon nanotubes; TEM, Transmission electron microscopy; THF, Tetrahydrofuran; UV, Ultraviolet; XRD, X-Ray diffraction.

* Corresponding authors.

E-mail addresses: thomas.scheibel@bm.uni-bayreuth.de (T. Scheibel), gregghq@unimelb.edu.au (G.G. Qiao).¹ These authors contributed equally to this work.<https://doi.org/10.1016/j.progpolymsci.2022.101557>

0079-6700/© 2022 Published by Elsevier B.V.

Nomenclature	
A	ALA alanine
C	CYS cysteine
D	ASP aspartic acid
E	GLU glutamic acid
F	PHE phenylalanine
G	GLY glycine
H	HIS histidine
I	ILE isoleucine
K	LYS lysine
L	LEU leucine
M	MET methionine
N	ASN asparagine
P	PRO proline
P	PRO proline
PADLG	poly(DL-allylglycine)
PBLA	poly(β -benzyl-L-aspartate)
PBLG	poly(γ -benzyl- α , L-glutamate)
PCL	poly(ϵ -caprolactone)
PDAla	poly(D-alanine)
PDGlu	poly(D-glutamic acid)
PDLAla	poly(DL-alanine)
PDLGlu	poly(DL-glutamic acid)
PDMS	polydimethylsiloxane
PEG	polyethylene glycol
PEI	polyethylenimine
PGI	polyglobalide
PGly	poly(glycine)
PHLG	poly [N5-(2-hydroxyethyl)-L-glutamine]
PLAla	poly(L-alanine)
PLArg	poly(L-arginine)
PLAsp	poly(L-aspartic acid)
PLGlu	poly(L-glutamic acid)
PLHis	poly(L-histidine)
PLIle	poly(L-isoleucine)
PLlys	poly(L-lysine)
PLLeu	poly(L-leucine)
PLPhe	poly(L-phenylalanine)
PLThr	poly(L-threonine)
PLTyr	poly(L-tyrosine)
PLX	poloxamer
PMLL	poly(L-lysine-g-methylacrylate)
PMMA	polymethylmethacrylate
PNIPAM	poly(N-isopropylacrylamide)
POLM	poly(sulfoxide methanoimine)
POSS	polyhedral oligomeric silsesquioxane
PPDL	polypentadecalactone
PPLG	amino propanol-modified PLGlu
PPO	poly(p-phenylene oxide)
PZLL	poly(carboxybenzyl-L-lysine)
Q	GLN Glutamine
R	ARG arginine
T	THR threonine
V	VAL valine
Y	TYR tyrosine

duce proteins with specific sequences [21,22]. Silk-like proteins synthesized in this fashion are amongst the most popular and extensively studied methods for achieving silk mimicry and have already been extensively reviewed [23–25]. The other common method for synthesizing specific sequences is using solid-state peptide synthesis, but the size of these peptides is restricted and lacks a high mass throughput [26,27]. The polymerization methods

for synthesizing polypeptides – *N*-carboxyanhydride ring-opening polymerization (NCA ROP) [28–31] and chemoenzymatic polymerization [32,33] – provide alternative techniques which can lead to the desired constructs. Comparatively, chemoenzymatic polypeptide synthesis is a less developed technique than NCA ROP, and while interesting work exists in the field, these works have previously been well reviewed. As NCA ROP has been well developed, multiple strategies uniquely available to polymerization-based techniques have emerged with interesting methods for synthesizing polypeptides with homopoly(amino acids) or copoly(amino acids) blocks (random or alternating depending on the polymerization method) blocks.

As interest in the field of biomimicry expands, and with the studies into synthetic methods ever-increasing, silk-inspired chemically synthesized polymers have intriguing prospects, with this review mainly focusing on the potential for NCA ROP to develop silk-mimetic polymers based on amino acid motifs that are typically not found in silk proteins. Previous bioinspired methods for silk-inspired chemical synthesis have been reviewed as well as other parallel strategies which can lead to bio-inspired pathways in the future. As with any attempts at biomimicry, a firm grasp of the structure-property relationship of silks is imperative. From there, the appropriate strategy for polypeptide synthesis can be determined. The Tang group has most recently reviewed the synthesis of bioinspired polymers [34], while the Sarkar et al. [35] and Numata [36] groups have recently reviewed the chemical synthesis of silk-like polymers. To complement these previous works, this review focuses on the properties of silk-like polypeptides and their potential applications. Particular attention is given to the role of molecular and nanoscale structure on the properties of silk-like polypeptide materials.

2. The structure of silk and the impact on properties

Before discussing the specifics of silk structure and the sequence-structure-function relationship, a fundamental understanding of the hierarchical structural nature of proteins is required.

Natural proteins are large folded biomacromolecules comprising up to 21 natural amino acids. Almost all amino acids consist of three unique groups extending from a chiral carbon (the α -carbon) – a carboxylic acid functional group, an amino-functional group, and a unique side chain different for each amino acid. As such, amino acids generally have two stereoisomers, with the L-isomer being the natural form of amino acids, though the D-isomer does occur in rare cases due to modifications after biological synthesis (referred to as posttranslational modifications). Conjugation of the carboxyl and amino functional groups stemming from the α -carbon results in peptide bonds, and the amino acid sequence in the polypeptides is called the protein primary structure. Supramolecular interactions between the amino acid residue side chains, such as hydrophobic interactions, π – π stacking, Van der Waals forces, and ionic bonding, cause this polypeptide chain to adopt thermodynamically stable secondary structures such as α -helices, β -sheets, and random coils. The spatial configuration of these secondary structure elements yields a 3D structure called the tertiary structure. In some cases, individual proteins will associate with each other to form a multimeric protein complex called a quaternary structure. Of these structural levels, the secondary structure is thermodynamically controlled and relies on the design of the primary structure.

Silks are best defined as a family of fibrous structural proteins consisting of highly repetitive sequences, which are processed from a concentrated protein solution (the protein itself is silk fibroin) before assembling into fibers outside the body [37]. Fibrous proteins consist of amino acid motifs that persist intrinsi-

cally unstructured in solution but can fold into rigid or flexible structures upon distinct processing, imparting high strength and toughness required for the fiber's performance [38]. This is distinct from globular proteins which have often a compact and spherical structure implying their function in solution to begin with [14]. In natural silks, the host organism stores the concentrated silk protein solution (otherwise referred to as a silk dope) within its silk glands [12]. From these glands, shear forces induce a highly controlled phase transition from an unfolded, soluble protein solution into a structured solid fiber alongside ion and pH gradients [39]. This spinning process induces structure formation resulting in a semicrystalline structure based on both protein primary structure and spinning conditions. It is these crystallites which regulate mechanical properties, with crystallite fraction, size and orientation differentiating between species and subsequent mechanical properties [40,41]. It should be noted that while shear forces are applied within the body in most organisms, exceptions occur where spinning are found post-excretion with rheological stress triggering assembly [42,43]. While a variety of arthropods produce silks, this section focuses on the two most prominent producers of silk – silkworms (*Bombyx mori* larvae) and spiders [8,44].

Silk can comprise one of five major secondary structures: extended β -sheets, cross β -sheets, α -helical coiled coils, collagen triple helices and polyglycine II [45]. The thermodynamically favorable packing of β -sheets dictates that amino acid side chains orientated towards the same face possess similar hydrophobicity and size. The orientation of such structures relative to the fiber axis is dictated through primary structure and spinning and defines the subcategory of structure. Extended β -sheet structures result from the packing of β -strands parallel to the fiber axis [46,47]. Cross- β structures instead result from the protein folding back on itself in a β -turn – usually due to periodic glycine within the crystallite [45,48,49]. Apart from β -sheet based structures, helix based structures are also present, though derived from different helical conformations. α -helical coiled-coils are particularly prevalent in aciniform silk (primarily used by spiders for wrapping prey), consisting of α -helices (right-handed twisting) winding around each other into a superhelix [50,51]. This is characterized by a repetitive heptad sequence with bulky nonpolar residues in the first and fourth position.[52] Collagen triple helix structures are far more rare, though are present in some silks (e.g. sawfly silk) [38]. They are characterized by the repetitive triad sequence GXY where X & Y are proline or hydroxyproline, resulting in left-handed helices which intertwine into a superhelix [53]. Polyglycine II structures are also rare, though are found in specific silks such as *Argiope trifasciata* flagelliform silk [54]. They consist of right-handed helices (3₁ helices), though more tightly wound than α -helices but instead of forming superhelices, they pack into a hexagonal lattice structure. The composition of such structures within crystallites subsequently contributes to mechanical properties, with coiled-coils contributing to high extension-at-break while β -sheet structures are far more rigid, contributing to mechanical strength [55].

In this review, the focus lies on the mimicry of silk-derived β -sheet structures and the resulting properties. Therefore, from now on the focus lies on the internal structure of the silks and not on the hierarchical structure of the silks. Another important aspect reviewing silks is that they can be regarded from a polymer chemistry view as block copolymer-like materials, since they comprise a defined amino acid sequence [56].

2.1. Silkworm silk

Bombyx mori silk consists of a heavy chain fibroin (~350-400 kDa), a small light chain fibroin (~25 kDa) linked to the heavy chain via disulfide bonds, and the P25 protein (a ~30 kDa glycoprotein) bonded to the other two components via hydrophobic

interactions [57–59]. The heavy chain is a hydrophobic polypeptide consisting primarily of glycine alternating with another amino acid (i.e., multiple repetitive GX motifs where G is glycine and X is another amino acid). Serine, tyrosine, valine, and threonine are all found in significant quantities as the second amino acid, while prominent motifs are GAGAGS, GAGAGY and GAAS (A is alanine, S is serine and Y is tyrosine) appearing in ~70 residue blocks and thus resulting in alanine-rich β -sheet nanocrystal forming blocks (Fig. 1a). The light chain, in contrast, making up the amorphous section of this protein is far less ordered with no repetition, consisting primarily of anionic glutamic acid and bulky hydrophobic and aromatic residues [60–62].

2.2. Dragline spider silk

The properties of dragline spider silk can significantly differ based on species but generally the fibers consist primarily of two different major ampullate spidroins (MaSp) (~200-350 kDa) (Fig. 1b) notated as MaSp1 and MaSp2, though recent studies have begun to research additional proteins such as MaSp3 and MaSp4 [63–66]. Numerous motifs are common within these, including poly(L-alanine) (PLAla), GGX and GPGXX motifs (almost exclusively in MaSp2), where P is proline and X is often tyrosine, glutamine, or leucine. The frequency of these motifs primarily affects the overall amino acid composition. It helps to differentiate the two MaSp – for example, the proline content in MaSp1 is less than 1% while it is greater than 10% for MaSp2. These MaSp consist of highly repetitive units of around 30-60 residues, including these motifs. The β -sheet nanocrystalline regions partially responsible for the superior mechanical properties are due to the PLAla blocks. These are made up of 5-14 residues depending on their species of origin and respective MaSp. Subsequently, hydrophobic association stacks these β -sheets to form aligned nanocrystals much smaller than that of silkworm silk, with spider silk β -sheet nanocrystals with dimensions in the range of 1 – 10 nm, although this varies between species. Importantly, silkworm silk β -sheet nanocrystals are at least twice as big as the dragline spider silk nanocrystals. The combination of nanocrystal alignment parallel to the fiber axis and size results in spider silk's significantly superior mechanical properties – precisely, strength and toughness are approximately double that of silkworm silk [67–69]. Apart from these regions are the glycine-rich regions which include the GGX as mentioned above and GPGXX motifs and, subsequently, are less well-defined, consisting of a mix of secondary structures [70–74]. This more amorphous region then provides the desired matrix for the β -sheet crystals to attain the desired mobility and thus achieve the superior flexibility and elasticity observed in such fibers. Besides from this repetitive core are flanking non-repetitive regions existing at the ends of the polypeptide sequence are primarily helical terminal domains. These terminal domains function as molecular switches preventing aberrant aggregation pre-spinning while promoting self-assembly during spinning [66,75].

3. Polypeptide synthesis through N-carboxyanhydride ring opening polymerization

Many strategies have implemented the previously detailed natural blueprints of the silkworm *B. mori* or different spider species like *N. clavipes*, with biocompatibility, biodegradability, and outstanding mechanical properties of natural silks driving this motivation. The aim is to produce a material that combines these properties, specifically synthetic polymers with silk-inspired polypeptide components using NCA ROP.

NCA ROP can be performed using numerous initiation methods (Scheme 1) [29]. The most common initiation method is

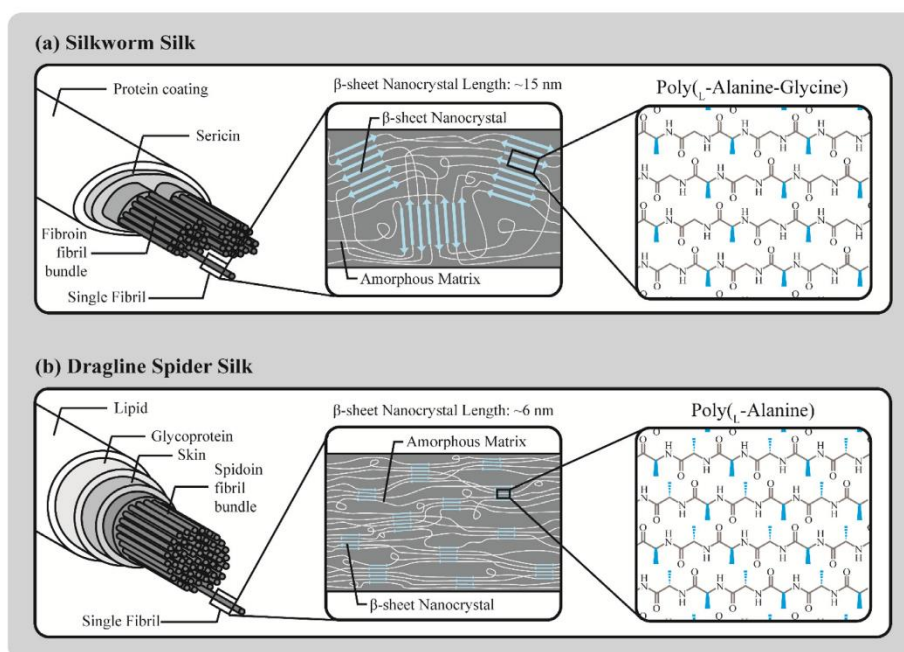
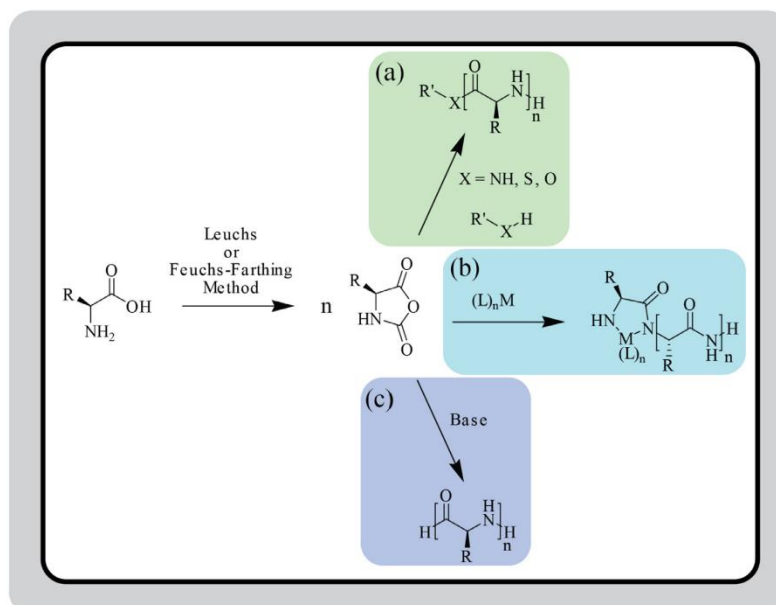


Fig. 1. Overall structure of (a) silkworm silk and (b) dragline spider silk. Both silks employ a “core-shell” structure with the core consisting of bundles of β -sheet nanofibrils. In spider silk, the β -sheet nanocrystals are based on poly(L-alanine) sequences with methyl group side chains alternating on a different side of the β -sheet plane (blue coming out of the page while red going into the page). Silkworm silk rather contains poly (glycine-L-alanine) motifs where side-chain alanine methyl groups would all remain on the same side of the plane (all coming out of the page).



Scheme 1. Synthesis of polypeptides via NCA ROP using the most common initiation methods: (a) nucleophile initiated ROP, often initiated by a primary amine; (b) transition metal initiated ROP; (c) base initiated ROP resulting in chain propagation via the activated monomer mechanism.

through nucleophilic attack (Scheme 1a) (most commonly a primary amine), resulting in chain-growth ring-opening polymerization via the normal amine mechanism. As the initiator remains attached to the polypeptide, facile synthesis of polypeptides with functional end groups can be performed. Furthermore, multiple initiating sites can be employed to design molecules with alternative architectures such as graft polypeptides and core-first stars. Alternatively, initiation via metal complexes (Scheme 1b) has been employed by the Deming group, which utilized nickel and cobalt initiators [76–78]. Through oxidative addition and amide proton migration upon reaction with other NCAs, five-membered amido-alkyl metallacycles, susceptible to further reaction by NCA monomers through the same sequences, are formed to achieve polymerization. Though residual metals must be removed, metal complex initiation offers reduced polydispersity and faster kinetics than nucleophilic attack. A third initiation strategy is to take advantage of the activated monomer mechanism (Scheme 1c) via deprotonation of the cyclic amine on the NCA monomers through a base. The deprotonated anionic amine acts as an initiator, ring-opening another NCA monomer resulting in a single NCA ring with a ring-opened amino acid installed onto the cyclic amine. Thus, it can act both as an initiator via the primary amine of the ring-opened amino acid group or as a cyclic monomer via this NCA ring. Though uncontrolled, this method yields high molecular weight polypeptides.

As with any synthetic technique, NCA ROP possesses specific qualities which inherently make them both more and less favorable to developing silk mimics. As a polymer synthesis technique, NCA ROP can yield polymers of high molecular weight (molecular weights on the order of 10 MDa have previously been reported) at a multigram scale within a comparable or shorter timescale compared to other techniques (24 h reaction times are often reported for the polymerization reaction). However, as they are synthetic polymers, they share characteristics which hinder their versatility. Of these characteristics, its non-sequence specific nature is the most notable as this complicates secondary structure-centered design considerably. This is even more pertinent in the pursuit of silk mimicry where the conformation of secondary structures is important. Furthermore, resultant polypeptides have a distribution of molecular weights centered around a targeted degree of polymerization (DP), otherwise known as a polydispersity index (PDI), instead of a specific molecular weight. In general, this means that polymers with a lower molecular weight distribution (i.e., lower PDI) will form more consistent substructures, but in the case of some polypeptide monoblocks residues such as poly(L-alanine) where the size of such blocks specifically dictates their secondary structure conformation, PDI in combination with molecular weight can ultimately determine secondary structure distribution and substructures.

The range of available residues for NCA ROP is also greatly increased beyond the traditional 21 canonical amino acids compared to other strategies. An NCA specific issue comes in the form of its susceptibility to nucleophilic attack and as such side-chain protection must commonly be employed for functional residues (e.g., glutamic acid, lysine). This introduces an extra deprotection step, though such modified amino acids have been utilized in their protected forms as the modified intermolecular interactions of such groups results in drastically altered secondary structure conformations. Furthermore, such modified amino acids cannot be easily utilized by techniques which require the identification of canonical amino acid (i.e., recombinant methods or chemoenzymatic polymerization). Another detail is the facile introduction of the unnatural D-isomer. In recombinant techniques, the introduction of the D-isomer is only possible through post-translational processes and clever design whereas NCA ROP allows introduction of the isomer during polymerization, allowing for physical and biological tuning

of properties. While these perspectives must be taken into consideration during synthesis, its potential as a polymerization method allows for unique strategies unavailable to other polypeptide synthesis strategies.

While coupling techniques are often required to append non-peptidic molecules, polymerization from an initiating group of pre-existing molecules allows for a more facile approach with further capabilities. Compared to coupling, such strategies assure high functionalization efficiency due to the reduced steric hinderance of a monomer instead of a polymer. Functional initiators allow for end-group functionalization with a functional group or polymer. Grafting-from strategies (or in the case of star polymers, core-first strategies) also become available for the purposes of developing graft polymers and polymer-based surfaces. In both cases, grafting from approaches yield high PDI, but can still yield high grafting efficiency or, in the case of surfaces, thicker surfaces. NCA ROP is established as a versatile and facile methodology for yielding silk-mimicking materials, but with its lack of sequence-control in particular, much can be garnered from studying the control of substructures using this technique.

4. Strategies towards silk-like polymer synthesis

Many strategies have implemented the previously detailed natural blueprints of the silkworm *B. mori* or different spider species like *Nephila clavipes*, with biocompatibility and biodegradability, utilizing NCA ROP to yield such structures [34,79]. Besides from precise strategies which mimic genetic blueprints to form the peptide sequence, the exploration of peripheral approaches, including poly(alanine) utilization and β -sheet fibrilization, gives further insight into the potential of silk-inspired polymers (Fig. 2). The general strategy implements rigid polypeptide secondary structures within an amorphous matrix as with natural silks to yield materials that can harness the desired properties. Based on the primary structure of silks, typically, amino acids glycine and alanine are modified to act as monomers. Then in further steps, the amino acids are coupled to polypeptides. Appendix A summarizes the strategies with specific sequences designed to mimic silk and their resulting secondary structure.

The Sogah group established the desired synthetic hybrid silk-mimic structures by catenating preformed building blocks with defined structure and functionality [80,81]. This strategy – which they have dubbed the Lego method – employs a combination of NCA ROP and anionic polymerization to link macromonomers consisting of soft synthetic polymeric segments such as poly(ethylene glycol) (PEG) already covalently coupled with the crystalline peptide sequence of alanine-glycine-alanine-glycine (Ala-Gly-Ala-Gly) [80,81]. Thus, it was possible to generate a library of protein-inspired polymers in which some segments are replaced with synthetic segments. NCA ROP strategies were particularly useful in such cases as the use of bifunctional polyethylene glycol (PEG) initiators prevented the need to multiple protection and deprotection steps. This enabled new opportunities to investigate the structure-property correlation, which is necessary to design new targeted bioinspired materials [80,81]. Their earlier templated approach used the rigid aromatic hairpin turn phenoxathiine as a template for β -sheet formation, even for weak hydrogen acceptors (Fig. 3) [82,83]. The second was a non-templated linear approach. The linking with PEG was performed in the same way as the templated approach [80–83]. Due to their linear architecture, the polymer can freely assemble into parallel or anti-parallel β -sheets via inter- or intramolecular interactions [81].

Such strategies also include studies where NCA ROP has not been utilized to develop the peptidic component, but its utilization provides simpler alternative pathways. One such aspect is the development of simpler methods of utilizing specific peptides

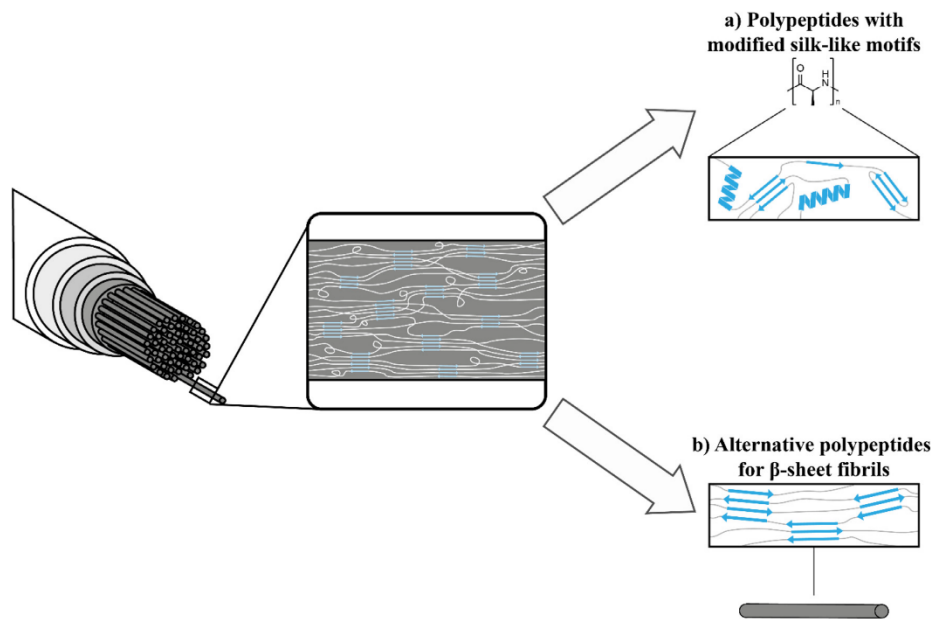


Fig. 2. Routes toward silk-inspired synthetic polymeric materials using (a) polypeptides with chemical similarity to β -sheet forming silk motifs, and (b) polypeptides with β -sheet fibrillar conformations after processing.

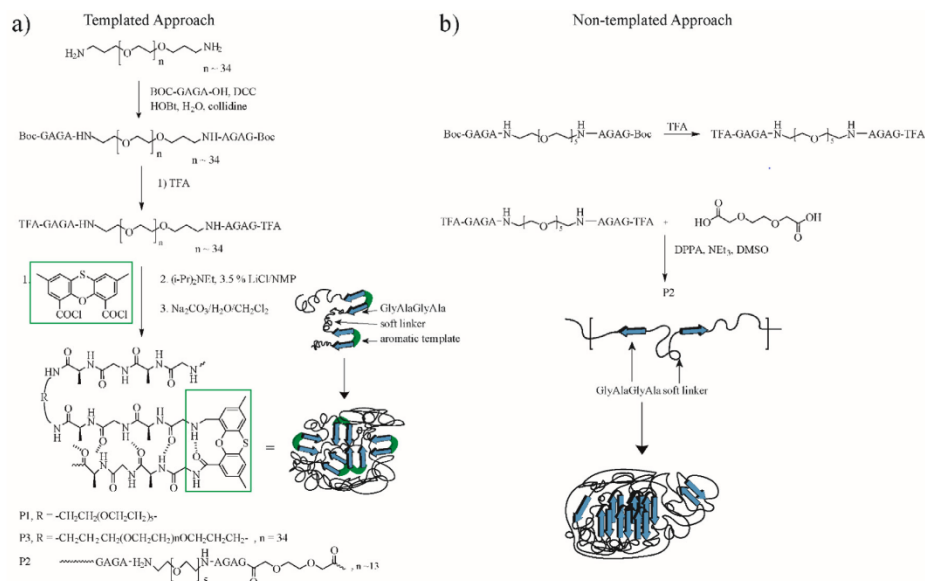


Fig. 3. The use of the molecular Lego method by the Sogah group. There are two different approaches presented: (a) the templated approach and (b) the non-templated approach [81]. Copyright 2001. Adapted with permission from the American Chemical Society.

with polymerizable end groups, resulting in a polymer with pendant peptides Ayres et al. [84]. Utilized the β -sheet forming sequence from silkworm silk modified with methacrylate end groups to employ atom-transfer radical polymerization (ATRP). However, the β -sheet forming sequence required a multi-step protocol involving multiple protection and deprotection steps whereas NCA

ROP would allow for the single-step synthesis of the desired peptide with a methacrylate-ended initiator. In other cases, the utilization of the end group amine still present after ROP can provide a versatile group for coupling. Smeenk et al., inspired by the triblock approach of the Sogah group, recombinantly produced polypeptide $((\text{AG})_3\text{EG})_{10}$ which was coupled *via* maleimide coupling to PEG

chains through the use of terminal tag peptides with cysteine [85]. In contrast, the use of a diamine initiator could have yielded the desired polypeptide with highly reactive amine groups which could be either modified themselves or directly coupled to the desired PEG chains. Thus, the potential of producing similar work utilizing NCA ROP as a synthetic strategy provides more versatility which in turn expands the field and provides potential scalability.

4.1. Polypeptides with modified silk-like motifs

Poly(alanine) is the major β -sheet forming unit in spider silk [58,71,74]. Poly(alanine) motifs natively found in silks remain below nine alanine units in length, thus achieving good thermodynamic stability in β -sheet conformations. However, beyond this upper threshold, these blocks favor α -helical structures [86]. Thus, careful design and manipulation are required to achieve β -sheets in pursuing primary and secondary structure mimicry. In this section, we focus on studies that utilize poly(alanine) in some way, including those which have poly(alanine) blocks interspersed with other residues (somewhat similar to silkworm silk and its GAGAGS motifs), with studies summarized in Appendix B. As mechanical properties are primarily dependent on the system, further clarification of general trends within studies have been stated.

4.1.1. Spacer residues within PLAla blocks

Early studies of alanine and glycine copolymerization investigated the relationship between the amino acid sequence and secondary structure using the simplest possible model [87]. In the late 1960s, Iwakura and coworkers reported the NCA-copolymerization of L-alanine, D-alanine, and glycine in different ratios and combinations in acetonitrile (ACN) or dimethylsulfoxide (DMSO) [88–90]. Poly(L-alanine) (PLAla) folded into α -helical structures, whereas a 1:1 mixture of glycine and L-alanine resulted in β -sheet conformations [89]. The resulting secondary structure was also dependent on the solvent used for polymerization. DMSO led to mainly β -sheet formation. The use of ACN resulted in α -helices [88,89].

Studies from Iio and Takahashi showed that the incorporation of higher ratios of glycine behaved destructively towards the α -helix formation of PAla in various organic solvents and water [87]. Conversely, it was found that the stability of an α -helix was higher in a polymer, in which glycine was at a ratio of 1:2 with alanine than a polymer where the ratio was 1:3 (glycine to alanine). The solubility of these copolymers depends on their molecular weight. Additionally, adding a D, L-glutamic acid (Glu) at the end of each polypeptide block increased the solubility without significant change to the resulting secondary structure. The introduction of charged amino acids like Glu can lead to a steric hindrance and favors the formation of inter- or intramolecular β -sheets.

It is important to note that upon the secondary structure change associated with introducing such residues, the stability and mechanical properties of these materials also change. For example, the Chen group has shown in their PLAla-*r*-poly(L-phenylalanine) (PLPhe)-*b*-PEG-*b*-PLAla-*r*-PLPhe based hydrogels the impact of introducing phenylalanine residues [91]. As LPhe is known to have a high β -sheet propensity, its insertion into PLAla blocks of around 30–40 units resulted in stiffer self-assembling hydrogels, with a storage modulus increase of 138 Pa up to 579 Pa with an increased LPhe to LAla ratio. Furthermore, the stereoisomerism of residues in the PAla block impacted overall stability. In a PEG-*b*-PAla-*r*-PLPhe hydrogel system (PAla DP ~10, PLPhe ~5), the introduction of D-alanine into blocks with primarily L-alanine led to a reduction in β -sheet structures (with an increase in other ordered structures) and a subsequent drop in mechanical stability with a storage modulus of ~500 Pa dropping to ~0.15 Pa with a racemic mixture. Interestingly, the use of solely D-isomers (i.e., poly(D-alanine)

(PDAla)) led to a slight increase in storage modulus (~100 Pa increase).

4.1.2. The impact of hydrophobic blocks outside of PAla chains

Hydrophobic components outside of the main PAla chain inherently affect intermolecular packing of chains either by improving the packing via hydrophobic association or disrupting the packing via the presence of bulky components.

Intriguingly, the Jeong group introduced a light-sensitive azobenzene unit within their linear polymers, resulting in molecular kinks, which impacted morphology alongside the effects of π - π stacking (Fig. 4) [92]. The N-termini of PEG_{22.7}-*b*-PLAla_{7.79} molecules were coupled together with an azobenzene-based diacyl chloride (azobenzene-4,4'-dicarbonyl dichloride), resulting in PEG_{22.7}-*b*-PLAla_{7.79}-Abz(azobenzene)-*b*-PLAla_{7.79}-*b*-PEG_{22.7}. A drastic decrease in β -sheet formation was observed compared to uncoupled copolymers (58% to below 45%), possibly due to the rigidity of the azobenzene group limiting interactions between L-alanine residues of the same polymer chain. The trans-to-cis configurational change of the central azobenzene group upon exposure to ultraviolet (UV) light (365 nm) was found to influence the π - π stacking of the molecules and thus the overall morphology of the hydrogels. In its cis configuration (under UV light), tighter, circular packing of the PLAla blocks resulted, with transmission electron microscopy (TEM) and dynamic light scattering (DLS) revealing the presence of spherical micellar structures of 60–82 nm in diameter. In its trans configuration (under visible light), the overall linear PLAla segments were found to stack upon each other with a slightly increased β -sheet content (44.1% compared to 40.8% in the cis configuration) with larger micellar structures of 95–147 nm being formed. Interestingly, these micelles remained spherical instead of worm-like nature, which may be expected from the parallel intermolecular stacking.

4.1.3. The impact of ionic components outside of PAla chains

Ionic bonding and repulsion profoundly affect the secondary structures and dominate the resulting secondary structures. This impact can be most easily observed in the poly(L-lysine) (PLLys)_{0.8}-*b*-PLAla_{4.5}-*b*-polaxmer (PLX)-*b*-PLAla_{4.5}-*b*-PLLys_{0.8} hydrogels synthesized by the Chu group [93]. The introduction of cationic L-lysine units prevented β -sheet formation via the short PLAla blocks despite being introduced at a minimal concentration (i.e., less than one-fifth of the amount of L-alanine). Upon heating from 20 to 60 °C, α -helical and β -sheet content decreased and increased, respectively, (α -helices: 60–58%; β -sheets: 2–4%), which was enough of a change to thermally induce gelation from an initial micellar formation, though these hydrogels remained relatively soft with a storage modulus of ~200 Pa. Conversely, ionic bonding can be amplified using polyionic complexation – using mixtures of polyanionic and polycationic polymers to induce β -sheet formation – as demonstrated by the Deming group, through the use of multiblock copolypeptides [94]. In their work, β -sheet formation was dominated by the number of polyionic blocks (i.e., PLLys and poly(L-glutamic acid) (PLGlu)) instead of the poly(sulfoxide methanoinine) (POLM)-*co*-PLAla blocks, reconfirming the dominance of ionic effects on such polypeptides. This led to a subsequent increase in storage moduli upon an increase from a diblock (~40 Pa at 10 wt%) to a pentablock polypeptide (~3000 Pa at 10 wt%). As such, it can be concluded that ionic components tend to dominate the secondary structure formation of these polypeptides, with the role of PLAla in such polypeptides not significantly extending into morphology.

4.1.4. Non-linear precursors

Asides from linear architectures, other molecular architectures have been employed with PAla blocks branching from a core or

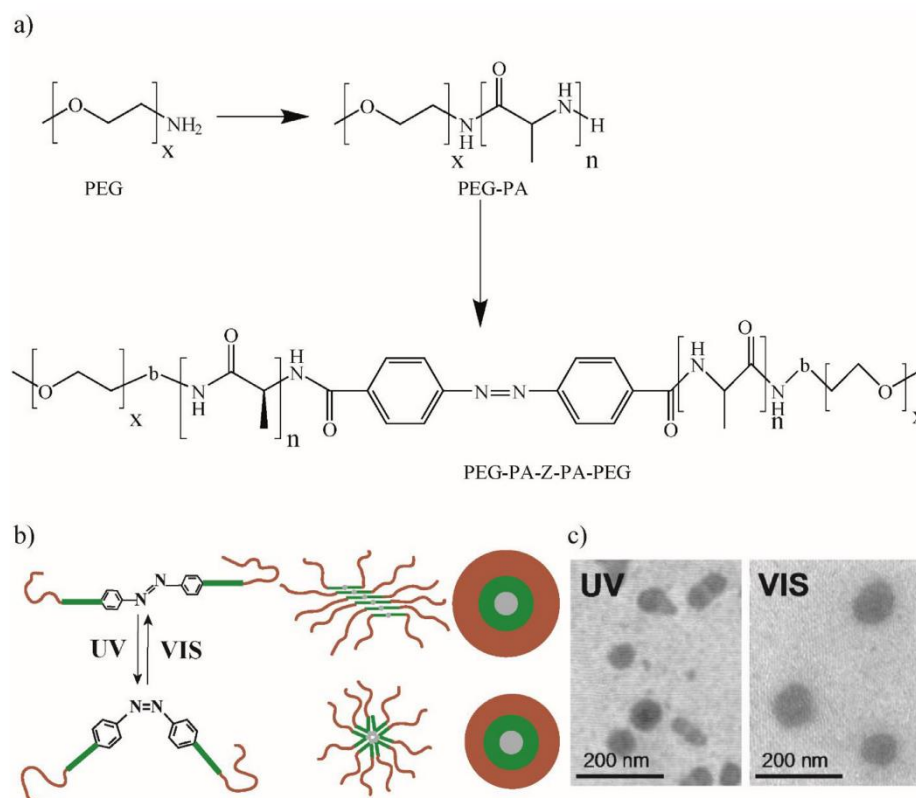


Fig. 4. (a) Synthetic route of azobenzene-centered copolymer production with PLAla blocks. (b) Schematic of transformation to cis (under UV) and trans (under visible light) forms. (c) TEM of micellar structures in the two conformations. [92], Copyright 2012. Adapted with permission from John Wiley and Sons.

backbone, resulting in increased proximity between PAAla blocks. Murphy et al. studied a series of hydrogels based on 8-arm stars with polypeptide arms terminated with hydrophobic, 5-unit homopolypeptide blocks, one of which was a PLAla₅ block [95]. Interestingly, despite the natural proclivity for PLAla₅ blocks to form β -sheets, 8- poly(carboxybenzyl-L-lysine) (PZLL)₄₀-PLAla₅ formed random coils identified by Fourier transform infrared spectroscopy (FTIR) and circular dichroism (CD) spectra, unable to gelate. Thornton et al. investigated their star-based system with a far more significant presence of α -helices and β -sheets [96]. Using a 4-arm PEG_{56,8} initiator, PLAla arms were polymerized with lengths ranging from DP 4-100. In contrast, Murphy et al. reported that their 4-PEG_{56,8}-*b*-PLAla₅ and 4-PEG_{56,8}-*b*-PLAla₁₀ stars were both found to gelate and exhibit significant α -helical structures, with the latter also possessing significant β -sheet content. This also contrasts against the expected primarily β -sheet conformations expected at low molecular weight PLAla. The explanation for the drastically observed difference in secondary structure is unclear but may be related to the relative bulkiness of side chains. While the PEG units of the 4-PEG_{56,8}-*b*-PLAla stars have no side chains, the bulk aromatic side chains of the PZLL blocks of the 8-PZLL₄₀-PLAla₅ likely hindered the interactions between neighboring arms. Furthermore, it should be noted that critical gelation and, presumably, mechanical stability increased upon increasing the PLAla length beyond five units.

Like stars, graft polymers potentially offer increased packing of neighboring PLAla blocks resulting in increased α -helical formation. Jeong and coworkers developed graft polymers by first synthesizing polypeptide-based arms and grafting them to a chitosan backbone [97]. On their own, the PLAla_{9,9}-*b*-PEG₄₅ copolymers would be expected to form β -sheets primarily. However, upon carbodiimide coupling *via* the N-terminus of the PLAla block to the dicarboxylic acid linker to couple to the amine of chitosan units, the subsequent graft polymer was found to possess a significant mix of both α -helical and β -sheet structures as shown by FTIR. Interestingly, the pH-sensitive behavior of the chitosan-containing hydrogel was not only altered upon the introduction of PLAla-*b*-PEG branches but outright reversed. As chitosan contains side chain amines (not coupled to by PLAla-*b*-PEG), their expected ionization under acidic conditions would usually result in electrostatic repulsion and thus softer hydrogels – a feature observed in other amine-based hydrogels [98]. However, storage moduli were instead found to increase with a decreasing pH (at 6 wt%, 43 Pa at pH 9.0 to 396 Pa at pH 3.0). This could partially be attributed to the slightly greater α -helical content at acidic pH. A shift in the ethylene oxide group of the carbon-13 nuclear magnetic resonance (¹³C-NMR) spectra from 72.4 ppm at pH 6.5 to 72.1 ppm at pH 3.0, as well as the broadening of the peak, suggest increased hydrogen bonding between the PEG and chitosan and restricted molecular motion which would further increase gelation.

4.2. Alternative polypeptides for β -sheet fibrils

As motif-based design does not exclusively render β -sheet conformations, the mimicry of silk-like structures without silk-like motifs provides an interesting alternative. Silk nanofibrils are similar but not identical to β -sheet-dominated amyloid fibrils at molecular and nanostructural levels [99–102]. Further to this, all amino acid sequences show some level of propensity towards β -sheet formation, though may be sterically hindered by side chains, and thus can be forced into this conformation [103,104]. As a result, much research has gone into investigating β -sheet-rich fibril structures for their individually strong nature, manipulation, and the subsequent impact on materials on a larger scale [48,105,106]. While these structures are not entirely congruent to those observed in silks, the pursuit of β -sheet fibrillar nanostructures is more easily attainable and thus presents more opportunities for investigation. Naturally, these structures tend to be larger than their silk-based counterparts, but with less stringent design criterion in relation to molecular weight, there is potentially more flexibility in tuning such materials to achieve specific properties. Specifically, this manifests in different β -strand spacings with the associated cross- β structures possessing interstrand spacings of 4.6 – 4.7 Å compared to the spacing of around 4.4 Å in spider silks due to glycine-rich components and the small side chains of this residue. Beyond this different spacing, however, the way in which such fibrillar structures manifest is largely based on the residue used and the strategies which have been employed to control their packing structure. This section seeks to observe how β -sheet fibrils have been produced, their conformations in relation to the residues used and subsequent implementation into different materials, with works summarized in Appendix C.

While this section is not focused on gel formation, the vast majority of the papers published on β -sheet fibrils focus on gelation. The self-assembly of β -sheet fibrils is primarily based on the system (e.g., spontaneous self-assembly, temperature-driven) instead of a singular universal environmental trigger. As the concentration of β -sheet-forming peptides are increased, the fibrils continue to increase in length before physical entanglement ensues.

4.2.1. β -sheet fibrils formed through canonical amino acids

Branched side chains on the β -carbon and aromatics have an affinity toward β -sheet formation, though this often manifests in uncontrolled aggregation,[107] often complicating the formation of specific nanostructures, with even micellar β -sheets potentially forming instead of an expected fibrillar state.[108] Amino acids which satisfy this prerequisite include isoleucine [109], tyrosine [110], phenylalanine, and threonine.

The hydrophobicity afforded by the formation of β -sheet structures and the large aromatic groups of poly(L-phenylalanine) (PLPhe) side chains makes them challenging to handle. The net result is far larger intersheet spacings than would usually be expected, as Puiggali and coworkers reported when using poly(L-lactic acid) (PLLA)-PLPhe [111,112]. Here, PPhe and PLLA blocks varied significantly concerning length and ratio, with FTIR providing evidence of high β -sheet content [111,112]. Throughout both works, PPhe and PLLA blocks varied significantly concerning length and ratio, with FTIR providing evidence of high β -sheet content. X-ray diffraction (XRD) spectra revealed the typical β -strand spacing of 4.7 Å typically associated with β -sheet crystals. Intriguingly, a reflection at 1.186 nm was also observed for all PLPhe lengths which is greater than typical cross- β structures assignment of interplanar spacing but can be attributed to the bulky aromatic rings causing this significant lamellar packing distance.

In direct contrast to the high hydrophobicity of PLPhe blocks, L-threonine blocks (PLThr) are the only polar block with high β -

sheet forming potential under benign conditions. Extensive publications by the Jan group reported using the coil-sheet forming poly(L-lysine) (PLLys)-PLThr to form a range of different β -sheet fibril-based assemblies (nanosheet/ribbons, hydrogel particles known as nanogels, hydrogels [113]). In all cases, copolypeptide formation was achieved using sequential NCA ROP. The impact of the β -sheet formation on these assemblies can be partially reflected in the hydrogels, where a series of copolymers with a PLLys length of ~20 DP and increasing PLThr sizes (DPs of 8, 16, and 41) correlated to an increase in β -sheet content determined by CD (45.3%, 46.6%, 54.8%) [113]. The presence of the cationic PLLys block was still required, as PLThr₂₀ was unable to form a gel at concentrations below 10 wt% despite attaining the highest β -sheet content (80.2%), though whether this was due to uncontrolled aggregation was unconfirmed. It was surmised that the charge-repulsion afforded by the PLLys blocks assisted with packing the PLThr blocks to achieve fibrillar formations. Investigation of small-angle X-ray scattering (SAXS) spectra revealed largely one-dimensional fibril assemblies with the XRD spectra revealing the typical d spacing of 4.6 Å associated with antiparallel β -sheets [114].

The inherently polar nature of threonine results in an increased chain length requirement to observe comparable mechanical properties to peptidic blocks with non-polar side chains. Despite having similar β -sheet propensities to other β -branched and aromatic amino acids [107], they are also less hydrophobic [115–118]. Due to the results of microphase separation of hydrophobic domains increasing crosslinking and thereby mechanical properties [119,120], this reduced hydrophobicity means that longer PLThr blocks are required resulting in an increased β -sheet content, increased hydrophobic microdomain density and subsequently increased mechanical properties. This impact can be seen from a mechanical standpoint in the Jan group's PLLys-PLThr system, where increasing PLThr resulted in increased β -sheet content and thus storage moduli in two separate cases (Fig. 5) [113]. At 5 wt% concentration, storage moduli increased from ~45 Pa for PLLys₂₀-*b*-PLThr₈ to ~200 Pa for PLLys₂₂-*b*-PLThr₁₆; and from ~100 Pa for PLLys₃₀-*b*-PLThr₁₂ to ~200 Pa for PLLys₃₀-*b*-PLThr₃₀ (Fig. 5b). In contrast, the PEG_{45,4}-poly(L-tyrosine) (PLTy_r) of the Heise group only required a peptide length of 6 units to achieve similar mechanical properties, though higher temperatures were required (~200 Pa at 2 wt%, 60 °C) [110].

While other hydrophobic residues also share a propensity towards β -sheet conformations, they simultaneously show a high propensity towards α -helix formation [107]. Thus, ingenious design strategies have been employed to force the tight packing required for preferential β -sheet formation.

Poly(L-leucine) (PLLeu) blocks follow a length-dependent secondary structure formation similar to PLAla [121], though β -sheet fibrils have been much less extensively explored. Generally, PLLeu blocks with DPs less than 10 primarily favor β -sheet conformation with increasing block length, leading to a slow evolution from β -sheet to α -helix [121,122]. The Deming group has performed extensive research on the use of PLLeu in diblock copolypeptides, but primarily as α -helical fibril formers [122–125]. As such, similar to PLAla, the use of non-peptidic components which may influence packing are used to modify secondary structure conformation. Higuschi et al. reported the design of poly(allylamine) with PLLeu grafted from the backbone [126]. Notably, the graft polymers were designed to have only 55% of allylamine group functionalized with PLLeu of DP 15, resulting in a backbone with pendant amine groups and thus in pH dependent morphology. With increased acidity and thus increased cationic charge of pendant amine groups, repulsive forces force a shift towards β -sheet formation in a similar fashion to the aforementioned effect of charge on PLAla chains. Furthermore, the alignment of such structures caused a transition from globular to fibrillar conformations which over a

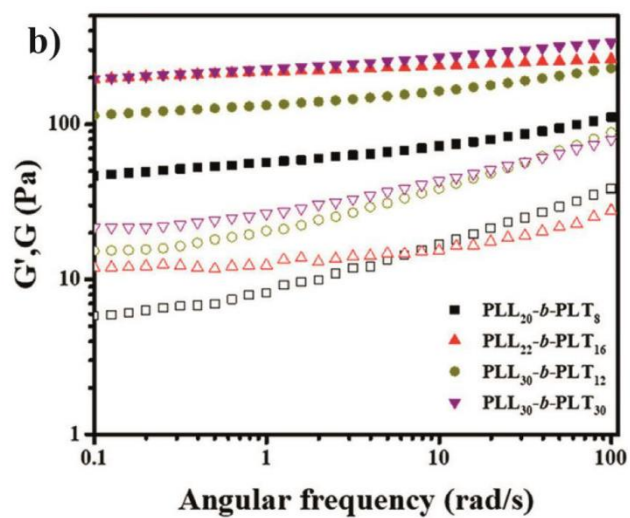
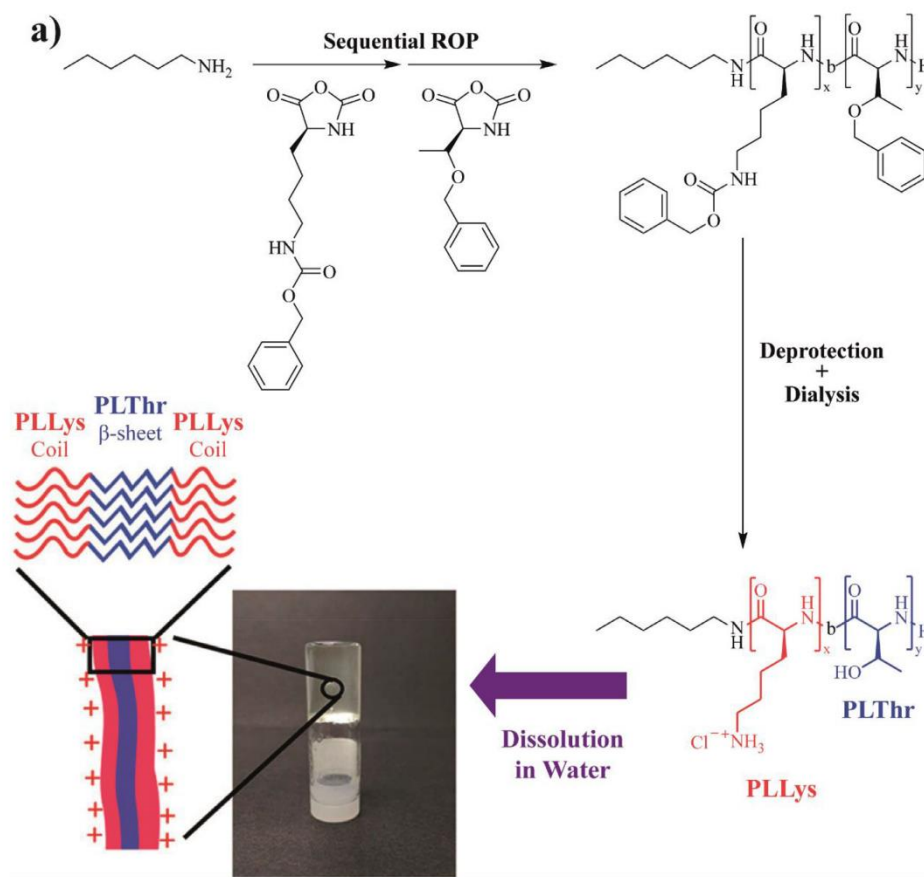


Fig. 5. (a) Schematic of PLThr PLLys block polypeptide synthesis and hydrogelation. After deprotection and subsequent dispersion in water, the repulsion forces of the PLLys help to force the PLThr blocks into the desired β -sheet nanoribbon conformation. (b) Storage modulus of hydrogels with differing block lengths at 5.0 wt%. [113]. Copyright 2018. Adapted with permission from the American Chemical Society.

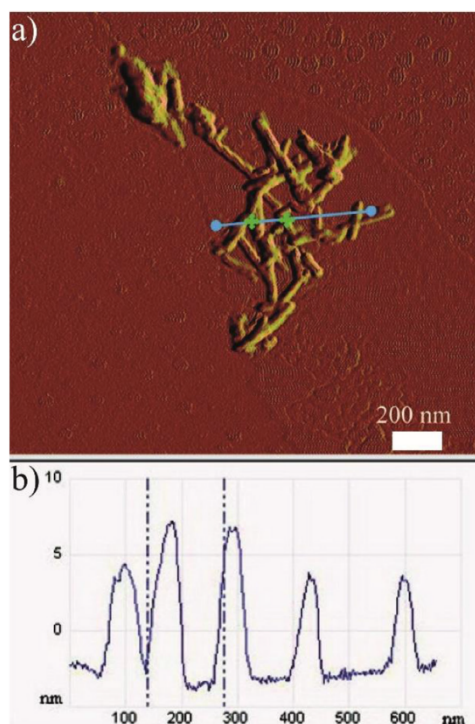


Fig. 6. Atomic force microscopy (AFM) images of PLGlu at pH 4.5. (a) Topography image of PLGlu nanofibers. (b) Cross-section height profiles of PLGlu nanofibers following the blue line in the topographical map. Green crosses on the blue line correlate to the position of the dotted lines on the height profile. [128], Copyright 2010. Adapted with permission from the American Chemical Society.

large time scale (18 days) would organize into sheet and eventually plate structures.

The influence of charge extends to charged amino acids which are susceptible to salt- and pH-dependent changes, which, in turn, affect their secondary structure. Typically, their charged state results in random coils due to the electrostatic repulsion preventing hydrogen bonding between peptide backbones. However, these repulsive forces can be rendered moot and thus strengthen their packing by either increasing the ionic strength of the solution [127] or reverting the residues to their uncharged states and thus increasing their hydrophobicity.

While not specifically an NCA ROP-based paper, the insights afforded by Dzwolak and coworkers into the conditions under which PLGlu and poly(*D*-glutamic acid) (PDGlu) form β -sheet fibrils provides a useful insight into design (Fig. 6) [128]. Acidification to pH \sim 4.1 and heating to temperatures above 65 °C resulted in the slow evolution of β -sheets from α -helical conformations after at least a 44 h incubation period. Stereoisomerism is an essential factor in structure formation as with other polypeptide blocks, with pure solutions of PLGA and PDGA of various molecular weights (15 – 50 kDa \sim 116 – 388 DP, center at DP 200) resulting in large, twisted bunches approximately 200 nm thick, with individual fibrils of 5 – 10 nm in width after incubation. Interestingly, scanning electron microscopy (SEM) uncovered the chirality-dependent twisting nature of these bundles, with PLGA and PDGA exhibiting left-handed and right-handed spirals, respectively. Equimolar

mixtures of these polypeptides exhibited a slower transition to β -sheet fibrils (evolution still occurring up to 99 h), with a lack of consistent twisting nature. A DP of 4 was found to be the critical length required for fibrillar aggregation of PLGlu, though the fibrillar bunches did not readily form until DP 10 [129].

4.2.2. β -Sheet fibrils formed through side chain modified amino acids

As stated before, protecting groups are often required with functional residues while using NCA ROP, though the altered intermolecular interactions results in β -sheet fibrils. Aromatic protecting groups are amongst the most investigated sidechain protecting groups. While they share the same ability to form π - π stacking bonds as their canonical counterparts, this does not translate to similar β -sheet forming propensities, with longer chains resulting in α -helical conformations [130].

Poly(benzyl-L-glutamate) (PBLG) stands out as a popular amino acid for fundamental studies. Though often used for its α -helical propensity, PBLG also experiences length dependent secondary structure though this cutoff is less than canonical amino acids with similar length dependence, with blocks with a DP less than 18 yielding β -sheets [130]. As with these residues though, non-peptidic components can influence this packing. Rodríguez-Hernández and coworkers interestingly worked on PBLG-polydimethylsiloxane (PDMS)-PBLG triblock polymers to observe the nanostructures that would form (Fig. 7) [131,132]. With increasing peptide length came the expected evolution of α -helical structures, with PBLG₅ maintaining primarily β -sheet structures (Fig. 10b) and with PBLG₁₀ attaining a more even mix of the two structures. Atomic force microscopy (AFM) revealed fibrillar morphologies up to 23 units in length, with a fibril thickness of 9 nm for DP 10 (Fig. 10c). It was surmised that PDMS formed coils while the flanking peptides would form the β -sheet structures in the low DP range. It can be extrapolated that non-peptidic components with stronger intermolecular influences such as the aforementioned charged backbones of PLLeu graft polymers could see a similar influence with PBLG.

Oligo(ethylene glycol)-functionalized L-glutamate blocks (PEGLG) are particularly interesting concerning their thermoresponsive secondary structure conformation. Much like poly(alanine), PEGLG tends to favor α -helical conformations. However, the Li group revealed through NMR spectroscopy that reversible dehydration of the ethylene glycol side chains of the PEG₄₅-PEGLG₄₃ copolymers through temperature increase resulted in increased hydrophobicity and subsequent β -sheet conformations as confirmed by FTIR [133]. TEM imaging revealed ribbon-like structures with a width of 60–80 nm in solutions at 80 °C – far larger than the fibrils reported using other residues. It was proposed that copolymers would first form wormlike micelles with α -helices associating to form cylindrical cores upon elevated temperatures. Further heating would result in the aforementioned β -sheet formation via intermolecular hydrogen bonding, resulting in nanoribbon packing.

The Li group further reported PEGLG in numerous fibrillar β -sheet organo- and hydrogel studies. A series of PEG-PEGLG diblock copolymers with shorter PEGLG blocks would spontaneously gelate when dispersed into water [134]. Larger PEGLG blocks were found to form gels at lower concentrations, with PEG₄₄-PEGLG₂₈ and PEG₄₄-PEGLG₁₅ due to an increase in β -sheet content. TEM and AFM imaging both presented significantly thinner fibrils with widths and heights of \sim 7–9 nm and \sim 1.0–1.5 nm, respectively, which may contribute to a continuous fibrillar network formation. Star polypeptides in a later work were found to produce gels with a far greater degree of mechanical tunability with storage moduli ranging between 24–3350 Pa solely via adjustment of arm length

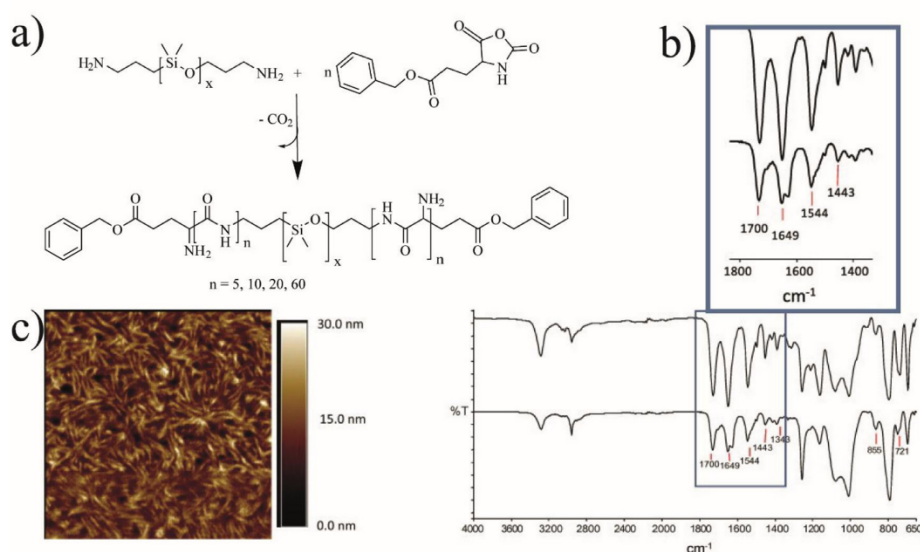


Fig. 7. (a) Synthetic route of PBLG-b-PDMS-b-PBLG copolyptide production via bifunctional PDMS. (b) FTIR of PBLG₆₀-b-PDMS-b-PBLG₆₀ (top) and PBLG₅-b-PDMS-b-PBLG₅ (bottom). (c) AFM images of PBLG₁₀-b-PDMS-b-PBLG₁₀. [131,132], Copyright 2007& 2010. Adapted with permission from Elsevier Science Ltd.

(DP 15-50) and number (8 and 32) [135]. However, the fibrillar hydrogels were only observed with the 8-arm copolyptides.

β -sheet fibril organogels formed from poly(D,L-allylglycine) (PADLG) assembly have been reported by the Wooley group [136]. Copolymers were synthesized using mono- and bi-functional PEG-based initiators to polymerize 12-residue long PADLG blocks. Using racemic blocks instead of a single consistent stereoisomer contradicts the usual strategy of triggering secondary structure formation. Nonetheless, gelation occurred after dissolution in polar solvents such as dimethylformamide (DMF), DMSO, and methanol (MeOH), with the sol-gel transition, found to reverse upon sonication. Attenuated total reflection Fourier transform infrared spectroscopy (ATR-FTIR) spectroscopy of dried diblock gels confirmed the role of secondary structure in gelation with primarily parallel β -sheet formation as well as significant antiparallel β -sheets [136]. Of note is the increased CGC (and hence, lower hydrogel stability) with increasing solvent polarity (where DMF has the lowest polarity and methanol has the highest) due to increased ease of dissolution. TEM and AFM imaging both revealed the fibrillar conformation of these structures, and AFM imaging of spin-coated mica samples showed exposed ribbon-like morphologies with heights and widths of ~ 2.5 and ~ 18 nm, respectively. Physically, these ribbon structures stacked similarly to monolayers, with hydrophilic tails flanking the hydrophobic core of the ribbons leading to β -sheet fibrillar structures, resulting in a stiff organogel in DMF (storage modulus of 15.2 kPa, compressive Young's modulus of 25.1 kPa).

5. Material morphology and fabrication strategies towards silk-like polymer synthesis

A natural progression from mimicking silk polypeptides at a chemical level is to process them into materials for practical applications. A common theme with all fabrication methods is the reliance on a high amount of intermolecular bonds between

molecules thus requiring high molecular weight polymers. Furthermore, the use of protected and modified residues is available using NCA ROP as stated before, resulting in potential strategies which cannot be emulated with other synthetic polypeptide techniques. Most of the reports utilizing NCA ROP result in the formation of gels as the final product. This is likely due to the minimal design constraints associated with homopolypeptides, block copolypeptides or random copolypeptides spontaneously forming the desired secondary structures and form the physical crosslinks necessary for gel formation in solution after the reaction. In some studies, further processing was performed to develop either films or fibers. Although this subset of studies is relatively small, many material morphologies for a vast suite of applications have been highlighted.

5.1. Fiber processing

Fiber processing is most successful through the utilization of long chain polymer precursors with a high density of intermolecular bonds, thus altering the approach available by NCA ROP polypeptides. Utilization of multiblock polymer-polypeptide hybrids as previously described is limited, thus step-growth polymerization via the end-to-end coupling of the hybrids as a prepolymer is often employed, allowing for the synthesis of high molecular weight polymers for spinning. Alternatively, the polypeptide itself can be designed to be high molecular weight using a base as an initiator, though this results in a less controlled reaction. Either of these strategies has been shown to yield NCA ROP polypeptides suitable for fiber formation.

The control of the molecular weight of peptidic components becomes an issue specifically related to NCA ROP. Based on the relationship between the size of some homopeptidic blocks and protein folding, the use of materials with minor molecular weight changes may yield significant changes in physical or chemical properties. Sogah and coworkers fabricated fibers from their

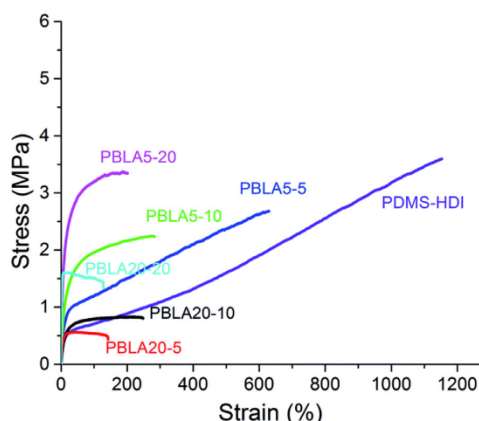


Fig. 8. Tensile properties of PDMS-PBLA (polydimethylsiloxane-poly-L-benzyl aspartate) cast films. All polymers are notated as PBLA X-Y, where X refers to the chain length of the PBLA block, and Y refers to the weight percentage concentration of peptide in the film. PDMS- (hexamethylene diisocyanate) HDI refers to films cast from polymers with no PBLA content. Films formed from short chain PBLA₅, which formed β -sheets generally possessing greater tensile strength and extension at break than their PBLA₂₀ counterparts (with a lower β -sheet content) [137]. Copyright 2014. Reproduced with permission from The Royal Society of Chemistry.

PLA₄₋₆-*b*-PEG₅-*b*-PLA₄₋₆ triblocks via wet spinning using the previously mentioned Lego method, developing fibers with PLA₄ blocks of DP 4 and 6 separately [80]. Integration across the radial axes found *d* spacings of 4.45 and 5.36 Å in both cases which are consistent with the spacing between β -sheets formed from PLA₄. Alignment of such structures was found to be more pronounced with PLA₄ blocks of DP 6. The net result was a comparatively more brittle but stronger fiber with the increase in Young's modulus and strength corresponding to an increase in β -sheet content (410 ± 35 MPa to 750 ± 156 MPa and 13.0 ± 1.4 MPa to 14.2 ± 2.7 MPa, respectively), as well as the corresponding drop in elongation at break ($22.9 \pm 13.6\%$ to $5.4 \pm 1.7\%$). Thus, even with a minor change in number of repeat units, assembly and consequential physical properties are already greatly affected.

5.2. Film casting and surface modification

Generally, the aforementioned molecular weight issues mentioned in fibers apply to films, with similar strategies employed. The Korley group reported the various factors which can contribute to the mechanical properties of polymer films. In all cases, similar polymers were synthesized – ABA triblock copolymers with a PDMS central block and peptidic flanking blocks (PZLL, Poly(β -benzyl-L-aspartate) (PBLA) or PBLG) synthesized as prepolymers and then linked using a di- or tri-functional isocyanate molecule. The utilization of aromatic-based protecting groups resulted in highly controllable secondary structure content by modification of the chain length. Johnson et al. investigated this system using a diisocyanate linker to compare different peptidic blocks (specifically PBLA and PZLL with different lengths) (Fig. 8) [137]. Using PBLA₅ as the peptide sequence (predominantly β -sheet forming) and casting from a mixture with 5 wt% peptides resulted in a tensile modulus, strength and strain-at-break of 14.5 MPa, 2.5 MPa and 669.5 %, respectively. However, PBLA₂₀ instead, which has 13% α -helical content, resulted in a drop in all these qualities (modulus of 9.26 MPa, strength of 0.8 MPa, strain-at-break

of 217.2%). Increased peptide wt% increased the α -helical content of the PBLA₂₀ films, but this increase in peptide concentration made films from both lengths of peptide more brittle with a strain-at-break reaching as low as 123.7% (PBLA₂₀ at 20 wt%). This extraordinary mechanical potential brought upon by β -sheet inclusion was not necessarily reflected once PZLL was introduced as the peptide unit, as the α -helical forming counterparts (PZLL₂₀) tended to outperform all the other combinations (at 5 wt%: modulus of 8.7 MPa, the strength of 5.2 MPa, strain-at-break of 821.9%). This inferiority can also be attributed to a lack of a truly fibrous β -sheet network compared to the use of PBLA.

A technique exclusively available to film formation is the development of covalently crosslinked networks during solvent evaporation. Using PBLA₅ as the peptide sequence with the same system as devised by the Korley group, Matolyak et al. investigated the impact of using a di- or tri-functional isocyanate molecule [138]. Breakdown of the antiparallel and parallel β -sheet content within the films revealed in ATR-FTIR spectra ($1620 - 1635$ cm⁻¹ for antiparallel β -sheets, and $1635 - 1645$ cm⁻¹ for parallel β -sheets) showed 100% parallel conformations when using the triisocyanate linker, while only 22–47% antiparallel β -sheet content was observed when using the di-isocyanate linker. Typically, antiparallel β -sheet structures are more favored due to their higher stability. However, the reduced chain mobility offered by the triisocyanate linker forced parallel- β -sheet formation instead and a reduction in fiber-like nanostructures (as confirmed by AFM).

Asides from conventional film synthesis techniques, the implementation of a polymerization-based synthetic method allows the unique use of grafting methods for polypeptide surface modification [139]. For surface initiated NCA ROP, surfaces need to be amminated such that nucleophilic end groups are available. Whitesell et al. investigated the use of an amine initiator with thiol groups for coupling to gold through thiolate-gold coupling [140]. In their work to develop helical structures from PLA₄, they specifically spaced initiating molecules at distances larger than the helix diameter (9 Å), however it is possible that initiating sites closer together would cause spatial restriction, resulting in a β -sheet rich surface. Alternatively, polymerization of polypeptide macromonomers provides another avenue towards polypeptide surface modification. Electrochemical polymerization was employed by Yagci and coworkers to achieve this, driving the deposition of PLA₄ chains to the electrode surface, which was then functionalized at the surface for biosensing applications [141,142]. Amino-functionalized thiophene was used to polymerize PLA₄ chains using NCA ROP [141]. A significant FTIR absorption peak at 1624 cm⁻¹ indicates β -sheet formation, supporting the theory that spatial constriction of such polypeptides can assist with increasing β -sheet content [141,142]. To achieve similar structures using other synthetic polypeptide techniques, end group coupling to the surface is required which ultimately does not assure the spatial restriction that may be desired.

5.3. Polypeptide based gels

Hydrogels have been extensively researched for their relative ease of fabrication compared to other architectures. In most cases, the critical gelation condition is reached when polypeptides undergo intermolecular secondary structure conformations, resulting in the physical crosslinks necessary for gelation. A wide range of environmental conditions can trigger this secondary structure formation. This breadth can further be modified using synthetic components including end groups or synthetic polymer which can be used as a (macro)initiator. Such components then modify the environmental sensitivity of the peptide component such as

PEG which undergoes a dehydration effect upon heating, resulting in hydrophobic interactions causing tightened packing [143]. Most relevantly, increasing temperatures from chilled (e.g. 4 °C) to physiological (37 °C) result in increased ordered structures for PLAla blocks, as shown by the Jeong group's PEG-PLAla system exhibited an increase in storage moduli from ~0.1 Pa to ~900 Pa [144].

The Jeong group has further extensively studied the gelation properties of PAla blocks when used in copolymers with synthetic blocks. With the implementation of DL-alanine along with L-alanine NCA monomers, they were able to tune the ratio between stereoisomers without completely sacrificing the formation of secondary structures [145–147]. In one of these works, PAla-PLX-PAla triblock with different amounts of L- and D- stereoisomers were introduced to achieve this secondary structure control [148]. As the hydrogels were designed for biological studies, a thermal gelation temperature of 37 °C was targeted in a 10 wt% aqueous solution, but this required increasing the peptide chain length with an increase in the mixture of DL-alanine along with L-alanine. With only the L-stereoisomer, this gelation temperature could be achieved with a DP of approximately 5.2 (370 Da). With 40 mol% of racemic alanine NCA, this increases to a DP of 6.5 (460 Da) and jumps to 12.4 (880 Da) with 100% racemic alanine to achieve the desired conformation. Secondary structure analysis revealed that the PLAla-based hydrogels had an α -helical and β -sheet content of 27% and 43%, respectively, but with 40 mol% being racemic, α -helical, and β -sheet content were found to change insignificantly (29% and 38%, respectively). However, the use of entirely racemic blocks yielded a significant rise in random coils (66%), and instead of the usual increase in α -helical content associated with an increase in block length, a drop in both α -helical and β -sheet content instead was observed (13% and 18%, respectively). Interestingly, this had minimal effect mechanically as all hydrogels investigated held a storage modulus of 1600 Pa.

As expected, the presence of different blocks or functional end-groups can significantly impact secondary structure formation and the subsequent morphology of specific systems. The Li group's work into PEGLG-based gels extended into fabricating nanoribbons focused on β -sheet organogels and hydrogels based on alkyl initiators, which completely changed the packing of the polymers. During the formation of hydrogels, hexyl-, dodecyl- and hexadecyl-PEGLG₁₁ were all found to maintain a CGC of 2 wt% [149]. However, CD and FTIR spectroscopy showed their secondary structure content changed significantly, with CD showing changes in α -helical and β -sheet content from 66% to 7% and 4 to 39%, respectively, with increasing alkyl chain size. TEM imaging still indicated nanoribbons within the fibrillar network, with widths in the range of 9–11 nm and heights of ~1 nm (found using AFM).

Organogels have been shown to form upon gelation of particular polypeptides in organic solvents. These are generally less popular, as their biological applications are severely restricted, but they are an important field of study for non-biological applications. Apart from the hydrogels mentioned above, the Li group has also observed the gelation characteristics of alkyl-terminated PEGLG-based organogels with the polar aprotic solvent tetrahydrofuran (THF) as the medium [150]. The effect of increasing alkyl chain size was far more pronounced in this solvent with hexyl-, dodecyl- and hexadecyl-PEGLG_{7,8} showing a steady decrease in CGC with increasing alkyl chain length (CGC is 5.0, 4.0 and 2.0 w/v%, respectively). Interestingly, FTIR spectroscopy showed the converse trend in secondary structure content with α -helical and β -sheet content from 19% to 26% and 60 to 36% with increasing alkyl chain size despite a similar mechanism to nanoribbon formation being proposed.

6. Applications

6.1. Drug/payload delivery

The method of drug delivery primarily depends on the morphology of the material, thus the greater sequence and subsequent morphological control of block copolymers/copolypeptides is favored over their random counterparts. Interestingly, majority groups utilizing NCA ROP-based silk analogues have reported the drug delivery capabilities of polypeptide hydrogel systems.

In its simplest form, hydrogels form in aqueous media with the payload dissolved or suspended within to achieve encapsulation [110,151]. As a hydrophobic block, PAla naturally associates with hydrophobic molecules and can be used for drug encapsulation and release. PAla is less hydrophobic than other amino acids, thus inducing a quicker release profile of drug molecules. The extensive study performed by Deming, Sofroniew, and coworkers looked at a range of different diblock copolypeptide hydrogels with a PLLys₁₈₀ block and a hydrophobic block for their potential use in drug delivery [152]. For the release of cholesterol, PLLys₁₈₀-b-PLAla₃₀ was found to have one of the fastest release profiles of the hydrogels tested, with ~90% cumulative release achieved over around 6 d. In comparison, PLLys₁₈₀-b-PLLeu₂₀ and PLLys₁₈₀-b-PLPhe₁₅, having more hydrophobic blocks, achieved ~70% and ~60% cumulative release over the same period.

The nanogels synthesized by the Jan group provide an alternative morphology for tuning drug release of hydrogels [153]. PLL₆₀-b-PLThr₁₅ were contained within the discrete water phase of a water-in-oil emulsion and chemically crosslinked using genipin. The subsequent nanogels were found to show membranolytic activity against the Gram-negative *K. pneumoniae*. Furthermore, almost instantaneous apoptotic action (3–6 min) against cells treated with lipopolysaccharides instead of those without the liposaccharides (15–18 min) further reinforced the aforementioned electrostatic mechanism of the antibacterial action. TNF-Related Apoptosis-Inducing Ligand (TRAIL) – a protein responsible for inducing cell apoptosis primarily in tumor cells – was also encapsulated within these cells to further increase the therapeutic action of the system. The effect was pronounced in mice infected with *K. pneumoniae*, where a much greater survival rate (~67%) was obtained upon treatment with the TRAIL-encapsulated nanogels instead of treatment with TRAIL or the nanogel alone (~30% and ~10% survival rate, respectively).

6.2. Cell toxicity and antimicrobial behavior

Generally, for NCA ROP-based antimicrobial polypeptides (AMPs), random copolypeptides of hydrophobic and cationic residues are well known to have high antimicrobial activity but also come with potentially high cytotoxicity resulting in the use of different architectures to restrict this cytotoxicity, leading to the use of β -sheet structures to allay this. PLLys segments are known to have antibacterial properties due to electrostatic effects – an impact reported by the Li group on short oligopeptide-based antibacterial hydrogels mixed with sodium alginate (amino propanol modified PLGlu (PPLG)-b-PLLys/sodium alginate (SA)). *Escherichia coli* (*E. coli*) was found to easily proliferate on PPLG₅/SA hydrogels as those lacked the electrostatic repulsion required for any antibacterial properties. However, substituting the PPLG unit for a lysine residue (PPLG₄-b-PLLys₁/SA) led to a decreased bacterial cell viability down to ~30%, with SEM revealing lesions and holes in the biofilm incubated with these hydrogels.

The Jan group expanded upon this, utilizing β -sheet fibril-based nanoribbons formed from DP 60 PLLys-b-PLThr polypeptides for

anticancer applications [154]. With the PLThr blocks being responsible for the nanoribbon formation, PLLys created a “fuzzy” exterior. In PLLys₅₀ samples (i.e., lacking PLThr), membranolytic activity was the greatest against cancer cells, though similarly high activity was observed against other human cells (LL2, H1299, A549-Luc). Increasing the ratio to PLThr₄₀-PLLys₂₀ resulted in decreased membranolytic activity in both cases and increased selectivity towards the cancer cells (LD₅₀ ~ 9 μM for A549 cancerous cells vs. LD₅₀ ~ 14 μM for BEAS-2B human cells). These results translated to positive *in vivo* results, where mouse models showed a significant decrease in tumor growth upon treatment with nanoparticles originating from PLThr₂₀-b-PLLys₄₀.

6.3. Tissue engineering

Tissue engineering relies on mimicry of the natural fibrous scaffolds excreted by cells called the extracellular matrix (ECM), which provides cells a platform for cell attachment, movement, and proliferation [155]. This mimicry takes on multiple aspects naturally fulfilled by silk-like structures, including biodegradation, molecular and structural mimicry, and mechanical properties, essential for cell differentiation [156,157]. Furthermore, having sufficient mechanical properties with prolonged stability prevents the polymer from being cleared away after insertion into the desired site and during the repair of the surrounding tissue. The ability to undergo environmentally sensitive crosslinking is necessary for hydrogels that form upon injection [158]. The aforementioned introduction of synthetic components. For thermogels, this requires preparing a thermally-sensitive solution at 10 – 20°C with hydrogelation occurring upon injection into the body at physiological temperatures (i.e., 37°C). The Jeong group has done extensive research on PAla-based copolymer systems as injectable thermogels for tissue engineering [144,148,159,160]. While there is naturally variation to their stiffness depending on the material, generally, storage moduli were found to be around 900 Pa or greater. Beyond injectability, cell signaling, and induced responses are vitally important to consider.

Bifunctional (macro)nitators have the side effect of introducing two N-termini which can be positively charged, thus introducing greater potential for ionic association. Park *et al* utilized hyaluronic acid as a polyanion to assist with the fibril formation and alignment of their PAla-b-PLX (Pluronic 127)-b-PAla triblock copolypeptides (Fig. 9) [147]. By aligning the fibrils, chondrocytes cultured on the scaffold showed better proliferation (from ~ 120% without hyaluronic acid to ~220% with 1 wt% hyaluronic acid, Fig. 9a) as well as increased mRNA expression for type II collagen, which is required for articular cartilage formation. This scaffold drastically outperformed the Matrigel™ control. It should be noted that these promising results are not likely solely due to the fibril alignment, as hyaluronic acid itself would interact with chondrocyte surface receptors [161]. Nonetheless, the overall impact of β-sheet fibrils cannot be discounted, as biomarker (i.e. sulfonated glycosaminoglycan (sGAG)) production in the controls was, at most, 4 times lower than in all β-sheet fibril bearing samples, including those without hyaluronic acid. The alignment of these fibers, however, appears to be more important than their mechanical properties, as despite samples containing the highest amount of hyaluronic acid having the lowest stiffness (270-400 Pa compared to 1000-1600 Pa with no hyaluronic acid), sGAG production and mRNA expression was ~25% and ~50% greater. This translated into a loss of spherical morphology within the controls (revealed via LIVE/DEAD assay) – a loss which was not reflected in the polypeptide-bearing samples.

Cell signaling will naturally occur due to the peptidic nature of PAla, with manipulation of this block length dictating

cell fate. Yeon *et al.* demonstrated the effect of manipulating PAla block length (DP 8.7 – 34.9) of PEG_{113.5}-b-PAla hydrogels on biomarker expression (Fig. 10) [162]. Adipose-tissue-derived stem cells (ADSCs) dispersed and cultured over 7 days within the hydrogels were all found to maintain their spherical morphology in a LIVE/DEAD assay; after 14 days, cells cultured in PEG_{113.5}-PAla_{8.7} hydrogels were found to lack sufficient adhesion and were washed away. Compared to a Matrigel™ control, the two-remaining peptide-based hydrogels (PEG_{113.5}-b-PAla_{15.5} and PEG_{113.5}-b-PAla_{34.9}) promoted cell proliferation (PAla_{15.5} cell proliferation of ~350%, PAla_{34.9} ~450%, control ~300%). However, while the longest PAla block supported cell proliferation best, cells cultured in the PAla_{15.5} block hydrogel produced the highest level of collagen II, a key protein for chondrogenesis, as mentioned above. As the storage moduli of all three hydrogels were similar, the drastic difference in biomarker expression is more directly related to the different PAla lengths causing different cell densities and triggering different signaling cues. Furthermore, *in vivo* injection of seeded PEG_{113.5}-b-PAla_{15.5} hydrogels and subsequent tissue staining around the remaining hydrogel revealed a clear presence of sulfated glycoaminoglycan (sGAG) – another biomarker for chondrogenesis.

With the emergence of 3D printing, the use of shear-thinning hydrogels is gaining more and more importance. Murphy *et al.* has reported PNLC₂₅-co-PLGlu₄₅-b-poly(L-isoleucine) (PLIle)₂₅ hydrogels for their potential as 3D printable materials, utilizing light-sensitive side-chain protecting groups to control chemical crosslinking [109]. Shear-thinning behavior was confirmed with a rheological strain sweep with the polypeptide hydrogels showing storage and loss moduli crossover at 80% strain. By extruding the hydrogel through a moving syringe (through an 18-gauge nozzle), each layer could be printed onto glass petri dishes resulting in a 3D scaffold with a degree of complexity despite its mechanical softness (storage modulus of 350 Pa). Alkyne-terminated 4-arm PEG molecules were printed along with the hydrogel, allowing the 3D scaffold to be stabilized using UV deprotection of the PNLC residues and subsequent thiolene ‘click’ chemistry crosslinking. While this chemically stabilized the print, the printed structure lost its fibrillar nature.

6.4. Further applications

6.4.1. Amphiphilic nanoparticle dispersant

Aside from the polypeptide-specific functions of β-sheet fibrils, some groups have instead taken advantage of the amphiphilic nature of many of these copolymers to employ them as a dispersant for single-wall carbon nanotubes (SWCNT) in organic solvents. The general strategy for dispersion involves finding one component which can associate with the SWCNT while the other is favorable within the solvent. While the component that associates with the SWCNT is often the β-sheet fibril, this is not always the case. Tang *et al.*, for example, required a pyrenyl end group to enable an association with the SWCNTs [164]. As a result, the properties of the SWCNT can be utilized for other applications, such as with the PEG-PADLG/SWCNT organogel systems employed by the Woolley group [165]. Due to the photosensitive nature of the PADLG-PEG-PADLG assemblies (partially afforded by the modified side chains of the peptidic regions), patterning was induced via light irradiation under yellow-red light (532 and 785 nm wavelength lights were tested), achieving highly complex patterns and lettering. This gel phase was then further stabilized by removing the solvent through evaporation or reverted into the sol state via sonication, giving a versatile patterning tool. Furthermore, the dispersed SWCNT resulted in a patterned film with a conductivity up to 130 S/m (based on SWCNT loading). The overall result is a con-

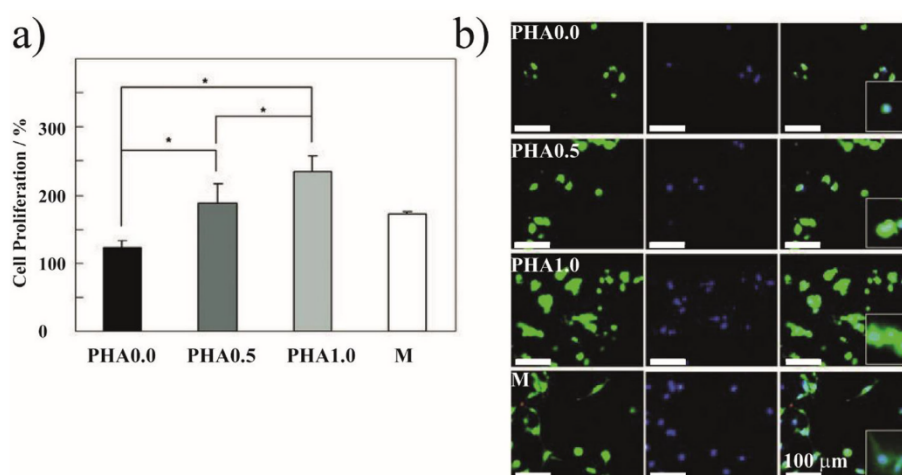


Fig. 9. Effect of hyaluronic inclusion within PEG-b-PALa-based hydrogels on chondrocytes compared to Matrigel™ (M). (a) Cell proliferation with increased hyaluronic acid content (b) Cell morphology as observed using a LIVE/DEAD assay (green and red indicates living and dead cells, respectively) and nuclei staining using Hoechst 33342 (blue). The scale bar is 100 μm. [147], Copyright 2012. Reproduced with permission from John Wiley and Sons.

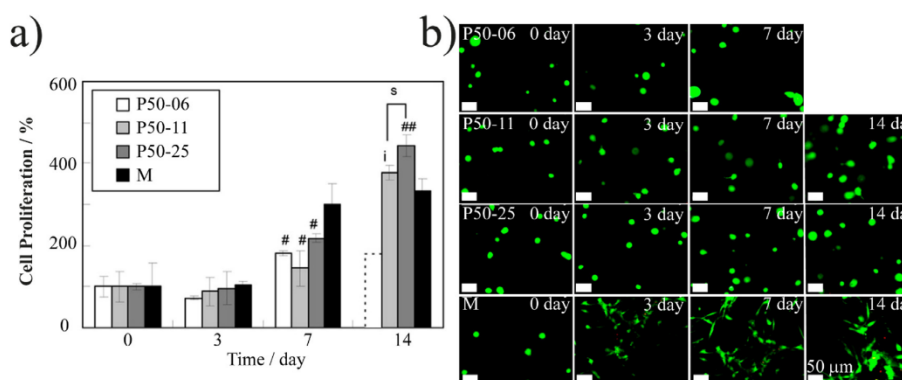


Fig. 10. (a) Cell proliferation of adipose-derived stem cells (ADSCs) over 14 days with different PLAla block sizes; (b) LIVE/DEAD assay (green and red indicates living and dead cells, respectively) revealing different morphologies after 14 days of culture [163]. The scale bar is 50 μm [163], Copyright 2013. Adapted with permission from the American Chemical Society.

ductive and rigid film resulting from the synergy of SWCNT and the β -sheet fibril network.

6.4.2. Molecule immobilization for biosensing

Yagci and coworkers have reported using surface grafted PLAla blocks to immobilize peptides and enzymes for biosensing purposes [141,142]. Thiophene-PLAla₁₆ synthesized using a thiophene functionalized initiator, yielding polypeptides which could be grafted-through without the need for further coupling. The thiophene end groups were electropolymerized and thus deposited onto glassy carbon electrodes. The sensing molecule was covalently coupled to the N-terminal amine via glutaraldehyde bonding, resulting in electrodes with different electrical resistances and subsequent different charge densities based on the target molecule concentration in solution. Upon conjugation of glucose oxidase, a

linear relationship between charge density and glucose concentration (0.05–1.0 mM) was observed (Fig. 11) [141]. Conversely, in the absence of PLAla, (i.e. only polythiophene), insufficient current density was obtained in the same range. While this is likely primarily due to the lack of binding sites for the covalent bonding of GOx, tests using a reduced density of PLAla chains exhibited the same issue, implying that the interaction between neighboring PLAla chains assists with inducing a response in charge density. Physical adsorption of glucose oxidase to the P(thiophene)-PLAla₁₆ surfaces did manage to yield sufficient response in the same range, but this response was not as sensitive. This technique was also successful for cocaine detection, with a covalently bonded cocaine aptamer registering a linear response in a 2.5–10 nM range for cocaine alone and 0.5–50 μM when the cocaine metabolite benzoylecgonine was also present [142].

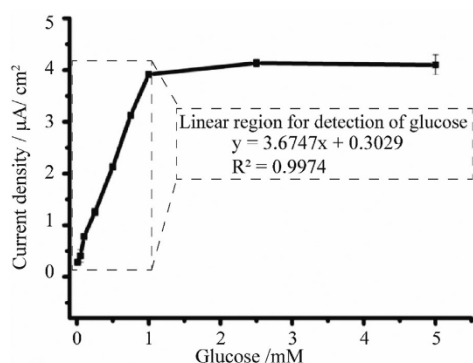


Fig. 11. Calibration curves for sensing glucose by measuring the charge density of PLAla coated electrodes up to 5 mM. Inset: Linear biosensing region for glucose concentrations up to 1.0 mM [141]. Copyright 2014. Reproduced with permission from The Royal Society of Chemistry.

7. Conclusions and future perspectives

In the pursuit of bioinspired materials, the synthesis of silk-inspired polymers via synthetic chemical techniques has shown much promise in designing materials with superior mechanical properties and interesting biological applications. The breadth of study in the field still relies heavily on NCA ROP, although chemoenzymatic polymerization has also shown promise in synthesizing such polypeptides. These approaches utilize β -sheets within an amorphous matrix to afford structural mobility and take advantage of the structure-property relationship found in natural silk. Intriguingly, the biological application of these approaches is limited despite the success of silk in drug delivery, tissue engineering, and other bioapplications.

To unlock the future potential of the field, we have also reviewed works with poly(alanine) blocks and with evidence of β -sheet fibrils for their facile implementation and thus introduc-

tion into more silk-inspired structures. Even with this expansion of scope, the potential for materials such as films and fibers has remained largely untapped. These directions feature particular potential in tissue engineering where evidence of degradation and cytocompatibility is a prerequisite for many applications. However, few of the existing publications take full advantage of the mechanical potential afforded by such structures. Thus, the intersection between these two areas represents the next hurdle for the field – implementing tough materials in bioapplications. With the field of biomimicry remaining as popular as ever, using silk as a template for the inspiration of chemically synthesized materials remains exciting for the potential bioapplications that will ensue.

Declaration of Competing Interest

The authors declare that they have no known competing financial interests or personal relationships that could have appeared to influence the work reported in this paper.

CRediT authorship contribution statement

Nicholas J. Chan: Conceptualization, Methodology, Investigation, Writing – original draft, Visualization. **Sarah Lentz:** Methodology, Investigation, Writing – original draft, Visualization. **Paul A. Gurr:** Methodology, Writing – review & editing. **Thomas Scheibel:** Conceptualization, Supervision, Writing – review & editing. **Greg G. Qiao:** Conceptualization, Supervision, Writing – review & editing.

Acknowledgments

N.J.C thanks The University of Melbourne for providing the Australian Government Research Training Program Scholarship (AGRTP) for providing funds for travel. This work is supported by grants DFG SCHE603/ 23-1. N.J.C, S.L, G.G.Q, and T.S. acknowledge funding from the German Academic Exchange Service (DAAD) through its thematic network Bayreuth-Melbourne Colloid/Polymer Network sponsored by the Federal Ministry of Education funds and Research (BMBF).

Appendix A. Overview of different β -sheet forming polypeptides, synthetic methods, and architectures for silk mimicry with the respective natural construct used as a blueprint and characterization methods

Peptidic component ^[a]	Structure Ref. ^[b]	Other peptides/ polymers/ materials	Natural Blueprint	Polymerization Method	Morphology	Secondary Structure Composition	Refs.
PLA1a	D1	None	None, compared against silk fibroin	NCA ROP	Films	Exact not specified	[89]
PLA1a-r-PDA1a	D2					Identification of secondary structure with FIR spectra bands	
PLA1a-r-poly(glycine) (PGly)	D3					Higher α -helical content in polymers in which glycine is in the i -th and the $(i+3)$ residue positions	[87]
PLA1a	D1	None	Silkworm Silk fibroin	Solid-phase synthesis and NCA ROP	None shown	Higher β -sheet content in polymers in which glycine is in the i -th residue positions ($i+2$) and ($i+4$)	
P(PLA1a ₂ -Gly)	D4					The less repeat units the less stable the α -helices.	
P(PLA1a ₃ -Gly)	D5						
P(LA1a-PGly ₂)	D6						
Poly(DL-glutamic acid)	D7						
(PDLGlu)-b-PLA1a-b-PDLGlu	D8						
PDLGlu-b-P(PLA1a ₂ -Gly)-b-PDLGlu	D9						
PDLGlu-b-P(PLA1a ₃ -Gly)-b-PDLGlu	D10						
PDLGlu-b-P(LA1a-PGly ₂)-b-PDLGlu							
P(LA1a-LVal-Gly)	D11	None	Silk fibroin	NCA ROP	None shown	Decreased by treatment with dichloroacetic acid from predominantly β -form to α -helical form	[166]
P(LVal-LA1a-Gly)	D12					Alternation of the simple tripeptide sequence change the conformation of the peptide	
PLA1a-r-PGly	D3	None	No mention	NCA ROP	Spherical aggregates		[167]
PLIys/PLGlu	D13/D14	None	Silk structure	NCA ROP	Fibers	Exact not specified	[168]
						Increase of glycine content increase the cross- β structure	
PLA1a	D1	Poly(2-acryloyloxyethyl-lactoside)	Spider silk	Sequential ATRP and NCA ROP	Spherical aggregates	Ratio of α -helix/ β -sheet secondary structure increased for PLA1a end blocks with increased block length	[169]
PLA1a	D1	Poly(ϵ -caprolactone) (PCL)	Spider silk	NCA ROP	Film	Exact not specified	[170]
						Predominant antiparallel β -sheet, less content of random coil conformation	
P((Gly-LA1a-Gly-LA1a)-b-PEG-b-(LA1a-Gly-LA1a-Gly))	D15	PEG	Nephila clavipes and Bombyx mori	Step-growth polymerization	Films	Solution synthesis led to antiparallel stacking of β -sheets - higher β -sheet content compared to other conformations	[80-83]
P(PLA1a-b-PEG-b-PLA1a)	D16					Interfacial polymerization led to lower β -sheet content and an increase in random coil proportion	

^aPolypeptides of repetitive amino acid sequences are indicated using the appropriate abbreviation

^bPolymer structure can be found in [Appendix D](#) under the corresponding code.

Appendix B. Overview of different poly(alanine)-based polymers, secondary structure, and other applicable properties

Peptide-bearing copolymer	Structure Ref. ^a	Morphology	Secondary Structure Composition	Mechanical Properties	Other materials and Applicable Properties	Refs.
PLAAla- <i>r</i> -poly(DL-alanine) (PDLAAla)- <i>b</i> -PLX- <i>b</i> -PLAAla- <i>r</i> -PDLAAla (end-capped with alkyl end group)	D17	Hydrogel	Not specified	Storage Moduli (50 °C): ~200-1000 Pa	Thermally induced gelation	[145]
PLAAla- <i>r</i> -PDLAAla- <i>b</i> -PLX- <i>b</i> -PLAAla- <i>r</i> -PDLAAla	D18	Hydrogel	Depending on ratio of L-DL-stereoisomer, (increasing DL increases random coils) β -sheet (18-43%), α -helix (13-29%) random coil (20-66%), others (3-12%)	Storage Moduli (37 °C after 100 min): ~1600-700 Pa Overall decrease with increasing DL	Morphological control in 2D and 3D chondrocyte cell cultures <i>In vivo</i> injection and native cell biomarker expression	[148]
Poly [N5-(2-hydroxyethyl)-L-glutamine] (PHLG)- <i>r</i> -PLAAla- <i>r</i> -Poly(L-lysine-g-methylacrylate) (PMLL)	D19	Hydrogel (crosslinked through methacrylate side chains)	No analysis	None shown	Chemically crosslinked with (Hydroxyethyl) methacrylate (HEMA) Porcine mesenchymal stem cells (MSC) culture on surface with cell adhesive motifs	[171]
PLAAla PEG- <i>b</i> -PLAAla PEG- <i>b</i> -PDLAAla	D1 D20 D21	Hydrogel	Decreased β -sheet and increased α -helix with increased PEG length β -sheet (36-74%), α -helix (4-42%) random coil (5-24%), others (5-17%) (Except for PDLAAla containing hydrogels which is majority random coils)	Storage Moduli (40 °C): ~10-1000 Pa Increase with increasing PEG length	Thermally induced gelation	[172]
chitosan- <i>g</i> -(PLAAla- <i>b</i> -PEG)	D22	Hydrogel	Non-specific, significant β -sheet and α -helical content, with α -helical content increasing with temperature and decreasing with pH	Storage Moduli (37 °C): 43-396 Pa Increase with decreasing pH	Thermally induced gelation	[97]
PLAAla- <i>r</i> -PLLeu- <i>b</i> -PLX- <i>b</i> -PLAAla- <i>r</i> -PLLeu	D23	Hydrogel	Increased β -sheet and decreased α -helix with β -sheet (31-42%), α -helix (37-48%), random coil (21-22%)	Storage Moduli (37 °C): 380 Pa	Thermally induced gelation ~50-95% mass loss over six days in proteinase K, elastase and MMP-12 <i>In vivo</i> injection, long term dissolution FITC-labeled bovine serum albumin (BSA) zeroth-order kinetics release over sustained period	[173]
PEG- <i>b</i> -PLAAla- <i>b</i> -PDLAAla PEG- <i>b</i> -PDLAAla- <i>b</i> -PLAAla	D24 D25	Hydrogel	Unspecified, but significant proportions of both α -helices and β -sheets	Storage Moduli (40 °C): PEG- <i>b</i> -PLAAla- <i>b</i> -PDLAAla: ~300 Pa PEG- <i>b</i> -PDLAAla- <i>b</i> -PLAAla: ~1000 Pa	None shown	[174]
PHLG- <i>r</i> -PLAAla- <i>r</i> -PMLL	D19	Hydrogel (crosslinked through methacrylate side chains)	No analysis performed	Not stated	>50% mass loss over six days in elastase	[175]

(continued on next page)

Peptide-bearing copolymer	Structure Ref. ^a	Morphology	Secondary Structure Composition	Mechanical Properties	Other materials and Applicable Properties	Refs.
PLAAla-r-PDLAAla-b-PLX-b-PLAAla-r-PDLAAla	D18	Hydrogel	Increased β -sheet with increased concentration β -sheet (37-47%), α -helix (22-25%), random coil (20-24%), others (9-18%)	Storage Moduli (37 °C): ~100-6000 Pa Increase with concentration	Thermally induced gelation 3D chondrocyte cell culture Cell biomarker expression None shown	[146]
PLAAla PBLG-b-PLAAla PBLG-b-PLAAla-b-PZLL PBLG-b-PLAAla-b-PZLL-b-PBLA PBLG-b-PZLL-b-PLAAla PLlys-b-PLAAla	D1 D26 D27 D28 D29	None	Unspecified, significant α -helix and β -sheet	N/A	None shown	[176]
	D30	Hydrogel (genipin crosslinking)	In all cases, predominantly random coil	Compressive Strength: 30-120 kPa Increase with overall polypeptide length	Biosilification (via calcination) Morphological control of 3T3 fibroblast cell culture on surface	[177]
PEG-b-PLAAla-Abz(azobenzene)-b-PLAAla-b-PEG	D31	Hydrogel	Under UV light: β -sheet (40.8%), α -helix (7.0%), random coil (46.4%), others (5.8%) Under visible light: β -sheet (44.1%), α -helix (8.2%), random coil (40.5%), others (7.2%)	Storage Moduli (37 °C): ~1000-1500 Pa Higher under UV	Thermally induced gelation	[92]
chitosan-g-(PLAAla-r-PLPhe-b-PEG)	D32	Hydrogel	Not broken down, primarily α -helix	Storage Moduli (37 °C): 128 Pa	Thermally induced gelation <i>In vivo</i> injection, long term dissolution Histologically compatible	[178]
PEG-b-PLAAla-r-PLPhe PEG-b-PDAAla-r-PDPhe	D33 D34	Hydrogel	Not broken down, primarily α -helix	Storage Moduli (37 °C): ~150 Pa	Thermally induced gelation <i>In vivo</i> injection, long term dissolution for L-isomer only Histologically compatible L-isomer, irritation with D-isomer	[159]
PEG-b-PLAAla-r-PLPhe	D33	Hydrogel	β -sheet (46%), α -helix (28%), random coil (26%)	Storage Moduli (37 °C): ~150 Pa	Thermally induced gelation <i>In vivo</i> injection, long term dissolution Marginal inflammatory response Human growth hormone (hGH) zeroth-order kinetics release over sustained period	[160]
PLlys PLAAla-r-PLlys	D13 D35	Hydrogel (chemical crosslinking via 6-arm PEG-ASG (NHS groups))	No analysis performed	Storage Moduli: 1400 Pa	3T3 fibroblast cell culture on surface with increased mitochondrial activity Inhibition against <i>E. coli</i> and <i>S. aureus</i>	[179]
PLAAla PDAAla	D1	None	<u>L-enantiomer</u> Predominantly α -helix <u>D-enantiomer</u> Predominantly β -sheet Predominantly α -helix in hexafluoroisopropanol (HFIP)	N/A	None shown	[86]
PEG-b-PLAAla	D20	Hydrogel	β -sheet (65%), α -helix (17%), random coil (14%), others (4%)	Storage Moduli (37 °C): 600 Pa	Thermally induced gelation Fibroblast cell culture within hydrogel with altered mRNA expression for collagen type I and II <i>In vivo</i> wound healing	[144]

(continued on next page)

Peptide-bearing copolymer	Structure Ref. ^a	Morphology	Secondary Structure Composition	Mechanical Properties	Other materials and Applicable Properties	Refs.
PLAAla	D1	None	No secondary structure analysis performed	N/A	None Shown	[180, 181]
PBLG- <i>b</i> -PLAAla	D26	Hydrogel	Predominantly β -sheet	Storage Moduli: 270-1600 Pa Increase with decreasing hyaluronic acid concentration	Fibril alignment upon inclusion of hyaluronic acid Chondrocyte cell culture within hydrogel Biomarker and mRNA expression for collagen type I and II	[147]
PLAAla- <i>r</i> -PDLAAla- <i>b</i> -PLX- <i>b</i> -PLAAla- <i>r</i> -PDLAAla	D18					
PBLG- <i>b</i> -PLAAla	D26					
PLAAla	D1	Film	Predominantly β -sheet	N/A Storage Modulus: ~400-1000 kPa Increase with decreasing PLAAla length	PCL and hexamethylene diisocyanate (HDI) linkers Strong tensile hysteresis	[182] [170]
PEG- <i>b</i> -PLAAla- <i>r</i> -PDALA- <i>b</i> -PLPhe	D36	Hydrogel	Predominantly β -sheet with increasing α -helix content with increasing D -enantiomer	Storage Modulus (37 °C): ~0.1-500 Pa Higher with only single stereoisomer	Thermally induced gelation Degraded polymer size over three days in elastase	[163]
4-arm PEG- <i>b</i> -PLAAla	D37	Hydrogel	Predominantly α -helix for DP 5, an increase of β -sheet content with arm length DP 10	Storage Modulus: ~10 kPa	Degradation over 18 h by elastase FITC-labeled albumin release sustained with elastase	[96]
PLAAla- <i>r</i> -PBLA- <i>r</i> -PLPhe- <i>b</i> -PLX- <i>b</i> -PLAAla- <i>r</i> -PBLA- <i>r</i> -PLPhe	D38 D39	Hydrogel	Increase in β -sheet and decrease of α -helix with increase temperature and deprotection of benzyl group on PLAsp	Storage Modulus (50 °C): ~0-600 Pa Increase with PBLA deprotection	Thermally induced gelation Low cytotoxicity to human retinal pigment epithelial cells	[183]
PLAAla- <i>r</i> -poly(L- aspartic acid)	D40	Hydrogel	Predominantly β -sheet	None shown	None shown	[184]
(PLAsp)- <i>r</i> -PLPhe- <i>b</i> -PLX- <i>b</i> -PLAAla- <i>r</i> -PLAsp- <i>r</i> -PLPhe						
Poly(L- arginine)	D41	Hydrogel	Predominantly α -helix	Storage Modulus (37 °C): 28-110 Pa Increase with decreasing ion binding affinity	Thermally induced gelation Cu ²⁺ , Zn ²⁺ and Ca ²⁺ binding to anionic ethylenediamine tetraacetic acid (EDTA)	[185]
(PLArg)- <i>b</i> -PLAAla						
P(PLAAla- <i>b</i> -PEG- <i>b</i> -PLAAla- <i>b</i> -EDTA)	D20	Hydrogel	None	Storage Modulus (37 °C): ~400 Pa	Incorporation of functionalized polystyrene microspheres Thermally induced gelation Morphological and cell differentiation control of tonsil-tissue-derived mesenchymal stem cells (TSMCs) cultured in hydrogels	[186]
PLlys- <i>b</i> -PLAAla	D30	Hydrogel	None performed	Storage Modulus: 10-50 Pa Increase with longer alanine peptides and lower cholesterol loading	Sustained cholesterol and temozolomide release <i>In vivo</i> injection, biomarker increase with tamoxifen release	[152]
PLlys- <i>b</i> -PLAAla- <i>r</i> -PLLeu	D42					
PLlys- <i>b</i> -PLLeu	D43					
PLlys- <i>b</i> -PLPhe						
PLAAla	D1	Films	None performed	N/A	Human mesenchymal stem cells cultured on crystals and films	[187]
PLlys	D13					
PLlys- <i>b</i> -PLAAla	D30					
Polyethyleneimine (PEI)- <i>g</i> -PLAAla	D44	Nanostructures	None performed	N/A	DNA transfection into HeLa, 293T, A549 and CHO cell lines	[188]

(continued on next page)

Peptide-bearing copolymer	Structure Ref. ^a	Morphology	Secondary Structure Composition	Mechanical Properties	Other materials and Applicable Properties	Refs.
P(thiophene)-g-PLAAla-glucose oxidase	D45	Surface/Film	None performed	None shown	Glucose sensing at range of 0.01-0.1 mM Moderate antimicrobial activity against <i>E. coli</i> and <i>S. aureus</i>	[141]
PLAAla	D1	None	None	N/A	None shown	[189]
PEG-b-PLAAla	D20	Hydrogel	Predominantly β -sheet	Storage Modulus (37 °C): 700-100 Pa	Thermally induced gelation Tonsil-Derived Mesenchymal Stromal Cells (TMSC) culture within hydrogels and differentiation with hepatogenic growth factors	[190]
PLGlu-r-PLLys-r-PLAAla-r-PLTyr	D46	Nanostructures	Increase in β -strands and decrease in α -helix with increase in temperature β -strand (9.2-29.4%), β -turn (18.4-21.5%), α -helix (15.2-37.8%), random coil (32.7-33.6%) Majority β -sheet	N/A	None-shown	[191]
PLAAla-b-poly(L-histidine) (PLHis)	D47	Nanostructures		N/A	Histidine tagging to gold nanoparticles	[192]
PEG-b-PLAAla-r-PLPhe	D33	Hydrogel	Decreased β -sheet and increased α -helices with increase in overall polymer size β -sheet (29-36%), α -helix (34-48%), random coil (20-22%), others (1-10%)	Storage Modulus (37 °C): 135-240 Pa (37 °C) Increase with overall increase in polymer length	Thermally induced gelation <i>in vivo</i> injection loaded with native cells rhGH (recombinant human growth hormone) release sustained <i>in vitro</i> and <i>in vivo</i>	[193]
PEG ₂ LG-r-PLAAla	D48	Hydrogel	Predominantly α -helical	Storage Modulus: 115-3600 Pa Increase with increased PEG size and decreased PEG ₂ LG length	Tunable thermally induced gelation	[194]
PEG ₂ DLG-b-PLLeu	D50	Hydrogels (Other polypeptides investigated in study, but focused on those presented)	Decrease in α -helix with increase in temperature for PEG ₂ DLG-b-PEG ₂ LG-r-PLLeu	Storage Modulus (40 °C): ~50-1000 Pa	Thermally induced gelation	[123]
PEG ₂ DLG-b-PEG ₁ LG-r-PEG ₂ LG-r-PLLeu	D51			Increase with increased PEG ₂ LG-r-PLLeu size	Sustained release of chicken egg white lysozyme	MSC cell compatibility
PEG ₂ DLG-b-PEG ₂ LG-r-PLAAla	D52					
PLAAla-b-PLGlu-C6-PLGlu-b-PLAAla ^{b1}	D53					
PLAAla-b-PLGlu-C6-PLGlu-b-PLAAla ^{b1}	D54	Hydrogel	Predominantly β -sheet at pH 7.4 Predominantly α -helix at pH 4	Storage Modulus: ~40-120 kPa Increase at pH 7.4 and PBS 0.15 M NaCl	Thermally induced gelation (cooling) pH sensitive gelation (pH 7.4 from 4)	[195]
8-arm PZLL-b-PLAAla	D55	Attempted Hydrogel (other residues found greater success)	Predominantly random coil	N/A	No gelation compared to other hydrophobic residues (valine, tyrosine, and phenylalanine)	[95]
PLAAla-O-R ^{c1}	D56	Hydrogel	Increase in β -sheet and decrease in α -helix with increased temperature β -sheet (2-4%), α -helix (58-61%), other (37-38%)	Storage Modulus (40 °C): ~8 Pa	Thermally induced gelation 2D and 3D MC3T3-E1 cell culture 32% mass loss over seven days in elastase BSA-FITC release with zeroth-order kinetics over ~180 h	[93]
PGly-O-R	D57					
PLAAla-r-PGly	D58					
PLLys-b-PLAAla-b-PLX-b-PLAAla-b-PLLys	D59					

(continued on next page)

Peptide-bearing copolymer	Structure Ref. ^a	Morphology	Secondary Structure Composition	Mechanical Properties	Other materials and Applicable Properties	Refs.
P(thiophene)- <i>g</i> -PLAAla-aptamer	D45	Surface	None shown	None shown	Cocaine sensing at range of 2.5–10 nM Benzoylcegonine sensing at range of 0.5–50 μ M	[142]
Bzl-PLAAla- <i>b</i> -PLGlu-C6-PLGlu- <i>b</i> -PLAAla-Bzl ^[9]	D60	Hydrogel	Predominantly β -sheet	Storage Moduli: ~10-200 kPa Increase at pH 4 and PBS 0.15 M NaCl	Thermally induced gelation (cooling) pH sensitive gelation (pH 4.0 from 6.5) Embedded with PCL-PEG-P2VP-PEG-PCL vesicles Sustained release of calcein A549 cell viability	[197]
PLAAla- <i>b</i> -PLX- <i>b</i> -PLAAla	D61	Hydrogel	Increasing α -helical content with alanine length	Storage Moduli: ~100-1000 kPa Increase with lower α -helical content	Thermally induced gelation Chondrocyte cultured within hydrogels <i>In vivo</i> injection	[198]
PEG- <i>b</i> -PLAAla- <i>r</i> -PLPhe	D33	Hydrogel	No analysis performed	Storage Modulus (40 $^{\circ}$ C): ~300 Pa	Thermally induced gelation Doxorubicin (DOX) and Combretastatin A4 (CA4) combined and sustained release 58.8-92.2% mass loss over 28 days in PBS pH 7.4 and elastase <i>In vivo</i> injection and tumor treatment	[199]
PEG- <i>b</i> -PLAAla	D20	Hydrogel	Predominantly α -helical	Storage Modulus (37 $^{\circ}$ C): ~600-1000 Pa Concentration adjusted to achieve range	Thermally induced gelation Morphological control of Adipose-tissue-derived stem cells (ADSC) cultured in hydrogels Biomarkers for neurogenesis and myogenesis observed during culture <i>In vivo</i> injection Histological compatibility None shown	[162]
PEG- <i>b</i> -PLHis- <i>r</i> -PLAAla	D62	Nanostructures	Primarily α -helix and random coil	N/A	None shown	[200]
PEG- <i>b</i> -PLAAla	D20	Hydrogels	Highly dependent on ratios and length	Storage modulus (40 $^{\circ}$ C): 100-600 Pa Increase with overall increase in polypeptide block length	Sustained nanosilver release with subsequent antibacterial activity against <i>S. aureus</i> and <i>B. subtilis</i>	[201]
PEG- <i>b</i> -PLAAla- <i>r</i> -PBLG	D63					
PEG- <i>b</i> -PLAAla- <i>r</i> -PGly- <i>r</i> -PLIle	D64	Hydrogels	Primarily β -sheet	Not shown	Thermally induced gelation ~50% mass loss over 10 days in Tris-HCl 0.05 M, pH 8.0 30-90% mass loss over four days in proteinase K and MMP-2 Sustained release of naproxen	[151]

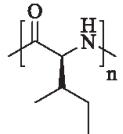
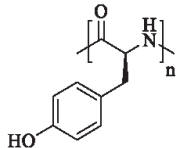
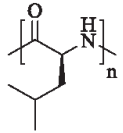
(continued on next page)

Peptide-bearing copolymer	Structure Ref. ^a	Morphology	Secondary Structure Composition	Mechanical Properties	Other materials and Applicable Properties	Refs.
PEG- <i>b</i> -PLAAla	D20	Hydrogel	Not analyzed	Storage modulus (40 °C): ~1.5 Pa	Thermally induced gelation ~15% mass loss over 7 days in PBS ~75% mass loss over 10 days in elastase 2D and 3D culture of MIN6 cells Sustained release of BSA <i>In vivo</i> injection, mild inflammation	[202]
PEG- <i>b</i> -PLAAla	D20	Hydrogel	Increase in antiparallel β -sheets with lower PLAAla DP (except for DP ~10 which has lower β -sheet content than DP ~13) antiparallel β -sheet (23.5-43.3%), parallel β -sheet (11.5-12.6%), α -helix (18.5-22.2%), random coil (40.7-42.6%)	Storage modulus (40 °C): 63-844 Pa Increase with increase PLAAla length	Thermally induced gelation Chondrocyte culture and resultant clustering within hydrogel with glycosaminoglycans (GAGs) and collagen	[203]
PLAAla- <i>b</i> -PEG- <i>b</i> -PLAAla PLAAla- <i>r</i> -PLPhe- <i>b</i> -PEG- <i>b</i> -PLAAla- <i>r</i> -PLPhe	D65 D66	Hydrogel	No analysis performed	Storage modulus (37 °C): 138-579 Pa Increase with increasing PLPhe length	Thermally induced gelation Bone marrow mesenchymal stem cell culture within hydrogel <i>In vivo</i> injection in osteochondral defects with increased GAGs and collagen type II expression	[91]
(Polypentadecalactone) PPDL- <i>b</i> -PLAAla (Polyglobalide) PGI- <i>g</i> -PLAAla	D67 D68	Nanostructures	Significant α -helix and β -sheets	N/A	None shown	[204]
PLLys- <i>b</i> -PLAAla- <i>b</i> -PLX- <i>b</i> -PLAAla- <i>b</i> -PLLys	D59	Hydrogel	Based on [93] Increase in β -sheet and decrease in α -helix with increased temperature β -sheet (2-4%), α -helix (58-61%), other (37-38%)	Not shown	Thermally induced gelation 293T cell culture within hydrogel ~55-82% mass loss over 14 days in PBS and elastase <i>In vivo</i> injection and sustained release of Tacrolimus	[205]
Poly(Sulfoxide methanoinine) (POLM)- <i>r</i> -PLAAla- <i>b</i> -PLLys POLM- <i>r</i> -PLAAla- <i>b</i> -PLLys- <i>b</i> -POLM- <i>r</i> -PLAAla POLM- <i>r</i> -PLAAla- <i>b</i> -PLLys- <i>b</i> -POLM- <i>r</i> -PLAAla POLM- <i>r</i> -PLAAla- <i>b</i> -PLGlu POLM- <i>r</i> -PLAAla- <i>b</i> -PLGlu- <i>b</i> -POLM- <i>r</i> -PLAAla POLM- <i>r</i> -PLAAla- <i>b</i> -PLGlu- <i>r</i> -POLM- <i>r</i> -PLAAla	D69 D70 D71 D72 D73 D74	Hydrogel	Predominantly random coil, significant β -sheet, increases with the number of blocks	Storage modulus: ~3-3000 Pa Increase with number of ionic blocks per polypeptide	Polypeptide mixtures to form hydrogel Self-healing	[94]
PLAAla C12- <i>b</i> -PLAAla Poly(N-isopropylacrylamide) (PNIPAM)- <i>b</i> -PLAAla PLAAla	D1 D75 D76	None shown	Predominantly random coil	N/A	None shown	[206]
PLAAla	D1	Fiber (electrospun mat)	Predominantly α -helix	Not shown	None shown	[207]

^aPolymer structure can be found in Appendix D under the corresponding code.

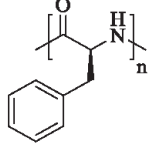
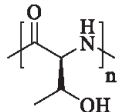
^bCX represents an alkane chain where X is the number of carbons in the alkane chain

^cR Represents a short chain alkane or a benzyl group.

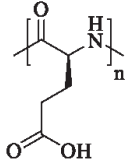
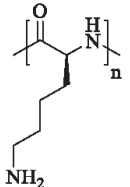
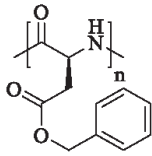
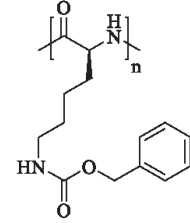
β -sheet Forming Peptide	Other peptides/ polymers/ materials	Morphologies	Fibril Dimension	Mechanical Properties	Applicable Properties	Ref.
PLLle 	PLGlu, PNBLC, 4-arm PEG	Hydrogel	Fibril width not stated	Storage modulus: 350 Pa	3D printable and crosslinkable Dermal fibroblast cell cultured within hydrogel	[109]
	PEG, PLAla (also likely contributes to β -sheet), PGly	Hydrogel	13.3 nm	Not shown	Thermally induced gelation ~50% mass loss over 10 days in Tris-HCl 0.05 M, pH 8.0 30-90% mass loss over four days in proteinase K and MMP-2 Sustained release of naproxen	[151]
	PEG	Hydrogel	Fibril width not stated	Storage Modulus (60 °C): ~125-200 Pa Increase with increase in temperature	Thermally induced gelation ~5-20% mass loss over 9 days in Krebs buffer (concentration dependent) Fast degradation in chymotrypsin Sustained release of desferrioxamine (DFO)	[110]
PLLleu 	PEG (mixture with and without PEG)	Nanostructures	Fibril width calculated (formed between spherical formations)	N/A	Not shown	[210]

(continued on next page)

Appendix C. Overview of different β -sheet fibril forming copolymers, synthesis methods and morphologies with mechanical and other applicable properties

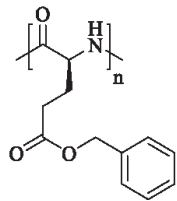
β -sheet Forming Peptide	Other peptides/ polymers/ materials	Morphologies	Fibril Dimension	Mechanical Properties	Applicable Properties	Ref.
PLPhe 	Poly(L-lactic acid)	Nanostructures	Fibril width not stated	N/A	None shown	[111, 112]
	None	Hydrogel	Fibril width not stated	None shown	HEK 293 cells cultured in polymer solutions	[208]
PLThr 	PLlys	Nanostructures	Fibril width not stated	N/A	Low cytotoxicity to BEAS-2B and BES-6 human cell lines cultured in polymer solutions Greater cytotoxicity to A549 and HEPG2 cancer cell lines cultured in polymer solutions Low haemolytic activity <i>In vivo</i> reduction of tumor growth Toxicity towards <i>K. pneumoniae</i> <i>In vivo</i> tumor necrosis factor (TNF)-related apoptosis-inducing ligands (TRAIL) release and action against towards <i>K. pneumoniae</i>	[154]
		Nanogels	Fibril width not stated	N/A	None shown	[153]
		Hydrogel	Fibril width not stated	Storage Modulus: ~40-200 Pa Increase with increasing PLThr length	None shown	[113]
	PLlys, PLGlu (separate polymer)	Films	Fibril width not stated	None shown	Biosilification (via calcination)	[209]

(continued on next page)

β -sheet Forming Peptide	Other peptides/ polymers/ materials	Morphologies	Fibril Dimension	Mechanical Properties	Applicable Properties	Ref.
	Poly(allylamine) (PLLeu branched from backbone)	Nanostructures	4.8 nm width	N/A	None shown	[126]
PLGlu 	Poly(norbornene) (grafted from backbone), Gold Nanoparticles (grafted from nanoparticles)	Nanostructures	Not stated	N/A	Grafted from gold nanoparticles	[211]
	PLLeu	Hydrogel	~ 3 nm from SAXS	Not shown	Hydroxyapatite nanocomposite inclusion	[125]
PLLys + PLGlu + PDLys + PDGlu	None	Nanostructures	Fibril width not stated	N/A	None shown	[212]
PBLA 	PDMS, difunctionalised and trifunctionalised isocyanates	Film	Fibril width not stated	Tensile Moduli: 9.8-72.5 MPa Elongation at Break: 52.1-285.0 % Toughness: 0.81-6.47 MJ/m ³ Overall modulus, extension at break and toughness increase with decreased covalent crosslinking and increased PDMS content	Strong tensile hysteresis	[138]
PZLL 	PEG, difunctionalised and trifunctionalised isocyanates	Film	Fibril width not stated	Tensile (only those with β -sheet) Moduli: 58-96 MPa Strength: 3-8 MPa Elongation at Break: 46-366 % Toughness: 1.3-21.1 MJ/m ³ Overall modulus, extension at break and toughness increase with decreased PEG content	None shown	[213]

(continued on next page)

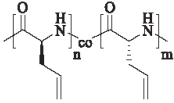
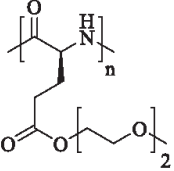
β -sheet Forming Peptide	Other peptides/ polymers/ materials	Morphologies	Fibril Dimension	Mechanical Properties	Applicable Properties	Ref.
	Poly(p-phenylene oxide) (PPO) or polyhedral oligomeric silsesquioxane (POSS)	Organogel (THF, Chloroform)	Fibril width not stated	Storage Modulus: 9-348 Pa Increase with overall PZLL length	None shown	[214]
PBLA + PZLL	PDMS, difunctionalised and trifunctionalised isocyanates	Film	Fibril width not stated	Tensile (only those without significant α -helix): Moduli: 8.6-43.8 MPa Strength: 1.6-3.4 MPa Elongation at Break: 202.5-669.5 % Toughness: 4.8-12.7 MJ/m ³ Overall modulus and strength increase with increased PDMS content, overall extension at break and toughness increase with lower PBLA or higher PZLL content	None shown	[137]
	Pyrenyl endgroup, SWCNT	Nanostructures	50 nm width after coating with SWCNT	N/A	Dispersant for SWCNT	[164]
	PCL (combination of dendron and linear, though linear promotes greatest β -sheet formation)	Organogel (toluene)	20 nm, 13 nm (SAXS)	None shown	Thermally induced gelation	[215]
	PDMS	Nanostructures	~12 nm (10 nm in SAXS)	N/A	None shown	[131]
		Films	4-9 nm	N/A	None shown	[132]



(Note: secondary structures focusing on short length)

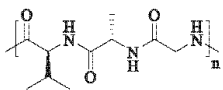
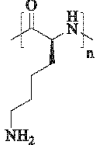
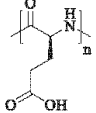
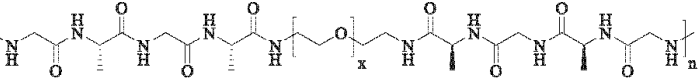
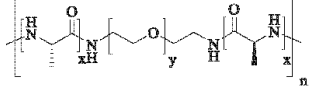
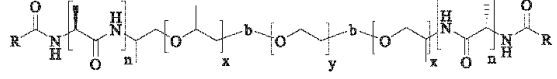
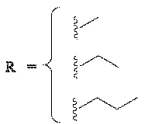
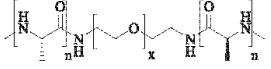
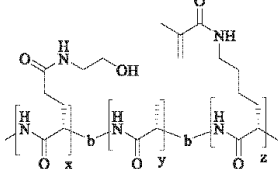
(Note: secondary structures focusing on short length)

(continued on next page)

β -sheet Forming Peptide	Other peptides/ polymers/ materials	Morphologies	Fibril Dimension	Mechanical Properties	Applicable Properties	Ref.
<p>PADLG</p> 	PEG, PGly	Organogel (DMF)	10.4-14.5 nm	Storage Modulus: 3.0-11.6 kPa Overall increase with increasing PGly content	Reversible gelation by sonication	[216]
	PEG	Organogel (DMF, DMSO, Methanol)	10-18 nm width 2.5 nm height	Storage Modulus: 20.7 kPa Compressive Modulus: 25 kPa Strength: >200 Pa Compression at break: >1.1%	Thermally induced gelation Reversible gelation by sonication	[136]
		Hydrogel	Not stated	Storage Modulus: ~4 kPa	Thermally induced gelation Reversible gelation by sonication ~90 wt% mass loss over 2-4 days in trypsin and proteinase ~80 wt% mass loss over 14 days in Tris HCl pH 8.0	[217]
	PEG, SWCNT (dispersed)	Organogel (DMF)	3.2-8.8 nm width	Storage Modulus: ~400 kPa	Reversible gelation by sonication Dispersant for SWCNT	[218]
Organogel (DMF), Film		2.4 - 18.9 nm width	Storage Modulus: 5-20 kPa Increase with increasing concentration	Reversible gelation by sonication Film formation upon light-induced crosslinking and drying Conductive upon SWCNT loading	[165]	
	PEG	Hydrogel	7.5-14 width 1.5-2.1 nm height	Storage Modulus (30 °C): ~60 Pa	Thermally modifiable storage modulus	[134]
	8- and 32- arm core (core first initiation) Alkyl endgroup	Hydrogel	16-23 nm width, 1.1 nm high	Storage Modulus: 24-3350 Pa Increase with increasing star number and peptide length	None shown	[219]
		Hydrogel	9-13 nm width, 1 nm high	Storage Modulus: ~1-1000 Pa Increase with increasing alkyl end group chain length	None shown	[149]

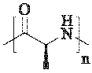
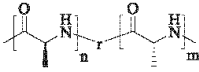
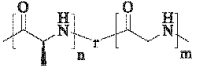
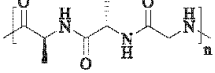
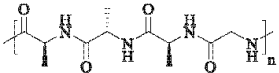
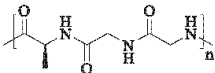
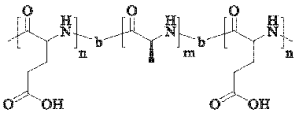
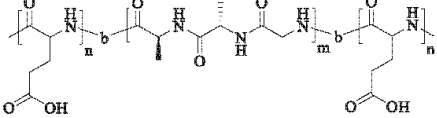
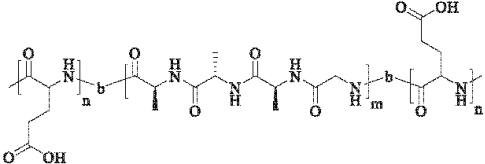
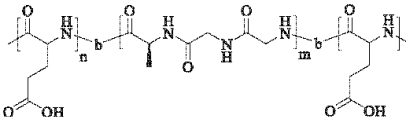
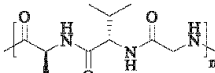
(continued on next page)

β -sheet Forming Peptide	Other peptides/ polymers/ materials	Morphologies	Fibril Dimension	Mechanical Properties	Applicable Properties	Ref.	
	PEG	Nanostructures	30-70 nm width	N/A	None shown	[133]	
	Alkyl endgroup	Organogel (THE, chloroform, dichloromethane (DCM))	8-17 nm width	Not shown	None shown	[150]	
	Alkyl endgroup	Hydrogel	4.5 nm width	Storage Modulus: ~20-20,000 Pa Increase with increasing sidechain length	None shown	[220]	
	<p>R = </p>	PLTyr (Also contributing to β -sheet)	Hydrogel, Nanogel	6-9 nm width, ~7 nm height	Storage Modulus: 100-656 Pa Increase with overall decrease in length	Further crosslinking with horseradish peroxidase crosslinking	[222]

Table Ref.	Polymer	
D12	P(LVal-LAla-Gly)	
D13	PLlys	
D14	PLGlu	
D15	P((Gly-LAla-Gly-LAla)-b-PEG-b-(LAla-Gly-LAla-Gly))	
D16	P(PLAla-b-PEG-b-PLAla)	 
D17	PLAla-r-PDLAla-b-PLX-b-PLAla-r-PDLAla (end-capped with alkyl end group)	
D18	PLAla-r-PDLAla-b-PLX-b-PLAla-r-PDLAla	
D19	PHLG-r-PLAla-r-PMLL	

(continued on next page)

Appendix D. Chemical structure of polymers presented

Table Ref.	Polymer	
D1	PLAla	
D2	PLAla- <i>r</i> -PDAla	
D3	PLAla- <i>r</i> -PGly	
D4	P(PLAla ₂ -Gly)	
D5	P(PLAla ₃ -Gly)	
D6	P(LAla-PGly ₂)	
D7	PDLGlu- <i>b</i> -PLAla- <i>b</i> -PDLGlu	
D8	PDLGlu- <i>b</i> -P(PLAla ₂ -Gly)- <i>b</i> -PDLGlu	
D9	PDLGlu- <i>b</i> -P(PLAla ₃ -Gly)- <i>b</i> -PDLGlu	
D10	PDLGlu- <i>b</i> -P(LAla-PGly ₂)- <i>b</i> -PDLGlu	
D11	P(LAla-LVal-Gly)	

(continued on next page)

Table Ref	Polymer	
D20	PEG- <i>b</i> -PLA _l Ala	
D21	PEG- <i>b</i> -PDLA _l Ala	
D22	chitosan- <i>g</i> -(PLA _l Ala- <i>b</i> -PEG)	
D23	PLA _l Ala- <i>r</i> -PLLeu- <i>b</i> -PLX- <i>b</i> -PLA _l Ala- <i>r</i> -PLLeu	
D24	PEG- <i>b</i> -PLA _l Ala- <i>b</i> -PDLA _l Ala	
D25	PEG- <i>b</i> -PDLA _l Ala- <i>b</i> -PLA _l Ala	
D26	PBLG- <i>b</i> -PLA _l Ala	
D27	PBLG- <i>b</i> -PLA _l Ala- <i>b</i> -PZLL	

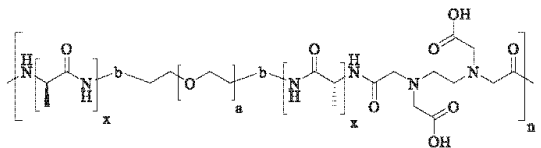
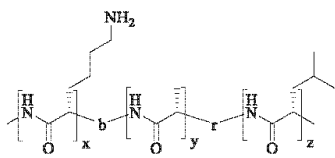
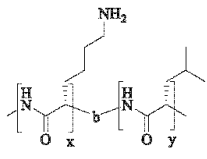
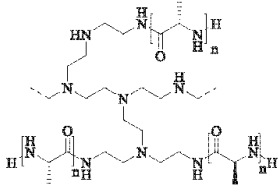
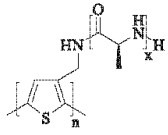
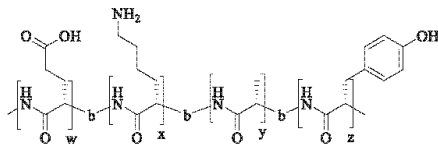
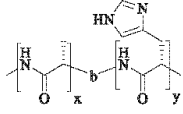
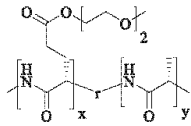
(continued on next page)

Table Ref.	Polymer	
D28	PBLG- <i>b</i> -PLAla- <i>b</i> -PZLL- <i>b</i> -PBLA	
D29	PBLG- <i>b</i> -PZLL- <i>b</i> -PLAla	
D30	PLIys- <i>b</i> -PLAla	
D31	PEG- <i>b</i> -PLAla-Abz(azobenzene)- <i>b</i> -PLAla- <i>b</i> -PEG	
D32	chitosan- <i>g</i> -(PLAla- <i>r</i> -PLPhe- <i>b</i> -PEG)	

(continued on next page)

Table Ref.	Polymer	
D33	PEG- <i>b</i> -PLAAla- <i>r</i> -PLPhe	
D34	PEG- <i>b</i> -PDAla- <i>r</i> -PDPhe	
D35	PLAAla- <i>r</i> -PLLys	
D36	PEG- <i>b</i> -PLAAla- <i>r</i> -PDAla- <i>b</i> -PLPhe	
D37	4-arm PEG- <i>b</i> -PLAAla	
D38	PLAAla- <i>r</i> -PBLA- <i>r</i> -PLPhe- <i>b</i> -PLX- <i>b</i> -PLAAla- <i>r</i> -PBLA- <i>r</i> -PLPhe	
D39	PLAAla- <i>r</i> -PLAsp- <i>r</i> -PLPhe- <i>b</i> -PLX- <i>b</i> -PLAAla- <i>r</i> -PLAsp- <i>r</i> -PLPhe	
D40	PLArg- <i>b</i> -PLAAla	

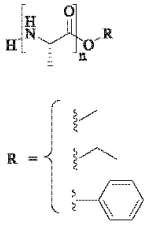
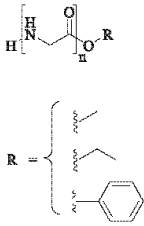
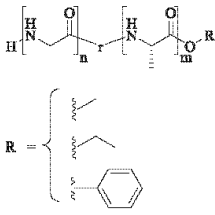
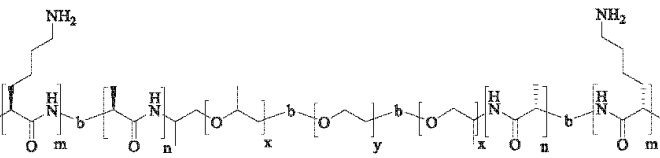
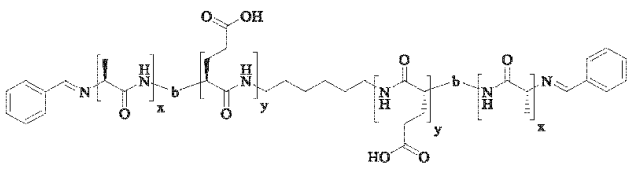
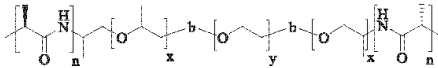
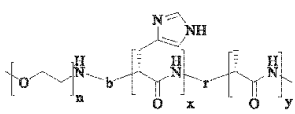
(continued on next page)

Table Ref.	Polymer	
D41	P(PLA1a- <i>b</i> -PEG- <i>b</i> -PLA1a- <i>b</i> -EDTA)	
D42	PLlys- <i>b</i> -PLA1a- <i>r</i> -PLLeu	
D43	PLlys- <i>b</i> -PLLeu	
D44	PEI- <i>g</i> -PLA1a	
D45	P(thiophene)- <i>g</i> -PLA1a	
D46	PLGlu- <i>r</i> -PLlys- <i>r</i> -PLA1a- <i>r</i> -PLTyr	
D47	PLA1a- <i>b</i> -PLHis	
D48	PEG ₂ LG- <i>r</i> -PLA1a	

(continued on next page)

Table Ref.	Polymer	
D49	PEG- <i>b</i> -PEG ₂ LG- <i>r</i> -PLA1a	
D50	PEG ₂ DLG- <i>b</i> -PLLeu	
D51	PEG ₂ DLG- <i>b</i> -PEG ₂ LG- <i>r</i> -PLLeu	
D52	PEG ₂ DLG- <i>b</i> -PEG ₁ LG- <i>r</i> -PEG ₂ LG- <i>r</i> -PLLeu	
D53	PEG ₂ DLG- <i>b</i> -PEG ₂ LG- <i>r</i> -PLA1a	
D54	PLA1a- <i>b</i> -PLGlu-C6-PLGlu- <i>b</i> -PLA1a	
D55	8-arm PZLL- <i>b</i> -PLA1a	

(continued on next page)

Table Ref.	Polymer
D56	PLAla-O-R 
D57	PLGly-O-R 
D58	PLAla-r-PGly-O-R 
D59	PLlys-b-PLAla-b-PLX-b-PLAla-b-PLlys 
D60	Bzl-PLAla-b-PLGlu-C6-PLGlu-b-PLAla-Bzl 
D61	PLAla-b-PLX-b-PLAla 
D62	PEG-b-PLHis-r-PLAla 

(continued on next page)

Table Ref.	Polymer	
D63	PEG- <i>b</i> -PLAla- <i>r</i> -PBLG	
D64	PEG- <i>b</i> -PLAla- <i>r</i> -PGly- <i>r</i> -PLIle	
D65	PLAla- <i>b</i> -PEG- <i>b</i> -PLAla	
D66	PLAla- <i>r</i> -PLPhe- <i>b</i> -PEG- <i>b</i> -PLAla- <i>r</i> -PLPhe	
D67	PPDL- <i>b</i> -PLAla	
D68	PGI- <i>g</i> -PLAla	
D69	POLM- <i>r</i> -PLAla- <i>b</i> -PLLys	

(continued on next page)

Table Ref.	Polymer	
D70	POLM-r-PLA1a-b-PLlys-b-POLM-r-PLA1a	
D71	POLM-r-PLA1a-b-PLlys-b-POLM-r-PLA1a-b-PLlys-b-POLM-r-PLA1a	
D72	POLM-r-PLA1a-b-PLGlu	
D73	POLM-r-PLA1a-b-PLGlu-b-POLM-r-PLA1a	
D74	POLM-r-PLA1a-b-PLGlu-b-POLM-r-PLA1a-b-PLGlu-r-POLM-r-PLA1a	
D75	C12-b-PLA1a	
D76	PNIPAM-b-PLA1a	

References

- [1] Balkenende DWR, Winkler SM, Messersmith PB. Marine-inspired polymers in medical adhesion. *Eur Polym J* 2019;116:134–43.
- [2] Wang J, Suhre MH, Scheibel T. A mussel polyphenol oxidase-like protein shows thiol-mediated antioxidant activity. *Eur Polym J* 2019;113:305–12.
- [3] Tadepalli S, Slocik JM, Gupta MK, Naik RR, Singamaneni S. Bio-optics and bio-inspired optical materials. *Chem Rev* 2017;117:12705–63.
- [4] Song B, Johansen VE, Sigmund O, Shin JH. Reproducing the hierarchy of disorder for morpho-inspired, broad-angle color reflection. *Sci Rep* 2017;7:46023.
- [5] Fu Y, Yuan C, Bai X. Marine drag reduction of shark skin inspired riblet surfaces. *Biosurf Biotribol* 2017;3:11–24.
- [6] Bixler GD, Bhushan B. Shark skin inspired low-drag microstructured surfaces in closed channel flow. *J Colloid Interface Sci* 2013;393:384–96.
- [7] Rising A, Withe M, Johansson J, Hedhammar M. Spider silk proteins: recent advances in recombinant production, structure–function relationships and biomedical applications. *Cell Mol Life Sci* 2011;68:169–84.
- [8] Hardy JG, Römer LM, Scheibel TR. Polymeric materials based on silk proteins. *Polymer* 2008;49:4309–27.
- [9] Hardy JG, Scheibel TR. Composite materials based on silk proteins. *Prog Polym Sci* 2010;35:1093–115.
- [10] Hakimi O, Knight DP, Vollrath F, Vadgama P. Spider and mulberry silkworm silks as compatible biomaterials. *Compos Part B: Eng* 2007;38:324–37.
- [11] Huang W, Ling S, Li C, Omenetto FG, Kaplan DL. Silkworm silk-based materials and devices generated using bio-nanotechnology. *Chem Soc Rev* 2018;47:6486–504.
- [12] Rising A, Johansson J. Toward spinning artificial spider silk. *Nat Chem Biol* 2015;11:309–15.
- [13] Keten S, Xu Z, Ihle B, Buehler MJ. Nanoconfinement controls stiffness, strength and mechanical toughness of β -sheet crystals in silk. *Nat Mater* 2010;9:359–67.
- [14] Heim M, Keerl D, Scheibel T. Spider silk: from soluble protein to extraordinary fiber. *Angew Chem Int Ed* 2009;48:3584–96.
- [15] Köhler T, Vollrath F. Thread biomechanics in the two orb-weaving spiders *Araneus diadematus* (Araneae, Araneidae) and *Uloborus walckenaerius* (Araneae, Uloboridae). *J Exp Zool* 1995;271:1–17.
- [16] Allmeling C, Jokuszies A, Reimers K, Kall S, Vogt PM. Use of spider silk fibres as an innovative material in a biocompatible artificial nerve conduit. *J Cell Mol Med* 2006;10:770–7.
- [17] Gellynck K, Verdonk PC, Van Nimmen E, Almqvist KF, Cheysens T, Schoukens G, et al. Silkworm and spider silk scaffolds for chondrocyte support. *J Mater Sci Mater Med* 2008;19:3399–409.
- [18] Chiarini A, Petriani P, Bozzini S, Dal Pra I, Armato U. Silk fibroin/poly (carbonate)-urethane as a substrate for cell growth: *in vitro* interactions with human cells. *Biomaterials* 2003;24:789–99.
- [19] Lu Q, Zhang B, Li M, Zuo B, Kaplan DL, Huang Y, et al. Degradation mechanism and control of silk fibroin. *Biomacromolecules* 2011;12:1080–6.
- [20] Horan RL, Antle K, Collette AL, Wang Y, Huang J, Moreau JE, et al. *In vitro* degradation of silk fibroin. *Biomaterials* 2005;26:3385–93.
- [21] Saric M, Scheibel T. Engineering of silk proteins for materials applications. *Curr Opin Biotechnol* 2019;60:213–20.
- [22] Wang J, Scheibel T. Recombinant production of mussel byssus inspired proteins. *Biotechnol J* 2018;13:1800146.
- [23] Tokareva O, Michalczewski-Lacerda VA, Rech EL, Kaplan DL. Recombinant DNA production of spider silk proteins. *Microb Biotechnol* 2013;6:651–63.
- [24] Humenik M, Smith AM, Scheibel T. Recombinant spider silks—biopolymers with potential for future applications. *Polymers* 2011;3:640.
- [25] Spiess K, Lammel A, Scheibel T. Recombinant spider silk proteins for applications in biomaterials. *Macromol Biosci* 2010;10:998–1007.
- [26] Varnava KG, Sarojini V. Making solid-phase peptide synthesis greener: a review of the literature. *Chem Asian J* 2019;14:1088–97.
- [27] Amblard M, Fehrentz JA, Martinez J, Subra G. Methods and protocols of modern solid phase peptide synthesis. *Mol Biotechnol* 2006;33:239–54.
- [28] He X, Fan J, Wooley KL. Stimuli-triggered sol-gel transitions of polypeptides derived from α -amino acid N-carboxyanhydride (NCA) polymerizations. *Chem Asian J* 2016;11:437–47.
- [29] Rasines Mazo A, Allison-Logan S, Karimi F, Chan NJA, Qiu W, Duan W, et al. Ring opening polymerization of α -amino acids: advances in synthesis, architecture and applications of polypeptides and their hybrids. *Chem Soc Rev* 2020;49:4737–834.
- [30] Huang J, Heise A. Stimuli responsive synthetic polypeptides derived from N-carboxyanhydride (NCA) polymerisation. *Chem Soc Rev* 2013;42:7373–90.
- [31] Deming TJ. Synthetic polypeptides for biomedical applications. *Prog Polym Sci* 2007;32:858–75.
- [32] Tsuchiya K, Numata K. Chemoenzymatic synthesis of polypeptides for use as functional and structural materials. *Macromol Biosci* 2017;17:1700177.
- [33] Numata K. Poly(amino acid)s/polypeptides as potential functional and structural materials. *Polym J* 2015;47:537–45.
- [34] Ganewatta MS, Wang Z, Tang C. Chemical syntheses of bioinspired and biomimetic polymers toward biobased materials. *Nat Rev Chem* 2021;5:753–72.
- [35] Sarkar A, Connor AJ, Koffas M, Zha RH. Chemical synthesis of silk-mimetic polymers. *Materials* 2019;12:4086.
- [36] Katashima T, Malay AD, Numata K. Chemical modification and biosynthesis of silk-like polymers. *Curr Opin Chem Eng* 2019;24:61–8.
- [37] Craig CL. Evolution of arthropod silks. *Annu Rev Entomol* 1997;42:231–67.
- [38] Rudall KM, Kenchington W. Arthropod silks: the problem of fibrous proteins in animal tissues. *Annu Rev Entomol* 1971;16:73–96.
- [39] Vollrath F, Knight DP. Liquid crystalline spinning of spider silk. *Nature* 2001;410:541–8.
- [40] Vehoff T, Glišović A, Schollmeyer H, Zippelius A, Salditt T. Mechanical properties of spider dragline silk: humidity, hysteresis, and relaxation. *Biophys J* 2007;93:4425–32.
- [41] Yazawa K, Malay AD, Masunaga H, Norma-Rashid Y, Numata K. Simultaneous effect of strain rate and humidity on the structure and mechanical behavior of spider silk. *Commun Mater* 2020;1:10.
- [42] Porter D, Vollrath F. Silk as a biomimetic ideal for structural polymers. *Adv Mater* 2009;21:487–92.
- [43] Iizuka E. The physico-chemical properties of silk fibers and the fiber spinning process. *Experientia* 1983;39:449–54.
- [44] Heim M, Römer L, Scheibel T. Hierarchical structures made of proteins. The complex architecture of spider webs and their constituent silk proteins. *Chem Soc Rev* 2010;39:156–64.
- [45] Sutherland TD, Young JH, Weisman S, Hayashi CY, Merritt DJ. Insect silk: one name, many materials. *Annu Rev Entomol* 2010;55:171–88.
- [46] Walker AA, Holland C, Sutherland TD. More than one way to spin a crystallite: multiple trajectories through liquid crystallinity to solid silk. *Proc R Soc B: Biol Sci* 2015;282:20150259.
- [47] Shao Z, Vollrath F, Sirichaisit J, Young RJ. Analysis of spider silk in native and supercontracted states using Raman spectroscopy. *Polymer* 1999;40:2493–500.
- [48] Dai B, Sargent CJ, Gui X, Liu C, Zhang F. Fibril self-assembly of amyloid–spider silk block polypeptides. *Biomacromolecules* 2019;20:2015–23.
- [49] Roche DB, Viet PD, Bakulina A, Hirsh L, Tosatto SCE, Kajava AV. Classification of β -hairpin repeat proteins. *J Struct Biol* 2018;201:130–8.
- [50] Addison B, Onofrei D, Stengel D, Blass B, Brennenman B, Ayon J, et al. Spider prey-wrapping silk is an α -helical coiled-coil/ β -sheet hybrid nanofiber. *Chem Commun* 2018;54:10746–9.
- [51] Sutherland TD, Trueman HE, Walker AA, Weisman S, Campbell PM, Dong Z, et al. Convergent evolution of structural anomalies in the coiled coil domains of insect silk proteins. *J Struct Biol* 2014;186:402–11.
- [52] Sutherland TD, Weisman S, Trueman HE, Sriskantha A, Trueman JWH, Haritos VS. Conservation of essential design features in coiled coil silks. *Mol Biol Evol* 2007;24:2424–32.
- [53] Bhattacharjee A, Bansal M. Collagen structure: the madras triple helix and the current scenario. *IUBMB Life* 2005;57:161–72.
- [54] Perea GB, Riekel C, Guinea GV, Madurga R, Daza R, Burghammer M, et al. Identification and dynamics of polyglycine II nanocrystals in *Argiope trifasciata* flagelliform silk. *Sci Rep* 2013;3:3061.
- [55] Jung D, Lee J, Park TY, Yang YJ, Cha HJ. Diverse silk and silk-like proteins derived from terrestrial and marine organisms and their applications. *Acta Biomater* 2021;136:56–71.
- [56] Borkner CB, Lentz S, Müller M, Fery A, Scheibel T. Ultrathin spider silk films: insights into spider silk assembly on surfaces. *ACS Appl Polym Mater* 2019;1:3366–74.
- [57] Zhou CZ, Confalonieri F, Esnault C, Zivanovic Y, Jacquet M, Janin J, et al. The 62-kb upstream region of *Bombyx mori* fibroin heavy chain gene is clustered of repetitive elements and candidate matrix association regions. *Gene* 2003;312:189–95.
- [58] Zhou CZ, Confalonieri F, Jacquet M, Perasso R, Li ZG, Janin J. Silk fibroin: structural implications of a remarkable amino acid sequence. *Protein Struct Funct Bioinf* 2001;44:119–22.
- [59] Tanaka K, Inoue S, Mizuno S. Hydrophobic interaction of P25, containing AS-N-linked oligosaccharide chains, with the H1 complex of silk fibroin produced by *Bombyx mori*. *Insect Biochem Mol Biol* 1999;29:269–76.
- [60] Asakura T, Saita K, Kameda T, Afonin S, Ulrich AS. Structural role of tyrosine in *Bombyx mori* silk fibroin, studied by solid-state NMR and molecular mechanics on a model peptide prepared as silk I and II. *Magn Reson Chem* 2004;42:258–66.
- [61] Zafar MS, Belton DJ, Hanby B, Kaplan DL, Perry CC. Functional material features of *bombyx mori* silk light versus heavy chain proteins. *Biomacromolecules* 2015;16:606–14.
- [62] Tanaka K, Kajiyama N, Ishikura K, Waga S, Kikuchi A, Ohtomo K, et al. Determination of the site of disulfide linkage between heavy and light chains of silk fibroin produced by *Bombyx mori*. *Biochim Biophys Acta (BBA) Protein Struct Mol Enzymol* 1999;1432:92–103.
- [63] Brooks AE, Steinkraus HB, Nelson SR, Lewis RV. An investigation of the divergence of major ampullate silk fibers from *nephila clavipes* and *argiope aurantia*. *Biomacromolecules* 2005;6:3095–9.
- [64] Saric M, Eissoldt L, Döring V, Scheibel T. Interplay of different major ampullate spidroins during assembly and implications for fiber mechanics. *Adv Mater* 2021;33:2006499.
- [65] Correa-Garhwal SM, Clarke TH, Janssen M, Crevecoeur L, McQuillan BN, Simpson AH, et al. Spidroins and silk fibers of aquatic spiders. *Sci Rep* 2019;9:13656.
- [66] Xu M, Lewis RV. Structure of a protein superfiber: spider dragline silk. *Proc Natl Acad Sci* 1990;87:7120–4.
- [67] Plaza GR, Pérez-Rigueiro J, Riekel C, Perea GB, Agulló-Rueda F, Burghammer M, et al. Relationship between microstructure and mechanical properties in spider silk fibers: identification of two regimes in the microstructural changes. *Soft Matter* 2012;8:6015–26.

- [68] Grubb DT, Jelinski LW. Fiber morphology of spider silk: the effects of tensile deformation. *Macromolecules* 1997;30:2860–7.
- [69] Riekel C, Bränden C, Craig C, Ferrero C, Heidelbach F, Müller M. Aspects of X-ray diffraction on single spider fibers. *Int J Biol Macromol* 1999;24:179–86.
- [70] Winkler S, Kaplan DL. Molecular biology of spider silk. *Rev Mol Biotechnol* 2000;74:85–93.
- [71] Kümmerlen J, Van Beek J, Vollrath F, Meier B. Local structure in spider dragline silk investigated by two-dimensional spin-diffusion nuclear magnetic resonance. *Macromolecules* 1996;29:2920–8.
- [72] Hijirida DH, Do KG, Michal C, Wong S, Zax D, Jelinski LW. ¹³C NMR of nephila clavipes major ampullate silk gland. *Biophys J* 1996;71:3442–7.
- [73] Liu Y, Sponner A, Porter D, Vollrath F. Proline and processing of spider silks. *Biomacromolecules* 2008;9:116–21.
- [74] Holland GP, Jenkins JE, Creager MS, Lewis RV, Yarger JL. Quantifying the fraction of glycine and alanine in β -sheet and helical conformations in spider dragline silk using solid-state NMR. *Chem Commun* 2008:5568–70.
- [75] Bauer J, Scheibel T. Conformational stability and interplay of helical N- and C-terminal domains with implications on major ampullate spider silk assembly. *Biomacromolecules* 2017;18:835–45.
- [76] Deming TJ. Cobalt and iron initiators for the controlled polymerization of α -amino acid-N-carboxyanhydrides. *Macromolecules* 1999;32:4500–2.
- [77] Deming TJ. Facile synthesis of block copolypeptides of defined architecture. *Nature* 1997;390:386–9.
- [78] Deming TJ, Curtin SA. Chain initiation efficiency in cobalt- and nickel-mediated polypeptide synthesis. *J Am Chem Soc* 2000;122:5710–17.
- [79] Chan NJA, Gu D, Tan S, Fu Q, Pattison TG, O'Connor AJ, et al. Spider-silk inspired polymeric networks by harnessing the mechanical potential of β -sheets through network-guided assembly. *Nat Commun* 2020;11:1630.
- [80] Rathore O, Sogah DY. Self-assembly of β -sheets into nanostructures by poly(alanine) segments incorporated in multiblock copolymers inspired by spider silk. *J Am Chem Soc* 2001;123:5231–9.
- [81] Rathore O, Sogah DY. Nanostructure formation through β -sheet self-assembly in silk-based materials. *Macromolecules* 2001;34:1477–86.
- [82] Wittingham MJ, Sogah DY. A modular approach to polymer architecture control via catenation of prefabricated biomolecular segments: polymers containing parallel β -sheets templated by a phenoxathiin-based reverse turn mimic. *Macromolecules* 1997;30:862–76.
- [83] Rathore O, Wittingham MJ, Sogah DY. A novel silk-based segmented block copolymer containing GlyAlaGlyAla β -sheets templated by phenoxathiin. *J Polym Sci Part A Polym Chem* 2000;38:352–66.
- [84] Ayres L, Adams P, Löwik D, van Hest JCM. β -Sheet side chain polymers synthesized by atom-transfer radical polymerization. *Biomacromolecules* 2005;6:825–31.
- [85] Smeenk JM, Schön P, Otten MJB, Speller S, Stunnenberg HG, van Hest JCM. Fibril formation by triblock copolymers of silklike β -sheet polypeptides and poly(ethylene glycol). *Macromolecules* 2006;39:2989–97.
- [86] Vanhelle M, Cornellie S, Smet M, Van Puyvelde P, Goderis B. Poly(alanine): structure and stability of the D and L-enantiomers. *Biomacromolecules* 2016;17:183–91.
- [87] Iio T, Takahashi S. Regular polypeptides of glycine and L-alanine (Special issue on polymer chemistry, VIII). *Polymers* 1971.
- [88] Iwakura Y, Uno K, Oya M. Polymerization of DL-alanine NCA and L-alanine NCA. *J Polym Sci Part A-1: Polym Chem* 1967;5:2867–74.
- [89] Itoh K, Nakahara T, Shimanouchi T, Oya M, Uno K, Iwakura Y. Far-infrared spectra of polyalanines with α -helical and β -form structures. *Biopolymers* 1968;6:1759–66.
- [90] Iwakura Y, Uno K, Oya M. Polymerization of α -amino acid N-carboxy anhydrides. III. Mechanism of polymerization of L- and DL-alanine NCA in acetonitrile. *J Polym Sci Part A-1: Polym Chem* 1968;6:2165–77.
- [91] Liu H, Cheng Y, Chen J, Chang F, Wang J, Ding J, et al. Component effect of stem cell-loaded thermosensitive polypeptide hydrogels on cartilage repair. *Acta Biomater* 2018;73:103–11.
- [92] Jeong SY, Moon HJ, Park MH, Joo MK, Jeong B. Molecular captain: a light-sensitive linker molecule in poly(ethylene glycol)-poly(L-alanine)-poly(ethylene glycol) triblock copolymer directs molecular nano-assembly, conformation, and sol-gel transition. *J Polym Sci Part A Polym Chem* 2012;50:3184–91.
- [93] Lin JY, Lai PL, Lin YK, Peng S, Lee LY, Chen CN, et al. A poloxamer-polypeptide thermosensitive hydrogel as a cell scaffold and sustained release depot. *Polym Chem* 2016;7:2976–85.
- [94] Sun Y, Deming TJ. Self-healing multiblock copolypeptide hydrogels via polyion complexation. *ACS Macro Lett* 2019;8:553–7.
- [95] Murphy R, Borase T, Payne C, O'Dwyer J, Cryan SA, Heise A. Hydrogels from amphiphilic star block copolypeptides. *RSC Adv* 2016;6:23370–6.
- [96] Thornton PD, Billah SMR, Cameron NR. Enzyme-degradable self-assembled hydrogels from polyalanine-modified poly(ethylene glycol) star polymers. *Macromol Rapid Commun* 2013;34:257–62.
- [97] Jang JH, Choi YM, Choi YY, Joo MK, Park MH, Choi BG, et al. pH/temperature sensitive chitosan-g-(PA-PEG) aqueous solutions as new thermogelling systems. *J Mater Chem* 2011;21:5484–91.
- [98] Yoshikawa HY, Rossetti FF, Kaufmann S, Kaindl T, Madsen J, Engel U, et al. Quantitative evaluation of mechanosensing of cells on dynamically tunable hydrogels. *J Am Chem Soc* 2011;133:1367–74.
- [99] Kenney JM, Knight D, Wise MJ, Vollrath F. Amyloidogenic nature of spider silk. *Eur J Biochem* 2002;269:4159–63.
- [100] Numata K, Kaplan DL. Differences in cytotoxicity of β -sheet peptides originated from silk and amyloid β . *Macromol Biosci* 2011;11:60–4.
- [101] Humenik M, Scheibel T. Nanomaterial building blocks based on spider silk-oligonucleotide conjugates. *ACS Nano* 2014;8:1342–9.
- [102] Yarger JL, Cherry BR, van der Vaart A. Uncovering the structure-function relationship in spider silk. *Nat Rev Mater* 2018;3:18008.
- [103] Costantini S, Colonna G, Facchiano AM. Amino acid propensities for secondary structures are influenced by the protein structural class. *Biochem Biophys Res Commun* 2006;342:441–51.
- [104] Jang H, Hall CK, Zhou Y. Thermodynamics and stability of a beta-sheet complex: molecular dynamics simulations on simplified off-lattice protein models. *Protein Sci* 2004;13:40–53.
- [105] Nova A, Keten S, Pugno NM, Redaelli A, Buehler MJ. Molecular and nanostructural mechanisms of deformation, strength and toughness of spider silk fibrils. *Nano Lett* 2010;10:2626–34.
- [106] Humenik M, Magdeburg M, Scheibel T. Influence of repeat numbers on self-assembly rates of repetitive recombinant spider silk proteins. *J Struct Biol* 2014;186:431–7.
- [107] Fujiwara K, Toda H, Ikeguchi M. Dependence of α -helical and β -sheet amino acid propensities on the overall protein fold type. *BMC Struct Biol* 2012;12:18.
- [108] Sinaga A, Hatton TA, Tam KC. Hydrogen bonded assembly of poly(acrylic acid)-block-poly(L-valine) in dilute solutions. *Macromolecules* 2007;40:9064–73.
- [109] Murphy RD, Kimmins S, Hibbitts AJ, Heise A. 3D-extrusion printing of stable constructs composed of photoresponsive polypeptide hydrogels. *Polym Chem* 2019;10:4675–82.
- [110] Huang J, Hastings CL, Duffy GP, Kelly HM, Raeburn J, Adams DJ, et al. Supramolecular hydrogels with reverse thermal gelation properties from (Oligo)tyrosine containing block copolymers. *Biomacromolecules* 2013;14:200–6.
- [111] Planellas M, Puiggali J. Synthesis and properties of poly(L-lactide)-b-poly(L-phenylalanine) hybrid copolymers. *Int J Mol Sci* 2014;15:3247–66.
- [112] Mayans E, Murase SK, Pérez-Madriral MM, Catiuela C, Alemán C, Puiggali J. Hybrid polypeptide/poly(lactide) copolymers with short phenylalanine blocks. *Macromol Chem Phys* 2018;219:1800168.
- [113] Hou SS, Fan NS, Tseng YC, Jan JS. Self-assembly and hydrogelation of coil-sheet poly(L-lysine)-block-poly(L-threonine) block copolypeptides. *Macromolecules* 2018;51:8054–63.
- [114] Rösler A, Klok HA, Hamley IW, Castelletto V, Mykhaylyk OO. Nanoscale structure of poly(ethylene glycol) hybrid block copolymers containing amphiphilic β -strand peptide sequences. *Biomacromolecules* 2003;4:859–63.
- [115] Eisenberg D. Three-dimensional structure of membrane and surface proteins. *Annu Rev Biochem* 1984;53:595–623.
- [116] Charton M, Charton BI. The structural dependence of amino acid hydrophobicity parameters. *J Theor Biol* 1982;99:629–44.
- [117] Kyte J, Doolittle RF. A simple method for displaying the hydropathic character of a protein. *J Mol Biol* 1982;157:105–32.
- [118] Wolfenden R, Andersson L, Cullis PM, Southgate CCB. Affinities of amino acid side chains for solvent water. *Biochemistry* 1981;20:849–55.
- [119] Jiang H, Duan L, Ren X, Gao G. Hydrophobic association hydrogels with excellent mechanical and self-healing properties. *Eur Polym J* 2019;112:660–9.
- [120] Tan S, Chan NJA, Collins J, Fu Q, Qiao GG. CHAPTER 13 new approaches towards the design of tough amphiphilic polymeric co-networks. In: Amphiphilic polymer co-networks: synthesis, properties, modelling and applications. The Royal Society of Chemistry; 2020. p. 277–308.
- [121] Stulz J, Müller D, Hull WE, Kricheldorf HR. Secondary structure of peptides, 10. FT-IR and ¹³C NMR CP/MAS study on tacticity and secondary structure of poly(D,L-leucine)s. *Die Makromol Chem* 1983;184:1311–22.
- [122] Holowka EP, Pochan DJ, Deming TJ. Charged polypeptide vesicles with controllable diameter. *J Am Chem Soc* 2005;127:12423–8.
- [123] Zhang S, Alvarez DJ, Sofroniew MV, Deming TJ. Design and synthesis of non-ionic copolypeptide hydrogels with reversible thermoresponsive and tunable physical properties. *Biomacromolecules* 2015;16:1331–40.
- [124] Breedveld V, Nowak AP, Sato J, Deming TJ, Pine DJ. Rheology of block copolypeptide solutions: hydrogels with tunable properties. *Macromolecules* 2004;37:3943–53.
- [125] Hu YY, Yusufoglu Y, Kanapathipillai M, Yang CY, Wu Y, Thiyyagarajan P, et al. Self-assembled calcium phosphate nanocomposites using block copolypeptide templates. *Soft Matter* 2009;5:4311–20.
- [126] Higuchi M, Inoue T, Miyoshi H, Kawaguchi M. pH-induced reversible conformational and morphological regulation of poly(ethylene glycol) grafted polyallylamine assembly in solution. *Langmuir* 2005;21:11462–7.
- [127] Grigsby JJ, Blanch HW, Prausnitz JM. Effect of secondary structure on the potential of mean force for poly-L-lysine in the α -helix and β -sheet conformations. *Biophys Chem* 2002;99:107–16.
- [128] Fulara A, Dzwolak W. Bifurcated hydrogen bonds stabilize fibrils of poly(L-glutamic) acid. *J Phys Chem B* 2010;114:8278–83.
- [129] Hernik A, Puławski W, Fedorczyk B, Tymecka D, Misicka A, Filippek S, et al. Amyloidogenic properties of short α -L-glutamic acid oligomers. *Langmuir* 2015;31:10500–7.
- [130] Papadopoulos P, Floudas G, Klok HA, Schnell I, Pakula T. Self-assembly and dynamics of poly(γ -benzyl-L-glutamate) peptides. *Biomacromolecules* 2004;5:81–91.
- [131] Ibarboure E, Papon E, Rodriguez-Hernández J. Nanostructured thermotropic PBLG-PDMS-PBLG block copolymers. *Polymer* 2007;48:3717–25.
- [132] Ibarboure E, Rodriguez-Hernández J. Supramolecular structures from self-assembled poly(γ -benzyl-L-glutamate)-polydimethylsiloxane-poly(γ -benzyl-

- l-glutamate) triblock copolypeptides in thin films. *Eur Polym J* 2010;46:891–9.
- [133] Shen J, Chen C, Fu W, Shi L, Li Z. Conformation-specific self-assembly of thermo-responsive poly(ethylene glycol)-b-polypeptide diblock copolymer. *Langmuir* 2013;29:6271–8.
- [134] Zhang S, Fu W, Li Z. Supramolecular hydrogels assembled from nonionic poly(ethylene glycol)-b-polypeptide diblocks containing OEGylated poly-l-glutamate. *Polym Chem* 2014;5:3346–51.
- [135] Shi SY, He YG, Chen WW, Liu N, Zhu YY, Ding YS, et al. Polypeptide-b-poly(Phenyl isocyanide) hybrid rod-rod copolymers: one-pot synthesis, self-assembly, and cell imaging. *Macromol Rapid Commun* 2015;36:1511–20.
- [136] Zou J, Zhang F, Chen Y, Raymond JE, Zhang S, Fan J, et al. Responsive organogels formed by supramolecular self-assembly of PEG-block-allyl-functionalized racemic polypeptides into β -sheet-driven polymeric ribbons. *Soft Matter* 2013;9:5951–8.
- [137] Johnson JC, Wanasekara ND, Korley IJ. Influence of secondary structure and hydrogen-bonding arrangement on the mechanical properties of peptidic-polyurea hybrids. *J Mater Chem B* 2014;2:2554–61.
- [138] Matolyak L, Keum J, Korley IJ. Molecular design: network architecture and its impact on the organization and mechanics of peptide-polyurea hybrids. *Biomacromolecules* 2016;17:3931–9.
- [139] Wibowo SH, Sulistio A, Wong EHH, Blencowe A, Qiao GG. Polypeptide films via N-carboxyanhydride ring-opening polymerization (NCA-ROP): past, present and future. *Chem Commun* 2014;50:4971–88.
- [140] Whitesell JK, Chang HK. Directionally aligned helical peptides on surfaces. *Science* 1993;261:73–6.
- [141] Akbulut H, Yavuz M, Guler E, Demirkol DO, Endo T, Yamada S, et al. Electrochemical deposition of polypeptides: bio-based covering materials for surface design. *Polym Chem* 2014;5:3929–36.
- [142] Bozokalfa G, Akbulut H, Demir B, Guler E, Gumus ZP, Odaci Demirkol D, et al. Polypeptide functional surface for the aptamer immobilization: electrochemical cocaine biosensing. *Anal Chem* 2016;88:4161–7.
- [143] Park MH, Yu Y, Moon HJ, Ko du Y, Kim HS, Lee H, et al. 3D culture of tonsil-derived mesenchymal stem cells in poly(ethylene glycol)-poly(L-alanine-co-L-phenyl alanine) thermogel. *Adv Healthcare Mater* 2014;3:1782–91.
- [144] Yun EJ, Yon B, Joo MK, Jeong B. Cell therapy for skin wound using fibroblast encapsulated poly(ethylene glycol)-poly(L-alanine) thermogel. *Biomacromolecules* 2012;13:1106–11.
- [145] Kim JY, Park MH, Joo MK, Lee SY, Jeong B. End groups adjusting the molecular nano-assembly pattern and thermal gelation of polypeptide block copolymer aqueous solution. *Macromolecules* 2009;42:3147–51.
- [146] Choi BG, Park MH, Cho SH, Joo MK, Oh HJ, Kim EH, et al. Thermal gelling polyalanine-ploxamine-polyalanine aqueous solution for chondrocytes 3D culture: Initial concentration effect. *Soft Matter* 2011;7:456–62.
- [147] Park MH, Choi BG, Jeong B. Complexation-induced biomimetic long range fibrous orientation in a rigid-flexible block copolymer thermogel. *Adv Funct Mater* 2012;22:5118–25.
- [148] Choi BG, Park MH, Cho SH, Joo MK, Oh HJ, Kim EH, et al. *In situ* thermal gelling polypeptide for chondrocytes 3D culture. *Biomaterials* 2010;31:9266–72.
- [149] Chen C, Wu D, Fu W, Li Z. Peptide hydrogels assembled from nonionic alkyl-polypeptide amphiphiles prepared by ring-opening polymerization. *Biomacromolecules* 2013;14:2494–8.
- [150] Chen C, Wu D, Fu W, Li Z. Tunable organogelator from alkyl-polypeptide diblock prepared by ring-opening polymerization. *Aust J Chem* 2014;67:59–65.
- [151] Fan J, Li R, Wang H, He X, Nguyen TP, Letteri RA, et al. Multi-responsive polypeptide hydrogels derived from N-carboxyanhydride terpolymerizations for delivery of nonsteroidal anti-inflammatory drugs. *Org Biomol Chem* 2017;15:5145–54.
- [152] Zhang S, Anderson MA, Ao Y, Khakh BS, Fan J, Deming TJ, et al. Tunable diblock copolypeptide hydrogel depots for local delivery of hydrophobic molecules in healthy and injured central nervous system. *Biomaterials* 2014;35:1989–2000.
- [153] Chen YF, Chen GY, Chang CH, Su YC, Chen YC, Jiang YS, et al. TRAIL encapsulated to polypeptide-crosslinked nanogel exhibits increased anti-inflammatory activities in Klebsiella pneumoniae-induced sepsis treatment. *Mater Sci Eng C* 2019;102:85–95.
- [154] Chen YF, Shiao AL, Chang SJ, Fan NS, Wang CT, Wu CL, et al. One-dimensional poly(L-lysine)-block-poly(L-threonine) assemblies exhibit potent anticancer activity by enhancing membranolytic. *Acta Biomater* 2017;55:283–95.
- [155] MacPhee CE, Woolfson DN. Engineered and designed peptide-based fibrous biomaterials. *Curr Opin Solid State Mater Sci* 2004;8:141–9.
- [156] Engler AJ, Sen S, Sweeney HL, Discher DE. Matrix elasticity directs stem cell lineage specification. *Cell* 2006;126:677–89.
- [157] Hiew VV, Simat SFB, Teoh PL. The advancement of biomaterials in regulating stem cell fate. *Stem Cell Rev Rep* 2018;14:43–57.
- [158] Liu M, Zeng X, Ma C, Yi H, Ali Z, Mou X, et al. Injectable hydrogels for cartilage and bone tissue engineering. *Bone Res* 2017;5:17014.
- [159] Kang EY, Yeon B, Moon HJ, Jeong B. PEG-I-PAF and PEG-d-PAF: comparative study on thermogelation and biodegradation. *Macromolecules* 2012;45:2007–13.
- [160] Shinde UP, Joo MK, Moon HJ, Jeong B. Sol-gel transition of PEG-PAF aqueous solution and its application for hGH sustained release. *J Mater Chem* 2012;22:6072–9.
- [161] Chow G, Knudson CB, Homandberg G, Knudson W. Increased expression of CD44 in bovine articular chondrocytes by catabolic cellular mediators. *J Biol Chem* 1995;270:27734–41.
- [162] Yeon B, Park MH, Moon HJ, Kim SJ, Cheon YW, Jeong B. 3D Culture of adipose-tissue-derived stem cells mainly leads to chondrogenesis in poly(ethylene glycol)-poly(L-alanine) diblock copolymer thermogel. *Biomacromolecules* 2013;14:3256–66.
- [163] Joo MK, Ko DY, Jeong SJ, Park MH, Shinde UP, Jeong B. Incorporation of d-alanine into poly(ethylene glycol) and l-poly(alanine-co-phenylalanine) block copolymers affects their nanoassemblies and enzymatic degradation. *Soft Matter* 2013;9:8014–22.
- [164] Tang H, Zhang D. Solid state self-assembly of the single-walled carbon nanotubes and poly(γ -benzyl-L-glutamate)s with different conformations. *J Polym Sci Part A Polym Chem* 2013;51:4489–97.
- [165] He X, Fan J, Zou J, Wooley KL. Reversible photo-patterning of soft conductive materials via spatially-defined supramolecular assembly. *Chem Commun* 2016;52:8455–8.
- [166] Katakai R, Oya M, Iwakura Y. Synthesis and conformational study of sequential polypeptides, (l-Ala-l-Val-Gly) n and (l-Val-l-Ala-Gly) n. *Biopolym Orig Res Biomol* 1975;14:1315–26.
- [167] Kim KY, Komoto T, Katakai R, Oya M, Kawai T. Growth mechanism of crystals of glycine-L-alanine copolymer in the course of polymerization. *Die Makromol Chem* 1975;176:373–89.
- [168] Hachisu M, Ohkawa K, Yamamoto H. Preparation of silk-like fibers designed by self-assembled ionic polypeptides. *Macromol Biosci* 2003;3:92–9.
- [169] Dong CM, Sun XL, Faucher KM, Apkarian RP, Chaikof EL. Synthesis and characterization of glycopolymer-polypeptide triblock copolymers. *Biomacromolecules* 2004;5:224–31.
- [170] Huang H, Hu J, Zhu Y. Shape-memory biopolymers based on β -sheet structures of polyalanine segments inspired by spider silks. *Macromol Biosci* 2013;13:161–6.
- [171] Studenovská H, Vodička P, Proks V, Hlučilová J, Motlík J, Rypáček F. Synthetic poly(amino acid) hydrogels with incorporated cell-adhesion peptides for tissue engineering. *J Tissue Eng Regen Med* 2010;4:454–63.
- [172] Choi YY, Jang JH, Park MH, Choi BG, Chi B, Jeong B. Block length affects secondary structure, nanoassembly and thermosensitivity of poly(ethylene glycol)-poly(L-alanine) block copolymers. *J Mater Chem* 2010;20:3416–21.
- [173] Moon HJ, Choi BG, Park MH, Joo MK, Jeong B. Enzymatically degradable thermogelling poly(alanine-co-leucine)-ploxamer-poly(alanine-co-leucine). *Biomacromolecules* 2011;12:1234–42.
- [174] Park SH, Choi BG, Moon HJ, Cho SH, Jeong B. Block sequence affects thermosensitivity and nano-assembly: PEG-I-PA-d-PA and PEG-d-PA-I-PA block copolymers. *Soft Matter* 2011;7:6515–21.
- [175] Sedláček T, Studenovská H, Rypáček F. Enzymatic degradation of the hydrogels based on synthetic poly(α -amino acids). *J Mater Sci: Mater Med* 2011;22:781.
- [176] Habraken GJM, Wilsens K, Koning CE, Heise A. Optimization of N-carboxyanhydride (NCA) polymerization by variation of reaction temperature and pressure. *Polym Chem* 2011;2:1322–30.
- [177] Jan JS, Chen PS, Hsieh PL, Chen BY. Silicification of genipin-cross-linked polypeptide hydrogels toward biohybrid materials and mesoporous oxides. *ACS Appl Mater Interfaces* 2012;4:6865–74.
- [178] Kang EY, Moon HJ, Joo MK, Jeong B. Thermogelling chitosan-g-(PAF-PEG) aqueous solution as an injectable scaffold. *Biomacromolecules* 2012;13:1750–7.
- [179] Song A, Rane AA, Christman KL. Antibacterial and cell-adhesive polypeptide and poly(ethylene glycol) hydrogel as a potential scaffold for wound healing. *Acta Biomater* 2012;8:41–50.
- [180] Ling J, Peng H, Shen Z. Deprotonation reaction of α -amino acid N-carboxyanhydride at 4-CH position by yttrium tris[bis(trimethylsilyl)amide]. *J Polym Sci Part A Polym Chem* 2012;50:3743–9.
- [181] Peng H, Ling J, Zhu Y, You L, Shen Z. Polymerization of α -amino acid N-carboxyanhydrides catalyzed by rare earth tris(borohydride) complexes: Mechanism and hydroxy-encapped polypeptides. *J Polym Sci Part A Polym Chem* 2012;50:3016–29.
- [182] Cao H, Yao J, Shao Z. Synthesis of poly(γ -benzyl-L-glutamate) with well-defined terminal structures and its block polypeptides with alanine, leucine and phenylalanine. *Polym Int* 2012;61:774–9.
- [183] Chiang PR, Lin TY, Tsai HC, Chen HL, Liu SY, Chen FR, et al. Thermosensitive hydrogel from oligopeptide-containing amphiphilic block copolymer: effect of peptide functional group on self-assembly and gelation behavior. *Langmuir* 2013;29:15981–91.
- [184] Hamley IW, Dehsorkhi A, Castelletto V, Seitsonen J, Ruokolainen J, Iatrou H. Self-assembly of a model amphiphilic oligopeptide incorporating an arginine headgroup. *Soft Matter* 2013;9:4794–801.
- [185] Joo JH, Ko DY, Moon HJ, Shinde UP, Park MH, Jeong B. Ion and temperature sensitive polypeptide block copolymer. *Biomacromolecules* 2014;15:3664–70.
- [186] Kye EJ, Kim SJ, Park MH, Moon HJ, Ryu KH, Jeong B. Differentiation of tonsil-tissue-derived mesenchymal stem cells controlled by surface-functionalized microspheres in PEG-polypeptide thermogels. *Biomacromolecules* 2014;15:2180–7.
- [187] Fagerland J, Finne-Wistrand A, Numata K. Short one-pot chemo-enzymatic synthesis of l-lysine and l-alanine diblock co-oligopeptides. *Biomacromolecules* 2014;15:735–43.
- [188] Guo Z, Tian H, Lin L, Chen J, He C, Tang Z, et al. Hydrophobic polyalanine modified hyperbranched polyethylenimine as high efficient pDNA and siRNA carrier. *Macromol Biosci* 2014;14:1406–14.

- [189] Peng H, Chen WL, Kong J, Shen ZQ, Ling J. Synthesis of α -hydroxy- ω -aminotelechelic polypeptide from α -amino acid N-carboxyanhydrides catalyzed by alkali-metal borohydrides. *Chin J Polym Sci* 2014;32:743–50.
- [190] Kim SJ, Park MH, Moon HJ, Park JH, Ko DY, Jeong B. Polypeptide thermogels as a three dimensional culture scaffold for hepatogenic differentiation of human tonsil-derived mesenchymal stem cells. *ACS Appl Mater Interfaces* 2014;6:17034–43.
- [191] Lai J, Fu W, Zhu L, Guo R, Liang D, Li Z, et al. Fibril aggregates formed by a glatiramer-mimicking random copolymer of amino acids. *Langmuir* 2014;30:7221–6.
- [192] Hamley IW, Kirkham S, Dehsorkhi A, Castelletto V, Adamcik J, Mezzenga R, et al. Self-assembly of a model peptide incorporating a hexa-histidine sequence attached to an oligo-alanine sequence, and binding to gold NTA/nickel nanoparticles. *Biomacromolecules* 2014;15:3412–20.
- [193] Shinde UP, Moon HJ, Ko DY, Jung BK, Jeong B. Control of rHG release profile from PEG-PAF thermogel. *Biomacromolecules* 2015;16:1461–9.
- [194] Yu L, Fu W, Li Z. Tuning the phase transition temperature of thermal-responsive OEGylated poly-L-glutamate via random copolymerization with L-alanine. *Soft Matter* 2015;11:545–50.
- [195] Popescu MT, Lontos G, Avgeropoulos A, Tsitsilianis C. Stimuli responsive fibrous hydrogels from hierarchical self-assembly of a triblock copolypeptide. *Soft Matter* 2015;11:331–42.
- [196] Ageitos JM, Yazawa K, Tateishi A, Tsuchiya K, Numata K. The benzyl ester group of amino acid monomers enhances substrate affinity and broadens the substrate specificity of the enzyme catalyst in chemoenzymatic copolymerization. *Biomacromolecules* 2016;17:314–23.
- [197] Popescu MT, Lontos G, Avgeropoulos A, Voulgari E, Avgoustakis K. Hydrogel TCI. Amplifying the pH sensitivity of a triblock copolypeptide by conjugating the N-termini via dynamic covalent bonding. *ACS Appl Mater Interfaces* 2016;8:17539–48.
- [198] Peng S, Lin JY, Cheng MH, Wu CW, Chu IM. A cell-compatible PEO-PPO-PEO (Pluronic®)-based hydrogel stabilized through secondary structures. *Mater Sci Eng C* 2016;69:421–8.
- [199] Wei L, Chen J, Zhao S, Ding J, Chen X. Thermo-sensitive polypeptide hydrogel for locally sequential delivery of two-pronged antitumor drugs. *Acta Biomater* 2017;58:44–53.
- [200] Skoulas D, Stavroulaki D, Santorinaios K, Iatrou H. Synthesis of hybrid-polypeptides m-PEO-b-poly (His-co-Gly) and m-PEO-b-poly (His-co-Ala) and study of their structure and aggregation. Influence of hydrophobic copolypeptides on the properties of poly (L-histidine). *Polymers* 2017;9:564.
- [201] Zhang Y, Song H, Zhang H, Huang P, Liu J, Chu L, et al. Fine tuning the assembly and gel behaviors of PEG ylated polypeptide conjugates by the copolymerization of L-alanine and γ -benzyl-L-glutamate N-carboxyanhydrides. *J Polym Sci Part A Polym Chem* 2017;55:1512–23.
- [202] Lin HC, Chen CY, Kao CW, Wu ST, Chen CL, Shen CR, et al. *In situ* gelling-polypeptide hydrogel systems for the subcutaneous transplantation of MIN6 cells. *J Polym Res* 2020;27:64.
- [203] Peng S, Wu CW, Lin JY, Yang CY, Cheng MH, Chu IM. Promoting chondrocyte cell clustering through tuning of a poly(ethylene glycol)-poly(peptide) thermosensitive hydrogel with distinctive microarchitecture. *Mater Sci Eng C: Mater Biol Appl* 2017;76:181–9.
- [204] Tinajero-Díaz E, Martínez de Iarduya A, Muñoz-Guerra S. Block and graft copolymers made of 16-membered macrolactones and L-Alanine: a comparative study. *Macromol Chem Phys* 2019;220:1900214.
- [205] Lin HC, Anggeli MR, Cheng CC, Ku KL, Cheng HY, Wen CJ, et al. A mixed thermosensitive hydrogel system for sustained delivery of tacrolimus for immunosuppressive therapy. *Pharmaceutics* 2019;11:413.
- [206] Tsuchiya K, Numata K. Facile terminal functionalization of peptides by protease-catalyzed chemoenzymatic polymerization toward synthesis of polymeric architectures consisting of peptides. *Polym Chem* 2020;11:560–7.
- [207] Devarayan K, Nakagami S, Suzuki S, Yuki I, Ohkawa K. Electrospinning and post-spun chain conformations of synthetic, hydrophobic poly (α -amino acid)s. *Polymers* 2020;12:327.
- [208] Ageitos JM, Baker PJ, Sugahara M, Numata K. Proteinase K-catalyzed synthesis of linear and star oligo(L-phenylalanine) conjugates. *Biomacromolecules* 2013;14:3635.
- [209] Chen KJ, Chen HL, Tang CC, Wu HH, Jan JS. Synthesis of silica/polypeptide hybrid nanomaterials and mesoporous silica by molecular replication of sheet-like polypeptide complexes through biomimetic mineralization. *J Colloid Interface Sci* 2019;542:243–52.
- [210] Centore R, Totsingan F, Amason AC, Lyons S, Zha RH, Gross RA. Self-assembly-assisted kinetically controlled papain-catalyzed formation of mPEG-b-Phe(Leu)_x. *Biomacromolecules* 2020;21:493–507.
- [211] Wang J, Lu H, Kamat R, Pingali SV, Urban VS, Cheng J, et al. Supramolecular polymerization from polypeptide-grafted comb polymers. *J Am Chem Soc* 2011;133:12906–9.
- [212] Perry SL, Leon L, Hoffmann KQ, Kade MJ, Priftis D, Black KA, et al. Chirality-selected phase behaviour in ionic polypeptide complexes. *Nat Commun* 2015;6:6052.
- [213] Matolyak LE, Thompson CB, Li B, Keum JK, Cowen JE, Tomazin RS, et al. Secondary-structure-mediated hierarchy and mechanics in polyurea-peptide hybrids. *Biomacromolecules* 2018;19:3445–55.
- [214] Naik SS, Savin DA. Poly(Z-lysine)-based organogels: effect of interfacial frustration on gel strength. *Macromolecules* 2009;42:7114–21.
- [215] You Y, Chen Y, Hua C, Dong CM. Synthesis and thermoreversible gelation of dendron-like polypeptide/linear poly(ϵ -caprolactone)/dendron-like polypeptide triblock copolymers. *J Polym Sci Part A Polym Chem* 2010;48:709–18.
- [216] Fan J, Zou J, He X, Zhang F, Zhang S, Raymond JE, et al. Tunable mechano-responsive organogels by ring-opening copolymerizations of N-carboxyanhydrides. *Chem Sci* 2014;5:141–50.
- [217] He X, Fan J, Zhang F, Li R, Pollack KA, Raymond JE, et al. Multi-responsive hydrogels derived from the self-assembly of tethered allyl-functionalized racemic oligopeptides. *J Mater Chem B* 2014;2:8123–30.
- [218] Zou J, He X, Fan J, Raymond JE, Wooley KL. Supramolecularly knitted tethered oligopeptide/single-walled carbon nanotube organogels. *Chem A Eur J* 2014;20:8842–7.
- [219] Shen Y, Zhang S, Wan Y, Fu W, Li Z. Hydrogels assembled from star-shaped polypeptides with a dendrimer as the core. *Soft Matter* 2015;11:2945–51.
- [220] Wan Y, Wang Z, Sun J, Li Z. Extremely stable supramolecular hydrogels assembled from nonionic peptide amphiphiles. *Langmuir* 2016;32:7512–18.
- [221] Wan Y, Liu L, Yuan S, Sun J, Li Z. pH-Responsive peptide supramolecular hydrogels with antibacterial activity. *Langmuir* 2017;33:3234–40.
- [222] Liu R, Shi Z, Sun J, Li Z. Enzyme responsive supramolecular hydrogels assembled from nonionic peptide amphiphiles. *Sci China Chem* 2018;61:1314–19.

Part IV - Chapter 2 - Crosslinked polypeptide films via RAFT mediated continuous assembly of polymers

Part IV – Chapter 2.1 - Chapter perspective and contribution

In this chapter, a novel polymerization method to produce crosslinked polypeptide films is presented, namely, RAFT-mediated continuous assembly of polymers (CAP-RAFT). These crosslinked polypeptide films comprised a unique secondary structure, particularly an unusually high proportion of random coils. Furthermore, we were able to degrade the crosslinked polymer films with two different enzymes, which proves the high potential of this method to produce surface-confined polypeptide crosslinked films with precise thickness and secondary structure. Nicholas Chan performed the synthesis and NMR analysis of the monomers, the RAFT agents and the crosslinked polypeptide films via RAFT mediated continuous assembly of polymers. The design of the experiments was performed by Nicholas Chan and myself. Nicholas Chan performed the AFM measurements of the polypeptide films. I performed the correlative AFM measurements and the ATR-FTIR, and the resulting secondary structure analysis. I performed the enzymatic degradation. The writing of the original draft and the visualization of the results was done by Nicholas Chan. Thomas Scheibel, Paul Gurr, Shereen Tan and Greg Qiao supervised the studies and edited the paper. I translated the whole manuscript into German for the German version of *Angewandte Chemie* (<https://doi.org/10.1002/ange.202112842>). All authors revised and approved the final version of the manuscript.

This chapter is a research article published in *Angewandte Chemie* which was available online 03.12.2021. The permission of reprint was granted by John Wiley and Sons with the license number: 5236130919983.

Part IV – Chapter 1.2 Full Paper



Polypeptide Films

How to cite: *Angew. Chem. Int. Ed.* **2022**, *61*, e202112842

International Edition: doi.org/10.1002/anie.202112842

German Edition: doi.org/10.1002/ange.202112842

Crosslinked Polypeptide Films via RAFT-Mediated Continuous Assembly of Polymers

Nicholas J. Chan, Sarah Lentz, Paul A. Gurr, Shereen Tan, Thomas Scheibel,* and Greg G. Qiao*

Abstract: Polypeptide coatings are a cornerstone in the field of surface modification due to their widespread biological potential. As their properties are dictated by their structural features, subsequent control thereof using unique fabrication strategies is important. Herein, we report a facile method of precisely creating densely crosslinked polypeptide films with unusually high random coil content through continuous assembly polymerization via reversible addition–fragmentation chain transfer (CAP-RAFT). CAP-RAFT was fundamentally investigated using methacrylated poly-L-lysine (PLLMA) and methacrylated poly-L-glutamic acid (PLGMA). Careful technique refinement resulted in films up to 36.1 ± 1.1 nm thick which could be increased to 94.9 ± 8.2 nm after using this strategy multiple times. PLLMA and PLGMA films were found to have 30–50% random coil conformations. Degradation by enzymes present during wound healing reveals potential for applications in drug delivery and tissue engineering.

Introduction

For decades, scientists have been deeply fascinated in surface modification via the introduction of synthetic polypeptides for a wide range of applications including biosensing,^[1] active molecule release^[2] and antibiofouling/antimicrobial applications.^[3] Polypeptides can be designed to bear application specific chemical and physical properties which largely is afforded by their ability to fold into different well-defined conformations known as secondary structures based on their specific amino acid sequence.^[4] Thus, the design and manipulation of secondary structures (e.g.

α -helices, β -sheets, random coils) forms a core directive for material scientists.^[5] While conventional techniques for coatings and film formation are well established, synthetic polypeptides formed through *N*-carboxyanhydride ring-opening polymerization (NCA ROP) offers the opportunity to lean into grafting polymerization techniques for the fabrication of polypeptide films.^[6] Grafting-to and grafting-from strategies both result in linear polymers with a terminal group anchored to the surface.^[7] However, films formed through grafting-to techniques tend to be limited by steric hindrance associated with tethering a large molecule to a surface, while films fabricated through a grafting-from approach are difficult to characterize after more than one monomer is introduced to the system.^[7] Grafting-through strategies aim to mitigate these issues, by using macromonomers with polymerizable end groups, instead of monofunctional monomers resulting in thicker films with well-defined polymer bottlebrushes.^[8,9] With all the advantages that result from using grafting-through methods, our group has developed a unique methodology, which yields unique, robust, crosslinked films, called continuous assembly polymerization (CAP).^[9]

As with grafting-through techniques, CAP utilizes polymers with a polymerizable group, but unlike traditional grafting-through techniques, these polymerizable groups are not restricted to a singular endgroup resulting in a macrocrosslinker.^[10] The result is a dense crosslinked polymeric network forming a robust film on the substrate surface with often a unique morphology, compared to even traditional grafting through methods. The technique itself is robust enough that multiple other macrocrosslinkers have already been utilized using this technique such as polyethylene glycol (PEG)-based,^[11] 2-hydroxyethylacrylate (HEA)-based,^[9a,c] and polythiophene^[12] polymers. Uniquely, this can be combined with macrocrosslinkers which already bear unique morphologies. For example, polyrotaxane-based macrocrosslinkers have been utilized to afford a film with the densely crosslinked nature of CAP films, along with the stimuli sensitivity associated with the “host–guest” chemistry of a cyclodextrin-based polyrotaxane network.^[13] The unique morphology afforded through CAP and the wide variety of macrocrosslinkers amenable to this process has enabled the synthesis of a range of films targeting a variety of different applications.^[10a,11a] Antifogging qualities of a PEG-based film have been shown using this technique after exposure of the film at -20 °C to ambient conditions, and films retained high light transmittance with a relatively low crosslinking density.^[11b] However, despite the aforementioned

[*] N. J. Chan, S. Lentz, P. A. Gurr, S. Tan, G. G. Qiao
 Polymer Science Group, Department of Chemical Engineering
 University of Melbourne
 Parkville, Melbourne, Victoria 3010 (Australia)
 E-mail: gregghq@unimelb.edu.au

N. J. Chan, S. Lentz, T. Scheibel
 Lehrstuhl Biomaterialien
 Universität Bayreuth
 Prof.-Rüdiger-Bormann-Str. 1, 95447 Bayreuth (Germany)
 E-mail: thomas.scheibel@uni-bayreuth.de

© 2021 The Authors. Angewandte Chemie International Edition published by Wiley-VCH GmbH. This is an open access article under the terms of the Creative Commons Attribution Non-Commercial License, which permits use, distribution and reproduction in any medium, provided the original work is properly cited and is not used for commercial purposes.

tioned versatility of polypeptides, they have yet to be utilized with this technique. In parallel to the established library of crosslinkers is the variety of techniques for CAP, which have since been established including various fabrication conditions.^[9a] Recently a unique patterning method has been developed employing CAP through microcontact printing which involves delivering material via a polymeric stamp.^[14] Alongside these advances, the development of CAP includes different polymerization methods such as ring-opening metathesis polymerization (ROMP)^[12,13] and atom transfer radical polymerization (ATRP).^[11] Fundamentally, the method of polymerization utilized impacts film properties due to the mechanistic differences and as such developing CAP using different polymerization techniques is of profound interest. A blue-light mediated system employed a thiocarbamate as a photoiniferter, but the film thickness's being limited to approximately 5 nm.^[9a] It is this variability in properties that highlights the need for investigating, the as yet unreported, reversible addition-fragmentation chain transfer (RAFT) polymerization as a CAP technique.

RAFT is identified as one of the most robust and versatile reversible-deactivation radical polymerization techniques.^[15] In a RAFT polymerization system, polymerization is controlled by the degenerative chain transfer of the chain transfer agent (CTA) in the form of a thiocarbonylthio compound (known as a RAFT agent) to the polymer chains, leading to the sequential insertion of monomer units to the initial RAFT agent.^[15d,16] As initiation is still free-radical based, there are numerous approaches to RAFT polymerization including initiation through enzymes, thermal initiators or acoustic cavitation of bubbles in the system via ultrasound. However, for a surface-initiated polymerization, light-based RAFT techniques provide a facile method of yielding grafted polymers.^[7c,17] Using our already developed techniques in both RAFT polymerization^[18] and NCA ROP,^[19] we aim to further develop the potential of CAP-RAFT while fabricating polypeptide-based films with secondary structure morphologies based on a fabrication technique rather than solely on polypeptide structure.

Herein, we expand on this film formation strategy, to perform blue light-mediated CAP-RAFT using synthetic polypeptide based macrocrosslinkers. This is the first instance of fabricating a chemically crosslinked NCA ROP/ based polypeptide film with precision control of thickness in one-step, controlled multilayer structures with designed composition and specifically formed peptide secondary structure resulting from the fabrication technique itself rather than solely on the polypeptide structure. Photoinitiator lithium phenyl-2,4,6-trimethylbenzoylphosphinate (LAP) was used in conjunction with two different model RAFT agents. A dithiobenzoate and a trithiocarbonate with differing kinetics were chosen to investigate their influence on the ability to form thick uniform films. Furthermore, we investigated the importance of RAFT agent in solution, which historically has been required to develop films of uniform thickness and its effects on both kinetics and uniformity. In furthering this work, we also explored the ability to produce stratified, multi-layered cross-linked films

by coupling RAFT agent to the initiating surface to re-initiate the CAP-RAFT process at the growing polymer surface. As a demonstration of versatility, a second polypeptide based macrocrosslinker was introduced into the system. In both cases, an unusually high random coil conformation was produced which, combined with the evident enzymatic degradation demonstrated, presents unique opportunities in drug delivery and tissue engineering.

Results and Discussion

Polypeptide macroinitiators were synthesized through NCA ROP, subsequent deprotection and methacrylation (Supporting Information Figure S1, S2). NCA ROP is known to be a facile method for creating long chain, non-sequence specific polypeptides.^[4b,20] With a selection of 21 canonical amino acids with varying degrees of hydrophobicity, physical properties and chemical functionality, it makes them a highly versatile polymer class for a wide range of applications.^[20b,21] To synthesize a model polypeptide macroinitiator, the homopolypeptide ϵ -carboxybenzyl-protected poly(L-lysine(Z)) (PZLL) was synthesized using hexylamine as the initiator. The use of PLL as the base polypeptide is rooted in its pendant amines which are ideal for material functionalization. The polypeptide was then treated with hydrobromic acid (HBr), removing the carboxybenzyl protecting group and revealing pendant primary amines of poly(L-lysine) (PLL) which would be amenable to methacrylation. This methacrylation was performed by first deprotonating the polypeptide in a 10 wt% aqueous solution by raising the pH to 10–11 and then addition of methacrylic anhydride, resulting in a methacrylation of 15% (Supporting Information Table S1). It should be noted that increasing macrocrosslinker functionalization will generally yield increased film thickness when utilizing CAP as demonstrated in a previous study.^[10c] However, 10% of repeat units with double bonds is generally sufficient for CAP process. While this results in poly(L-lysine-g-methacrylate) (PLLMA) as intended, a fortuitous side-effect is that the polypeptide remains deprotonated allowing for CAP to be performed in organic solvents (Figure 1).

To prepare the surfaces for CAP, RAFT agent was immobilized onto aminated silica surfaces. Silica surfaces were aminated with 3-aminopropargyl triethoxysilane (APTES) using previously established methods.^[22] The subsequent amine groups were susceptible to carbodiimide coupling with carboxylic acid-terminated RAFT agents (Supporting Scheme S3). To establish the validity of this method, 4-cyano-4-(phenylcarbonothioylthio)pentanoic acid (CPADB) was anchored as a model dithiobenzoate RAFT agent, allowing CAP-RAFT to be performed using PLLMA macrocrosslinker. CPADB has been used previously as a model dithiobenzoate RAFT agent for the study of methacrylamine monomers in solution,^[23] and thus was deemed an appropriate model RAFT agent in this instance.

CAP-RAFT was performed by soaking the treated surfaces in a DMSO solution of PLLMA macrocrosslinker and LAP photoinitiator and irradiated under blue light

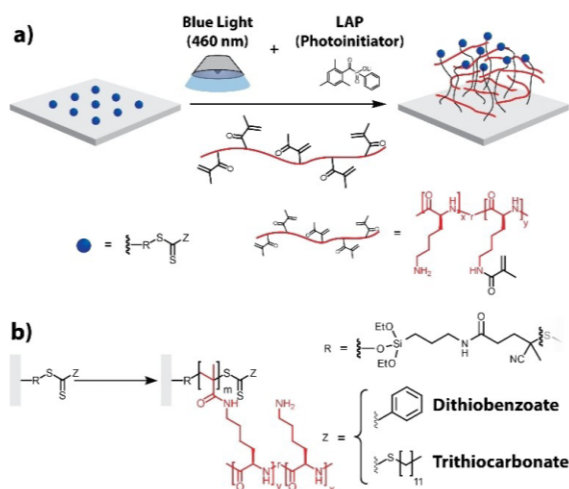


Figure 1. Schematic for CAP-RAFT using a polypeptide macroinitiator onto a surface functionalized with RAFT agent. a) Graphical schematic of CAP-RAFT of PLLMA macrocrosslinker through the use of blue light (4 mW cm^{-2} , $\lambda_{\text{max}} = 460 \text{ nm}$). b) Chemical schematic representing the use of model dithiobenzoate and trithiocarbonate RAFT agents.

(4 mW cm^{-2} , $\lambda_{\text{max}} \approx 460 \text{ nm}$). To confirm that film formation is due to CAP rather than solely adhesion of the macroinitiator to the surface, control experiments were performed with specific elements absent from the system (Supporting Information Table S2). All samples showed very small amount (1.31–5.60 nm) of film formation due to adhesion of deposited polypeptide. As would be expected, surfaces without surface initiator resulted in films of similar thicknesses, indicating a lack of surface confined polymerization (Figure 1). Furthermore, samples kept in the dark (i.e. no blue light exposure) also showed a lack of surface confined polymerization confirming the requirement for blue light for RAFT polymerization. Our group has previously shown that RAFT polymerization can be initiated with blue light without the use of a photoinitiator with a significantly lowered rate of polymerization, compared to other known RAFT mechanisms.^[24] However, only samples with photoinitiator showed any evidence of polymerization, with film thickness of at least 30 nm observed, providing strong evidence of surface confined RAFT polymerization.

Previous papers have shown that surface initiated RAFT polymerization in general requires the use of a RAFT agent in solution to ensure consistent film thickness.^[7c] Recently, Seo et al. demonstrated the use of SI-PET-RAFT without RAFT agent in the solution to yield patternable polymer brushes.^[25] This is in agreement with our results indicating polymerization is confined to the film surface. Thus, to observe the degree of polymerization occurring both with and without RAFT agent in solution, analysis of the aggregate size was performed. DLS revealed an increase in particle size after irradiation under blue light as long as photoinitiator was present in solution (from $0.901 \pm 0.0590 \text{ nm}$ to $2.47 \pm 0.210 \text{ nm}$ with LAP and without func-

tionized surfaces) (Supporting Figure S6 and S7). A decrease in particle size correlating to a decrease in polymerization in the supernatant was observed with the introduction of functionalized surfaces, signifying an increase in control upon their introduction; for reactions without RAFT agent in solution, particles with a diameter of $2.47 \pm 0.210 \text{ nm}$ were observed after reaction without surfaces compared to $2.04 \pm 0.360 \text{ nm}$ with surfaces. With RAFT agent in solution, particles with a diameter of $4.01 \pm 0.513 \text{ nm}$ without surfaces were observed compared to $3.19 \pm 0.41 \text{ nm}$ with surfaces. However, the degree of polymerization in solution was found to be decreased without any free RAFT agent in solution signifying greater surface confinement of the reaction.

To further investigate the necessity of sacrificial RAFT agent when using polymeric macroinitiators, experiments with and without RAFT agent in solution were performed (Figure 2). In the presence of sacrificial RAFT agent, films were found to reach a maximum of $36.1 \pm 1.1 \text{ nm}$ after 16 h (Figure 2ai) with an RMS roughness of 6.1 nm (Figure 2aii). Without RAFT agent in solution, surfaces grew slower (24 h maximum), rougher and thinner ($31.5 \pm 2.4 \text{ nm}$ with an RMS roughness of 9.4 nm), however remained relatively uniform in thickness, despite more regions of varied thickness (Figure 2b). In both cases, surfaces were found to have relatively high RMS roughness with respect to the film thickness. Furthermore, the overall homogeneity of the surface was found to be decreased without RAFT agent in solution. Though both films were relatively homogeneous, large regions with denser films were also observed. This has been observed in previous instances of the use of CAP which is due to the decreased availability of initiator at the film surface as it is covered by macrocrosslinker during film growth, with differences in homogeneity emerging based on the polymerization technique utilized and the macromonomers.^[10] Furthermore, RAFT agents are susceptible to aminolysis by primary amines, potentially causing the degradation.^[26] To determine if this was occurring, analysis of the supernatant after reaction both with and without RAFT agent in solution was performed. Dialysis was performed to remove excess CPADB (RAFT agent) and LAP, with the resulting ^1H NMR revealing splitting patterns consistent with aromatic rings which would only be present due to aminolysis of CPADB (Supporting Figure S8). Although solution experiments have confirmed that aminolysis can occur with PLLMA, direct confirmation on the surface is challenging due to the low concentration of the RAFT end groups. On the other hand, uneven growth of CAP layer can also be due to other reasons such as monomer type, polymerization methods as well as efficiency of re-initiation as observed before in other systems. Furthermore, while there is a relatively significant impact upon the introduction of RAFT agent in solution, it is not a crucial requirement in this system.

To observe if this trend remained consistent with other initiators, 4-cyano-4-[(dodecylsulfanylthiocarbonyl)sulfanyl]pentanoic acid (CDTPA)—a trithiocarbonate-based RAFT agent—was introduced in the same manner as the dithiobenzoate initiator. Trithiocarbonates typically have a high

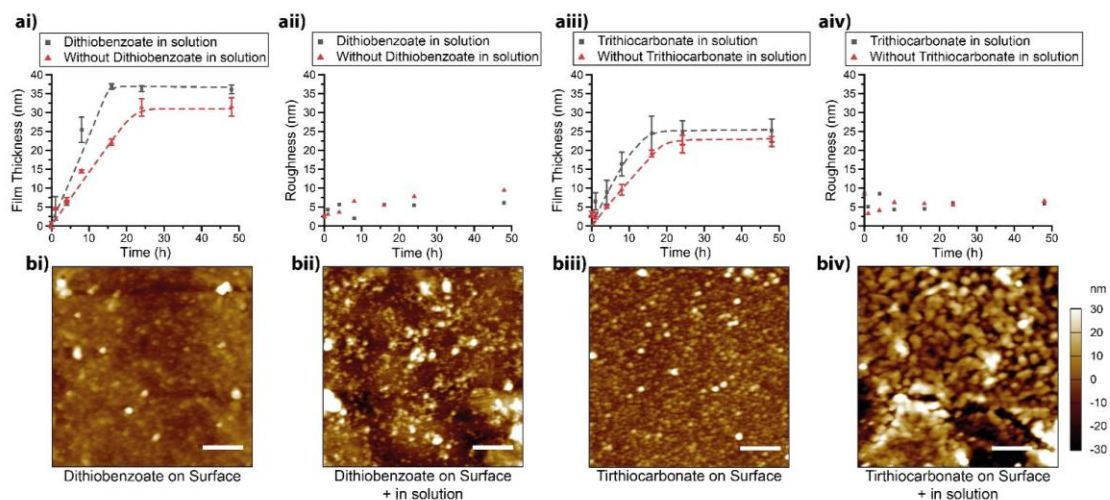


Figure 2. AFM imaging and analysis of CAP-RAFT films using a PLLMA macrocrosslinker utilizing different model RAFT agents. ai, aii) Analysis of film growth utilizing a dithiobenzoate RAFT agent observing kinetics of film growth (ai) and film roughness (a ii) both with and without RAFT agent in solution. aiii, aiv) Analysis of film growth utilizing a trithiocarbonate RAFT agent observing kinetics of film growth (a iii) and film roughness (a iv) both with and without RAFT agent in solution. b) Surface morphology after 48 h of CAP-RAFT utilizing systems imaged using AFM with bi) a dithiobenzoate RAFT agent anchored to the surface as well as in RAFT agent in solution; bii) a dithiobenzoate RAFT agent anchored to the surface but not in the reaction solution; biii) a trithiocarbonate RAFT agent anchored to the surface as well as in RAFT agent in solution; and biv) a trithiocarbonate anchored to the surface but not in the reaction solution (scale bars = 1 μm).

affinity towards methacrylamides^[27] and would provide some insight toward specific variability associated with using CAP (Figure 2). The time to reach maximum film thickness was the same as with the dithiobenzoate initiator, with and without sacrificial RAFT agent (16 h and 24 h respectively), but thicknesses were significantly reduced both with and without RAFT agent (25.3 ± 3.0 and 22.3 ± 1.3 nm respectively) (Figure 2a iii–iv). Furthermore, the morphologies of the films were found to have more significant aggregation (Figure 2b iii–iv). This appears to concur with the general principal that trithiocarbonates are known to be less active than their dithiobenzoate counterparts.^[15d] However, they are less susceptible to aminolysis,^[26c] supporting the hypothesis that the lower overall homogeneity of the dithiobenzoate samples is due to RAFT agent degradation by aminolysis. Nonetheless, as we aim to develop this method by keeping polymerization surface confined, we continued testing without RAFT agent in solution.

One advantage of CAP is the ability to increase the film thickness without concern for maintaining chain-end fidelity through re-initiation. As lysine residues have primary amine side chains, these films are uniquely susceptible to modification using the same carbodiimide chemistry employed for immobilization of the carboxylic acid-functional RAFT agent. From this RAFT agent-functionalized layer, a second layer of CAP could be performed (Figure 3a). This process could theoretically be continuously repeated to yield thicker films based on desired functionality. Using this strategy, we were able to grow films with 94.9 ± 8.24 nm in thickness after 4 layers (Figure 3b). It should be noted that a prominent increase in regions aggregation was also observed as more

and more layers were introduced to the system (Figure 3d). Furthermore, these pendant primary amines are no longer available for carbodiimide coupling after attacking another immobilized RAFT agent. While this did not seem to have a significant effect on the first or second layers, this irregular morphology was much more pronounced in the third and fourth layers. Nonetheless, this demonstrates the potential to develop multilayered systems which can be increased further based on previous works demonstrating similar capabilities.^[10]

With the use of polypeptides in the formation of these films comes the presence of secondary structures typical for proteins and polypeptides with poly-L-lysine being no exception.^[28] ATR-FTIR spectra around the Amide I band ($1600\text{--}1720\text{ cm}^{-1}$) are often used to analyze the secondary structure content of proteins.^[28] By observing this region of the spectra, the bottom three layers were found to share similar structures based on the major peaks (Figure 3c). However, the introduction of the fourth layer appeared to have a drastic effect with the peak at 1649 cm^{-1} splitting into two peaks (1658 and 1642 cm^{-1}) and a drop of the peak at 1696 cm^{-1} both indicating a drop in β -sheet formation.

To further determine the secondary structures present, lineshape analysis was performed according to Chirgadze et al.^[29] for IR analysis of polypeptides. High molecular weight poly-L-lysine is well known to form random coils in solution while charged,^[30] which is changed to a primarily α -helical structure under alkali aqueous conditions (i.e. uncharged primary amines).^[28d] Poly-L-lysine films formed utilizing different methodologies including dip coating quartz in an alkali aqueous media or grafting the polypep-

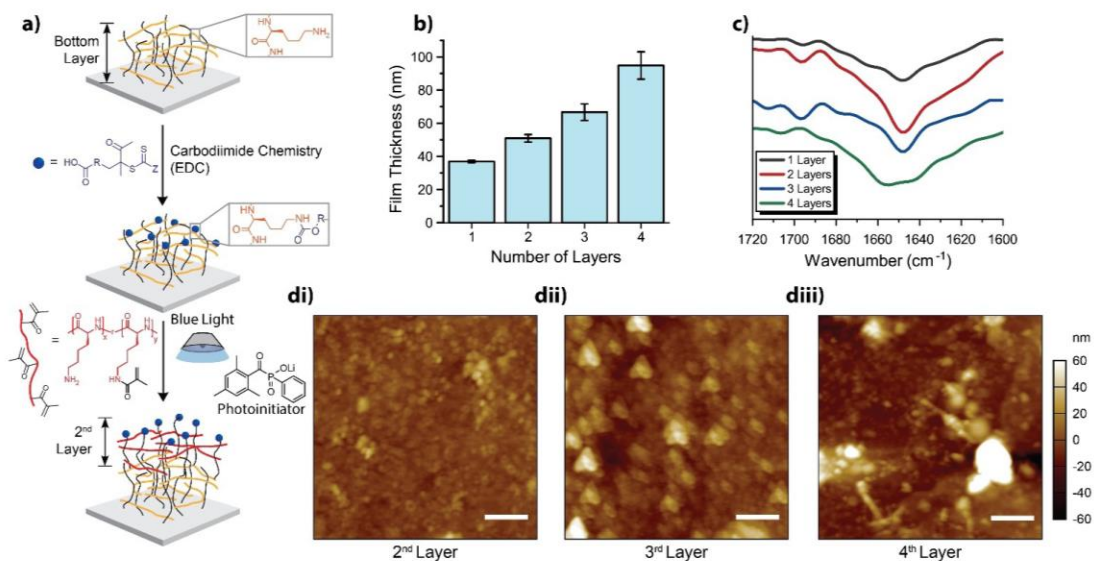


Figure 3. Multiple layers synthesized using CAP-RAFT. a) Schematic for reinitiation and execution of multiple layers of CAP-RAFT. b) Film thickness for multiple layers with PLLMA macrocrosslinker determined using AFM. c) FTIR spectra of the Amide I band of each layer. d) Surface morphology as revealed by AFM imaging of the di) 2nd, dii) 3rd and diii) 4th layers. (scale bars = 1 μm). EDC is 1-ethyl-3-(3-dimethylaminopropyl) carbodiimide.

tide directly to the surface showed this α -helical structure while in their uncharged state.^[31] Subsequently, it might be reasonable to assume that since polylysine favors α -helices,^[32] the films may form the same secondary structure. However, this was not the case when using CAP-RAFT as they instead preferentially formed random coils and β -sheets in the majority of the films (Table 1). While random coil content tended to vary significantly between 30 to 50%, the β -sheet content remained between 32 to 39%. This deviation from the expected α -helical structures is likely due to the unique covalently crosslinked morphology of films formed through CAP, resulting in reduced mobility of the PLLMA chains and thus preventing their usual favored conformation. Interestingly, the four-layer films seem to trend back towards the expected norm with β -sheet and random coil content dropping to 21 and 19% respectively, while α -helical structure rose from around 13–19% to 26%. Furthermore, β -turns were observed in a far more significant quantity at 27%. The issues stated before, pertaining to localized film growth, would also lead to lower crosslinking density. Subsequently, chain mobility would be increased, allowing the PLLMA chains to begin to take on their more favorable conformations. This unusually high random coil conformation grants these films a more amorphous structure which can assist with accessibility to functional groups or motifs desired for further surface modification or the specific binding of molecules making them a prime candidate for drug delivery or tissue engineering where such signaling molecules and molecular payloads are desired.

To further establish the versatility of this technique, poly(L-glutamic acid-r-L-lysine-g-methacrylate) (PLGMA)

was investigated in a similar fashion as PLLMA (Supporting Information Figure S3, Table S3) with similarly modifiable functional group side chains (i.e. carboxylic acids). By performing CAP with PLGMA in aqueous media, a slightly thicker film of 41.2 ± 1.4 nm was observed, possibly attributed to PLGMA's inability to undergo aminolysis (Figure 4a). However, the comparative increase in film thickness was more pronounced when CAP was performed on a reinitiated PLLMA layer with a jump to 76.0 ± 9.4 nm. Since the reaction was performed at pH 7 (deionized water), PLLMA and PLGMA layers exist in both the cationic and anionic forms. This would potentially result in ionic attraction of the layers accounting for the observed increased film thickness.

Despite one sample including a PLLMA layer below the PLGMA layer, both samples with PLGMA share similar FTIR spectra around the Amide I band (Figure 4b). Using the same logic as before, as poly-L-glutamic acid is expected to take predominantly random coil conformations at neutral pH,^[33] the high random coil content of the PLGMA films ($37 \pm 2\%$) is unsurprising, though there are still significant quantities of other secondary structures which might be due to localized confinement afforded by the unique morphology of CAP films. However, analogous to layer-by-layer (LbL) films fabricated from poly-L-glutamic acid and poly-L-lysine^[34] our PLLMA/PLGMA films would be expected to form primarily β -sheet formations, due to polyionic complexation. In contrast, this was not observed and, instead, a similar secondary structure breakdown to the solely PLGMA films (with the exception of β -turns at $23 \pm 14\%$) was elucidated. It can be surmised that after the initial layer

Table 1: Secondary structure elements of multi-layered PLLMA and PLGMA films (determined using ATR-FTIR).

Layer Number	2	3	4 (top)	β -Sheets [%]	α -Helices [%]	Random Coils [%]	β -Turns [%]	Others ^[a] [%]
1 (bottom)								
PLLMA	–	–	–	37 ± 6	19 ± 11	35 ± 11	9 ± 5	N/A
PLLMA	PLLMA	–	–	32 ± 7	13 ± 3	50 ± 5	5 ± 2	N/A
PLLMA	PLLMA	PLLMA	–	39 ± 2	15 ± 3	40 ± 2	6 ± 2	N/A
PLLMA	PLLMA	PLLMA	PLLMA	21 ± 4	26 ± 1	19 ± 2	27 ± 4	6 ± 4
PLGMA	–	–	–	19 ± 1	29 ± 2	37 ± 2	13 ± 2	2 ± 1
PLLMA	PLGMA	–	–	14 ± 4	25 ± 8	37 ± 12	23 ± 14	2 ± 1

[a] In some cases, the amount of “other” secondary structure was negligible and thus denoted as “N/A”.

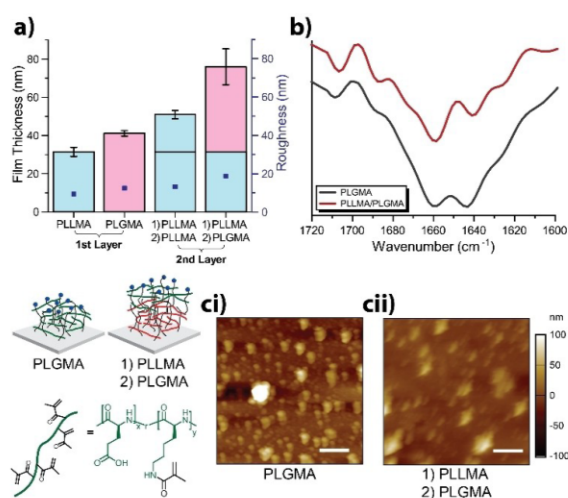


Figure 4. a) Comparative film thickness and roughness upon introduction of PLGlu as the initial layer and the second layer; b) FTIR spectra of top PLGlu layer; c) surface morphology of PLGlu layer as the ci) initial layer and cii) the second layer (scale bars = 1 μ m).

of PLGMA, the subsequently deposited PLGMA layer no longer interacts strongly with the preceding PLLMA layer to form the polyionic complex as before.

Alongside their ability to form secondary structures, polypeptides are favourable in bio applications such as drug delivery and tissue engineering due to their ability to undergo enzymatic degradation.^[35] To evaluate this susceptibility, the PLLMA- and PLGMA-based films were incubated with both α -chymotrypsin and protease type XIV as model proteases. α -chymotrypsin is a digestive enzyme present in the mammalian gut,^[36] while protease type XIV is a protease mixture known to break down β -sheet structures and is often used in wound healing studies since it mimics the cocktail of metalloproteases (MMP's) found in wounds.^[37] In general, proteases are expected to hydrolyse the amide bonds of the polypeptide backbone in multiple locations while leaving the hydrocarbon backbone formed through RAFT polymerization intact (Figure 5a). Thus, while it is expected that residual polymer remains, the majority of the film is degraded. AFM analysis of films at the same site of the PLLMA-based films before and after incubation (Figure 5b and d) revealed significant change

using both enzymes. After the use of α -chymotrypsin, a noticeable increase in roughness was observed with both higher and lower regions of the films expanding relative to each other as a result of degradation in these lower regions in particular (Figure 5b). While this could also be observed in presence of protease type XIV (Figure 5d), a large piece was found missing after incubation indicating successful degradation. Interestingly, treatment of PLGMA films with these enzymes also yielded degradation, but it had little changes in the presence of α -chymotrypsin (Figure 5c), and none in the presence of protease type XIV showing resistance to this protease (Figure 5d). This suggests that degradation against certain enzymes can be controlled through selection of different amino acids though as is typical for proteases, since this control is enzyme specific. Thus, evidence of controllable enzymatic degradation has been demonstrated using both model enzymes, further suggesting potential in biological systems as scaffolds and drug delivery systems.

Conclusion

In summary, the first instance of CAP-RAFT has been established to form crosslinked polypeptide films with unique secondary structure features. Through the use of PLLMA as an initial model macrocrosslinker, investigations were performed with model dithiobenzoate and trithiocarbonate initiators and with and without sacrificial RAFT agent in solution. While the thickest films were obtained using surface confined dithiobenzoate RAFT agent (thickness of 36.1 ± 1.1 nm), films of comparable thickness (31.5 ± 2.4 nm) and uniformity were obtained with sacrificial RAFT agent in solution. As a result, further experiments which ensured greater surface confinement were performed in the absence of RAFT agent in solution. In this way, multi-layered films reaching a thickness of 94.9 ± 8.24 nm were achieved. Secondary structure analysis showed an unusually high proportion of random coil structures (35–50%), despite expected high α -helical formation for PLLMA. This is likely due to the reduced mobility of the surface confined PLLMA, and hence its ability to form the usually favored secondary structure. Similar trends were observed when the PLGMA macrocrosslinker was utilized. As a result, we have established CAP-RAFT as a viable strategy to create surface confined polypeptide crosslinked films with precision thick-

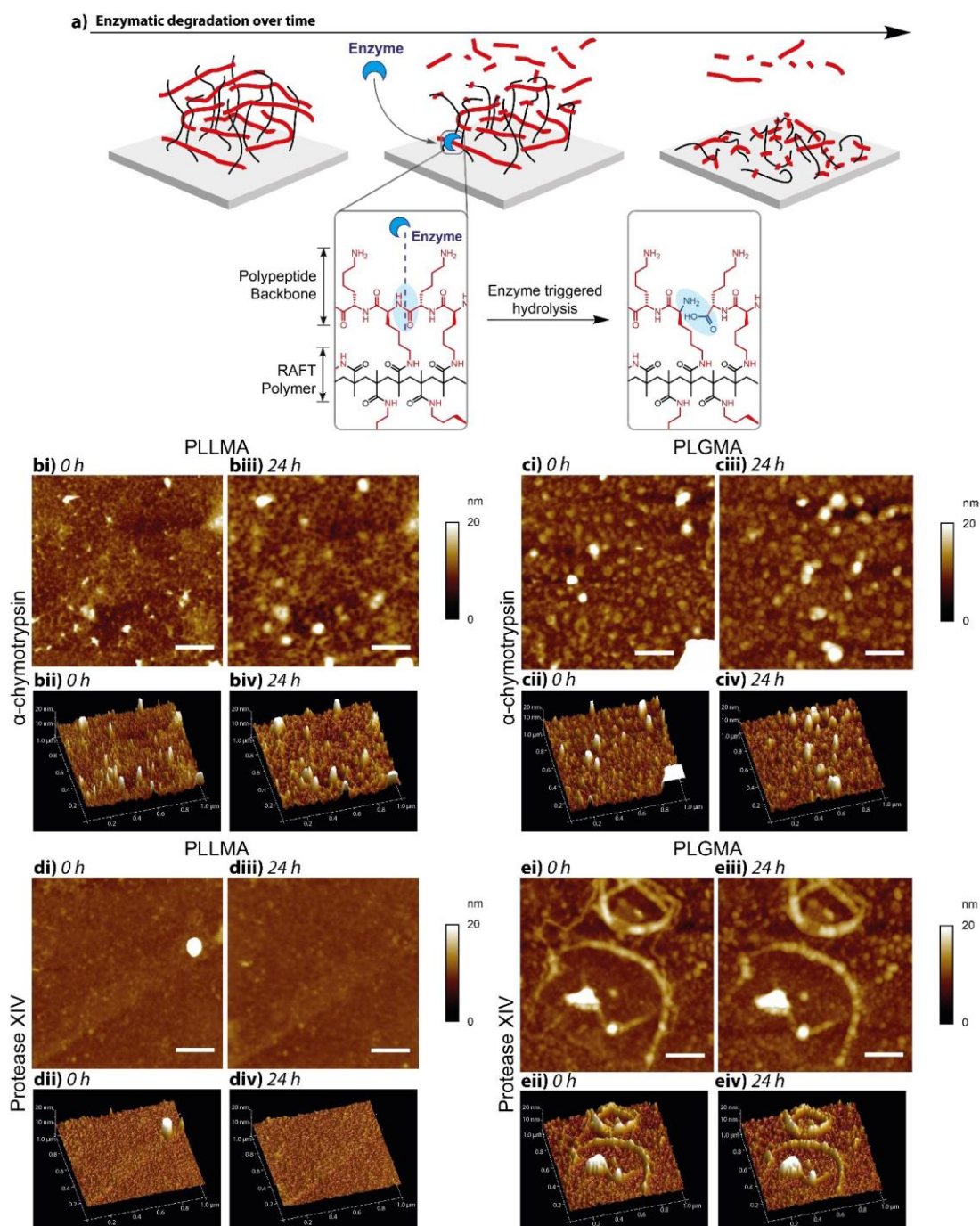


Figure 5. a) Schematic of enzymatic degradation of polypeptide films via hydrolysis of amide bonds in the polypeptide backbone (in red). Notably, the RAFT polymer remains intact (in black). b–e) AFM images of films treated with enzyme. b) PLLMA-based films before (bi, bii) and after incubation (biii, biv) with 1 mg mL^{-1} α -chymotrypsin at 25°C . c) PLGMA-based films before (ci, cii) and after incubation (ciii, civ) with 1 mg mL^{-1} α -chymotrypsin at 25°C . d) PLLMA-based films before (dii, dii) and after incubation (diii, div) with 1 mg mL^{-1} Protease XIV at 37°C . e) PLGMA-based films before (ei, eii) and after incubation (eiii, eiv) with 1 mg mL^{-1} Protease XIV at 37°C . For b–e): 2D (i, iii) and 3D (ii, iv) image maps were utilized. Protease solutions used were 1 mg mL^{-1} α -chymotrypsin at 25°C (b, c) and 1 mg mL^{-1} Protease XIV at 37°C (d, e) (scale bars = 200 nm).

ness control and unique properties such as specific secondary structure formations and degradation. This secondary structure control combined with enzymatic degradation shows high potential for numerous biological applications including drug delivery and tissue engineering which will be subject to further investigation in future studies.

Acknowledgements

This work was performed in part at the Materials Characterization and Fabrication Platform (MCFP) at the University of Melbourne. We further thank Prof. Laforsch for access to the Harrick VariGATR. S.L. thanks Markus Hund for technical assistance with AFM measurements. N.J.C. thanks The University of Melbourne for providing Australian Government Research Training Program Scholarship (AGRTP) for providing funds for travel. This work is supported by grants DFG SCHE603/ 23-1. N.J.C., S.L., G.G.Q. and T.S. acknowledge funding from the German Academic Exchange Service (DAAD) through its thematic network Bayreuth-Melbourne Colloid/Polymer Network sponsored from funds of the Federal Ministry of Education and Research (BMBF). Open Access funding enabled and organized by Projekt DEAL.

Conflict of Interest

The authors declare no conflict of interest.

Keywords: CAP-RAFT • Crosslinked • Polypeptide • Surface-initiated polymerization • Secondary structure

- [1] a) G. Bozokalfa, H. Akbulut, B. Demir, E. Guler, Z. P. Gumus, D. Odaci Demirkol, E. Aldemir, S. Yamada, T. Endo, H. Coskunol, S. Timur, Y. Yagci, *Anal. Chem.* **2016**, *88*, 4161–4167; b) B. Demir, T. Yilmaz, E. Guler, Z. P. Gumus, H. Akbulut, E. Aldemir, H. Coskunol, D. G. Colak, I. Cianga, S. Yamada, S. Timur, T. Endo, Y. Yagci, *Talanta* **2016**, *161*, 789–796; c) T. Yilmaz Sengel, E. Guler, Z. P. Gumus, E. Aldemir, H. Coskunol, H. Akbulut, D. Goen Colak, I. Cianga, S. Yamada, S. Timur, T. Endo, Y. Yagci, *Sens. Actuators B* **2017**, *246*, 310–318.
- [2] a) K. Park, H. Jeong, J. Tanum, J.-C. Yoo, J. Hong, *J. Ind. Eng. Chem.* **2019**, *69*, 263–268; b) B. Jiang, B. Li, *Int. J. Nanomed.* **2009**, *4*, 37–53; c) B. Jiang, E. DeFusco, B. Li, *Biomacromolecules* **2010**, *11*, 3630–3637.
- [3] a) Q. Gao, M. Yu, Y. Su, M. Xie, X. Zhao, P. Li, P. X. Ma, *Acta Biomater.* **2017**, *51*, 112–124; b) G. P. Sakala, M. Reches, *Adv. Mater. Interfaces* **2018**, *5*, 1800073; c) J. S. Rudra, K. Dave, D. T. Haynie, *J. Biomater. Sci. Polym. Ed.* **2006**, *17*, 1301–1315; d) Q. Yang, L. Wang, W. Lin, G. Ma, J. Yuan, S. Chen, *J. Mater. Chem. B* **2014**, *2*, 577–584.
- [4] a) T. J. Deming, *J. Polym. Sci. Part A* **2000**, *38*, 3011–3018; b) T. J. Deming, *Nature* **1997**, *390*, 386–389; c) C. Nacar, *Protein J.* **2020**, *39*, 21–32; d) K. Fujiwara, H. Toda, M. Ikeguchi, *BMC Struct. Biol.* **2012**, *12*, 18.
- [5] a) N. J.-A. Chan, D. Gu, S. Tan, Q. Fu, T. G. Pattison, A. J. O'Connor, G. G. Qiao, *Nat. Commun.* **2020**, *11*, 1630; b) D. T. Haynie, L. Zhang, J. S. Rudra, W. Zhao, Y. Zhong, N. Palath, *Biomacromolecules* **2005**, *6*, 2895–2913; c) S. H. Wibowo, A. Sulistio, E. H. H. Wong, A. Blencowe, G. G. Qiao, *Chem. Commun.* **2014**, *50*, 4971–4988; d) T. Borase, A. Heise, *Adv. Mater.* **2016**, *28*, 5725–5731.
- [6] a) C. Zhang, J. Yuan, J. Lu, Y. Hou, W. Xiong, H. Lu, *Biomaterials* **2018**, *178*, 728–737; b) A. Heise, H. Menzel, H. Yim, M. D. Foster, R. H. Wieringa, A. J. Schouten, V. Erb, M. Stamm, *Langmuir* **1997**, *13*, 723–728; c) Y.-C. Chang, C. W. Frank, *Langmuir* **1996**, *12*, 5824–5829; d) F. Audouin, M. Fox, R. Larragy, P. Clarke, J. Huang, B. O'Connor, A. Heise, *Macromolecules* **2012**, *45*, 6127–6135.
- [7] a) K. Kato, E. Uchida, E.-T. Kang, Y. Uyama, Y. Ikada, *Prog. Polym. Sci.* **2003**, *28*, 209–259; b) Y. Uyama, K. Kato, Y. Ikada, *Grafting/Characterization Techniques/Kinetic Modeling* **1998**, 1–39; c) M. Li, M. Fromel, D. Ranaweera, S. Rocha, C. Boyer, C. W. Pester, *ACS Macro Lett.* **2019**, *8*, 374–380.
- [8] a) E. Roeven, A. R. Kuzmyn, L. Scheres, J. Baggerman, M. M. J. Smulders, H. Zuilhof, *Langmuir* **2020**, *36*, 10187–10199; b) Y. Zhang, K. Kang, N. Zhu, G. Li, X. Zhou, A. Zhang, Q. Yi, Y. Wu, *J. Mater. Chem. B* **2020**, *8*, 7428–7437.
- [9] a) E. H. H. Wong, S. N. Guntari, A. Blencowe, M. P. van Koevorden, F. Caruso, G. G. Qiao, *ACS Macro Lett.* **2012**, *1*, 1020–1023; b) T. K. Goh, S. N. Guntari, C. J. Ochs, A. Blencowe, D. Mertz, L. A. Connal, G. K. Such, G. G. Qiao, F. Caruso, *Small* **2011**, *7*, 2863–2867; c) D. Mertz, C. J. Ochs, Z. Zhu, L. Lee, S. N. Guntari, G. K. Such, T. K. Goh, L. A. Connal, A. Blencowe, G. G. Qiao, F. Caruso, *Chem. Commun.* **2011**, *47*, 12601–12603; d) E. Nam, J. Kim, S. N. Guntari, H. Seyler, Q. Fu, E. H. H. Wong, A. Blencowe, D. J. Jones, F. Caruso, G. G. Qiao, *Chem. Sci.* **2014**, *5*, 3374–3380.
- [10] a) S. N. Guntari, A. C. H. Khin, E. H. H. Wong, T. K. Goh, A. Blencowe, F. Caruso, G. G. Qiao, *Adv. Funct. Mater.* **2013**, *23*, 5159–5166; b) E. H. H. Wong, M. P. van Koevorden, E. Nam, S. N. Guntari, S. H. Wibowo, A. Blencowe, F. Caruso, G. G. Qiao, *Macromolecules* **2013**, *46*, 7789–7796; c) S. N. Guntari, T. K. Goh, A. Blencowe, E. H. H. Wong, F. Caruso, G. G. Qiao, *Polym. Chem.* **2013**, *4*, 68–75.
- [11] a) Q. Fu, J. Kim, P. A. Gurr, J. M. P. Scofield, S. E. Kentish, G. G. Qiao, *Energy Environ. Sci.* **2016**, *9*, 434–440; b) E. Nam, E. H. H. Wong, S. Tan, Q. Fu, A. Blencowe, G. G. Qiao, *Macromol. Mater. Eng.* **2017**, *302*, 1600199.
- [12] E. Nam, E. H. H. Wong, S. Tan, S. N. Guntari, Q. Fu, J. Kim, B. Delalat, A. Blencowe, G. G. Qiao, *Polym. Chem.* **2016**, *7*, 3251–3258.
- [13] S. Tan, E. Nam, J. Cui, C. Xu, Q. Fu, J. M. Ren, E. H. H. Wong, K. Ladewig, F. Caruso, A. Blencowe, G. G. Qiao, *Chem. Commun.* **2015**, *51*, 2025–2028.
- [14] T. G. Pattison, A. Spanu, A. M. Friz, Q. Fu, R. D. Miller, G. G. Qiao, *ACS Appl. Mater. Interfaces* **2020**, *12*, 4041–4051.
- [15] a) G. Moad, E. Rizzardo, S. H. Thang, *Chem. Asian J.* **2013**, *8*, 1634–1644; b) G. Moad, *Polym. Chem.* **2017**, *8*, 177–219; c) M. D. Nothling, Q. Fu, A. Reyhani, S. Allison-Logan, K. Jung, J. Zhu, M. Kamigaito, C. Boyer, G. G. Qiao, *Adv. Sci.* **2020**, *7*, 2001656; d) G. Moad, E. Rizzardo, S. H. Thang, *Polymer* **2008**, *49*, 1079–1131; e) R. Whitfield, K. Parkatidis, N. P. Truong, T. Junkers, A. Anastasaki, *Chem* **2020**, *6*, 1340–1352; f) K. Parkatidis, H. S. Wang, N. P. Truong, A. Anastasaki, *Chem* **2020**, *6*, 1575–1588.
- [16] a) S. Allison-Logan, F. Karimi, Y. Sun, T. G. McKenzie, M. D. Nothling, G. Bryant, G. G. Qiao, *ACS Macro Lett.* **2019**, *8*, 1291–1295; b) A. Reyhani, S. Allison-Logan, H. Ranji-Burachaloo, T. G. McKenzie, G. Bryant, G. G. Qiao, *J. Polym. Sci. Part A* **2019**, *57*, 1922–1930.
- [17] a) A. R. Kuzmyn, A. T. Nguyen, L. W. Teunissen, H. Zuilhof, J. Baggerman, *Langmuir* **2020**, *36*, 4439–4446; b) Q. Wang, L. Hu, Z. Cui, P. Fu, M. Liu, X. Qiao, X. Pang, *ACS Appl. Mater. Interfaces* **2020**, *12*, 42161–42168.

- [18] a) S. Allison-Logan, Q. Fu, Y. Sun, M. Liu, J. Xie, J. Tang, G. G. Qiao, *Angew. Chem. Int. Ed.* **2020**, *59*, 21392–21396; *Angew. Chem.* **2020**, *132*, 21576–21580; b) T. G. McKenzie, E. H. H. Wong, Q. Fu, A. Sulistio, D. E. Dunstan, G. G. Qiao, *ACS Macro Lett.* **2015**, *4*, 1012–1016.
- [19] a) S. J. Lam, N. M. O'Brien-Simpson, N. Pantarat, A. Sulistio, E. H. H. Wong, Y.-Y. Chen, J. C. Lenzo, J. A. Holden, A. Blencowe, E. C. Reynolds, G. G. Qiao, *Nat. Microbiol.* **2016**, *1*, 16162; b) S. J. Shirbin, S. J. Lam, N. J.-A. Chan, M. M. Ozmen, Q. Fu, N. O'Brien-Simpson, E. C. Reynolds, G. G. Qiao, *ACS Macro Lett.* **2016**, *5*, 552–557.
- [20] a) G. J. M. Habraken, K. H. R. M. Wilsens, C. E. Koning, A. Heise, *Polym. Chem.* **2011**, *2*, 1322–1330; b) Z. Song, Z. Tan, J. Cheng, *Macromolecules* **2019**, *52*, 8521–8539; c) G. J. M. Habraken, M. Peeters, C. H. J. T. Dietz, C. E. Koning, A. Heise, *Polym. Chem.* **2010**, *1*, 514–524.
- [21] a) H. Lu, J. Wang, Z. Song, L. Yin, Y. Zhang, H. Tang, C. Tu, Y. Lin, J. Cheng, *Chem. Commun.* **2014**, *50*, 139–155; b) N. Hadjichristidis, H. Iatrou, M. Pitsikalis, G. Sakellariou, *Chem. Rev.* **2009**, *109*, 5528–5578.
- [22] M. D. Nothling, T. G. McKenzie, I. A. Eastland, H.-C. Chien, J. Collins, A. S. Meyer, G. G. Qiao, *Chem. Commun.* **2019**, *55*, 8544–8547.
- [23] a) Y. A. Vasilieva, C. W. Scales, D. B. Thomas, R. G. Ezell, A. B. Lowe, N. Ayres, C. L. McCormick, *J. Polym. Sci. Part A* **2005**, *43*, 3141–3152; b) P. Singhsa, H. Manuspiya, R. Narain, *Polym. Chem.* **2017**, *8*, 4140–4151.
- [24] T. G. McKenzie, Q. Fu, E. H. H. Wong, D. E. Dunstan, G. G. Qiao, *Macromolecules* **2015**, *48*, 3864–3872.
- [25] S. E. Seo, E. H. Discekici, Y. Zhang, C. M. Bates, C. J. Hawker, *J. Polym. Sci.* **2020**, *58*, 70–76.
- [26] a) J. Xu, J. He, D. Fan, X. Wang, Y. Yang, *Macromolecules* **2006**, *39*, 8616–8624; b) C. Boyer, A. Granville, T. P. Davis, V. Bulmus, *J. Polym. Sci. Part A* **2009**, *47*, 3773–3794; c) G. B. Desmet, D. R. D'hooge, M. K. Sabbe, M.-F. Reyniers, G. B. Marin, *J. Org. Chem.* **2016**, *81*, 11626–11634.
- [27] a) Y. Shi, E. T. A. van den Dungen, B. Klumperman, C. F. van Nostrum, W. E. Hennink, *ACS Macro Lett.* **2013**, *2*, 403–408; b) K. Luo, J. Yang, P. Kopečková, J. Kopeček, *Macromolecules* **2011**, *44*, 2481–2488.
- [28] a) X. Zhou, Z. Li, *Adv. Healthcare Mater.* **2018**, *7*, 1800020; b) J. Huang, A. Heise, *Chem. Soc. Rev.* **2013**, *42*, 7373–7390; c) N. H. Lee, L. M. Christensen, C. W. Frank, *Langmuir* **2003**, *19*, 3525–3530; d) K. Ciešlik-Boczula, *Biochimie* **2017**, *137*, 106–114.
- [29] a) A. Barth, *Biochim. Biophys. Acta Bioenerg.* **2007**, *1767*, 1073–1101; b) Y. N. Chirgadze, B. V. Shestopalov, S. Y. Venyaminov, *Biopolymers* **1973**, *12*, 1337–1351.
- [30] D. Huesmann, A. Birke, K. Klinker, S. Türk, H. J. Räder, M. Barz, *Macromolecules* **2014**, *47*, 928–936.
- [31] a) A. Di Mauro, F. Mirabella, A. D'Urso, R. Randazzo, R. Purrello, M. E. Fragalà, *J. Colloid Interface Sci.* **2015**, *437*, 270–276; b) Y. Wang, Y. C. Chang, *Macromolecules* **2003**, *36*, 6511–6518.
- [32] A. Mirtič, J. Grdadolnik, *Biophys. Chem.* **2013**, *175–176*, 47–53.
- [33] K. Inoue, N. Baden, M. Terazima, *J. Phys. Chem. B* **2005**, *109*, 22623–22628.
- [34] A.-M. Pilbat, V. Ball, P. Schaaf, J.-C. Voegel, B. Szalontai, *Langmuir* **2006**, *22*, 5753–5759.
- [35] a) S. J. Shirbin, F. Karimi, N. J.-A. Chan, D. E. Heath, G. G. Qiao, *Biomacromolecules* **2016**, *17*, 2981–2991; b) M. Byrne, P. D. Thornton, S.-A. Cryan, A. Heise, *Polym. Chem.* **2012**, *3*, 2825–2831; c) M. K. Joo, D. Y. Ko, S. J. Jeong, M. H. Park, U. P. Shinde, B. Jeong, *Soft Matter* **2013**, *9*, 8014–8022.
- [36] a) D. M. Blow, *Acc. Chem. Res.* **1976**, *9*, 145–152; b) W. Appel, *Clin. Biochem.* **1986**, *19*, 317–322.
- [37] a) J. Brown, C.-L. Lu, J. Coburn, D. L. Kaplan, *Acta Biomater.* **2015**, *11*, 212–221; b) S. Müller-Herrmann, T. Scheibel, *ACS Biomater. Sci. Eng.* **2015**, *1*, 247–259.

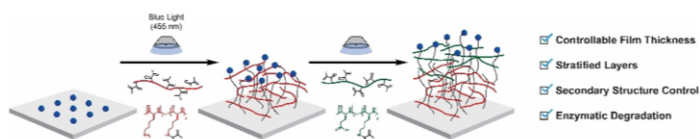
Manuscript received: September 21, 2021
 Accepted manuscript online: December 3, 2021
 Version of record online: ■■■ ■■■

Research Articles

Polypeptide Films

N. J. Chan, S. Lentz, P. A. Gurr, S. Tan,
T. Scheibel,* G. G. Qiao* — e202112842

Crosslinked Polypeptide Films via RAFT-Mediated Continuous Assembly of Polymers



Research into polypeptide films extends beyond polypeptide characterization into their fabrication. Herein, we report the novel fabrication of chemically cross-linked polypeptide films using reversible addition–fragmentation chain transfer

(RAFT) polymerization. Secondary structure analysis reveals unusually high random coil formation and such films further demonstrate biodegradability useful for tissue engineering and drug delivery.

Supporting Information

Crosslinked Polypeptide Films via RAFT-Mediated Continuous Assembly of Polymers

N. J. Chan, S. Lentz, P. A. Gurr, S. Tan, T. Scheibel, G. G. Qiao**

Supporting Information

Materials and Methods

Materials

Acetone (>99.5%, AR Grade, Merck), 3-aminopropargyl triethoxysilane (APTES, 99%, Merck), diethyl ether (Et₂O, AR grade, Chem-Supply), *N*-(3-(dimethylamino)propyl)-*N'*-ethylcarbodiimide hydrochloride (EDCI, ≥98%, Merck), 4-cyano-4-[(dodecylsulfanylthiocarbonyl)sulfanyl]pentanoic acid (CDTPA, 98%, Aldrich) 4-cyano-4-(phenylcarbonothioylthio)pentanoic acid (CPADB; 98%, Aldrich), dimethyl sulfoxide (DMSO; AR grade, Ajax Finechem), glacial acetic acid (AcOH; AR Grade, Chem-Supply), hydrobromic acid (HBr; 33% in acetic acid, Merck), hexylamine (≥98%, Merck), *N*-hydroxysuccinimide (NHS; ≥98%, Fluka), isopropanol (iPrOH, AR grade, Chem-Supply), lithium phenyl-2,4,6-trimethylbenzoylphosphinate (LAP, >98% HPLC grade, Tokyo Chemical Industry), H-L-Lys(Z)-OH (>99%, Mimotopes), H-L-Glu(OBzl)-OH (>99%, Mimotopes), magnesium sulfate (anh. MgSO₄, ≥97%, Merck), methanol (AR grade, Chem-Supply), α-pinene (98%, Merck), sodium hydrogen carbonate (NaHCO₃, AR grade, Chem-Supply), triphosgene (≥98%, Merck), sodium hydroxide (NaOH; ≥97%, Merck), trifluoroacetic acid (TFA; Merck) were used as received without further purification. Saturated brine solution was prepared from sodium chloride (NaCl, AR grade, Chem-Supply) in DI water. Tetrahydrofuran (anh. THF, inhibitor free, >99.9%, Merck), ethyl acetate (anh. EtOAc, >99.9 Honeywell) and dimethylformamide (anyhd. DMF, 99.8%, Acros) were purified by passage through a solvent purification system (SBPT-1, LC Technologies, USA) containing 4Å sieves under Argon gas. Hexane (AR, Chem-Supply) was distilled over calcium hydride under nitrogen prior to use.

Instrumentation

^1H NMR analysis was performed using a Varian Unity Plus 400 MHz NMR spectrometer using referenced deuterated solvent (D_2O , $\text{d}_6\text{-DMSO}$ or CDCl_3).

GPC analysis was performed on a Shimadzu liquid chromatography system fitted with a PostNova Analytics MALS detector ($\lambda = 658 \text{ nm}$), a Shimadzu RID-10 refractometer ($\lambda = 633 \text{ nm}$), and a Shimadzu SPD-20A UV-vis detector, using three phenogel columns (Phenomenex, $5 \mu\text{m}$) in series and HPLC grade DMF with 0.05 M LiBr as the mobile phase (1 mL/min). The oven temperature was set to $50 \text{ }^\circ\text{C}$ to maintain an acceptable pressure across the system, and the detectors were temperature controlled to $25 \text{ }^\circ\text{C}$. Nova MALS software (PostNova) was used to determine the molecular weights and PDI using poly(ethylene glycol) standards.

DLS was performed using ZetaSizer NanoZS (Malvern Instruments, Worcestershire, U.K.) to analyze aggregation of macromonomer post-modification at concentrations of 0.01 mg/mL in reaction solution and diluted with DMSO.

The characterization of the thin films was performed using ATR-FTIR spectroscopy with a Bruker Hyperion 1000 microscope with a dedicated ATR-objective (Bruker Optics GmbH, Ettlingen, Germany). The ATR-crystal was brought into contact with the sample. The microscope was continuously purged with dry air, and the MCT detector was cooled with liquid nitrogen. The FTIR spectra were recorded with a resolution of 2 cm^{-1} . One hundred scans per measurement were performed. Three samples per layer with three spots per sample were measured.

Atomic force microscopy (AFM) for surface morphology and film thickness was performed in air-tapping mode on an Asylum Research Cypher (Asylum Research, Santa Barbara) with a silicon tip. CAP film thicknesses were estimated by film scratching (mechanical removal) and by tracing a profile along the film and the scratched zone. The thickness measurements reported represent mean values over 3 different analysis sites per substrates.

AFM was used to identify surface morphology before and after enzyme degradation and was acquired with a Dimension Icon (Bruker Nano Inc.) in tapping mode in air with a resolution of 512 to 512 datapoints at 0.5 to 1 Hz. Silicon cantilevers (OTESPA-R3, Bruker, Karlsruhe, Germany) were used with a force constant of 26 Nm^{-1} . The x- and y positions were exactly stored and used before and after enzymatic degradation. The same cantilever was used for the measurements.

Macromonomer Synthesis

Z-protected lysine N-Carboxyanhydride (Lys(Z) NCA) and Benzyl-protected Glutamic Acid (Glu(OBzl) NCA)

Both NCAs were synthesized using modified versions of previous reported methods. In a typical experiment Lys(Z) (5.00 g, 17.8 mmol) was added to a 500 mL three-necked RBF and suspended in 200 mL of anh. THF with α -pinene (6.00 mL, 37.5 mmol, 1.15 excess moles) under nitrogen. After heating to $60 \text{ }^\circ\text{C}$, triphosgene (2.11 g, 7.14 mmol, 1.2 excess moles) was added and the mixture was stirred at temperature for 2 h. Solvent was then removed from the now clear solution under reduced pressure and replaced with 100 mL of anh. EtOAc. The solution was cooled to $-18 \text{ }^\circ\text{C}$ before washing with sat. brine and 5 w/v% sodium hydrogen carbonate and the organic phase was dried over MgSO_4 . The filtered solution was reduced under reduced pressure and recrystallized using anh. hexane at $-18 \text{ }^\circ\text{C}$ over 16 h. The solids were then filtered and redissolved into anh. EtOAc before being precipitated into anh. hexane. The precipitate was then dried under vacuum over 24 h and stored under argon at $-80 \text{ }^\circ\text{C}$ (yields $\sim 80\%$).

Lys(z) NCA: ^1H NMR (400 MHz, CDCl_3): δ 1.30–1.60 (m, 4H, -NH-CH₂-CH₂-CH₂-CH₂-), 1.81–2.07 (m, 2H, -NH-CH₂-CH₂-CH₂-CH₂-), 3.20 (m, 2H, -NH-CH₂-CH₂-CH₂-), 4.27 (t, 1H, $J = 5.6 \text{ Hz}$, CHN), 4.92 (s, 1H, side chain NH), 5.10 (s, 2H, CH₂-ArH), 6.83 (s, 1H, ring NH), 7.22–7.37 (m, 5H, ArH).

Glu(OBzl) NCA: ^1H NMR (400 MHz, CDCl_3): δ 2.06–2.32 (m, 2H, $\text{CH}_2\text{-CH}_2\text{-CO}$), 2.58 (t, 2H, $J = 6.8$ Hz, $\text{CH}_2\text{-CH}_2\text{-CO}$), 4.36 (t, 1H, $J = 6.0$ Hz, CHN), 5.12 (s, 2H, $\text{CH}_2\text{-ArH}$), 6.59 (s, 1H, ring NH), 7.29–7.41 (m, 5H, ArH).

Poly(L-glutamic acid(OBzl)-r-L-lysine(Z)) synthesis

Both Glu(OBzl) NCA (3.00 g, 11.4 mmol, 80 mol% of overall NCA monomer) and Lys(Z) NCA (0.873 g, 2.85 mmol, 20 mol% of overall NCA monomer) were dissolved in anh. DMF under nitrogen in a 50 mL RBF. To the stirring solution was added hexylamine (23.5 μL , 54.3 μmol , $M/I = 90$), and the clear solution was stirred under an argon bleed at room temperature for 24 h. The reaction mixture was then precipitated into and subsequently rinsed with Et_2O which was then dried and stored under vacuum to afford a clear tacky solid as the final product (2.84 g, yield: 78.5%).

M_n (GPC) = 7.2 kDa; PDI 1.30. ^1H NMR ($d_6\text{-DMSO}$): δ 1.20–1.90 (m, Lys -NH- $\text{CH}_2\text{-CH}_2\text{-CH}_2\text{-CH}_2\text{-}$), 2.0–2.40 (m, Glu - $\text{CH}_2\text{-CH}_2\text{-CO}$ -), 2.94 (s, Lys -NH- $\text{CH}_2\text{-CH}_2\text{-CH}_2\text{-CH}_2\text{-}$), 3.92 (s, CH-NH backbone), 4.99 (m, $\text{CH}_2\text{-ArH}$), 5.76 (m, $\text{CH}_2\text{-CH}$ -), 7.26 (s, ArH), 8.38 (brs, CO-NH)

Deprotection of poly(L-glutamic acid(OBzl)-r-L-lysine(Z))

To a 25 mL RBF was added the protected poly(L-glutamic acid(OBzl)-r-L-lysine(Z)) (2.84 g, (0.12 mmol) followed by 20 mL of TFA. The solution was stirred until the polymer was completely dissolved, followed by the dropwise addition of HBr (33 vol% in AcOH diluted to 16.7 vol% with AcOH, 20 mL). The resulting solution was stirred with thick precipitate observed soon after. The reaction mixture was stirred for a total of 16 h with the suspension then dropwise precipitated into diethyl ether, washed in ether ($\times 2$), then dried in vacuo overnight. The solid was then dissolved in DI water and added to 3.5 kDa dialysis tubing for dialysis against 2 L DI water ($\times 3$) for 24 h before being freeze-dried to obtain a white, fluffy solid (~ 1.4 g).

Deprotection of poly(L-glutamic acid(OBzl)-r-L-lysine(Z))

To a 25 mL RBF was added the protected poly(L-glutamic acid(OBzl)-r-L-lysine(Z)) (2.84 g, (0.12 mmol) followed by 20 mL of TFA. The solution was stirred until the polymer was completely dissolved, followed by the dropwise addition of HBr (33 vol% in AcOH diluted to 16.7 vol% with AcOH, 20 mL). The resulting solution was stirred with thick precipitate observed soon after. The reaction mixture was stirred for a total of 16 h with the suspension then dropwise precipitated into diethyl ether, washed in ether ($\times 2$), then dried in vacuo overnight. The solid was then dissolved in DI water and added to 3.5 kDa dialysis tubing for dialysis against 2 L DI water ($\times 3$) for 24 h before being freeze-dried to obtain a white, fluffy solid (~ 1.4 g). ^1H NMR (D_2O , 400 MHz): 1.06–1.43 (m, 4H, $-\text{NH}-\text{CH}_2-\text{CH}_2-\text{CH}_2-\text{CH}_2-$), 1.89–1.99 (m, Glu $-\text{CH}_2-\text{CH}_2-\text{CO}-$), 2.23 (m, Glu $-\text{CH}_2-\text{CH}_2-\text{CO}-$), 2.56 (m, 2H, Lys $-\text{NH}-\text{CH}_2-\text{CH}_2-\text{CH}_2-\text{CH}_2-$), 4.27 (m, CH-NH backbone).

Methacrylation of poly(L-lysine) to form PLLMA

In a 28 mL glass vial, poly(L-lysine) (1.00 g, 4.78 mmol lysine units) was dissolved in DI water. pH was adjusted to 10 using 2.5 M NaOH before being chilled in an ice bath while stirring. Methacrylic anhydride (143 μL , 0.957 mmol, 20% mole equivalent to lysine units), was then added dropwise and the mixture was allowed to stir for 24 h. The resulting mixture was added to 3.5 kDa dialysis tubing for dialysis against 2 L DI water ($\times 3$) for 24 h before being freeze-dried to obtain a white fluffy solid (~ 300 mg). The polymer was purged with argon and stored at -18 °C. ^1H NMR (D_2O , 400 MHz): δ 1.04–1.40 (m, 4H, Lys methacrylated $-\text{NH}-\text{CH}_2-\text{CH}_2-\text{CH}_2-\text{CH}_2-$), 1.41–1.73 (m, 4H, Lys $\text{NH}_2-\text{CH}_2-\text{CH}_2-\text{CH}_2-\text{CH}_2-$), 1.84 (m, 3H, methacrylate $-\text{CO}-\text{C}(\text{CH}_3)=\text{CH}_2$), 2.78 (m, Lys $\text{NH}_2-\text{CH}_2-\text{CH}_2-\text{CH}_2-\text{CH}_2-$), 3.13 (m, Lys methacrylated $-\text{NH}-\text{CH}_2-\text{CH}_2-\text{CH}_2-\text{CH}_2-$), 4.12 (m, CH-NH backbone), 5.27 (s, 1H, methacrylate $-\text{NH}-\text{CO}-\text{C}(\text{CH}_3)=\text{CH}_2$), 5.56 (s, 1H, methacrylate $-\text{NH}-\text{CO}-\text{C}(\text{CH}_3)=\text{CH}_2$)

Methacrylation of poly(L-lysine-r-L-glutamic acid) to form PLGMA

In a 28 mL glass vial, poly(L-glutamic acid-r-L-lysine) (1.00 g, 0.868 mmol of lysine units) was dissolved in DI water. pH was adjusted to 10 using 2.5 M NaOH before being chilled in an ice bath while stirring. Excess methacrylic anhydride (388 μ L, 2.60 mmol, 3 times excess mole equivalent to lysine units) was then added dropwise, and the mixture was stirred for 24 h. The resulting mixture was added to 3.5 kDa dialysis tubing for dialysis against 2 L DI water (\times 3) for 24 h before being freeze-dried to obtain a white, fluffy solid (\sim 300 mg). The polymer was purged with argon and stored at -18 $^{\circ}$ C. 1 H NMR (D_2O , 400 MHz): δ 1.06–1.53 (m, 4H, Lys methacrylated $-NH-CH_2-CH_2-CH_2-CH_2-$), 1.77 (m, 3H, methacrylate $-CO-C(CH_3)=CH_2$), (m, 4H, Lys $NH_2-CH_2-CH_2-CH_2-CH_2-$), 1.84 (m, 3H, methacrylate $-CO-C(CH_3)=CH_2$), 1.87-2.12 (m, Glu $-CH_2-CH_2- CO-$), 2.24-2.55 (m, 2H, Lys $-NH-CH_2-CH_2-CH_2-CH_2-$), 3.21 (m, Lys methacrylated $-NH-CH_2-CH_2-CH_2-CH_2-$), 3.85-4.27 (m, CH-NH backbone), 5.24 (s, 1H, methacrylate $-NH-CO-C(CH_3)=CH_2$), 5.58 (s, 1H, methacrylate $-NH-CO-C(CH_3)=CH_2$)

Wafer Modification

Silica wafers were sonicated in acetone (30 m) and isopropanol (30 m) before being rinsed in isopropanol and dried *in vacuo*. Surfaces were silanized using previously established procedures. Silica wafers were soaked in a solution of APTES in acetone (4 v/v%) at 45 $^{\circ}$ C for 24 h. Wafers were then rinsed in acetone thoroughly before being dried *in vacuo*. Using CDTPA as an example, CDTPA (50.0 mg, 0.179 mmol, 1 mol eq.), EDCI (137 mg, 0.716 mmol, 4 mol eq.) and NHS (20.6 mg, 0.179 mmol, 1 mol eq.) were added to a 100 mL RBF and dissolved in anhyd. DCM (50 mL). The solution was stirred for 2 h under nitrogen before adding to a beaker containing the washed silicon wafers. The beaker was placed in a desiccator purged with N_2 (g) which was shaken on a plate agitator at 80 RPM for 48 h. The wafers were

removed and washed thoroughly with DCM and isopropanol and left to dry *in vacuo*. Wafers were stored in methanol at 4 °C for later use.

PLLMA CAP-RAFT on pretreated silica substrates

PLLMA (30.0 mg, 31.9 μmol of methacrylated units) dissolved in DMSO (973.8 μL , totalling to 30 mg/mL concentration after addition of stock solutions) was treated with DMSO solutions of CTA (25.8 μL , 1.00 mg/mL, 63.8 nmol, 1/500 mole equivalent of methacrylate units) and LAP (0.470 μL , 1.00 mg/mL, 1.56 nmol, 1/40 mole equivalent of CTA). Functionalized wafers were submersed face up in solution, and high purity argon was bubbled through the solution for 20 min. The degassed mixture was left sealed and irradiated in blue light (4 mW/cm², λ_{max} = 460 nm) for various intervals up to 24 h. Upon completion, the wafers were sonicated for 10 s in fresh DMSO, and the supernatant was extracted. The wafers themselves were thoroughly washed with DMSO (x3), DCM and iPrOH, before being dried under a nitrogen stream for 1 min. Treated wafers were then stored *in vacuo* prior to analysis.

The supernatant was also added to 3.5 kDa dialysis tubing for dialysis against 1 L DMSO (x3) for 24 h to remove leftover CTA and LAP and then analyzed by ¹H NMR.

PLGMA CAP-RAFT on pretreated silica substrates

PLGMA (30.0 mg, 27.5 μmol of methacrylated units) dissolved in DI water (984.2 μL , totalling to 30 mg/mL concentration after addition of stock solutions) was treated with DI water of CTA (15.4 μL , 1.00 mg/mL, 55.1 nmol, 1/500 mole equivalent of methacrylate units) and LAP (0.405 μL , 1.00 mg/mL, 1.38 nmol, 1/40 mole equivalent of CTA). Functionalized wafers were submersed face up in solution and high purity argon was bubbled through the solution for 20 min. The degassed mixture was left sealed and irradiated in blue light for various intervals up to 24 h. Upon completion, the wafers were sonicated for 10 s in fresh DI water, and then

thoroughly washed with DI water (x3), then DMSO and isopropanol, before being dried under a nitrogen stream for 1 min. Treated wafers were then stored *in vacuo* prior to analysis.

Characterization

Line shape analysis (LSA) for the quantification of secondary structure elements from FTIR

Line shape analysis was performed according to Chirgadze for IR analysis of polypeptides. The sum of the measured absorbance $A(\nu)$ of the components (i) was calculated using Equation (1).

$$A(\nu) = \sum A_i(\nu) \quad (1)$$

The maximum ν_i^{max} and the half-width at half-weight (w_i) and the integral of the component (B_i) were calculated. The starting values for the curve fit (Local-least-squares and Levenberg-Marquardt) were a mixture of 50% Lorentzian and 50% Gaussian lineshape.^[1] For curve fitting, the OPUS software 8.1 (Bruker Optics GmbH, Ettlingen, Germany) was used. The recorded spectra were cut before curve fitting to the amide I region (1590 cm^{-1} - 1720 cm^{-1}), smoothed by 9 points, and baseline corrected with one iterative step. The number of components was determined by calculating the second derivative of the spectra. The negative peaks of the second derivative were used as wavenumber positions for the LSA. The half-widths for each component except the unordered random coil component around $1655\text{-}1660 \text{ cm}^{-1}$ were set to $w_i = 20 \text{ cm}^{-1}$ and for the random coil structure $w_{\text{random coil}}$ was set to 50 cm^{-1} according to Chirgadze.^[1] All spectra were fitted according to this procedure. The secondary structure proportions were calculated by summing up all the component integrals assigned to the respective secondary structures.^[1] The quotient of the integral of one secondary structure component and the sum of all integrals multiplied by 100 is the secondary proportion in percent as shown in Equations (2) – (6).^[2]

$$Q_{\text{random coil}} = \frac{\sum B_{1638-1655 \text{ cm}^{-1}}}{(B_{(\text{random coil})} + B_{(\beta\text{-sheet})} + B_{(\beta\text{-turn})} + B_{(\alpha\text{-helices})} + B_{(\text{Other})})} \quad (2)$$

$$Q_{\beta\text{-sheets}} = \frac{\sum B_{1614-1638 \text{ cm}^{-1}} + B_{1696-1708 \text{ cm}^{-1}}}{(B_{(\text{random coil})} + B_{(\beta\text{-sheet})} + B_{(\beta\text{-turn})} + B_{(\alpha\text{-helices})} + B_{(\text{Other})})} \quad (3)$$

$$Q_{\alpha\text{-helices}} = \frac{B_{1655-1664 \text{ cm}^{-1}}}{(B_{(\text{random coil})} + B_{(\beta\text{-sheet})} + B_{(\beta\text{-turn})} + B_{(\alpha\text{-helices})} + B_{(\text{Other})})} \quad (4)$$

$$Q_{\beta\text{-turns}} = \frac{\sum B_{1664-1696\text{ cm}^{-1}}}{(B_{(\text{random coil})} + B_{(\beta\text{-sheet})} + B_{(\beta\text{-turn})} + B_{(\alpha\text{-helices})} + B_{(\text{Other})})} \quad (5)$$

$$Q_{\text{Other (side chains, aggregated chain strands)}} = \frac{B_{1604-1613\text{ cm}^{-1}}}{(B_{(\text{random coil})} + B_{(\beta\text{-sheet})} + B_{(\beta\text{-turn})} + B_{(\alpha\text{-helices})} + B_{(\text{Other})})} \quad (6)$$

Film Degradation

Degradation experiments were performed according to Müller-Herrmann and Scheibel.^[3] Experiments were performed in TCNB buffer (50 mM Tris/HCl, 10 mM CaCl₂, 150 mM NaCl, 0.05% Brij 35, pH 7.5) at room temperature. The samples were incubated with 250 μL of PXIV or CHC solution (175 μg/mL in TCNB buffer) for 24 h. Control experiments without enzymes were conducted in 250 μL TCNB buffer. AFM analysis was performed with a Dimension Icon (Bruker Nano Inc.) in tapping mode as previously stated elaborated.

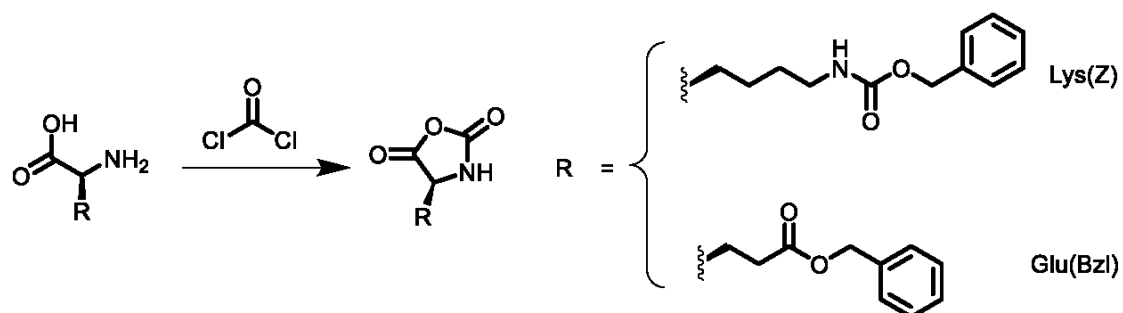


Figure S1: Scheme for synthesis of *N*-carboxyanhydrides

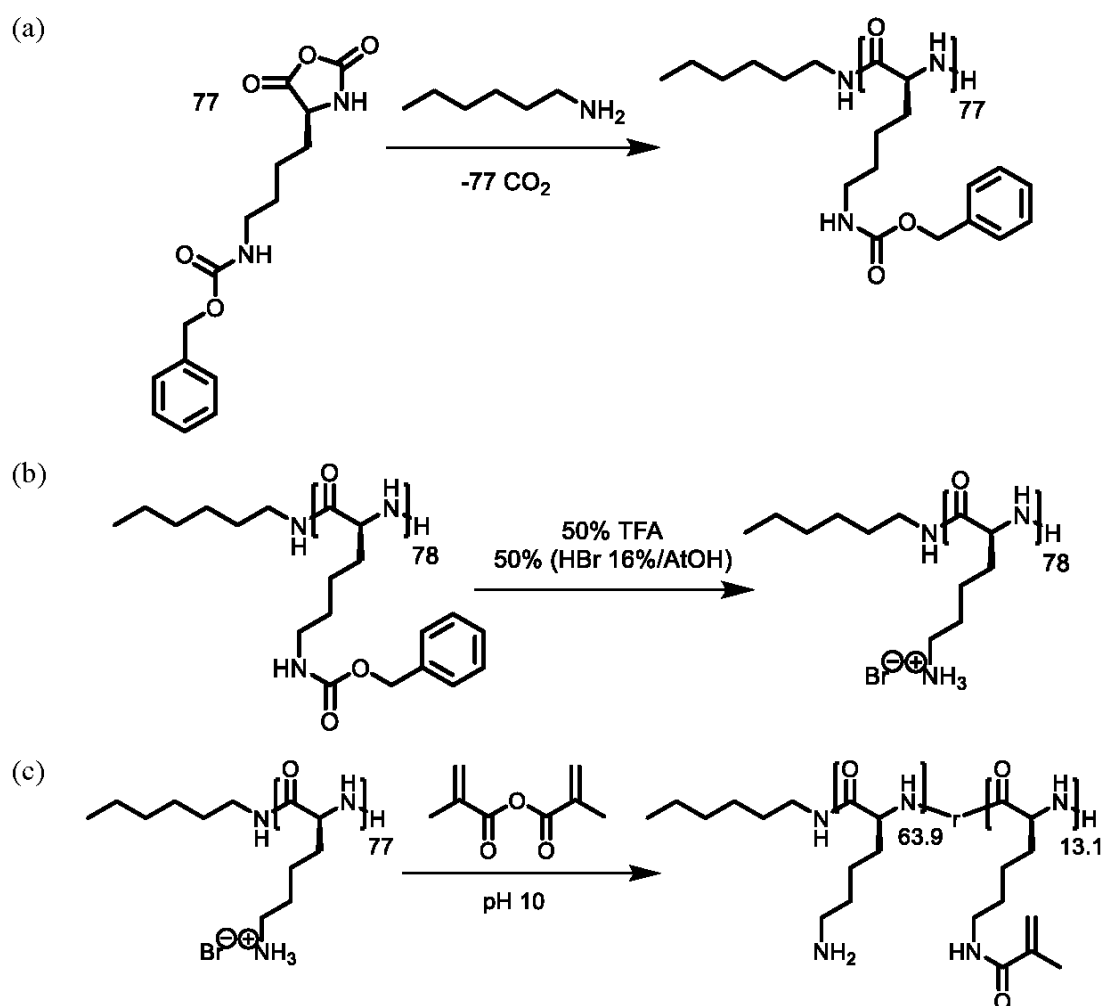


Figure S2: Synthesis of poly(*L*-lysine-*r*-*L*-lysine-*g*-methacrylamide) (PLLMA) (a) NCA ROP of Lys(Z) NCA using hexylamine as an initiator; (b) Deprotection of Z-protecting group using HBr, (c) Methacrylation of exposed amine groups with methacrylic anhydride.

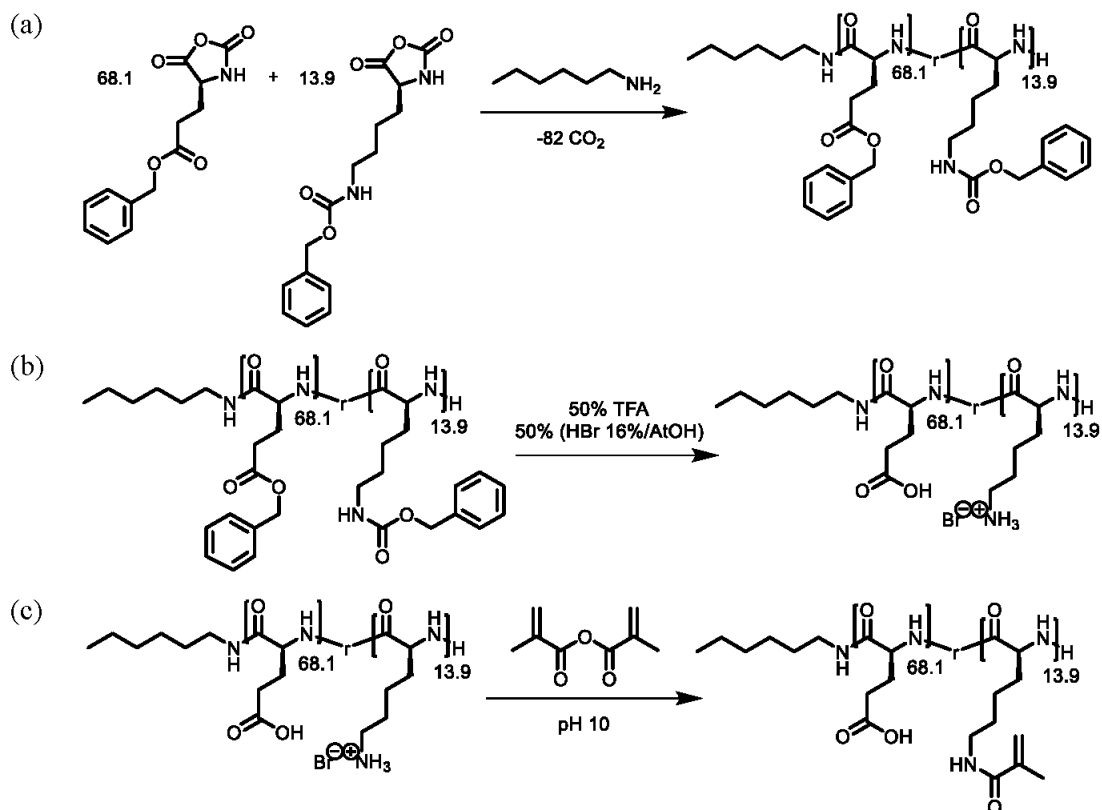


Figure S3: Synthesis of poly(L-glutamic acid-*r*- L-lysine-*g*-methacrylamide) (PLGMA) (a) NCA ROP of Lys(Z) and Glu(Bzl) NCA using hexylamine as an initiator; (b) Deprotection of Z-protecting group using HBr; (c) Methacrylation of exposed amine groups with methacrylic anhydride.

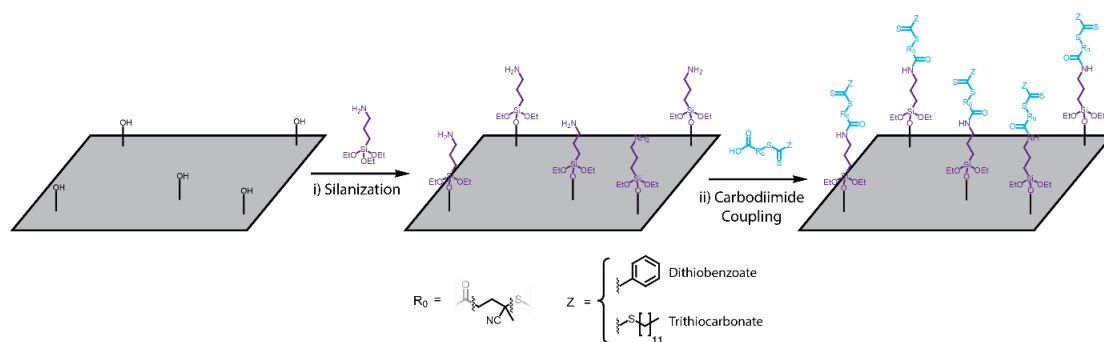


Figure S4: Anchoring of initiator to silicon wafers

Table S1: Summary of PLLMA macromonomer

M_w ^[a]	DP ^[a]	PDI ^[a]	Methacrylation ^[b]
8318	77.9	1.22	15%

^[a]Molecular weight (and subsequently degree of polymerization) and PDI determined using GPC with PEG standards; ^[b]Methacrylation determined by ¹H NMR.

Table S2: Thickness of films in the absence of specific elements used in the CAP-RAFT procedure

Surface Initiator ^[a]	Free CTA in solution ^[a]	Photoinitiator ^[a]	Light ^[a]	Thickness (nm) ^[b]	RMS (nm) ^[b]
N	N	Y	Y	3.45 ± 0.15	3.12
N	Y	Y	Y	5.60 ± 0.29	2.74
Y	N	N	Y	4.05 ± 0.26	3.67
Y	Y	N	Y	1.31 ± 0.51	1.15
Y	N	Y	N	4.98 ± 0.75	3.55
Y	Y	Y	N	4.37 ± 1.10	3.31
Y	N	Y	Y	31.46 ± 2.41	9.39
Y	Y	Y	Y	36.09 ± 1.13	6.11

^[a] “N” indicates element absent in experiment, “Y” indicates element present in experiment;

^[b]Thickness and RMS roughness determined using AFM

Table S3: Summary of PLGMA macromonomer

M_n ^[a]	DP ^[a]	PDI ^[a]	Methacrylation ^[b]
8723	82.1	1.39	17%

^[a]Number average molecular weight (M_n) (and subsequently degree of polymerization) and PDI determined using GPC with PEG standards; ^[b]Methacrylation determined using ¹H NMR.

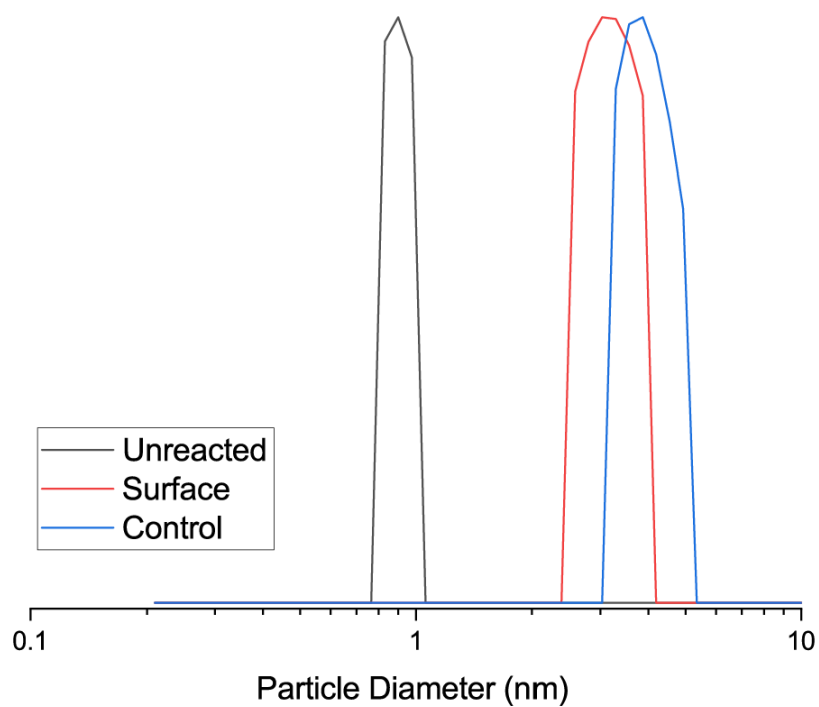


Figure S6: DLS of supernatant with CTA present in 0.5 mg/mL solutions of DMSO.

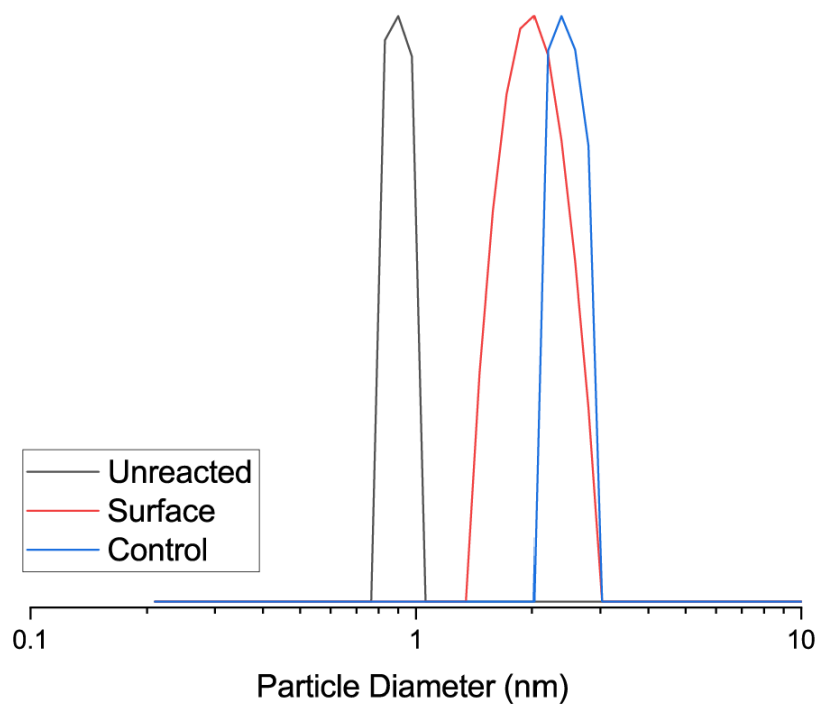


Figure S7: DLS of supernatant without CTA present in 0.5 mg/mL solutions of DMSO.

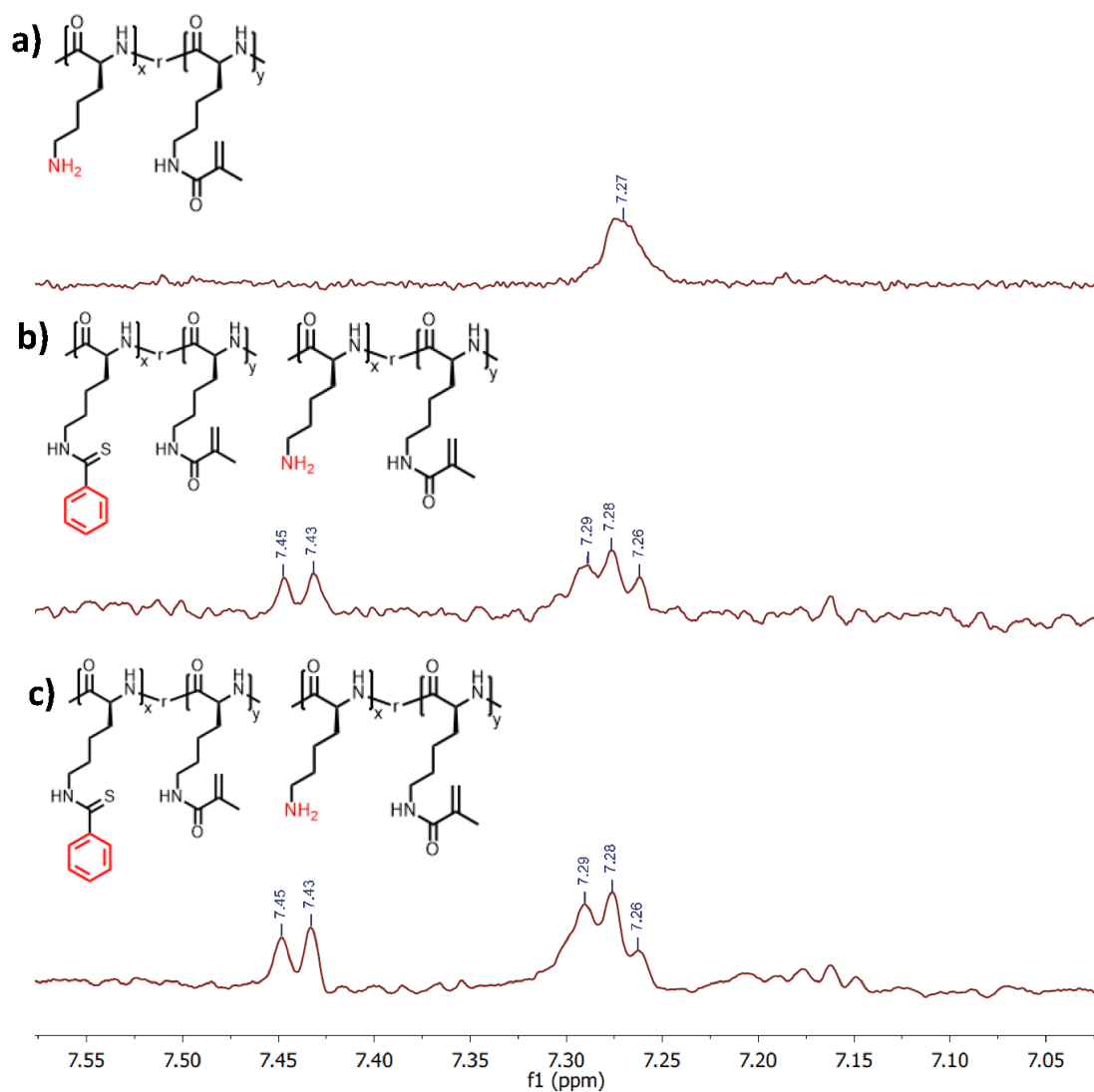


Figure S8: ^1H NMR (in DMSO) between 7.0 and 7.6 ppm of PLLMA a) before reaction and b) after reaction without CTA in solution and c) after reaction with CTA in solution. Reaction supernatant was dialysed against DMSO, revealing splitting patterns consistent with aromatic rings which would only be present after degradation of RAFT agent by free amines on the PLLMA.

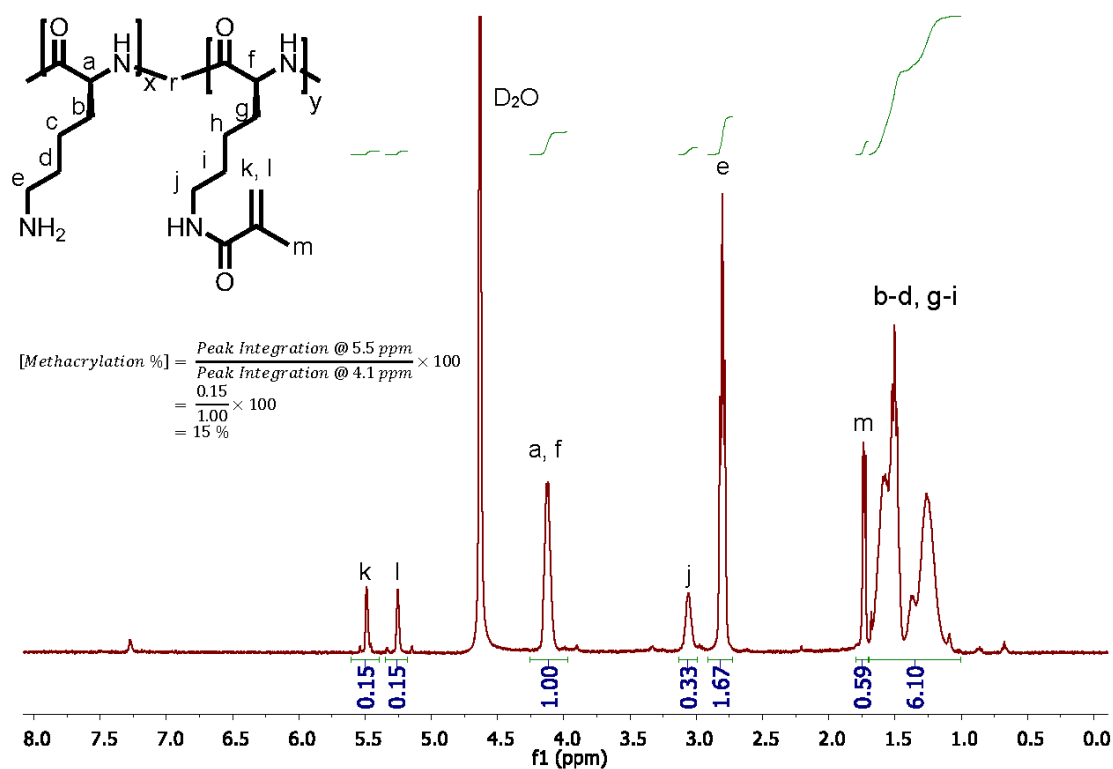


Figure S9: ¹H NMR of PLLMA including calculation for methacrylation percentage

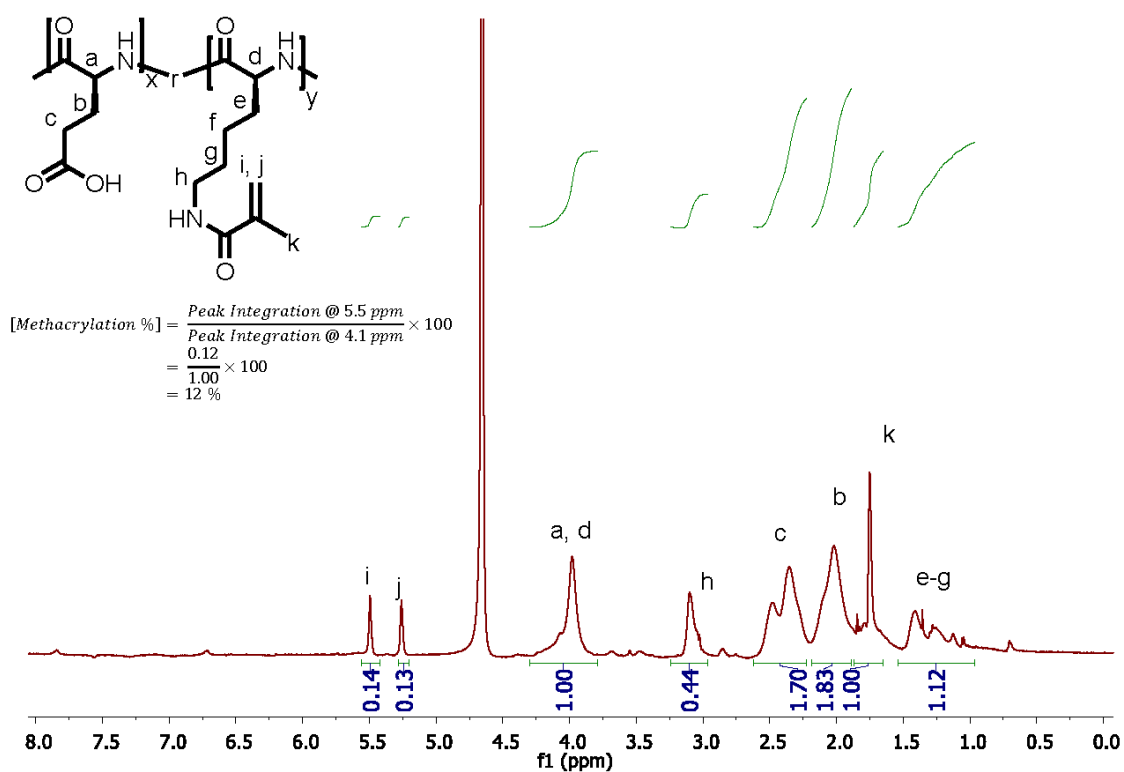


Figure S10: ¹H NMR of PLGMA including calculation for methacrylation percentage

References

- [1] Y. N. Chirgadze, B. V. Shestopalov, S. Y. Venyaminov, *Biopolymers* **1973**, *12*, 1337-1351.
- [2] A. Barth, *Biochimica et Biophysica Acta (BBA) - Bioenergetics* **2007**, *1767*, 1073-1101.
- [3] S. Müller-Herrmann, T. Scheibel, *ACS Biomaterials Science & Engineering* **2015**, *1*, 247-259.

Part V – Appendix

Part V – 1 - List of Abbreviations

A or Ala	Alanine
ATR	Attenuated total reflection
ADF	<i>Araneus diadematus</i> fibroin
AFM	Atomic force microscopy
apt	After post-treatment with Methanol
bpt	Before post-treatment with Methanol
BSA	Bovine serum albumin
c	Concentration
C	Cysteine
CA	Contact angle
CD	Circular dichroism
CLSM	Confocal laser scanning microscopy
D	Aspartic acid
Da	Dalton
DAPI	4',6-diamino-2-phenylindole
DCM	Dichloromethane
DLS	Dynamic Light Scattering
DMF	Dimethylformamide
DMSO	Dimethylsulfoxide
DP	Degree of polymerization
E	Glutamic acid
eADF	engineered <i>Araneus diadematus</i> fibroin
<i>E.Coli</i>	<i>Escherichia coli</i>

EDTA	Ethylenediaminetetraacetic acid
et al.	et alii
EtOH	Ethanol
F	Phenylalanine
FA	Formic acid
FBS	Fetal bovine serum
FCS	Fetal calf serum
FSD	Fourier self-deconvolution
FTIR	Fourier transform infrared
G	Glycine
GPC	Gel permeation chromatography
HFIP	Hexafluoroisopropanol
I	Isoleucine
IMAC	Immobilized metallion affinitychromotography
kDa	Kilodalton
KPFM	Kelvin probe force microscopy
L	Leucine
M_n	Number-averaged molecular weight
M_w	Weight-averaged molecular weight
MALDI – TOF	Matrix - assisted laser desorption/ionization time of flight mass spectrometry
MeOH	Methanol
MQ water	Ultrapure water
MW	Molecular weight
N	Asparagine
NCA	N-carboxyanhydride

NMR	Nuclear magnetic resonance
P	Proline
PBS	Phosphate buffered saline
pH	pondus Hydrogenii
Q	Glutamine
QCM-D	Quartz crystal microbalance with dissipation monitoring
R	Arginine
RI	Refractive index
ROP	Ring-opening polymerization
rpm	revolutions per minute
rss	Recombinant spider silk
rssp	Recombinant spider silk protein
RT	Room temperature
SC	Spin-coating
SDS-PAGE	Sodium dodecyl sulfate polyacrylamide gel electrophoresis
SEM	Scanning electron microscopy
sFTIR	Synchrotron-coupled Fourier Transform Infrared spectroscopy
THF	Tetrahydrofuran
TIRF	Total internal reflection fluorescence microscopy
UV	Ultraviolet
V	Valine
W	Tryptophane
Y	Tyrosine

Part V – 2 - List of Figures

Figure 1: This is a schematic overview of the classification of polymers according to composition, architecture, molecular structure, and origin. Figure created based on ¹⁻³..... 1

Figure 2: The figure shows an exemplary, theoretical phase diagram of a diblock copolymer. The x-axis displays the fraction of block A. The y-axis shows the Flory-Huggins interaction parameter, the χ -parameter, and N stands for the total degree of polymerization. If the volume fraction of block A is increased, equilibrium morphologies of AB diblock copolymers change from body-centered cubic (BCC) to hexagonal cylinders (HEX) to gyroid (GYR) to lamellar (LAM) phases in bulk.¹⁷ 4

Figure 3: R Representative architectures of different kinds of block copolymers. A - D represents the most common terblock copolymers, namely linear BCP (A), “Comb“ graft terpolymer (B), Cyclic BCP (C), and miktoarm star terpolymer (D). E - G represents complex polymer structures like star BCP (E), “Comb“ star copolymer (F), and “Comb“ graft polymer (G). The figure was drawn according to ¹⁸ 5

Figure 4: Schematic representation of the formation of a peptide bond by a condensation reaction of the C-terminus of AA1 and the N-terminus of AA2, which results in the removal of one water molecule. Figure adapted from ^{20, 22, 23, 25} 6

Figure 5: Overview of 20 naturally used amino acids of proteins. The amino acids are divided into different classes. The separation was done according to their effects and properties. Each amino acid is shown with its chemical structure, name, and abbreviations of this and molecular weight. Figure adapted from ²⁶. 7

Figure 6: Four levels of a PP and protein structures. Firstly, the amino acid sequence is the lowest hierarchical level, which assembles into secondary structure elements like β -sheets, α -helices, or remains unordered as random coil. The secondary structure elements assemble into the tertiary protein structure. When multiple protein chains interact, the quaternary protein structure is formed. 8

Figure 7: Overview of poly(amino acid) synthesis using the NCA method. (A) displays the Leuchs method of NCA synthesis. (B) shows the Fuchs Farthing method of NCA production. (C) is a schematic presentation of the normal amine mechanism (NAM) for ROP of α -AA NCAs. (D) represents the mechanism of the activated monomer mechanism (AMM). Figure adapted from ^{20, 21} 10

- Figure 8:** The principle of grafting to (A) and grafting from (B) methods are shown exemplarily for NCA ROP. Figure created based on ²¹..... 12
- Figure 9:** This figure shows the seven different kinds of spider silk produced by *Araneus diadematus*: (1) *Minor Ampullate* silk (2) *Dragline* silk (3) *Aggregate* silk (4) *Flagelliform* silk (5) *Piriform* silk (6) *Aciniform* silk (7) *Tubuliform* silk..... 13
- Figure 10:** Core-shell model of an *Araneus diadematus* dragline silk fiber. The fiber can be divided into four parts. The outer shell is a lipid layer. The second layer is the glycoprotein layer, which protects the inner layer, the *minor ampullate silk ADF1*, and *ADF2*. The core is semi-crystalline *major ampullate* silk comprising at least two MaSp named *ADF3* and *ADF4* and consists of fibrils representing the crystalline part of the silk. Figure created based on ^{42, 43, 45} 14
- Figure 11:** Schematic overview of recombinant spider silk production from the consensus sequence pool (step 1) to the technical approach. The designed spider silk module sequences are translated in Step 2 to transgenic DNA, which is then transferred to a plasmid (Step 3), which can be introduced in the host organism *E.coli* (Step 4) for recombinant expression (Step 5) in fermenters. After the biotechnological production, the protein is purified using different purification steps (Step 6) and, upon lyophilization, yields a white protein powder. Figure adapted from ⁴¹ 15
- Figure 12:** Names, amino acid sequences, and molecular weight of the spider silk proteins and peptides used in this thesis. The *ADF4* derived spider silk variants eADF4(C16), eADF4(κ 16), and eADF4(Ω 16) with corresponding charge and molecular weight are depicted in (A). Furthermore, (B) shows the *ADF3*-derived spider silk variants, eADF3(AQ)₁₂ and eADF3(AQ)₂₄. All recombinant spider silk variants in (A) and (B) can be genetically engineered and fused with functional tags, in this thesis with C-terminal tags like -RGD, -E₈G, or -R₈G⁶⁰ (C). After protein purification, the recombinant spider silk proteins are a lyophilized white powder that can be processed using various processing methods into different morphologies like films, fibers, non-woven meshes, foams, hydrogels, particles, and capsules (D). Figure was adapted from ⁶²..... 17
- Figure 13:** Schematic figure displaying the different blocks of the amino acid sequence of the eADF4-derived C-module and the eADF3-derived A- and Q-module (A). The microphase separation model, according to *Wohlrab et al.*, is shown in (B) for a hydrophilic and a hydrophobic substrate.⁶¹ The microphase separation of polymer chains depending on

the fraction of the crystalline block A f_a (orange) and amorphous block B (dark blue) is depicted in (C). Figure B was adapted from ⁶¹. 19

Figure 14: Requirements of a biomaterial and biomaterial surfaces. The three most important points are that the material is biocompatible, biodegradable, and can be adapted towards the biological environment. Sometimes, biodegradability is not desired; instead, durability is more important for the used biomaterial, such as hip implants. A biomaterial surface can be described from two different perspectives, the physicochemical perspective, where the surface morphology, mechanical properties, and hydrophilicity are the most determining factors; the biological perspective, where the biocompatibility and no or low immune response are desired. Surface engineering can be useful to achieve the requirements of a biomaterial. Methods like self-assembly of polymers or proteins or chemical coupling are methods for surface modifications. 20

Figure 15: Requirements and properties of a biomaterial surface. The physicochemical properties affect the biocompatibility of a biomaterial. The shown properties are valuable parameters to tune the biomaterial surface. The biological perspective of the surface is highly important because biocompatibility and the immune response are the most important factors for a good biomaterial surface. Surface engineering is useful to achieve the desired surface properties. Figure created based on findings of ^{52, 68, 69}. 22

Figure 16: Purification strategy of recombinant spider silk proteins. The obtained cell pellet with the target protein is lysed, and the cells get disrupted using ultrasound or high-pressure homogenization. The cell lysate is heated to around 70 °C to precipitate all *E.coli*-derived proteins and other impurities. The cell debris is removed using centrifugation. The purification continues with a precipitation step with ammonium sulfate and vigorously washing. After multiple washing steps, the pure protein can be lyophilized. The green star indicates the target protein. The brown cylinders depict *E.coli* bacteria. 23

Figure 17: Schematic representation of spider silk film formation upon spin-coating.^{76, 80} The protein solution is applied onto the substrate (A), and then rotational forces are applied to the substrate. The excess protein solution is slung away from the substrate, the protein molecules come close together (B), and the solvent evaporates completely (C→D). 24

Figure 18. Formation of a coating using drop-casting. The dissolved protein is applied to the surface. The protein molecules, which can be divided into hydrophilic, amorphous blocks, and hydrophobic polyalanine stretches, are randomly distributed in the droplet. (A)

The solvent starts to evaporate, the degree of freedom of the proteins decreases due to the declining volume of the solvent. (B) The protein molecules come closer together and start to self-assemble. (B) After the complete evaporation of the solvent, a homogenous, self-assembled film is formed. (C).....25

Figure 19: Schematic setup of the fundamental functionality of an Atomic force microscope (AFM): The sample is placed on the sample plate, which is movable in x, y, and z-direction driven by a piezoelectric motor. A laser beam is focused on the backside of a cantilever to record the changes in the cantilever deflections during scanning of the surface. A position-sensitive photodiode is used to detect the reflection of the laser beam. A piezoelectric scanner controls the lateral and vertical position of the AFM cantilever by getting feedback relative to the sample surface (A). Depending on the distance to the surface of the sample, the deflection of the cantilever changes. Different interaction forces apply depending on the distance between the tip and the surface of the sample (B). If the distance of the cantilever is approximate 100 nm from the surface, it gets attracted upon van der Waals forces. (C) schematically shows the tapping mode. Figure based on descriptions and adapted figures from ⁸²⁻⁸⁵26

Figure 20: Generation of different electrons in the diffusion cloud by the interaction of an electron beam with a solid sample.^{88, 90} The different emitted and transmitted electrons (backscattered electrons (BSE), secondary electrons (SE), Auger electrons (AE) and transmitted electrons), the characteristic X-rays (EDX), cathodoluminescence (CL), and Bremsstrahlung provide different information concerning the analyzed matter. The corresponding information is shown below the electrons. Figure adapted from ⁸⁷⁻⁹⁰27

Figure 21: Fluorescence is the property of molecules to absorb light with a distinct wavelength and to emit light at higher wavelengths. In this process, the electron jumps from the ground state S_0 to an excited state (S_1) and then subsequently emits with a loss of energy back to the ground state. (A) The fluorophore absorption profile of Alexa fluoro 555 is shown as an example. The difference between the absorption spectral profile and the emission spectral profile is called the Stokes shift. (B) The setup of a standard widefield fluorescence microscope (Epi) is shown in (C). The simplified light paths and the penetration of the light for Epi-Fluorescence (D), TIRF-M (E), and CLSM (F) are depicted in (D), (E), and (F). Excited fluorophores are depicted in red, non-excited fluorophores in green. Epi-Fluorescence penetrates the whole cell, and all fluorophores in the light path are excited (D). Using TIRF-M, the incidence angle of the light can be varied to achieve total

internal reflection. This leads to the effect that only the fluorophores in the first 200 nm of the cell are excited (E). CLSM comprises the variation of the penetration depth. The laser can scan the cell layer by layer using galvanometer mirrors and excite different fluorophores by varying the scanning depth. Figure adapted from^{91, 92, 94, 98-106}.....30

Figure 22: A negatively charged (spider silk) protein particle suspended in an aqueous buffer. The negatively charged particle is migrating towards the positive electrode. Figure adapted from¹¹¹.....32

Figure 23: A mixture of proteins are in solution with a different charge without consistency (A-I) is mixed with sodium dodecyl sulfate (SDS). The negatively charged SDS binds evenly because of its long aliphatic tail to the protein. The SDS has a strong binding affinity; thus, the original charges of the protein are overpowered upon the addition of SDS. A direct charge/length relationship is established for most proteins (A-II). After adding SDS to the protein mixture, the solution can be applied to a polyacrylamide gel. A schematic setup of a polyacrylamide gel is shown (B). The upper part of the gel is the so-called stacking gel. Here, the protein mixture is applied into one pocket of the gel. This polyacrylamide gel has larger pores and a lower ionic strength than the lower part of the gel, the resolving gel. Here, the acrylamide concentration is increased, and thus the pores are smaller and comprise higher pH. In general, all polyacrylamide gels are running with molecular weight (MW) standard sample. It is a molecular ruler for the unknown protein samples (B-I). The negatively charged proteins travel to the cathode if an electric field is applied. In the beginning, the proteins are collected in the stacking gel in the looser polyacrylamide mesh (B-II-III). Then all proteins enter the resolving gel simultaneously and separate, dependent on their molecular weight. Bigger molecules get entangled in the smaller pores of the resolving gel. Smaller molecules can pass the gel faster. After finishing the separation, the separated proteins can be visualized upon staining with Coomassie brilliant blue or silver staining (BI; V-VI). Figure was created based on¹¹²⁻¹¹⁶.....33

Figure 24: The infrared wavelength region with corresponding wavenumbers is shown (A). The fingerprint region reaches from 400 cm^{-1} to 1450 cm^{-1} , the group frequency region from 1450 cm^{-1} to 4000 cm^{-1} .¹¹⁰ The different vibration modes of molecules are exemplarily shown for formaldehyde (B).¹¹⁰ The grazing incidence angle attenuated total reflection (GATR) IR principle is shown. The surface of a coating is measured at the interface air/coating. The penetration depth of the IR beam is marked (C).¹¹⁰ The single-beam-sample-reference (SBSR) cell is an individual setup from the IPF in Dresden. Here, the

sample is directly coated onto the sample cell, and the IR beam can penetrate the sample cell so that the bottom of the film can be measured.¹²¹ The IR beam penetrates the whole sample in the case of transmission measurements (E).¹¹⁰ Dichroic ATR-FTIR is a method where parallel (p) and vertical (s) polarized IR light is measured individually. The parameter which can be determined with this method is the so-called dichroic ratio RT. This is the ratio of the integrated absorbances of p- and s-polarized light (F).¹¹⁰35

Figure 25: A) Schematic setup of a CD-spectrometer: White unpolarized light is generated from a high-intensity light source (I). The light is transformed into single wavelength, linear polarized light passing a monochromator and a linear polarizer (II). The photoelastic modulator splits the light into right or left polarized light (RPL/LPL) (III). The RPL/LPL passes the CD active medium (IV). Due to the chiral molecules preference, the proportion of RPL or LPL increases, and the photomultiplier (V) transforms the signal into a voltage, from which the ellipticity is calculated. The linearly polarized light can be seen as a superposition of RPL/LPL. If RPL and LPL are absorbed equally by the sample, then no CD signal is detectable (B-i), but if RPL/LPL are absorbed unequally, then ellipticity can be measured as a function of wavelength. But this ellipticity is still dependent on the sample concentration, the thickness of the cuvette, the number of peptide bonds, and the CD signal. According to the Lambert-Beer-Law, the concentration-independent molar ellipticity $[\theta]$ can be calculated with the equation (C). Also, the relationship between the differential absorption coefficient of RPL/LPL and the molar ellipticity is given. D) Representative CD-spectra of polypeptides and proteins with α -helical (black), β -sheet, and random coil (green) conformation are shown. The curve characteristics for each secondary structure element can be found in table 1.¹²⁴37

Figure 26: Schematic illustration of a QCM-D sensor chip: The active and counter electrode sandwich a piezo quartz crystal (A). The frequency changes if mass (layer of interest) is adsorbed to the sensor surface. The penetration depth of the different overtones of the fundamental frequency increases with increasing odd numbers (B). The course of frequency and dissipation in situ for the adsorption of rigid particles (C) follow the Sauerbrey equation (G). In contrast to the course of frequency and dissipation for rigid particles, the course for Δf and ΔD of soft materials like proteins are displayed in (D). The resulting decay curves are shown below each diagram (E for C) and F for D). The relevant equations for the determination of adsorbed mass (Sauerbrey equation), the estimation of

the thickness of the adsorbed layer, and the dissipation are shown in (G). adapted from^{125, 126, 129, 132}40

Figure 27: The maskless lithography device (Smartprint®) setup consists of a light source that passes an LCD matrix, a filter, and gets focused by a focusing lens and directly exposed to a photoresist (A). The device comprises two different objectives. The 2.5x objective narrows the light beam compared to the 1x objective. This results in smaller features while using the 2.5x objective (B). The processing of patterning photoresists is schematically depicted in C. The photoresist should be a homogeneous coating (1), then the photoresist coating is exposed to the light beam, which exposes the areas from the digital mask (2). The exposed photoresist is immersed in the developer solution, and then the42

Figure 28: The Young Laplace equation describes the relation between the specific surface energy γ_{SG} of a substrate, a water drop γ_{SL} and the surface tension of the water drop γ_{LG} and the corresponding contact angle θ (A). Three ideal degrees of wetness exist, the partially, the complete and the non-wetting state. A water contact angle of 0° defines the complete wetting. A water contact angle between 0° and 180° comprises partially wetting. No wetting state is defined with a water contact angle above 180° (B).^{137, 138, 140}43

Figure 29: Structure of the thesis. This thesis is divided into two main topics, the assembly of spider silk-inspired materials into films and the structure-property relationship of spider silk-inspired materials. The first part is developing a thickness-dependent structural assembly and phase separation model for recombinant spider silk proteins from the nanoscale up to the microscale (Part II-1) and studying the structure formation of recombinant spider silk proteins and the orientation of β -sheet crystals within these films (Part II-2). A method for continuous assembly polymerization via reversible addition-fragmentation chain transfer (CAP-RAFT) of polypeptides into crosslinked film with tunable layer thickness is developed (Part IV-2) as well. The second main topic is the structure-property relationship of the spider silk-inspired materials concerning various surface properties and modifications and their effects on degradation biocompatibility, such as blood coagulation behavior, protein adsorption, and cell adhesion behavior.46

Figure 30: Classification of five different recombinant spider silk variants for coating applications based on their properties.....57

Figure 31: Schematic illustration of the fabrication of patterned recombinant spider silk protein films.....59

Figure 32: Correlative measurements of murine (Balb) and human (BJ) fibroblasts adhered to three different intruding patterns in a recombinant spider silk protein film.....60

Part V – 3 - List of Tables

Table 1: Maxima and minima for certain secondary structure elements in CD-spectra. ^{122,} ¹²³	39
Table 2: Overview of used protein and synthetic polypeptides and where the associated publications can be found	56